

博士論文

**Elastic wave propagation through unsaturated soils
concerning early warning of rain-induced landslides**

[降雨による斜面崩壊の早期警報のための不飽和土内の弾性波速度の研究]

by

Muhammad Irfan
ムハマドイルファン

A dissertation submitted in partial fulfillment of the
requirements for the degree of

Doctor of Philosophy

in

Civil Engineering

東京大学大学院工学系研究科
社会基盤学専攻
Department of Civil Engineering,
The University of Tokyo, Tokyo, Japan
March, 2014

*Dedicated to my wonderful parents,
Rasheed Ahmed & Shabana Nasreen;
without their nurturing love, I wouldn't be a shadow of my
present being.*

THESIS APPROVAL

Student Name : Muhammad Irfan
Student I.D. : 37-117006
Institute : The University of Tokyo
Department : Civil Engineering
Laboratory : Geotechnical Engineering
Subject : Elastic wave propagation through unsaturated soils concerning
early warning of rain-induced landslides
Submission : March, 2014

This is to certify that we have read this thesis and that in our opinion it is fully adequate,
in scope and quality, as a thesis for the degree of Doctor of Philosophy.

Research Supervisor:

Prof. Dr. Taro UCHIMURA

Advisory Committee Members:

Prof. Dr. Ikuo TOWHATA

Prof. Dr. Junichi KOSEKI

Prof. Dr. Reiko KUWANO

Prof. Dr. Satoru SHIBUYA

Department of Civil Engineering,
The University of Tokyo, Tokyo, Japan
March, 2014

Elastic Wave Propagation through Unsaturated Soils Concerning Early Warning of Rain-induced Landslides

[降雨による斜面崩壊の早期警報のための不飽和土内の弾性波速度の研究]

Muhammad Irfan

Ph.D. Thesis – Civil Engineering

March 2014

Supervisor: Prof. Taro Uchimura

ABSTRACT

Rapid growth in world's population is pressing its inhabitants to uncover the unexplored avenues of accommodation and transportation. Under these severe demographic and economic pressures, widespread construction projects are being carried out in hilly areas and thus are exposed to landslides. Landslides cause severe damage to infrastructure and life all around the globe every year. Citing the vast aerial spread of such disasters, typical landslide remediation approaches of constructing retaining structures or soil improvement are not economically feasible anymore. Rather, there is a need for more robust and economically viable solutions like real-time landslide early warning systems. Current landslide early warning systems rely on monitoring slope movements by means of inclinometers or tilt sensors, in combination with soil moisture monitoring by means of dielectric moisture sensors or tensiometers, etc. This study is an attempt to improve the currently available landslide early warning systems by introducing a new technique to predict landslide movements by means of elastic wave propagation in soil.

The fundamental understanding of behavior of elastic wave velocities (compression wave velocity (V_p), and shear wave velocity (V_s)) during landslides was envisaged through laboratory element tests. An advanced triaxial apparatus with independent controls of axial, and lateral stress (required for replicating field stress path during landslides), and capable of measuring elastic wave velocities in unsaturated soil

specimens was developed. Measurement of elastic wave velocities was made possible by means of a novel disk shaped piezoelectric transducer, which was able to generate and measure both compression and shear wave velocities. Separate series of triaxial tests were conducted to explore the effects of soil moisture, and soil yielding on elastic wave velocities. In another series of tests, field stress path during rain-induced landslides was reproduced to study the behavior of corresponding wave velocities.

Through the aforementioned test series, sensitivity of elastic wave velocities (V_p and V_s) to soil moisture as well as soil yielding, was confirmed. It was concluded that, both compression and shear wave velocities decrease with a nearly uniform rate as soil becomes wet. Compression wave velocity however, approached sonic wave velocity in water, for fully saturated soil. These observations are useful to monitor the saturation state of an actual soil slope. Soil yielding was also found to cause a decrease in elastic wave velocities. Also, the rate of decrease of wave velocities was observed to be consistent with rate of soil yielding. This finding is of practical importance with reference to real-time slope monitoring, as the actual slope movements in a slope surface can be identified by monitoring the rate of decrease of wave velocities.

Keywords: Landslide monitoring; early warning; wave velocity; unsaturated soil.

ACKNOWLEDGEMENTS

Completing my PhD degree has been the most challenging, and at the same most enlightening activity of my life so far. I feel so blessed to have been given this opportunity, as it taught me to ‘*think*’ and to discover my true passions which might keep me engaged and entertained for a lifetime. Throughout this journey, I might have travelled in a vacuum without constant blessings and guidance of Almighty **Allah**. Words fail me in expressing my thankfulness to Him. He is surely worthy of “*Alhamdu Lillahi Rabbil Aalamin*” (*All praise is due to Allah, Lord of the worlds (Al-Quran, 1:2)*).

I am extremely grateful to have worked with **Prof. Taro Uchimura**, my PhD research supervisor. Accomplishing this dream would not have been possible without his edifying guidance. The well-directed research freedom provided by him always encouraged me to think out of the box and try innovative options. Our long and stimulating discussions not only helped me improve my research but also helped nourishing my critical thinking abilities. Dear “Sensei”, thank you very much from the core of my heart.

My appreciation and gratitude is extended to members of my research advisory committee **Prof. Ikuo Towhata**, **Prof. Junichi Koseki**, **Prof. Reiko Kuwano**, and **Prof. Satoru Shibuya** for their enlightening discussions and constructive comments on my research in general and this thesis in particular. I am grateful that they took time out of their busy schedules to be part of the evaluation committee. **Prof. Reiko Kuwano** and her lab member **Dr. Laxmi Suwal** are especially acknowledged for their intellectual as well as material input in solving various issues related to elastic wave measurement.

Special appreciation is extended to **administrative staff** of Civil Engineering Department, **Foreign Student Officers** and **Japanese Language teachers** for their consistent guidance and support during my stay in Japan. It would be unfair not to mention **Ms. Hirano**, secretary Geotechnical Laboratory, who took care of several administrative matters related to my research and travel. It was the continuous assistance of these people in handling the academic and administrative matters which kept me focused on my studies.

My years in Todai would not have been the same without the fellowship and camaraderie of my fellow geotechnical graduate students. I would like to thank all the laboratory members for making our workspace such a lively and wonderful place. Special appreciation is extended to **Otsubo, Aoyama, Ali Derakhshani, Yu, Umar, Mohsin, Rouzbeh, Monoi, Ghani, Luki, Yolanda, Naveed, Ali Falak** for their warm friendship and assistance whenever it was required.

Time spent in Japan not only helped me strengthen some old friendships but also gave me some wonderful new friends. I am grateful to **Tayyab, Umair Baig, Ali Ahmed, Nabeel, Dr. Tauqir, Saifullah, Awais, Saad bhai**, for their warm and cheerful friendship. Presence of these amazing people around me always made me feel at home, away from home. A very special thanks is due to **Nauman Khalid**, not only for being a great friend but also for helping settle several issues during my early days in Japan.

My three years at the University of Tokyo, were made possible by the scholarship funded by the Ministry of Education, Culture, Sports, Science & Technology (**MEXT**) Japan, which is greatly acknowledged. Research funding provided by **Grant-in-Aid for Science Research** and **JSPS Core-to-core program** are also appreciated. **University of Engineering & Technology (UET), Lahore**, my parent university, is gratefully acknowledged for granting me study leave.

I finish with Pakistan, where the most basic source of my life and energy reside; my parents, my family. Thank you my dearest **Maa G**, my mother, for your overwhelming love, innumerable prayers, and never-ending motivation in making me what I am today. Thank you my dearest **Abbu Jaan**, my father, for your unconditional love and care, and for motivating me to pursue a PhD. I feel really proud to have fulfilled your dream. My wonderful little **sister**, always kept my spirits high, encouraged and motivated me. Thank you **sis**, for all the laughs, fights, and everything in between. Last but not the least; I am indebted to my lovely fiancé, **Naamal**, for believing in me, and for standing by my side throughout this long journey. Very special thanks as well for proof-reading this manuscript and providing critical feedback on sentence structure, and writing style.

Finally, I would like to thank everybody who was important to the successful realization of this thesis. At the same time I express my apology that I could not mention each and everyone in person.

Muhammad Irfan

March 2014

Tokyo, Japan

TABLE OF CONTENTS

Dedication	i
Thesis Approval	ii
Abstract	iii
Acknowledgements	v
Table of Contents	vii
List of Figures	xiii
List of Tables	xxx
Symbols & Abbreviations	xxxi
1. DISSERTATION OVERVIEW.....	1-1
1.1. Prologue	1-1
1.2. Motivation & Significance.....	1-1
1.3. Problem Statement	1-3
1.4. Aims & Objectives.....	1-4
1.5. Scope of Work and Limitations	1-5
1.6. Unit System.....	1-6
1.7. Time Scale and Location of Research.....	1-6
1.8. Thesis Organization	1-6
1.9. References	1-8
2. LITERATURE REVIEW	2-1
2.1. Introduction	2-1
2.2. Rain-induced Slope Failures	2-1

2.2.1	Mechanism of Rain-induced Landslides.....	2-2
2.2.2	Field Stress Conditions	2-3
2.2.3	Field Stress Path.....	2-5
2.3.	Landslide Early Warning Systems	2-8
2.3.1	Landslide Susceptibility Maps.....	2-8
2.3.2	Early Warning Based on Rainfall Thresholds	2-9
2.3.3	Real-time Landslide Monitoring through Instrumentation.....	2-10
2.4.	Elastic Wave Propagation in Soil.....	2-12
2.4.1	Factors Influencing Elastic Wave Propagation in Soil	2-14
2.5.	Summary	2-22
2.6.	References	2-23
3.	EXPERIMENTAL SETUP	3-1
3.1.	General	3-1
3.2.	Modified Triaxial Compression System for Testing Unsaturated Soils	3-1
3.2.1	General Structure	3-2
3.2.2	Loading System	3-3
3.2.3	Measurement Devices.....	3-7
3.2.4	Pressure Transducers	3-17
3.2.5	Pore Water Pressure of Unsaturated Specimens.....	3-18
3.2.6	Differential Pressure Transducer (<i>DPT</i>).....	3-24
3.2.7	Data Acquisition System	3-25
3.3.	Elastic Wave Measurement System.....	3-29
3.3.1	Function Generator	3-31
3.3.2	Power Amplifier	3-31
3.3.3	Recording Unit.....	3-33
3.4.	Summary	3-35
3.5.	References	3-36

4. MATERIALS & METHODOLOGY	4-1
4.1. Test Material	4-1
4.1.1 Material Preparation	4-1
4.1.2 Physical Properties of Test Material	4-1
4.2. Experimental Program	4-3
4.3. General Experimental Procedures	4-4
4.3.1 Unsaturated Specimens (<i>ICCW</i> , <i>ICWI</i> , <i>CWRSR</i> and <i>CSWI</i> tests)	4-4
4.3.2 Saturated Specimens (<i>ICCW</i> and <i>CWRSR</i> tests).....	4-18
4.4. Fundamental Relationships & Calculations	4-21
4.4.1 Weight-Volume Relationships.....	4-21
4.4.2 Elastic Wave Velocities	4-26
4.4.3 Stress-Strain Relationships	4-28
4.5. Summary	4-32
4.6. References	4-33
5. DISK SHAPED PIEZOELECTRIC TRANSDUCER – DEVELOPMENT AND PERFORMANCE ANALYSIS –	5-1
5.1. Piezoelectricity and its Application in Geotechnical Engineering.....	5-1
5.2. <i>P</i> & <i>S</i> -wave Velocity in Element Tests.....	5-2
5.3. Combined Monitoring of <i>P</i> & <i>S</i> -wave Velocities	5-3
5.4. Disk Transducer Fabrication	5-4
5.4.1 Water Insulation.....	5-9
5.5. Calibrations	5-10
5.5.1 Time Lag.....	5-10
5.5.2 Polarity.....	5-13
5.5.3 Travel Path.....	5-14
5.6. Signal Interpretation.....	5-14
5.6.1 Time Domain Analysis	5-16

5.6.2	Frequency Domain Analysis.....	5-18
5.7.	Performance Evaluation of Disk Transducer System	5-18
5.7.1	Transmission Cables	5-18
5.7.2	Electromagnetic Coupling – Crosstalk	5-22
5.7.3	Resolution of Recording Unit.....	5-23
5.7.4	Shape of Input Waveform.....	5-30
5.7.5	Excitation Frequency	5-32
5.7.6	Combined Measurement of <i>P</i> & <i>S</i> wave Velocity	5-56
5.8.	Concluding Remarks	5-58
5.9.	References	5-59
6.	INVESTIGATION OF SOIL MOISTURE EFFECTS ON ELASTIC WAVE PROPAGATION	6-1
6.1.	General Remarks	6-1
6.2.	Test Conditions	6-1
6.3.	Isotropic Compression Constant Water content (<i>ICCW</i>) tests	6-3
6.3.1	Methodology	6-4
6.3.2	Normalization of Void Ratio and Density	6-6
6.3.3	Effects of Isotropic Stress on Wave Velocities	6-9
6.3.4	Deformation Characteristics of Specimens.....	6-33
6.3.5	Effects of Soil Moisture on Wave Velocities	6-36
6.4.	Isotropic Compression Water Injection (<i>ICWI</i>) Tests.....	6-43
6.4.1	Methodology	6-43
6.4.2	Initially Dry Specimens	6-44
6.4.3	Initially Moist Specimens	6-49
6.5.	Wave Velocities as a Function of Matric Suction.....	6-55
6.6.	Summary	6-61
6.7.	References	6-62

7. BEHAVIOR OF ELASTIC WAVE VELOCITIES DURING RAIN-INDUCED LANDSLIDES	7-1
7.1. General	7-1
7.2. Test Conditions	7-1
7.3. Constant Water Radial Stress Reduction (CWRSR) tests.....	7-4
7.3.1 Methodology	7-4
7.3.2 Effects of Initial Saturation on Failure Initiation.....	7-6
7.3.3 Effects of Soil Yielding on Wave Velocities.....	7-9
7.3.4 Dependency of V_s and V_p on Principle Stress Direction.....	7-16
7.3.5 Application for Landslide Monitoring.....	7-18
7.4. Constant Shear Stress Water Injection (CSWI) Tests	7-19
7.4.1 Methodology	7-19
7.4.2 Effects of Initial Relative Density	7-22
7.4.3 Effects of Principle Stress Ratio	7-29
7.5. Moisture Distribution through Helical Filter Paper	7-37
7.5.1 Ceramic Disk/Filter Paper Technique.....	7-37
7.5.2 Moisture Distribution in Specimens	7-41
7.5.3 Deformation Characteristics	7-50
7.6. Summary	7-56
7.7. References	7-57
 8. FIELD APPLICATION OF ELASTIC WAVE VELOCITIES FOR LANDSLIDE PREDICTION.....	 8-1
8.1. General	8-1
8.2. Conceptual Framework	8-1
8.3. Key Concerns for Practical Application	8-3
8.4. Field Application – Ideas	8-6
8.4.1 Single Exciter, Multiple Receivers Approach	8-6
8.4.2 Monitoring Based on Seismic Refraction.....	8-8

8.5. Concluding Remarks	8-12
8.6. References	8-13
9. CONCLUSIONS & RECOMMENDATIONS.....	9-1
9.1. General	9-1
9.2. Conclusions	9-2
9.2.1 Disk Transducer – Performance Analysis	9-2
9.2.2 Soil Moisture Effects on Wave Velocities.....	9-3
9.2.3 Wave Velocities during Landslides	9-5
9.3. Recommendations for Future Research	9-6
9.4. References	9-9
A. TRIAXIAL APPARATUS EQUIPMENTS	A-1
A.1. Guide to Make Local Deformation Transducer (LDT).....	A-1
A.2. Determination of Load Cell Capacity	A-12
B. Trigger and Receiver Devices for Elastic Wave Measurement in Lab.....	B-1
B.1. Trigger Devices	B-1
B.1.1 Electromagnetic Type Trigger Device.....	B-2
B.1.2 Piezoelectric Speaker Type Trigger Device	B-5
B.2. Receiving Devices.....	B-6

LIST OF FIGURES

Figure 1.1: Typical landslide protection works; (a) along railway tracks (FHWA, 2003), (b) along highways (Hongbai county, Wenchuan, China).....	1-2
Figure 1.2: Determination of soil moisture on a slope surface; typical moisture sensors versus moisture detection by elastic wave propagation (T. Uchimura, 2011).....	1-4
Figure 2.1: Schematic representation of forces acting on an infinite slope surface (after S. A. Anderson and Sitar (1995)).	2-3
Figure 2.2: Resolution of stresses acting on a soil element during slope failure (after S. A. Anderson and Sitar (1991)).....	2-4
Figure 2.3: Field stress path adopted by soil element during rain-induced slope failures (after S. A. Anderson and Sitar (1995)).....	2-5
Figure 2.4: Behavior of soil element undergoing water infiltration (after Cascini et al. (2009)); (a) Stress path; (b) Development of strain with time; (c) Variation of resisting and disturbing force.	2-6
Figure 2.5: A comparison of field stress path with various types of conventional triaxial tests (after Brand (1981)).....	2-8
Figure 2.6: Schematic representation of methodology adopted by Japan railway (JR-East) to avoid landslide related accidents.	2-9
Figure 2.7: Precipitation intensity and duration thresholds for landslide occurrence in various States of US (R. Baum & Godt, 2010).....	2-10
Figure 2.8: Particle motion in (a) Compression waves; (b) Shear waves (Kramer, 1996)	2-12
Figure 2.9: Typical variation in compression wave velocity with degree of saturation changing from 99.4% to 100% for sand (after Allen et al. (1980)).....	2-13

List of Figures

Figure 2.10: Variation of shear wave velocity with confining pressure and void ratio for saturated and dry crushed quartz sand (B. O. Hardin & Richart, 1963).2-15

Figure 2.11: Shear wave velocity variation with void ratio for different stress states (after B. O. Hardin and Richart (1963)).....2-16

Figure 2.12: Shear wave velocity variation with void ratio. Wave velocities normalized by using Eq. 2.3 to cancel the effect of stress state (after B. O. Hardin and Richart (1963)).2-16

Figure 2.13: Shear stiffness of unsaturated soils versus (a) degree of saturation and confining pressure, (b) degree of saturation and fine content, and (c) degree of saturation confining pressure as tested in a resonant column device. (after Qian et al. (1991))2-19

Figure 2.14: (a) Initial shear stiffness in controlled-suction resonant column tests. (b) Response of shear stiffness to suction at a mean net stress of 400 kPa. (Mancuso et al., 2002)2-20

Figure 2.15: Shear wave velocity versus degree of saturation; (a) Granite Powder; (b) Sandboil sand. (Cho & Santamarina, 2001)2-21

Figure 2.16: Variation of shear wave velocity (in terms of shear modulus) with degree of saturation. (Alramahi et al., 2009).....2-21

Figure 3.1: Modified triaxial testing apparatus used in this study.....3-4

Figure 3.2: Schematic layout of modified triaxial apparatus.....3-5

Figure 3.3: Schematic layout – pressure control system of modified triaxial apparatus. 3-6

Figure 3.4: Working principle of axial loading system.3-7

Figure 3.5: Axial load cell employed for this study.3-8

Figure 3.6: Calibration characteristics of axial load cell (a) calibration curve (b) long-term stability of load cell.3-9

Figure 3.7: <i>LVDT</i> used in present study (0-30mm range).	3-10
Figure 3.8: Calibration characteristics of <i>LVDT</i>	3-11
Figure 3.9: Calibration characteristics of local deformation transducers (<i>LDTs</i>).....	3-13
Figure 3.10: Setting up local deformation transducers (<i>LDTs</i>) and clip gauges (<i>CGs</i>) on specimen surface.	3-15
Figure 3.11: Calibration characteristics of clip gauges used in this study.....	3-16
Figure 3.12: Calibration characteristics of pressure transducers.	3-17
Figure 3.13: Modified base pedestal of triaxial apparatus.....	3-19
Figure 3.14: Miniature pressure sensor for pore water pressure measurement during water injection tests.	3-20
Figure 3.15: Arrangement for calibration of miniature pore pressure transducer.	3-21
Figure 3.16: Calibration curve of miniature pressure transducer.	3-22
Figure 3.17: Reliability test of miniature sensor for measuring soil pore water pressure.	3-23
Figure 3.18: Comparison of pore water pressure of soil specimen measured by two pore pressure sensors.	3-23
Figure 3.19: Photograph of <i>DPT</i> employed for this study.....	3-24
Figure 3.20: Calibration characteristics of differential pressure transducer (<i>DPT</i>).....	3-25
Figure 3.21: Schematic layout of data acquisition system.....	3-26
Figure 3.22: Calibration curves of electro-pneumatic (<i>E/P</i>) transducers.	3-29
Figure 3.23: Modified pedestal and top cap of triaxial apparatus, fitted with disk type piezoelectric transducers at their respective centers.	3-30
Figure 3.24: Schematic layout of elastic wave measurement system.....	3-30

Figure 3.25: <i>Tektronix AFG-3022C</i> function generator used in this study.	3-31
Figure 3.26: Photographs of power amplifiers used in this study.	3-32
Figure 3.27: Response of ordinary custom-built amplifier against <i>NF HSA4012</i> high speed amplifier.....	3-33
Figure 3.28: Wave recording devices used in this study.	3-33
Figure 4.1: Particle size distribution of Edosaki sand.	4-2
Figure 4.2: Compaction characteristics of Edosaki sand.....	4-2
Figure 4.3: Saturation of ceramic disk. (a) Vacuum system for saturating ceramic disks and deairation of water (b) Saturation chamber close-up (c) Close-up view of ceramic disks submerged in water.....	4-5
Figure 4.4: Saturation check of ceramic disk.	4-6
Figure 4.5: Suction response of miniature sensor to various air-tightening techniques. .4-8	8
Figure 4.6: Specimen preparation steps - 1. (a) membrane is fastened to pedestal. (b) split mould is set up. (c) helical filter paper is set up (only in water injection tests). (d) soil is poured inside the mould. (e) tamping and checking the height of each layer. (f) roughening up surface to achieve a good bond with overlying layer.	4-9
Figure 4.7: Wet tamping procedure of specimen preparation.	4-10
Figure 4.8: Template of helical filter paper used in water injection tests.....	4-11
Figure 4.9: Specimen preparation steps-2 (a) miniature PWP sensor placed inside the groove (b) filter paper is wrapped over the tenth layer (c) top cap is placed and membrane is fastened to it (d) split mould is removed carefully (e) LDTs and clip gauges are attached through pseudo hinges (f) clip gauges are balanced and aligned	4-12
Figure 4.10: Initial matric suction of unsaturated Edosaki sand specimen during an <i>ICCW</i> test, measured by an external pressure transducer connected to the saturated ceramic disk.	4-15

Figure 4.11: Initial matric suction measurement during CSWI tests; (a) comparison of matric suction measured by ceramic disk and miniature pore pressure sensor; (b) zoomed-in view of (a) showing, disturbance to initial matric suction during sampling, removal of split mold, and application of stress.	4-17
Figure 4.12: Saturation process: schematic layout of de-airing and water flushing stages.	4-20
Figure 4.13: Systematic explanation of <i>B</i> -value check.....	4-21
Figure 4.14: Three-phase depiction of soil system.	4-21
Figure 4.15: Soil as a two-phase system; (a) water saturated; (b) oven dried.	4-22
Figure 4.16: Simplified block diagram of an unsaturated soil mass, indicating various parameters of a three-phase soil system.	4-22
Figure 4.17: Travel time determination of compression wave signals.	4-27
Figure 4.18: Travel time determination of shear wave signals.....	4-28
Figure 5.1: Comparison of shear wave velocity from resonant column and bender element tests (Thomann & Hryciw, 1990).....	5-2
Figure 5.2: Bender elements, and its application for hard/stiff specimens (after Pantazopoulos and Atmatzidis (2012)).....	5-4
Figure 5.3: Schematic illustration describing the nature of polarization and mode of vibration of an <i>S</i> -type piezoelectric disk/plate (after Strassburger (1982)).	5-5
Figure 5.4: Schematic illustration describing the nature of polarization and mode of vibration of a <i>P</i> -type piezoelectric disk/plate (after Strassburger (1982)).....	5-6
Figure 5.5: (a) <i>P</i> and <i>S</i> -type piezoelectric ceramics in comparison to Japanese 5 yen coin; (b) <i>P</i> and <i>S</i> -type ceramics bonded by Araldite; (c) Piezoelectric ceramics fitted in the metal housing by Araldite; before filling silicon in the top periphery of sensor; (d) The finished product.	5-8
Figure 5.6: Schematic diagram of piezoelectric disk transducer.	5-9

List of Figures

Figure 5.7: Disk transducers fitted at the center of top cap and base pedestal by means of an O-ring.....5-9

Figure 5.8: Top cap and pedestal placed directly in-contact with each other for conducting ‘time lag calibrations’.5-11

Figure 5.9: Determination of 'time lag' in compression wave response.5-12

Figure 5.10: Determination of 'time lag' in shear wave response.5-13

Figure 5.11: Determination of compression wave travel time.....5-15

Figure 5.12: Determination of shear wave travel time; disturbances due to compression wave and near-field effects are encircled.5-16

Figure 5.13: Typical S-wave signal waveform within near-field; point-A: first deflection; point-B: First bump maximum; point-C: zero crossover; point-D: first major peak. (after Kawaguchi et al. (2001))5-17

Figure 5.14: Comparison of compression wave response when monitored through (a) Ordinary coaxial cables, and (b) Low-noise coaxial cables.5-20

Figure 5.15: Comparison of shear wave response when monitored through (a) Ordinary coaxial cables, and (b) Low-noise coaxial cables.....5-21

Figure 5.16: Comparison of compression wave signals received (a) Without grounding, and (b) With grounding, highlighting the effects of crosstalk.....5-22

Figure 5.17: Comparison of shear wave signals received (a) Without grounding, and (b) With grounding, highlighting the effects of crosstalk.5-23

Figure 5.18: Typical shear wave signals recorded with (a) *Keyance NR-500* data logger, and (b) *Hioki 8860-50* hi-resolution oscilloscope.....5-24

Figure 5.19: Frequency response function of shear wave signals recorded with (a) *Keyance NR-500* data logger, and (b) *Hioki 8860-50* hi-resolution oscilloscope.5-25

Figure 5.20: Typical compression wave signals recorded with (a) *Keyance NR-500* data logger, and (b) *Hioki 8860-50* hi-resolution oscilloscope.5-27

Figure 5.21: Frequency response function of compression wave signals recorded with (a) <i>Keyance NR-500</i> data logger, and (b) <i>Hioki 8860-50</i> hi-resolution oscilloscope.	5-28
Figure 5.22: Inherent noise in (a) <i>Keyance NR-500</i> data logger, and (b) <i>Hioki 8860-50</i> hi-resolution oscilloscope; obtained by short-circuiting the receiver terminals (0 Volt input).	5-29
Figure 5.23: Effect of shape of input waveform on shear wave receiver signals; (a) Square pulse, (b) Sine pulse.	5-30
Figure 5.24: Frequency response of commonly used driving waveforms; (a) square pulse (b) sine pulse. (after (Blewett et al., 2000)).	5-31
Figure 5.25: schematic illustration describing the generation of two side lobes of <i>P</i> -waves (responsible for near-field effect) in addition to <i>S</i> -waves, upon shear excitation of bender elements (J. Lee & Santamarina, 2005).	5-32
Figure 5.26: Effects of excitation frequency on shear wave signals obtained in dry Edosaki sand ($S_r = 0\%$) at 50 kPa isotropic stress.	5-35
Figure 5.27: Effects of excitation frequency on shear wave signals obtained in dry Edosaki sand ($S_r = 0\%$) at 100 kPa isotropic stress.	5-36
Figure 5.28: Effects of excitation frequency on shear wave signals obtained in dry Edosaki sand ($S_r = 0\%$) at 200 kPa isotropic stress.	5-37
Figure 5.29: Effects of excitation frequency on shear wave signals obtained in partially saturated Edosaki sand ($S_r = 45\%$) at 50 kPa isotropic stress.	5-38
Figure 5.30: Effects of excitation frequency on shear wave signals obtained in partially saturated Edosaki sand ($S_r = 45\%$) at 100 kPa isotropic stress.	5-39
Figure 5.31: Effects of excitation frequency on shear wave signals obtained in partially saturated Edosaki sand ($S_r = 45\%$) at 200 kPa isotropic stress.	5-40
Figure 5.32: Effects of excitation frequency on shear wave signals obtained in partially saturated Edosaki sand ($S_r = 74\%$) at 50 kPa isotropic stress.	5-41

Figure 5.33: Effects of excitation frequency on shear wave signals obtained in partially saturated Edosaki sand ($S_r = 74\%$) at 100 kPa isotropic stress.5-42

Figure 5.34: Effects of excitation frequency on shear wave signals obtained in partially saturated Edosaki sand ($S_r = 74\%$) at 200 kPa isotropic stress.5-43

Figure 5.35: Effect of L/λ ratio of shear wave velocity in dry Edosaki sand specimen, tested under 50 kPa, 100 kPa, 200 kPa, and 300 kPa effective confining pressure.....5-44

Figure 5.36: Effect of L/λ ratio of shear wave velocity in partially saturated Edosaki sand specimen ($S_r = 45\%$), tested under 50 kPa, 100 kPa, 200 kPa, and 300 kPa effective confining pressure.....5-44

Figure 5.37: Effect of L/λ ratio of shear wave velocity in partially saturated Edosaki sand specimen ($S_r = 74\%$), tested under 50 kPa, 100 kPa, 200 kPa, and 300 kPa effective confining pressure.....5-45

Figure 5.38: Effects of excitation frequency on compression wave signals obtained in dry Edosaki sand ($S_r = 0\%$) at 50 kPa isotropic stress.5-46

Figure 5.39: Effects of excitation frequency on compression wave signals obtained in dry Edosaki sand ($S_r = 0\%$) at 100 kPa isotropic stress.5-47

Figure 5.40: Effects of excitation frequency on compression wave signals obtained in dry Edosaki sand ($S_r = 0\%$) at 200 kPa isotropic stress.5-48

Figure 5.41: Effects of excitation frequency on compression wave signals obtained in partially saturated Edosaki sand ($S_r = 45\%$) at 50 kPa isotropic stress.....5-49

Figure 5.42: Effects of excitation frequency on compression wave signals obtained in partially saturated Edosaki sand ($S_r = 45\%$) at 100 kPa isotropic stress.....5-50

Figure 5.43: Effects of excitation frequency on compression wave signals obtained in partially saturated Edosaki sand ($S_r = 45\%$) at 200 kPa isotropic stress.....5-51

Figure 5.44: Effects of excitation frequency on compression wave signals obtained in partially saturated Edosaki sand ($S_r = 74\%$) at 50 kPa isotropic stress.....5-52

Figure 5.45: Effects of excitation frequency on compression wave signals obtained in partially saturated Edosaki sand ($S_r = 74\%$) at 100 kPa isotropic stress.....5-53

Figure 5.46: Effects of excitation frequency on compression wave signals obtained in partially saturated Edosaki sand ($S_r = 74\%$) at 200 kPa isotropic stress.....5-54

Figure 5.47: Response of compression wave signals in fully saturated Edosaki sand ($S_r = 100\%$) at 300 kPa isotropic stress.....5-55

Figure 5.48: Observing near-field effects through simultaneous records of *P*-type and *S*-type receivers; (a) Response on shear-type excitation; (b) Response on compression-type excitation.....5-56

Figure 5.49: Compression and shear wave velocities measured in 50% saturated Edosaki sand specimen.5-57

Figure 6.1: Stress path in *ICCW* tests.6-4

Figure 6.2: Typical variation of void ratio during *ICCW* tests.6-5

Figure 6.3: Effect of saturation ratio on volume change during *ICCW* tests.....6-8

Figure 6.4: Response of shear wave velocity to isotropic loading, $S_r=0\%$; (a) observed shear wave velocity, V_s ; (b) shear wave velocity corrected for void ratio and density, V_s''6-10

Figure 6.5: Response of shear wave velocity to isotropic loading, $S_r=9\%$; (a) observed shear wave velocity, V_s ; (b) shear wave velocity corrected for void ratio and density, V_s''6-11

Figure 6.6: Response of shear wave velocity to isotropic loading, $S_r=20\%$; (a) observed shear wave velocity, V_s ; (b) shear wave velocity corrected for void ratio and density, V_s''6-12

Figure 6.7: Response of shear wave velocity to isotropic loading, $S_r=45\%$; (a) observed shear wave velocity, V_s ; (b) shear wave velocity corrected for void ratio and density, V_s''6-13

Figure 6.8: Response of shear wave velocity to isotropic loading, $Sr=74\%$; (a) observed shear wave velocity, V_s ; (b) shear wave velocity corrected for void ratio and density, V_s'' 6-14

Figure 6.9: Response of shear wave velocity to isotropic loading: Saturated specimen ($B = 0.80$); (a) observed shear wave velocity, V_s ; (b) shear wave velocity corrected for void ratio and density, V_s'' 6-15

Figure 6.10: Response of shear wave velocity to isotropic loading: Saturated specimen ($B = 0.968$); (a) observed shear wave velocity, V_s ; (b) shear wave velocity corrected for void ratio and density, V_s'' 6-16

Figure 6.11: Response of compression wave velocity to isotropic loading, $Sr=0\%$; (a) observed shear wave velocity, V_p ; (b) shear wave velocity corrected for void ratio and density, V_p'' 6-20

Figure 6.12: Response of compression wave velocity to isotropic loading, $Sr=9\%$; (a) observed shear wave velocity, V_p ; (b) shear wave velocity corrected for void ratio and density, V_p'' 6-21

Figure 6.13: Response of compression wave velocity to isotropic loading, $Sr=20\%$; (a) observed shear wave velocity, V_p ; (b) shear wave velocity corrected for void ratio and density, V_p'' 6-22

Figure 6.14: Response of compression wave velocity to isotropic loading, $Sr=45\%$; (a) observed shear wave velocity, V_p ; (b) shear wave velocity corrected for void ratio and density, V_p'' 6-23

Figure 6.15: Response of compression wave velocity to isotropic loading, $Sr=74\%$; (a) observed shear wave velocity, V_p ; (b) shear wave velocity corrected for void ratio and density, V_p'' 6-24

Figure 6.16: Response of compression wave velocity to isotropic loading: Saturated specimen ($B = 0.80$); (a) observed shear wave velocity, V_p ; (b) shear wave velocity corrected for void ratio and density, V_p'' 6-25

Figure 6.17: Response of compression wave velocity to isotropic loading: Saturated specimen ($B = 0.80$); (a) observed shear wave velocity, V_p ; (b) shear wave velocity corrected for void ratio and density, V_p''	6-26
Figure 6.18: Typical variation of void ratio during reloading of isotropic stress.	6-30
Figure 6.19: Typical variation of shear wave velocity during reloading of isotropic stress; (a) $S_r=20\%$; (b) $S_r=45\%$	6-31
Figure 6.20: Typical variation of compression wave velocity during reloading of isotropic stress; (a) $S_r=20\%$; (b) $S_r=45\%$	6-32
Figure 6.21: Deformation characteristics of unsaturated specimen, $S_r=45\%$; (a) Variation of isotropic stress; (b) Comparison of axial displacement transducers; (c) Radial deformation characteristics.....	6-34
Figure 6.22: Deformation characteristics of unsaturated specimen, $S_r=74\%$; (a) Variation of isotropic stress; (b) Comparison of axial displacement transducers; (c) Radial deformation characteristics.....	6-35
Figure 6.23: Behavior of V_s'' with soil saturation during unloading of isotropic stress in <i>ICCW</i> tests.	6-36
Figure 6.24: Behavior of V_s'' with soil saturation during loading of isotropic stress in <i>ICCW</i> tests.	6-37
Figure 6.25: Behavior of V_p'' with soil saturation during unloading of isotropic stress in <i>ICCW</i> tests; (a) V_p'' ; (b) V_p'' (Zoomed-in).	6-38
Figure 6.26: Behavior of V_p'' with soil saturation during loading of isotropic stress in <i>ICCW</i> tests; (a) V_p'' ; (b) V_p'' (Zoomed-in).	6-39
Figure 6.27: Behavior of shear wave velocity, V_s , with soil saturation in <i>ICCW</i> tests; (a) During loading phase; (b) During unloading phase.....	6-41
Figure 6.28: Behavior of compression wave velocity, V_p , with soil saturation in <i>ICCW</i> tests; (a) During loading phase; (b) During unloading phase.	6-42

Figure 6.29: Variation in saturation ratio, S_r , of *ICWI* specimens upon water injection. 6-45

Figure 6.30: Volume response of *ICWI* specimens upon water infiltration. 6-46

Figure 6.31: Variation of elastic wave velocities upon water injection in *ICWI* tests; (a) Shear wave velocity, V_s ; (b) Compression wave velocity, V_p 6-47

Figure 6.32: Variation of normalized elastic wave velocities upon water injection in *ICWI* tests; (a) Normalized shear wave velocity, V_s'' ; (b) Normalized compression wave velocity, V_p'' 6-48

Figure 6.33: Variation in saturation ratio, S_r , of initially moist *ICWI* specimens upon water injection..... 6-49

Figure 6.34: Volume response of initially moist *ICWI* specimens upon water infiltration. 6-50

Figure 6.35: Variation of normalized elastic wave velocities upon water injection in initially moist *ICWI* tests; (a) Normalized shear wave velocity, V_s'' ; (b) Normalized compression wave velocity, V_p'' 6-51

Figure 6.36: Variation of elastic wave velocities upon water injection in initially moist *ICWI* tests; (a) Shear wave velocity, V_s ; (b) Compression wave velocity, V_p 6-52

Figure 6.37: Wave velocities plotted against volume response of specimens during *ICWI* tests on initially moist specimens; (a) Normalized shear wave velocity, V_s'' ; (b) Normalized compression wave velocity, V_p'' 6-54

Figure 6.38: Soil water characteristic curve (*SWCC*) of Edosaki sand based on initial suction of *ICCW* tests, test data from Gallage and Uchimura (2010), and Fredlund and Xing (1994) curve fitting. 6-57

Figure 6.39: Zones of a typical *SWCC* (after Oh and Vanapalli (2011)). 6-58

Figure 6.40: Dependence of elastic wave velocities on zones of *SWCC*. 6-59

Figure 6.41: Change in the particle contact area with saturation of soil; (a) Dry soil, wave travel possible only through inter-particle ‘ <i>contact points</i> ’; (b) Partially saturated soil, wave travels through inter-particle contacts plus ‘ <i>meniscus points</i> ’; (c) Evolution of inter-particle contact area with soil wetting (after Santamarina (2003)).	6-60
Figure 7.1: Relationship between saturation ratio and Skempton's <i>B</i> -value (after Gu et al. (2013)).	7-5
Figure 7.2: Stress path adopted for <i>CWRSR</i> tests.	7-6
Figure 7.3: Response of <i>CWRSR</i> specimens to radial stress reduction.	7-7
Figure 7.4: Definition of yield point in <i>CWRSR</i> tests.	7-8
Figure 7.5: Effects of soil yielding on elastic wave velocities; (a) Compression wave velocities, V_p ; (b) Shear wave velocities, V_s	7-10
Figure 7.6: Variation of dry density during the course of <i>CWRSR</i> tests.	7-11
Figure 7.7: Effects of soil yielding on elastic wave velocities normalized for void ratio ($e_o = 0.673$) and density ($(\gamma_d)_o = 1.578 \text{ g/cm}^3$); (a) Normalized compression wave velocity, V_p'' ; (b) Normalized shear wave velocity, V_s'' .	7-12
Figure 7.8: Variation of corrected elastic wave velocities ($e_o = 0.673$; $(\gamma_d)_o = 1.578 \text{ g/cm}^3$), normalized with respective initial values; (a) Compression wave velocities, $V_p''/V_p''_{(ini)}$; (b) Shear wave velocities, $V_s''/V_s''_{(ini)}$.	7-14
Figure 7.9: Dependence of elastic wave velocities on specimen dilation; (a) Compression wave velocities, $V_p''/V_p''_{(ini)}$; (b) Shear wave velocities, $V_s''/V_s''_{(ini)}$.	7-15
Figure 7.10: Dependence of shear and compression wave velocities on principle stress direction.	7-17
Figure 7.11: Variation of normalized shear wave velocities with axial strain in specimens.	7-18
Figure 7.12: Schematic representation of stress path adopted for <i>CSWI</i> tests.	7-20
Figure 7.13: Schematic description of triaxial specimens used in this study.	7-21

Figure 7.14: Effect of relative density of soil on failure initiation during rain-induced landslides; (a) Variation of saturation ratio (S_r) with time; (b) Axial strain (ϵ_a) response upon water infiltration; (c) Variation of pore water pressure/matric suction (S_u). 7-24

Figure 7.15: Response of elastic wave velocities at different specimen densities during shearing infiltration tests; (a) Variation of saturation ratio (S_r) with time; (b) Compression wave velocity (V_p) response; (c) Shear wave velocity (V_s) response. .. 7-26

Figure 7.16: Effect of relative density on strain path during shearing infiltration tests. . 7-27

Figure 7.17: Response of elastic wave velocities (normalized corresponding to $e_o = 0.673$, and $\gamma_d = 1.578 \text{ g/cm}^3$) at different specimen densities during shearing infiltration tests; (a) Saturation ratio (S_r) versus time; (b) Normalized compression wave velocities ($V_p''/V_p''(initial)$); (c) Normalized shear wave velocities ($V_s/V_s(initial)$)..... 7-28

Figure 7.18: Relationship between principle stress ratio (K) and slope inclination (after K Farooq (2002)). 7-30

Figure 7.19: Effect of principle stress ratio (K) on failure initiation during rain-induced landslides; (a) Variation of saturation ratio (S_r) with time; (b) Axial strain (ϵ_a) response upon water infiltration; (c) Variation of pore water pressure/matric suction (S_u). 7-31

Figure 7.20: Effect of principle stress ratio (K) on strain path during shearing infiltration tests. 7-32

Figure 7.21: Response of elastic wave velocities at different principle stress ratios (K) during shearing infiltration tests; (a) Variation of saturation ratio (S_r) with time; (b) Compression wave velocity (V_p) response; (c) Shear wave velocity (V_s) response. .. 7-34

Figure 7.22: Response of elastic wave velocities (normalized corresponding to $e_o = 0.673$, and $\gamma_d = 1.578 \text{ g/cm}^3$) at different principle stress ratios (K) during shearing infiltration tests; (a) Saturation ratio (S_r) versus time; (b) Normalized compression wave velocities ($V_p''/V_p''(initial)$); (c) Normalized shear wave velocities ($V_s/V_s(initial)$). 7-36

Figure 7.23: Water injection in a triaxial specimen using a ceramic disk and filter paper; (a) High AEV ceramic disk embedded in pedestal; water injected through application of back pressure; (b) Helical filter paper assembled inside latex membrane; (c) Specimen preparation by wet temping; (d) Completed soil specimen. 7-38

Figure 7.24: End of test moisture distribution in triaxial specimen; (a) Specimen removed from triaxial cell; (b) Pedestal is detached carefully and membrane is cut open; (c)(d) Fifteen equal sections are marked and specimen is divided into 15 equal parts; (e) Sample collected for moisture content from center of each part. 7-39

Figure 7.25: Nomenclature for labeling end of test moisture distribution; (a) Longitudinal sections; (b) Transverse sections..... 7-40

Figure 7.26: Effect of helical filter paper on strain response of Edosaki sand specimens ($D_r = 56\%$, $K = 3.0$, $\sigma_3 = 25$ kPa). 7-42

Figure 7.27: End of test moisture distribution when helical filter paper was not used ($D_r = 56\%$, $K = 3.0$, $\sigma_3 = 25$ kPa); (a) Moisture variation along specimen height; (b) Moisture variation along specimen diameter..... 7-44

Figure 7.28: End of test moisture distribution when helical filter paper was used ($D_r = 56\%$, $K = 3.0$, $\sigma_3 = 25$ kPa); (a) Moisture variation along specimen height; (b) Moisture variation along specimen diameter. 7-45

Figure 7.29: Comparison of end of test moisture distribution in the specimens with, and without using helical filter paper ($D_r = 30\%$, $K = 3.4$, $\sigma_3 = 25$ kPa). 7-47

Figure 7.30: Comparison of end of test moisture distribution in the specimens with, and without using helical filter paper ($D_r = 56\%$, $K = 3.7$, $\sigma_3 = 25$ kPa). 7-47

Figure 7.31: Comparison of strain response of specimens with, and without using helical filter paper ($D_r = 30\%$, $K = 3.4$, $\sigma_3 = 25$ kPa). 7-48

Figure 7.32: Comparison of strain response of specimens with, and without using helical filter paper ($D_r = 56\%$, $K = 3.7$, $\sigma_3 = 25$ kPa). 7-49

Figure 7.33: Deformation characteristic during shearing infiltration test when helical filter paper was used ($Dr = 56\%$, $K = 3.4$, $\sigma_3 = 25$ kPa); (a) Axial strain response; (b) Radial strain response.7-51

Figure 7.34: Deformation characteristic during shearing infiltration test when helical filter paper was used ($Dr = 56\%$, $K = 3.0$, $\sigma_3 = 25$ kPa); (a) Axial strain response; (b) Radial strain response.7-52

Figure 7.35: Deformation characteristic during shearing infiltration test when helical filter paper was not used ($Dr = 56\%$, $K = 3.7$, $\sigma_3 = 25$ kPa); (a) Axial strain response; (b) Radial strain response.7-54

Figure 7.36: Deformation characteristic during shearing infiltration test when helical filter paper was not used ($Dr = 56\%$, $K = 3.7$, $\sigma_3 = 25$ kPa); (a) Axial strain response; (b) Radial strain response.7-55

Figure 8.1: Expected response of elastic wave velocities during rainfall-induced landslides.8-3

Figure 8.2: Possible orientations of exciter and receiver in field conditions; (a) Cross-hole type; (b) Down-hole type.8-4

Figure 8.3: Schematic showing single exciter, multiple receiver assembly.8-7

Figure 8.4: Schematic representation of wave excitation deep into soil surface.8-8

Figure 8.5: Schematic illustration showing the ray paths of the incident wave (SB) striking the boundary at critical angle (i_c), and the refracted wave (BC) traveling along the boundary with velocity $V_2 (>V_1)$. The latter is refracted back to the first medium (V_1) at the same angle (i_c) and re-emerges with a ray path such as CD. Advancement of the wavefronts is shown from the instant ($t = 0$) when the incident ray strikes the boundary B. (after Palmer (1986)).....8-9

Figure 8.6: Wavefronts for the first-arriving waves in a seismic refraction survey. Note that first arrivals near the source are from direct waves but, at the distance greater than the critical distance, x_c , the first arrivals are from the head waves. (after U.S. Corps of Engineers (1979)).8-10

Figure 8.7: Typical plot of seismic refraction test. 8-10

Figure 8.8: Schematic illustration describing the layout of sensors and wave propagation paths of seismic waves when used for landslide monitoring. 8-11

Figure 8.9: Schematic illustration of variation of wave velocities in a seismic refraction test during rainfall-induced landslides. 8-12

Figure A.1: Schematic views of load cell used in this study. A-13

Figure B.1: Different excitation devices used for generating elastic waves in triaxial specimen. B-2

Figure B.2: Orientation of electromagnetic type trigger for generating *P*-waves and *S*-waves in triaxial specimen. B-3

Figure B.3: Typical test results obtained by electromagnet type exciter. Receiver-1 is the piezoelectric wave receiver located in top cap whereas receiver-2 is a similar receiver located in base pedestal. B-4

Figure B.4: Piezoelectric speaker type trigger device glued to triaxial top cap. B-6

Figure B.5: Development of piezo-beam receivers. B-7

Figure B.6: Schematic illustration explaining installation of piezo-beam receivers. ... B-8

Figure B.7: Piezo-beam receivers installed on triaxial specimen. B-9

LIST OF TABLES

Table 2.1: Void ratio function, $F(e)$, as suggested by various researchers (after (Yimsiri, 2001)).	2-17
Table 3.1: Salient features of <i>Tektronix AFG-3022C</i> function generator.	3-31
Table 3.2: Salient features of <i>Hioki 8860-50</i> oscilloscope (all features corresponds to when installed with <i>Hioki 8957</i> hi-resolution input module).	3-34
Table 4.1: Physical properties of Edosaki sand.	4-3
Table 5.1: Basic properties of <i>P</i> -type and <i>S</i> -type piezoelectric ceramics disks used in this study.	5-7
Table 5.2: Main features of signal recorders used in this study.	5-29
Table 6.1: Initial test conditions in <i>ICCW</i> tests	6-2
Table 6.2: Initial test conditions in <i>ICWI</i> tests.	6-3
Table 6.3: Summary of fitting parameter, C , from shear wave velocity plots.	6-17
Table 6.4: Summary of fitting parameter, n , from shear wave velocity plots.	6-18
Table 6.5: Summary of fitting parameter, C , from compression wave velocity plots.	6-28
Table 6.6: Summary of fitting parameter, n , from compression wave velocity plots.	6-28
Table 7.1: Initial test conditions in <i>CWRSR</i> tests.	7-2
Table 7.2: Initial test conditions in <i>CSWI</i> tests.	7-3
Table A.1: Capacity of load cell, as determined from Eq. A.1.	A-14

SYMBOLS & ABBREVIATIONS

<i>A</i>	Area
<i>A/D</i>	Analog to digital converter
<i>AEV</i>	Air Entry Value
<i>B</i>	Skempton's pore pressure parameter
<i>C_u</i>	Coefficient of uniformity (D_{60}/D_{10})
<i>C_c</i>	Coefficient of curvature/gradation ($D_{30}^2/(D_{10} \times D_{60})$)
<i>CG</i>	Clip Gauge
<i>CWRSR</i>	Constant Water Radial Stress Reduction tests
<i>CSWI</i>	Constant Shear stress Water Injection tests
<i>D/A</i>	Digital to analog signal converter
<i>DPT</i>	Differential pressure transducer
<i>D_r</i>	Relative density
<i>D_{r_o}</i>	Reference relative density for normalization
<i>D₅₀</i>	Grain diameter for which 50% of specimen particles are finer
<i>D₁₀</i>	Grain diameter for which 10% of specimen particles are finer
<i>D₆₀</i>	Grain diameter for which 60% of specimen particles are finer
<i>E/P</i>	Electro pneumatic transducer
<i>e</i>	Void ratio
<i>e_o</i>	Reference void ratio for normalization
<i>e_{min}</i>	Minimum void ratio
<i>e_{max}</i>	Maximum void ratio
<i>F_c</i>	Fines content

<i>FP</i>	Helical Filter Paper
<i>F(e)</i>	Void ratio function
<i>f_{in}</i>	Frequency of Input/excitation signal
<i>f_{out}</i>	Frequency of output/received signal
<i>G_s</i>	Specific gravity
<i>G, G_{max}, G_o</i>	Maximum/Initial shear modulus
<i>H (or L)</i>	Specimen height
<i>ICCW</i>	Isotropically Consolidated Constant Water Content tests
<i>ICWI</i>	Isotropically Consolidated Water Injection tests
<i>K</i>	Principle stress ratio
<i>LDT</i>	Local Deformation Transducer
<i>LVDT</i>	Linear Variable Displacement Transducer
<i>Mini PWP</i>	Miniature Pore Water Pressure Sensor
<i>M</i>	Constrained compression modulus
<i>NFE</i>	Near-field effect
<i>n</i>	Porosity
<i>OMC</i>	Optimum moisture content
<i>PWP</i>	Pore water pressure
<i>q</i>	Deviator stress
<i>S_r</i>	Degree of saturation/Saturation ratio
<i>S_u</i>	Matric suction
<i>SWCC</i>	Soil-water characteristic curve
<i>u_a</i>	Pore air pressure
<i>u_w</i>	Pore water pressure
<i>V_p</i>	Compression/Dilatation wave velocity

V_s	Shear wave velocity
V_p'	Compression wave velocity normalized for void ratio
V_s'	Shear wave velocity normalized for void ratio
V_p''	Compression wave velocity normalized for void ratio and density
V_s''	Shear wave velocity normalized for void ratio and density
WI	Rate of water injection (ml/hr)
w	Gravimetric water content

Greek Symbols

σ_1	Total axial stress
σ_3	Total radial stress
σ_1'	Effective axial stress
σ_3'	Effective radial stress
θ_v	Volumetric water content
γ_d	Dry density/unit weight
γ_b	Bulk/moist/total density
$\gamma_{d(max)}$	Maximum dry density
γ_w	Unit weight of water (= 1 g/cm ³)
ϵ_a, ϵ_1	Axial strain
ϵ_r, ϵ_3	Radial strain
ϵ_{vol}	Volumetric strain
γ	Shear strain
λ	Wavelength

DISSERTATION OVERVIEW

Chapter 1

CHAPTER 1

DISSERTATION OVERVIEW

1.1. PROLOGUE

Rapid growth in world's population is pressing its inhabitants to uncover the unexplored avenues of accommodation and transportation. Under these severe demographic and economic pressures, widespread construction projects are being carried out in hilly areas and thus are exposed to landslides. Landslides cause severe damage to infrastructure and life all around the globe every year. For instance, annual losses resulting from landslides in United States alone are estimated to be 25 to 50 lives and \$3.5 billion worth of infrastructure damage (USGS, 2004). Similarly in Canada 570 deaths over a 160 year period (1840-1999) have been attributed to disastrous landslides (Evans, 2001). Death tolls in less developed, populated regions are even higher (e.g. Ancash, Peru, 1970, 18,000 deaths; Layte, Philippines, 2006, 1800 fatalities) (Mosher, 2008). Citing the vast aerial spread of such disasters, typical landslide remediation approaches of constructing retaining structures or soil improvement are not economically feasible anymore. Rather there is a need for more robust and economically viable solutions like real-time landslide early warning systems. This study is an attempt to improve the currently available landslide early warning systems by introducing a new technique to predict landslide movements by means of elastic wave propagation in soil.

1.2. MOTIVATION & SIGNIFICANCE

Landslides are among the most devastating natural disasters. According to the GLIDE number record of 134 landslides between 1999 and 2012, around 63% were triggered

by rainfall (www.glidenumber.net). Over the years, rainfall induced landslides have caused substantial damage in several countries such as Japan, China, Pakistan, Brazil, Hong Kong, Italy, etc. (Brand, 1981; Wolle & Hachich, 1989; Ng & Pang, 2000; Farooq et al., 2004). The most common landslide protection works used around the world include various '*hard measures*' including several soil retaining techniques (retaining walls, wire mesh support, etc.) and, soil improvement by means of soil nailing, anchor bolting, shotcrete, etc. Since the aerial spread of rain-induced landslides is generally very large (Uchimura et al., 2010), such protection measures are sometimes required to cover very large areas (Figure 1.1). Thus, such hard measures are often neither practically viable nor economically feasible.



Figure 1.1: Typical landslide protection works; (a) along railway tracks (FHWA, 2003), (b) along highways (Hongbai county, Wenchuan, China)

Early warning of a possible landslide disaster provides a suitable alternative. The concept of landslide early warning is somehow similar to a fire-alarm, which might not be able to prevent the fire itself but at least warn the inhabitants to evacuate, thus saving valuable lives. Similarly, a landslide early warning system may not be able to prevent the landslide from occurring but it can at least give timely caution to people in its surrounding. If the warning is early enough, it can also be used to take necessary action to prevent the landslide itself. Even if the infrastructure damage may not be prevented to large extent by early warning systems, yet saving human lives is a large enough contribution to invest in this field.

Study of soil behavior during rainfall is primitive to devise an effective landslide/slope failure prediction strategy. The current landslide prediction methods primarily involve monitoring based on rainfall intensity, with warning issued when rainfall exceeds a certain critical value (Caine, 1980; Chan et al., 2003; Cannon et al., 2008; Baum & Godt, 2010). However, there is no standard criteria for issuing the warning; as the warning criteria is generally based on magnitude (intensity, duration, etc) of past rainfall events triggering landslides. Therefore, there is no consideration of prevalent soil mechanics or physical properties of soil, in issuing landslide warnings. Direct monitoring of slope movements and soil moisture content may prove efficient in devising a generalized landslide predicting strategy (Uchimura et al., 2010). Elastic wave velocity in soil can provide an assessment of degree of saturation of soil specimen (Brignoli et al., 1996). Variation of elastic wave velocity in soil during rainfall, can therefore be used to predict slope failures and landslides (Taro Uchimura, 2011).

1.3. PROBLEM STATEMENT

The current practice of physical landslide early warning is mainly focused on monitoring actual slope movements, and soil moisture/matric suction. A variety of sensors are currently being used to monitor physical movements of slope surfaces. These include draw wire sensors (Arnhardt et al., 2007), inclinometers (Lollino et al., 2002; Uchimura et al., 2010; Uchimura, Towhata, et al., 2011), extensometers (Angeli et al., 2000; Uchimura, Suzuki, et al., 2011), etc. Similarly, typical instrumentation to indicate soil moisture in unsaturated soils include ceramic cups or tensiometers for determining soil matric suction, and dielectric moisture sensors for measurement of volumetric water content of soil (Uchimura et al., 2010; Ramesh & Vasudevan, 2012). All such sensors are however point sensors, and hence, sensitive only to deformation and moisture changes in their own vicinity (Figure 1.2). To cover a wide potential landslide area, a large number of such sensors would therefore be required. This could significantly increase the project cost but on the other hand, reducing the number of sensors would decrease efficiency of landslide prediction thereby making the technology itself questionable.

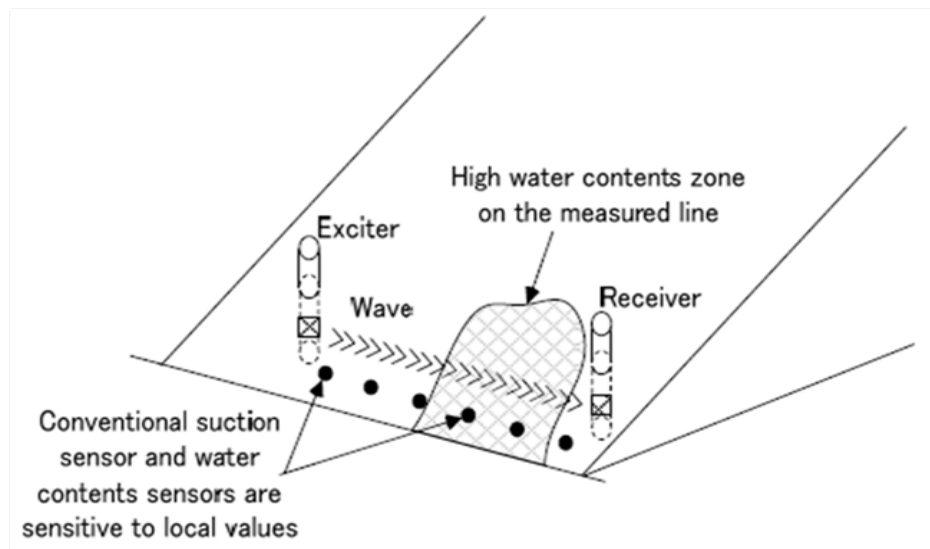


Figure 1.2: Determination of soil moisture on a slope surface; typical moisture sensors versus moisture detection by elastic wave propagation (T. Uchimura, 2011).

In this study, an idea to monitor slope deformations, and soil moisture variations by using elastic wave velocities is presented. A single pair of elastic wave exciter and receiver installed on the slope surface can cover a considerably large area (Figure 1.2). Laboratory elements tests were conducted to explore the behavior of elastic wave velocities with soil deformations, and varying soil moisture content. The tests were designed to reproduce the prevalent landslide conditions. Corresponding test results and related discussions shed light on the mechanism of elastic wave velocity variation during actual landslide conditions; since understanding the mechanism properly is the first step towards its practical application.

1.4. AIMS & OBJECTIVES

This research is aimed towards developing the fundamental understanding of elastic wave propagation in unsaturated soils with reference to landslides. Clear and comprehensive understanding of mechanism of wave velocity variation during soil wetting/drying, and slope movements is integral for its application in practical landslide early warning systems. The main objectives of this study can be outlined as follows;

- Development of appropriate experimental facilities to enable the combined measurement of compression wave (V_p), and shear wave velocity (V_s) in unsaturated soil specimens. The designed experimental apparatus was required to possess the following specific attributes;
 - a. Independent control of axial and lateral stresses acting on the specimen. This is required for reproducing actual field stress path in laboratory element tests.
 - b. In order to replicate the effects of rainfall, the apparatus was required to possess ability to inject water in the specimen.
 - c. Ability to measure soil matric suction which is integral in understanding unsaturated soil behavior.
 - d. Combined measurement of V_p and V_s over the same travel path in the specimen.
- Explore the effects of soil moisture on elastic wave propagation.
- Explore the effects of soil deformations/yielding on elastic wave propagation.
- Explore the behavior of elastic wave propagation during landslide conditions (combined effect of water infiltration and soil yielding).
- Devise a strategy to predict landslides by means of elastic wave velocities.

1.5. SCOPE OF WORK AND LIMITATIONS

The scope of this research encompasses comprehensive studies to explore the variation of elastic wave velocities with soil saturation, and with soil yielding. The objective of this research is to explore the mechanism of elastic wave velocities variation during landslides. During a rainfall event, initially unsaturated slope surfaces start becoming saturated. Very small or no deformations are expected in the slope surface during this initial phase. Hence, it is desired to explore the effects of soil saturation on wave velocities in isolation. Similarly near the saturation stage, when the failure is initiated and the slope actually starts to move; soil yields without any appreciable change in moisture. A separate study is required to explore the effects of soil yielding during landslides, in constant water content conditions. The experimental plan was so defined to explore the effects of soil saturation, and soil yielding at

constant water content first. And then another series of experiments was conducted to reproduce actual field stress path during landslides, and wave velocities were examined during actual landslide conditions, i.e. by combining the effects of soil moisture and soil yielding.

Due to the limitation of time, findings of this research could not be expanded to other soil types. Numerical modeling could also be done to validate the findings of this research. This study is however limited to exploring the behavior of elastic wave velocities during landslides by means of laboratory element tests only. Validity of said findings in actual landslide conditions is yet to be proved.

1.6. UNIT SYSTEM

The S.I. system of measurement units, acronymically known as “International System of Units” was employed for this study. Following the usual sign convention adopted in soil mechanics, stresses and strains in compression were designated as positive, whereas those in tension were represented as negative.

1.7. TIME SCALE AND LOCATION OF RESEARCH

The experimental work and all the related laboratory tests were conducted at the Geotechnical Engineering Laboratory of the University of Tokyo located at 7-3-1 Hongo, Bunkyo-ku, Tokyo 113-8656, Japan. The study presented herein was conducted from April 2011 to March 2014.

1.8. THESIS ORGANIZATION

Considering the desired objectives and scope of this research work, the thesis is arranged in eight chapters providing a detailed overview of the work done and the main findings of this research program. A broad outline of the thesis is as follows.

Chapter 1 is an introduction of this research, and provides a broad synopsis of this research. The research curriculum is elucidated by discussing in detail, the problem

statement and its significance, objectives and specific aims as well as the scope of work and its limitations.

Chapter 2 provides a brief review of previous studies related to rain-fall induced landslides and landslide protection approaches.

Chapter 3 presents the detailed description of the development and use of experimental setup employed for this study.

Chapter 4 describes the overall research methodology. The physical properties of test material, detailed experimental plan and step by step procedure for the performance of each type of experiment are outlined in this chapter.

In Chapter 5 the evolution of wave measurement apparatus of this study is outlined. A detailed description of development of disk type piezoelectric transducer, its performance evaluation, and a comprehensive layout of elastic wave measurement procedure is outlined in this chapter.

Chapter 6 discusses the behavior of elastic wave velocities with changing soil moisture conditions. Test results from different series of experiments are used to shed light on the said phenomenon.

In Chapter 7, the results of triaxial tests on unsaturated specimens simulating landslide conditions are presented and the corresponding effects on elastic wave velocities are discussed.

Chapter 8 combines the results and discussions of previous two chapters to layout plans for field application of elastic wave velocities for landslide prediction.

Finally, Chapter 9 summarizes the conclusion drawn from this research along with the associated recommendations for future studies.

1.9. REFERENCES

- Angeli, M.-G., Pasuto, A., & Silvano, S. (2000). A Critical Review of Landslide Monitoring Experiences. *Engineering Geology*, 55(3), 133-147.
- Arnhardt, C., Asch, K., Azzam, R., Bill, R., Fernandez-Steeger, T., Homfeld, S., . . . Toloczyki, M. (2007). Sensor Based Landslide Early Warning System-Slews. Development of a Geoservice Infrastructure as Basis for Early Warning Systems for Landslides by Integration of Real-Time Sensors. *Geotechnologien science report*, 10, 75-88.
- Baum, R., & Godt, J. (2010). Early Warning of Rainfall-Induced Shallow Landslides and Debris Flows in the USA. *Landslides*, 7(3), 259-272. doi: 10.1007/s10346-009-0177-0
- Brand, E. W. (1981). Some Thoughts on Rain-Induced Slope Failures. *Proc. of 10th International Conference on Soil Mechanics and Foundation Engineering*, 3, 373-376.
- Brignoli, E. G. M., Gotti, M., & Stokoe, K. H. (1996). Measurement of Shear Waves in Laboratory Specimens by Means of Piezoelectric Transducers. *Geotechnical Testing Journal*, GTJODJ, 19(4), 384-397. doi: 10.1520/GTJ10716J
- Caine, N. (1980). The Rainfall Intensity–Duration Control of Shallow Landslides and Debris Flows. *Geografiska Annaler*, 62A, 23-27.
- Cannon, S. H., Gartner, J. E., Wilson, R. C., Bowers, J. C., & Laber, J. L. (2008). Storm Rainfall Conditions for Floods and Debris Flows from Recently Burned Areas in Southwestern Colorado and Southern California. *Geomorphology*, 96, 250-269.
- Chan, R., Pang, P., & Pun, W. (2003). *Recent Developments in the Landslip Warning System in Hong Kong*. Proceedings: Proceedings of the 14th Southeast Asian Geotechnical Conference), Balkema, Lisse, The Netherlands.

- Evans, S. G. (2001). Landslides. *A Synthesis of Geological Hazards in Canada, Geological Survey of Canada Bulletin 578*, 43-79.
- Farooq, K., Orense, R., & Towhata, I. (2004). Response of Unsaturated Sandy Soils under Constant Shear Stress Drained Condition. *Soils and foundations*, 44(2), 1-13.
- FHWA. (2003). Soil Nail Walls, Geotechnical Engineering Circular No 7. *Report No. FHWAO-IF-03-017*. Federal Highway Administration.
- Lollino, G., Arattano, M., & Cuccureddu, M. (2002). The Use of the Automatic Inclinometric System for Landslide Early Warning: The Case of Cabella Ligure (North-Western Italy). *Physics and Chemistry of the Earth, Parts A/B/C*, 27(36), 1545-1550.
- Mosher, D. C. (2008). *Submarine Mass Movements in Canada: Geohazards with Far-Reaching Implications*. Proceedings: 4th Canadian Conference on Geohazards: From Causes to Management (pp. 55-62), Quebec, Canada.
- Ng, C. W., & Pang, Y. (2000). Influence of Stress State on Soil-Water Characteristics and Slope Stability. *Journal of Geotechnical and Geoenvironmental Engineering*, 126(2), 157-166.
- Ramesh, M., & Vasudevan, N. (2012). The Deployment of Deep-Earth Sensor Probes for Landslide Detection. *Landslides*, 9(4), 457-474. doi: 10.1007/s10346-011-0300-x
- Uchimura, T. (2011). *Wave Velocity in Unsaturated Slopes in Relation to Moisture and Stability*. Paper presented at the The 14th Asian Regional Conference on Soil Mechanics and Geotechnical Engineering, Hong Kong.
- Uchimura, T. (2011). *Wave Velocity in Unsaturated Slopes in Relation to Moisture and Stability*. Proceedings: Proc. of The 14th Asian Regional Conference on Soil Mechanics and Geotechnical Engineering), Hong Kong, China.

- Uchimura, T., Suzuki, D., & Hongkwan, S. (2011). *Combined Monitoring of Water Content and Displacement for Slope Instability*. Proceedings: Proc. of 4th Japan-Korea Geotechnical Workshop (pp. 67-72), Kobe, Japan.
- Uchimura, T., Towhata, I., Lan Anh, T., Fukuda, J., Bautista, C. B., Wang, L., . . . Sakai, N. (2010). Simple Monitoring Method for Precaution of Landslides Watching Tilting and Water Contents on Slopes Surface. *Landslides*, 7(3), 351-357. doi: 10.1007/s10346-009-0178-z
- Uchimura, T., Towhata, I., Wang, L., & Qiao, J. P. (2011). *Miniature Ground Inclinator for Slope Monitoring*. Proceedings: Proc. of The 14th Asian Regional Conference on Soil Mechanics and Geotechnical Engineering, ATC3 session), Hong Kong, China.
- USGS. (2004). Landslide Types and Processes, Fact Sheet 2004-3072, July 2004 Retrieved 18/12/2013, from <http://pubs.usgs.gov/fs/2004/3072/pdf/fs2004-3072.pdf>
- Wolle, C., & Hachich, W. (1989). *Rain-Induced Landslides in Southeastern Brazil*. Proceedings: The 12 th International Conference on Soil Mechanics and Foundation Engineering, Rio de Janeiro, Br, 08/13-18/89 (pp. 1639-1642).

LITERATURE REVIEW

Chapter 2

CHAPTER 2

LITERATURE REVIEW

2.1. INTRODUCTION

Keeping in view the various aspects of problem statement and research objectives of this study presented in the previous chapter, this chapter has been designed to present a brief overview of published scientific work related to the mechanism rain-induced slope failures and the currently available landslide early warning systems. Various types of landslide early warning systems currently in practice around the world are described, and their limitations are discussed. Different types of sensors used for predicting landslides are also introduced. The subject demands a thorough understanding of not only the mechanism of rain-induced landslides but also the propagation of elastic waves in soils. In the past, extensive research has been conducted on the propagation of shear waves in saturated soils. However, the response of shear and compressive waves in unsaturated soils requires further exploration. Only a handful of studies discussing the response of shear wave velocities in unsaturated soils are available at present. Even lesser information is available about the response of compression wave velocities in unsaturated soils. Thorough understanding of elastic wave propagation in unsaturated soils is the core of this study. Therefore, a comprehensive review of existing literature related to the response of elastic waves in saturated and unsaturated soils is presented.

2.2. RAIN-INDUCED SLOPE FAILURES

Rainfall-induced slope failures are among the most destructive natural hazards that have caused substantial damage in various parts of the world including, but not

limited to, Taiwan (Lin et al., 2000; Chen et al., 2006), Hong Kong (Brand, 1981; Au, 1998; Fuchu et al., 1999; Dai & Lee, 2002), Singapore (Pitts, 1983; Toll, 2001), Japan (Sidle & Chigira, 2004; Ayalew et al., 2005; Yoshimatsu & Abe, 2006), Pakistan (Shroder Jr, 1998), United States (Iverson, 2000; R. L. Baum et al., 2005; Guzzetti et al., 2008; R. Baum & Godt, 2010), Italy (Guzzetti et al., 1999; Guzzetti et al., 2004; Capparelli & Tiranti, 2010), etc. Slope failures caused by infiltration of rain water typically occur in slopes which are marginally stable and consisting of various types of soils, such as colluvial and residual soils (Y Tsukamoto et al., 1998; Angeli et al., 2000). Besides being shallow in nature (generally less than 3 meters), rainfall-induced landslides are generally small in scale but large in aerial extent (Taro Uchimura et al., 2010). This fact reduces efficiency and economic viability of traditional landslide protection methods such as retaining structures, and soil improvement, etc. A useful and cost-efficient alternative is real-time monitoring of susceptible slope surfaces and issuing an early warning to reduce potential damages.

2.2.1 Mechanism of Rain-induced Landslides

The mechanism of rain-induced landslides has been investigated by several researchers (Brand, 1981; S. A. Anderson & Sitar, 1995; Farooq et al., 2004; Sorbino & Nicotera, 2012). Soil on a slope surface is generally in unsaturated state with soil matric suction forming a large part of soil shear strength. During a rainfall event, rainwater infiltrates the slope surface, thereby decreasing matric suction which in turn decreases the available shear strength of soil. The underlying mechanism along the potential failure plane is that, decreasing matric suction reduces the effective normal stress acting along the potential failure plane, which in turn diminishes the available shear strength to a point when equilibrium can no longer be sustained hence resulting in failure of slope. Although, the shear stress may actually increase as the soil profile becomes saturated, possibly increasing the stability of slope. However, in most of instances, failure occurs after some period of rainfall, at which point the increase in weight due to the final stage of saturation is quite small (Johnson, 1987). Moreover, S. Anderson (1992) showed that the increase in shear stress due to increase in weight is less than about 5%. Therefore, it is a safe assumption to ignore the increase in bulk unit weight due to water infiltration. Thus, ignoring the increase in bulk unit weight of

soil due to water infiltration, the process leading to failure essentially takes place under constant total stress condition and increasing pore water pressure.

2.2.2 Field Stress Conditions

Rain-induced slope failures generally occur in slopes which are steep and marginally stable (S. A. Anderson & Sitar, 1995; Y Tsukamoto et al., 1998). It shows that the initial stress state in the field is often quite close to failure and even small disturbance can trigger failure. The in-situ stresses within the soil layer are functions of slope angle, the unit weight of the soil, and depth of the soil (S. A. Anderson & Sitar, 1991, 1995). Seepage force, during and after rainfall, may also develop and add to gravity induced shear stress. In an infinite slope, these stresses can easily be resolved on a plane parallel to the slope, as shown in Figure 2.1. The resulting state of stress is anisotropic, with the degree of anisotropy depending on the slope angle.

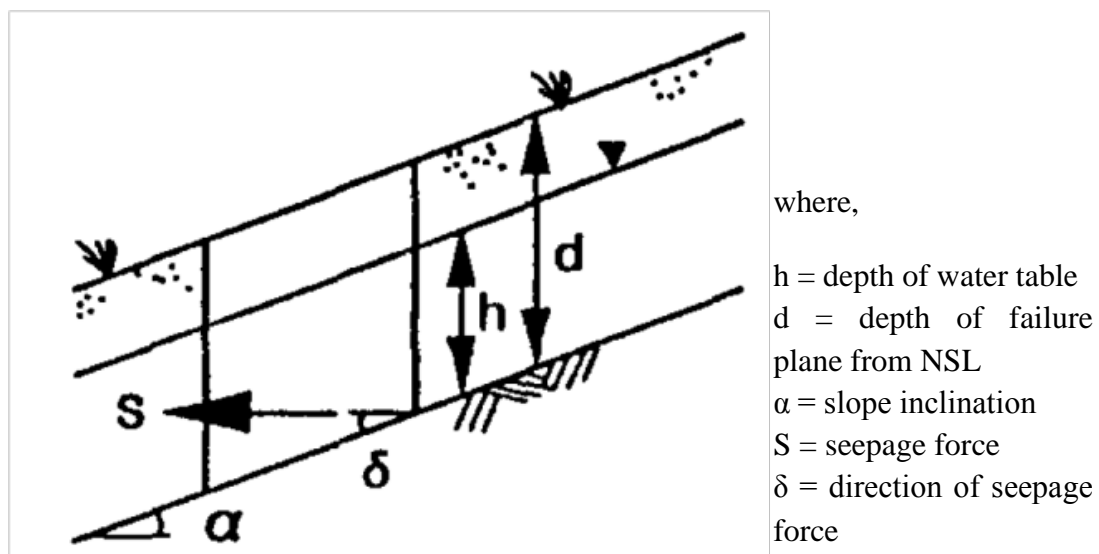


Figure 2.1: Schematic representation of forces acting on an infinite slope surface (after S. A. Anderson and Sitar (1995)).

Considering a well drained, infinite and planar slope and assuming that there is no linear strain on plane parallel to the surface of the slope, Vaughan and Kwan (1984) inferred the following equation for calculating initial principal stresses:

$$\sigma'_1 = \gamma Z \cos^2 \beta (1 - \tan \beta \cot 2\omega + \tan \beta \operatorname{cosec} 2\omega) \quad (2.1)$$

$$\sigma'_3 = \gamma Z \cos^2 \beta (1 - \tan \beta \cot 2\omega + \tan \beta \operatorname{cosec} 2\omega) \quad (2.2)$$

Where γ = unit weight of soil, Z = depth of the soil element, β = angle of the slope, ω = inclination angle of the principal stress with respect to the horizontal plane.

Lowe (1967) on the contrary, assumed that the initial principal stress orientations are approximately the same as their orientation at failure as shown in Figure 2.2. At failure, the major (σ'_1) and minor (σ'_3) principal stress directions are inclined to the failure plane at $(45 - \phi'/2)$ and $(45 + \phi'/2)$, respectively. This is an assumption that is probably reasonable for steep slopes that exist naturally at a state close to failure. Taking this assumption into account and neglecting seepage and capillary effects, S. A. Anderson and Sitar (1995) further derived the result that the in-situ principal stress ratio is independent of depth and has values approximately equal to one-tenth of the slope angle. Typical values of principal stress ratio (K), representing the field consolidation state, used in the laboratory testing by various researchers varies in the range of 1.4 ~ 5 (Brenner et al., 1985; S. A. Anderson & Sitar, 1995; Y Tsukamoto et al., 1998; Farooq et al., 2004; Melinda et al., 2004).

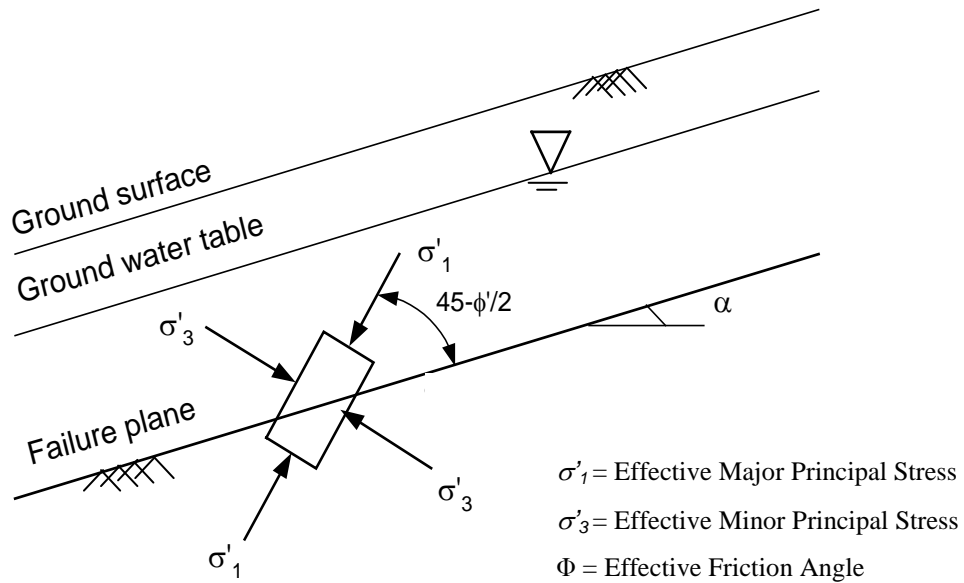


Figure 2.2: Resolution of stresses acting on a soil element during slope failure (after S. A. Anderson and Sitar (1991)).

2.2.3 Field Stress Path

In conventional triaxial tests, a soil element is subjected to increasing axial stress (σ_1) while maintaining the radial stress (σ_3) constant. However, such tests do not correctly depict the in-situ stress path followed by soil during rainfall induced failure. Brand (1981) postulated that the process leading to failure generally takes place under constant total stress condition and increasing pore water pressure from an initially unsaturated state. He further suggested that the field stress path can be simulated in laboratory element tests by one of the following tests methods;

1. Application of constant total stress (σ_1, σ_3 : constant) and increasing pore water pressure from initial negative value until the failure occurs.
2. Decreasing the radial stress (σ_3) while maintaining the axial stress (σ_1) constant.

Although both the methods yield the same stress path but the latter method is unable to simulate actual failure mechanism (Brand, 1981; Brenner et al., 1985). A description of such field stress path was provided by S. A. Anderson and Sitar (1995), as shown in Figure 2.3.

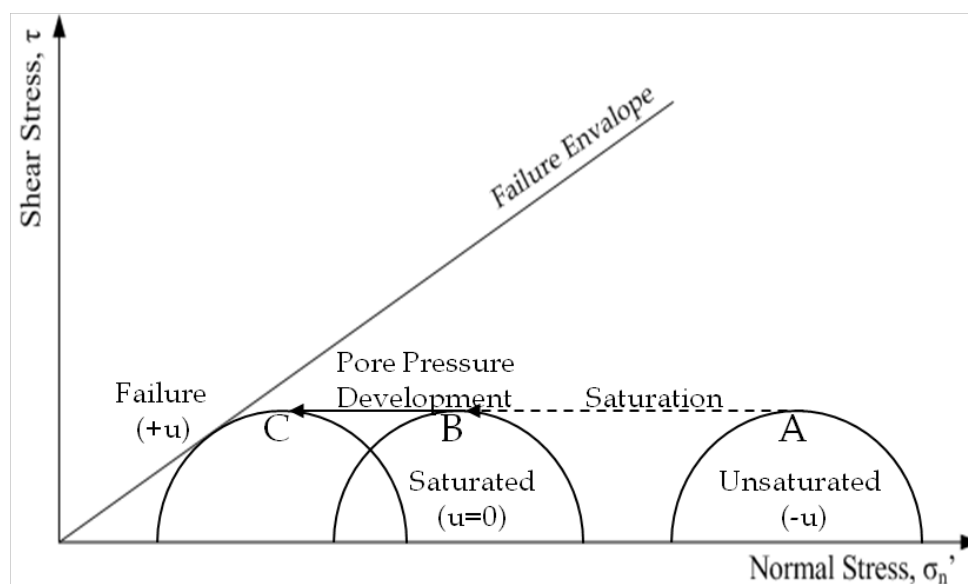
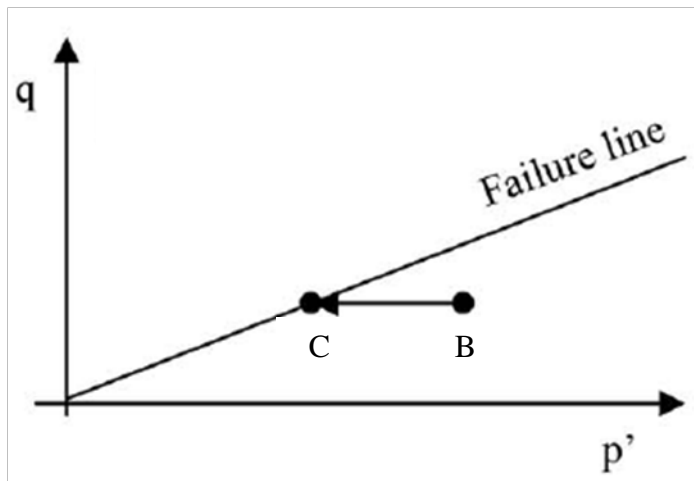


Figure 2.3: Field stress path adopted by soil element during rain-induced slope failures (after S. A. Anderson and Sitar (1995)).

A soil element lying on the slope surface is generally in the unsaturated state and possesses matric suction (negative pore water pressure); this state of soil element is shown by Mohr circle A in Figure 2.3. Matric suction gradually dissipates with water infiltration, causing a reduction in available shear strength and as a result Mohr circle shifts to point B. Further infiltration of water will cause an increase in pore water pressure and the Mohr circle of soil element would shift to point C, and ultimately reach failure. It is pertinent to consider that depending on the location of failure plane, slope may or may not fail at point B; e.g., for very steep slopes, the loss of shear strength only due to suction dissipation may be enough to trigger a failure; whereas Mohr circle may reach failure envelope only after sufficient positive pore water pressure has developed.



where,

δ = displacement

t = time

F_r = Resisting force

F_d = Disturbing force

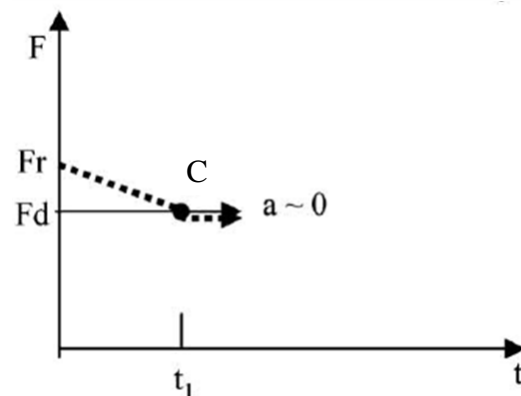
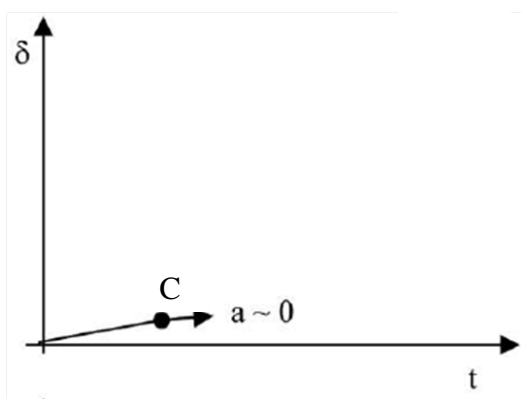


Figure 2.4: Behavior of soil element undergoing water infiltration (after Cascini et al. (2009)); (a) Stress path; (b) Development of strain with time; (c) Variation of resisting and disturbing force.

Further evidence of Mohr circle presented in Figure 2.4 was provided by Cascini et al. (2009), who showed that soil keep on deforming gradually upon water infiltration during rainfall; and on failure initiation (represented by point C), deformations continue at an accelerated rate (Figure 2.4(b)). Moreover he concluded that, the disturbing force does not vary much with rainfall, rather the failure occurs due to the decrease in resisting force as shown in Figure 2.4(c).

Several researchers have found that the most common failure mode is analogous to Mohr circle C (Figure 2.3), and requires the generation of positive pore water pressure for failure to be attained (Eckersley, 1990; Johnson & Sitar, 1990; Sitar et al., 1992). This implies that the soil element along the potential failure plane, at the time of failure, is nearly saturated and any increase in the bulk unit weight of the soil due to saturation is negligible. In other words, the field stress path followed by a soil element during rainfall is characterized by pore pressure increase at almost constant shear stress condition as represented by horizontal line in Figure 2.3. Note that the magnitude of shear stress during the hydrologic response of soil to rainfall can change depending on the direction of seepage flow, and the field stress path may deviate from horizontal. However, such deviation may be considered relatively small and the exact nature of seepage flow is unknown (S. A. Anderson & Sitar, 1995). Therefore, the horizontal stress path can be considered a reasonable assumption for the hydrologic response of soil due to rainfall.

Brand (1981) further suggested that the typical stress ranges over which triaxial tests are usually conducted are not appropriate for laboratory simulation of rain-induced slope failures. Owing to the shallow depth of majority of rain-induced landslides, stresses lower than conventional triaxial tests are required to be applied. Figure 2.5 illustrates the disparity between the stress paths normally followed in conventional triaxial tests, i.e., consolidated undrained (CU) and consolidated drained (CD), and the path which reflects the field condition. In order to obtain the meaningful shear properties from laboratory tests for the analysis and design of slopes subjected to rainwater infiltration, it is essential to simulate the field stress path as close as possible while conducting the laboratory testing.

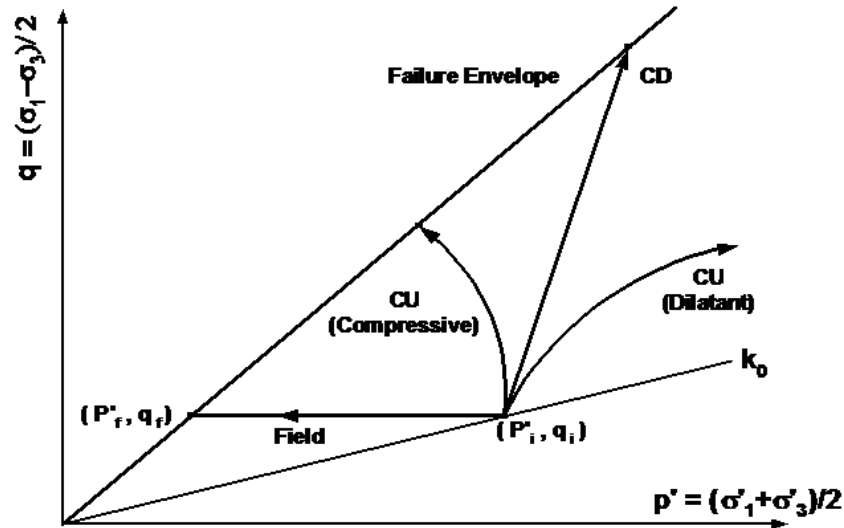


Figure 2.5: A comparison of field stress path with various types of conventional triaxial tests (after Brand (1981)).

2.3. LANDSLIDE EARLY WARNING SYSTEMS

Although the practical use of landslide prediction systems is still scarce, yet slowly but gradually, the world is realizing the significance of landslide early warning system. In recent years several researchers have presented various ideas for the prediction of landslides and have also discussed their significance (Zan et al., 2002; Hong & Adler, 2007; Intrieri et al., 2012; Thiebes et al., 2013). Landslide prediction around the world is generally done through landslide hazard maps, by using rainfall thresholds, or through real-time monitoring. A brief description of these methods along with their pros and cons is described in the following sections.

2.3.1 Landslide Susceptibility Maps

Majority of landslide hazard maps are mainly derived through rainfall ~ landslide historical data. Although such maps are often useful by emergency managers and general public to locate possible danger zones but beyond that, they can not identify exact locations of slope failures. However, maps of real-time storm rainfall estimates can be overlaid on landslide hazard maps through geographic information system (GIS). This can help emergency managers to identify which areas are at great risk during a particular storm (R. Baum & Godt, 2010).

2.3.2 Early Warning Based on Rainfall Thresholds

The most commonly used landslide hazard prediction method around the world is based on various rainfall thresholds e.g., quantity, duration or intensity of a storm; or in some cases the amount of antecedent rainfall is also used as warning criteria (Terlien, 1998; Brigandi et al., 2012; Rossi et al., 2012). To avoid landslide based accidents, Japan Railway Company (JR-East) employs a similar concept for safe operation of its rail cars during rainfall. Based on the combination of rainfall intensity (mm/hr) and accumulated rainfall (mm), the train service is regulated or even completely stopped between two stations, as schematically shown in Figure 2.6.

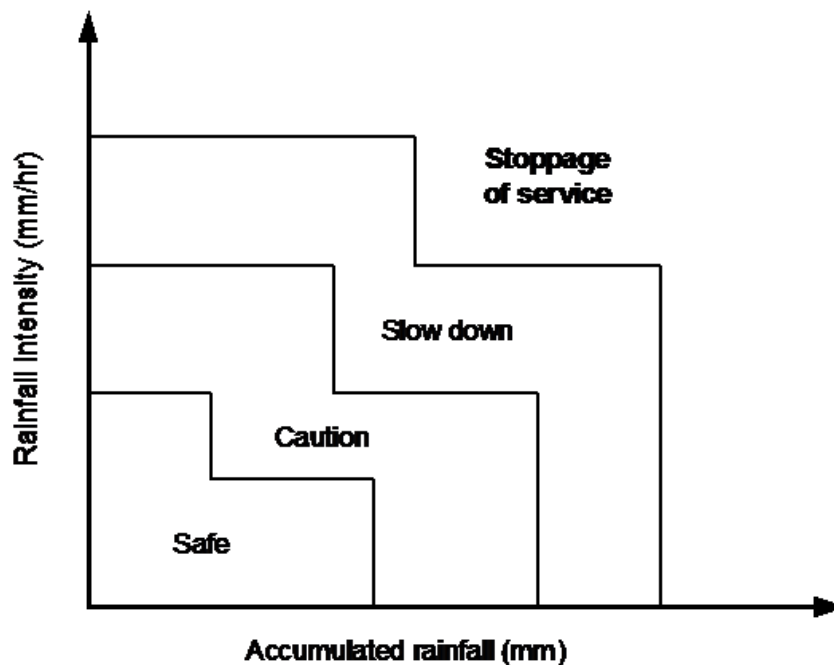


Figure 2.6: Schematic representation of methodology adopted by Japan railway (JR-East) to avoid landslide related accidents.

Majority of rainfall thresholds are mainly based on the analysis of historical landslide and rainfall data and developing such thresholds for new areas is very time consuming and tedious task. Additionally, the amount of rainfall required to initiate landslide varies with soil type, geology, climate, vegetation, topography, etc., therefore such thresholds exhibit a high degree of variability from place to place (R. Baum & Godt,

2010). This phenomenon is highlighted in Figure 2.7, which shows the rainfall thresholds for various regions across United States.

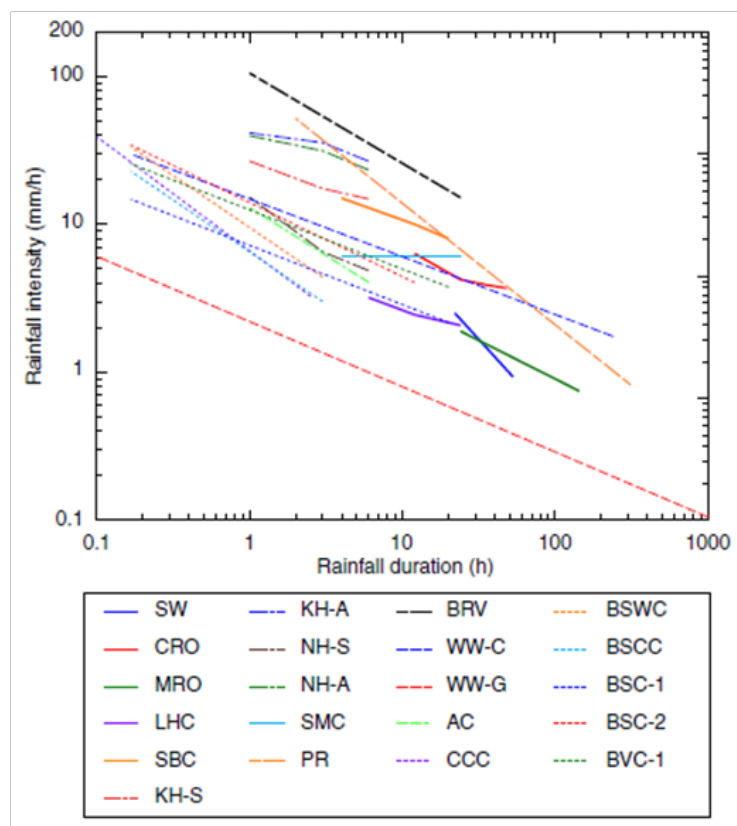


Figure 2.7: Precipitation intensity and duration thresholds for landslide occurrence in various States of US (R. Baum & Godt, 2010).

Note: Symbols in the legend are acronyms of different States.

2.3.3 Real-time Landslide Monitoring through Instrumentation

Landslide hazard maps and rainfall thresholds for landslides can provide an idea about the possibility of occurrence of a landslide; however, prediction by these methods can be highly uncertain and inefficient. Nature of soil profile, drainage conditions, depth of ground water, vegetation, etc., which can greatly affect landslide initiation, are generally not considered in various rainfall threshold models. Actual monitoring of slope movements, soil moisture/suction, etc., lay down new avenues for landslide early warning and can also help overcoming the previously mentioned limitations of landslide hazard maps, and rainfall threshold models. Key questions required to be answered for real-time slope monitoring include “*what parameters to monitor?*” and

“when to issue the warning?”. Various researchers have successfully monitored physical movements of slope surfaces leading to a failure by means of extensometers (Angeli et al., 2000; Taro Uchimura et al., 2011), inclinometers (Lollino et al., 2002; Taro Uchimura et al., 2010; T. Uchimura, 2011), draw wire displacement transducers (Arnhardt et al., 2007), etc. Taro Uchimura et al. (2010) showed that monitoring of soil moisture is necessary for efficient landslide prediction. Monitoring of soil moisture condition during rainfall is generally carried out by means of ceramic cups or tensiometers (for determining matric suction), and dielectric moisture sensors for the determination of volumetric water content of soil (Taro Uchimura et al., 2010; Ramesh & Vasudevan, 2012). Although the changes in slope displacements and soil moisture/suction have proved to give indications of failure; however, the formulation of an efficient early warning criterion is still restricted because of the absence of ample data. Some preliminary ideas towards the development of real-time landslide early warning criteria include Taro Uchimura et al. (2013) and M.-I. Kim et al. (2013). Based on landslide monitoring of an artificial rainfall experiment, Taro Uchimura et al. (2013) suggested to watch the slope movements by means of tilt sensor. Failure was observed to trigger when rates of tilting were between 0.1 and 0.5 degree/hour. Thus an early warning system based on tilt angle can be suggested, e.g., a preliminary warning can be issued when rate of slope movement reaches about 0.01 degree/hour, and on similar lines, a final emergency can be announced when slope starts moving at a rate of about 1 degree/hour. Similarly, (M.-I. Kim et al., 2013) suggested an early warning criterion based on soil volumetric water content gradient. They showed volumetric water content of soil to be more efficient in predicting slope failure compared to pore water pressure. They also observed the landslides to be triggered when volumetric water content gradient exceeded 0.1. Based on this observation they suggested issuing an early warning when volumetric water content gradient exceeded 0.1; at the same time they suggested a need to verify this criterion for other site conditions.

2.4. ELASTIC WAVE PROPAGATION IN SOIL

In an infinite medium, two fundamental modes of seismic waves, namely compression waves and shear waves exist (Kolsky, 1963; White, 1983; Achenbach, 1984). In compression waves (also known as primary waves or *P*-waves), particles of the medium vibrate in a direction parallel to the direction of propagation of wave, whereas in shear waves (also known as secondary waves or *S*-waves) vibration of particles is perpendicular to the direction of wave propagation (Figure 2.8).

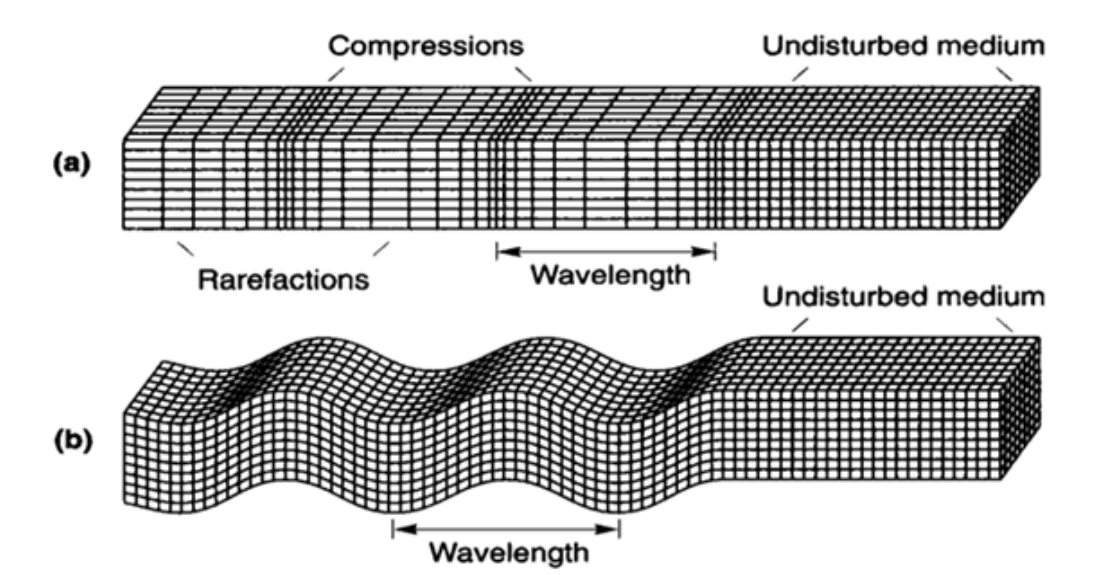


Figure 2.8: Particle motion in (a) Compression waves; (b) Shear waves (Kramer, 1996)

In geotechnical engineering, elastic waves have been widely used for geomaterials, and site characterization. One of their major benefits is the non-invasive/non-destructive nature of majority of geophysical experiments. Thus, the required geomaterials or site characterization can be achieved without causing any noticeable disturbance to soil. Majority of geotechnical laboratory studies are focused solely on shear wave propagation in soil, because soil is mostly loaded in shear and thus its behavior is better explained by shear modulus. Also until recently, majority of geotechnical engineering laboratory studies, were conducted in saturated soil

conditions. As P -wave can propagate not only through soil skeleton but also through pore fluid, thus they could not be used to determine requisite geotechnical properties. Various researchers including Allen et al. (1980), Kokusho (2000), and Yoshimichi Tsukamoto et al. (2002) have studied the effect of saturation (only close to full saturation state) on compression wave velocities. Typical variation of compression wave velocity with degree of saturation (from 99.4% to 100%) is shown in Figure 2.9.

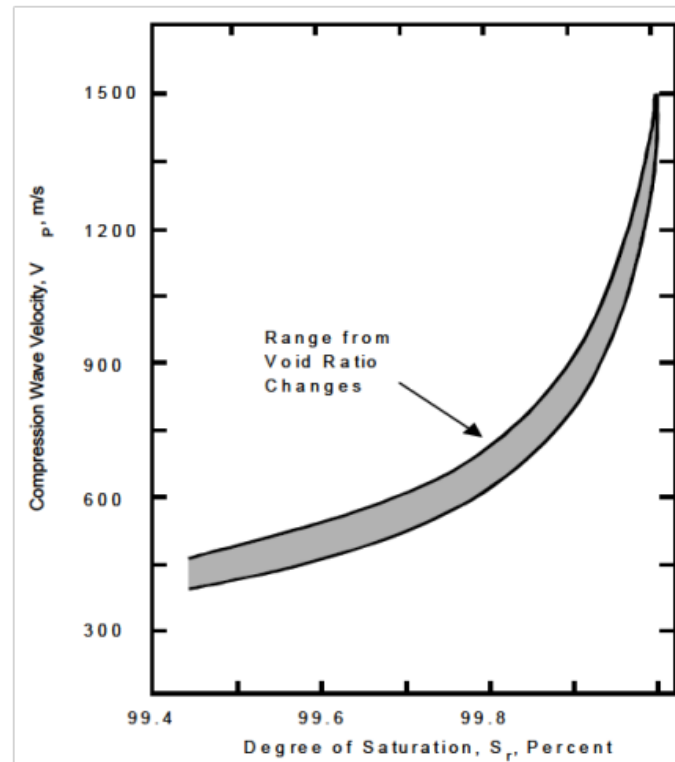


Figure 2.9: Typical variation in compression wave velocity with degree of saturation changing from 99.4% to 100% for sand (after Allen et al. (1980)).

Shear wave velocity on the other hand remains largely unaffected by very small changes in saturation ratio near the fully saturated state (Kokusho, 2000; K. H. Stokoe & Santamarina, 2000). This is mainly because of zero shear stiffness of pore fluids, and thus shear waves propagate solely through the soil skeleton. However, an emerging interest in unsaturated soil mechanics is making the use of compression wave velocities more and more meaningful as it can provide an assessment of saturation ratio as well as porosity of unsaturated soil specimen (Brignoli et al., 1996).

2.4.1 Factors Influencing Elastic Wave Propagation in Soil

Early studies on elastic wave propagation in soil were carried out by means of resonant column apparatus, in which wave velocities were determined in terms of small-strain stiffness of soil. Due to the reasons described in previous section, these studies were limited to determination of shear modulus (based on shear wave velocity only). The generalized relationship explaining shear wave velocity, V_s , can be expressed as (B. O. Hardin & Richart, 1963; B. O. Hardin, 1978);

$$V_s = C_s \cdot \sqrt{F(e)} \cdot \left(\frac{\sigma'_o}{P_a} \right)^n \quad (2.3)$$

where σ'_o represents effective isotropic stress, C_s and n are material constants associated with the type of grains, the nature of contacts and the stability of soil skeleton. P_a is the atmospheric pressure which is in the same units as σ'_o , and $F(e)$ is known as the void ratio function. In unsaturated soil, constrained compression wave velocity, V_p , was assumed to follow the same functional relationship with the only change being the difference in material constant, C_p .

2.4.1.1 Effective Stress State

Some of the earliest studies exploring the effects of effective stress state on shear wave velocities in dry and saturated soils were conducted by B. O. Hardin and Richart (1963), B. Hardin and Black (1968), and B. O. Hardin and Drnevich (1972). Based on experimental evidence, as reproduced in Figure 2.10, and mathematical relationships similar to the one presented in Eq. 2.3, they suggested that both shear and compression wave velocities vary with approximately $1/4$ power of confining pressure. The existence of a similar phenomenon for various other types of soils was also reported by several other researchers (Marcuson & Wahls, 1972; Iwasaki et al., 1978; Kokusho, 1980; T. Kim & Novak, 1981).

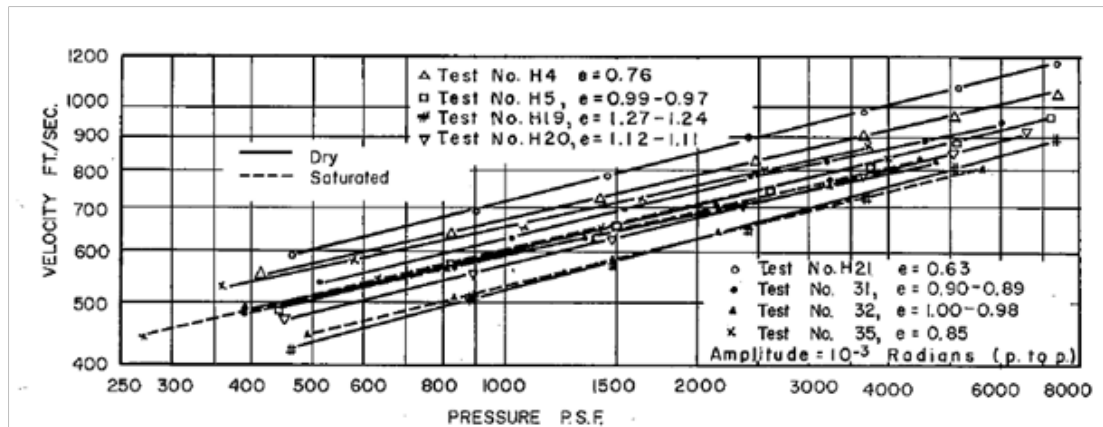


Figure 2.10: Variation of shear wave velocity with confining pressure and void ratio for saturated and dry crushed quartz sand (B. O. Hardin & Richart, 1963).

More recent studies with reconstituted soils subjected to anisotropic stress states have shown the dependency of elastic wave propagation on principle stress directions (Roesler, 1979; K. Stokoe et al., 1991; Bellotti et al., 1996). Compression wave velocity, V_p , depends only the state of stress in the direction of wave propagation, whereas the magnitude of shear wave velocity, V_s , is found to be dependent on the state of stress in the direction of wave propagation as well as particle vibration (Stokoe II et al., 1995; K. H. Stokoe & Santamarina, 2000).

2.4.1.2 Void Ratio

Some of the earliest studies related to elastic wave propagation realized the significance of void ratio on wave velocities (B. O. Hardin & Richart, 1963; B. Hardin & Black, 1968; Iwasaki et al., 1978). By using resonant-column experiments, B. O. Hardin and Richart (1963) provided experimental evidence for the behavior of shear wave velocity with void ratio, as shown in Figure 2.11.

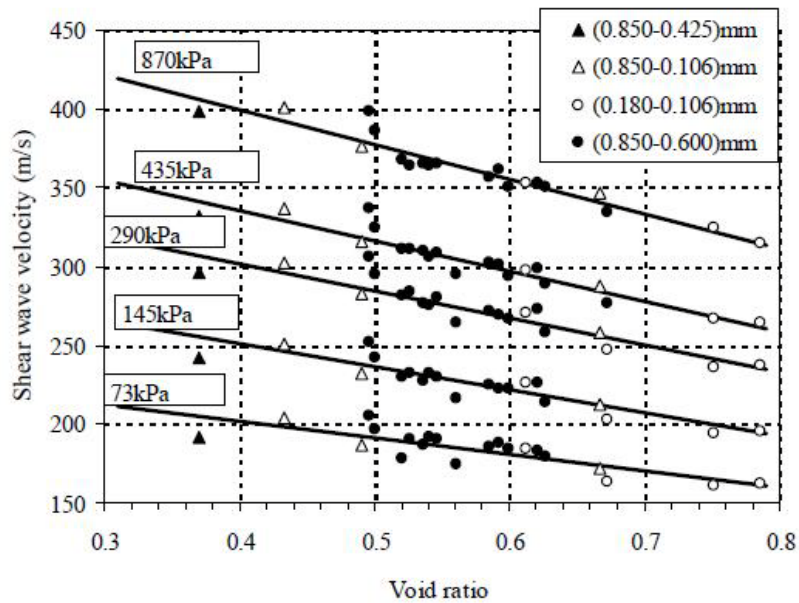


Figure 2.11: Shear wave velocity variation with void ratio for different stress states (after B. O. Hardin and Richart (1963))

To account for the varying stress conditions in Figure 2.11, shear wave velocities can be normalized by using Eq. 2.3. Shear wave velocities, normalized for isotropic stress level show a near linear decrease with void ratio (Figure 2.12).

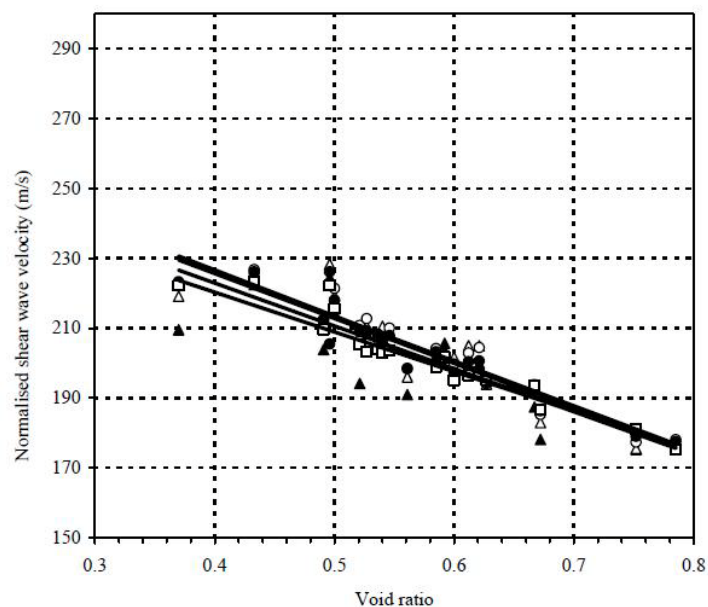


Figure 2.12: Shear wave velocity variation with void ratio. Wave velocities normalized by using Eq. 2.3 to cancel the effect of stress state (after B. O. Hardin and Richart (1963)).

During triaxial experiments, changes in stress level and/or other parameters cause a change in void ratio, which would in turn affect shear wave velocities. Void ratio function, $F(e)$, defined in Eq 2.3, is therefore used to normalize wave velocities for any changes in void ratio. Using different soil types and ranges of void ratio, several researchers have proposed different models of $F(e)$ which are summarized in Table 2.1.

Table 2.1: Void ratio function, $F(e)$, as suggested by various researchers (after (Yimsiri, 2001)).

<i>Soil type</i>	<i>A</i>	<i>F(e)</i>	<i>n</i>	<i>Void ratio range</i>	<i>Test Method</i>	<i>Reference</i>
Sand						
Round-grain Ottawa sand	6,900	$\frac{(2.174 - e)^2}{1 + e}$	0.5	0.3-0.8	RC	(B. O. Hardin & Richart, 1963)
Angular-grain crushed quartz	3270	$\frac{(2.973 - e)^2}{1 + e}$	0.5	0.6-1.3	RC	(B. O. Hardin & Richart, 1963)
Several Sands	9000	$\frac{(2.17 - e)^2}{1 + e}$	0.4	0.6-0.9	RC	(Iwasaki et al., 1978)
Toyoura Sand	8000	$\frac{(2.17 - e)^2}{1 + e}$	0.5	0.6-0.8	Cyclic TX	(Kokusho, 1980)
Several cohesionless and cohesive soils	4500-140000	$\frac{1}{0.3 + 0.7e^2}$	0.5	N/A	RC	(B. O. Hardin & Blandford, 1989)
Ticino Sand	7100	$\frac{(2.27 - e)^2}{1 + e}$	0.43	0.6-0.9	RC and TS	(Lo Presti et al., 1993)

Clays						
Reconstituted NC Kaoline	3270	$\frac{(2.973 - e)^2}{1 + e}$	0.5	0.5-1.5	RC	(B. Hardin & Black, 1968)
Several undisturbed NC clays	3270	$\frac{(2.973 - e)^2}{1 + e}$	0.5	0.5-1.7	RC	(B. Hardin & Black, 1968)
Reconstituted NC Kaoline	4500	$\frac{(2.973 - e)^2}{1 + e}$	0.5	1.1-1.3	RC	(Marcuson & Wahls, 1972)
Reconstituted NC bentonite	450	$\frac{(4.4 - e)^2}{1 + e}$	0.5	1.6-2.5	RC	(Marcuson & Wahls, 1972)
Several Undisturbed silts and clays	893- 1726	$\frac{(2.973 - e)^2}{1 + e}$	0.46- 0.61	0.4-1.1	RC	(T. Kim & Novak, 1981)
Undisturbed NC clay	90	$\frac{(7.32 - e)^2}{1 + e}$	0.6	1.7-3.8	Cyclic TX	(Kokusho et al., 1982)
Undisturbed Italian Clays	4400- 8100	$e^{-1.3}$ (average from e^{-x} : $x=1.11-1.43$) $e^{-1.5}$	0.40- 0.58	0.6-1.8	RC and BE	(Jamiolkowski et al., 1995)
Several soft clays	5000	$e^{-1.5}$	0.5	1-5	SCPT	(Satoru Shibuya & Tanaka, 1996)
Several Soft Clays	18000- 30000	$\frac{1}{(1 + e)^{2.4}}$	0.5	1-6	SCPT	(S Shibuya et al., 1998)

RC: resonant column test, TX: triaxial test, TS: torsional shear test, BE: bender element test, SCPT: seismic cone test

2.4.1.3 Degree of Saturation

Shear wave depends on the shear stiffness of soil skeleton. Compression wave velocity, on the other hand is governed by constrained compression modulus of soil, $M=B+4G/3$, therefore it is influenced by both, the pore fluid and soil skeleton (K. H. Stokoe & Santamarina, 2000). Qian et al (1991) used resonant column to study the response of shear wave velocities in low saturation ranges (0% to 50% saturation). They expressed shear wave velocity in terms of small strain shear modulus, G , of soil. They observed the presence of a certain peak in shear modulus with soil saturation. This peak was found to be dependent upon external confining pressure and percentage of fines. However, the peak remained unaffected by mean particle size of soil. A summary of their experimental study is presented in Figure 2.13.

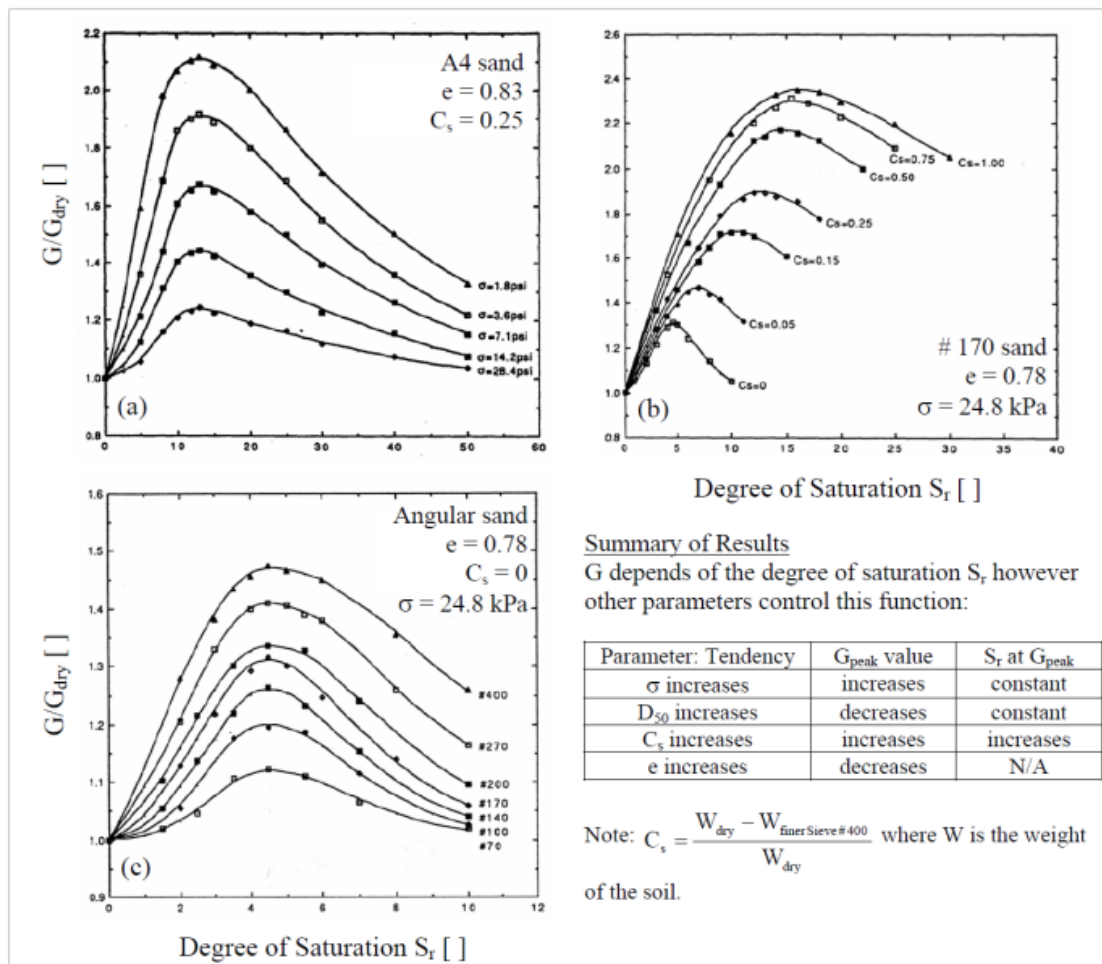


Figure 2.13: Shear stiffness of unsaturated soils versus (a) degree of saturation and confining pressure, (b) degree of saturation and fine content, and (c) degree of saturation confining pressure as tested in a resonant column device. (after Qian et al. (1991))

Mancuso et al. (2002) investigated the small strain behavior of unsaturated compacted silty sand using a resonant column – torsional shear cell fitted with a suction control assembly. They also expressed the results of observed shear wave velocities in terms of initial shear stiffness, G_o . They observed S-shaped shear stiffness versus suction variation. They explained it based on the progressive change from bulk-water regulated soil response, observed close to saturation state, to a menisci-water regulated soil response which was observed at relatively drier stages of the experiment, as shown in Figure 2.14. They also noted that for suction values higher than 200 kPa, shear stiffness mainly depended on net stress level only.

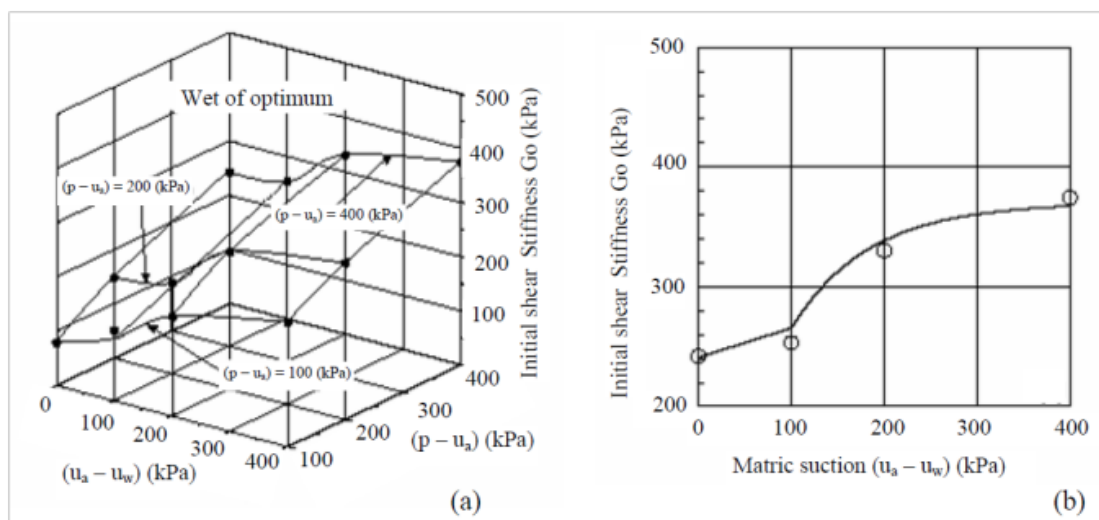


Figure 2.14: (a) Initial shear stiffness in controlled-suction resonant column tests. (b) Response of shear stiffness to suction at a mean net stress of 400 kPa. (Mancuso et al., 2002)

Cho & Santamarina (2001) conducted bender element tests on various cohesive soils specimens. They examined the variation of shear wave velocity with soil saturation. Specimens were allowed dry from an initially saturated state and shear wave velocities were determined at various saturation ratios. As the specimens dried, they observed a gradual increase in shear wave velocities; however, a rapid increase in V_s was observed close to fully dry state, as shown in Figure 2.15. They explained this increase in wave velocity based on the increased bonding between fine-grained soil particles with drying. A similar observation was later made by Alramahi et al (2010),

when he conducted similar experiments on clay and silt specimens with different pore fluids (Figure 2.16).

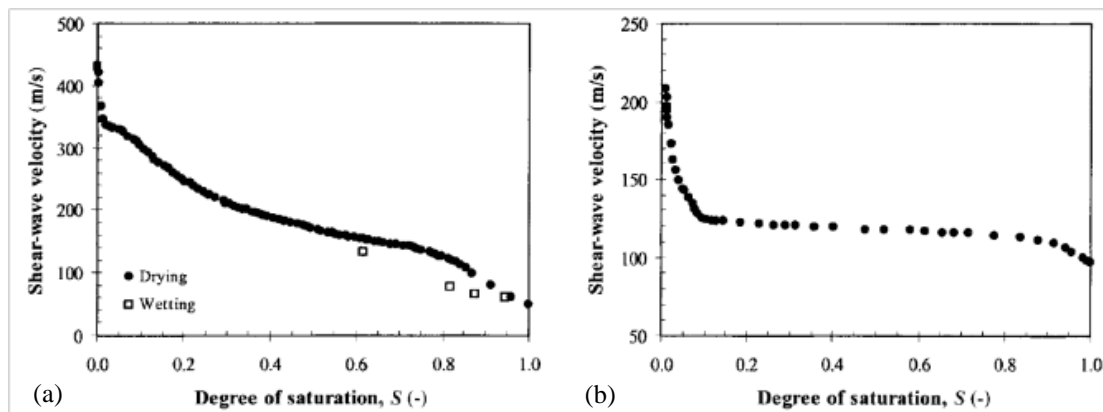


Figure 2.15: Shear wave velocity versus degree of saturation; (a) Granite Powder; (b) Sandboil sand. (Cho & Santamarina, 2001)

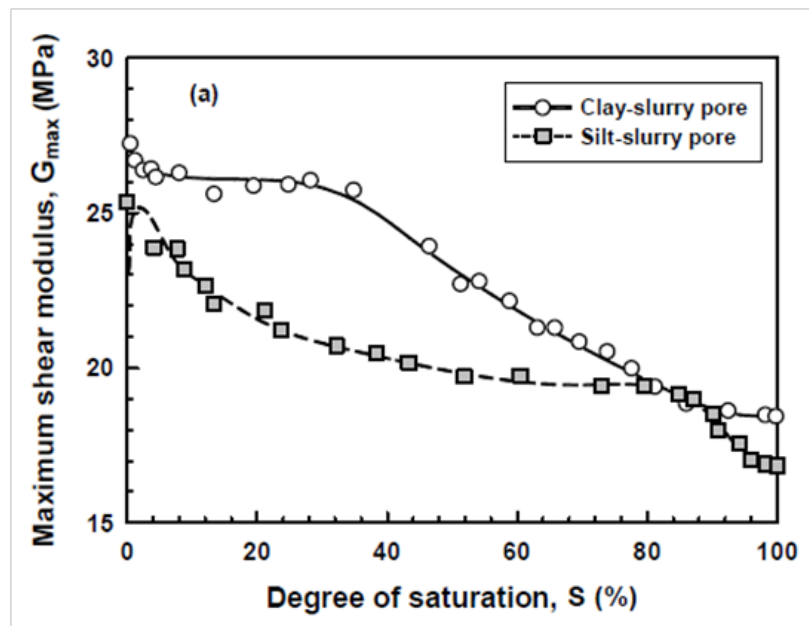


Figure 2.16: Variation of shear wave velocity (in terms of shear modulus) with degree of saturation. (Alramahi et al., 2009)

As can be observed from the discussion hereinbefore, most of these studies were limited to fine grained soils, and mainly explored the behavior during drying stage. The corresponding behavior for sands/silty sands, which form a large portion of natural slopes in Japan and various other parts of the world, is still unexplored. Also during rainfall-induced landslides, soil progressively gets wet from an initially dry state. Behavior of wave velocities during soil wetting is therefore required to be investigated. Additionally, almost all of the above mentioned studies were limited to shear wave velocities, and none of them directly explored the variation of compression wave velocity with changing soil saturation. Thus in the present study, the response of shear wave, as well as compression wave velocities with soil saturation state are explored.

2.5. SUMMARY

The fundamental concepts which form the backbone of this study are discussed in this chapter. The overall discussion presented in this chapter is categorized in two broad fields; *(i)* rainfall-induced landslides, and *(ii)* elastic wave propagation in soil. In the first section, basic mechanism of rain-induced and the importance of field stress path is discussed. Various landslide early warning systems, along with their merits and demerits are presented. Since the main aim of this study is to devise a landslide prediction method based on elastic waves, thus second half of this chapter was dedicated in presenting a comprehensive overview of elastic wave propagation in soils. An extensive literature survey compiling the results of several previous researches in this regard is also presented.

2.6. REFERENCES

- Achenbach, J. (1984). *Wave Propagation in Elastic Solids*. North-Holland, New York.
- Allen, N. F., Richart Jr, F., & Woods, R. (1980). Fluid Wave Propagation in Saturated and Nearly Saturated Sands. *Journal of Geotechnical and Geoenvironmental Engineering*, 106(ASCE 15286).
- Alramahi, B., Alshibli, K. A., & Fratta, D. (2009). Effect of Fine Particle Migration on the Small-Strain Stiffness of Unsaturated Soils. *Journal of Geotechnical and Geoenvironmental Engineering*, 136(4), 620-628.
- Anderson, S. (1992). *The Role of Hydrologic Response and Soil Behavior in the Initiation of Rainfall-Induced Debris Flows*. PhD Thesis, Univeristy of California, Berkeley, California.
- Anderson, S. A., & Sitar, N. (1991). *Influence of Stress Path on Soil Strength Parameters and Analysis of Rainfall Induced Slope Failures*. Proceedings: Symp. Eng. Geol. Geotech. Eng (pp. 21-26).
- Anderson, S. A., & Sitar, N. (1995). Analysis of Rainfall-Induced Debris Flows. *Journal of Geotechnical Engineering*, 121(7), 544-552.
- Angeli, M.-G., Pasuto, A., & Silvano, S. (2000). A Critical Review of Landslide Monitoring Experiences. *Engineering Geology*, 55(3), 133-147.
- Arnhardt, C., Asch, K., Azzam, R., Bill, R., Fernandez-Steeger, T., Homfeld, S., . . . Toloczyki, M. (2007). Sensor Based Landslide Early Warning System-Slews. Development of a Geoservice Infrastructure as Basis for Early Warning Systems for Landslides by Integration of Real-Time Sensors. *Geotechnologien science report*, 10, 75-88.
- Au, S. (1998). Rain-Induced Slope Instability in Hong Kong. *Engineering Geology*, 51(1), 1-36.
- Ayalew, L., Yamagishi, H., Marui, H., & Kanno, T. (2005). Landslides in Sado Island of Japan: Part II. Gis-Based Susceptibility Mapping with Comparisons of

- Results from Two Methods and Verifications. *Engineering Geology*, 81(4), 432-445.
- Baum, R., & Godt, J. (2010). Early Warning of Rainfall-Induced Shallow Landslides and Debris Flows in the USA. *Landslides*, 7(3), 259-272. doi: 10.1007/s10346-009-0177-0
- Baum, R. L., Coe, J. A., Godt, J. W., Harp, E. L., Reid, M. E., Savage, W. Z., . . . McKenna, J. P. (2005). Regional Landslide-Hazard Assessment for Seattle, Washington, USA. *Landslides*, 2(4), 266-279.
- Bellotti, R., Jamiolkowski, M., Lo Presti, D., & O'Neill, D. (1996). Anisotropy of Small Strain Stiffness in Ticino Sand. *Geotechnique*, 46(1), 115-132.
- Brand, E. W. (1981). Some Thoughts on Rain-Induced Slope Failures. *Proc. of 10th International Conference on Soil Mechanics and Foundation Engineering*, 3, 373-376.
- Brenner, R. P., Tam, H. K., & Brand, E. W. (1985). Field Stress Path Simulation of Rain-Induced Slope Failure. *Proc. of 11th International Conference on Soil Mechanics and Foundation Engineering*, 2, 991-996.
- Brigandi, G., Aronica, G., Basile, G., Pasotti, L., & Panebianco, M. (2012). *An Experimental Operative System for Shallow Landslide and Flash Flood Warning Based on Rainfall Thresholds and Soil Moisture Modelling*. Proceedings: EGU General Assembly Conference Abstracts (pp. 11730).
- Brignoli, E. G. M., Gotti, M., & Stokoe, K. H. (1996). Measurement of Shear Waves in Laboratory Specimens by Means of Piezoelectric Transducers. *Geotechnical Testing Journal, GTJODJ*, 19(4), 384-397. doi: 10.1520/GTJ10716J
- Capparelli, G., & Tiranti, D. (2010). Application of the Moniflair Early Warning System for Rainfall-Induced Landslides in Piedmont Region (Italy). *Landslides*, 7(4), 401-410.

- Cascini, L., Cuomo, S., Pastor, M., & Sorbino, G. (2009). Modeling of Rainfall-Induced Shallow Landslides of the Flow-Type. *Journal of Geotechnical and Geoenvironmental Engineering*, 136(1), 85-98.
- Chen, H., Dadson, S., & Chi, Y.-G. (2006). Recent Rainfall-Induced Landslides and Debris Flow in Northern Taiwan. *Geomorphology*, 77(1), 112-125.
- Cho, G. C., & Santamarina, J. C. (2001). Unsaturated Particulate Materials-Particle-Level Studies. *Journal of Geotechnical and Geoenvironmental Engineering*, 127(1), 84-96.
- Dai, F., & Lee, C. (2002). Landslide Characteristics and Slope Instability Modeling Using Gis, Lantau Island, Hong Kong. *Geomorphology*, 42(3), 213-228.
- Eckersley, D. (1990). Instrumented Laboratory Flowslides. *Geotechnique*, 40, 489-502.
- Farooq, K., Orense, R., & Towhata, I. (2004). Response of Unsaturated Sandy Soils under Constant Shear Stress Drained Condition. *Soils and foundations*, 44(2), 1-13.
- Fuchu, D., Lee, C., & Sijing, W. (1999). Analysis of Rainstorm-Induced Slide-Debris Flows on Natural Terrain of Lantau Island, Hong Kong. *Engineering Geology*, 51(4), 279-290.
- Guzzetti, F., Cardinali, M., Reichenbach, P., Cipolla, F., Sebastiani, C., Galli, M., & Salvati, P. (2004). Landslides Triggered by the 23 November 2000 Rainfall Event in the Imperia Province, Western Liguria, Italy. *Engineering Geology*, 73(3), 229-245.
- Guzzetti, F., Carrara, A., Cardinali, M., & Reichenbach, P. (1999). Landslide Hazard Evaluation: A Review of Current Techniques and Their Application in a Multi-Scale Study, Central Italy. *Geomorphology*, 31(1), 181-216.
- Guzzetti, F., Peruccacci, S., Rossi, M., & Stark, C. P. (2008). The Rainfall Intensity-Duration Control of Shallow Landslides and Debris Flows: An Update. *Landslides*, 5(1), 3-17.

- Hardin, B., & Black, W. (1968). Vibration Modulus of Normally Consolidated Clay. *J. Soil Mech. and Found. Div., ASCE*, 94, 353-369.
- Hardin, B. O. (1978). *The Nature of Stress-Strain Behavior for Soils*. Proceedings: ASCE Geotechnical Engineering Division Specialty Conference: Earthquake Engineering and Soil Dynamics (pp. 3-91), Pasadena, California.
- Hardin, B. O., & Blandford, G. E. (1989). Elasticity of Particulate Materials. *Journal of Geotechnical Engineering*, 115(6), 788-805.
- Hardin, B. O., & Drnevich, V. P. (1972). Shear Modulus and Damping in Soils: Design Equation and Curves. *J. Soil Mech. Found. Engng. Div., ASCE* 98(7), 667-691.
- Hardin, B. O., & Richart, F. E. (1963). Elastic Wave Velocities in Granular Soils. *J. Soil Mech. and Found. Div., ASCE*, 89(1), 33-65.
- Hong, Y., & Adler, R. (2007). Towards an Early - Warning System for Global Landslides Triggered by Rainfall and Earthquake. *International journal of remote sensing*, 28(16), 3713-3719.
- Intrieri, E., Gigli, G., Mugnai, F., Fanti, R., & Casagli, N. (2012). Design and Implementation of a Landslide Early Warning System. *Engineering Geology*.
- Iverson, R. M. (2000). Landslide Triggering by Rain Infiltration. *Water Resources Research*, 36(7), 1897-1910.
- Iwasaki, T., Tatsuoka, F., & Takagi, Y. (1978). Shear Moduli of Sands under Cyclic Torsional Shear Loading. *Soils and Foundations*, 18(1), 39-56.
- Jamiolkowski, M., Lancellotta, R., & Lo Presti, D. (1995). *Remarks on the Stiffness at Small Strains of Six Italian Clays*. Proceedings: Pre-failure Deformation of Geomaterials (pp. 817-836), Sapporo, Japan.
- Johnson, K. (1987). *An Investigation of the Mechanisms of Debris Flow Initiation*. PhD Thesis, University of California Berkeley, California.

- Johnson, K., & Sitar, N. (1990). Hydrologic Conditions Leading to Debris-Flow Initiation. *Canadian Geotechnical Journal*, 27(6), 789-801.
- Kim, M.-I., Lee, M., Kim, M., Cho, G., & Chae, B.-G. (2013). *Monitoring of the Variation of Volumetric Water Content Due to Rainfall Infiltration for Landslide Early Warning*. Proceedings: 3rd Korea-Japan Joint Workshop on Unsaturated Soils (pp. 89-105), Seoul, South Korea.
- Kim, T., & Novak, M. (1981). Dynamic Properties of Some Cohesive Soils of Ontario. *Canadian Geotechnical Journal*, 18(3), 371-389.
- Kokusho, T. (1980). Cyclic Triaxial Test of Dynamic Soil Properties for Wide Strain Range. *Soils and foundations*, 20(2), 45-60.
- Kokusho, T. (2000). Correlation of Pore-Pressure B-Value with P-Wave Velocity and Poisson's Ratio for Imperfectly Saturated Sand or Gravel. *Soils and foundations*, 40(4), 95-102.
- Kokusho, T., Yoshida, Y., & Esashi, Y. (1982). Dynamic Properties of Soft Clay for Wide Strain Range. *Soils and foundations*, 22(4), 1-18.
- Kolsky, H. (1963). *Stress Waves in Solids* (Vol. 1098): Courier Dover Publications.
- Kramer, S. L. (1996). *Geotechnical Earthquake Engineering*: Pearson Education India.
- Lin, H., Kung, J., Rahardjo, H., Toll, D., & Leong, E. (2000). *Rainfall-Induced Slope Failures in Taiwan*. Proceedings: Asian Conference on Unsaturated Soils, UNSAT-Asia 2000, Singapore, 18-19 May, 2000. (pp. 801-806).
- Lo Presti, D. C. F., Pallara, O., Lancellotta, R., Armandi, M., & Maniscalco, R. (1993). Monotonic and Cyclic Loading Behaviour of Two Sands at Small Strains. *Geotechnical Testing Journal*, 16, 409-424.
- Lollino, G., Arattano, M., & Cuccureddu, M. (2002). The Use of the Automatic Inclinometric System for Landslide Early Warning: The Case of Cabella

- Ligure (North-Western Italy). *Physics and Chemistry of the Earth, Parts A/B/C*, 27(36), 1545-1550.
- Lowe, J. (1967). Stability Analysis of Embankments. *Journal of Soil Mechanics & Foundations Div.*
- Mancuso, C., Vassallo, R., & d'Onofrio, A. (2002). Small Strain Behavior of a Silty Sand in Controlled-Suction Resonant Column Torsional Shear Tests. *Canadian Geotechnical Journal*, 39(1), 22-31.
- Marcuson, W. F., & Wahls, H. E. (1972). Time Effects on Dynamic Shear Modulus of Clays. *Journal of the Soil Mechanics and Foundations Division*, 98(12), 1359-1373.
- Melinda, F., Rahardjo, H., Han, K., & Leong, E. (2004). Shear Strength of Compacted Soil under Infiltration Condition. *Journal of Geotechnical and Geoenvironmental Engineering*, 130(8), 807-817. doi: doi:10.1061/(ASCE)1090-0241(2004)130:8(807)
- Pitts, J. (1983). The Form and Causes of Slope Failures in an Area of West Singapore Island. *Singapore Journal of Tropical Geography*, 4(2), 162-168.
- Qian, X., Gray, D., & Woods, R. (1991). Resonant Column Tests on Partially Saturated Sands. *Geotechnical Testing Journal*, 14(3).
- Ramesh, M., & Vasudevan, N. (2012). The Deployment of Deep-Earth Sensor Probes for Landslide Detection. *Landslides*, 9(4), 457-474. doi: 10.1007/s10346-011-0300-x
- Roesler, S. K. (1979). Anisotropic Shear Modulus Due to Stress Anisotropy. *Journal of the Geotechnical Engineering Division*, 105(7), 871-880.
- Rossi, M., Peruccacci, S., Brunetti, M., Marchesini, I., Luciani, S., Ardizzone, F., . . . Fiorucci, F. (2012). *Sanf: National Warning System for Rainfall-Induced Landslides in Italy*. Proceedings: Proceeding of the 11th International Symposium on Landslides (ISL) and the 2nd North American Symposium on Landslides (NASL).

- Shibuya, S., Hwang, S., & Mitachi, T. (1998). Elastic Shear Modulus of Soft Clays from Shear Wave Velocity Measurement. *Pre-failure deformation behaviour of geomaterials*, 207.
- Shibuya, S., & Tanaka, H. (1996). Estimate of Elastic Shear Modulus in Holocene Soil Deposits. *Soils and foundations*, 36(4), 45-55.
- Shroder Jr, J. F. (1998). Slope Failure and Denudation in the Western Himalaya. *Geomorphology*, 26(1), 81-105.
- Sidle, R. C., & Chigira, M. (2004). Landslides and Debris Flows Strike Kyushu, Japan. *Eos, Transactions American Geophysical Union*, 85(15), 145-151.
- Sitar, N., Anderson, S., & Johnson, K. (1992). *Conditions Leading to the Initiation of Rainfall-Induced Debris Flows*. Proceedings: Geotech Eng Div Specialty Conf: Stability and Perf. of Slopes and Embankments-II. ASCE, New York (pp. 834-839).
- Sorbino, G., & Nicotera, M. V. (2012). Unsaturated Soil Mechanics in Rainfall-Induced Flow Landslides. *Engineering Geology*.
- Stokoe II, K., Hwang, S., Lee, J.-K., & Andrus, R. D. (1995). *Effects of Various Parameters on the Stiffness and Damping of Soils at Small to Medium Strains*. Proceedings: Pre-Failure Deformation of Geomaterials, Sapporo, Japan.
- Stokoe, K., Hwang, S., & Lee, S.-H. (1991). *Characterization of Soil in Calibration Chambers with Seismic Waves*. Proceedings: 1st Int. Symposium on Calibration Chamber Testing, Potsdam, New York.
- Stokoe, K. H., & Santamarina, J. (2000). Seismic-Wave-Based Testing in Geotechnical Engineering. *GeoEng 2000*, 1490-1536.
- Terlien, M. T. (1998). The Determination of Statistical and Deterministic Hydrological Landslide-Triggering Thresholds. *Environmental Geology*, 35(2-3), 124-130.

- Thiebes, B., Bell, R., Glade, T., Jäger, S., Mayer, J., Anderson, M., & Holcombe, L. (2013). Integration of a Limit-Equilibrium Model into a Landslide Early Warning System. *Landslides*, 1-17.
- Toll, D. (2001). Briefing: Rainfall-Induced Landslides in Singapore. *Proceedings of the ICE-Geotechnical Engineering*, 149(4), 211-216.
- Tsukamoto, Y., Ishihara, K., Nakazawa, H., Kamada, K., & Huang, Y. (2002). Resistance of Partly Saturated Sand to Liquefaction with Reference to Longitudinal and Shear Wave Velocities. *Soils and foundations*, 42(6), 93-104.
- Tsukamoto, Y., Ishihara, K., & Nosaka, Y. (1998). On the Initiation of Rainfall Induced Soil Failure. *Geotechnical Hazards*, 883-890.
- Uchimura, T. (2011). *Wave Velocity in Unsaturated Slopes in Relation to Moisture and Stability*. Paper presented at the The 14th Asian Regional Conference on Soil Mechanics and Geotechnical Engineering, Hong Kong.
- Uchimura, T., Gizachew, G., Wang, L., Nishie, S., & Seko, I. (2013). *Deformation and Water Seepage Observed in a Natural Slope During Failure Process by Artificial Heavy Rainfall*. Proceedings: 18th International Conference on Soil Mechanics and Geotechnical Engineering (pp. 2273-2276), Paris, France.
- Uchimura, T., Suzuki, D., & Hongkwan, S. (2011). *Combined Monitoring of Water Content and Displacement for Slope Instability*. Proceedings: Proc. of 4th Japan-Korea Geotechnical Workshop (pp. 67-72), Kobe, Japan.
- Uchimura, T., Towhata, I., Lan Anh, T., Fukuda, J., Bautista, C. B., Wang, L., . . . Sakai, N. (2010). Simple Monitoring Method for Precaution of Landslides Watching Tilting and Water Contents on Slopes Surface. *Landslides*, 7(3), 351-357. doi: 10.1007/s10346-009-0178-z
- Vaughan, P., & Kwan, C. (1984). Weathering, Structure and in Situ Stress in Residual Soils. *Geotechnique*, 34(1), 43-59.
- White, J. E. (1983). *Underground Sound: Application of Seismic Waves*: Elsevier Amsterdam.

Yimsiri, S. (2001). *Pre-Failure Deformation Characteristics of Soils: Anisotropy and Soil Fabric*. PhD Thesis, University of Cambridge, Cambridge, England.

Yoshimatsu, H., & Abe, S. (2006). A Review of Landslide Hazards in Japan and Assessment of Their Susceptibility Using an Analytical Hierarchic Process (Ahp) Method. *Landslides*, 3(2), 149-158.

Zan, L., Latini, G., Piscina, E., Polloni, G., & Baldelli, P. (2002). *Landslides Early Warning Monitoring System*. Proceedings: Geoscience and Remote Sensing Symposium, 2002. IGARSS'02. 2002 IEEE International (pp. 188-190).

EXPERIMENTAL SETUP

Chapter 3

CHAPTER 3

EXPERIMENTAL SETUP

3.1. GENERAL

For the characterization of geomaterials and their intrinsic properties, a variety of laboratory element tests are in practice nowadays. Each of the available testing approach has its own merits and demerits. Careful consideration is therefore required to select an apparatus which can best reproduce the required in-situ characteristics (in-situ stress state, field stress path during shearing, drainage/seepage characteristics, etc.) during element tests.

The field stress path followed by a soil element during rainfall-induced landslides is a specialized one, as explained in Chapter 2. A special soil testing apparatus is therefore required to mimic such stress path. An ordinary stress-controlled triaxial testing apparatus (A. W. Bishop & Henkel, 1962) was modified to suite necessary requirements for replicating field stress path. Detailed description of all the modifications, and the working of various parts and systems of modified triaxial apparatus are discussed in this chapter.

3.2. MODIFIED TRIAXIAL COMPRESSION SYSTEM FOR TESTING UNSATURATED SOILS

Triaxial testing systems are among the most commonly used laboratory equipments for determining shear strength parameters of soils. However, conventional triaxial systems are primarily designed for testing saturated soil specimens and appropriate modifications, considering the nature of unsaturated soils, are required to test

unsaturated soil specimens. The main concerns involved in unsaturated soil testing include accurate determination of specimen volume, and soil matric suction.

In the present study, a conventional triaxial apparatus was modified to test initially unsaturated soil specimens. Moreover, the apparatus was fitted with peripheral electronics to enable the measurement of elastic wave velocities during the course of experiments. The following section explains the details and functions of various parts of modified triaxial apparatus.

3.2.1 General Structure

The general structure of modified triaxial apparatus employed in this study is shown in Figure 3.1 and Figure 3.2. The main parts of triaxial system used in this study are as follows;

- a. Pressure control system; controlling the axial and lateral load acting on the specimen.
- b. Triaxial cell; containing soil specimen.
- c. Response measuring devices; to determine axial, radial and volumetric changes in specimen.
- d. Ceramic disk; for injecting water into triaxial specimens in order to replicate rainfall conditions and/or determining initial matric suction of specimens.
- e. Miniature pressure sensor; for determining matric suction of unsaturated soil specimen during water injection tests.
- f. An *A/D* (analogue to digital) converter board; for converting electrical response of transducers from analogue to computer understandable digital format.
- g. A set of amplifiers; to amplify output from transducers improving measurement resolution, and to filter high frequency noise in digital signals.
- h. A *D/A* (digital to analogue) converter board; for converting digital control signals from computer, to analogue format in order to control axial load, cell pressure and infiltration pressure (back pressure), etc.
- i. Elastic wave measurement system; comprising of function generator, power amplifier, piezoelectric transducers, oscilloscopes, etc.

3.2.2 Loading System

3.2.2.1 Pressure Control System

The terminal pressure source was an air compressor, supplying air compressed from 800 to 1000 kPa. This compressed air was first collected in an air tank which acted as a water trap and a pressure accumulator. Air accumulation in this air tank ensured the supply of constant air pressure to associated systems. Next the compressed air was passed through a filter (to remove dust and other floating objects) and then distributed to regulators. The cell pressure was controlled by electro-pneumatic (*E/P*) transducers whereas, the axial load controlling pressures were controlled through a combination of *E/P* transducers and air volume boosters, as explained in next section. During specimen preparation, negative pressure is required, initially to stretch the membrane and then to keep the specimen standing on the removal of split mould. This negative pressure was applied through a *CONVUUM*, which provided a partial vacuum through a fast flow of air. Various components of pressure control system are schematically shown in Figure 3.3.

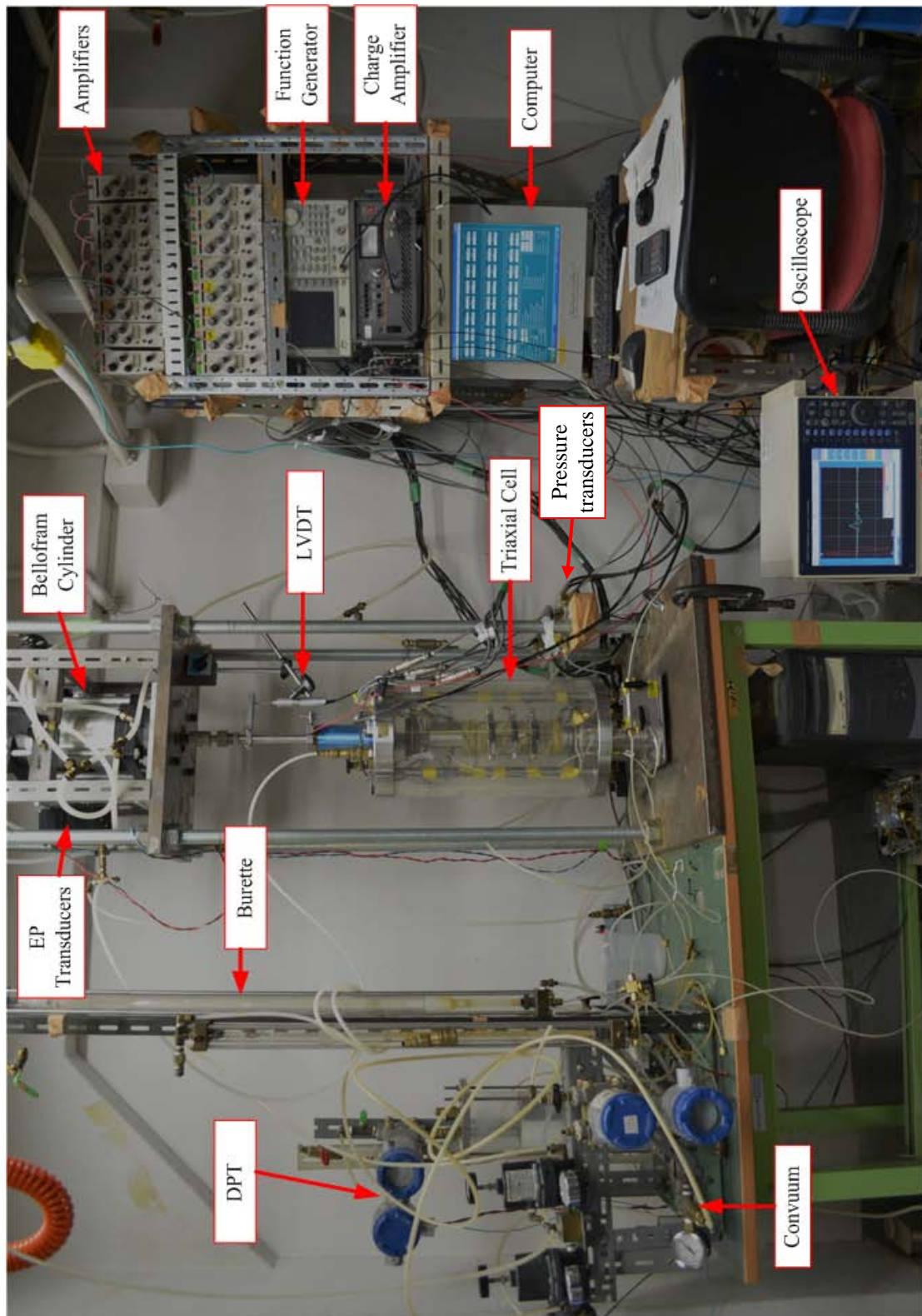
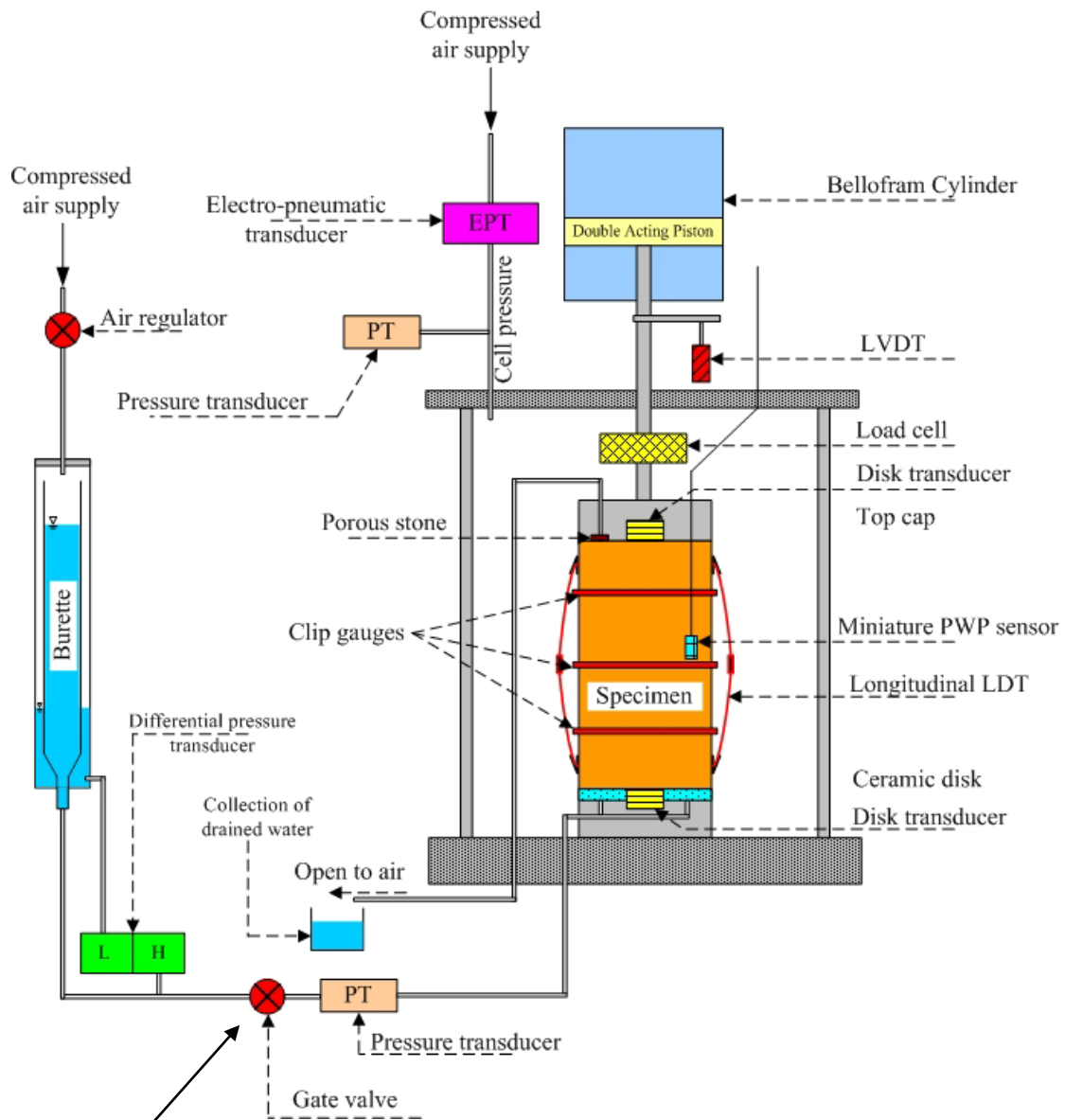


Figure 3.1: Modified triaxial testing apparatus used in this study.



Notes:

1. For measuring matric suction using ceramic disk (*ICCW*, and *CWRSR* tests), this gate valve is closed.
2. This gate valve is open when water injection through ceramic disk is required (*ICWI*, and *CSWI* tests).

Figure 3.2: Schematic layout of modified triaxial apparatus.

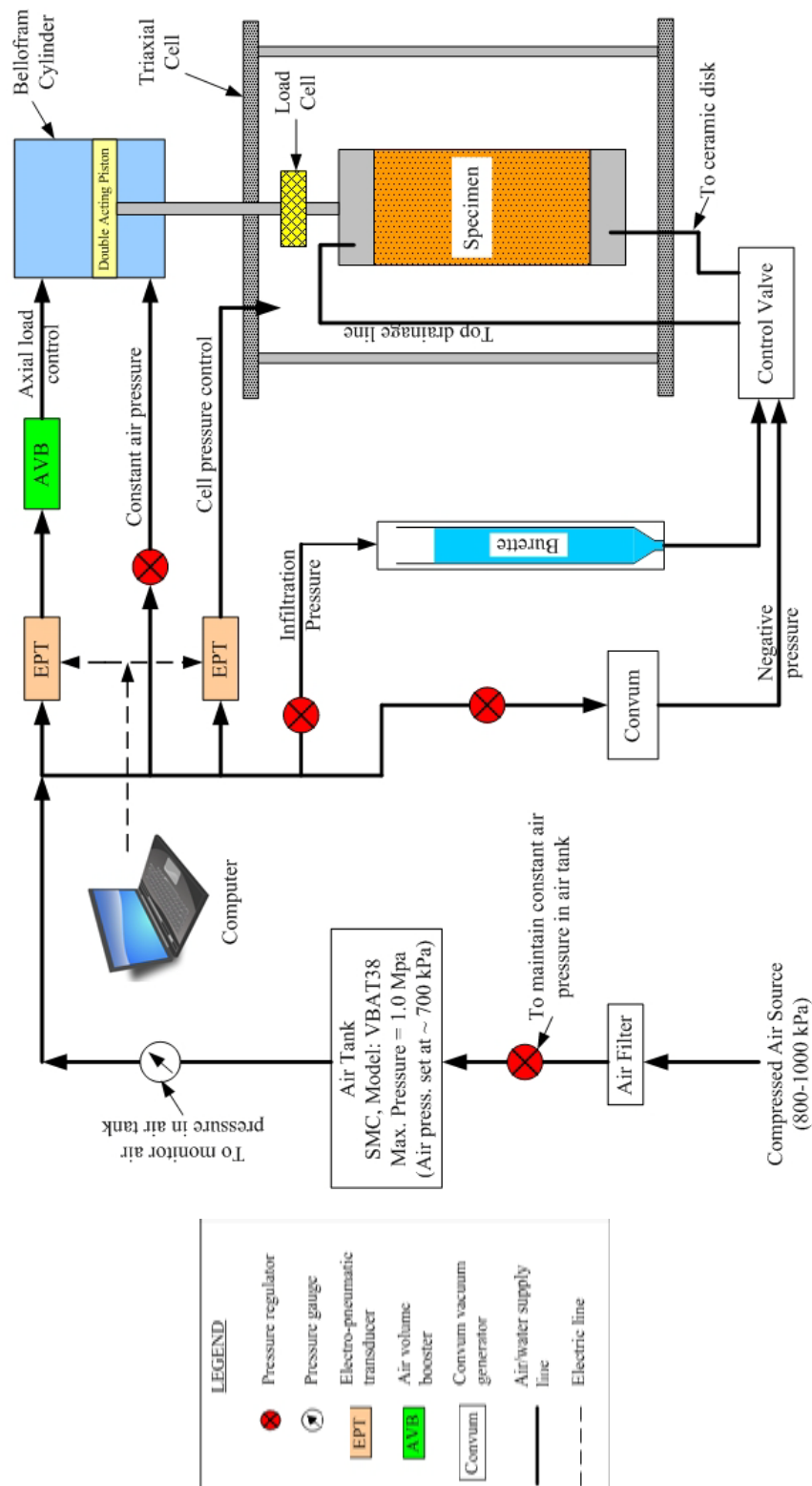


Figure 3.3: Schematic layout – pressure control system of modified triaxial apparatus.

3.2.2.2 Axial Loading System

A rigid frame mounted on a loading table served as the foundation of loading system. A double action Bellofram cylinder (*Fujikura Co. Ltd., Model: SCD-125-140-BO*), mounted with a loading piston which in turn was connected to the loading shaft of triaxial cell, was fixed at the top of metal frame. The Bellofram cylinder, which is the main component of loading system, comprised of two compartments separated by a moving piston. A constant air supply, through the compressed air tank, was provided to the lower compartment of Bellofram cylinder. Air pressure in the upper compartment was controlled through *E/P* transducers. Pressure output from *E/P* transducer is proportional to input voltage, which was controlled through computer program. Constant shear stress application on soil specimen could therefore be maintained by loading system through quick continuous adjustments in the axial load. Fundamental working of loading system is explained schematically in Figure 3.4.

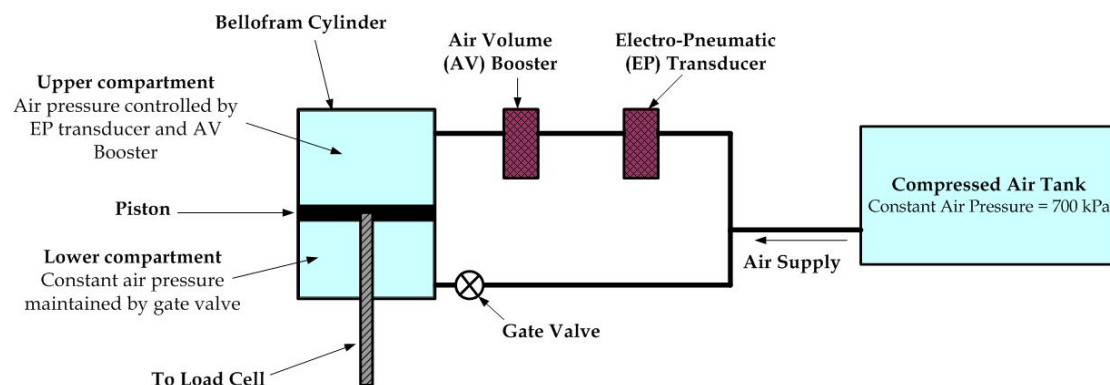


Figure 3.4: Working principle of axial loading system.

3.2.3 Measurement Devices

3.2.3.1 Axial Load Cell

The load cell used was an electronic-resistant strain gauge type transducer. Its main body was made from a block of phosphor-bronze. Following the basic design by Tani et al. (1983), four suitably placed electronic-resistant strain gauges (two on

compression zone and two on extension zone), forming a Wheatstone bridge, were the essential elements of this type of load cell. The load cell used for this study (shown in Figure 3.5) had a capacity of 5 kN. Basic design of load cell and derivation of its load carrying capacity is explained in Appendix-A.



Figure 3.5: Axial load cell employed for this study.

The load cell was placed inside the triaxial cell, screwed to the top cap and the loading piston. The measured axial load was therefore free from piston friction. Standard calibration procedure was adopted for the calibration of load cell. A series of known dead loads was applied to the load cell, and the corresponding response signals from the strain amplifier were recorded. A correlation between the applied loads and response voltage was thus established. The calibration characteristics of load cell are shown in Figure 3.6(a). Perfect linearity and repeatability can be observed from the load cell calibration plot. In some of the experiments, load cell was expected to apply a constant load for long durations of time. Therefore, the stability of load cell and its ability to maintain a constant load for a long duration was tested. A rubber dummy specimen was subjected to 1010 N load for about 48 hours. Test results shown in Figure 3.6(b) shows a fluctuation of ± 5 N (error of less than 1%), which corresponds to about 0.003 kPa of axial stress. This fluctuation is comparable with the uncertainty in the pressure controlling system, so for all practical purposes this fluctuation was considered insignificant.

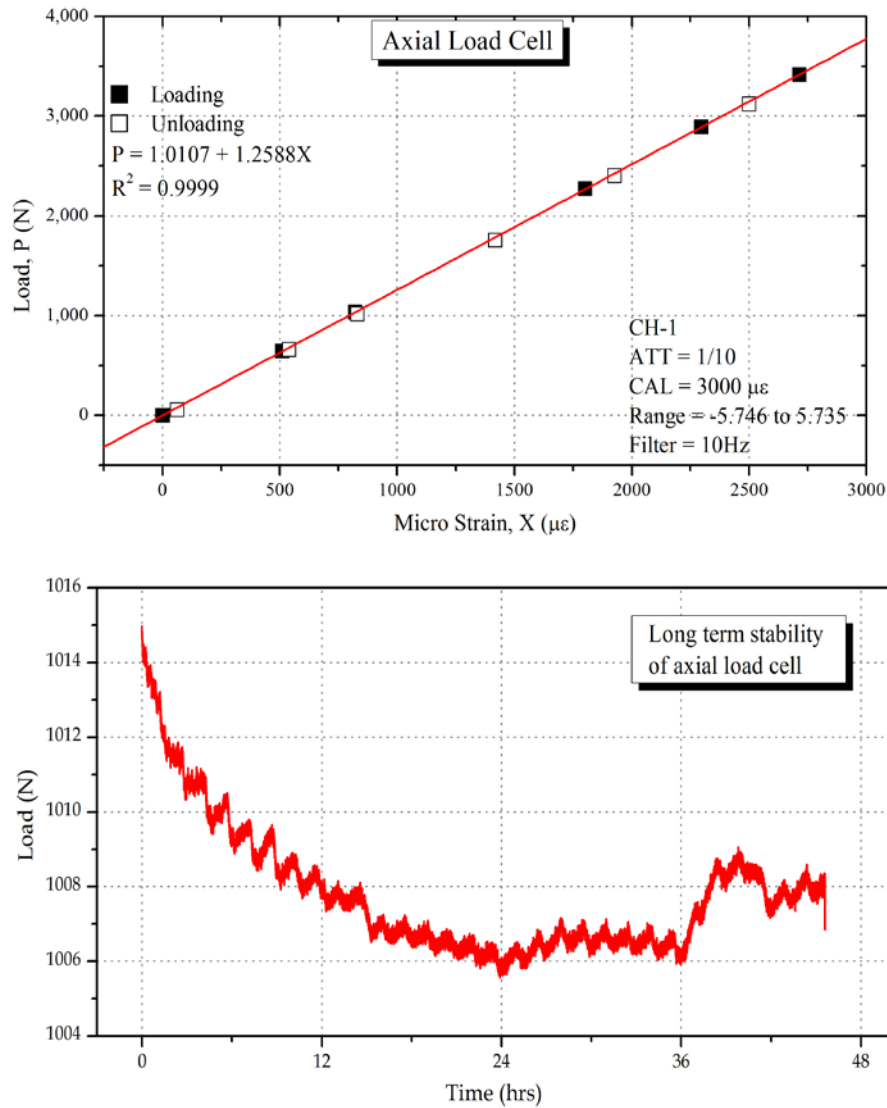


Figure 3.6: Calibration characteristics of axial load cell (a) calibration curve (b) long-term stability of load cell.

3.2.3.2 Strain Measurement

Measurement of specimen deformations, particularly the specimen volume, can be a challenging task in unsaturated soil testing. In saturated soil, the total volume change of the soil specimen is generally assumed to be equal to the change in water volume (considering the water to be incompressible) and it can be measured relatively easily by using a volume gauge. In an unsaturated soil however, the total volume change generally comprises two components: changes in the volume of air and changes in the volume of water in void spaces (C WW Ng et al., 2002). Some of the existing methods for the determination of volume change in unsaturated soil specimen include:

(i) measurement of cell fluid (A. Bishop & Donald, 1961; Cui & Delage, 1996), (ii) measurement of air and water volumes separately (Geiser et al., 2000), (iii) measurement of overall specimen volume by recording the differential pressure due to changes in water level inside an open-ended inner cell caused by volume change in the specimen and the reference tube using an accurate differential pressure transducer (C WW Ng et al., 2002), and (iv) direct measurement of soil specimen (Chiu, 2001; Charles WW Ng & Chiu, 2001). However, in order to simplify the water proofing of piezoelectric transducers used for elastic wave measurement (discussed in Chapter 5), direct measurement of soil specimen was preferred. Various transducers used for this purpose are explained in the following section.

a) External Displacement Transducer (LVDT)

The axial deformation of the test specimen was monitored by an externally mounted LVDT (*Linear Variable Differential Transducer*). It was fixed on a metal plate attached to the upper horizontal frame and it measured the displacement of axial rod clamped to the loading piston. LVDT manufactured by *KYOWA Electronic Co. Ltd.*, *Model: DTH-A-30*, having maximum capacity of 30 mm was employed for this study. Calibration of LVDT was performed with a standard *block gauge apparatus*. LVDT's response to known displacements, imparted using standard block gauges, was recorded. Perfect linearity and repeatability can be observed from calibration characteristics curve of LVDT used in this study, as shown in Figure 3.8.



Figure 3.7: LVDT used in present study (0-30mm range).

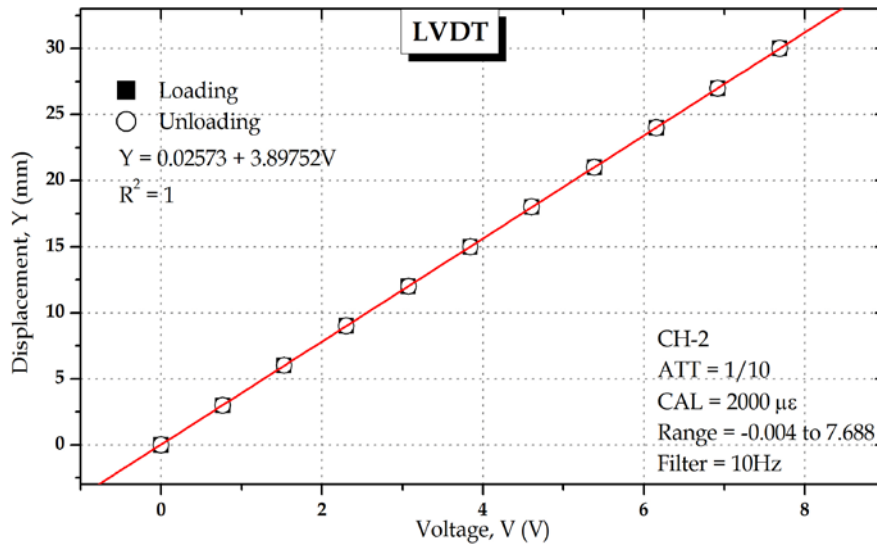


Figure 3.8: Calibration characteristics of *LVDT*.

b) Local Deformation Transducer (*LDT*)

Axial deformation measured by using externally mounted *LVDT* always results in some overestimation due to the imperfect contact between the soil specimen and the top cap, generally termed as bedding error (Sarsby et al., 1980; Tatsuoka et al., 1994). In order to examine the influence of bedding error and to accurately evaluate axial strains, a pair of locally manufactured local deformation transducers (*LDT*) (Goto et al., 1991; Hoque et al., 1997) was installed directly on the opposite sides of specimen's lateral surfaces. Each *LDT* was held at both ends of strip by a pair of pseudo hinges (Figure 3.10) attached in align on the surface of specimen. The distance between the two ends, i.e. two hinges was to be slightly less than the unstressed length of *LDT* so that the strip can be balanced by its own elastic force against the hinges. *LDTs* were made of a thin phosphor-bronze strip on which four electronic-resistance strain gauges (*KYOWA Electronic Co. Ltd., Type: KFG-1N-120-C1-16*) were placed, two on the compression side and two on the tension side, forming a Wheatstone bridge. When the *LDT* is subjected to any bending deformation associated with axial compression between both ends, a consistent change in voltage by strain gauges is obtained, which provides the basis for developing the relationship between deformation and response voltage. These *LDTs* can measure strains less than 0.0005% without a second stage amplification. A pair of *LDTs* having length 112 mm

was prepared to test 150 mm high specimens. Details of manufacturing procedure are explained in Appendix-A.

The calibration of *LDTs* was performed by setting them on similar pseudo hinges on a stand supported by precision ball-bearing. Precise increments of displacements were given by means of a micrometer and the corresponding voltage response was established. The calibration/regression characteristics of *LDTs* used in this study are shown in Figure 3.9. As evident from the figures that both *LDTs* possess perfect repeatability and a second degree parabola fits the data well. The parameters of fitted curves were fed into the computer program in order to obtain axial deformation directly in 'mm'.

The *LDTs* used in this study can measure specimen deformations only up to 3 mm, which was not sufficient for most parts of this study (e.g. *CWRSR* and *CSWI* tests). Therefore, axial deformations beyond the range of *LDTs* were determined by *LVDT*. This is not expected to cause any discrepancy because the bedding error only appears to affect small strain measurements.

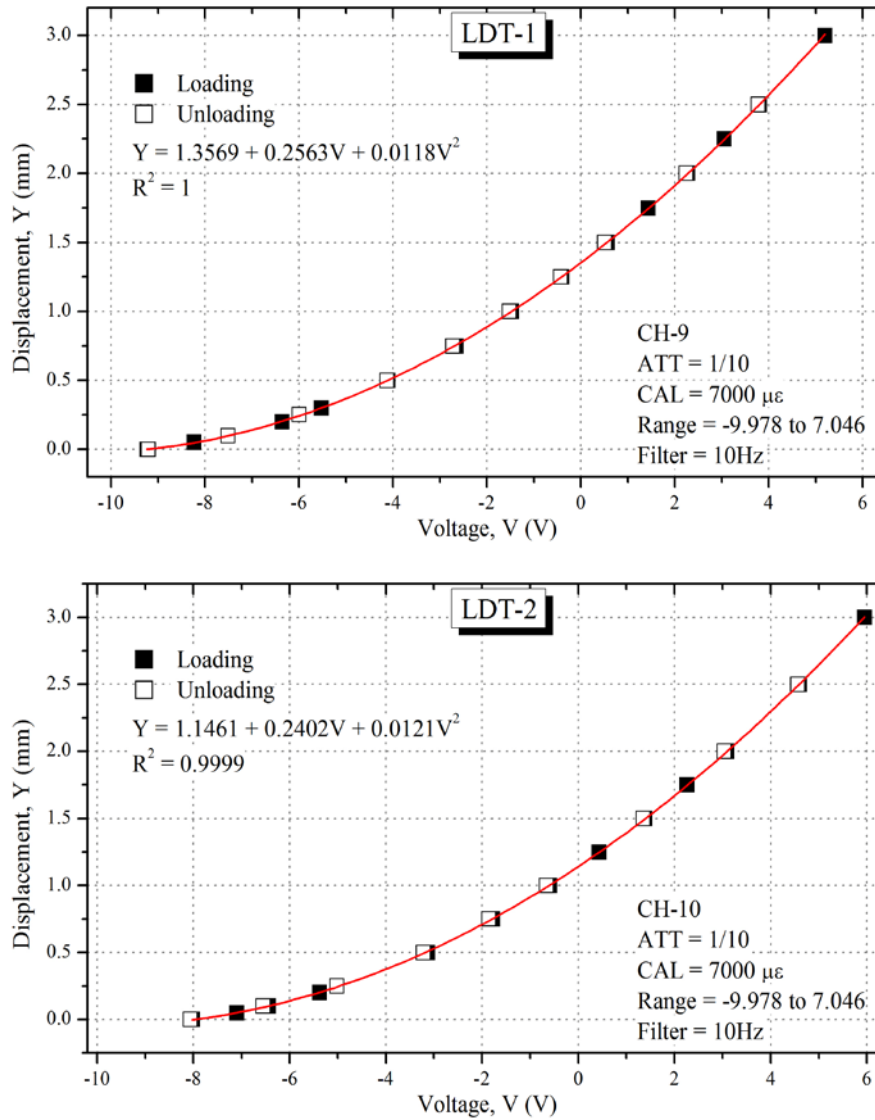


Figure 3.9: Calibration characteristics of local deformation transducers (*LDTs*).

c) Clip Gauge (*CG*)

Radial displacements of unsaturated soil specimens were monitored by using clip gauge type transducers. Three clip gauges manufactured by *Tokyo Sokki Kenkyujo Co. Ltd. (TML)*, (*Model: PI-5-100*) were mounted at different heights of specimen, as shown in Figure 3.10. The clip gauges consisted of a U-shaped metal frame having four strain gauges (two on compression side and two on extension side), forming a Wheatstone bridge, attached at its centre. Custom-made legs were attached to the U-shaped central frame in order to support them on specimen surface. In order to mount

the clip gauge on specimen surface custom-made block-hinge attachments were glued to the specimen surface (membrane) to support the clip gauge legs (Figure 3.10), whereas the central U-shaped frame was hung by means of a string (Figure 3.10) which passed through the top of triaxial cell by means of an O-ring. The clip gauges were able to measure radial displacements of ± 5 mm (5 mm in compression and 5 mm in dilation). In order to avoid damage to clip gauges, the strings supporting them were pulled to dismount the clip gauges as radial deformation approached the clip gauge maximum capacity.

Calibration of clip gauges was done by setting them on the same ball-bearing displacement stand used for the calibration of *LDTs*. Clip gauges were set in the exactly same way as on soil specimen and known increments of displacement were applied by using micrometer. By recording the corresponding voltage changes the calibration characteristics of three clip gauges were established, as shown in Figure 3.11. As clear from the calibration charts, all the clip gauges possessed perfect linearity and repeatability both in dilation and compression.

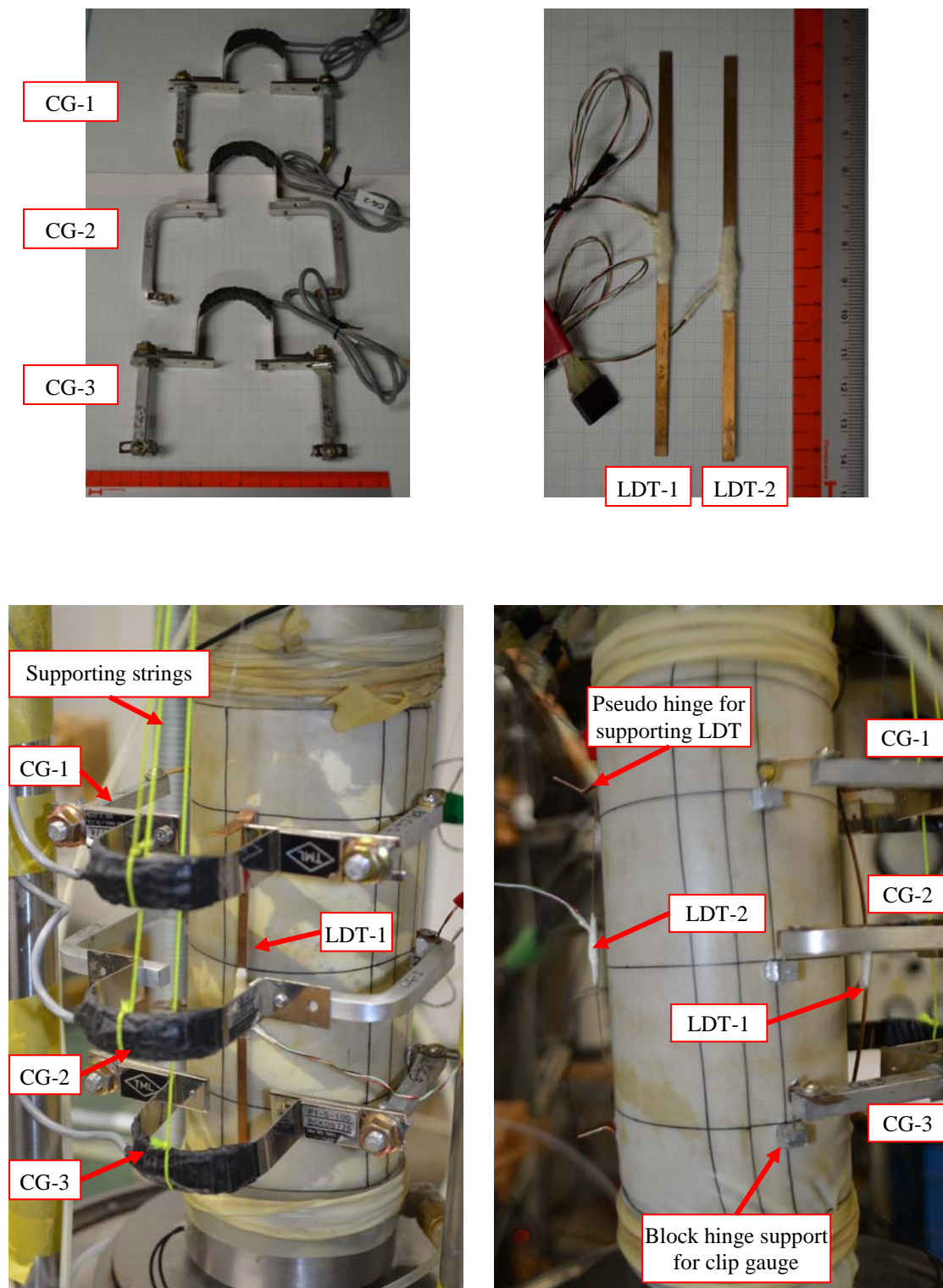


Figure 3.10: Setting up local deformation transducers (*LDTs*) and clip gauges (*CGs*) on specimen surface.

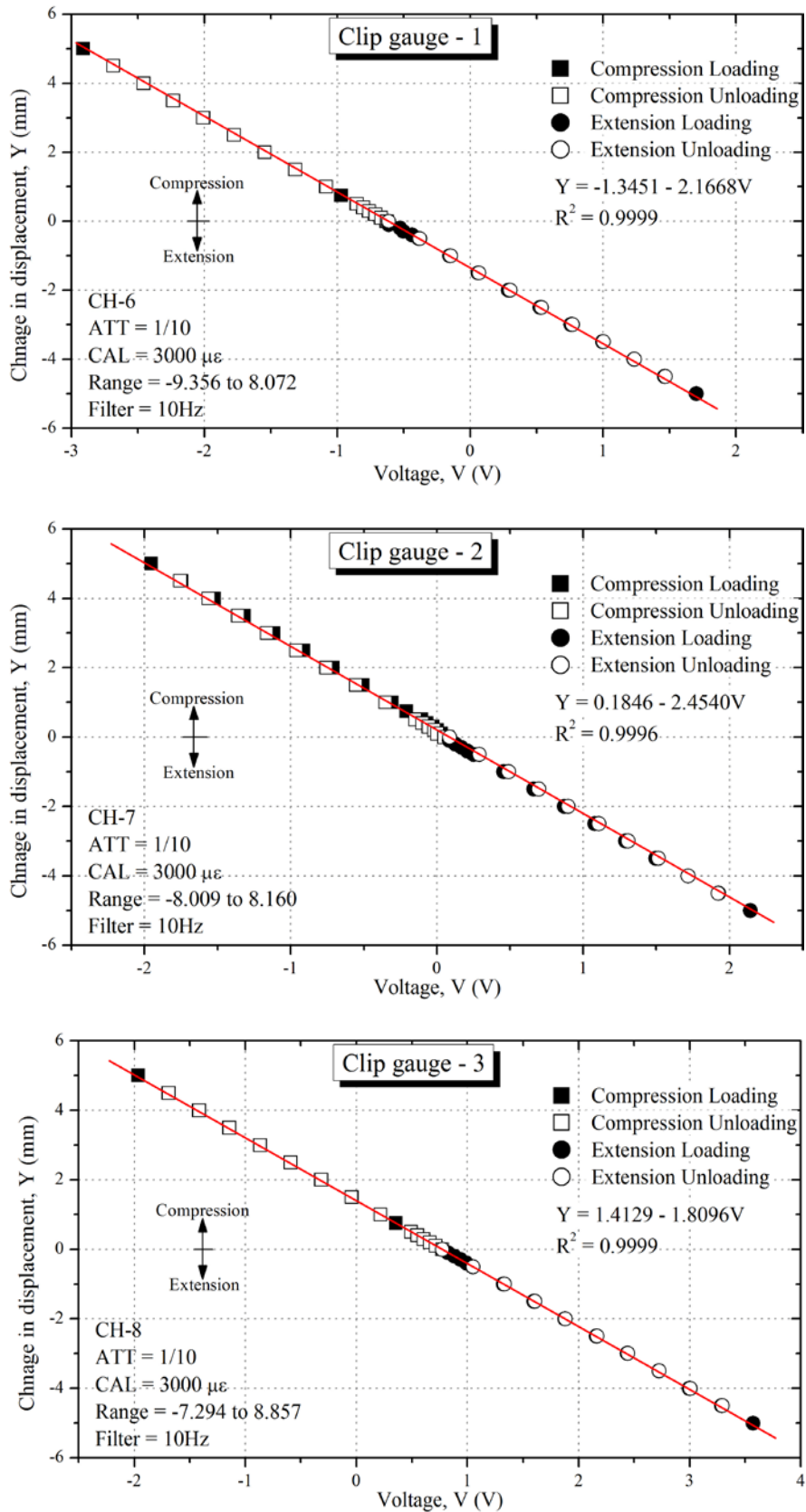


Figure 3.11: Calibration characteristics of clip gauges used in this study.

3.2.4 Pressure Transducers

In order to monitor the pore water pressure (including matric suction through ceramic disk) and the cell pressure, two pressure transducers (*KYOWA Electronic Co. Ltd.*, *Model: PGM-10KH, Capacity 1000 kPa*), installed outside triaxial cell (Figure 3.1), were used. The voltage output of pressure transducers varied as a function of applied pressure. The calibration characteristics of these transducers are shown in Figure 3.12. Perfect linearity and repeatability within the calibration range can be observed from these calibration plots.

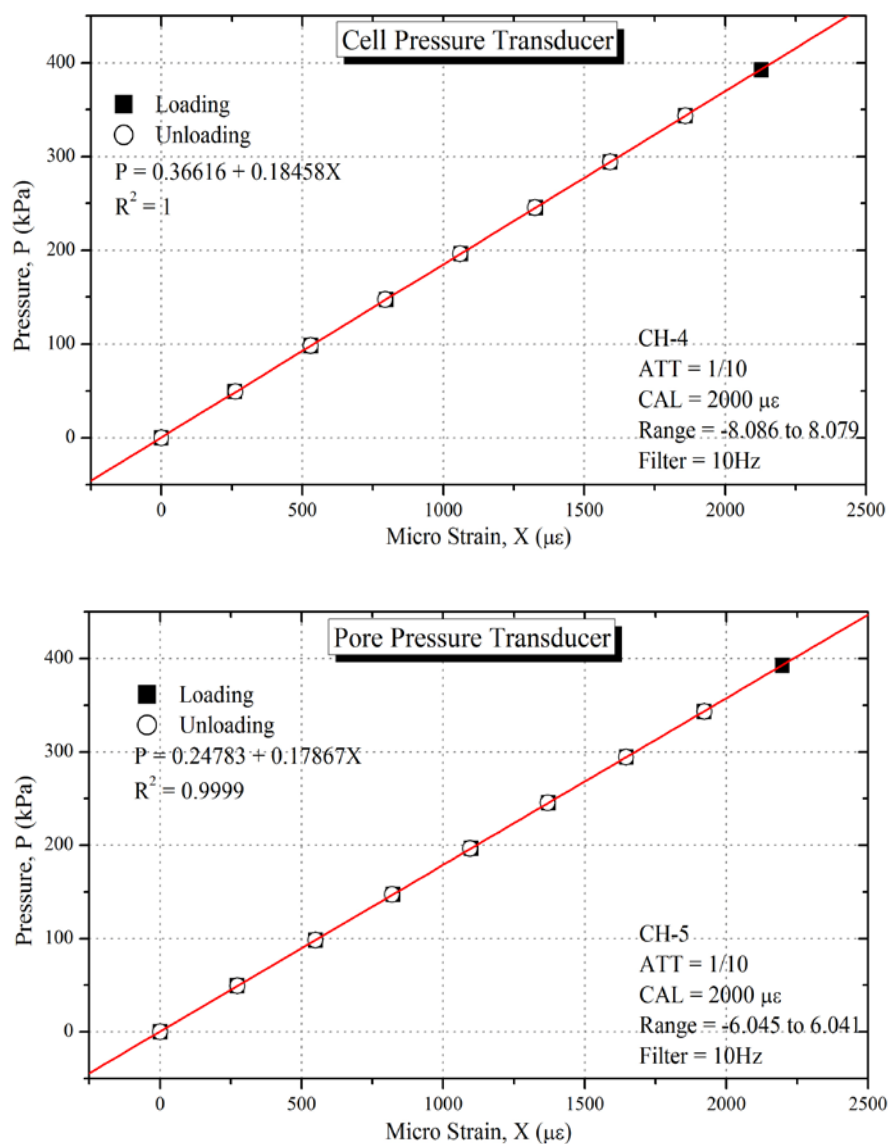


Figure 3.12: Calibration characteristics of pressure transducers.

3.2.5 Pore Water Pressure of Unsaturated Specimens

The modified triaxial apparatus was equipped with two measurements of pore water pressure of unsaturated soil specimen. A donut-shaped ceramic disk sealed to the pedestal of triaxial apparatus, and a miniature pore pressure sensor placed inside the specimen were used to determine the positive as well as negative (suction) pore water pressure. The following sections explain the details of pore water pressure measurement systems.

3.2.5.1 High Air-entry Value Ceramic Disk

A saturated ceramic disk serves as a means of continuity between pore water in an unsaturated soil specimen and the measuring system (a pressure transducer in this case). The capacity of a ceramic disk to measure soil matric suction depends on its air entry value (*AEV*). The *AEV* is the maximum magnitude of soil matric suction at which surface tension of water, filling ceramic disk pores, is exceeded and the air commences to pass through the saturated ceramic disk. As long as the soil matric suction remains less than *AEV* and the associated measuring system remains properly saturated, the continuity between pore water in soil and the measuring system is maintained by means of ceramic disk; and the pore water pressure (positive or negative) can easily be measured by associated pressure measuring device. However, when suction value in the soil exceeds the *AEV*, air bubbles enter the measuring system breaking the continuity between pore water and the measuring system, resulting in erroneous measurement of pore water pressure. The detailed construction and working principles of ceramic disks have been discussed by Fredlund and Rahardjo (1993) whereas a comparison between suction measurement by ceramic disk and other methods is presented by Agus and Schanz (2005).

In this study, a donut-shaped ceramic disk (68 mm outer diameter, 37 mm inner diameter, and 5 mm thickness) with *AEV* of 100 kPa was embedded and sealed to the pedestal of triaxial apparatus, as shown in Figure 3.13. Donut shape of ceramic disk was adopted to accommodate the disk type piezoelectric transducer (discussed in Chapter 5) at the centre of base pedestal and it covered 64.6% of base pedestal's surface area. The compartment below the ceramic disk was connected to a pressure transducer (to measure positive and negative water pressure) and a water supply

burette (to inject water in soil specimen). Before the start of each test, the ceramic disk and associated system was saturated by a procedure explained in Section 4.3.1.1 (Chapter 4). The pressure transducer, connected to the ceramic disk, was calibrated by standard calibration procedure of applying known increments of pressure and recording the corresponding change in voltage response. The same pore pressure transducer, explained in previous section, was used for this purpose.

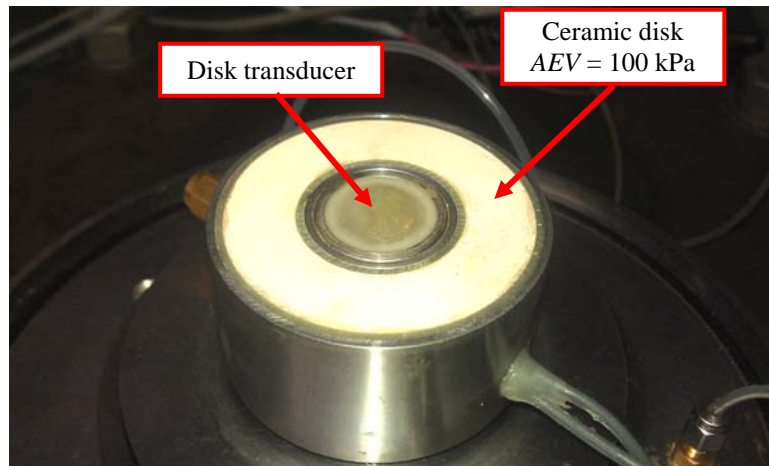


Figure 3.13: Modified base pedestal of triaxial apparatus.

3.2.5.2 Miniature Pressure Sensor

During the water injection tests (*ICWI* tests, and *CSWI* tests), water was injected into the specimens through ceramic disk. Thus, an alternate assembly was required to record the variation of pore water pressure during water injection. A miniature pressure sensor manufactured by *SSK Corp. Ltd.* (Model: *P306AV-5*; Maximum capacity = 50 kPa) was used for this purpose. The sensor was placed inside the specimen at mid-height, and its cable was taken out through the apparatus top cap. Miniature sensor, as shown in Figure 3.14, was 10 mm in height and 8 mm in diameter. The wire mesh in the front of sensor was replaced with a high air entry value ceramic disk ($AEV=200$ kPa) in order to enable the measurement of both positive and negative pore water pressure (Figure 3.14)

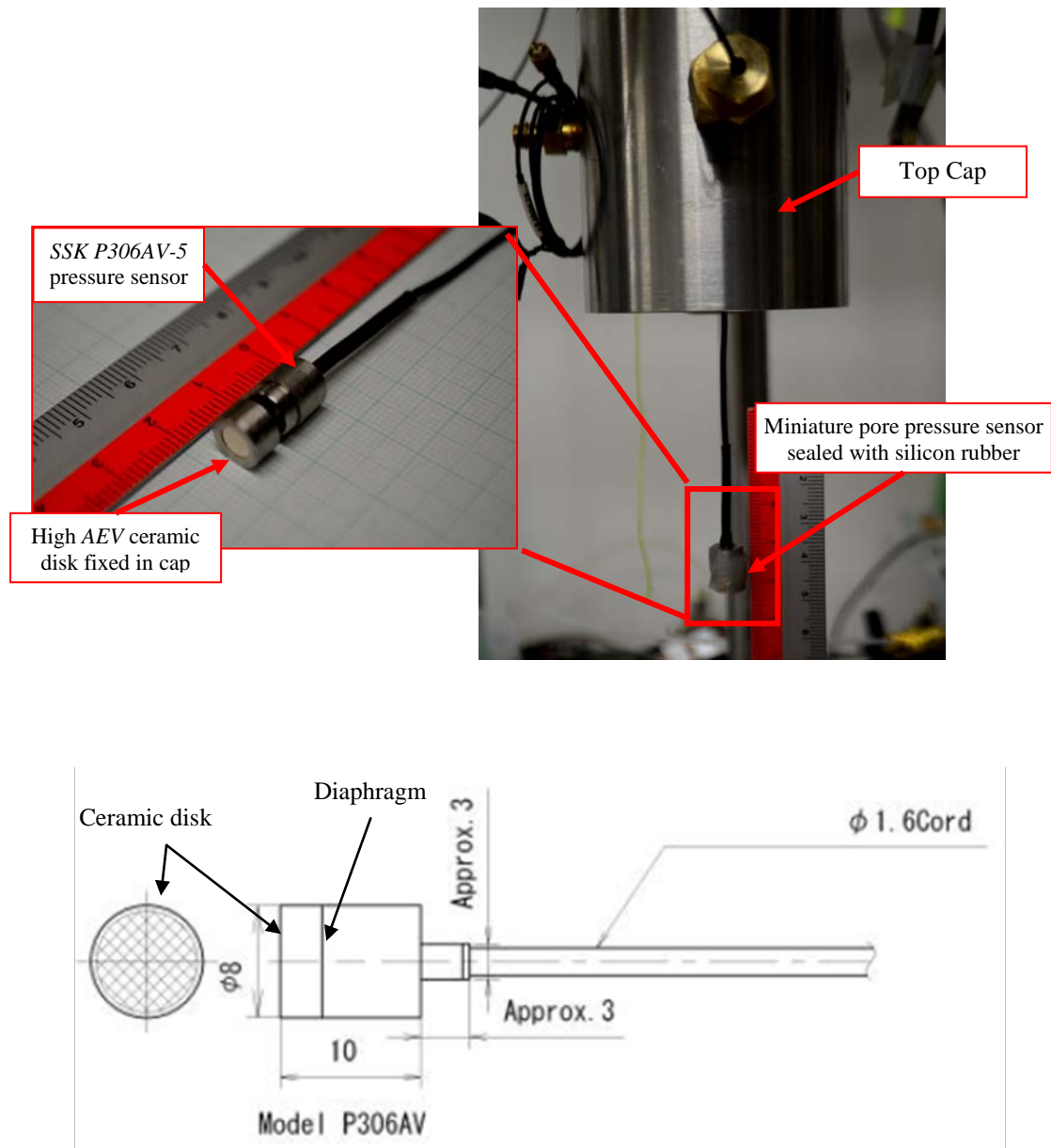


Figure 3.14: Miniature pressure sensor for pore water pressure measurement during water injection tests.

Accurate determination of pore water pressure (both positive and negative) is only possible if the miniature sensor is properly saturated. The miniature sensor and its ceramic disk were thus saturated by a procedure explained in Section 4.3.1.2 of Chapter 4. Calibration of miniature pore water pressure sensor was done with respect to the pore pressure sensor connected to base pedestal. The base pedestal containing the saturated ceramic disk, and the saturated miniature pressure transducer (assembled with its ceramic disk and sealed with silicon rubber), were submerged in de-aired

water inside the triaxial cell, as shown in Figure 3.15. Positive as well as negative pressures were applied to triaxial cell and the miniature pressure sensor voltage was calibrated against the pressure reading obtained from ceramic disk pressure sensor. The calibration curve of miniature pressure sensor is shown in Figure 3.16.

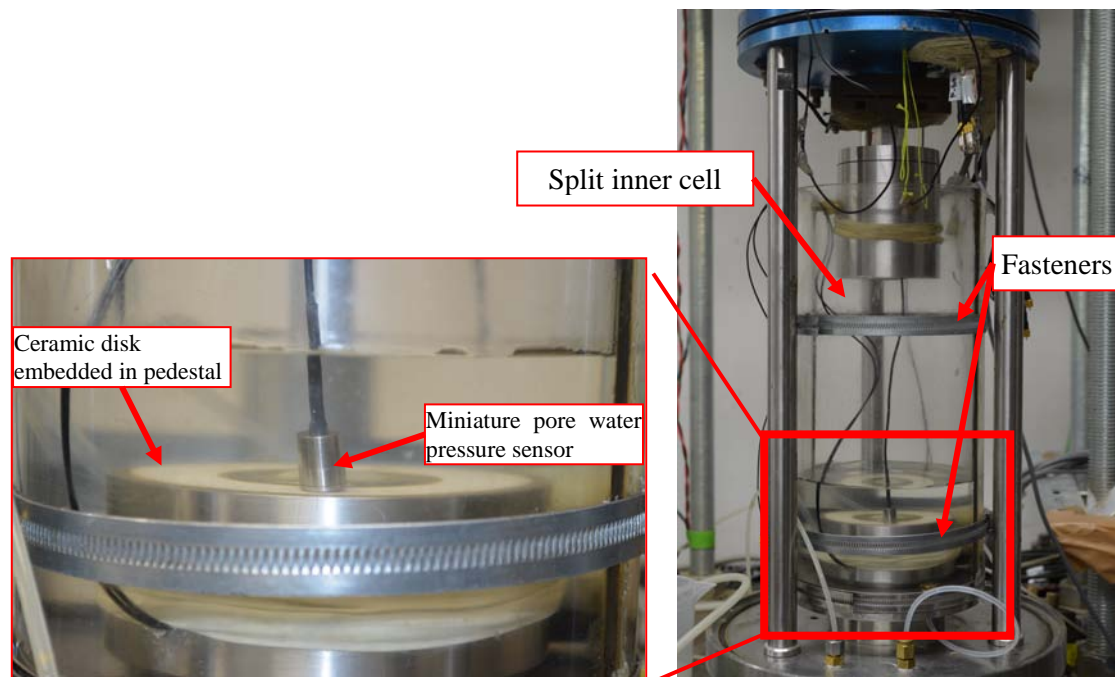


Figure 3.15: Arrangement for calibration of miniature pore pressure transducer.

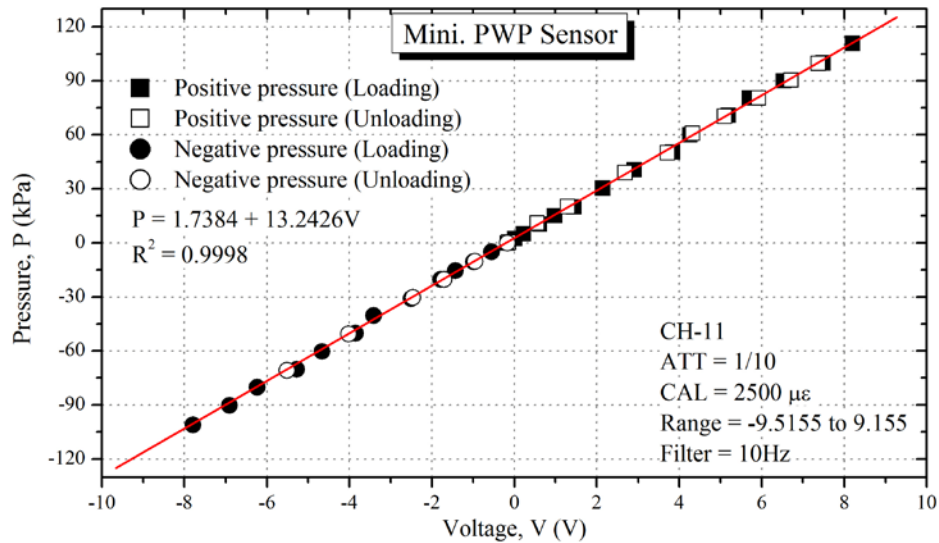


Figure 3.16: Calibration curve of miniature pressure transducer.

To validate the reliability and accuracy of miniature sensor for soil pore water pressure measurement, a 4 cm thick unsaturated soil layer (14% volumetric water content) was prepared on top of the saturated ceramic disk sealed to base pedestal and connected with an external pressure transducer. Saturated miniature sensor was placed inside the soil layer, close to the base pedestal ceramic disk (Figure 3.17). The soil layer was then subjected to air drying-wetting cycles, and the response of soil pore water pressure from both sensors was recorded. As shown in Figure 3.18, pore water pressure measurements from both sensors were identical and consistent. This verified the accuracy and reliability of pore water pressure measurements by means of miniature sensor.

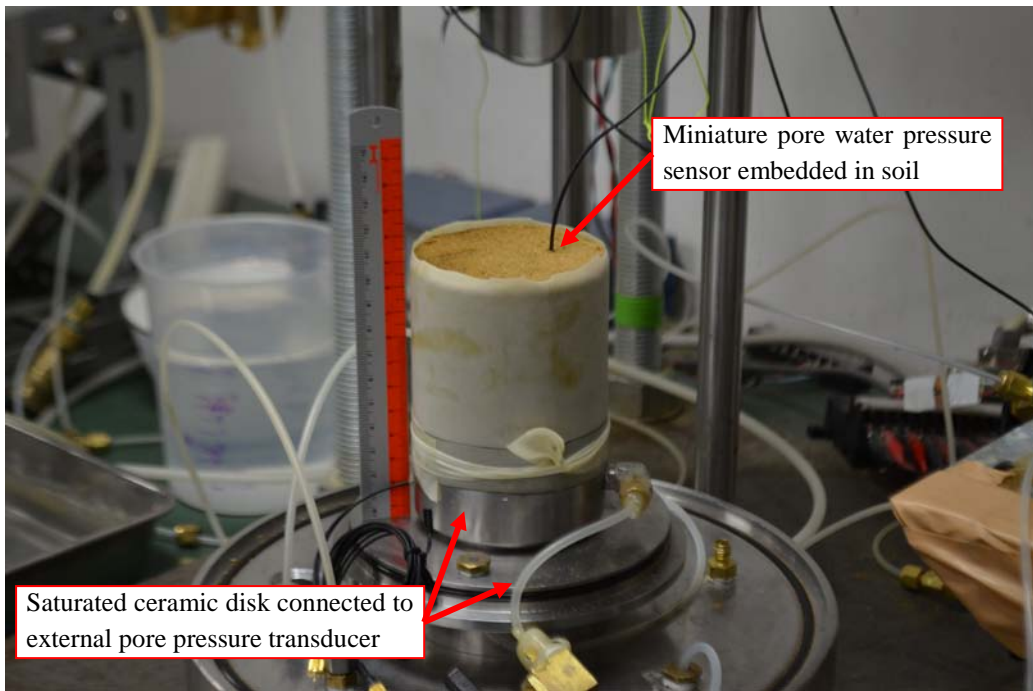


Figure 3.17: Reliability test of miniature sensor for measuring soil pore water pressure.

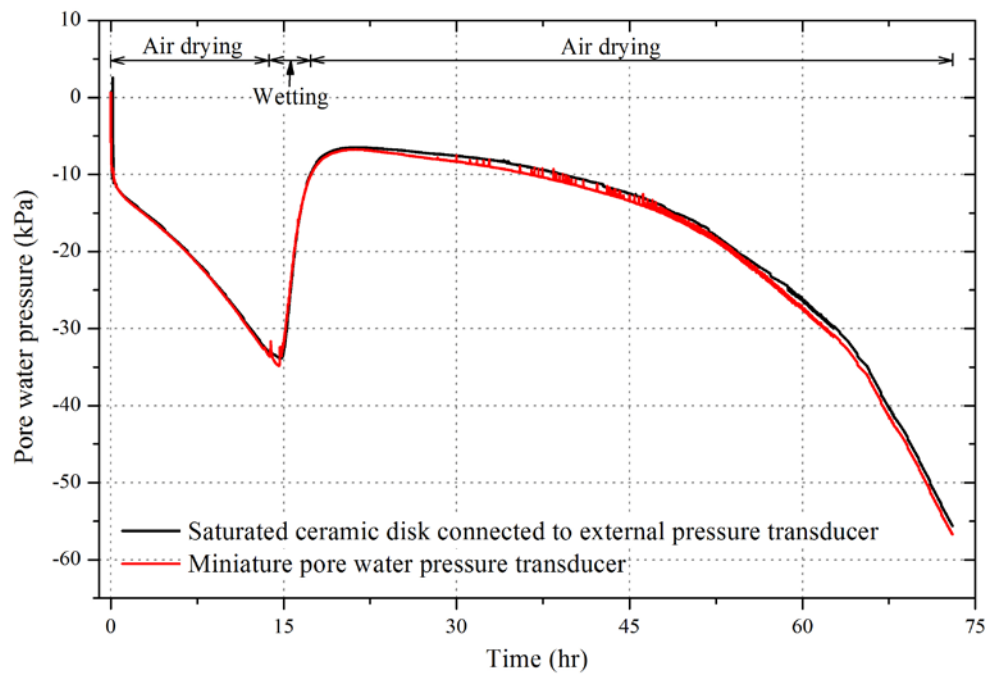


Figure 3.18: Comparison of pore water pressure of soil specimen measured by two pore pressure sensors.

3.2.6 Differential Pressure Transducer (*DPT*)

A low capacity differential pressure transducer (*Fuji Electronic Co. Ltd.; Model: FHC122V2-BABYY-AA-Z; Range = 0~6.0 kPa; Maximum working pressure = 10 MPa*) was used to continuously record the volume of water injected into the unsaturated specimens. A photograph of *DPT* used in this study is shown in Figure 3.19. *DPT* was connected to a double column burette (Figure 3.2); with an outer column having fixed water level (serving as reference pressure), and an inner burette, connected to the specimen, whose water level varies as the water is injected into the specimen. The system works on the principle of measuring the pressure difference between the reference water column, and the burette connected to specimen. This pressure difference appears as voltage which can be monitored by the computer program. The accuracy of low capacity *DPT* measurement has been studied by (Pradhan et al., 1986). While testing saturated specimens, the same assembly was used to measure volumetric expansion or contraction by monitoring the volume of water drawn in or expelled out by the specimen respectively (Tatsuoka, 1981).



Figure 3.19: Photograph of *DPT* employed for this study.

The calibration of *DPT* was performed by collecting and draining out definite amount of water from the burette and recording the corresponding voltage change. Figure 3.20 shows the calibration curve of *DPT* used in this study. It can be seen from the calibration plot that there is perfect linearity and repeatability between volume change

of water and monitored voltage. The calibration factors were fed to the computer program to obtain the volume of water injected/drained out from the specimen directly in cubic centimeters (cm^3).

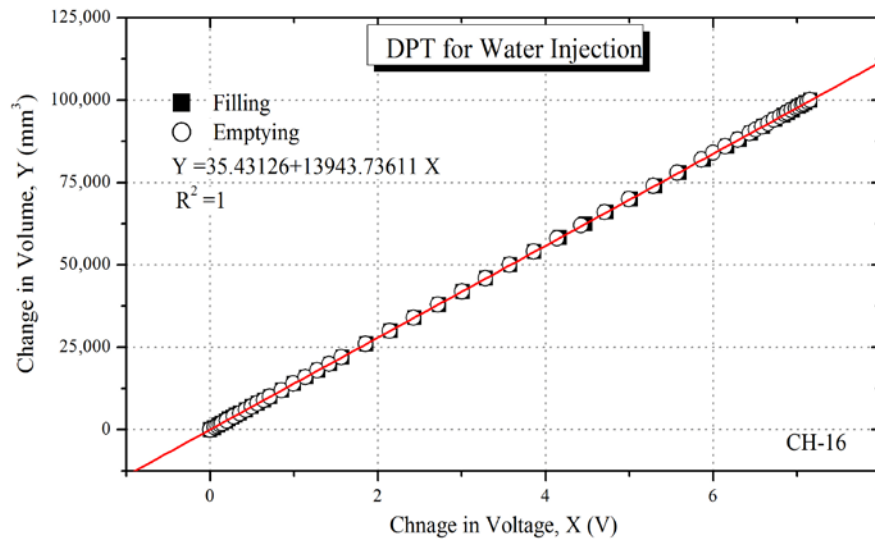
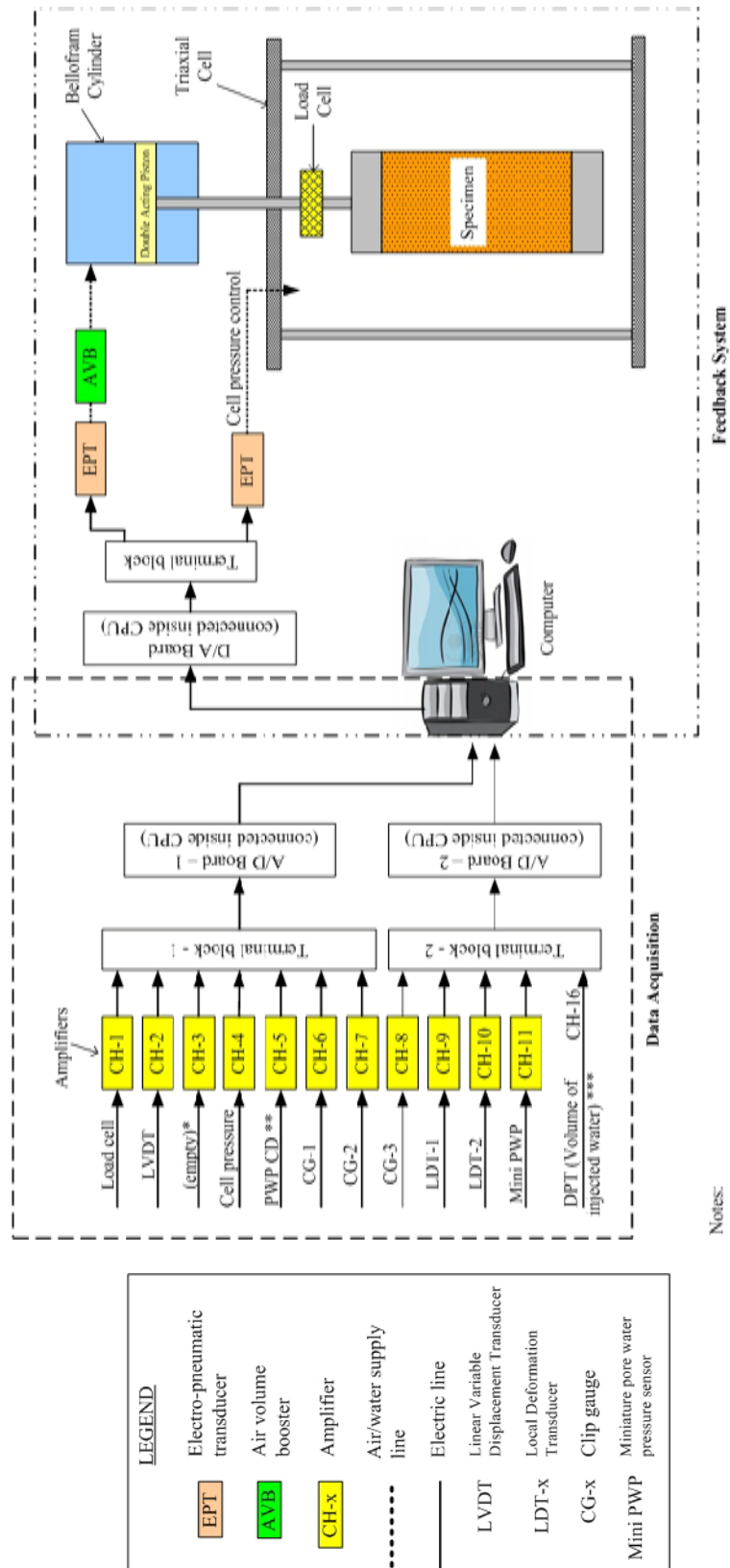


Figure 3.20: Calibration characteristics of differential pressure transducer (*DPT*).

3.2.7 Data Acquisition System

The output signals from electronic transducers were amplified by a set of amplifiers, converted into digital format, and then sent to the computer where data sampling at required frequency was done. Schematic layout of the data acquisition system is shown in Figure 3.21. There are two main components of the data acquisition system as explained briefly in the following section.



Notes:
 * : For unsaturated tests only, for saturated tests PWP sensor was used.
 ** : Pore water pressure sensor connected to ceramic disk. Only for unsaturated specimens.
 ***: For saturated tests, used for volume change of specimen.

Figure 3.21: Schematic layout of data acquisition system.

3.2.7.1 *A/D (analogue to digital) Converter*

Various transducers installed on the triaxial apparatus provide feedback (output) in the form of voltage. The function of analogue to digital (*A/D*) converter board is to convert this instantaneous voltage from the transducers into digital format to be fed to the computer port for subsequent data processing and logging. Two 16 bit (4.9 mV), 8 channel *A/D* differential converter boards (*NEC; Model: AD12-16T(98)H*) connected inside the CPU through PCI slots were used in this study. Analogue signals from various sensors were fed to *A/D* boards through terminal blocks (*Interface; Model: TRM-7000*). The breakdown of channels used in this study is as follows:

- | | |
|----------|--|
| 1. CH1 | Axial load cell |
| 2. CH2 | LVDT |
| 3. CH3 | (empty) |
| 4. CH4 | Cell pressure |
| 5. CH5 | Pore water pressure/matric suction (connected to ceramic disk) |
| 6. CH6 | Clip gauge-1 |
| 7. CH7 | Clip gauge-2 |
| 8. CH8 | Clip gauge-3 |
| 9. CH9 | LDT-1 |
| 10. CH10 | LDT-2 |
| 11. CH11 | Miniature pressure sensor |
| 12. CH16 | DPT |

3.2.7.2 *Feedback System*

The feedback control system consisted of digital to analogue (*D/A*) converter, electro-pneumatic (*E/P*) transducers, and air volume (*A/V*) boosters. The feedback system controlled the axial load, cell pressure and pore water pressure/infiltration pressure during the experiments according to the instructions of controlling computer program. A brief description of components of feedback system is as follows.

a) *D/A (digital to analogue) Converter*

The digital to analogue (*D/A*) converter board employed for this study had 12 bit conversion resolution on each of its 8 channels. The function of *D/A* board was to convert the digital instructions from computer into analogue form to drive various

feedback control components. The breakdown of *D/A* board channel usage is as follows;

1. CH1 Axial load control unit
2. CH2 Cell pressure control
3. CH3 Back pressure/infiltration pressure control
4. CH4 (empty)

b) *E/P* (electro-pneumatic) Transducers and Air Volume (*A/V*)

Booster

Two electro-pneumatic (*E/P*) transducers, one to control axial load, and another to control cell pressure were used in this study. The *E/P* transducers used, were *FAIRCHILD* product, *model: TT6000-026U*, operating over range of 0 ~ 800 kPa on a scale of 0 ~ 10V DC with input air supply range of 860 ~ 1000 kPa. The calibration of *E/P* transducers was conducted by recording the pressure output from *E/P* transducers on the application of a known input voltage. Calibration curves for *E/P* transducers used in this study, shown in Figure 3.22, depict perfect linearity and repeatability. Calibration of *E/P* transducers is of significant importance to control the axial/radial loading rate properly.

It is to be noted that output air volume from *E/P* transducers is generally small, thus, the pressure stabilization takes a long time. Whereas, to maintain the required magnitude of axial load during stress controlled tests, rapid changes in air pressure are required. Therefore, for obtaining faster stabilization of axial load controlling pressure, the output air from the axial load *E/P* transducers was connected to an air volume booster. Air volume (*A/V*) booster manufactured by *Fujikura Co. Ltd.*, (*Model: RR-HR*) with an operating range of 14 ~ 840 kPa and a maximum supply pressure of 990 kPa, was used in this study.

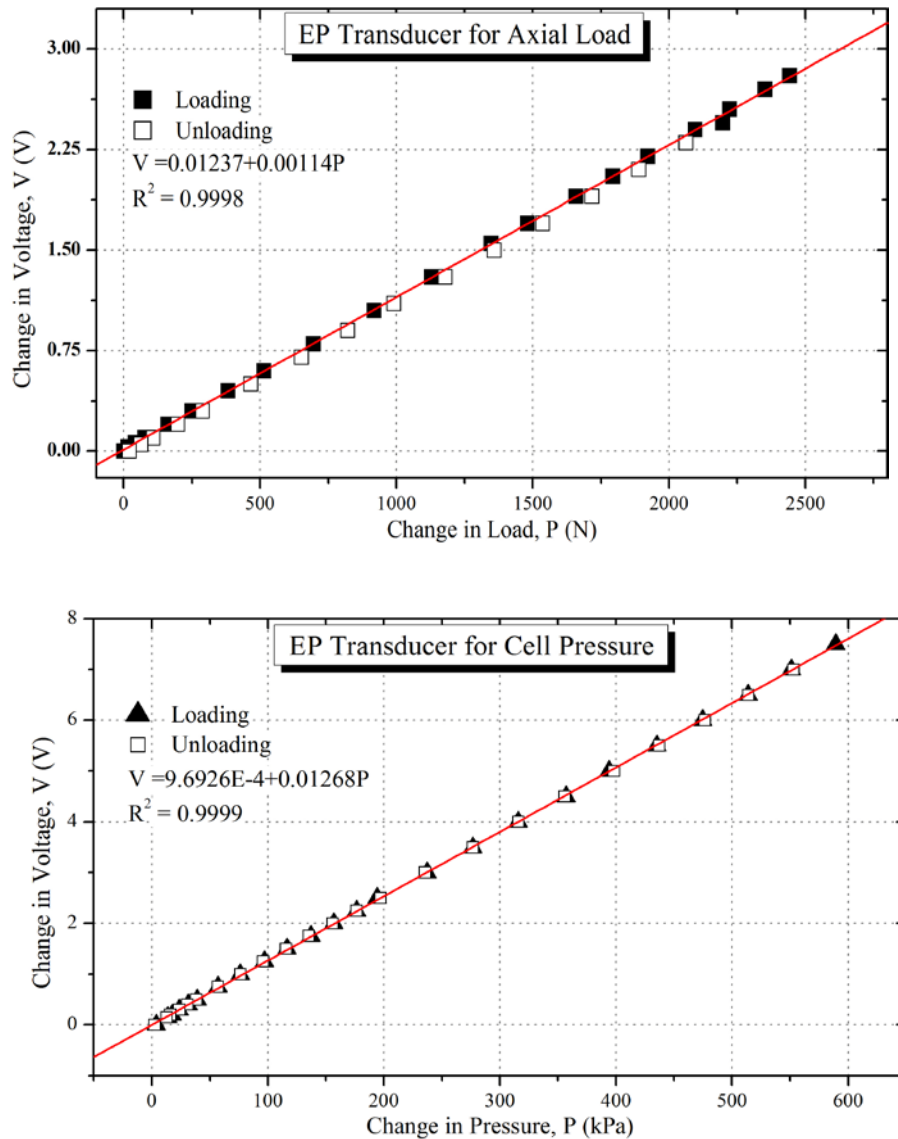


Figure 3.22: Calibration curves of electro-pneumatic (E/P) transducers.

3.3. ELASTIC WAVE MEASUREMENT SYSTEM

The base pedestal of triaxial cell was modified to house piezoelectric disk transducer (explained in Chapter 5), which was held firmly at the center of pedestal by means of an O-ring. The corresponding top cap was modified accordingly. The modified top cap and pedestal are shown in Figure 3.23.

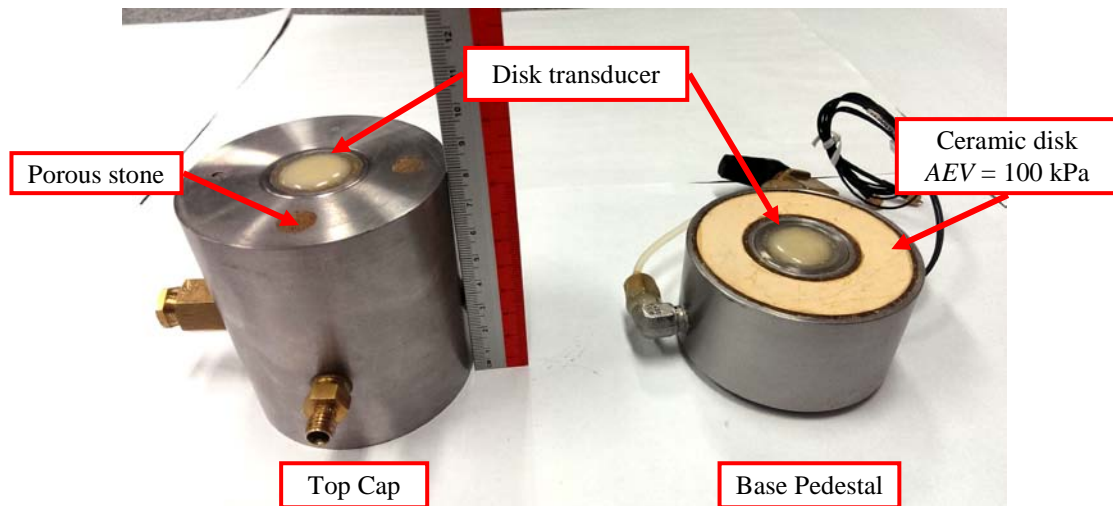


Figure 3.23: Modified pedestal and top cap of triaxial apparatus, fitted with disk type piezoelectric transducers at their respective centers.

Besides the disk transducers, a chain of equipments was used to generate, amplify, and then receive the elastic waves which are explained in the following sections and are schematically shown in Figure 3.24.

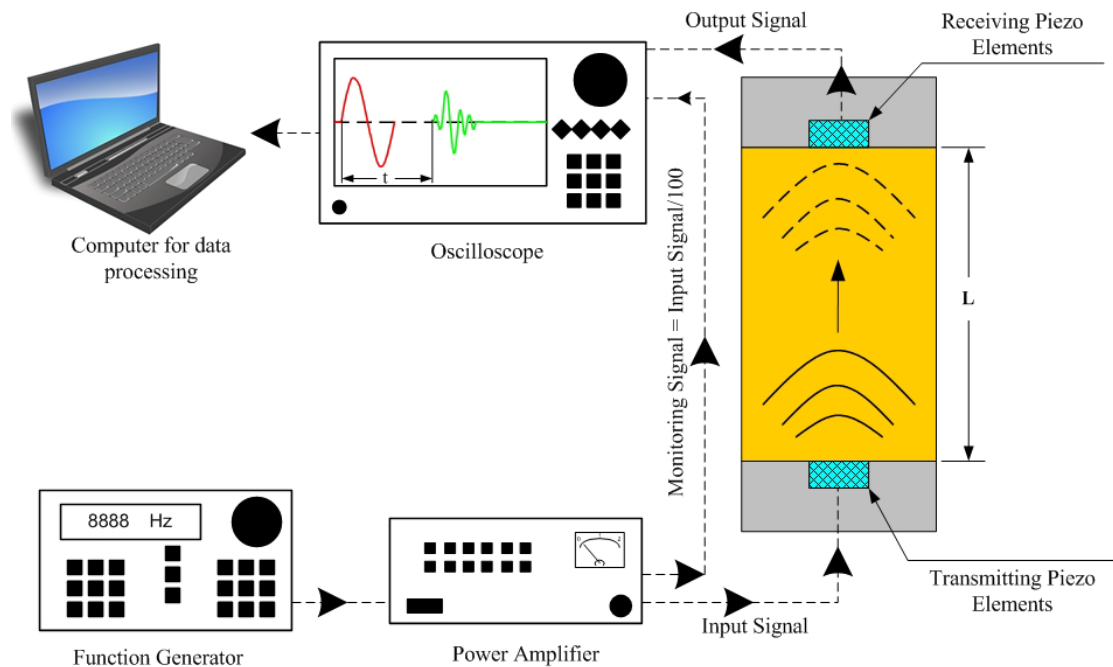


Figure 3.24: Schematic layout of elastic wave measurement system.

3.3.1 Function Generator

For generating the input signals, a function generator manufactured by *Tektronix Co. Ltd.*, Model *AFG-3022C*, was used. It was capable of producing twelve different kinds of input waveforms with a maximum peak to peak voltage of 10 V ($10 V_{PP}$). A photograph of said function generator is shown Figure 3.25 while a summary of its features is presented in Table 3.1.

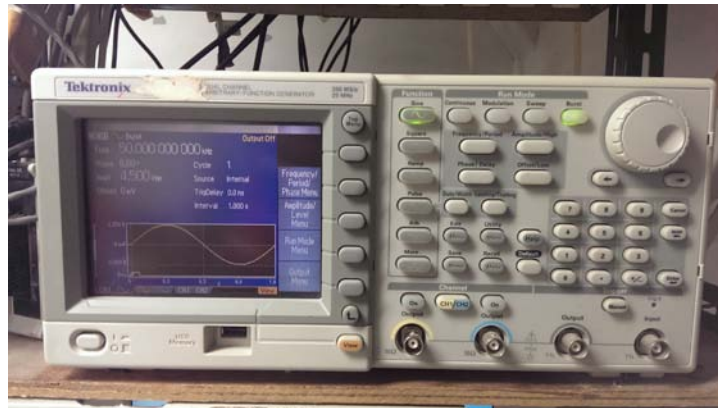


Figure 3.25: *Tektronix AFG-3022C* function generator used in this study.

Table 3.1: Salient features of *Tektronix AFG-3022C* function generator.

<i>Feature</i>	<i>Value</i>
Number of output channels	2
Peak to peak voltage (maximum)	10 V
Frequency range	0.001 Hz to 25 MHz
Trigger rate	1 ms to 500 s
Maximum sampling rate	250 MS/s
Resolution (vertical)	14 bits
Display	5.6 inches color display

3.3.2 Power Amplifier

The function generator could only generate an excitation up to a maximum of $10 V_{PP}$. This amplitude of excitation was not enough to generate signals which were discernible by the receiving piezoelectric transducer. The input signals were therefore

amplified by a power amplifier manufactured by *NF Corporation Japan*, Model: *HSA4012* (Figure 3.26). This amplifier was rated as “*high speed amplifier*”, which ensured that even for high frequency input waves, the signals were amplified without any distortion or time lag. For instance, the response of *NF* high speed amplifier was compared with an ordinary custom-built amplifier. The response of a single square wave pulse, generated by function generator, and amplified by the power amplifiers is shown in Figure 3.27. It can clearly be seen that, due to the slow response of custom-built amplifier, the square input wave is distorted and is converted into a trapezoidal shape. The high speed amplifier on the other hand, managed to preserve the original shape of input waveform. For all the experiments conducted in this study, *NF HSA4012* high speed amplifier was thus used.



Ordinary custom-built amplifier



NF HSA4012 High speed amplifier

Figure 3.26: Photographs of power amplifiers used in this study.

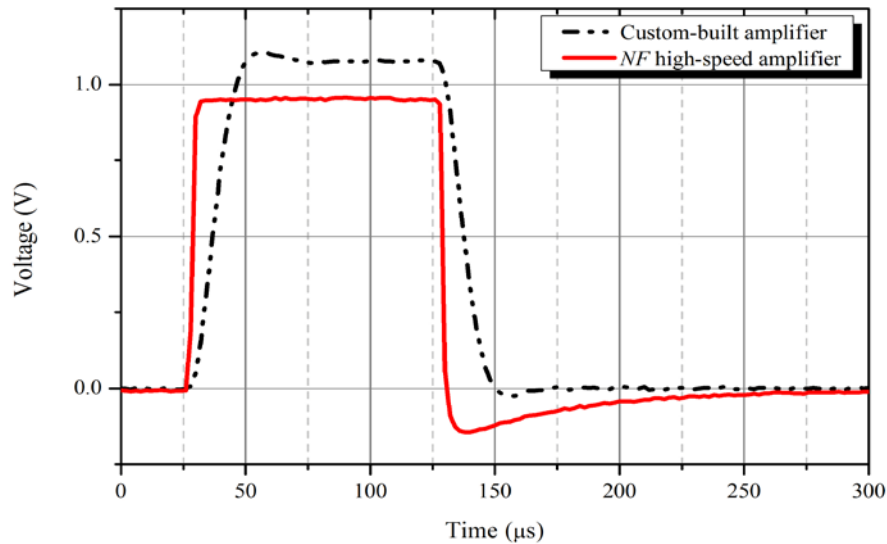


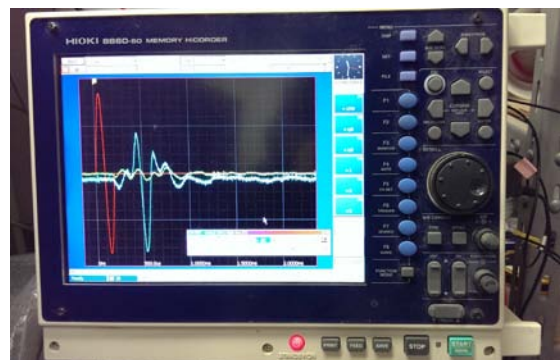
Figure 3.27: Response of ordinary custom-built amplifier against *NF HSA4012* high speed amplifier.

3.3.3 Recording Unit

A data logger “*Keyence Corporation Ltd., Model: NR-500*” with “*NR-HA08 hi-speed measurement unit*” (Figure 3.28(a)), was initially used. However due to persistent noise problems, it was replaced by a high resolution multi-channel digital oscilloscope “*Hioki 8860-50*” with “*Hioki 8957 hi-resolution input module*” (Figure 3.28(b)). A performance comparison of two recording units presented in Chapter 5 clearly highlights the superiority of *Hioki* oscilloscope over *Keyence* data logger. Therefore, for all the subsequent triaxial tests *Hioki* oscilloscope was used for recording received waveforms. Salient features of *Hioki* oscilloscope are presented in Table 3.2.



(a) *Keyence NR-500* Data Logger



(b) *Hioki 8860-50* Oscilloscope

Figure 3.28: Wave recording devices used in this study.

Table 3.2: Salient features of *Hioki 8860-50* oscilloscope (all features corresponds to when installed with *Hioki 8957* hi-resolution input module).

<i>Feature</i>	<i>Value</i>
No. of input units	Max. 4 units
No. of channels	Max. 16 analogue channels (max. 64 units with scanner unit) + 16 logic channels (standard configuration)
Measurement range	5mV to 20V/div, 12 ranges; low-pass filter: 5Hz/50Hz/500Hz/5kHz/50kHz.
Measurement resolution	1/1600 of measurement range (using 16-bit A/D conversion of 8860-50 model)
Highest sampling rate	2MS/s (simultaneous sampling in multiple channels)
Accuracy	DC amplitude: $\pm 0.2\%$ of full scale (with filter 5Hz) Zero position: $\pm 0.1\%$ of full scale (with filter 5Hz after zero adjustment)
Frequency characteristics	DC to 10MHz
Max. allowable input	DC 400V
Time axis at memory function	5 μ s to 5min/div
Memory capacity	12-bits x 32M-Words/ch (for 1 channel) to 2M-Words/ch (for 16 channels). Memory can be expanded 32 times (Optimal memory board)

3.4. SUMMARY

An efficient experimental apparatus is the key to successful research. Details of the experimental equipment used for this research have been discussed in length in this chapter. Modifications done to a typical triaxial apparatus to suit the needs of this study have been outlined. Detailed description of various machine parts and equipments is highlighted by means of properly labeled photographs and schematic illustrations. Basic working principles, salient features, as well as the calibration procedures of various equipments are discussed in detail. Various components of elastic wave measurement system, which forms the core of this study, have also been presented and main features of various components are summarized in tabular form.

3.5. REFERENCES

- Agus, S. S., & Schanz, T. (2005). Comparison of Four Methods for Measuring Total Suction. *Vadose Zone J.*, 4(4), 1087-1095. doi: 10.2136/vzj2004.0133
- Bishop, A., & Donald, I. (1961). *The Experimental Study of Partly Saturated Soil in the Triaxial Apparatus*. Proceedings: Proceedings of the 5th International Conference on Soil Mechanics and Foundation Engineering, Paris (pp. 13-21).
- Bishop, A. W., & Henkel, D. J. (1962). *The Measurement of Soil Properties in the Triaxial Test* (2nd ed.). London: St. Martin's Press.
- Chiu, C. F. (2001). *Behaviour of Unsaturated Loosely Compacted Weathered Materials*. Ph.D. thesis, The Hong Kong University of Science and Technology, Hong Kong.
- Cui, Y., & Delage, P. (1996). Yielding and Plastic Behaviour of an Unsaturated Compacted Silt. *Geotechnique*, 46(2), 291-311.
- Fredlund, D. G., & Rahardjo, H. (1993). *Soil Mechanics for Unsaturated Soils*: Wiley-Interscience Publication, John Wiley & Sons, New York.
- Geiser, F., Laloui, L., Vulliet, L., Rahardjo, H., Toll, D., & Leong, E. (2000). *On the Volume Measurement in Unsaturated Triaxial Test*. Proceedings: Unsaturated soils for Asia. Proceedings of the Asian Conference on Unsaturated Soils, UNSAT-Asia 2000, Singapore, 18-19 May, 2000. (pp. 669-674).
- Goto, S., Tatsuoka, F., Shibuya, S., You-Seong, K., & Sato, T. (1991). A Simple Gauge for Local Small Strain Measurements in the Laboratory. *Soils and Foundations*, 31(1), 169-180.
- Hoque, E., Sato, T., & Tatsuoka, F. (1997). Performance Evaluation of Ldts for Use in Triaxial Tests. *ASTM geotechnical testing journal*, 20(2), 149-167.
- Ng, C. W., & Chiu, A. C. (2001). Behavior of a Loosely Compacted Unsaturated Volcanic Soil. *Journal of Geotechnical and Geoenvironmental Engineering*, 127(12), 1027-1036.

- Ng, C. W., Zhan, L., & Cui, Y. (2002). A New Simple System for Measuring Volume Changes in Unsaturated Soils. *Canadian Geotechnical Journal*, 39(3), 757-764.
- Pradhan, T. B. S., Tatsuoka, F., & Molenkamp, F. (1986). Accuracy of Automated Volume Change Measurement by Means of a Differential Pressure Transducer. *Soils and Foundations*, 26(4), 150-158.
- Sarsby, R., Kalteziotis, N., & Haddad, E. (1980). Bedding Error in Triaxial Tests on Granular Media. *Geotechnique*, 30(3).
- Tani, Y., Hatamura, Y., & Nagao, T. (1983). Development of Small Three Component Dynamometer for Cutting Force Measurement. *Bulletin of the Japanese Society of Mechanical Engineering*, 26(214), 650-658.
- Tatsuoka, F. (1981). A Simple Method for Automatic Measurement of Volume Change in Laboratory Tests. *Soils and Foundations*, 21(3), 104-106.
- Tatsuoka, F., Teachavorasinskun, S., Dong, J., Kohata, Y., & Sato, T. (1994). Importance of Measuring Local Strains in Cyclic Triaxial Tests on Granular Materials. *ASTM Special Technical Publication*, 1213, 288-288.

MATERIALS & METHODOLOGY

Chapter 4

CHAPTER 4

MATERIALS & METHODOLOGY

4.1. TEST MATERIAL

The main aspire of this study was to explore the mechanism of wave velocity variation during actual landslides. The understanding of such mechanism was deemed necessary to use it in practical landslide early warning. Edosaki sand, a brown colored natural sand, which makes up several natural slope surfaces across Japan, was used as test material of this study. The following sections explain the procedure of soil procurement and physical properties of tested material.

4.1.1 Material Preparation

Edosaki sand used in this study was procured from a trench pit in Tsukuba, Japan. In order to ensure consistency of tested material, soil from several soil bags was thoroughly mixed together. Soil was first air, and then oven-dried. Particles larger than 2 mm diameter were removed through sieving. In this manner, a sufficient quantity of homogenous soil was procured.

4.1.2 Physical Properties of Test Material

The particle size distribution of test ready Edosaki sand is shown in Figure 4.1 whereas Figure 4.2 shows the compaction characteristics of the same. Table 1 summarizes physical properties of Edosaki sand. All the tests for the determination of index properties were performed according to Japanese Geotechnical Society (*JGS*) standards. Where G_s is the specific gravity of soil solids, e_{min} and e_{max} refer to minimum and maximum void ratios, D_{50} correspond to mean particle diameter, U_c is

the coefficient of uniformity defined as D_{60}/D_{10} , obtained from particle size distribution curve, and F_c is the percentage of fines passing sieve size 0.075 mm.

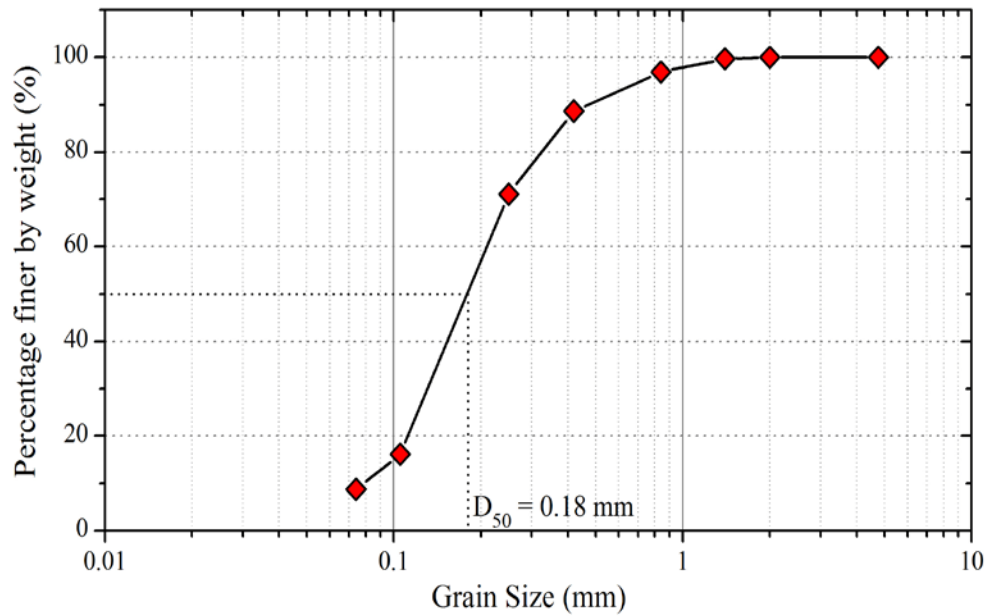


Figure 4.1: Particle size distribution of Edosaki sand.

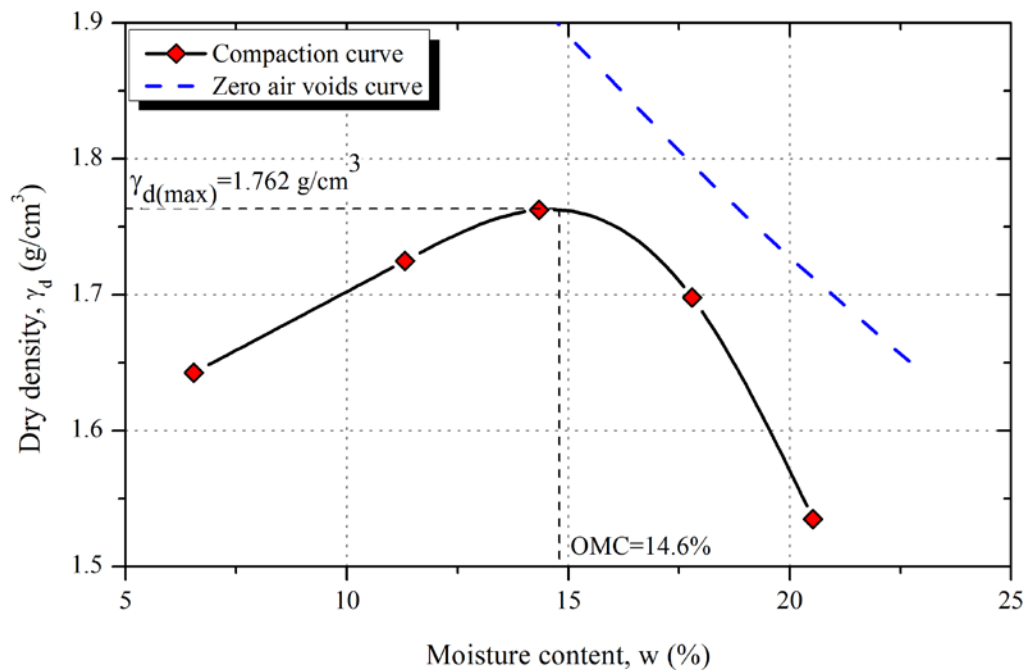


Figure 4.2: Compaction characteristics of Edosaki sand.

Table 4.1: Physical properties of Edosaki sand.

<i>Property</i>	<i>Value</i>
Specific gravity, G_s	2.639
Minimum void ratio, e_{min}	0.647
Maximum void ratio, e_{max}	1.160
Fines (%)	9
Coefficient of uniformity, C_u	2.82
Coefficient of curvature, C_c	1.157
Maximum dry density (g/cm^3)	1.762
Optimum moisture content (%)	14.6

4.2. EXPERIMENTAL PROGRAM

In order to conduct laboratory investigation on rainfall-induced slope failures and the corresponding effects on elastic wave propagation, a comprehensive testing program was formulated. The testing program was so defined that effects of soil moisture, and soil yielding on elastic wave propagation could be explored with considerable comprehension. An additional series of tests was designed to combine the effects of soil moisture and yielding, i.e. to replicate the actual landslide conditions. Various triaxial test series performed as part of this research are summarized below;

1. *ICCW* – Isotropically Consolidated Constant Water content tests
2. *ICWI* – Isotropically Consolidated Water Injection tests
3. *CWRSR* – Constant Water Radial Stress Reduction tests
4. *CSWI* – Constant Shear stress Water Injection tests

It is to be noted that hereafter, these tests will be referred by their above mentioned code names. The following sections explain the general experimental procedures of each test series.

4.3. GENERAL EXPERIMENTAL PROCEDURES

The laboratory investigation was mainly conducted by means of triaxial tests. Test procedures of various kinds of tests series performed in this study are explained in the following sections;

4.3.1 Unsaturated Specimens (*ICCW, ICWI, CWRSR and CSWI tests*)

Majority of tests conducted as part of this study were performed on initially unsaturated sand specimens. The following sections explain the general steps involved in conducting triaxial tests on initially unsaturated specimens.

4.3.1.1 *Saturation of Ceramic Disk*

For the measurement of initial matric suction of soil specimens, a high air entry value (*AEV*) ceramic disk of 100 kPa was embedded in the pedestal of triaxial apparatus. The ceramic disk was of donut shape (Figure 3.13), to accommodate the disk type piezoelectric transducer at the center of the base pedestal. For accurate determination of matric suction, ceramic disk and the associated measuring system (compartment below the ceramic disk, pressure transducer, lines connecting base pedestal with pressure transducer) were required to be fully saturated. Presence of air bubbles inside the measuring system reduces the measurement efficiency due to compressibility of air.

For saturation, ceramic disk embedded base plate was immersed in a chamber filled with water (Figure 4.3(a)). To avoid water entering the disk transducer and disturbing its electrical connections, the base pedestal was placed upside down in the chamber (Figure 4.3(b)). The chamber was subjected to vacuum of 101.3 kPa for about 24 hours. During this period, the chamber was tapped gently by a wooden hammer to remove air entrapped in water and, the pores of ceramic disk itself. After this process, the base pedestal was carefully removed from the chamber, set in the triaxial apparatus, and connected to the pressure transducer. The pressure transducer itself, and the line connecting it with ceramic disk was saturated by flushing water through it.

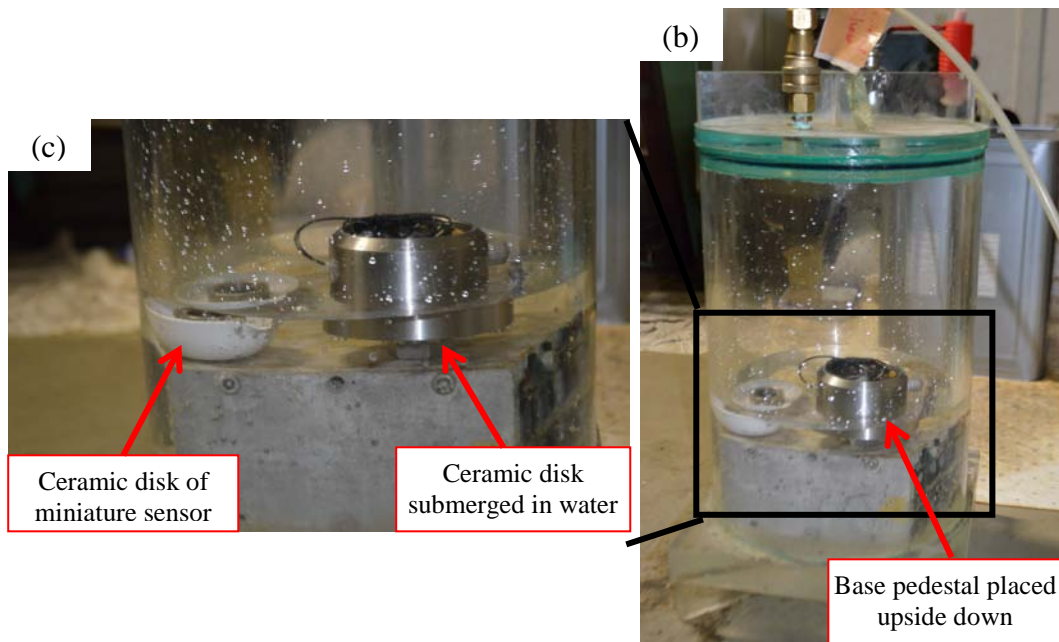
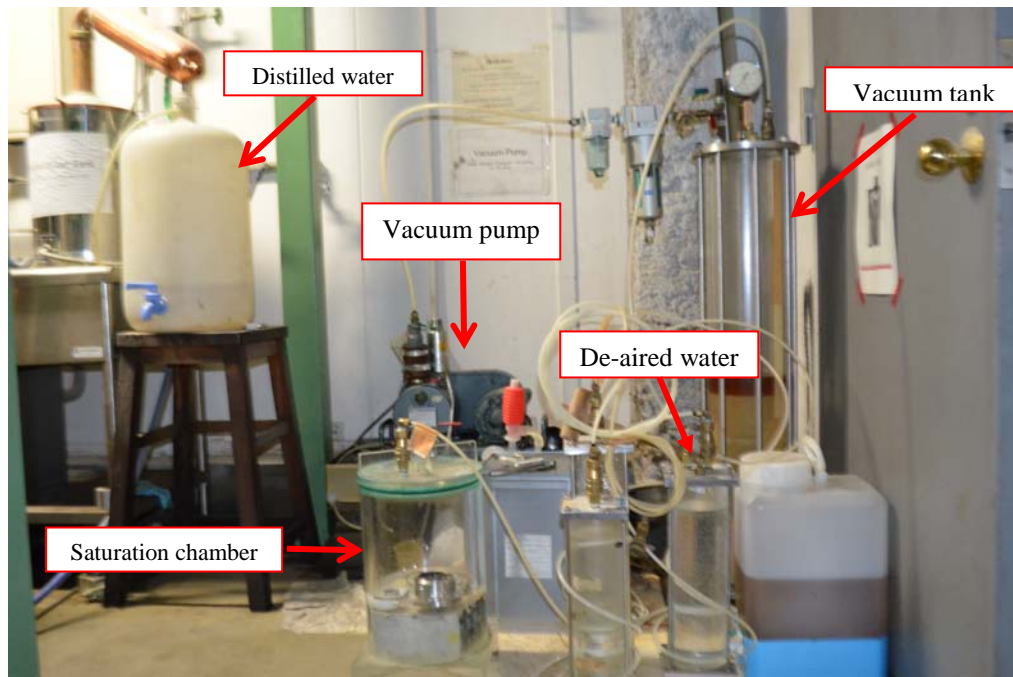


Figure 4.3: Saturation of ceramic disk. (a) Vacuum system for saturating ceramic disks and deairation of water (b) Saturation chamber close-up (c) Close-up view of ceramic disks submerged in water.

To ensure proper saturation of ceramic disk and associated measuring system, a check was made following the guidelines provided by (Huang, 1994). Water was briefly flushed through ceramic disk to refill the pores which might have dried due to evaporation. Water connection was then closed and the surface of saturated ceramic disk was wiped with a soft cloth/tissue paper. Due to the evaporation of water from the ceramic disk (due to air drying), negative pressure gradually started to develop. Change in negative pressure with time was recorded. Saturation of ceramic disk and the associated measuring system was considered perfect when a negative pressure could develop up to 60-70 kPa (Huang, 1994). If not, the whole process was repeated. Typical response of ceramic disk saturation check is shown in Figure 4.4 (after Huang (1994)). Once the saturation is confirmed, water is again flushed through the base of ceramic disk in order to saturate the top portion which dried-up during the saturation check.

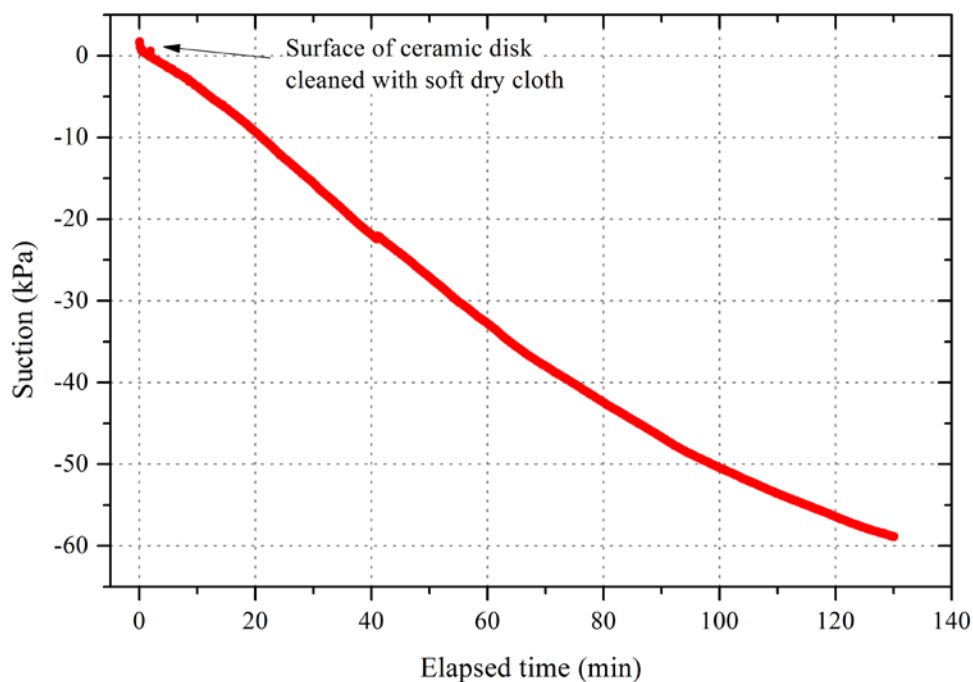


Figure 4.4: Saturation check of ceramic disk.

4.3.1.2 Saturation of Miniature Pore Pressure Sensor

During water injection tests (ICWI and CSWI tests), water was injected through the base pedestal ceramic disk. This rendered the measurement of matric suction with base pedestal ceramic disk impossible. Therefore, to continuously monitor the variation of pore water pressure upon water injection, a miniature pore water pressure was placed mid-height of the specimen. The connecting cable of transducer was taken out of the specimen through top cap. The detailed description of miniature pore pressure sensor and its calibration is discussed in Section 3.2.5.2 of Chapter 3.

For accurate measurement of pore water pressure, the miniature sensor and the ceramic at its front were required to be properly saturated. The front cap of miniature sensor which housed the ceramic disk was removed. It was then submerged in water and subjected to a negative pressure of 101.3 kPa for 18-24 hours (Figure 4.3). Gentle tapping of the chamber with a wooden hammer helped to remove entrapped air from the ceramic disk. Upon the completion of saturation, it was removed from vacuum chamber but was kept submerged in water (inside a small bowl of water). Miniature sensor was then immersed in the same bowl of water. Any small air bubbles inside the miniature sensor were removed carefully. Keeping them submerged in water, the cap (containing the saturated ceramic disk) was then housed over the miniature sensor and the screw was tightened. Since, cap and sensor were kept submerged in water during the whole process, so no air could enter the sensor and the assembly remained saturated.

In order to confirm the saturation of miniature sensor and check for possible leakages, the saturated miniature sensor was suspended in air and the ceramic disk was wiped with a soft cloth (tissue paper). As the ceramic disk dried in air, suction started to develop in miniature sensor. However, it was found that the thread between sensor and cap could only hold negative pressure of 4~5 kPa. This was observed by a sudden drop in negative pressure as soon as it reached about 4.5 kPa. In order to strengthen the sealing, the screw between the sensor and cap was coated with a layer of high vacuum grease (*Silicon High Vacuum Grease manufactured by Dow Corning Co., Ltd.*). Suction holding capacity was improved to about 20 kPa, beyond which air bubbles again seeped through the thread. As a further improvement, in addition to greasing the threads, the sensor was also coated with a layer of silicon rubber (*Shin-*

Etsu Silicon; Model: *KE45T*). Silicon rubber requires 12-24 hours for gaining strength. During this time, the sensor was kept submerged in water so as to avoid de-saturation of ceramic disk; silicon rubber thus hardened inside water. This made the sensor air-tight and enabled measurement of suction to the maximum capacity of sensor, i.e. 50 kPa. A comparison of miniature sensor response to various sealing techniques is shown in Figure 4.5.

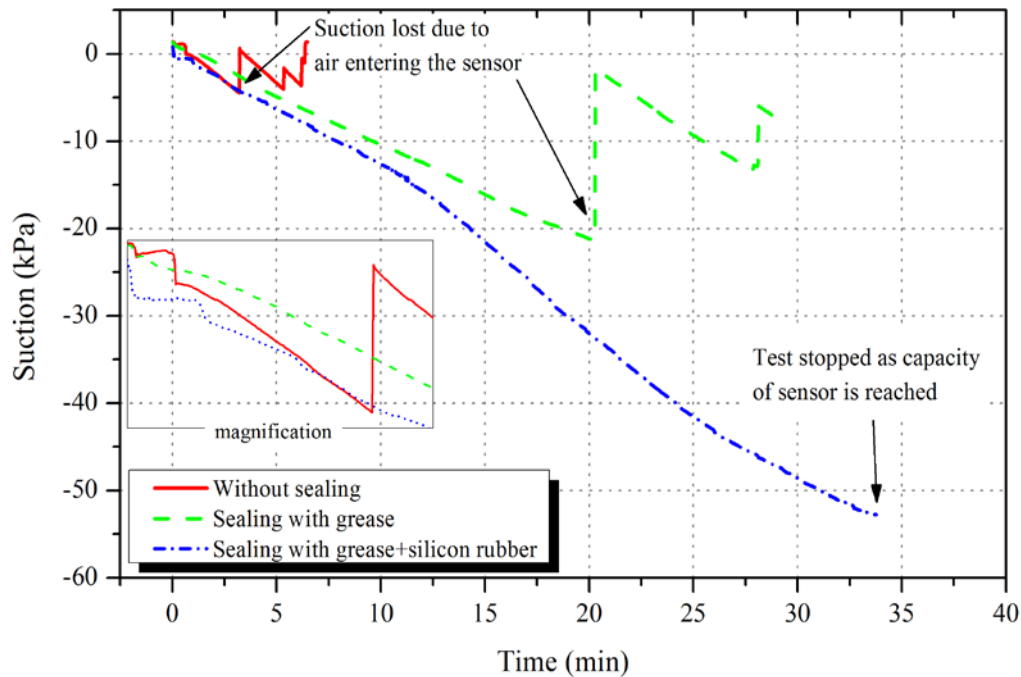


Figure 4.5: Suction response of miniature sensor to various air-tightening techniques.

4.3.1.3 Specimen Preparation

After saturation check, the base plate was connected to a water chamber in order to avoid de-saturation of ceramic disk and associated system. A rubber membrane (0.3 mm thick) was fastened to the circumference of ceramic disk by means of O-ring (or by stretching and tying up a strip of rubber membrane). The split mould was then set up and membrane was stretched out to the inside face of the split mould by applying negative air pressure into the space between membrane and the inside face of split mould (Figure 4.6(a), (b)). The water connection to ceramic disk was then closed, its surface was wiped with a tissue paper and data acquisition was started.

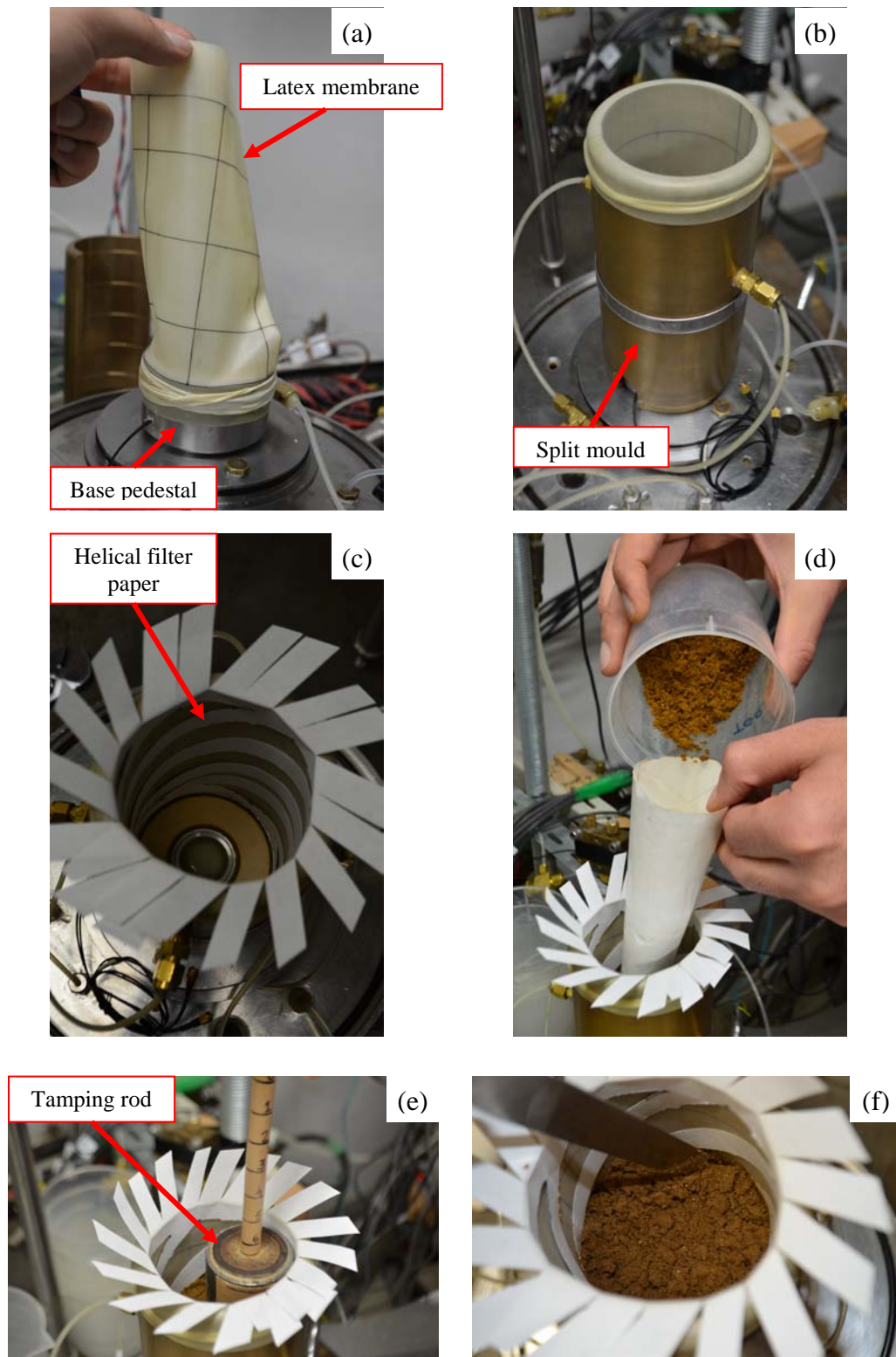


Figure 4.6: Specimen preparation steps - 1. (a) membrane is fastened to pedestal. (b) split mould is set up. (c) helical filter paper is set up (only in water injection tests). (d) soil is poured inside the mould. (e) tamping and checking the height of each layer. (f) roughening up surface to achieve a good bond with overlying layer.

The specimen was then directly prepared on top of saturated ceramic disk by the method of moist placement (wet tamping) in ten equal layers of 15 mm each. Oven dried soil was mixed with pre-calculated amount of water to obtain specified degree of saturation (S_r). This moist soil was then poured inside the split mould and each layer was prepared by using the same amount of moist soil with the same height. The moist soil was strewn evenly inside the mold and then compacted gently with a mass held by a rod until the predetermined height was reached. Same procedure was repeated for all ten layers. To improve the bond between two layers and to enhance the uniformity of specimen, the surface of each compacted layer was roughened before pouring the next layer. The finished specimens used for this study were of cylindrical shape having height of 153 mm and diameter 75 mm. Moist temping method of specimen preparation was advantageous for this study because it allowed good control over specified void ratio and initial degree of saturation of prepared specimens. Wet tamping procedure of specimen preparation is schematically shown in Figure 4.7.

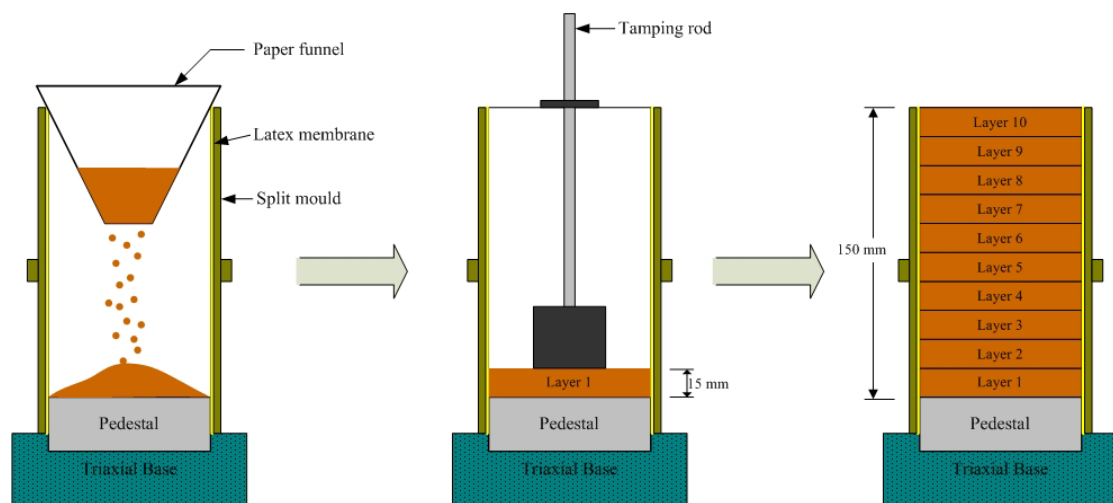


Figure 4.7: Wet tamping procedure of specimen preparation.

For test series comprising of injecting water into soil specimen (*ICWI* and *CSWI* tests), a helical shaped filter paper was set up inside the latex membrane before pouring soil into the mould (Figure 4.6(c)). Helical shape was formed by cutting a sheet of filter paper in such a way that it could be rolled into a helix. A photograph of template, used to form helical filter paper is shown in Figure 4.8. Presence of filter paper around soil specimen ensured more uniform distribution of moisture upon water injection (further details in Chapter 7; Section 7.5).

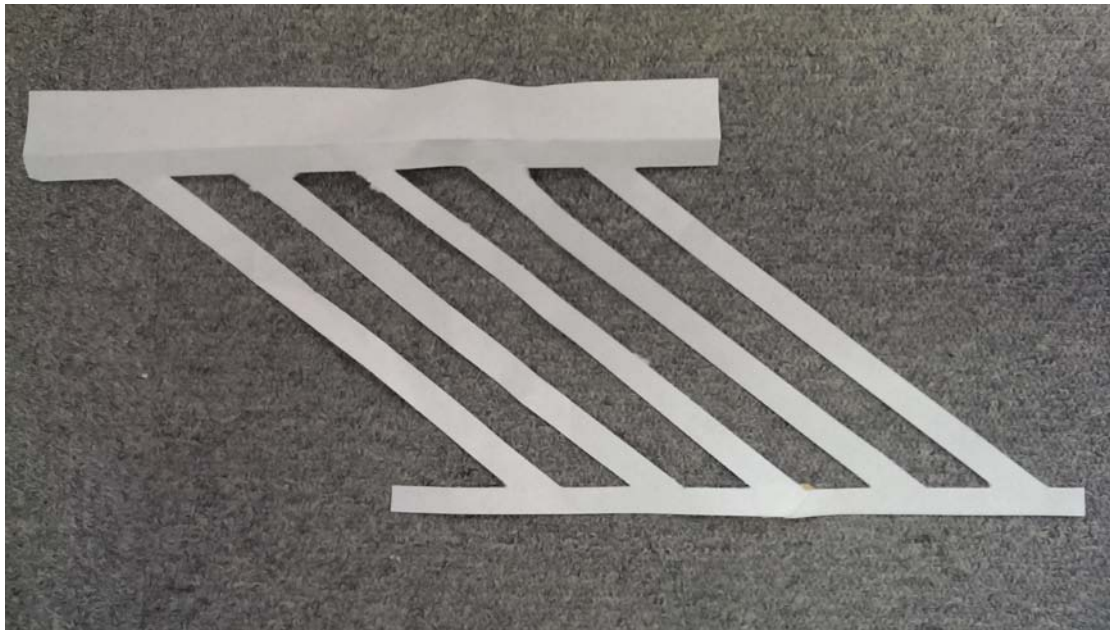


Figure 4.8: Template of helical filter paper used in water injection tests.

For *CSWI* test series a miniature pore water pressure sensor was used to monitor the variation of matric suction upon water injection. The sensor was placed at mid-height of the specimen. After pouring the sixth layer of soil, a small groove was made and the sensor was carefully placed inside the groove (Figure 4.9(a)). The sensor cable was taken out from the specimen through a small hole in top cap. Various stages of specimen preparation are shown in Figure 4.6 and Figure 4.9.

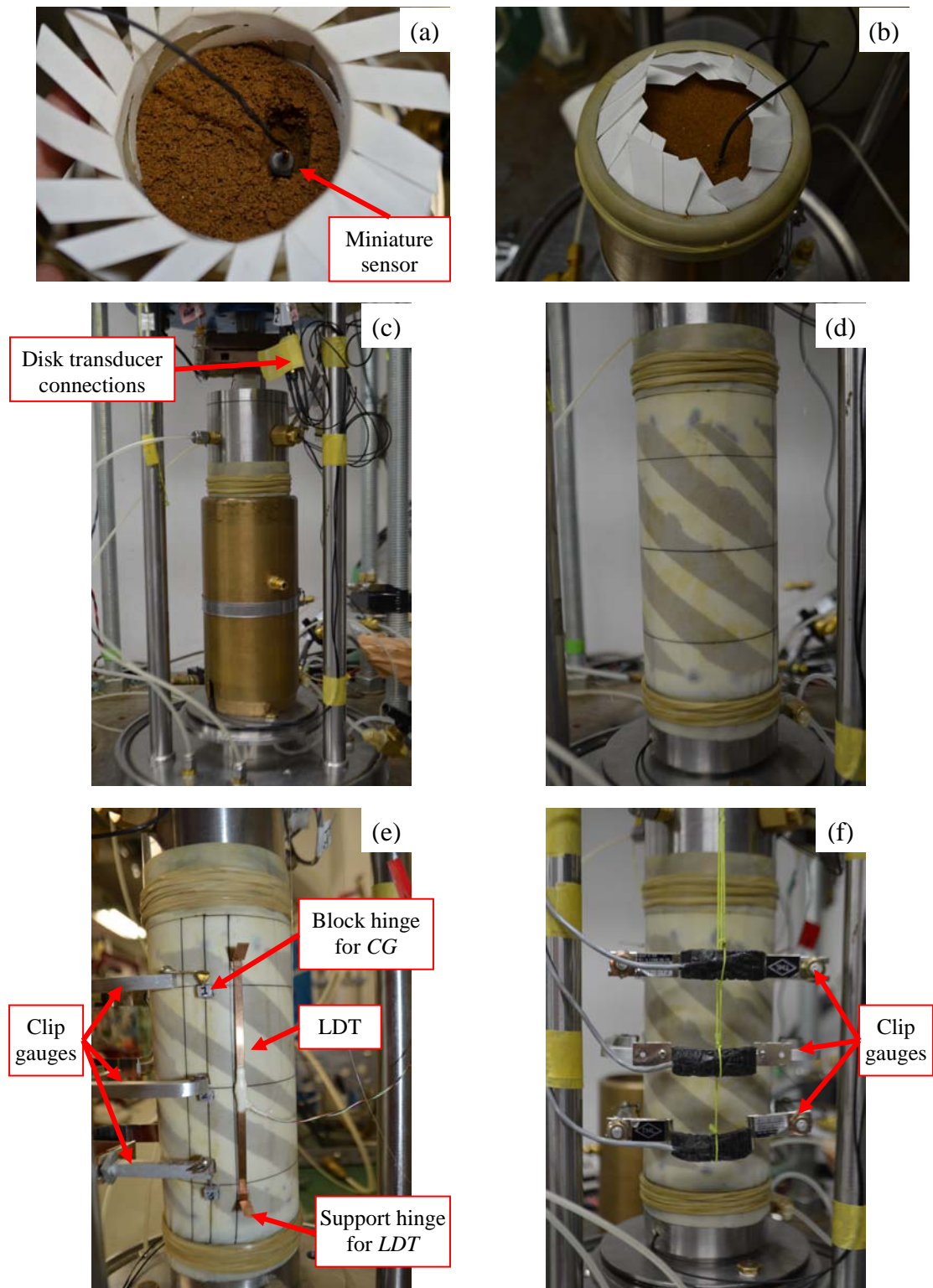


Figure 4.9: Specimen preparation steps-2 (a) miniature PWP sensor placed inside the groove (b) filter paper is wrapped over the tenth layer (c) top cap is placed and membrane is fastened to it (d) split mould is removed carefully (e) LDTs and clip gauges are attached through pseudo hinges (f) clip gauges are balanced and aligned

4.3.1.4 Assembling Triaxial Cell

After preparing the specimen inside the mold, the triaxial cell is set up over base plate of triaxial apparatus. The steps involved in assembling the triaxial cell are outlined below;

- The amplifiers were turned on approximately one hour before the start of the test, so that they could achieve their optimal operating temperature (in order to reduce electrical noise). Calibration parameters of all the sensors were fed to the computer and the respective connections were checked.
- The load cell, whose vertical movement is restricted by means of a clamp, was set to zero.
- The top cap was unclamped and then lowered slowly to a level such that it merely touched the soil specimen without imposing any stress on it. At this level, top cap was clamped again to restrict its movement. The membrane was then stretched up and fastened to the top cap.
- Disk transducer cables from base pedestal and top cap were connected to cables leading to outside the triaxial cell by means of pin connectors (Figure 4.9(c)).
- The split mould was then removed very carefully and the specimen was allowed to stand with its own weight (Figure 4.9(d)). It is worth considering that negative air pressure was not applied inside the specimen because it would have disturbed matric suction of specimen. Since most of the specimens were prepared in relatively well compacted state with certain initial moisture, the apparent cohesion between soil particles of Edosaki sand ensured them to stand on their own without any support.
- The top cap was vented to atmosphere to make pore-air pressure zero. Since rainfall-induced landslides typically occur at shallow depths, generally less than 3 meters (Brand et al., 1984; Anderson & Sitar, 1995; Collins & Znidarcic, 2004; Farooq et al., 2004; Xie et al., 2004), the pore air pressure can safely be assumed as zero. Thus, during all the tests on unsaturated specimens (*ICCW*, *ICWI*, *CWRSR* and *CSWI* tests), pore air pressure was maintained at atmospheric level.

- Height and diameter of specimen were measured by vernier calipers and pi-tape respectively.
- Hinges to support *LDTs* and clip gauges were glued to the membrane (Figure 4.9(e)). *LDTs* and clip gauges were then carefully attached to the specimen through their respective hinges (Figure 4.9(e) and Figure 4.9(f)). Care was taken to align the clip gauges properly about the vertical plane, so that they remain vertically aligned even after considerable axial deformation of specimen.
- The acrylic cell was placed on the base plate of the triaxial cell and was clamped tightly with the top plate.
- By means of an air regulator, a small cell pressure (5~8 kPa) was applied to the triaxial cell, in order to support the specimen in standing.
- The whole setup was placed coaxially with the vertical loading shaft coming from the bellofram cylinder and both shafts (one connected to the sample top cap) were connected together.
- Cell air pressure supply from air regulator was replaced with supply from *E/P* transducer. And an isotropic stress of 10 kPa was applied to the specimen by means of isotropic loading control of digit show basic software.

4.3.1.5 Monitoring Initial Matrix Suction

Matrix suction is defined as the difference between pore-air and pore-water pressure of soil. Since all the specimens were vented to atmosphere, (i.e. pore-air pressure, $u_a = 0$), matrix suction could be obtained by only monitoring the magnitude of pore water pressure (u_w). Pore water pressure of the specimen was thus measured by means of an external pressure transducer connected to the saturated ceramic disk.

Matrix suction is generally determined in a pressure plate (tempe pressure cell) apparatus without the application of any external stress. However, for testing unsaturated specimens in a triaxial apparatus, a small cell pressure had to be applied to keep the specimen standing. As described in the previous section, cell pressure of 10 kPa was applied to support the specimen. As soon as the soil was poured on top of saturated ceramic disk, the pore pressure transducer started measuring matrix suction (equal to negative pore pressure reading of pressure transducer). Matrix suction took

considerable time to equalize. Depending on specimen density, and its own magnitude, matric suction was typically equalized in 24~48 hours, as seen in Figure 4.10. Negative pore water pressure at the end of equalization was taken as initial matric suction of specimen. Matric suction is observed to decrease slightly when the specimen is subjected to isotropic stress (initial part of Figure 4.10). This may be because of increase in pore air pressure. However, the trend of matric suction returns to its original initial trend soon afterwards, as the increased pore air pressure dissipates.

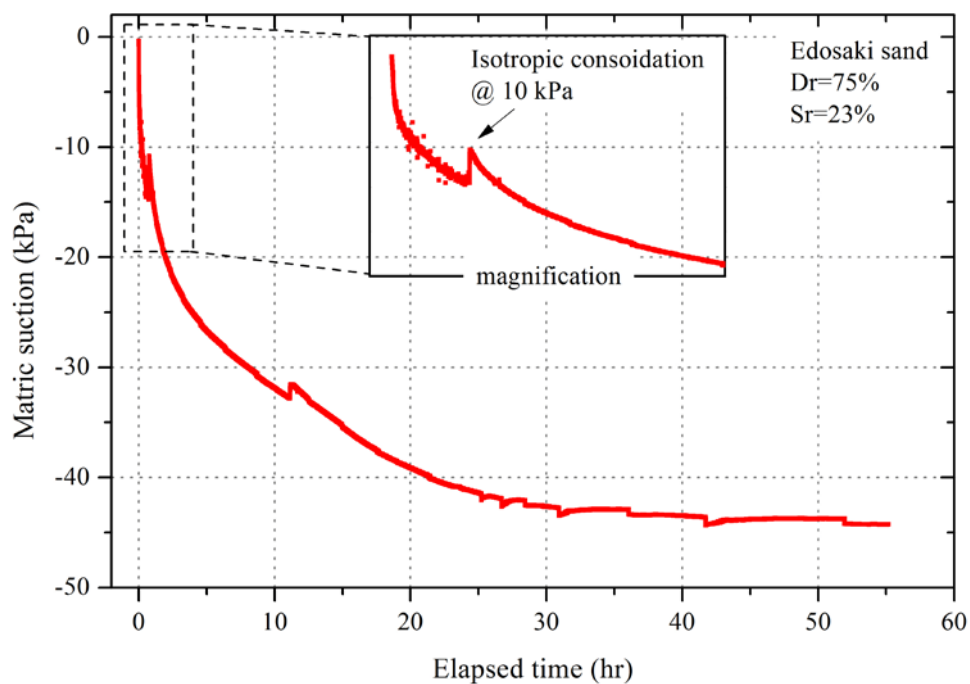


Figure 4.10: Initial matric suction of unsaturated Edosaki sand specimen during an *ICCW* test, measured by an external pressure transducer connected to the saturated ceramic disk.

In a similar way, initial matric suction of all the specimens of *ICCW* tests was determined. However, since the air entry value of ceramic disk was limited to 100 kPa, specimens with initial matric suction greater than 100 kPa could not be determined. In such cases ($S_r = 0\%$, and 10%), the capillary barrier at the interface of saturated ceramic disk and soil was broken and air entered the measurement system making

suction measurement impossible. Initial matric suction of various specimens in *ICCW* tests is summarized in Table 6.1 (Chapter 6).

During water injection in the *CSWI* tests, ceramic disk could not be used to measure matric suction of soil (since it was being used to inject water in specimen). However, it was used to determine the initial matric suction, before the start of water injection. Since all the *CSWI* tests were conducted at a confining pressure of 25 kPa, the initial matric suction was thus recorded after bringing the specimens to 25 kPa (as opposed to 10 kPa in *ICCW* tests). Similar to the ceramic disk, miniature pore pressure sensor also started recording suction as soon as it was brought in contact with soil. Due to the small surface area and less thickness of miniature sensor ceramic disk, it was generally observed to be more sensitive to suction changes, as compared to ceramic disk. Thus, miniature sensor generally took less time to develop the same matric suction. However, at the end of suction equalization, suction recorded by both sensors was found to be nearly equal, as shown in Figure 4.11(a).

Ceramic disk started developing matric suction as soon the soil was poured on top of it. However, the development of matric suction is disturbed due to tamping of soil during specimen preparation, as can be seen from the initial part of Figure 4.11(b). A small time lag exists in the initial part of suction curves obtained by two sensors (Figure 4.11(b)). This time lag is because of the delay in bringing the sensor in contact with soil; i.e., the ceramic disk came in contact with soil as soon as the first layer of soil was poured, whereas the miniature pressure sensor came in contact with the soil when the fifth layer was placed (since it was placed mid-height of the specimen).

Matric suction is observed to increase slightly as soon as the split mold is removed. This may be because of the increase in negative pore water pressure due to volumetric expansion of specimen, on removing the mold. On the contrary, matric suction decreases slightly when the specimen is subjected to isotropic stress of 25 kPa. This may be because of the increase in pore air pressure, which dissipated gradually and matric suction returned to its original trend.

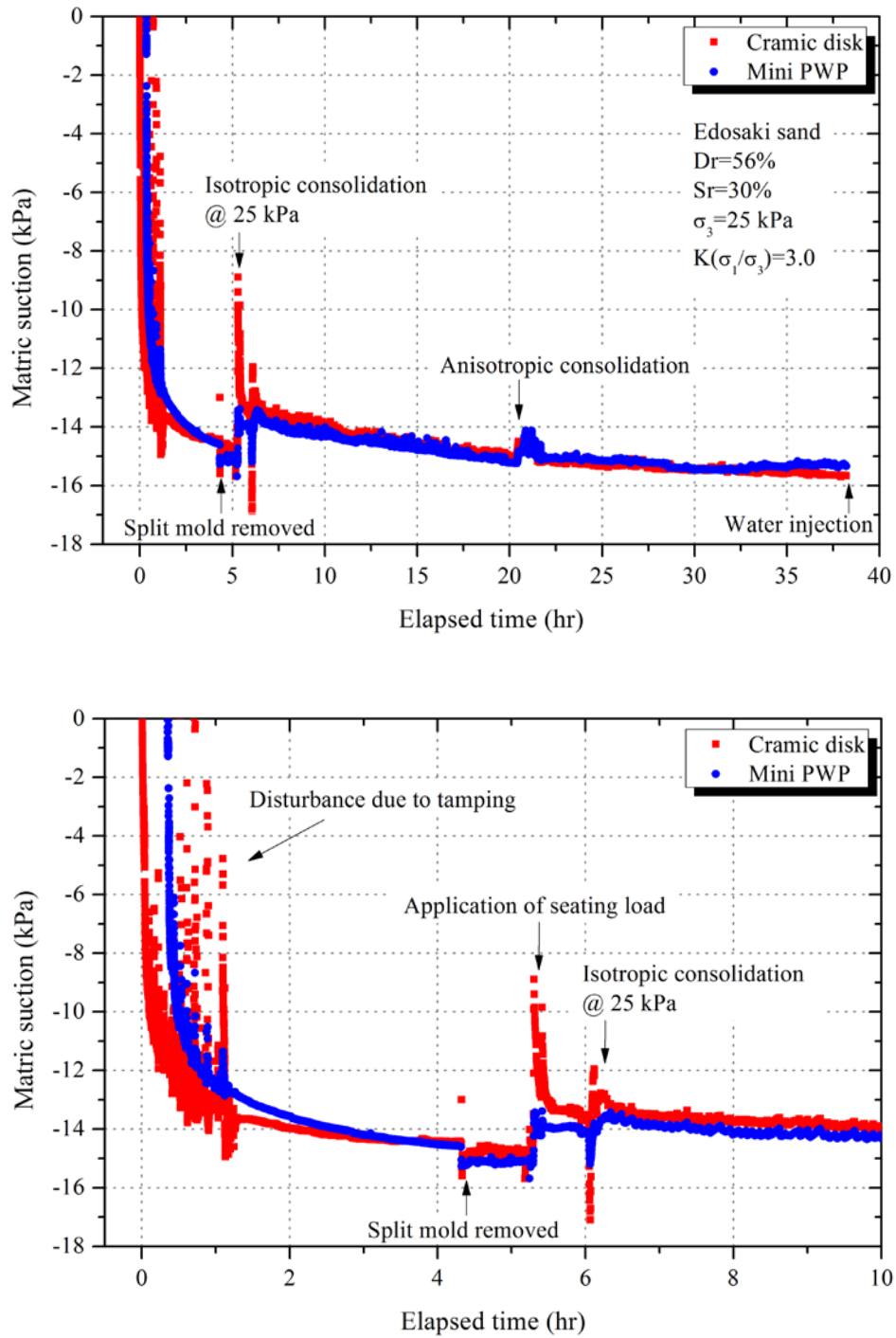


Figure 4.11: Initial matric suction measurement during CSWI tests; (a) comparison of matric suction measured by ceramic disk and miniature pore pressure sensor; (b) zoomed-in view of (a) showing, disturbance to initial matric suction during sampling, removal of split mold, and application of stress.

4.3.2 Saturated Specimens (ICCW and CWRSR tests)

Only a few tests were conducted on initially saturated triaxial specimens. The steps followed for conducting saturated triaxial tests are outlined below.

- The specimens were prepared by tamping into 10 equal layers in exactly the same way as explained in previous section. Specimens were prepared in initially dry condition, so that the pore air could easily be removed by applying vacuum.
- Negative pressure of 15 kPa was applied from top cap to keep the specimen standing on the removal of split mould.
- Triaxial cell was set up, calibration factors of sensors were fed to computer and the load cell was connected to loading shaft. The procedures adopted were similar to the ones explained for unsaturated specimens in previous section.
- Cell pressure was increased gradually to 15 kPa and at the same time negative pressure inside the specimen was reduced to zero. By doing so, the effective stress acting on the specimen at any time remained 15 kPa; but now the specimen was standing because of the positive pressure applied outside the specimen instead of the negative pressure applied inside the specimen.
- **De-airing the specimen:** A slight modification of ‘dry setting method’ proposed by Ampadu and Tatsouka (1993) was used for de-airing soil specimen. Vacuum inside the specimen was increased gradually in increments of -5 kPa (from top cap), at the same time cell pressure was decreased by equal magnitude. Thus, the cell pressure was decreased to 10 kPa, 5 kPa, 0 kPa, -5 kPa, -10 kPa, (and so on) for the corresponding negative pressures of -5 kPa, -10 kPa, -15 kPa, -20 kPa, -25 kPa, (and so on) inside the specimen. This process was continued until negative pressure inside the specimen reached 90 kPa and the corresponding cell pressure became 75 kPa. In this way, the effective stress acting on the specimen at any time remained -15 kPa. Since the base pedestal had a ceramic disk embedded in it, so the air was not only required to be removed from the specimen itself but also from the ceramic disk, the compartment underneath it, and the lines connecting to it. To do so, vacuum lines were connected to the specimen, not only from the top cap but also through the bottom pedestal. This process of de-airing the specimen

was continued for 24 hours to ensure the removal of all the air from specimen, base ceramic disk and its associated assembly.

- **Water flushing:** Figure 4.12 shows schematic layout of assembly used for flushing water through the specimen during saturation. Once the specimen was de-aired, tank A, connected to the base pedestal, was raised to about 0.5 meter height. This created a net pressure head of 5 kPa from tank A towards tank B; and the de-aired water started flowing into the specimen through its base. Water slowly moved from bottom to top of specimen, filling the pores with water. The presence of low permeability ceramic disk (instead of a typically used porous stone) at the base of test specimen caused the water to flow at a very slow rate. The process of saturation was completed in 24~48 hours.
- After saturation, cell pressure was slowly brought from -75 kPa to 15 kPa and at the same time the corresponding pressure inside the specimen was varied from -90 kPa to 0 kPa. This process was done in increments of 5 kPa, so as to avoid disturbing the specimen.
- **B-value check:** Saturation state of specimen was determined through *B*-value check (Bishop, 1954; Skempton, 1954). *B*-value is the ratio of change in pore pressure (Δu) to the corresponding change in confining pressure ($\Delta \sigma_3$).
 - To check the *B*-value, drainage valve from the specimen was closed.
 - Cell pressure was increased by 50 kPa and the corresponding change in pore pressure was observed. The ratio of increase in pore pressure (Δu) to the corresponding change in cell pressure ($\Delta \sigma_3$) gives the *B*-value. Systematic explanation of *B*-value check is given in Figure 4.13.
- Once the desired degree of saturation was confirmed through *B*-value check, the specimen was subjected to stress path of specified test series as explained in respective sections of this thesis.

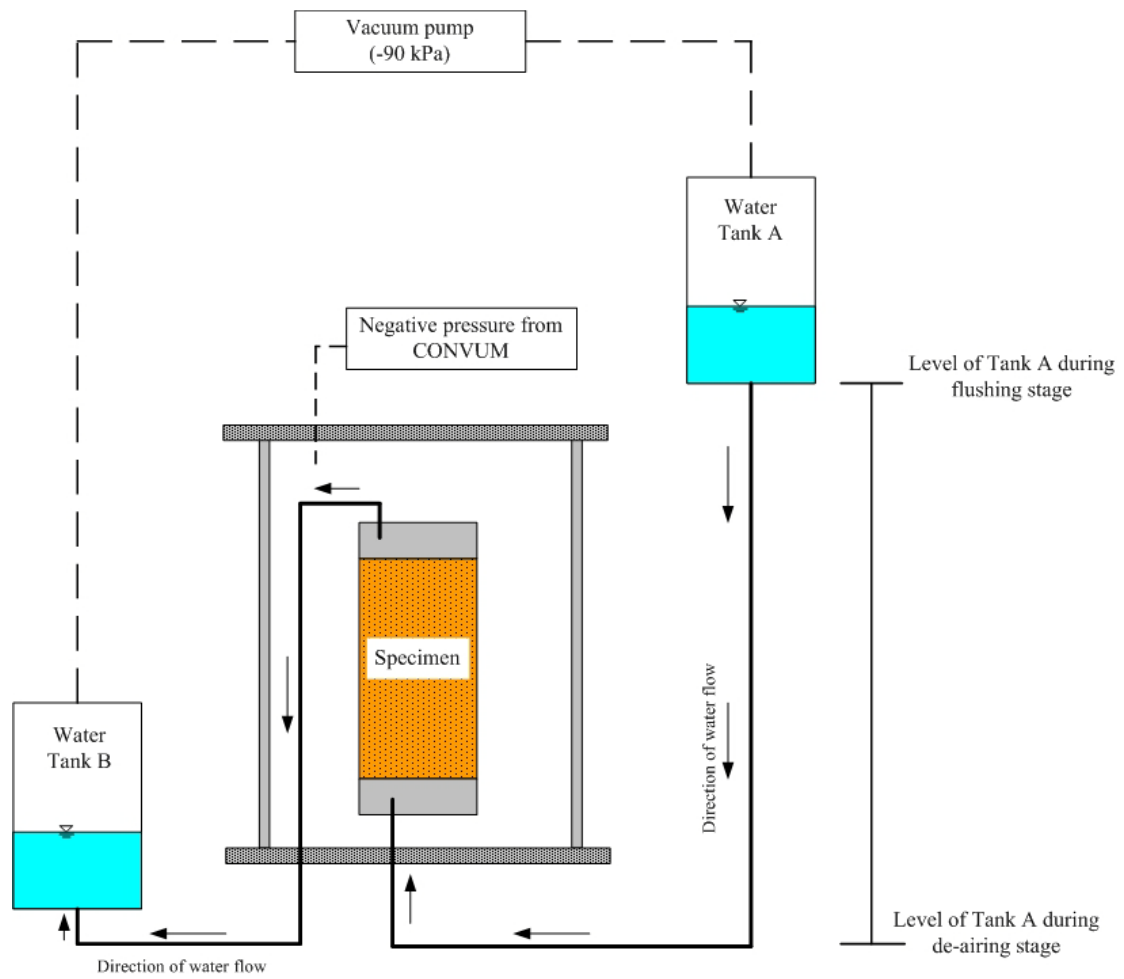


Figure 4.12: Saturation process: schematic layout of de-airing and water flushing stages.

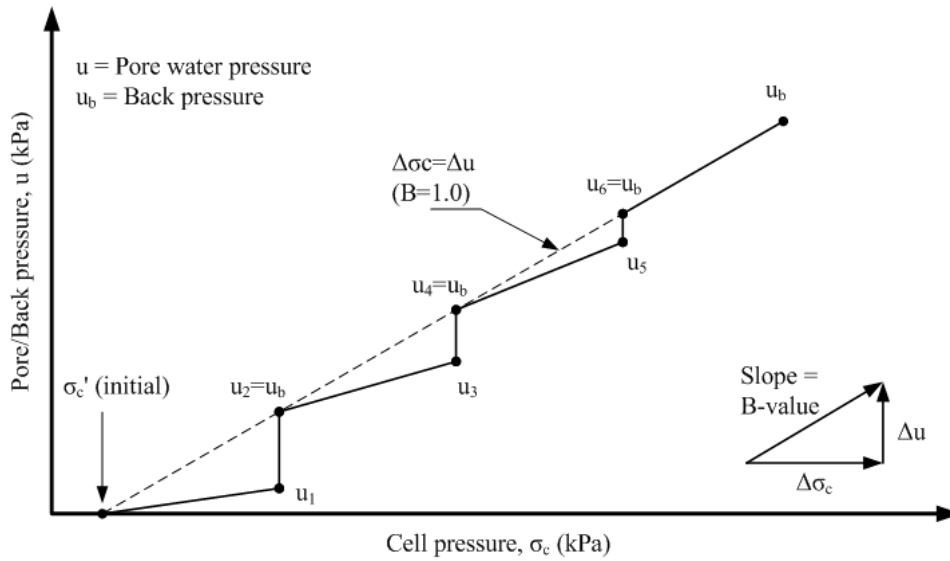


Figure 4.13: Systematic explanation of B -value check.

4.4. FUNDAMENTAL RELATIONSHIPS & CALCULATIONS

4.4.1 Weight-Volume Relationships

Soil is a particulate mineral matter, and is generally composed of solid, liquid, and gaseous/air phases. This three-phase depiction of soil mass system is shown in Figure 4.14.

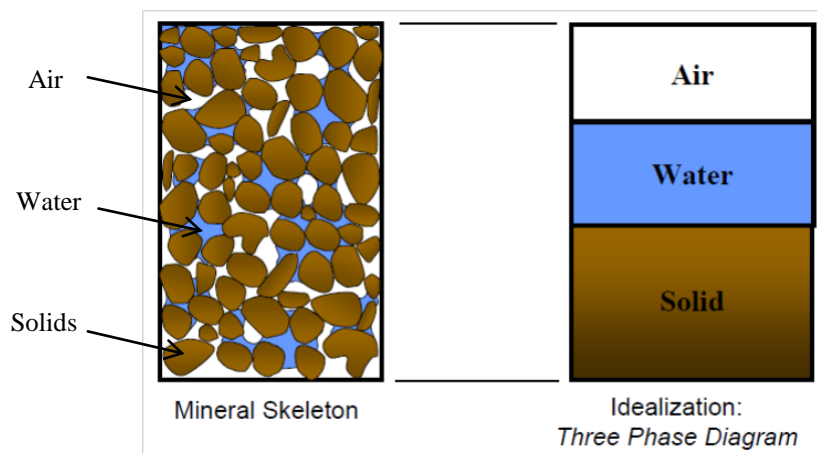


Figure 4.14: Three-phase depiction of soil system.

The amount of each of these constituents (solid, liquid, and air) directly affects soil properties. Depending on the prevailing field conditions, soil mass may contain some, or all of the above mentioned three phases; e.g. the above mentioned three-phase soil system may be reduced to a two-phase system when the soil is saturated (all voids filled with water), or when oven dried (all voids filled with air). Thus, two-phase soil systems are special cases of three-phase soil system, as shown in Figure 4.15.

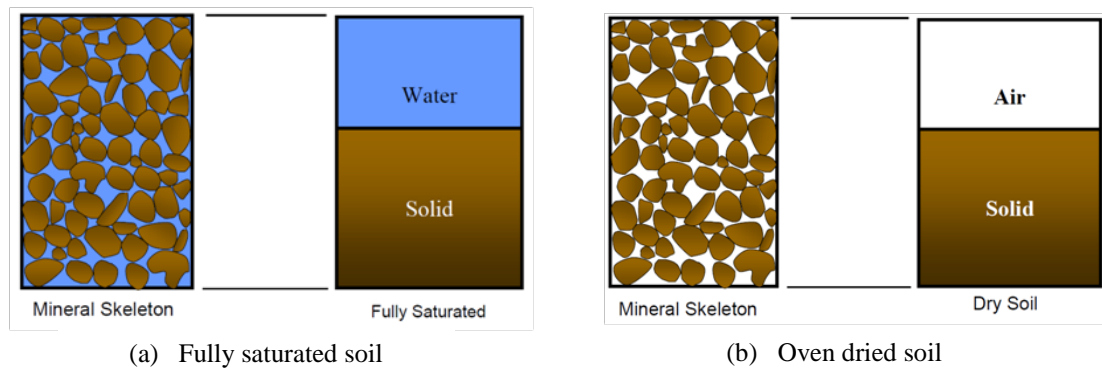


Figure 4.15: Soil as a two-phase system; (a) water saturated; (b) oven dried.

The fundamental relationships used in this study for various basic calculations related to weight and volume of soil can be derived by considering a simplified block representation of an unsaturated soil mass, as shown in Figure 4.16.

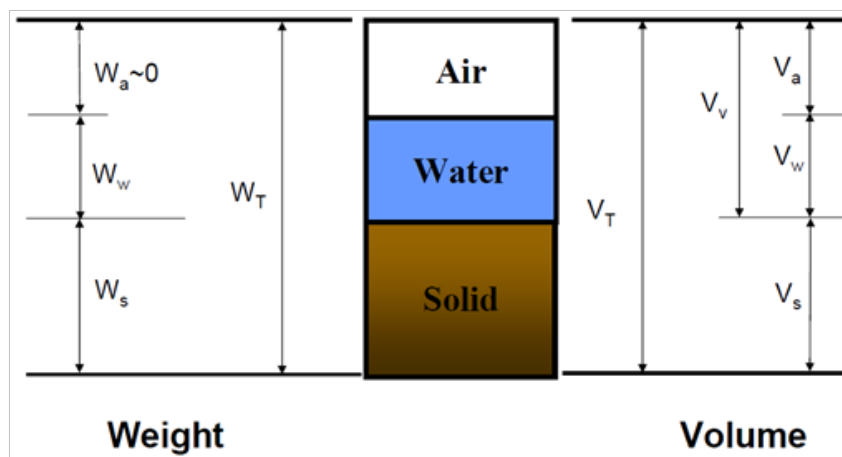


Figure 4.16: Simplified block diagram of an unsaturated soil mass, indicating various parameters of a three-phase soil system.

As shown in Figure 4.16, various parameters of a three-phase soil system can be described as;

V_T = Total volume of soil mass

V_v = Volume of voids/pores

V_s = Volume of solid soil particles

V_w = Volume of water

V_a = Volume of air

W_T = Total weight of soil mass

W_s = Weight of soil particles

W_w = Weight of water

W_a = Weight of air = 0; since it is quite insignificant comparing with W_T , W_s , and W_w .

Void ratio, e , of soil specimen, is generally expressed as a decimal number and is computed as;

$$e = \frac{V_v}{V_s} \tag{4.1}$$

The volume of voids occupying the total volume of soil specimen, expressed as percentage is known as porosity, n ;

$$n = \frac{V_v}{V_T} \times 100 \tag{4.2}$$

Considering $V_s = 1$, then $V = V_v + V_s = 1$ (from Figure 4.16), and from Equation 4.2 we get;

$$n = \frac{e}{1 + e} \tag{4.3}$$

or

$$e = \frac{n}{1-n} \quad (4.4)$$

The amount of water contained in a soil mass is generally expressed either in terms of volume, i.e., saturation ratio (S_r), and volumetric water content (θ_v); or weight, i.e. gravimetric water content (w). Saturation ratio is described as the percentage of voids filled with water;

$$S_r = \frac{V_w}{V_v} \times 100 \quad (4.5)$$

Thus, a fully saturated soil would have all its voids filled with water ($S_r=100\%$), and a 50% saturated soil would mean that half of the voids in soil skeleton are filled with water.

Volumetric water content, θ_v , on the other hand considers the overall volume of soil skeleton. It is the ratio of volume of water compared with the overall volume of soil mass, given as;

$$\theta_v = \frac{V_w}{V_T} \quad (4.6)$$

Knowing the porosity (n) of soil, saturation ratio (S_r) can be related to volumetric water content (θ_v) as;

$$\theta_v = n \cdot S_r \quad (4.7)$$

Due to the simplicity of its determination procedure, gravimetric water content is often the most commonly used measure of expressing the amount of water in soil. It is given by the following expression;

$$w = \frac{W_w}{W_s} \times 100 \quad (4.8)$$

For most part of this study, water content in terms of saturation ratio (S_r) is used, since in physical terms, it provides a better explanation of saturation state of soil specimen. For example, it is easier to imagine that a specimen having $S_r=50\%$ is lying mid-way between dry and saturated state irrespective of specimen density. However, the same can not be predicted of a specimen whose volumetric water content is known to be ($\theta_v=$) 0.5. Additional information about specimen density/void ratio is required to predict the saturation state by using θ_v . Information about saturation state of soil specimens is important to extend the results of element tests to actual landslides.

The specimens were equipped with instruments to continuously record the axial and radial displacements during the experiments. They were used to determine the volumetric strains at any instant of time during the test. By knowing the current volume of specimen, dry density (dry unit weight) of specimen was computed as;

$$\gamma_d = \frac{W_s}{V_T} \quad (4.9)$$

where, the W_s was determined during specimen preparation, and remained the same throughout the experiment. By knowing the dry unit weight, void ratio could be computed by using the expression;

$$e = \frac{G_s \cdot \gamma_w}{\gamma_d} - 1 \quad (4.10)$$

During water injection experiments, the degree of saturation/saturation ratio (S_r) varied with water injection, and was computed as;

$$S_r = \frac{w \cdot G_s}{e} \quad (4.11)$$

Similarly, the volumetric water content was computed by using Equation 4.7, as described earlier.

Bulk density (moist unit weight) of the specimens was computed by using the expression;

$$\gamma = \frac{W_T}{V_T} = \gamma_d \cdot (1 + w) \quad (4.12)$$

Density of the each specimen was represented on the basis of minimum and maximum void ratio, in terms of relative density. Relative density (D_r) reflects the degree of packing of soil particles with respect to the minimum and maximum possible density. It is generally expressed as;

$$D_r = \frac{e_{\max} - e}{e_{\max} - e_{\min}} \times 100 \quad (4.13)$$

4.4.2 Elastic Wave Velocities

The basic formulation of velocity; i.e., displacement covered per unit time, is valid for determining wave velocities as well. Thus compression wave (V_p) and shear wave (V_s) velocities were computed by using the expressions given as;

$$V_p = H / t \quad (4.14)$$

$$V_s = H / t \quad (4.15)$$

where, H is the travel distance of the wave and t is the corresponding time of flight of compression and shear waves respectively.

In case of bender elements type piezoelectric transducers, travel distance of waves is found to be equivalent to tip-to-tip distance between transmitter and receiver bender elements (Dyvik & Madshus, 1985; Viggiani & Atkinson, 1995; Kawaguchi et al., 2001). Following the same principle, transverse distance between transmitter and receiver disk transducer was assumed to be the travel distance of elastic waves. Since, disk transducers were flat in shape, and were flush with the surface of pedestal/top cap, an assumption of wave travel distance equivalent to instantaneous height of the specimen was reasonably accurate. Height of the specimen at any instant was

determined by knowing the axial deformations through *LVDT* (or *LDT*), thus giving the wave travel distance any time during the experiment.

Travel time, t , of each wave was computed by analyzing the corresponding response of transmitted and received signals. For compression wave, the first deflection of receiver signal is considered as the arrival of compression wave. This interpretation of first arrival time is valid because compression waves are the fastest propagating waves and thus arrive at the receiver first. Time between the first deflection of input, and output signals was thus considered as the time of flight of compression waves, as depicted in Figure 4.17.

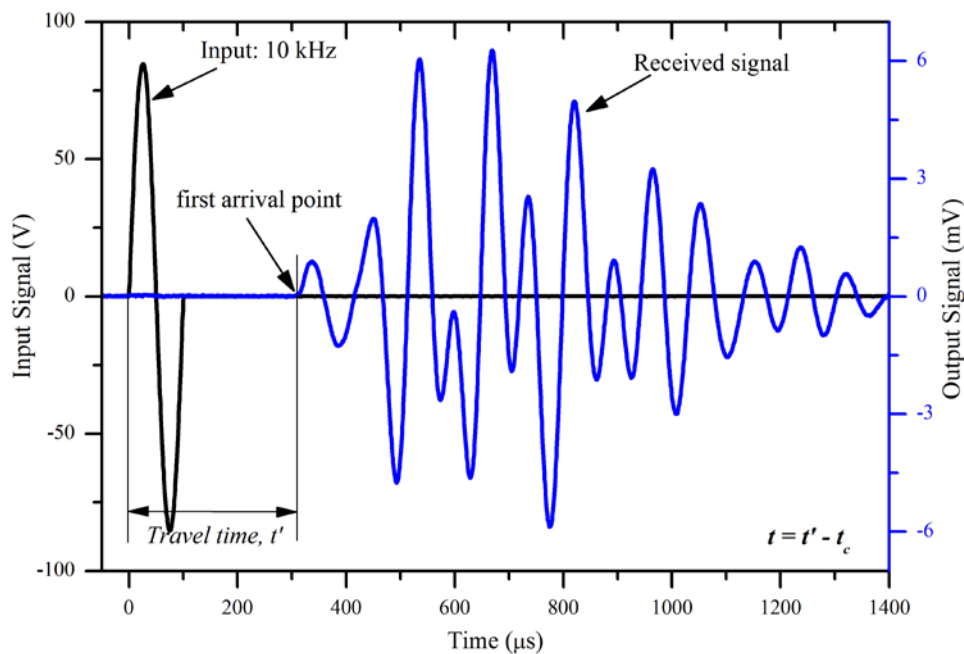


Figure 4.17: Travel time determination of compression wave signals.

Travel time determination of shear waves is not as simple as compression waves because the first deflection of shear wave signal may not correspond to the arrival of *S*-wave, but rather to the arrival of the so-called “near-field” component, which travels with the velocity of *P*-waves (Mancuso & Vinale, 1988). By ignoring the initial disturbance due to *P*-wave, and near-field effect, shear wave travel time was calculated as the difference between the start of transmitted signal and the start of first

major positively polarized rise up; i.e., “*first-zero cross over*” method (Kawaguchi et al., 2001; Lee & Santamarina, 2005), as shown in Figure 4.18.

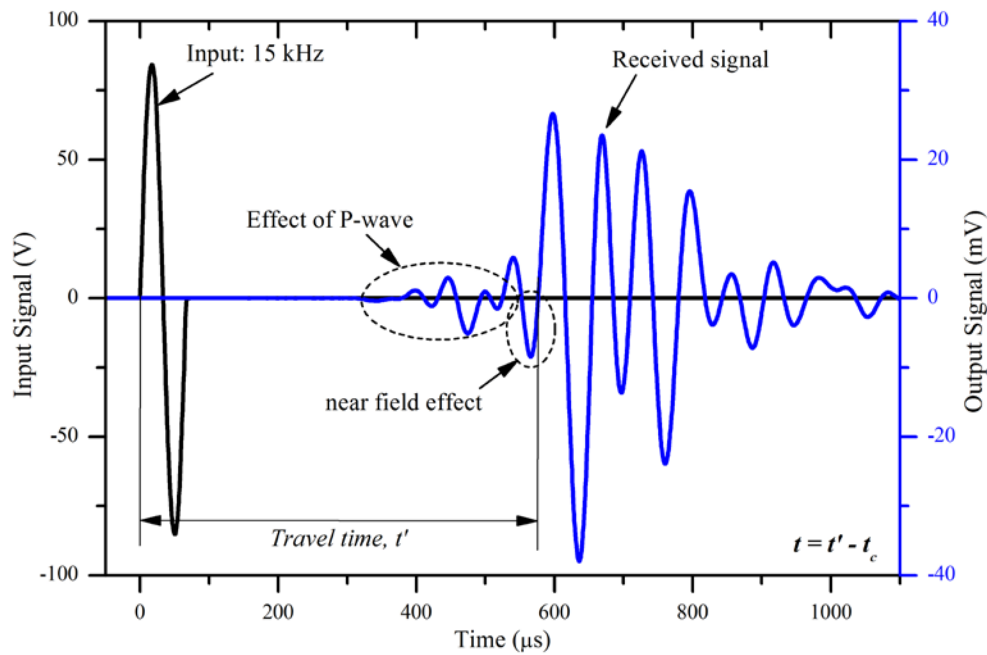


Figure 4.18: Travel time determination of shear wave signals.

4.4.3 Stress-Strain Relationships

Proper understanding of stress transfer and corresponding strains increments is integral for processing and obtaining meaningful information from triaxial test data. This section enlists the expressions used for the computation of stresses and strains for various types of triaxial tests conducted in this study.

4.4.3.1 Stress Components

The sign convention typically used in soil mechanics is opposite to that of continuum mechanics; i.e. in soil mechanics, compressive stresses and strains are taken as positive while tensile stresses and strains are considered negative. This is because soil is mostly loaded in compression and is considered to transfer only compressive normal stresses.

Total major principal stress at mid-height of specimen, σ_1 is given as;

$$\sigma_1 = \frac{F_a + (A - A_r)\sigma_c + \frac{1}{2}W_s}{A} \quad (4.16)$$

Since the load cell was placed inside the triaxial chamber and was directly connected to the top cap, thus $A_r = 0$, and equation 3.1 is reduced to;

$$\sigma_1 = \frac{F_a + A\sigma_c + \frac{1}{2}W_s}{A} \quad (4.17)$$

Major effective principle stress, σ_1' , (only for saturated specimens);

$$\sigma_1' = \sigma_1 - u_w \quad (4.18)$$

Total minor principal stress, σ_3 :

$$\sigma_3 = \sigma_c \quad (4.19)$$

Minor effective principle stress, σ_3' , (only for saturated specimens);

$$\sigma_3' = \sigma_3 - u_w \quad (4.20)$$

Matric suction, S_u , is the difference between pore air pressure and pore water pressure, given as:

$$S_u = u_a - u_w \quad (4.21)$$

Since top cap was vented to atmosphere, thus $u_a = 0$, and equation 4.21 reduces to;

$$S_u = -u_w \quad (4.22)$$

Deviator stress, q :

$$q = \sigma_1 - \sigma_3 = \sigma_1' - \sigma_3' \quad (4.23)$$

where:

F_a = axial load measured by the load cell (N)

A = current cross-sectional area of the specimen (mm^2)

A_r = cross-section area of the loading rod (mm^2)

σ_c = cell pressure (kPa)

u_a = pore air pressure (kPa)

u_w = pore-water pressure applied/measured through ceramic disk (kPa)

W_s = weight of the sample calculated considering corresponding water content (N)

4.4.3.2 Strain Components

Axial strain, ε_a :

$$\varepsilon_a = \frac{\Delta h}{h_i} \quad (4.24)$$

Radial strain, ε_r :

$$\varepsilon_r = \frac{\Delta d_m}{d_i} \quad (4.25)$$

Volumetric strain, ε_v :

$$\varepsilon_v = \varepsilon_a + 2\varepsilon_r \quad (4.26)$$

Shear strain, γ :

$$\gamma = \varepsilon_a - \varepsilon_r \quad (4.27)$$

where:

Δh = change in the height of the specimen measured by *LVDT* (mm)

h_i = initial height of the specimen (before consolidation) (mm)

ΔD_m = change in the level of the inner cell water measured by *DPT-1* (mm)

D_o = inside cross-sectional area of the inner cell (mm²)

A_c = cross-section area of the sample top cap (mm²)

A = current cross-section area of the specimen

In the above calculations, membrane force and membrane penetration were not taken into account because their influences were demonstrated negligible for silty sands by Huang (1994).

4.5. SUMMARY

This chapter started by presenting the physical properties of test material used in this study. The overall experimental program designed to achieve the objectives of this research was presented. Details of experimental procedures, including preparation of suction measuring devices (saturation of ceramic disk, saturation and sealing of miniature pressure sensor), specimen preparation, installation of strain measurement devices, etc, were discussed in detail. Separate sections were dedicated for the discussion on experimental procedures of unsaturated and saturated triaxial tests. Measurement of initial matric suction by ceramic disk and miniature pore pressure sensor placed mid-height inside the specimen was compared, and found to be reasonably in agreement with each other.

Basic calculations related to the determination of state of specimen during the experiment, e.g., density, void ratio, degree of saturation, etc., were presented. A detailed discussion on the determination of elastic wave velocities and the determination of travel time is presented. Furthermore, equations for the calculation of stresses and strains in both saturated and unsaturated triaxial specimens were discussed.

A. REFERENCES

- Ampadu, S., & Tatsouka, F. (1993). Effect of Setting Method on the Behaviour of Clays in Triaxial Compression from Saturation to Undrained Shear. *Soils and Foundations*, 33(2), 14-34.
- Anderson, S. A., & Sitar, N. (1995). Analysis of Rainfall-Induced Debris Flows. *Journal of Geotechnical Engineering*, 121(7), 544-552.
- Bishop, A. W. (1954). The Use of Pore-Pressure Coefficients in Practice. *Geotechnique*, 4(4), 148-152.
- Brand, E. W., Premchitt, J., & Phillipson, H. B. (1984). *Relationship between Rainfall and Landslides in Hong Kong*. Proceedings: 4th International Symposium on Landslides (pp. 377-384), Ontario, Canada.
- Collins, B. D., & Znidarcic, D. (2004). Stability Analyses of Rainfall Induced Landslides. *Journal of Geotechnical and Geoenvironmental Engineering*, 130(4), 362-372.
- Dyvik, R., & Madshus, C. (1985). *Lab Measurements of Gmax Using Bender Elements*. Proceedings: Advances in the art of testing soils under cyclic conditions (pp. 186-196).
- Farooq, K., Orense, R., & Towhata, I. (2004). Response of Unsaturated Sandy Soils under Constant Shear Stress Drained Condition. *Soils and foundations*, 44(2), 1-13.
- Huang, Y. (1994). *Effect of Suction on Strength and Deformation Behavior of Unsaturated Collapsible Soils*. PhD Thesis, University of Tokyo, Japan.
- Kawaguchi, T., Mitachi, T., & Shibuya, S. (2001). *Evaluation of Shear Wave Travel Time in Laboratory Bender Element Test*. Paper presented at the 15th International Conference on Soil Mechanics and Geotechnical Engineering (ICSMGE).

- Lee, J., & Santamarina, J. (2005). Bender Elements: Performance and Signal Interpretation. *Journal of Geotechnical and Geoenvironmental Engineering*, 131(9), 1063-1070. doi: doi:10.1061/(ASCE)1090-0241(2005)131:9(1063)
- Mancuso, C., & Vinale, F. (1988). Propagazione Delle Onde Sismiche: Teoria E Misure in Sito. *Atti del Convegno Nazionale del Coordinamento per gli Studi di Ingegneria Geotecnica*, 115-138 [In Italian].
- Skempton, A. (1954). The Pore-Pressure Coefficients a and B. *Geotechnique*, 4(4), 143-147.
- Viggiani, G., & Atkinson, J. (1995). Stiffness of Fine-Grained Soil at Very Small Strains. *Geotechnique*, 45(2), 249-265.
- Xie, M., Esaki, T., & Cai, M. (2004). A Time-Space Based Approach for Mapping Rainfall-Induced Shallow Landslide Hazard. *Environmental Geology*, 46(6-7), 840-850.

DISK SHAPED PIEZOELECTRIC TRANSDUCER – DEVELOPMENT & PERFORMANCE ANALYSIS –

Chapter 5

CHAPTER 5

DISK SHAPED PIEZOELECTRIC TRANSDUCER – DEVELOPMENT AND PERFORMANCE ANALYSIS –

5.1. PIEZOELECTRICITY AND ITS APPLICATION IN GEOTECHNICAL ENGINEERING

Piezoelectricity is a property exhibited by certain materials (ceramics, crystals and biological matter, etc) to accumulate electric charge in response to the applied mechanical stress or vice versa. The phenomenon of piezoelectricity was discovered by Curie brothers (Jacques and Pierre) in 1880 (Curie & Curie, 1880). The use of piezoelectric elements for geotechnical engineering applications was first introduced by Lawrence (1963, 1965) who used piezoelectric crystals to generate one dimensional compression waves through sand, and glass beads. Since then, various types of piezoelectric transducers are being used for laboratory studies of geomaterials properties; some of them include the bender elements (Shirley, 1978; Shirley & Hampton, 1978), frictional/pulsate bender elements (Fioravante, 2000), and, bender/extender elements (Lings & Greening, 2001; E. C. Leong et al., 2009), etc. Among these, bender elements for the determination of shear wave (*S*-wave) velocities (and the corresponding shear modulus) have gained outright popularity. Experimental evidence by Dyvik and Madshus (1985), Thomann and Hryciw (1990), etc, showed good agreement between maximum shear modulus, G_{max} , measured with bender element and resonant column (Figure 5.1).

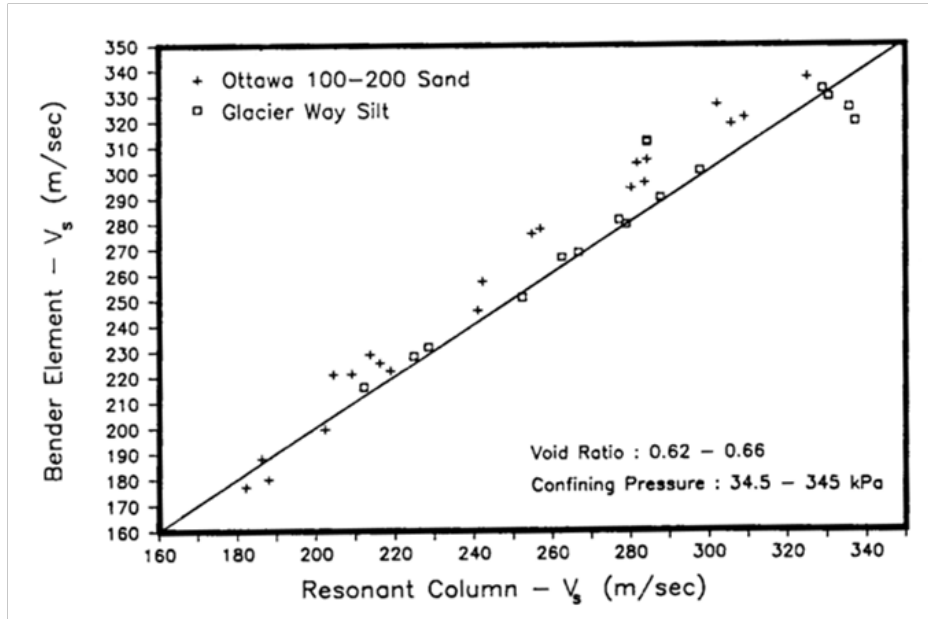


Figure 5.1: Comparison of shear wave velocity from resonant column and bender element tests (Thomann & Hryciw, 1990).

On the contrary, the usage of piezoelectric transducers for compression/dilatational wave (P -wave) velocity (and the corresponding *constrained compression modulus*, K) determination is not as widespread. This is because for majority of geotechnical engineering applications, soil is loaded in shear; and thus the deformation behavior of soil is better explained by shear modulus. Large energy dissipation of P -waves in dry and moist granular media (de Alba et al., 1984), and the inability to measure P -wave velocity in saturated soils (as P -wave travels faster through the water phase than through the soil skeleton) (E. C. Leong et al., 2009), limit the usage of P -wave piezoelectric transducers. However, with the emerging interest in unsaturated soil mechanics, the measurement of P -wave velocity is becoming more meaningful as it can provide an assessment of the saturation ratio as well as the porosity of unsaturated soil specimen (Brignoli et al., 1996).

5.2. P & S -WAVE VELOCITY IN ELEMENT TESTS

Elastic waves propagate through soil due to vibration of soil particles in longitudinal (P -wave) or lateral (S -wave) plane; thus subjecting the soil to extremely small strains. Several laboratory techniques have been developed to measure directly the small-

strain shear modulus, most notably the torsional resonant column and cyclic torsional shear technique (Stokoe II et al., 1980; ASTM, 2007). In these experiments, shear moduli are measured at strains generally less than 0.001%. At such small strain, moduli are independent of strain amplitude and the terms ‘*elastic*’, ‘*linear*’, or ‘*small-strain*’ are typically used to describe the measurements and results. Beside these techniques, soil dynamics texts (Richart et al., 1970; Prakash, 1981) describe a sonic technique utilizing direct-transmission measurements for this purpose. In this test, an elastic shear wave is generated by a piezoelectric transducer placed on one end of a confined soil specimen and is received at the other end of the specimen by another piezoelectric transducer. The distance between the two transducers, L , and the time required by the wave to cover this distance, t , are used to calculate wave propagation velocity, V , as $V=L/t$.

5.3. COMBINED MONITORING OF P & S -WAVE VELOCITIES

Various researchers have worked on the idea of combined determination of shear and compression wave velocities by using a pair of S -wave, and a pair of P -wave piezoelectric transducers mounted in the same apparatus (e.g. (Schultheiss, 1981; Bates, 1989; de Alba & Baldwin, 1991; Brignoli et al., 1996; Nakagawa et al., 1996; Fioravante & Capoferri, 2001; Uchimura, 2011)). However, the use of separate pairs of P -wave and S -wave transducers meant V_p and V_s were being measured over different paths in the specimen. Lings and Greening (2001) introduced a single hybrid transducer called “*bender/extender element*”, by introducing an innovative modification in bender element wiring, producing an *extender element* capable of transmitting and receiving P -waves. The bender/extender element was therefore capable of measuring P -wave and S -wave velocities over the exact same path. However, all of these transducers were essentially modifications of the original bender elements, requiring penetration into the soil specimen in order to generate elastic waves. The specimens were required to be grooved to accommodate this protrusion. This not only caused disturbance to the specimens but also made elastic wave velocity in hard/stiff specimens (e.g., rock specimens, cement/lime treated specimen, etc) a challenging task (Figure 5.2).



Figure 5.2: Bender elements, and its application for hard/stiff specimens (after Pantazopoulos and Atmatzidis (2012)).

The following sections explain the construction, use, and performance evaluation of a new flat shaped piezoelectric transducer, called *disk transducer*, for combined determination P -wave and S -wave velocity in triaxial specimen. Disk transducer, besides being flat in plan (not penetrating into soil specimen), is capable of measuring both P -wave and S -wave velocities over the same path in triaxial specimen.

5.4. DISK TRANSDUCER FABRICATION

Activation of the piezoelectric property in ceramics, typically called *polarization*, is obtained by applying a high DC voltage between a pair of electrode faces. The mode of deformation of a piezoelectric element depends on the type of ceramic (shape and composition, etc), polarization direction, and the location of applied electrical field. Based on nature of polarization, piezoelectric ceramics can generate (or sense) both compression and shear waves. Various types of piezoelectric ceramic elements are used nowadays; however, some of the earliest use of piezoelectric ceramics for geotechnical engineering purposes was in the form of piezoelectric disk/plate elements. Lawrence (1963, 1965) was the first one to employ piezoelectric plate/disk elements for the determination of S -wave velocity in clay and sand specimens.

However, their use has been limited because of their large size and a requirement of greater driving voltage. Also shear plates were found to be more effective at higher confining stresses and with very coarse soils (Brignoli et al., 1996). For the generation of *S*-waves through a shear plate/disk transducer, the electrodes are applied to two faces that are parallel to the polarization direction as shown in Figure 5.3. The same figure also shows the deformation created by transmitting transducer when a given voltage of specified polarity is applied to the electrodes. A deformation in the same direction generates, in the transducer used as receiver, an inverted polarity in voltage to that of the source.

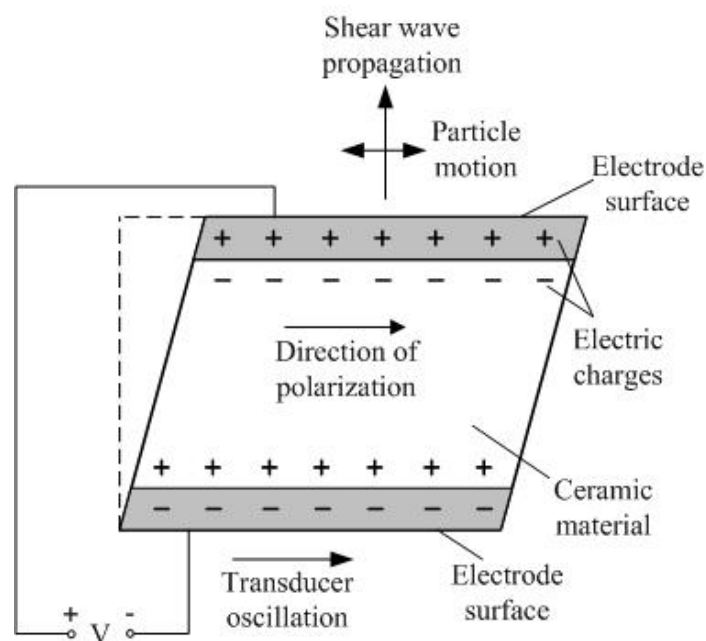


Figure 5.3: Schematic illustration describing the nature of polarization and mode of vibration of an *S*-type piezoelectric disk/plate (after Strassburger (1982)).

For the generation of *P*-waves, ceramic elements are polarized in the thickness direction, and electrodes are placed on the element faces normal to the polarization direction. The direction of polarization and the mode of vibration of a *P*-type piezoelectric disk element is shown in Figure 5.4.

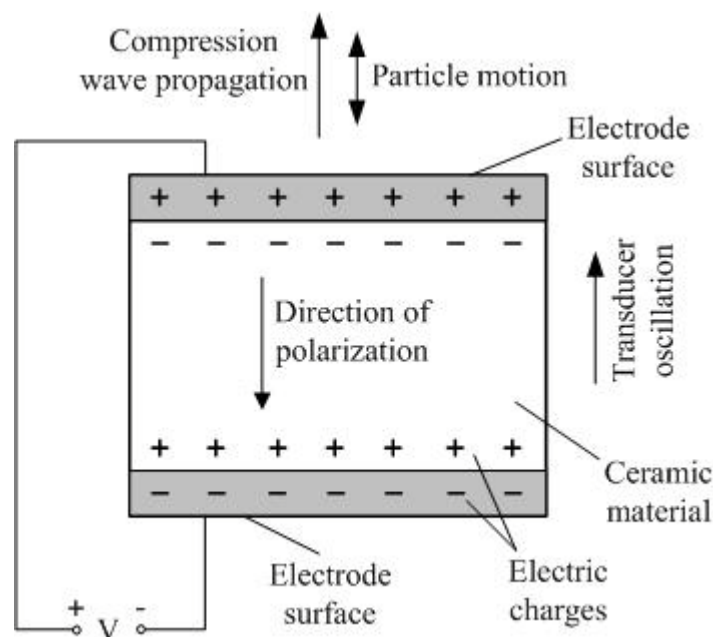


Figure 5.4: Schematic illustration describing the nature of polarization and mode of vibration of a *P*-type piezoelectric disk/plate (after Strassburger (1982)).

Plate type piezoelectric elements, similar to the ones used by Lawrence (1963, 1965), but more versatile and much smaller in size were used in this study. A pair of compression (*P*-type) and a pair of shear (*S*-type) ceramic plate transducers, manufactured by *Fuji ceramics corporation* (Model: *P*-type: Z2T20D-SYX (C-6); *S*-type: SZ5T20D-LLYX (C-6)) were employed in this study. The flat disk shaped piezoelectric elements consisted of a central core of polarized piezoelectric ceramic (*Lead Zirconate Titanate*, $[Pb(Ti.Zr)O_3]$) sandwiched between two thin electrodes covering the top and bottom surfaces. The ceramic plates were 20 mm in diameter with a thickness of 2 mm and 5 mm for *P* and *S* type respectively, as shown in Figure 5.5(a). Basic properties of piezoelectric ceramic disks used in this study are summarized in Table 5.1.

Table 5.1: Basic properties of *P*-type and *S*-type piezoelectric ceramics disks used in this study.

Use	<i>P</i> -type				<i>S</i> -type			
	kp*	C**	Dia.	Thick.	k15*	C**	Dia.	Thick.
	(%)	(pF)	(mm)	(mm)	(%)	(pF)	(mm)	(mm)
Transmitter	66.2	2960	19.98	2.02	64.8	1310	20.01	4.98
Receiver	65.4	2890	19.98	2.01	65.2	1310	20.01	4.97

Notes:

Lead Zirconate Titanate, [Pb(Ti,Zr)O₃] piezoelectric ceramics, manufactured by Fuji Ceramics Co. Ltd.

* kp, k15: Coupling factors

** C: electrostatic capacity

In order to form a single transducer capable of measuring both shear and compression waves, *P* and *S* type disks were bonded together with araldite (a two-component epoxy glue) (Figure 5.5(b)). This component besides bonding together the two piezoelectric ceramic disks ensured electrical insulation of the surfaces of two disks. Once the epoxy hardened and the bond gained strength, the elements were encapsulated in a metal housing (Figure 5.5(c)). In order to fix the piezoelectric elements inside metal housing, the space at the base of elements was filled with araldite; this also served as a rigid base providing reaction surface to *P*-type piezoelectric disk. Besides, being good at electrical insulation and water proofing, araldite is ductile enough to allow transducers to move, yet is supportive and also makes them sturdy. Space in the top of metal housing was filled with silicon rubber to make the transducer more ductile and to allow easy movement of *S*-type piezo disk (Figure 5.5(d)). A thin layer of Araldite was also coated on the surface of transducer to protect it against direct exposure of testing material and also to make it waterproof. Surface of the transducers was thus kept smooth, as smooth surface of transducer is proved to impart less bedding error compared with corrugated surface (Suwal & Kuwano, 2010b). The completed assembly, as schematically represented in Figure 5.6,

was thus capable of measuring both P -wave and S -wave velocities and was named as disk transducer following the initial design by Suwal & Kuwano (2009, 2010a). The base pedestal of triaxial apparatus was modified to house the disk transducer, which was held firmly at the center of pedestal by means of O-ring, as shown in Figure 5.7. The corresponding top cap was modified accordingly.

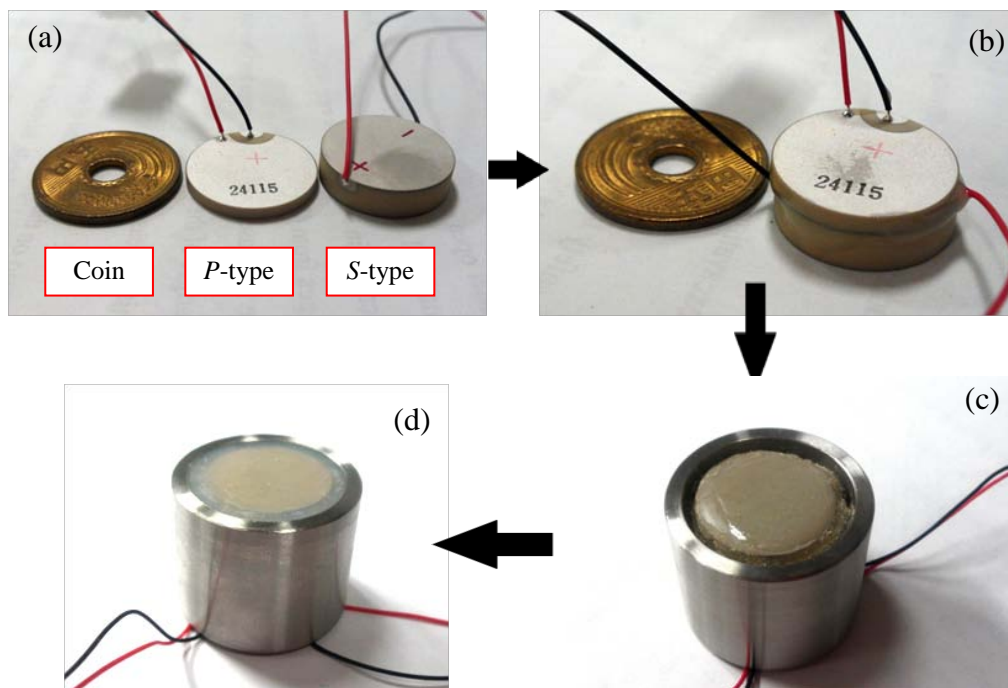


Figure 5.5: (a) P and S -type piezoelectric ceramics in comparison to Japanese 5 yen coin; (b) P and S -type ceramics bonded by Araldite; (c) Piezoelectric ceramics fitted in the metal housing by Araldite; before filling silicon in the top periphery of sensor; (d) The finished product.

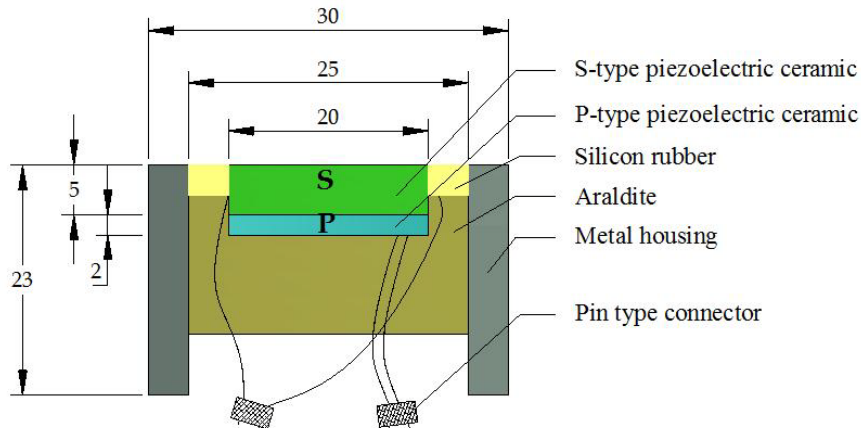


Figure 5.6: Schematic diagram of piezoelectric disk transducer.

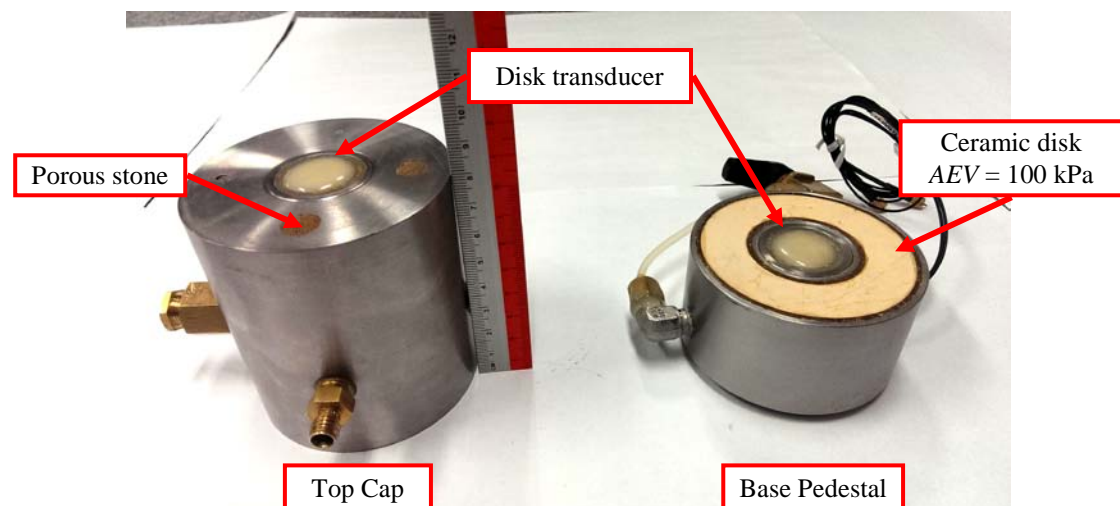


Figure 5.7: Disk transducers fitted at the center of top cap and base pedestal by means of an O-ring.

5.4.1 Water Insulation

Piezoelectric transducers are required to be properly waterproofed, in order to avoid malfunctioning due to short-circuiting. Several steps were taken to ensure water insulation of disk transducers throughout the course of experiments. Piezoelectric disks were coated with Araldite during fabrication, and any gaps/openings in the pedestal (and top cap) which could allow water entry were sealed with silicon rubber.

Additional precaution was practiced while coating the corners of piezoelectric elements, because surface tension of liquid coating material makes it very difficult to apply a uniform coat around the corners. For maintaining cell pressure during triaxial tests, air was used instead of water. Although the use of air for cell pressure can be dangerous (ASTM, 2011), but since most of the tests were conducted at low confining pressure, therefore the use of air did not offer any potential threat. While saturating ceramic disk in the saturation tank, it was submerged upside down with water level reaching approximately mid-height of pedestal. Additionally, rear end of pedestal (which could expose transducer cables to water) was covered with plastic sheet to avoid any scattered water entering the sensor during saturation.

5.5. CALIBRATIONS

5.5.1 Time Lag

The wave transmission/receiving system is prone to undesired delay times induced in the measurements by peripheral electronics, coating materials and ceramics, etc. For disk transducers, *P*-wave sensors were located underneath the *S*-wave sensors (Figure 5.6). The actual travel distance of compression waves was thus greater than the specimen length. Additionally, since both sensors were coated with a layer of Araldite epoxy resin, the time required by waves to travel through ceramics and epoxy resin was required to be considered. This additional travel time of waves is known as '*time lag*', and the corresponding corrections are required to be applied to observed travel times for accurate determination of wave velocities. The existence of phase lag between applied voltage and response of bender elements was also depicted by Arulnathan et al. (1998) by means of finite element analysis.

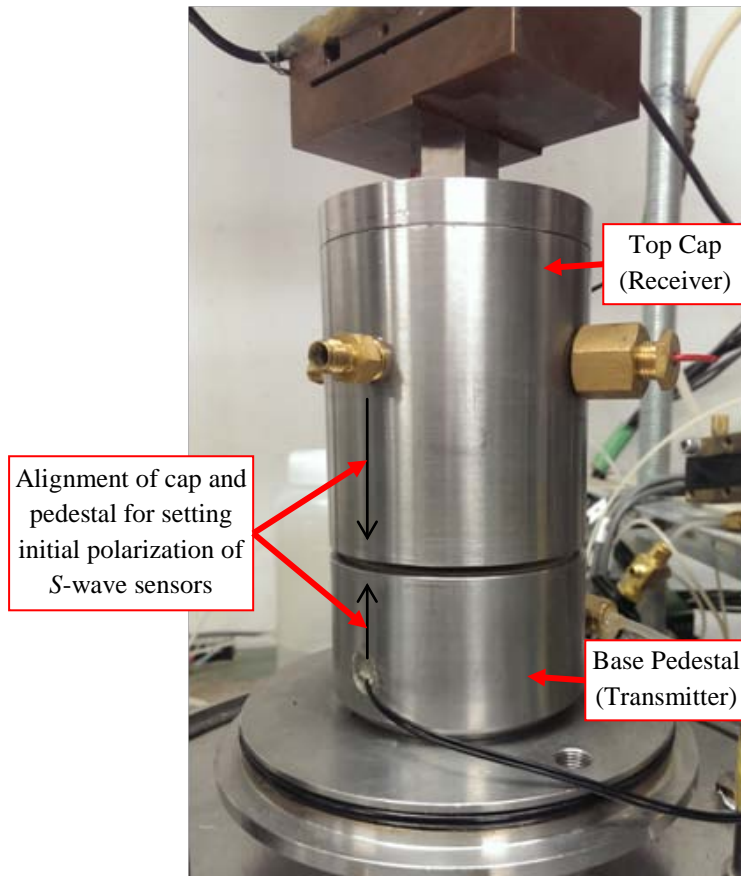


Figure 5.8: Top cap and pedestal placed directly in-contact with each other for conducting ‘time lag calibrations’.

Calibration of the system was carried out by placing the transmitting and receiving elements directly in contact with each other, as shown in Figure 5.8. In order to ensure proper contact between transmitter and receiver, dead load of 10 N was applied on top cap. Input voltage was applied to the transmitter and the corresponding response was recorded. The time interval (t_c) between the initiation of electrical pulse input to the transmitter and the initial arrival of the pulse at the receiving transducer was computed for various input frequencies. Typical examples of calibration test response for compression wave and shear wave are shown in Figure 5.9, and Figure 5.10 respectively. Time lag of 7 μ s and 4 μ s was observed for compression waves and shear waves respectively. Additionally, input frequency was not found to have any effect on the observed time lag. Time lag corrections determined from Figure 5.9, and

Figure 5.10 were therefore applied to all the corresponding wave measurements made in this study.

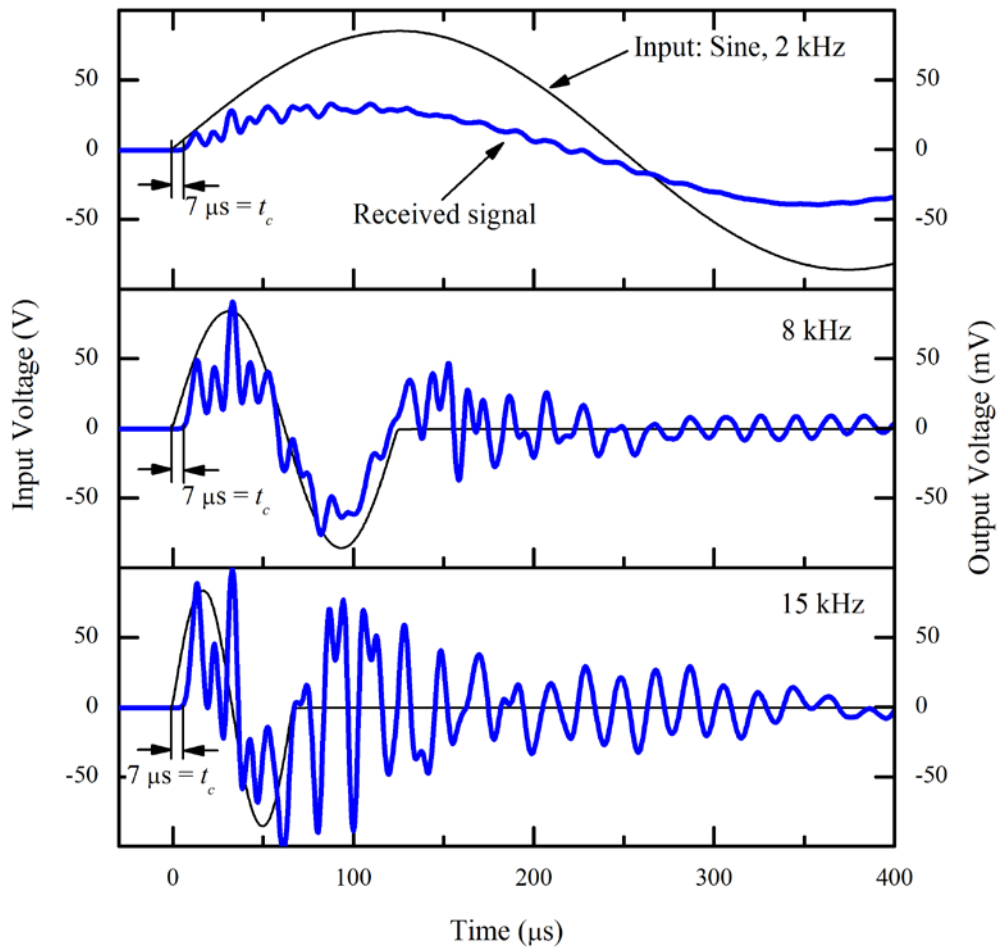


Figure 5.9: Determination of 'time lag' in compression wave response.

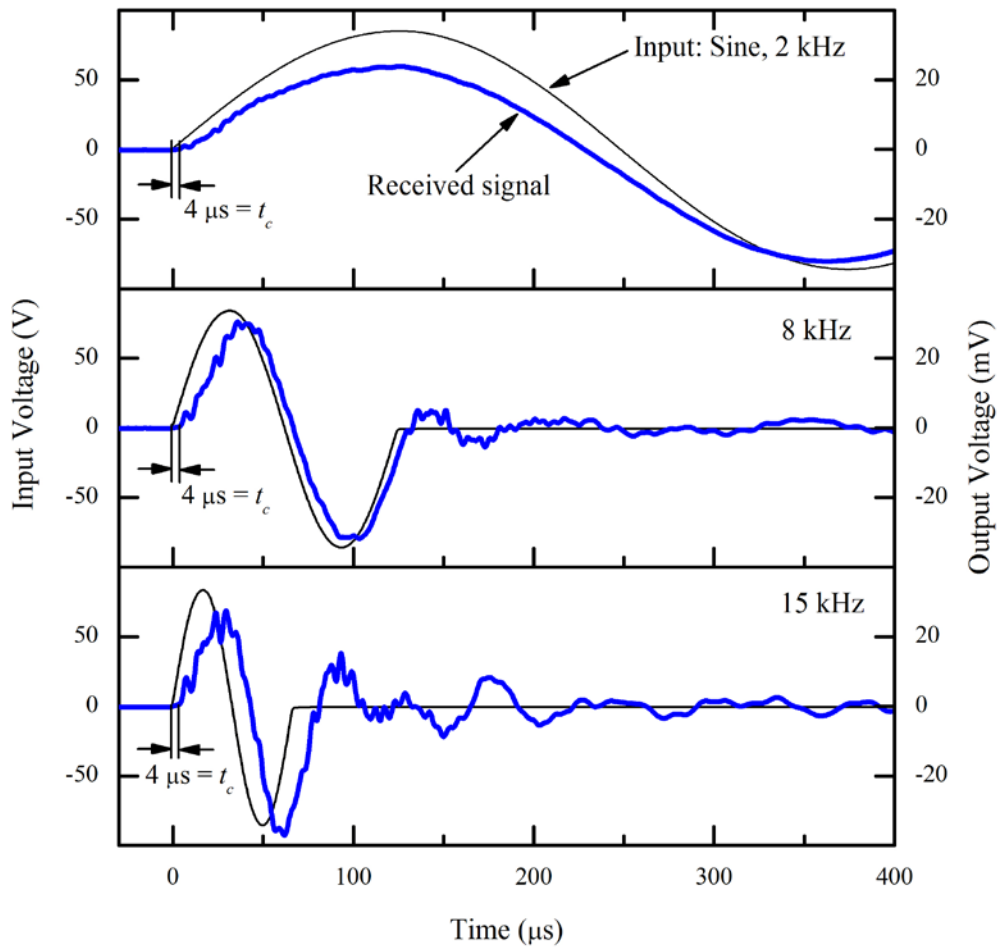


Figure 5.10: Determination of 'time lag' in shear wave response.

5.5.2 Polarity

Besides time lag calibration, the initial polarization of signals are important to be known (Brignoli et al., 1996). Initial polarization of shear wave transducers is important in order to distinguish actual arrival of shear wave from the near-field effects. The alignment of transducers was therefore fixed at the time of fabrication. The corresponding polarities of transmitter and receiver were determined during calibration tests (Figure 5.8), and the same arrangement was maintained throughout the course of this study.

5.5.3 Travel Path

Elastic waves can travel through the metal frame of triaxial apparatus instead of the soil skeleton itself (Brignoli et al., 1996). In such a case, the observed travel time would not be representative of soil specimen. To make sure that the only travel path available to elastic waves is the soil specimen, a test was conducted without soil specimen. Triaxial platens were fixed apart from each other inside an air filled triaxial cell and the transmitter disk transducer was excited. The receiving disk transducer did not detect any signal, therefore, confirming the absence of any travel path other than the soil specimen.

5.6. SIGNAL INTERPRETATION

The fundamental expression governing elastic wave velocity measurement using piezoelectric devices is given as;

$$V_p \text{ or } V_s = \frac{L}{t} \quad (5.1)$$

where, L represents the travel path of elastic wave which is considered equivalent to specimen height. V_p and V_s are compression and shear wave velocities and t is the corresponding travel time of each wave. The efficiency of wave velocity measurement in soil is therefore governed by the accurate determination of travel time, t , and travel distance, L . Surface-to-surface distance between transmitter and receiver disk transducer was considered as the travel path of elastic waves. This assumption follows the well-established practice in bender element testing in which tip-to-tip distance between transmitter and receiver bender element is taken as wave travel distance (Dyvik & Madshus, 1985; Viggiani & Atkinson, 1995). Time of flight of elastic waves is determined by analyzing the transmitted and received signals. Interpretation of compression wave signals and the determination of its travel time is quite straightforward. Figure 5.11 shows a typical compression wave signal obtained by disk transducer system. The first deflection of received signals is considered as the arrival of compression wave, and the time interval between first deflection of transmitted wave and received wave is taken as time of flight of compression wave.

This interpretation of first arrival time is valid because compression waves are the fastest propagating waves and therefore arrive at the receiver first. Travel times determined from first deflection method were then subtracted from compression wave calibration factor (t_c) to determine the correct travel time (t) of compression waves, which was therefore used for further analysis.

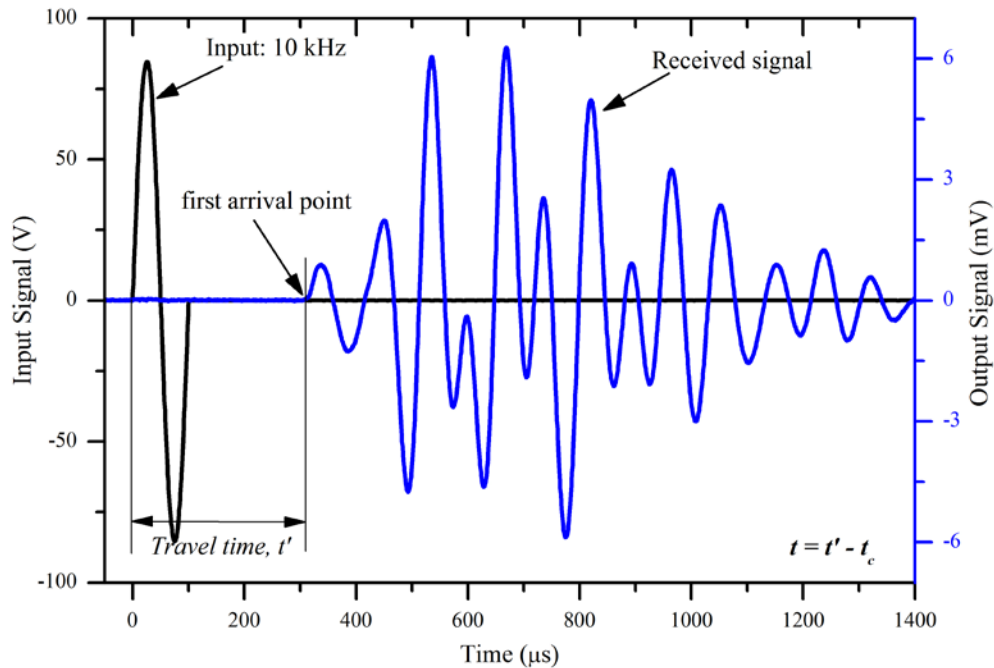


Figure 5.11: Determination of compression wave travel time.

Travel time determination of shear waves is rather tricky because the first deflection of shear wave signal, may not correspond to the arrival of S -wave, but rather to the arrival of the so-called “*near-field*” component, which travels with the velocity of P -wave (Mancuso & Vinale, 1988). Shear waves signals may also be affected by reflected waves which may arrive at the receiver before actual shear waves and make the travel time determination more difficult. A typical shear wave signal recorded in Edosaki sand shown in Figure 5.12, highlights the disturbance caused due to compression waves and near-field effect.

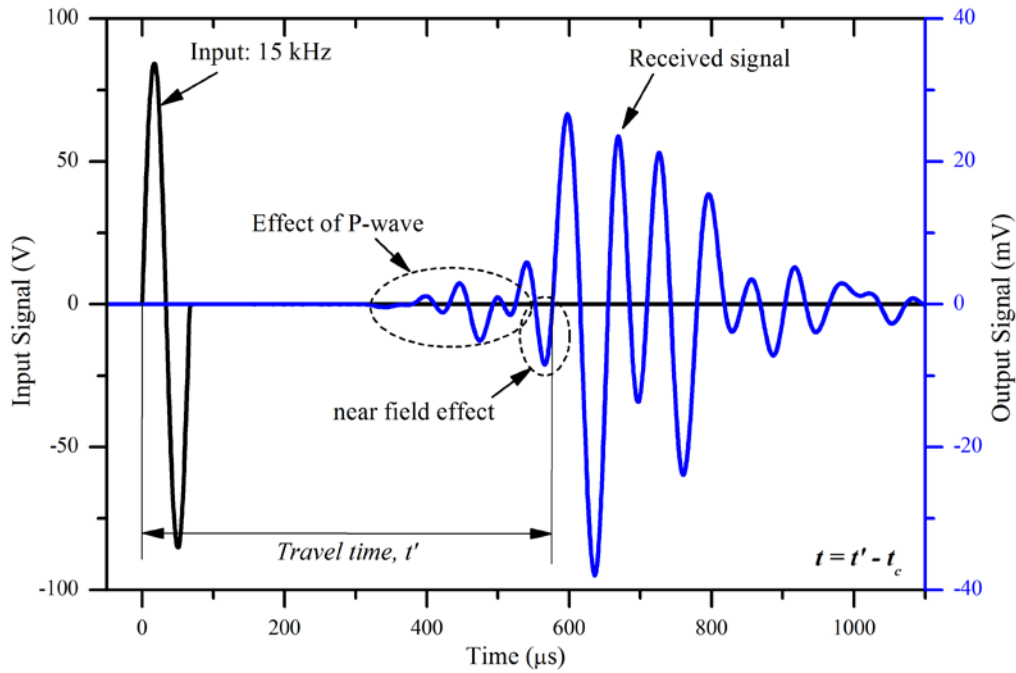


Figure 5.12: Determination of shear wave travel time; disturbances due to compression wave and near-field effects are encircled.

Several researchers have proposed different techniques for accurate determination of shear wave arrival time. Many of these techniques involve analysis of received signals in the time domain (Viggiani & Atkinson, 1995; Arulnathan et al., 1998; Clayton et al., 2004; E.C. Leong et al., 2005); whereas several frequency domain analysis have also been proposed (Viggiani & Atkinson, 1995; Brocanelli & Rinaldi, 1998; Blewett et al., 2000; Arroyo, 2001). A brief summary of these methods with their advantages and disadvantages is presented in the following sections.

5.6.1 Time Domain Analysis

Time domain techniques involve direct extraction of shear wave propagation time based on the input and the received signal response. Different approaches of time domain analysis consider different parts of received signal for travel time determination, as summarized in Figure 5.13. Although some approaches for automatic determination of travel time in time domain are available (Mohsin & Airey, 2003; Rees et al., 2013), yet visual inspection of recorded signals remains the most popular approach of travel time determination.

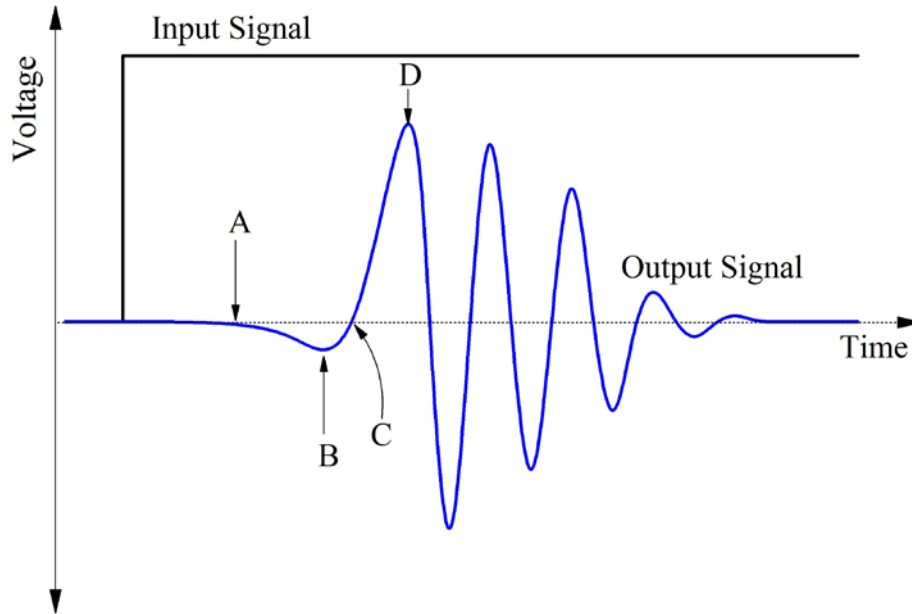


Figure 5.13: Typical *S*-wave signal waveform within near-field; point-A: first deflection; point-B: First bump maximum; point-C: zero crossover; point-D: first major peak. (after Kawaguchi et al. (2001))

5.6.1.1 Zero Crossover Method

This is the most commonly used approach for shear wave signals interpretation. Shear wave travel time is calculated as the difference between the start of transmitted signal and the start of first major positively polarized up rise (or negatively polarized downward signal depending on the polarity of sensors); i.e. “*first-zero cross over*” (Jovicic et al., 1996; Kawaguchi et al., 2001; Lings & Greening, 2001; J. Lee & Santamarina, 2005). A typical description of first zero cross over point is presented as point C in Figure 5.13. However, difficulties arise in this method when point C is masked by near field effects. Such problems are particularly evident when making measurements at low input frequencies (Kawaguchi et al., 2001; E.C. Leong et al., 2005; E. C. Leong et al., 2009).

Because of its simplicity, zero crossover method was adopted for the analysis of all the data in this study. Corrected travel times (t), for shear wave propagation were

calculated by subtracting measured travel time (t') from shear wave calibration factors (t_c).

5.6.1.2 First Major Peak-to-Peak Method

To overcome the problem of distortion due to near field effects peak-to-peak time interval between input signal and the first major peak of received signal (represented by point D in Figure 5.13) can be used to estimate the shear wave time of flight (Viggiani & Atkinson, 1995). This method requires the shape of input and output waves to be similar; thus effectively only 'sine pulse' type of input waves can be used. Additionally, due to dispersion and attenuation of waves in the specimen, it is often very difficult to define the first major peak of received signal in the presence of several consecutive peaks with similar amplitudes.

5.6.2 Frequency Domain Analysis

Frequency domain approaches involve spectral breakdown of signals and comparison of component phase shifts (Viggiani & Atkinson, 1995; Brocanelli & Rinaldi, 1998; Blewett et al., 2000; Arroyo, 2001). Phase delay method, initially proposed by Viggiani and Atkinson (1995) has recently been used by Paul D Greening and Nash (2004), Chan (2010), M. Styler and Howie (2012), M. A. Styler and Howie (2013), etc. However, P. D. Greening et al. (2003) reported underestimation of shear wave velocities measured with frequency domain methods. Additionally, the complexity of frequency domain analysis over time domain analysis limits its adoption by masses. Cross-correlation and cross-spectrum methods are among the most commonly used frequency domain methods.

5.7. PERFORMANCE EVALUATION OF DISK TRANSDUCER SYSTEM

5.7.1 Transmission Cables

The excitation amplitude of disk transducer is naturally lower than bender elements because of its flat shape. Even for very large excitation voltage, the amplitude of receiver signal may still be very low. Very low amplitude receiver signals are prone

not only to interference from external noise, but also to the self-induced noise within the cable. Noise-free transmission lines are necessary to maintain signal integrity. Standard coaxial cables are susceptible to self-induced noise, due to vibration, bending, twisting, friction and fluctuation of pressure, a phenomenon known as *triboelectric noise*. The performance of ordinary coaxial cables in receiving low-amplitude disk transducer signals was compared with low noise coaxial cables (*Fuji ceramics Co. Ltd., Model: LN-030*). The ordinary coaxial cable used in this study had an outer diameter of 2.90 mm whereas the outer diameter of low noise cables was 2.30 mm.

The basic structure of both the cables consisted of a central electrically insulated conductor surrounded by a braided shield. The input signal is transmitted to the sensor through the central core, and the return path is provided by braided outer cable. However, the central conductor of low noise cables had special fluorinated ethylene propylene (FEP) sheathing which not only reduced self-induced cable noise but also provided additional shielding against coupled electromagnetic noise. The quality of transmission cables was analyzed in terms of signal to noise, *SNR*, of received signal. Expression devised by Carlson (1986) was used for calculating *SNR*, and is given as;

$$SNR = 20 \log \frac{\text{Signal Amplitude}}{\text{Signal Noise}} \quad (5.2)$$

Figure 5.14 shows a comparison of compression wave measurement response in Edosaki sand when measured with both cables. Use of low noise coaxial cables significantly reduced the noise generated within the cable, thereby increasing signal to noise ratio, *SNR*, of received signal by about 2.5 times (Figure 5.14(b)). Signal to noise ratio of shear wave signals is naturally higher than compression waves because of less damping, and higher amplitude, under identical conditions. Similar to compression waves, shear wave signals shown in Figure 5.15, show a much smoother response when low noise coaxial cables were used.

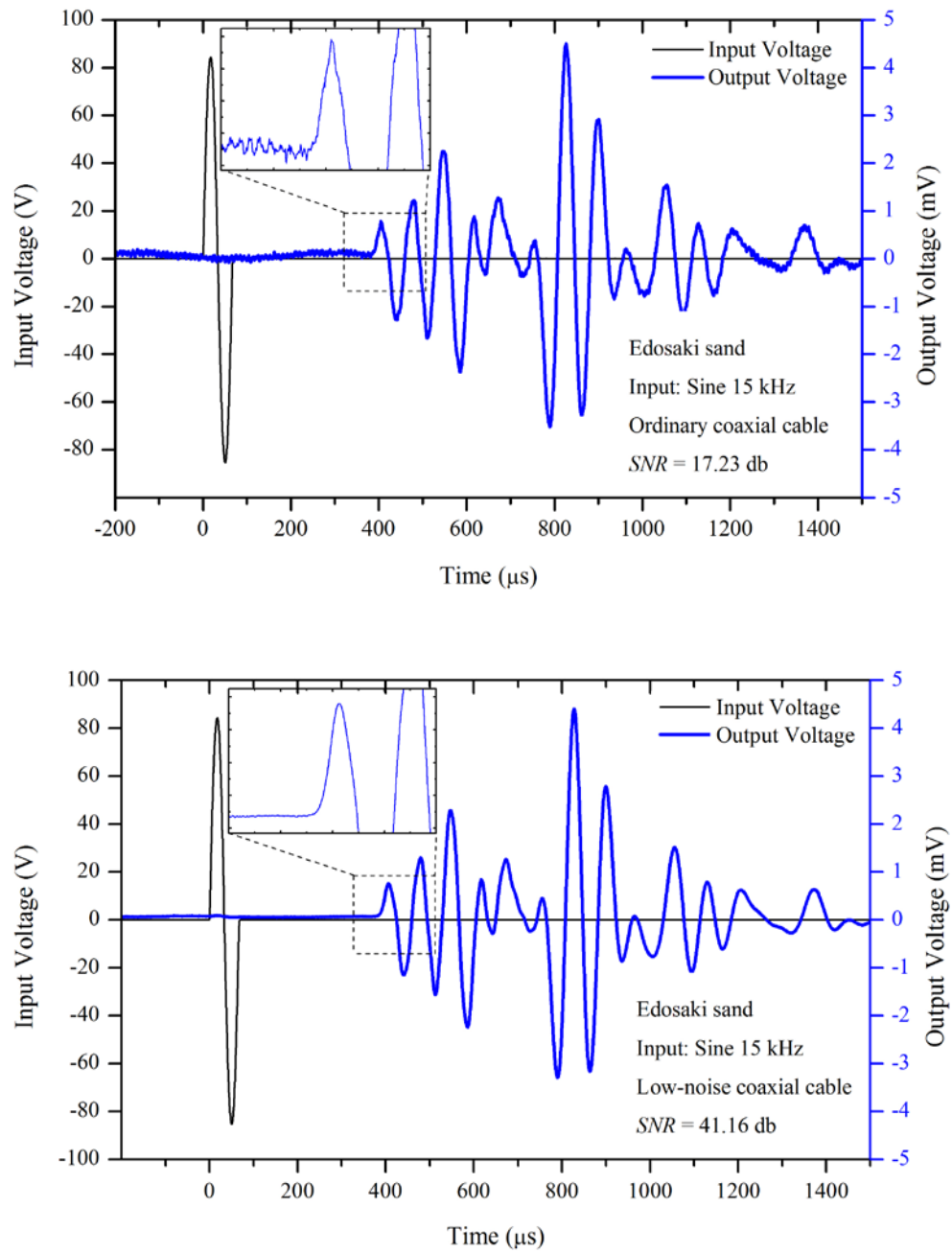


Figure 5.14: Comparison of compression wave response when monitored through (a) Ordinary coaxial cables, and (b) Low-noise coaxial cables.

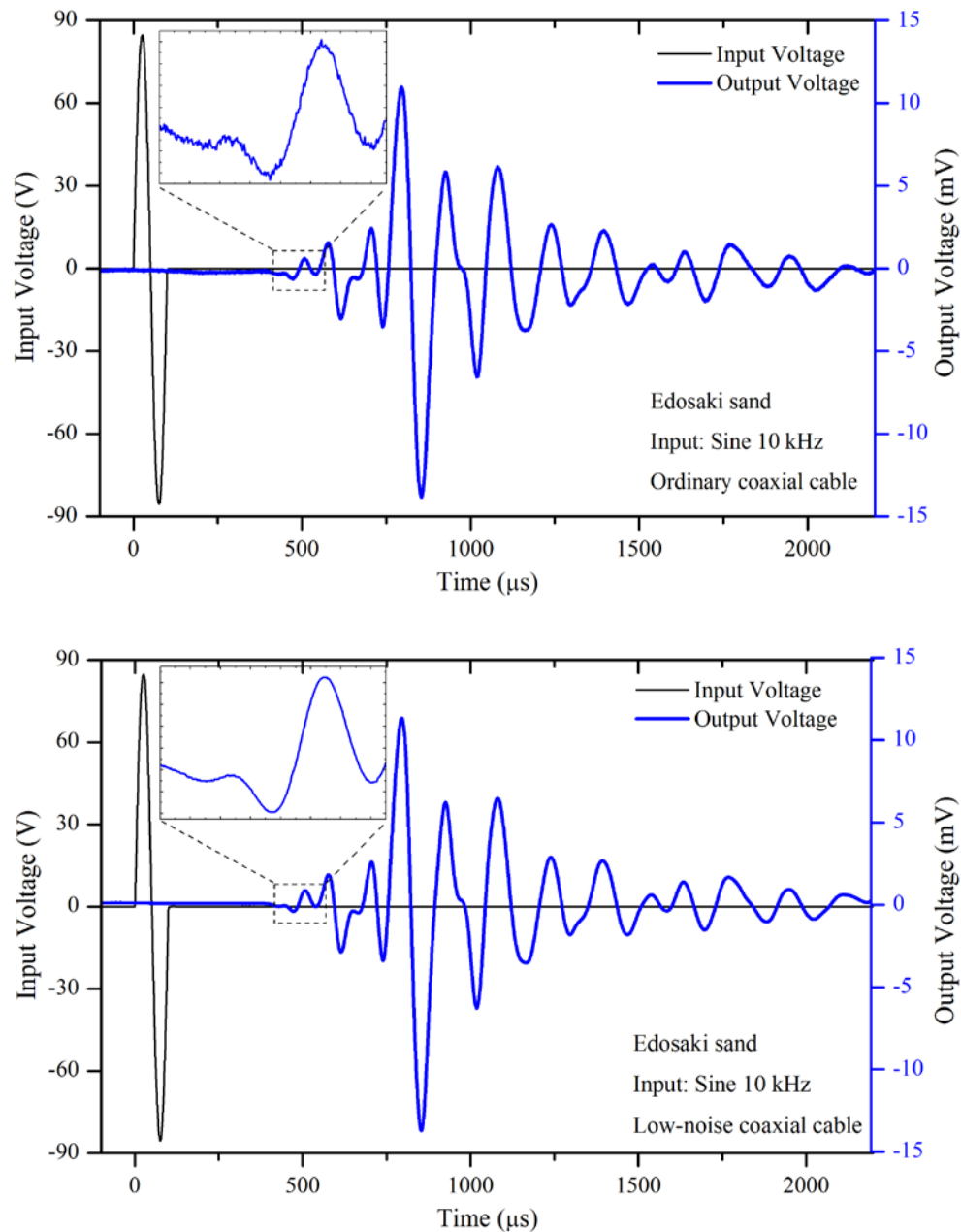


Figure 5.15: Comparison of shear wave response when monitored through (a) Ordinary coaxial cables, and (b) Low-noise coaxial cables.

Although magnitude of self-induced cable noise compared with received signal is not very significant, still it adds to instability of entire system. Moreover, the effect of cable noise can become very significant when the amplitude of received signals is very low, e.g. in saturated/near saturated conditions, aggressive environments (Montoya et al., 2012), etc.

5.7.2 Electromagnetic Coupling – Crosstalk

Electromagnetic coupling between source and receiver piezoelectric transducer causes the deterioration of output signal in the form of an early component which is quasi-simultaneous with the input signal, known as “crosstalk” (J. Lee & Santamarina, 2005). Figure 5.16 and Figure 5.17 show typical examples of crosstalk in *P*-wave and *S*-wave disk transducer signals respectively. The actual arrival point of received signals appears to be masked by crosstalk. As a result, the first arrival appears at a time later than the actual arrival time; consequently the computed wave velocity is lower than the actual value. Crosstalk in disk transducers was found to be removed by grounding the transmitter disk transducer. It was also observed that 50 Hz noise from commercial power supply can be eliminated by grounding the receiver disk transducer. For grounding, the negative terminals of both *P* and *S* transducers were connected to a grounded cable. Both transmitter and receiver disk transducers were therefore, properly grounded in all subsequent tests conducted in this study.

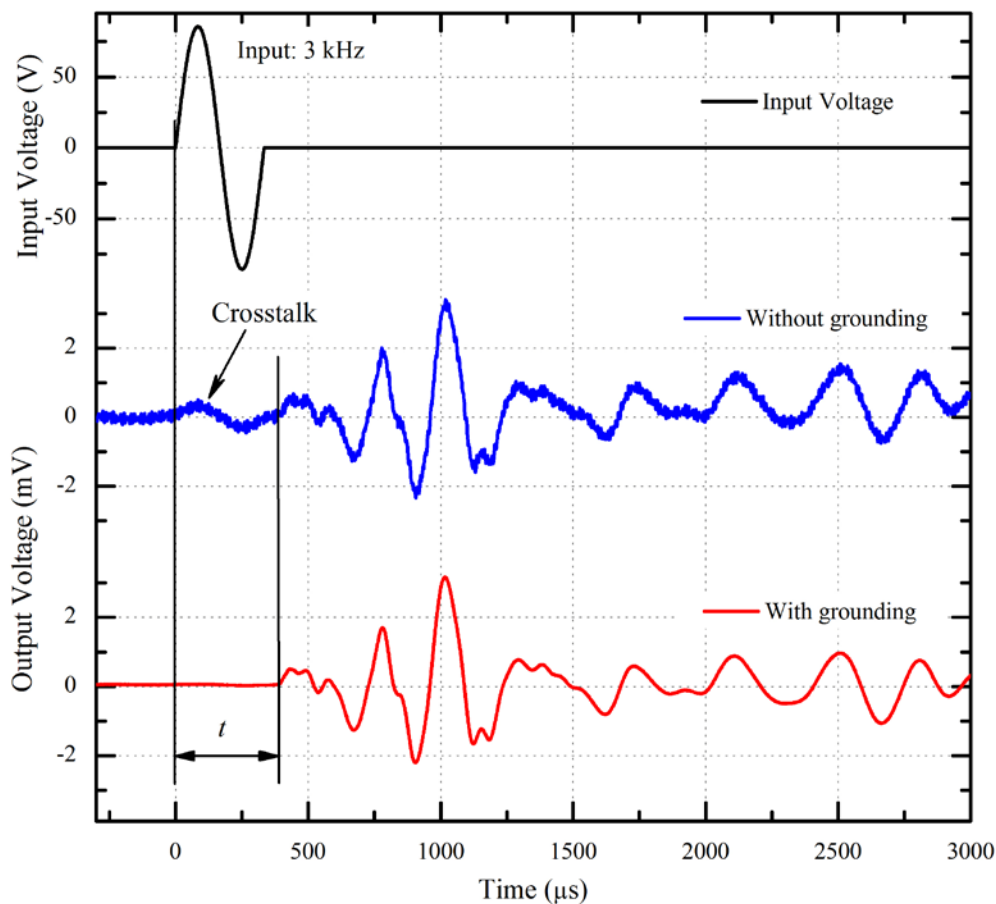


Figure 5.16: Comparison of compression wave signals received (a) Without grounding, and (b) With grounding, highlighting the effects of crosstalk.

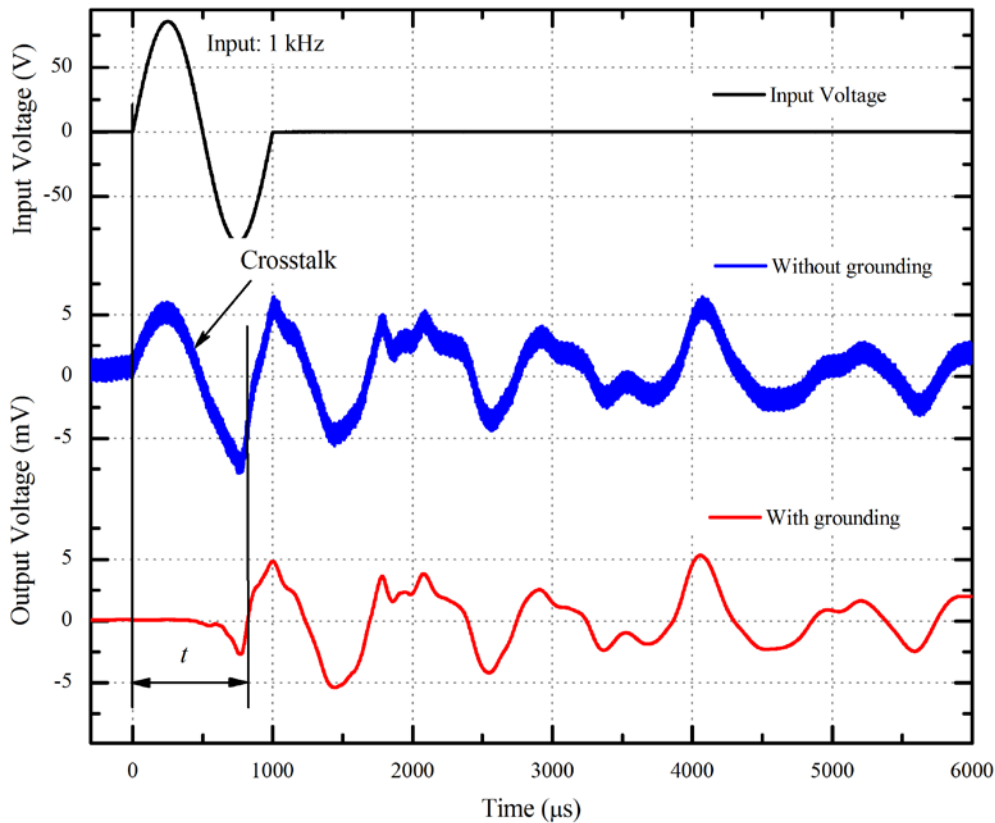


Figure 5.17: Comparison of shear wave signals received (a) Without grounding, and (b) With grounding, highlighting the effects of crosstalk.

5.7.3 Resolution of Recording Unit

Low magnitude received signals from disk transducers are prone to be affected by various sources of signal noise. Quality of signal recording unit directly affects the received signals making signal interpretation difficult. Received signals with low *SNR* may require rigorous signal processing for travel time determination. The effect of recording unit quality on disk transducer received signals was evaluated by comparing signals recorded by a data logger (*Keyence NR-500 data logger with NR-HA08 hi-speed measurement unit*) and a digital oscilloscope (*Hioki 8860-50 digital oscilloscope with model 8957 hi-resolution measurement unit*).

Figure 5.18 shows typical *S*-wave receiver signals in a dry Edosaki sand specimen, recorded on both *Keyence NR-500* data logger and *Hioki 8860-50* oscilloscope. The corresponding frequency spectrums, obtained through Fast Fourier Transform (*FFT*)

of received signals are shown in Figure 5.19. Although the frequency spectrum of both the recorders showed a similar dominant frequency but the signal to noise ratio as well as the signal amplitude of signal recorded by *Hioki 8860-50* oscilloscope was much higher. Moreover, the signal obtained through *Hioki 8860-50* oscilloscope was much clearer compared to its counterpart making travel time determination rather easy.

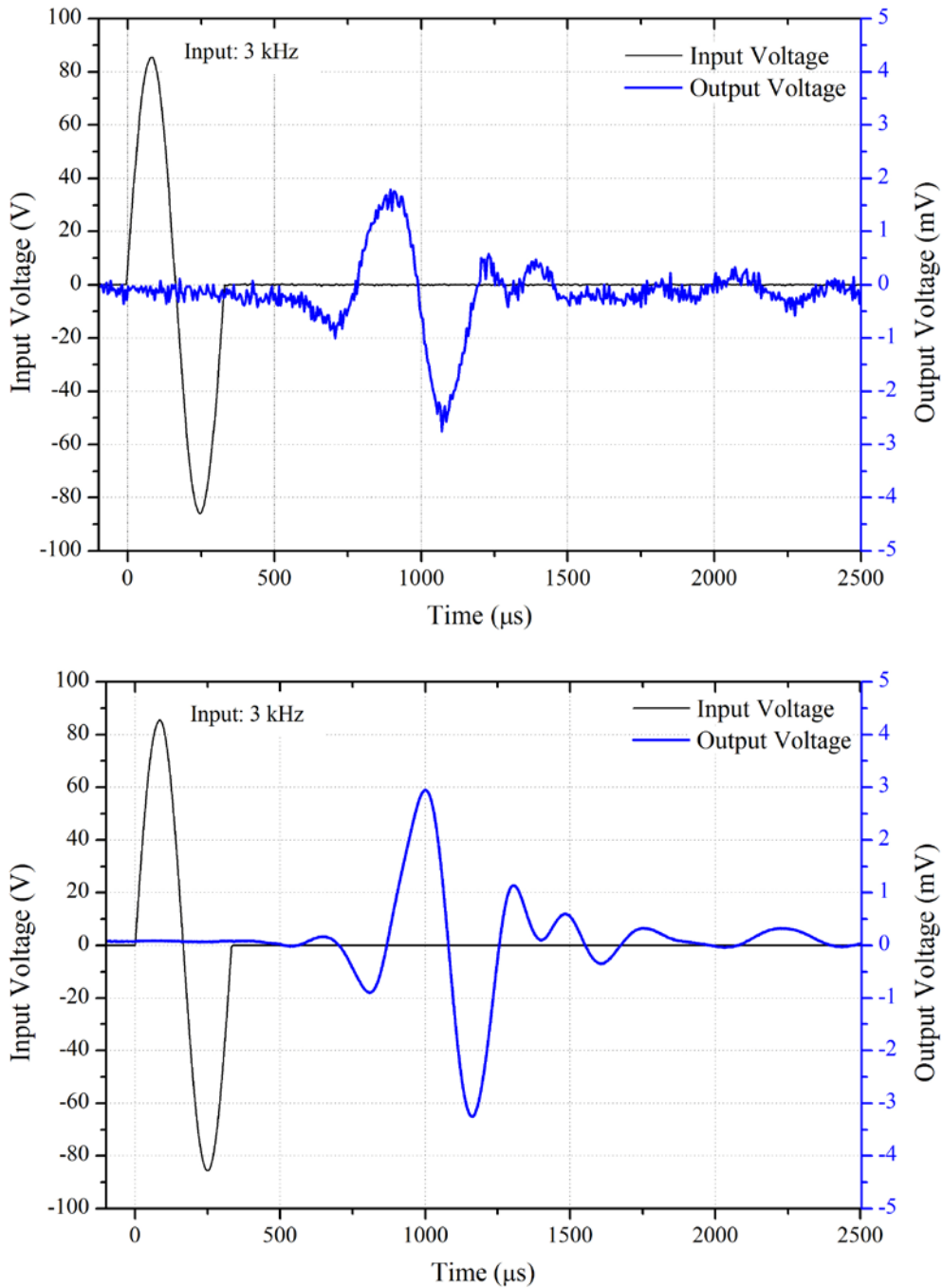


Figure 5.18: Typical shear wave signals recorded with (a) *Keyance NR-500* data logger, and (b) *Hioki 8860-50* hi-resolution oscilloscope.

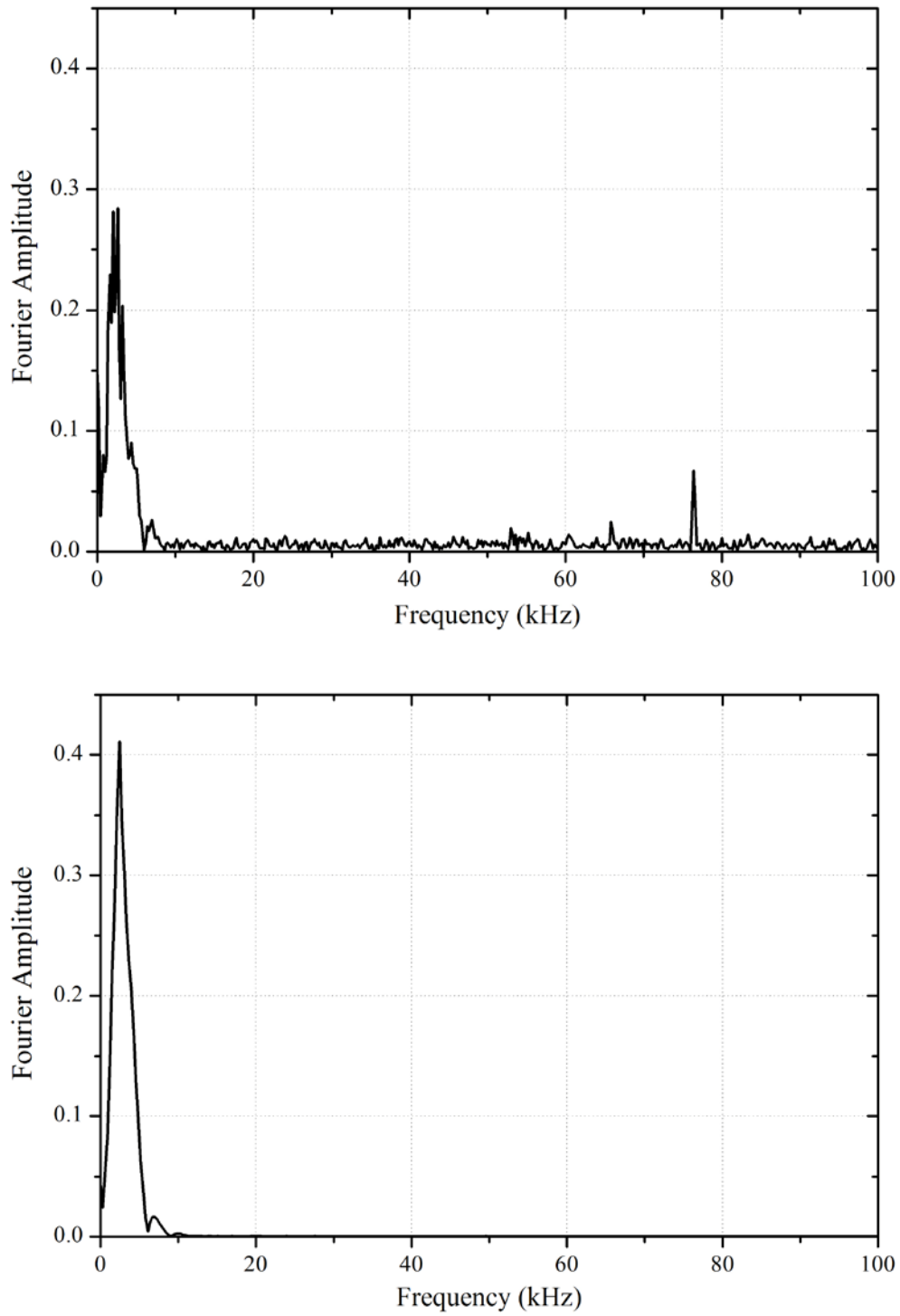


Figure 5.19: Frequency response function of shear wave signals recorded with (a) *Keyence NR-500* data logger, and (b) *Hioki 8860-50* hi-resolution oscilloscope.

Typical *P*-wave receiver signals in the same dry Edosaki sand specimen obtained through both recorders are shown in Figure 5.20, and their corresponding frequency spectrums are shown in Figure 5.21. Similar to *S*-waves, *P*-wave receiver signal obtained by *Hioki 8860-50* oscilloscope was much clearer than the signal obtained by *Keyence NR-500* data logging unit. High levels of noise in *Keyence NR-500* data logger signals mean a very low signal to noise ratio, resultantly no dominant frequency can be observed from its frequency spectrum. On the contrary, a dominant frequency of about 15 kHz, similar to the excitation frequency, can be observed from the frequency spectrum of signal recorded by *Hioki 8860-50* oscilloscope. Due to electromagnetic coupling between the transmitter and receiver, cross-talk can be observed in the signal recorded by data logger. However, no crosstalk was observed for *Hioki 8860-50* oscilloscope.

A comparison of main features of both recording units is presented in Table 5.2. Four separate recording units can be installed on *Hioki 8860-50* oscilloscope. This enables transmitter and receiver signals to be recorded on individual recording units, thereby reducing the chances of electromagnetic crosstalk, as can be observed in Figure 5.20. Besides a higher analog to digital (*A/D*) conversion resolution, *Hioki 8860-50* oscilloscope offers a much higher sampling rate resulting in a smoother signal. The voltage sensitivity of recorder is expressed in terms of least significant bit (*LSB*) voltage, which is the minimum voltage discernible by the recorder. The *LSB* voltage of *Keyence NR-500* was limited to 0.01 mV as compared to 3.125 μ V for *Hioki 8860-50* oscilloscope; hence any change in voltage smaller than 0.01 mV could not be detected by *NR-500* data logger, as can be seen in Figure 5.20(b). In order to determine the inherent noise level, both recorders were fed with 0 V input (i.e. short-circuited) and the resulting signal was recorded. *Keyence NR-500* data logger possessed a very high inherent noise of about 0.08 mV as compared to 0.001 mV of *Hioki 8860-50* oscilloscope, as shown in Figure 5.22. Hence, signals recorded by *Keyence NR-500* data logger having peak-to-peak amplitude of less than 0.08 mV would be difficult to observe because of being masked by inherent noise. Therefore, a signal recorder having separate recording units for transmitter and receiver, high *A/D* conversion resolution, sampling rate, voltage resolution; and low inherent noise is necessary for disk transducer element tests.

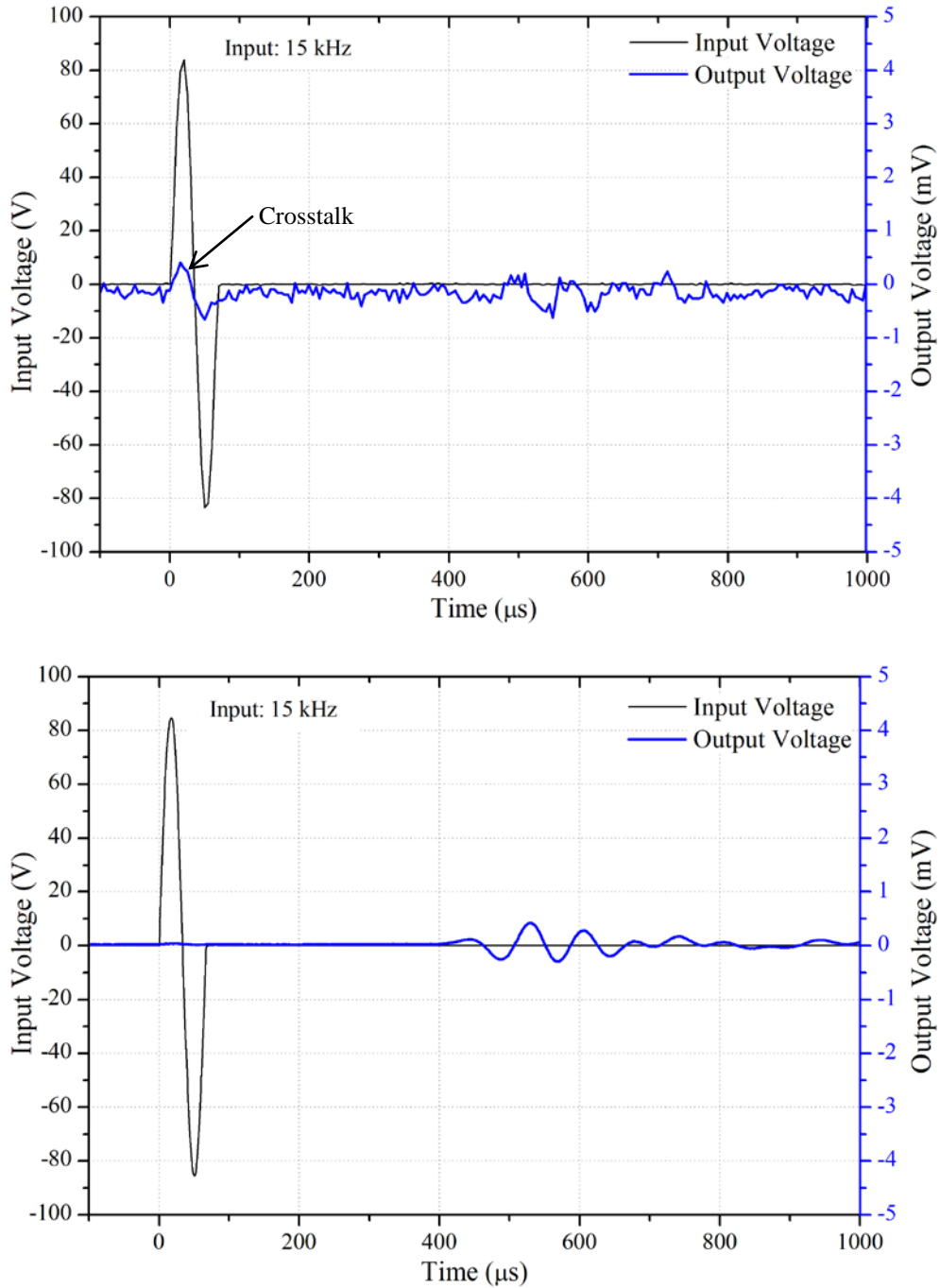


Figure 5.20: Typical compression wave signals recorded with (a) *Keyence NR-500* data logger, and (b) *Hioki 8860-50* hi-resolution oscilloscope.

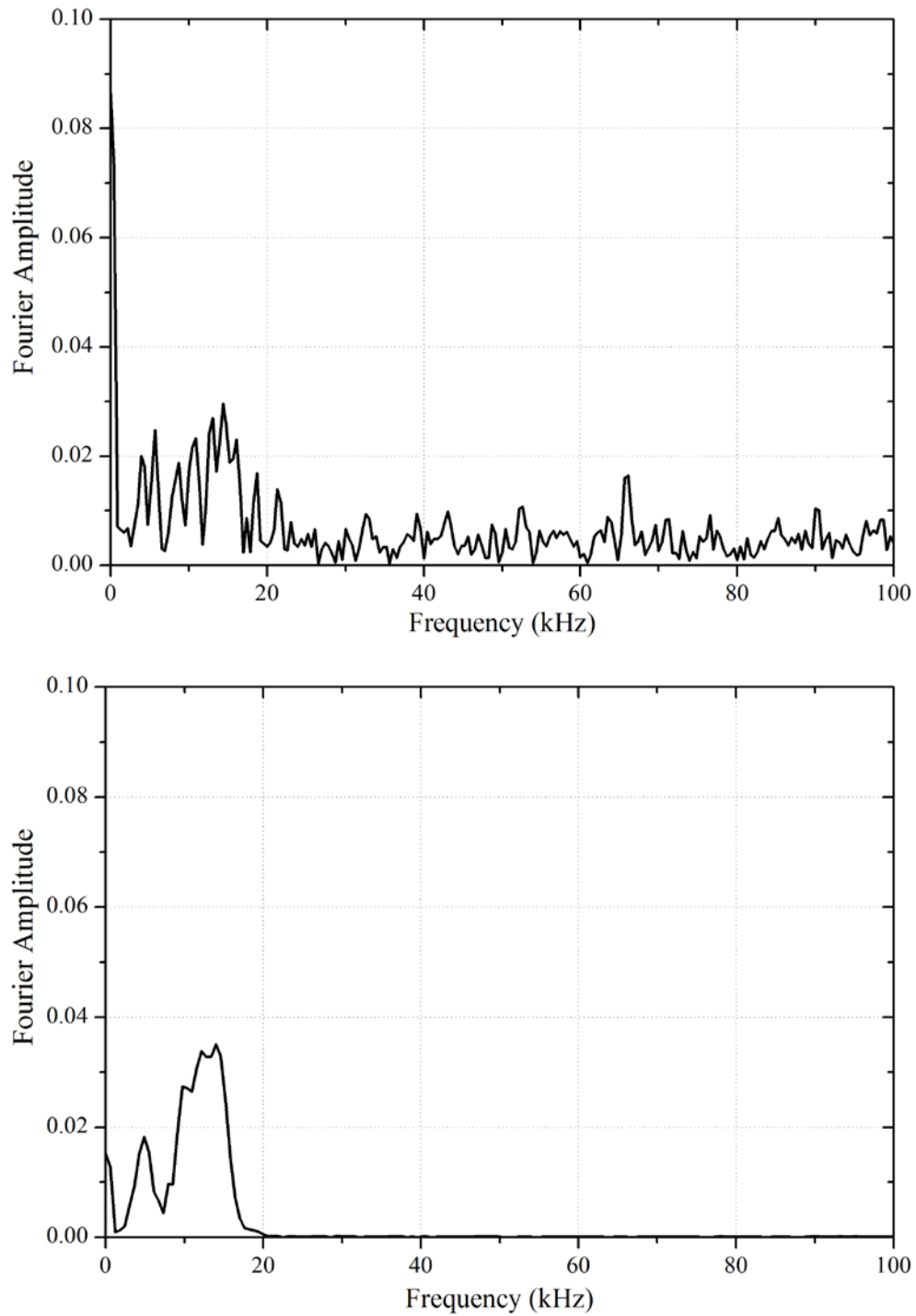


Figure 5.21: Frequency response function of compression wave signals recorded with (a) *Keyence NR-500* data logger, and (b) *Hioki 8860-50* hi-resolution oscilloscope.

Table 5.2: Main features of signal recorders used in this study.

<i>Feature</i>	<i>Keyence NR-500 Data Logger with NR-HA08 Measurement Unit</i>	<i>Hioki 8860-50 Oscilloscope with 8957 Hi-resolution Measurement Unit</i>
Max. input channels	4	16
A/D conversion resolution	14 bit	16 bit
Maximum sampling rate	2 μ s/S (500 kHz)	50 ns/S (20 MHz)
Voltage resolution	0.01 mV	3.125 μ V
Inherent noise	≈ 0.08 mV	≈ 0.001 mV

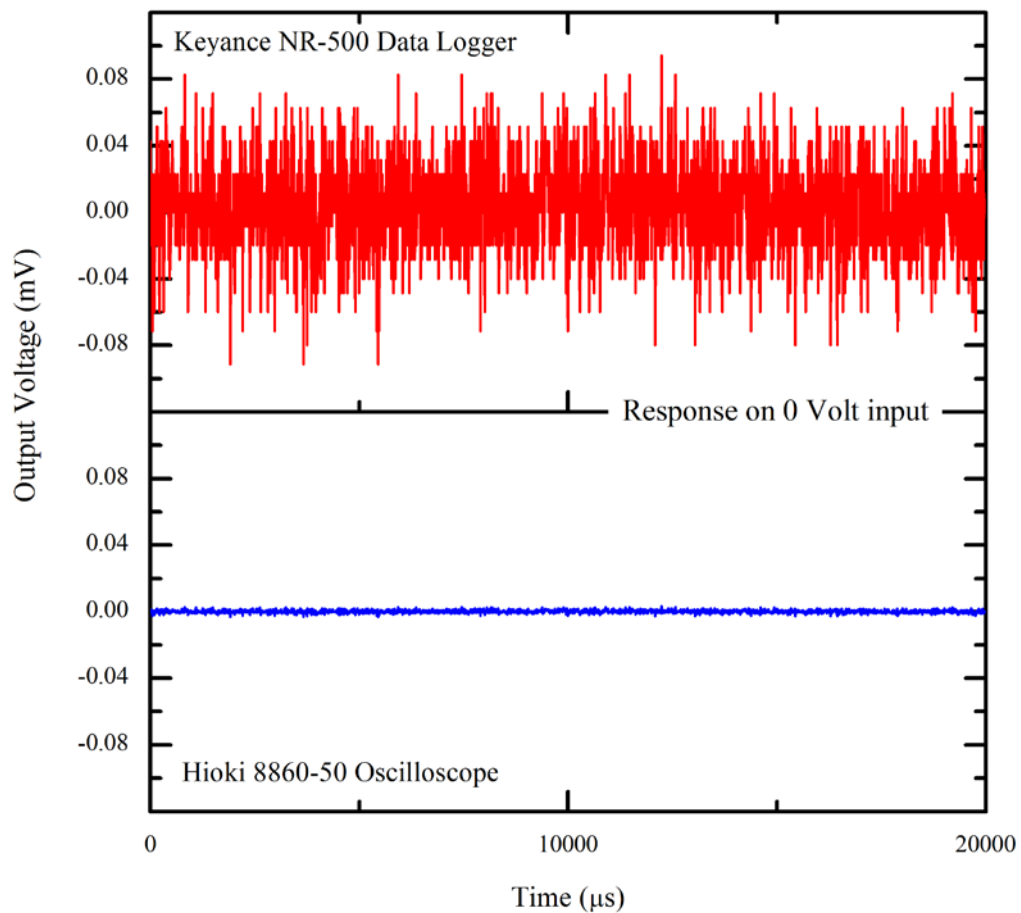


Figure 5.22: Inherent noise in (a) *Keyence NR-500* data logger, and (b) *Hioki 8860-50* hi-resolution oscilloscope; obtained by short-circuiting the receiver terminals (0 Volt input).

5.7.4 Shape of Input Waveform

Two types of input waveforms are commonly used by researchers; square (Dyvik & Madshus, 1985; Bates, 1989; Lohani et al., 1999; Rodríguez & Moreno-Carrizales, 2001), and sinusoidal (Viggiani & Atkinson, 1995; Blewett et al., 2000; Pennington et al., 2001; E.C. Leong et al., 2005; C. J. Lee & Huang, 2007; E. C. Leong et al., 2009). Response of square and sinusoidal waves to disk transducer measurements were evaluated in this study. Figure 5.23 shows receiver signals for square and sinusoidal wave in 70% saturated Edosaki sand specimen.

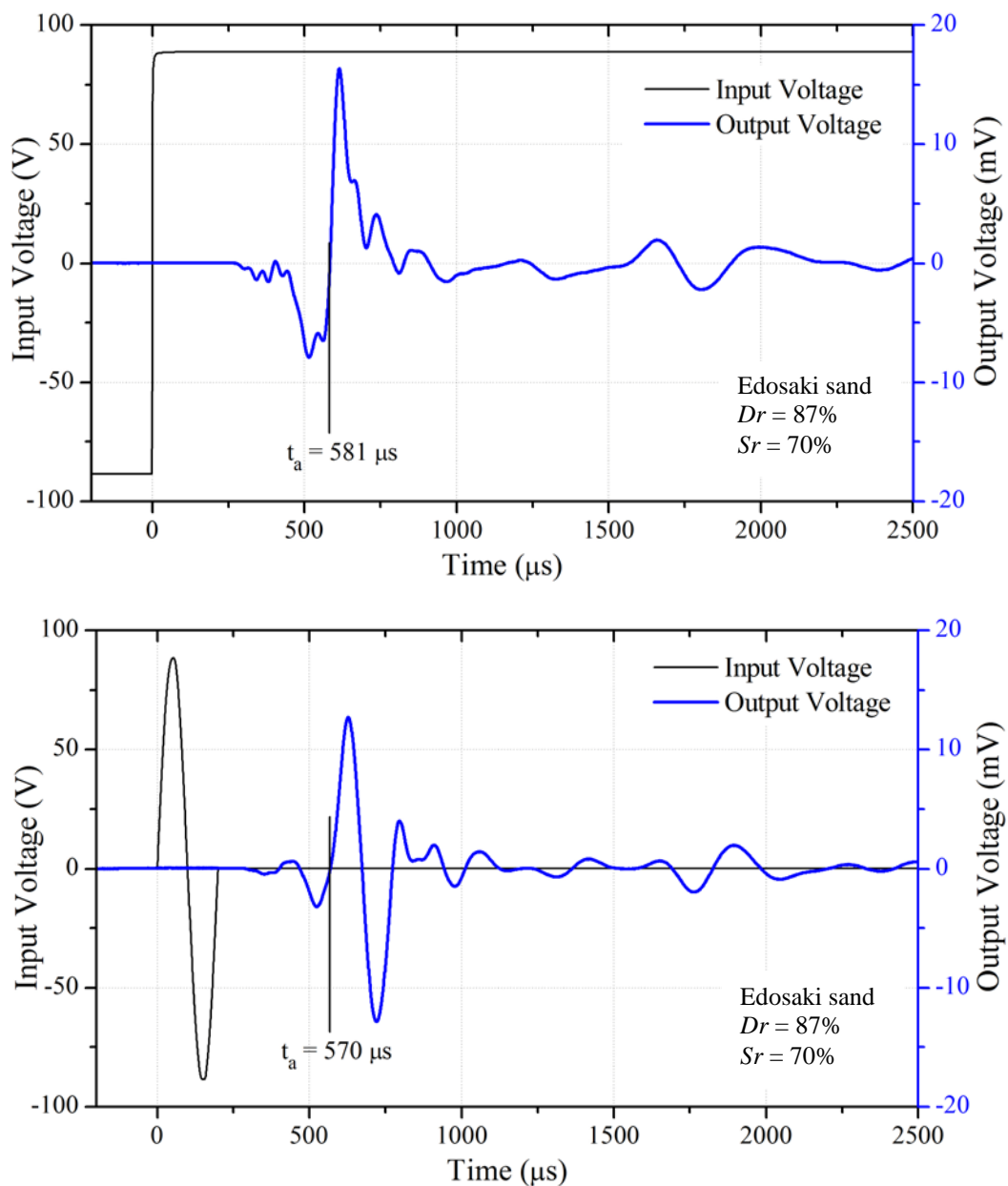


Figure 5.23: Effect of shape of input waveform on shear wave receiver signals; (a) Square pulse, (b) Sine pulse.

In case of square input, more distortion was observed before the actual arrival causing greater ambiguity in determination of travel time (Figure 5.23(a)). Also the received signal does not resemble the input signal; this observation is consistent with the observations made by Jovicic et al. (1996), Blewett et al. (2000), and E.C. Leong et al. (2005). High distortion for square wave input can be explained on the basis of large number of frequency components contained within it (Figure 5.24(a)). Group velocity dispersion within the specimen leads to separation of different frequency components within the voltage-edge waveform. These propagate at different speeds, arriving at different times, and producing a severely distorted receiver waveform (Blewett et al., 2000). Conversely, sinusoidal wave input causes comparatively less distortion due to the presence of fewer frequency components (Figure 5.24(b)). Receiver signals for sinusoidal wave input resembled the input signal and less distortion observed at the beginning of signal, made travel time determination comparatively easy (Figure 5.23(b)). This behavior was observed to be independent of relative density, and degree of saturation of specimen. Sinusoidal input waveform is therefore, used for all subsequent tests in this study.

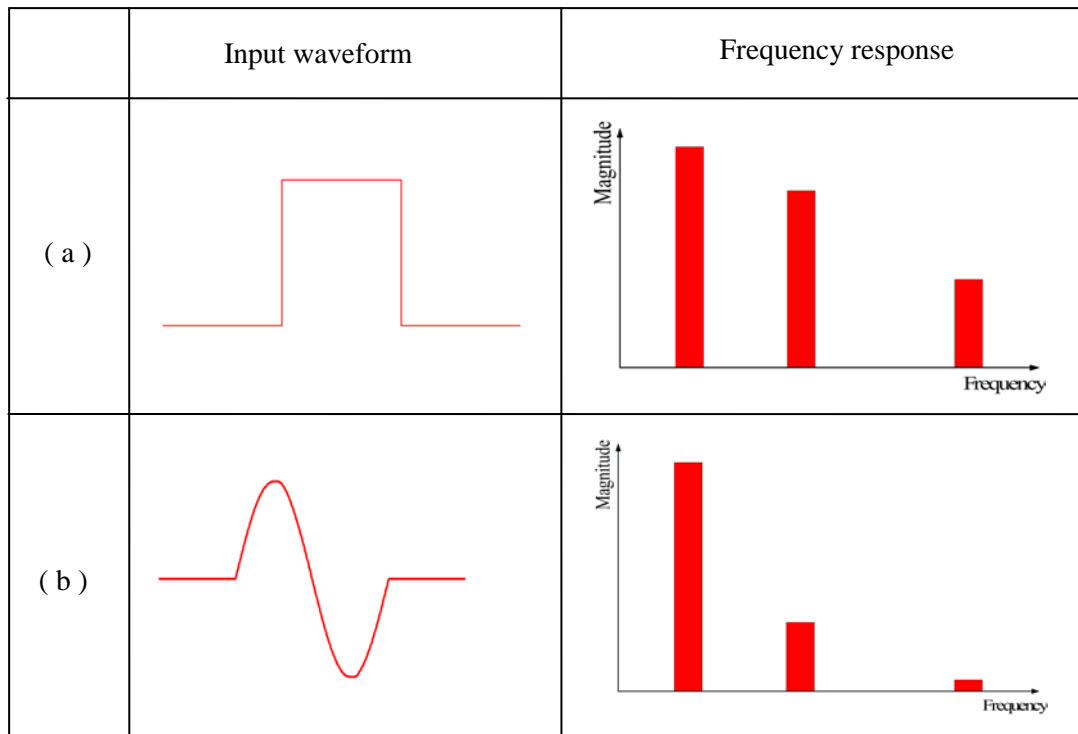


Figure 5.24: Frequency response of commonly used driving waveforms; (a) square pulse (b) sine pulse. (after (Blewett et al., 2000))

5.7.5 Excitation Frequency

Interpretation of elastic wave signals, i.e., the ability to detect the arrival time of wave, depends largely on the amplitude of received signals. For efficient determination of shear wave velocity, E.C. Leong et al. (2005) suggested signal to noise ratio (*SNR*) of received signal to be at least 4 db. Amplitude of received signals is enhanced when the frequency of excitation approaches resonant frequency of piezoelectric element – soil system (Jovicic et al., 1996; Kawaguchi et al., 2001; J. Lee & Santamarina, 2005; Wang et al., 2007).

During shear excitation, disk transducer, generates two *P*-wave side lobes parallel to its plane of vibration (Figure 5.25). These lobes are generated due to the compression effect associated with shear vibration. Difference in travel velocity prevents interference of shear and compression waves. However, test result of shear waves show some traces of distorted *P*-waves making the identification of first arrival ambiguous. Sanchez-Salinero et al. (1986) showed that the *S*-wave signal is always accompanied by propagation of another signal of opposite polarity travelling with the velocity of *P*-waves. This phenomenon known as “*near-field*” effect is quantified in terms of wave path length (*L*) to wavelength (λ) ratio. Inverting the polarity of input voltage does not help in removing near-field effect as by doing so the polarity of whole signal, including the near-field component is reversed (Mancuso & Vinale, 1988).

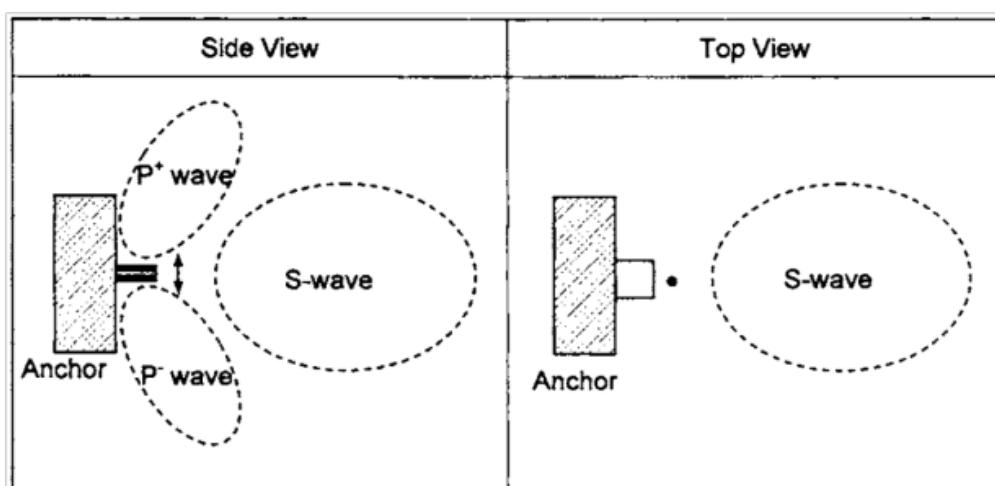


Figure 5.25: schematic illustration describing the generation of two side lobes of *P*-waves (responsible for near-field effect) in addition to *S*-waves, upon shear excitation of bender elements (J. Lee & Santamarina, 2005).

Effects of excitation frequency on shear and compression wave signals were evaluated by subjecting each specimen in *ICCW* test series (Chapter 6) to various input frequencies. Excitation frequencies ranged from 0.25 kHz – 25 kHz for shear waves, and 1 kHz – 30 kHz for compression waves. Effects of input frequency on shear wave signals are summarized in Figure 5.26 to Figure 5.37, whereas the corresponding effects on compression wave velocities are presented in Figure 5.38 to Figure 5.39. Resonant frequency of disk transducer – soil system appeared to be increasing with confining pressure; e.g., for dry specimen maximum amplitude of received signals were observed at 5 kHz, 7.5 kHz and 10 kHz for 50 kPa, 100 kPa, and 200 kPa confining pressure respectively. Stiffness of soil specimens increased with confining pressure, and stiffer specimens would naturally resonate with low time period and high frequency. A similar trend was observed for specimens with different saturation ratio as well.

Shear wave arrival time was also found to be dependent on magnitude of input frequency. Several researchers have previously reported the sensitivity of shear wave arrival time to input frequency because of near-field effect distortions (Brignoli et al., 1996; Kawaguchi et al., 2001; J. Lee & Santamarina, 2005; E.C. Leong et al., 2005; E. C. Leong et al., 2009). Near-field effect is evaluated in terms of L/λ ratio, i.e. number of wavelengths between transmitter and receiver. Due to low damping in dry specimen ($Sr = 0\%$), amplitude of compression waves, arriving prior to shear waves increases with excitation frequency. At considerably large input frequencies, compression wave signal may be as strong as shear wave signal itself (e.g., Figure 5.26, $f_{(in)} = 15$ kHz). However, for partially saturated specimens ($Sr = 45\%$, and $Sr = 74\%$), the magnitude of near-field effect is found to decay considerably with increasing L/λ (Figure 5.29 to Figure 5.34). This observation is consistent with several other researchers including Sanchez-Salinero et al. (1986), Brignoli et al. (1996), Arulnathan et al. (1998), and E.C. Leong et al. (2005), etc. Also due to near-field effects, the arrival time of shear waves was found to decrease with excitation frequency. However, this variation in S -wave arrival time decreased considerably with L/λ . Based on ASTM standards (ASTM, 2008), Leong (2005; 2009) suggested to use minimum L/λ of 3.33 in order to avoid near-field effect distortions. Shear wave velocities, plotted against L/λ in Figure 5.35 to Figure 5.37 show almost negligible

variation in shear wave velocity beyond $L/\lambda = 3.33$. It can also be surmised that the empirical lower bound of $L/\lambda = 3.33$ works well irrespective of soil saturation state. In summary, near-field effects distortion in shear wave signals can be reduced by using a higher excitation frequency. However, increased wave attenuation and overshooting of signals (J. Lee & Santamarina, 2005; Wang et al., 2007) at high frequencies limits the maximum excitation frequency and hence the L/λ ratio.

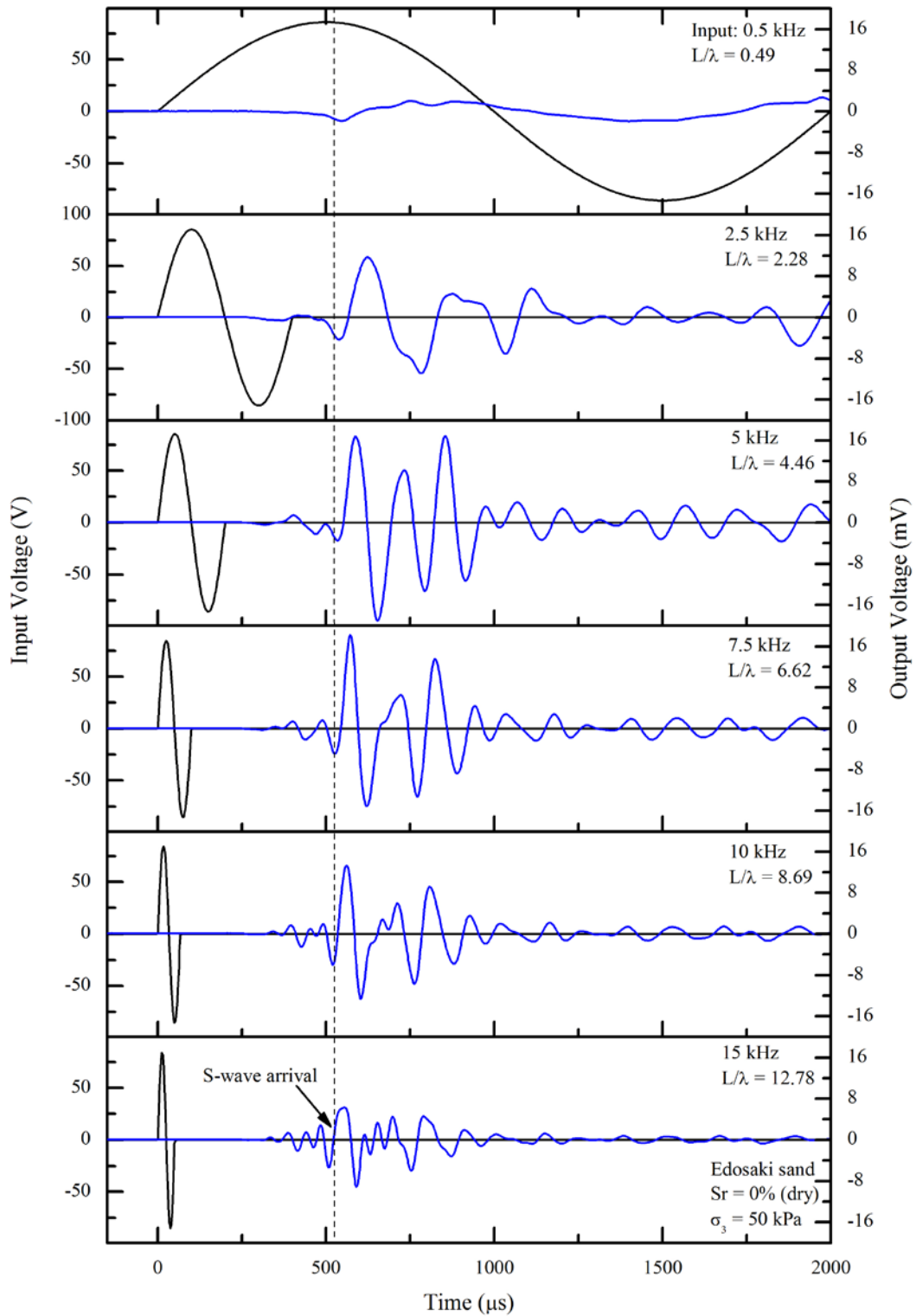


Figure 5.26: Effects of excitation frequency on shear wave signals obtained in dry Edosaki sand ($S_r = 0\%$) at 50 kPa isotropic stress.

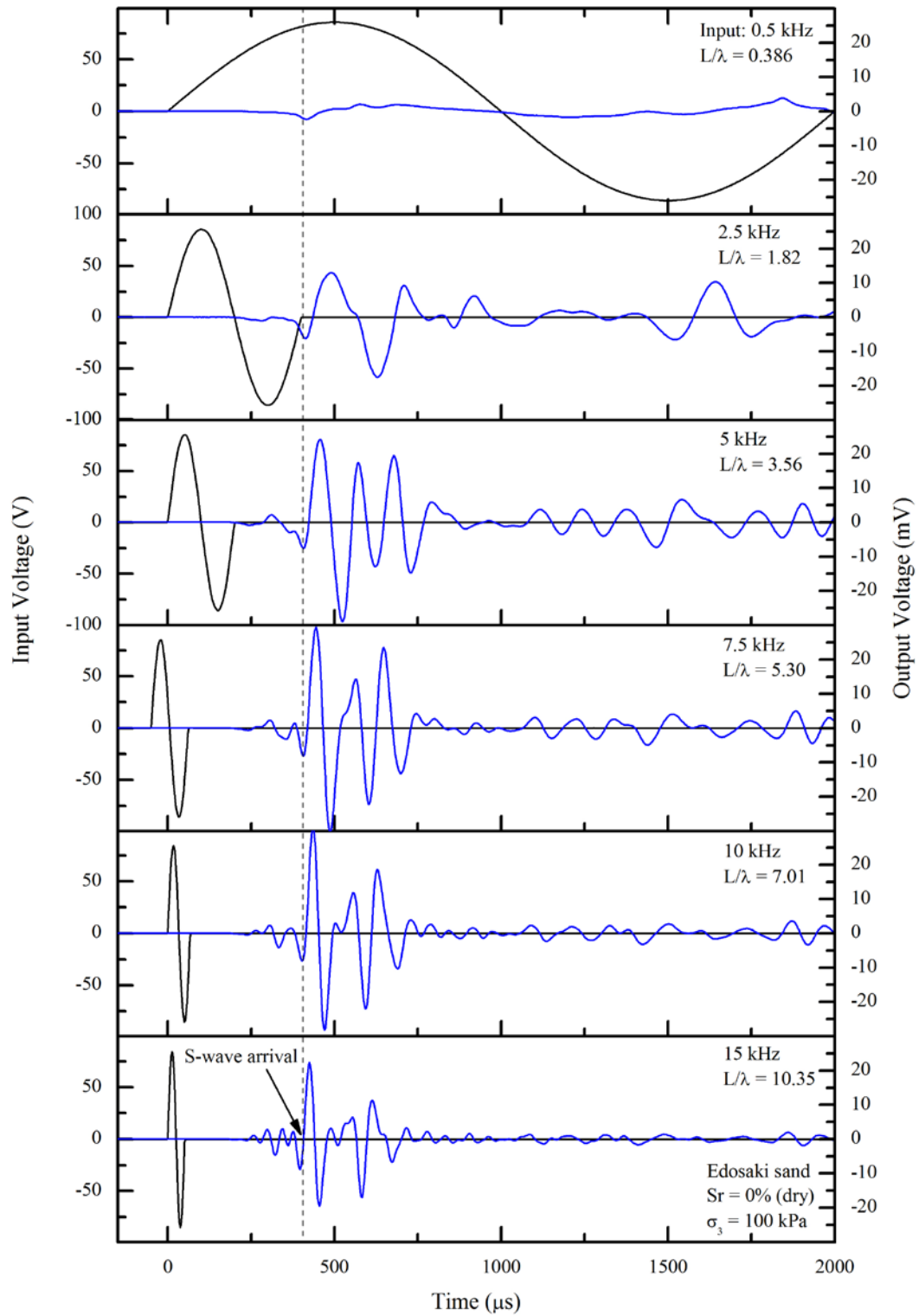


Figure 5.27: Effects of excitation frequency on shear wave signals obtained in dry Edosaki sand ($S_r = 0\%$) at 100 kPa isotropic stress.

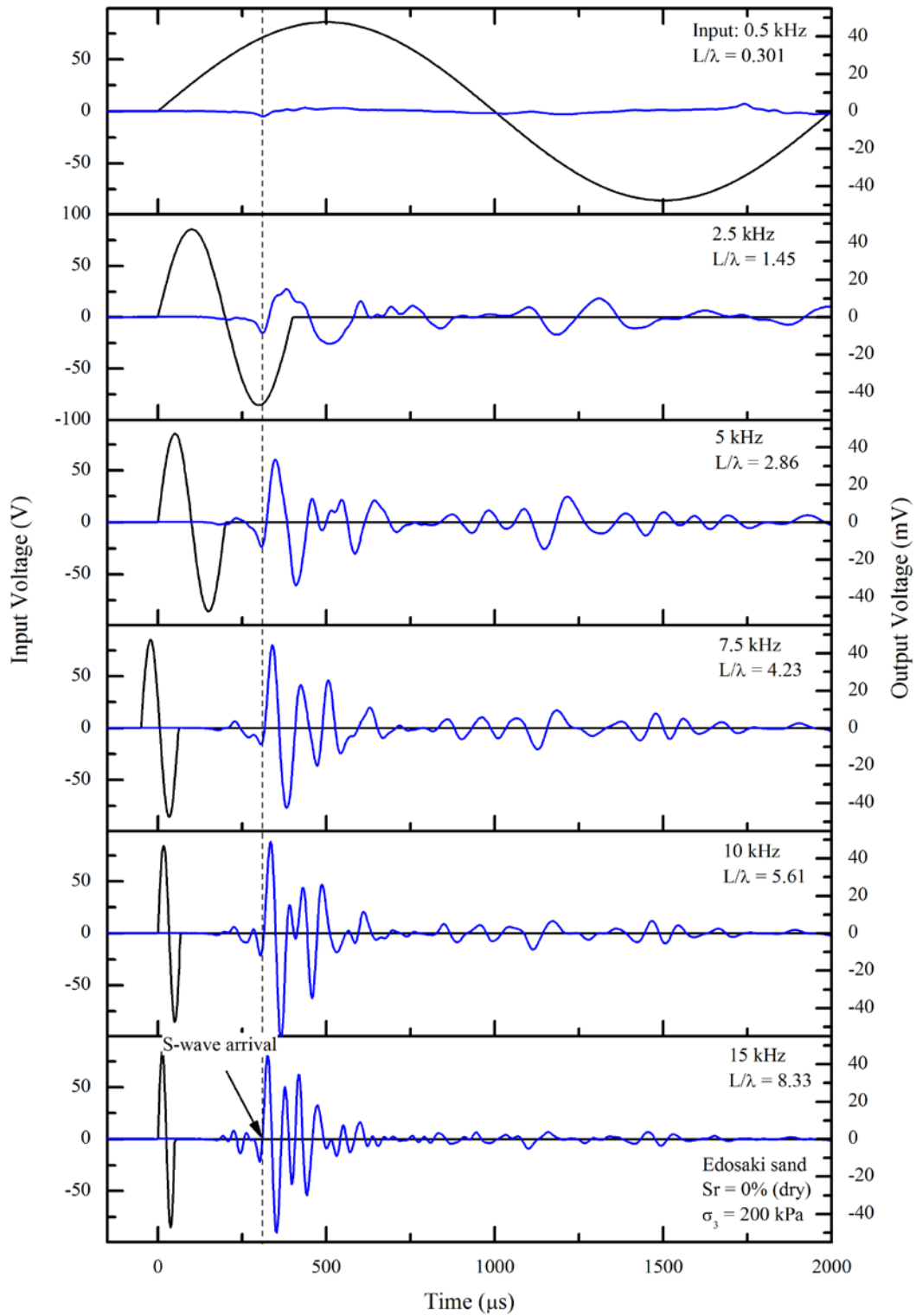


Figure 5.28: Effects of excitation frequency on shear wave signals obtained in dry Edosaki sand ($S_r = 0\%$) at 200 kPa isotropic stress.

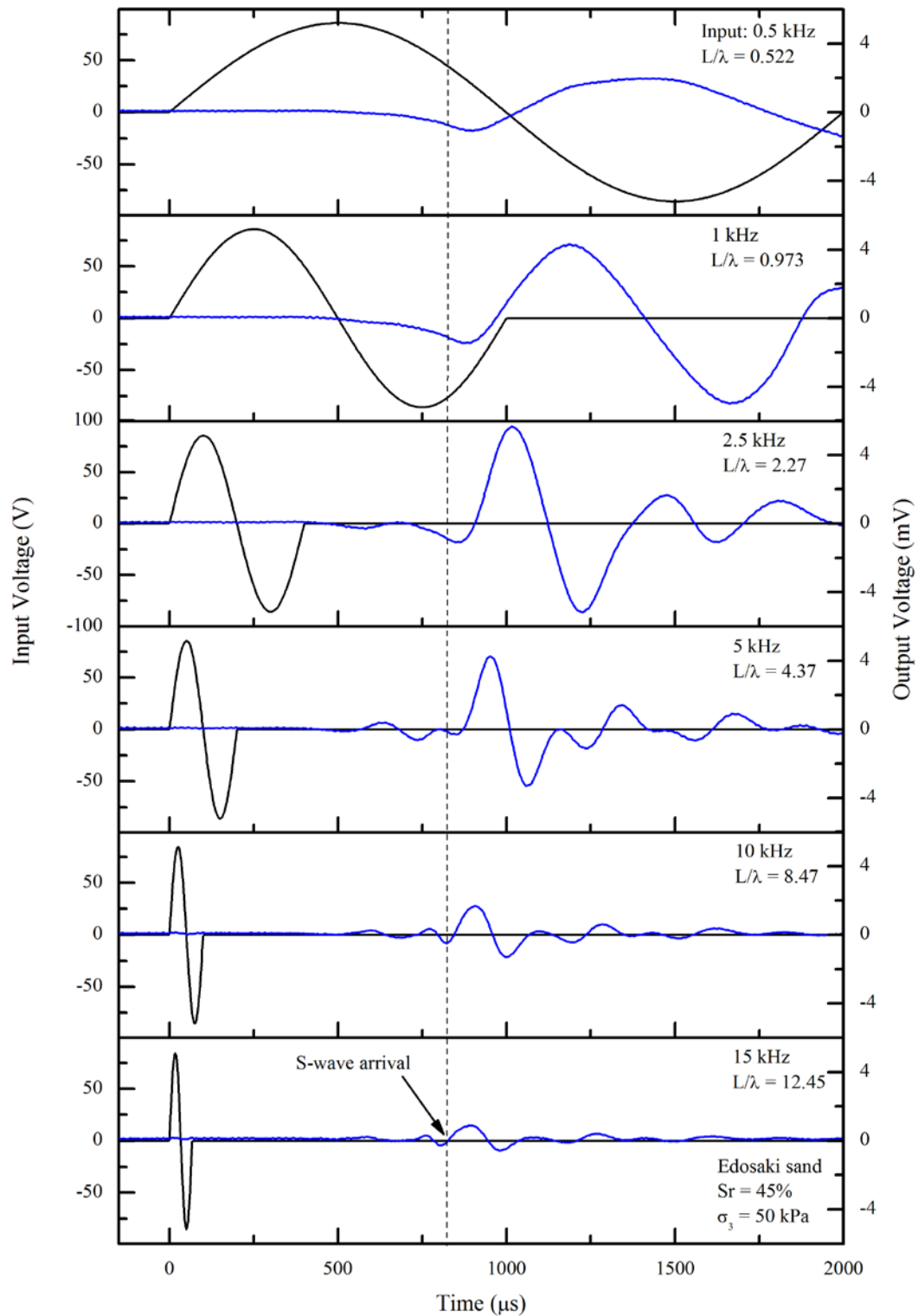


Figure 5.29: Effects of excitation frequency on shear wave signals obtained in partially saturated Edosaki sand ($S_r = 45\%$) at 50 kPa isotropic stress.

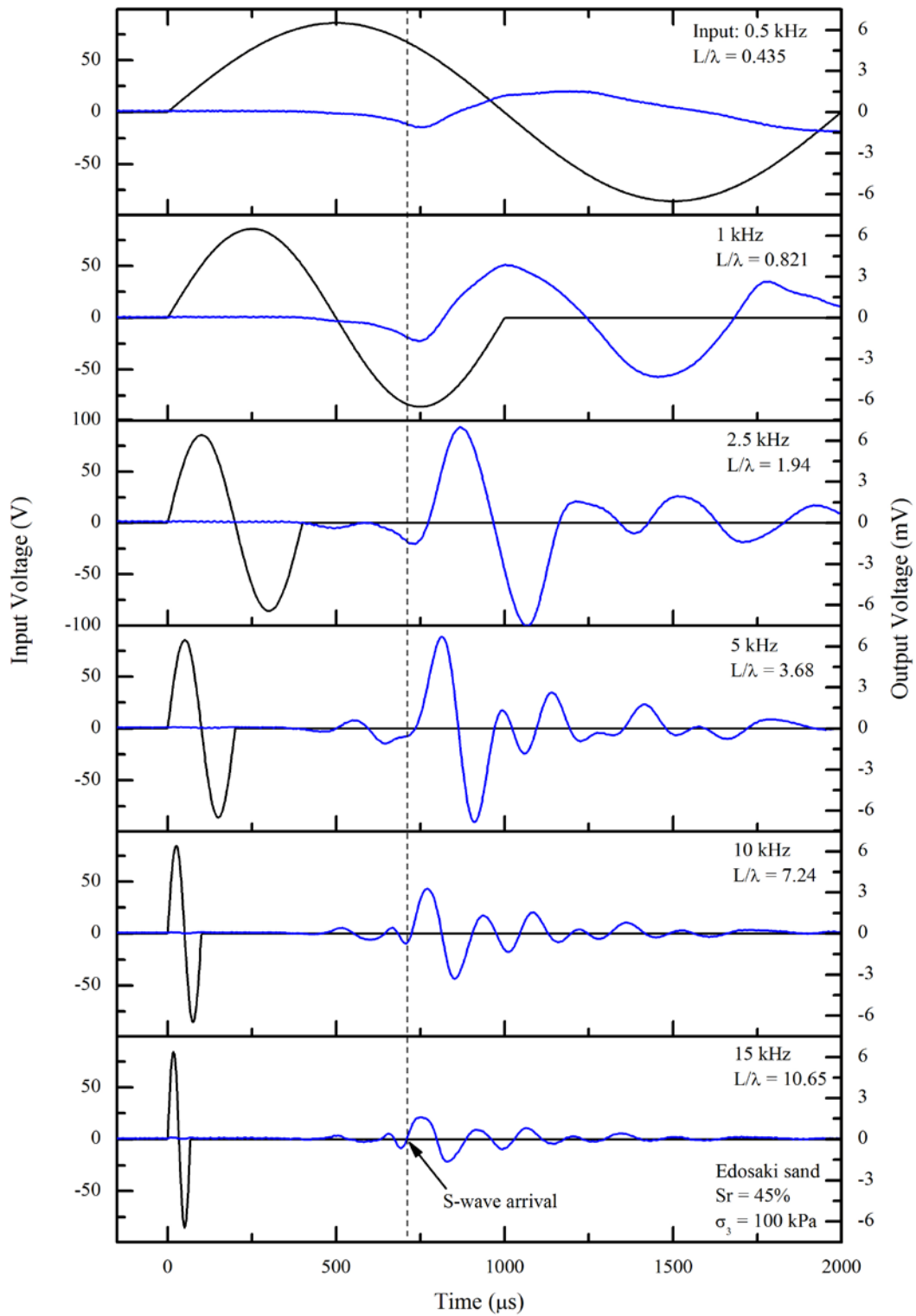


Figure 5.30: Effects of excitation frequency on shear wave signals obtained in partially saturated Edosaki sand ($S_r = 45\%$) at 100 kPa isotropic stress.

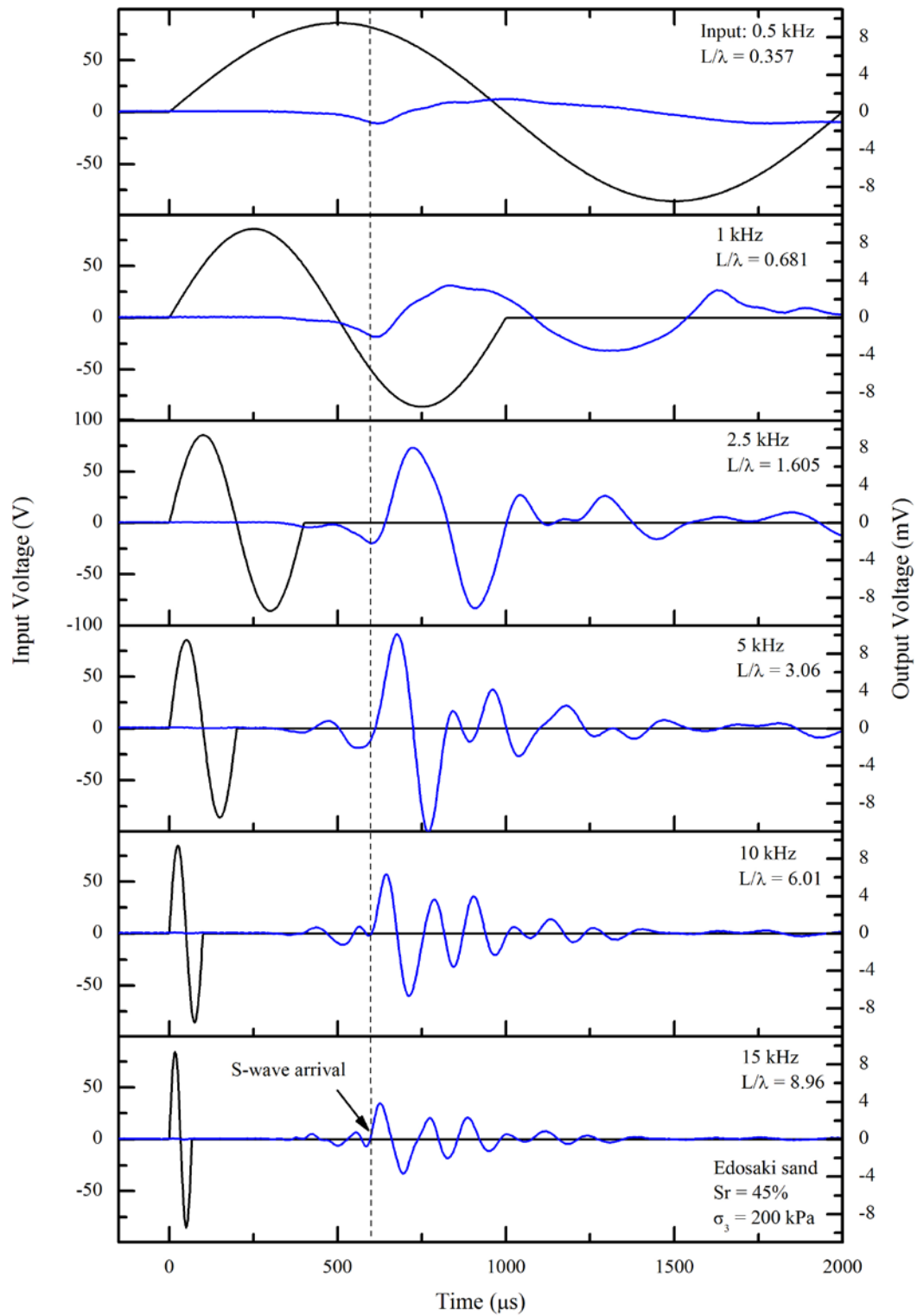


Figure 5.31: Effects of excitation frequency on shear wave signals obtained in partially saturated Edosaki sand ($S_r = 45\%$) at 200 kPa isotropic stress.

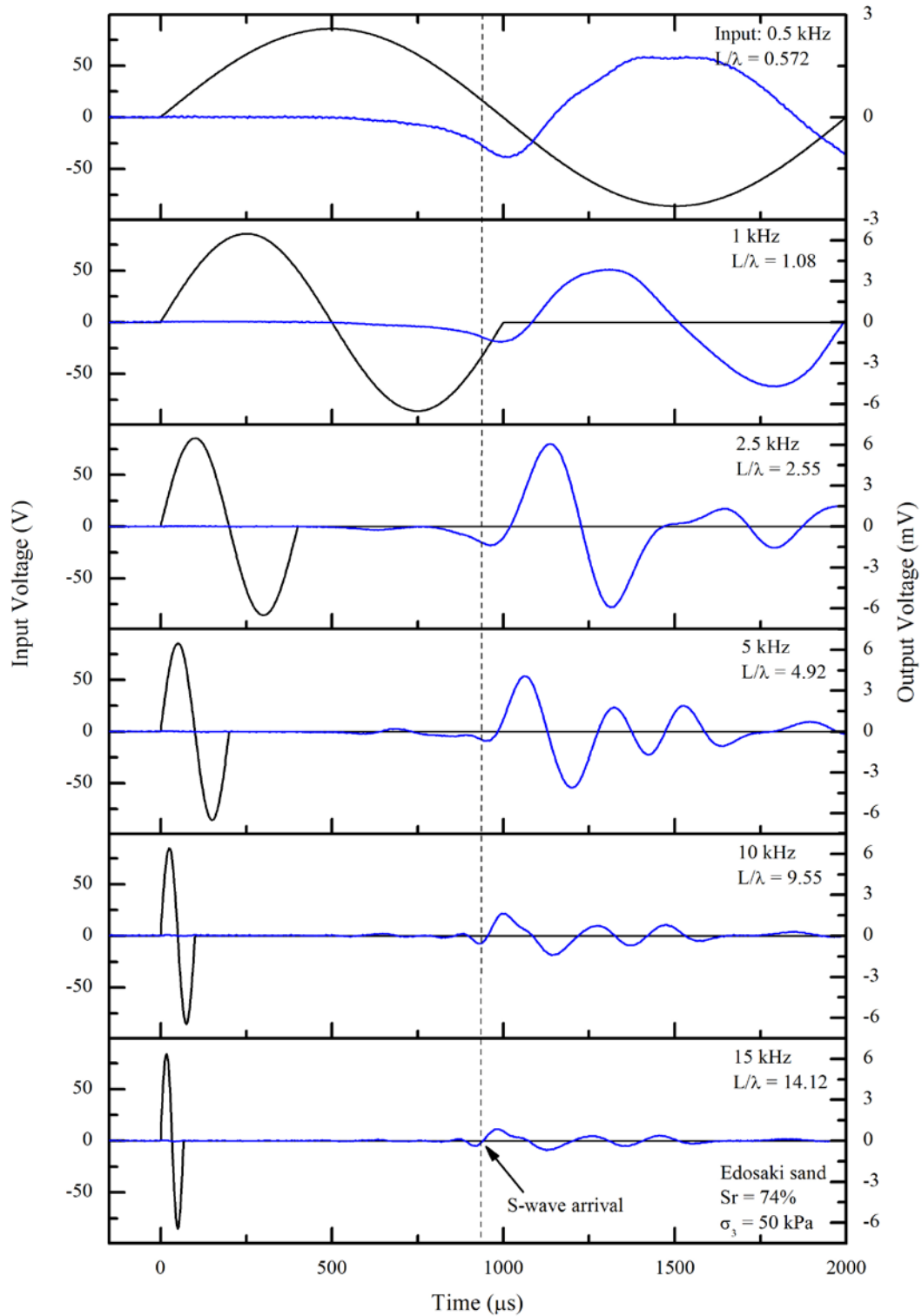


Figure 5.32: Effects of excitation frequency on shear wave signals obtained in partially saturated Edosaki sand ($Sr = 74\%$) at 50 kPa isotropic stress.

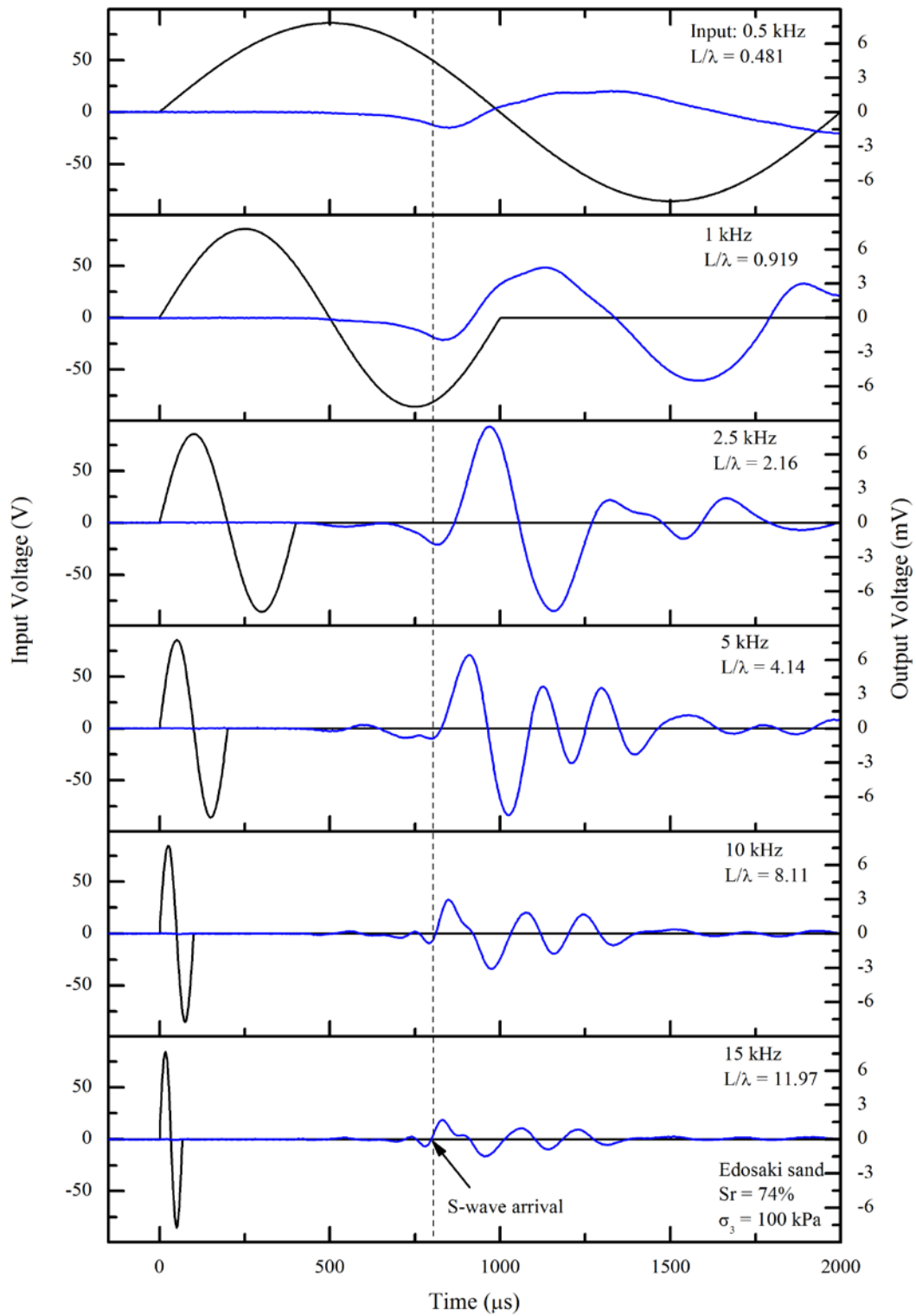


Figure 5.33: Effects of excitation frequency on shear wave signals obtained in partially saturated Edosaki sand ($S_r = 74\%$) at 100 kPa isotropic stress.

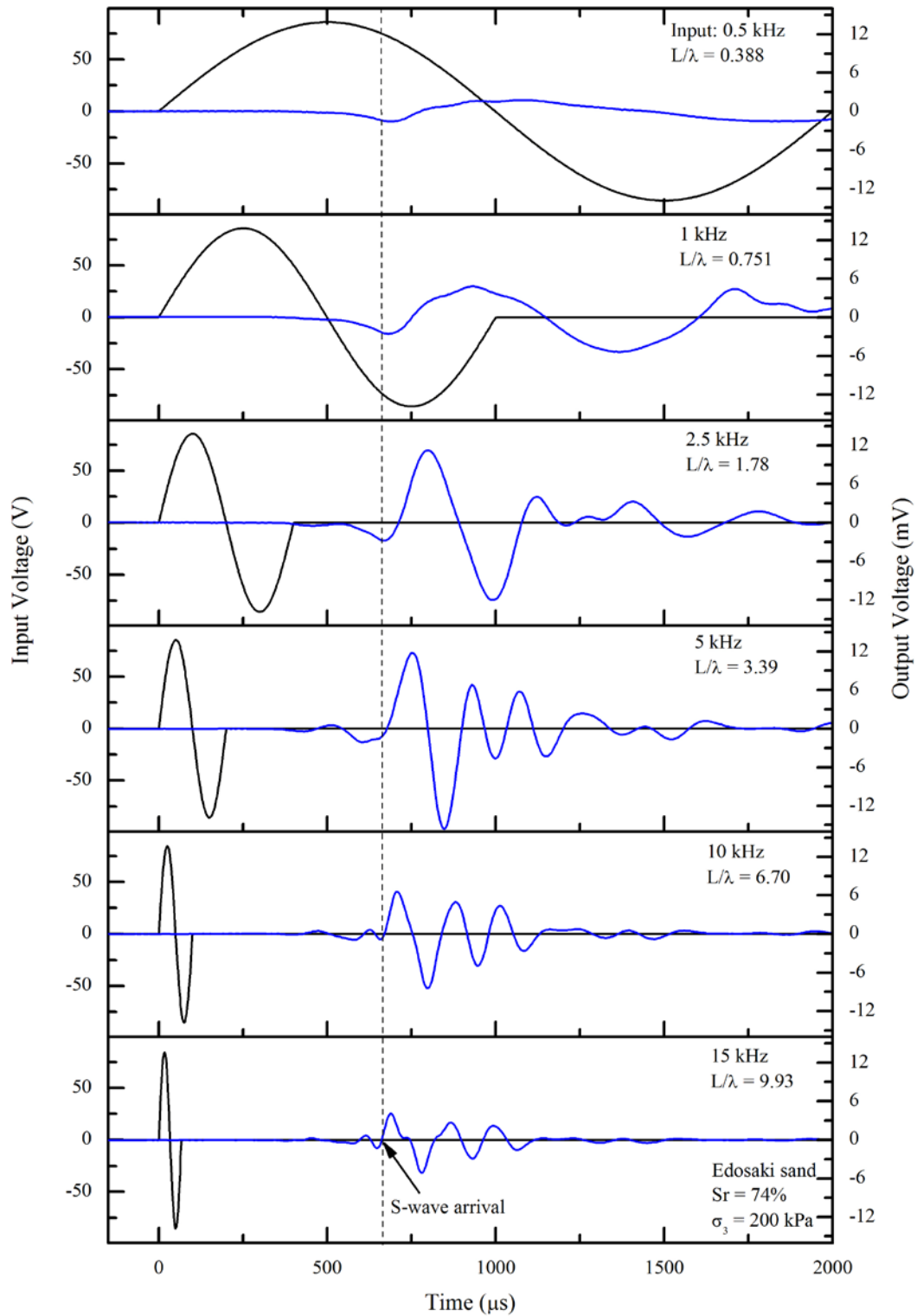


Figure 5.34: Effects of excitation frequency on shear wave signals obtained in partially saturated Edosaki sand ($S_r = 74\%$) at 200 kPa isotropic stress.

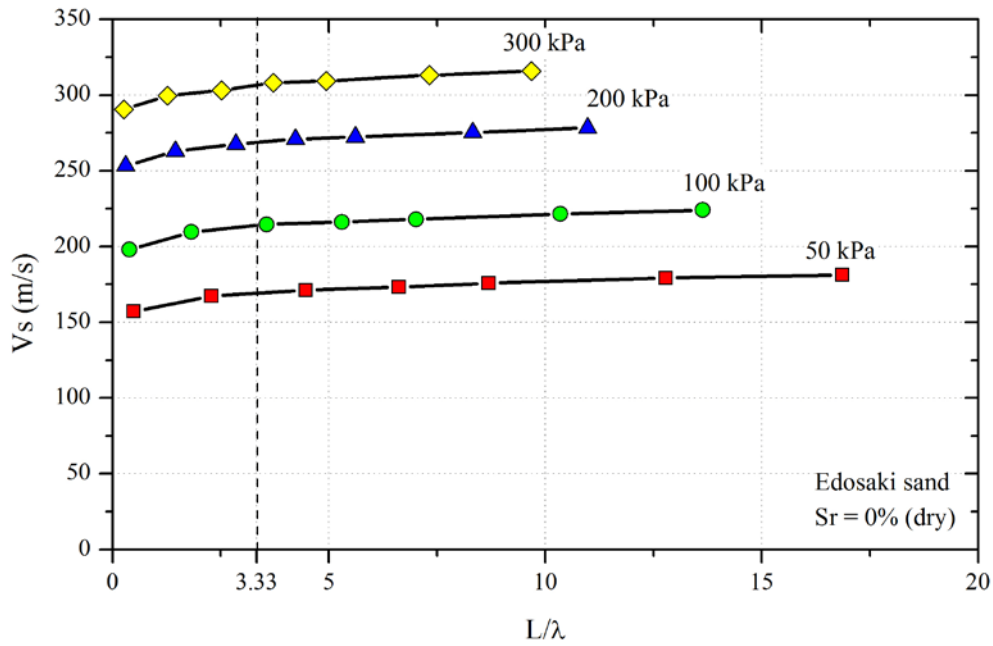


Figure 5.35: Effect of L/λ ratio of shear wave velocity in dry Edosaki sand specimen, tested under 50 kPa, 100 kPa, 200 kPa, and 300 kPa effective confining pressure.

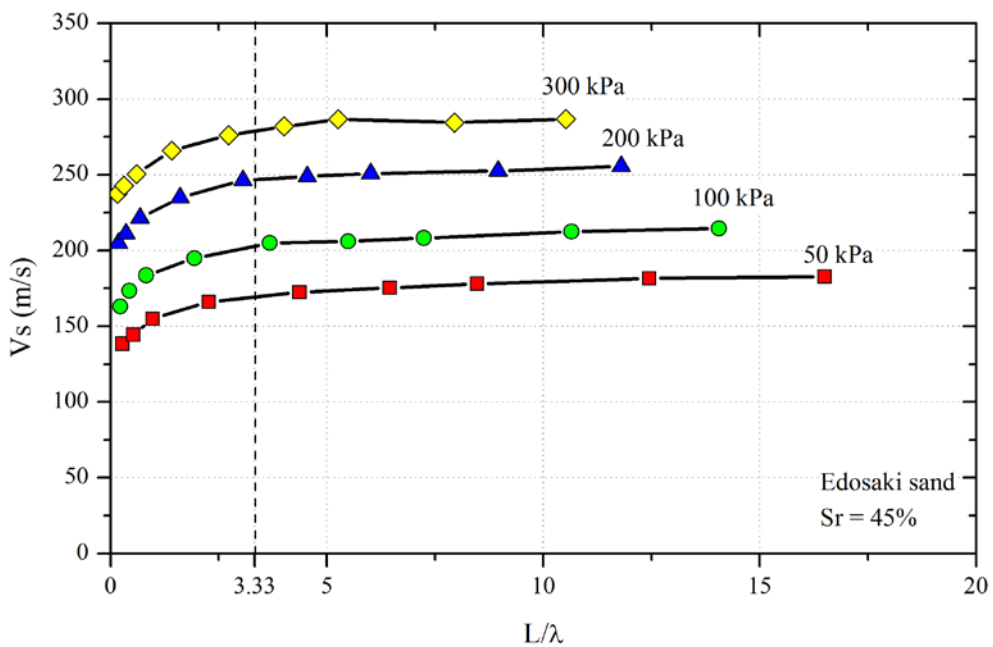


Figure 5.36: Effect of L/λ ratio of shear wave velocity in partially saturated Edosaki sand specimen ($S_r = 45\%$), tested under 50 kPa, 100 kPa, 200 kPa, and 300 kPa effective confining pressure.

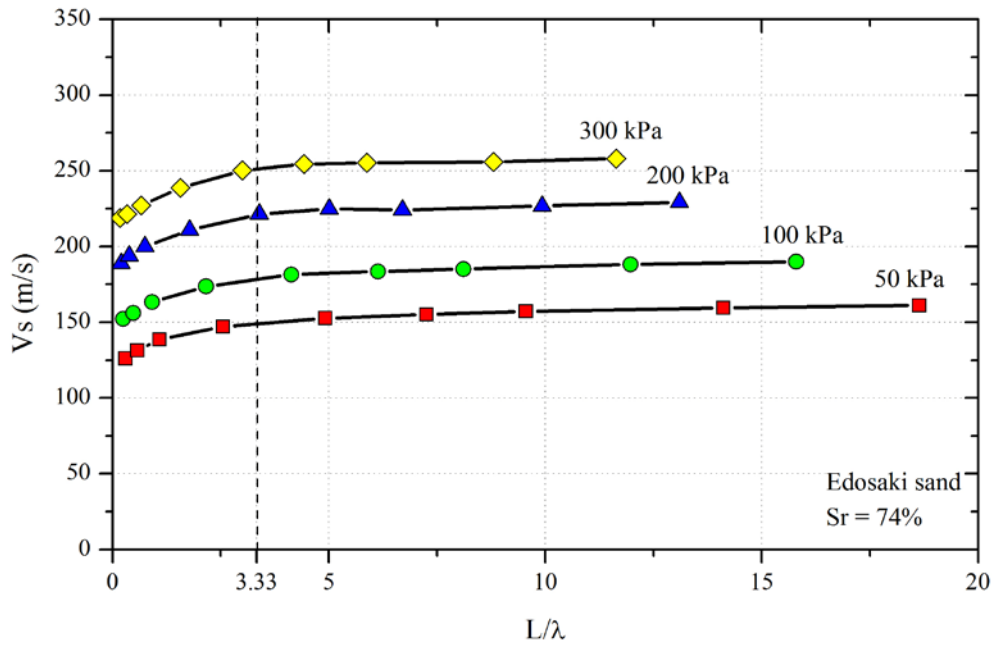


Figure 5.37: Effect of L/λ ratio of shear wave velocity in partially saturated Edosaki sand specimen ($S_r=74\%$), tested under 50 kPa, 100 kPa, 200 kPa, and 300 kPa effective confining pressure.

Figure 5.38 to Figure 5.46 show compression wave signals obtained from same *ICCW* test specimens tested under identical conditions. Excitation frequencies were varied from 1 kHz to 30 kHz. Unlike shear waves, compression wave travel times were not observed to be affected by magnitude of excitation frequency. However, the amplitude of received signal varied depending on the input frequency. Excitation frequency of the strongest signal provided an approximation of resonant frequency of the system (J. Lee & Santamarina, 2005).

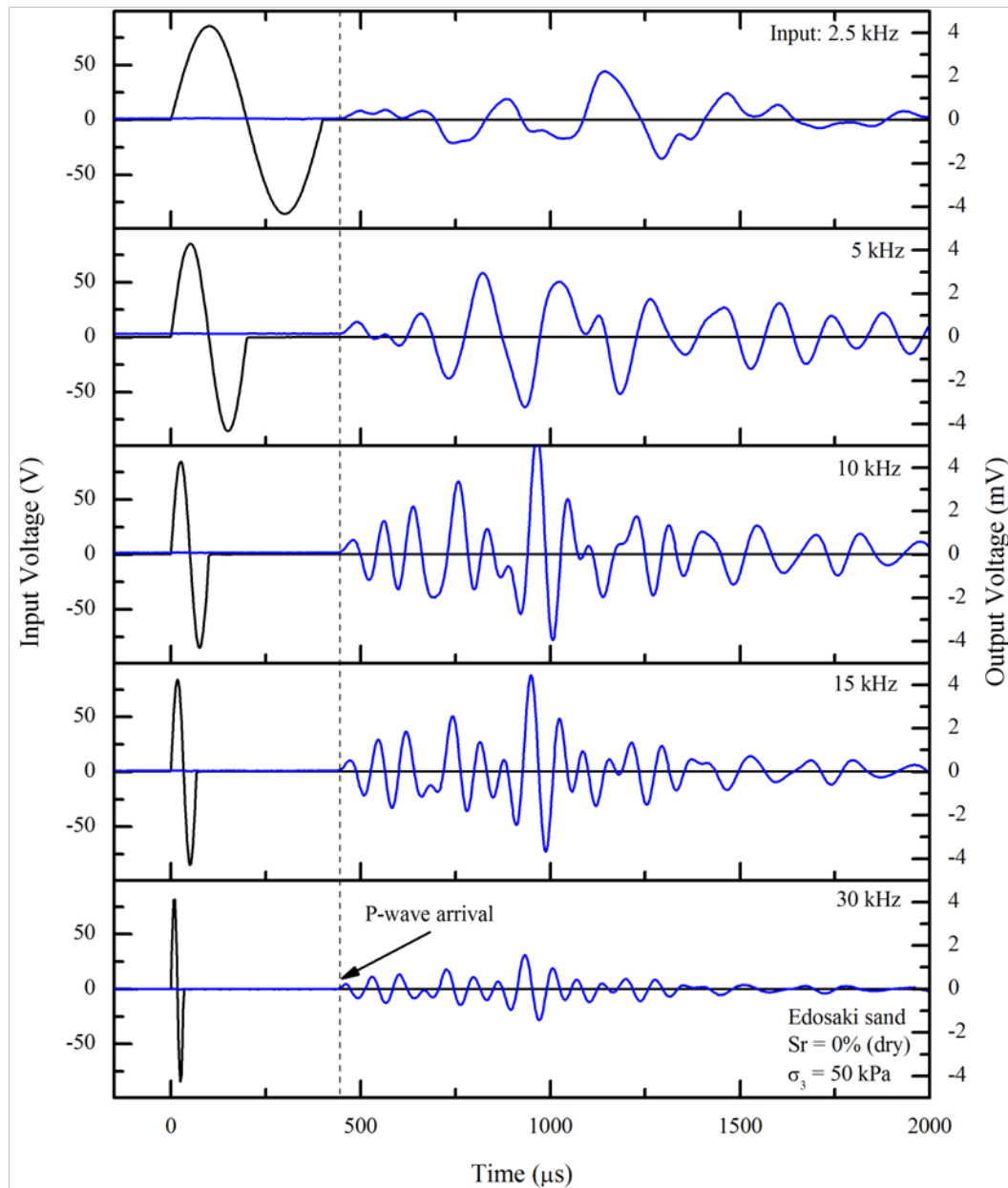


Figure 5.38: Effects of excitation frequency on compression wave signals obtained in dry Edosaki sand ($Sr = 0\%$) at 50 kPa isotropic stress.

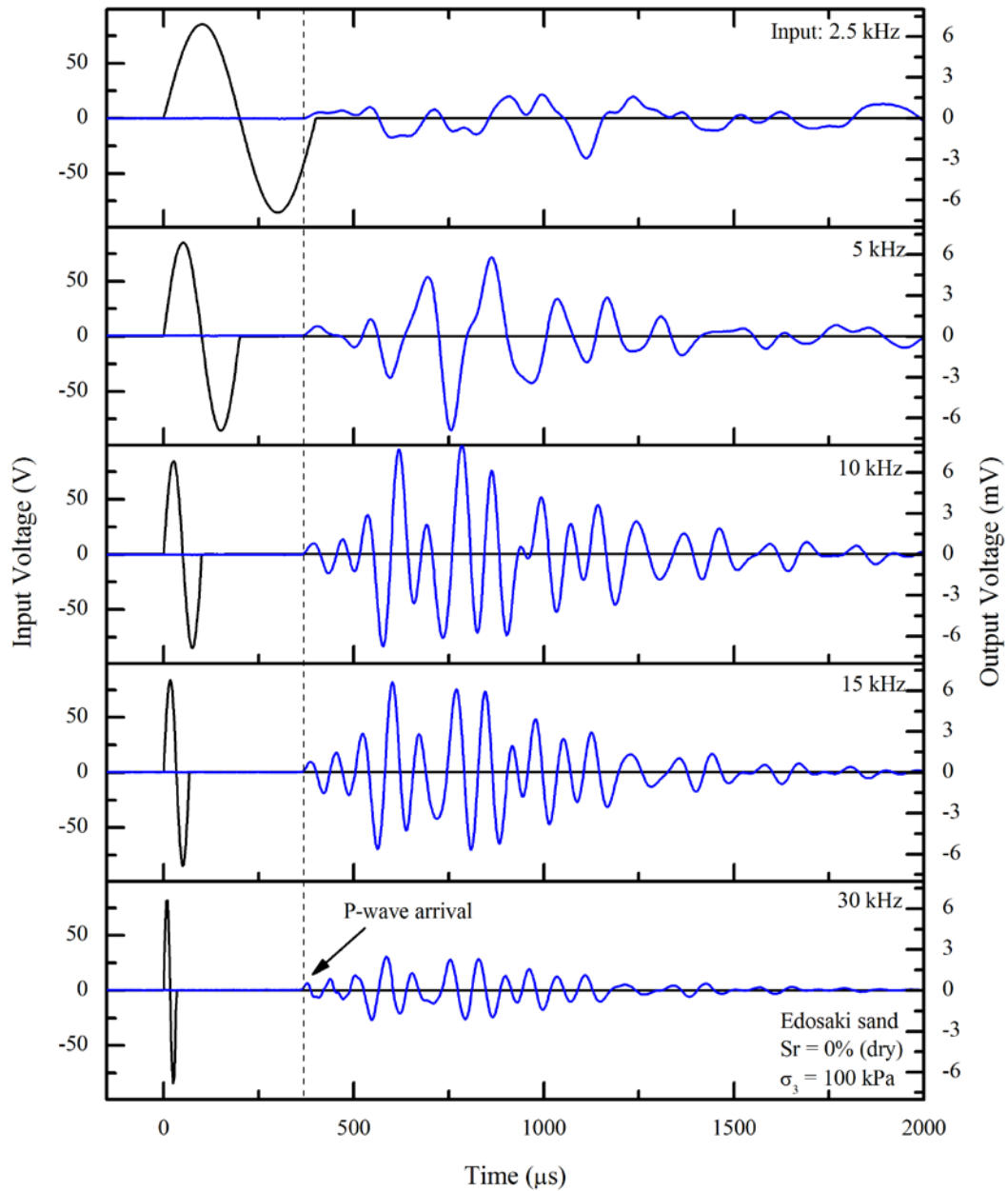


Figure 5.39: Effects of excitation frequency on compression wave signals obtained in dry Edosaki sand ($S_r = 0\%$) at 100 kPa isotropic stress.

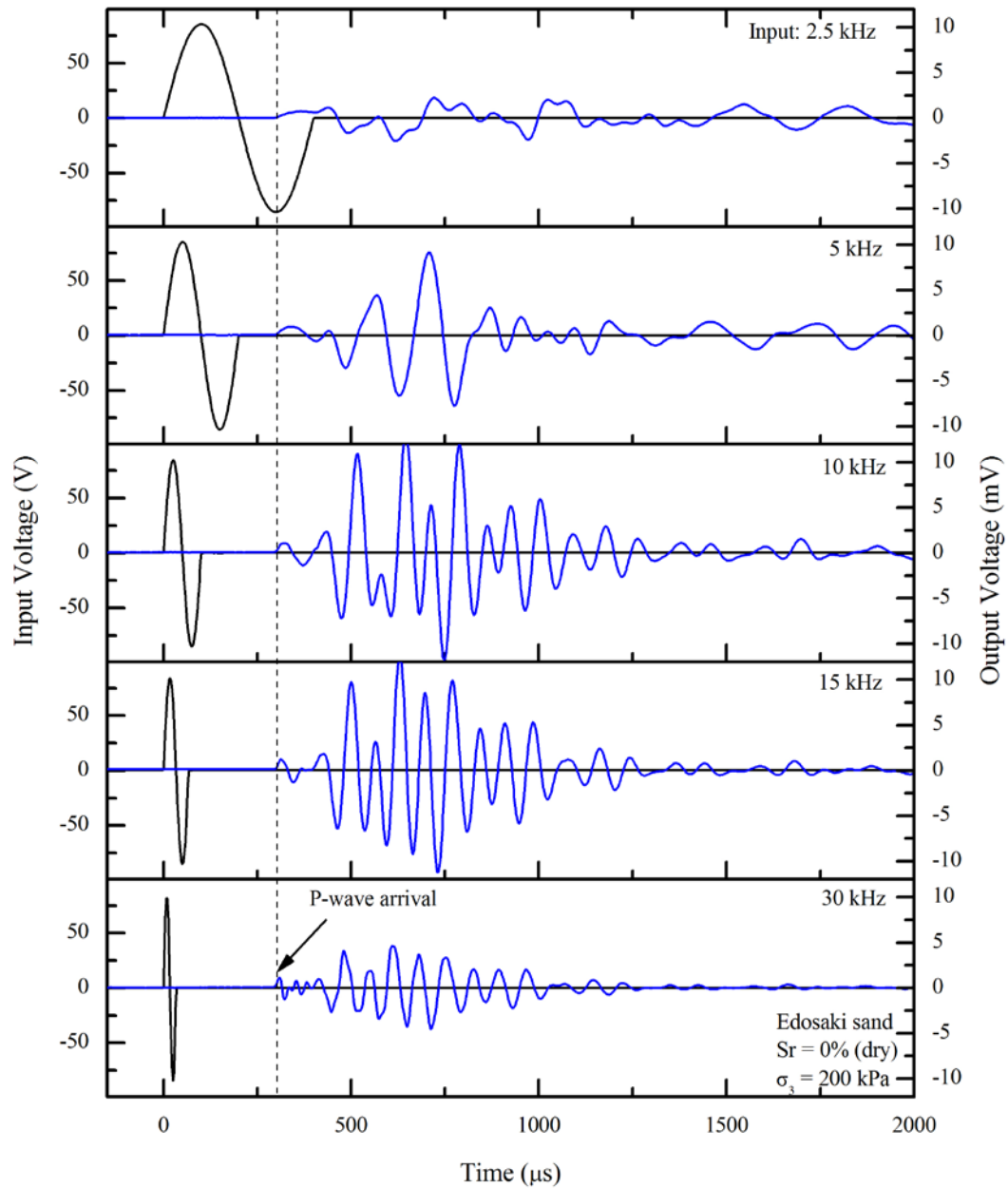


Figure 5.40: Effects of excitation frequency on compression wave signals obtained in dry Edosaki sand ($S_r = 0\%$) at 200 kPa isotropic stress.

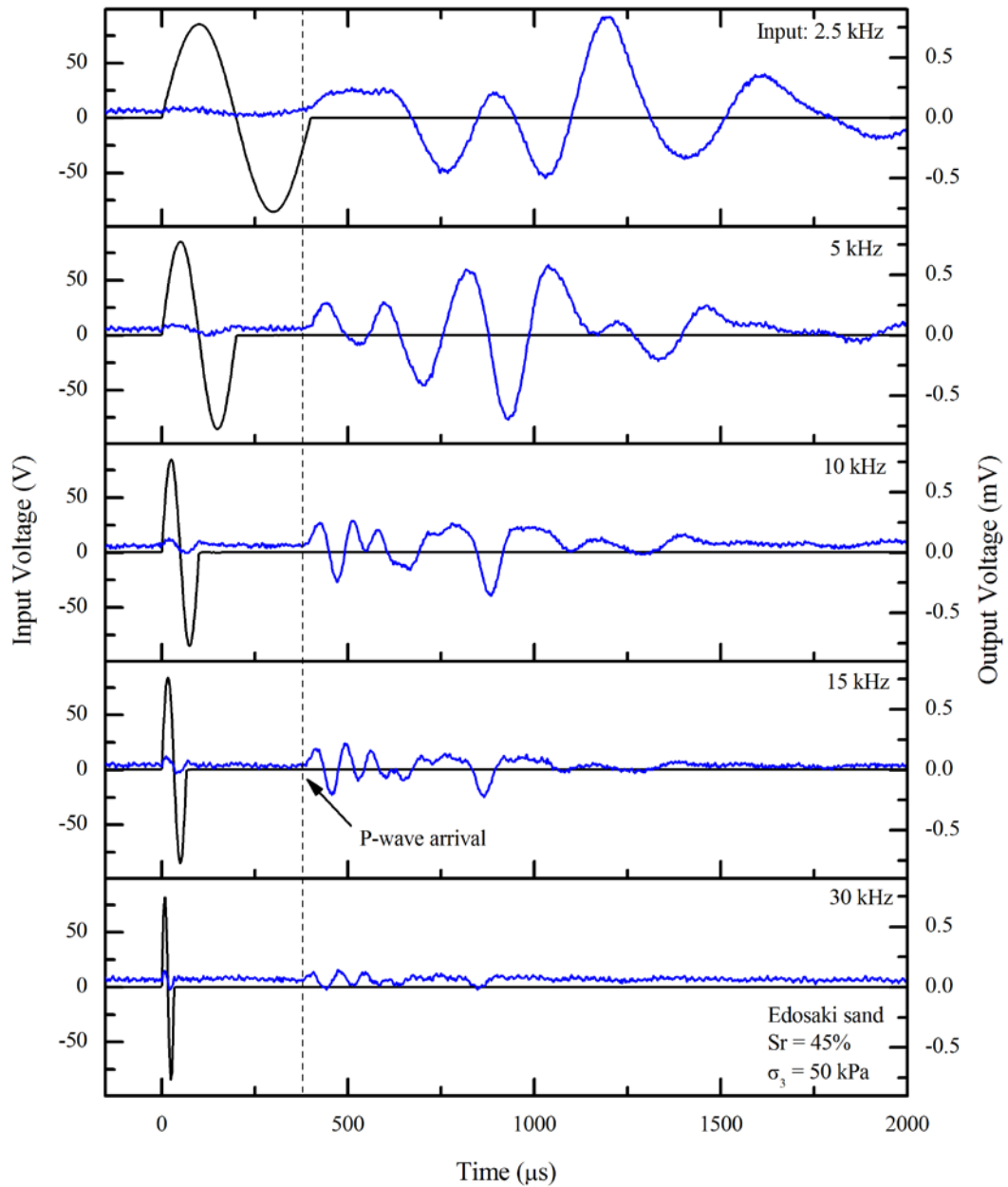


Figure 5.41: Effects of excitation frequency on compression wave signals obtained in partially saturated Edosaki sand ($S_r = 45\%$) at 50 kPa isotropic stress.

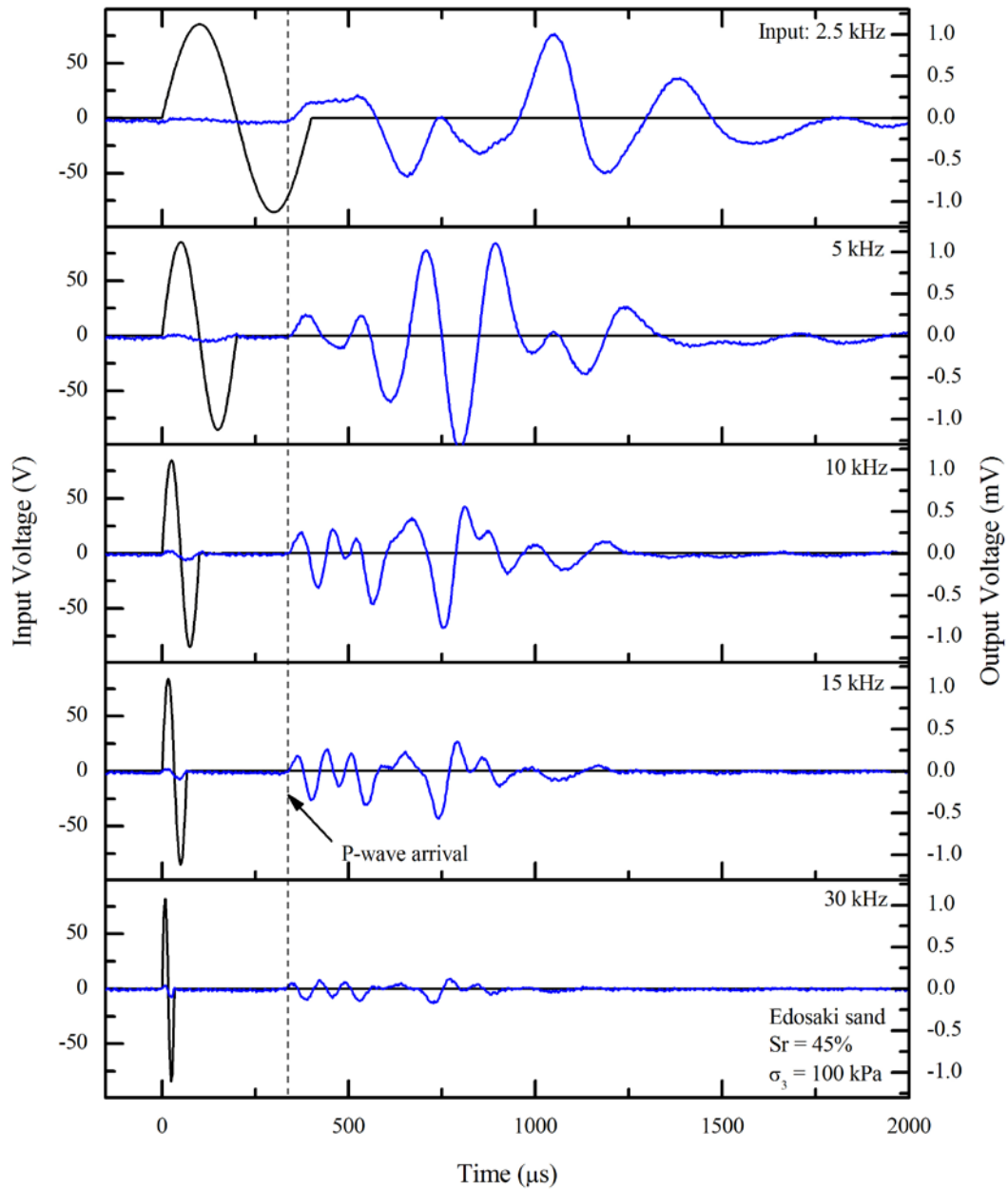


Figure 5.42: Effects of excitation frequency on compression wave signals obtained in partially saturated Edosaki sand ($S_r = 45\%$) at 100 kPa isotropic stress.

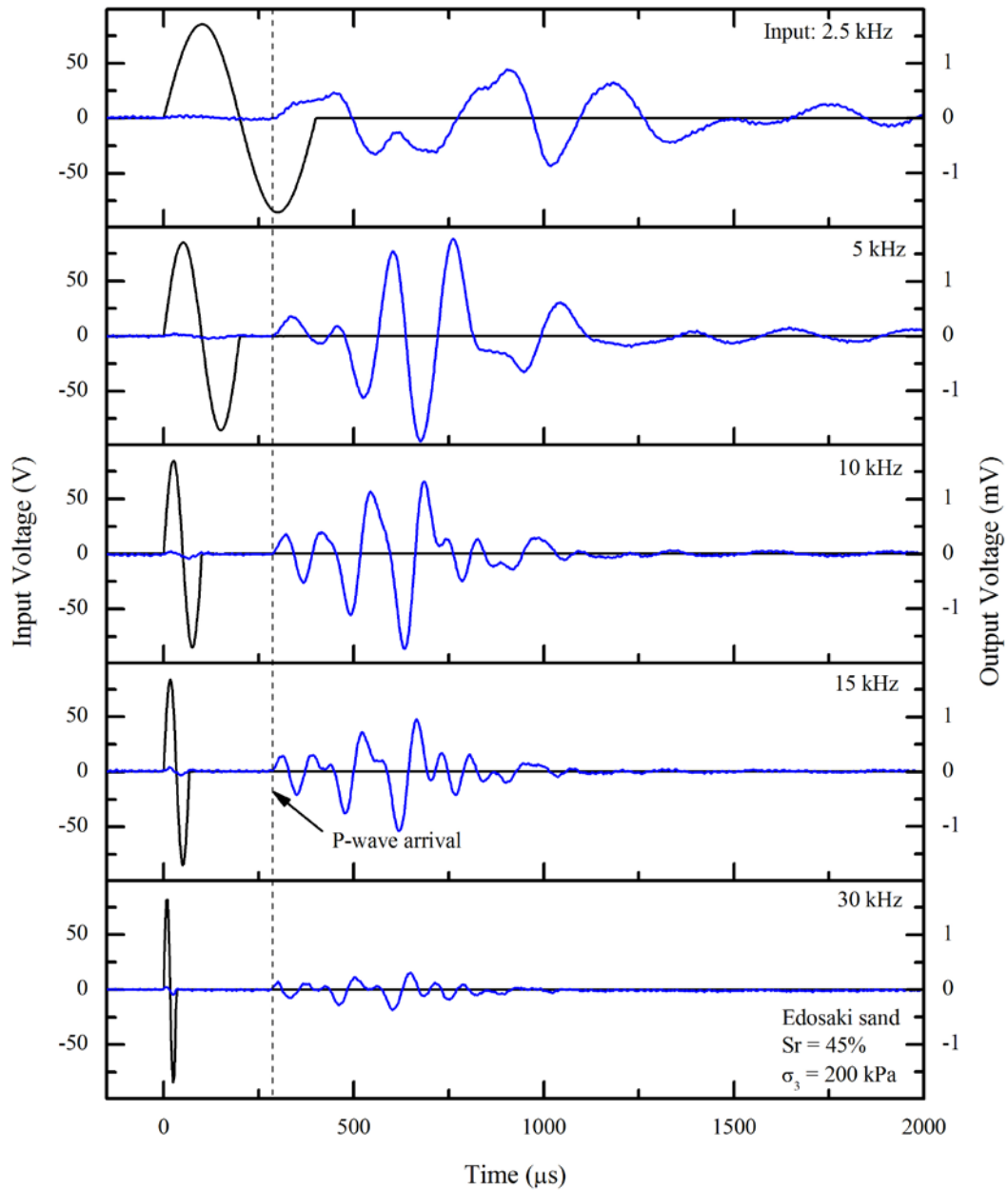


Figure 5.43: Effects of excitation frequency on compression wave signals obtained in partially saturated Edosaki sand ($S_r = 45\%$) at 200 kPa isotropic stress.

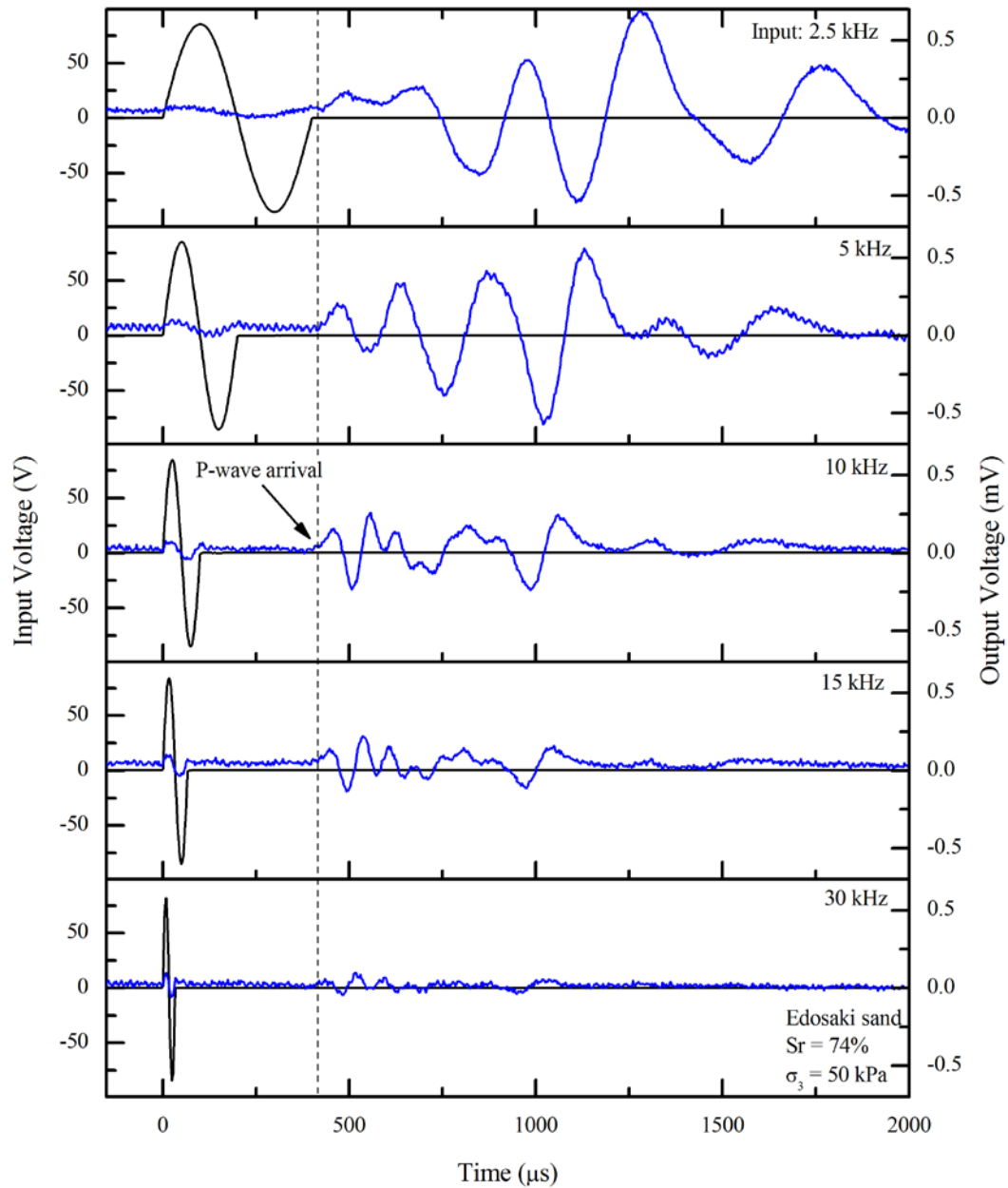


Figure 5.44: Effects of excitation frequency on compression wave signals obtained in partially saturated Edosaki sand ($S_r = 74\%$) at 50 kPa isotropic stress.

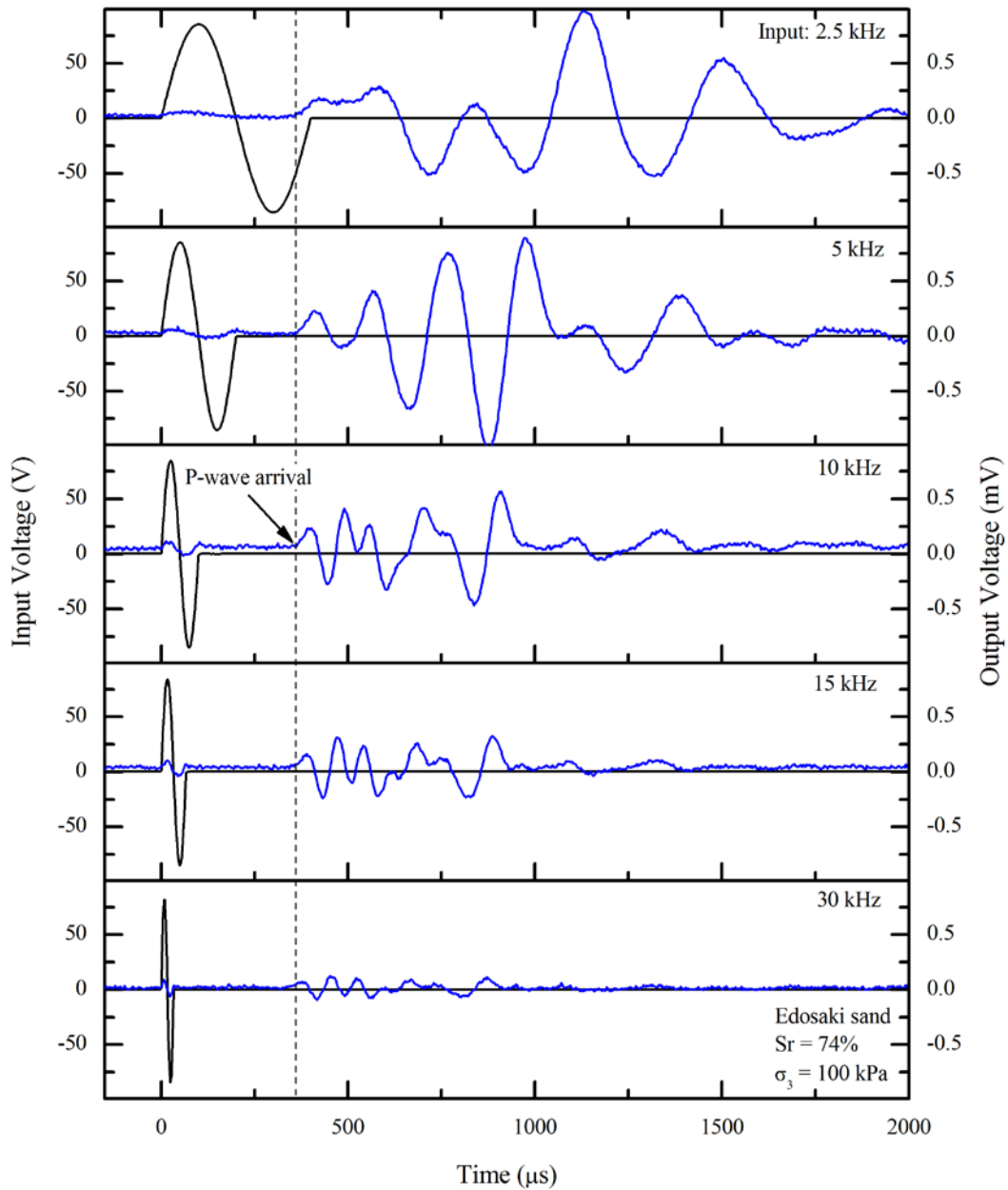


Figure 5.45: Effects of excitation frequency on compression wave signals obtained in partially saturated Edosaki sand ($S_r = 74\%$) at 100 kPa isotropic stress.

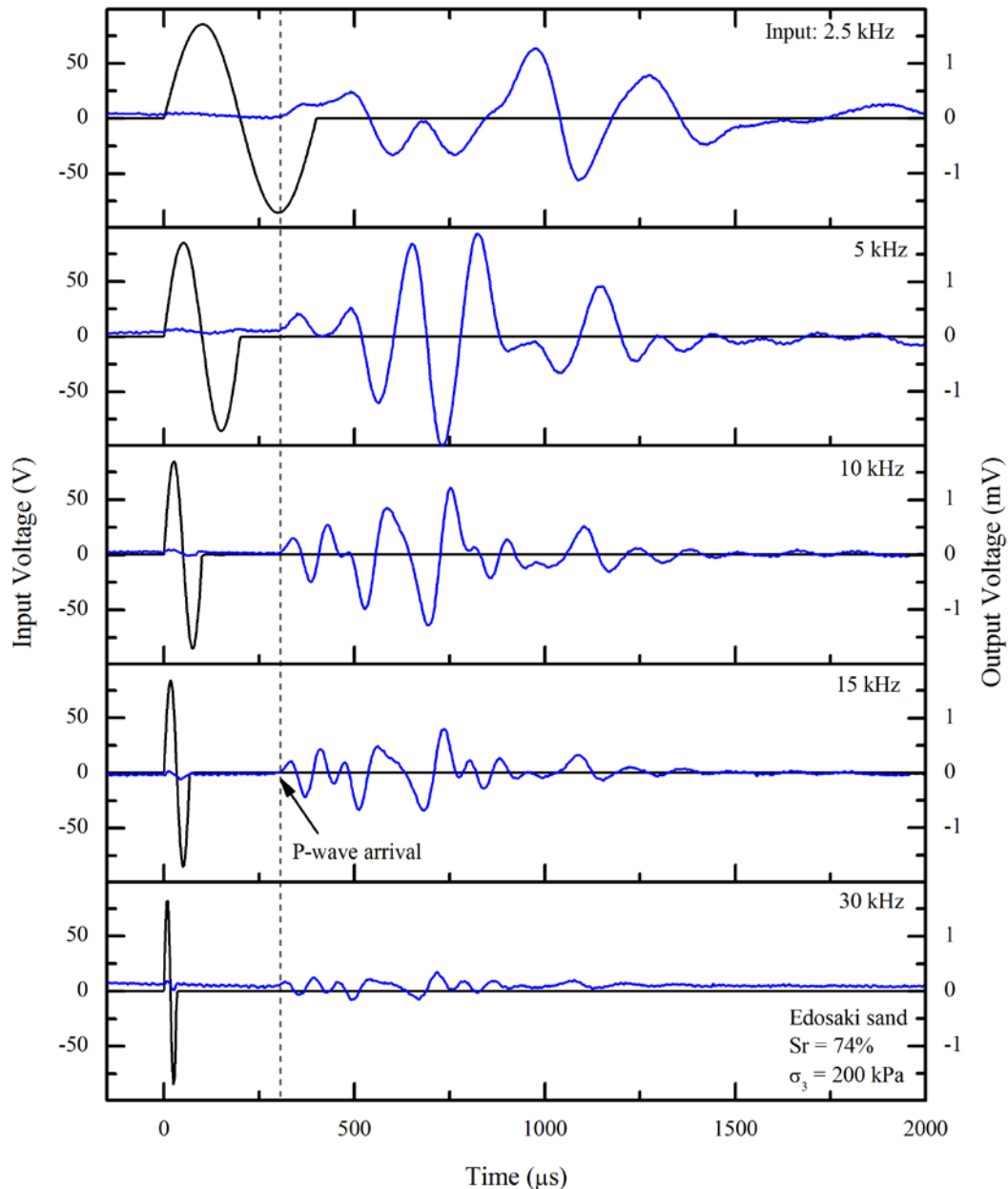


Figure 5.46: Effects of excitation frequency on compression wave signals obtained in partially saturated Edosaki sand ($S_r = 74\%$) at 200 kPa isotropic stress.

Amplitude of both compression and shear wave received signals was observed to increase with confining pressure. The number of particle contact points within the specimen increase with confining stress. It not only reduced the wave flight time, but also enhances the amplitude of received signals. On the contrary, increase in soil moisture caused a decrease in wave amplitudes. This may be because of the decrease in stiffness of soil particles, or the general softening of soil specimen with increased

saturation. Thus, it may become very difficult to discern wave arrival when testing under low confinements and high moisture conditions.

In fully saturated soil specimens, compression wave travels through the pore fluid instead of soil particles. First deflection of compressive wave therefore reflects wave travel time through the fluid phase and not through the soil skeleton itself. Results of compression wave propagation in saturated conditions are therefore not meaningful. A typical example of compression wave response in saturated conditions is shown in Figure 5.47.

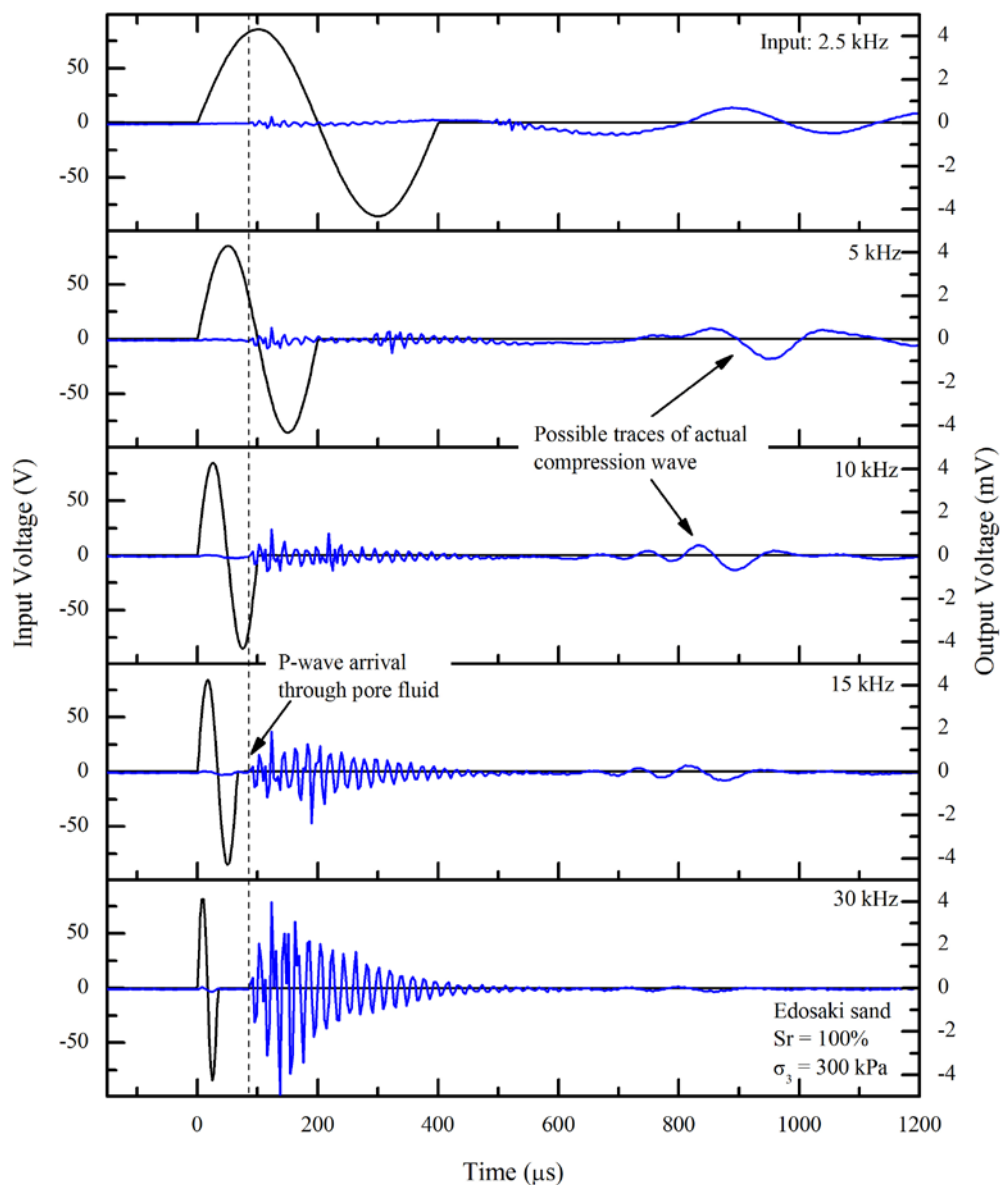


Figure 5.47: Response of compression wave signals in fully saturated Edosaki sand ($S_r = 100\%$) at 300 kPa isotropic stress.

5.7.6 Combined Measurement of P & S wave Velocity

The ability of disk transducer to measure both P -wave and S -wave velocity over the same travel path in the triaxial specimen makes it suitable for studying the near-field effect (i.e., a P -wave component of opposite polarity associated with S -wave propagation). Near-field effect obscures the actual arrival point of S -wave and adds to the complexity of S -wave velocity determination.

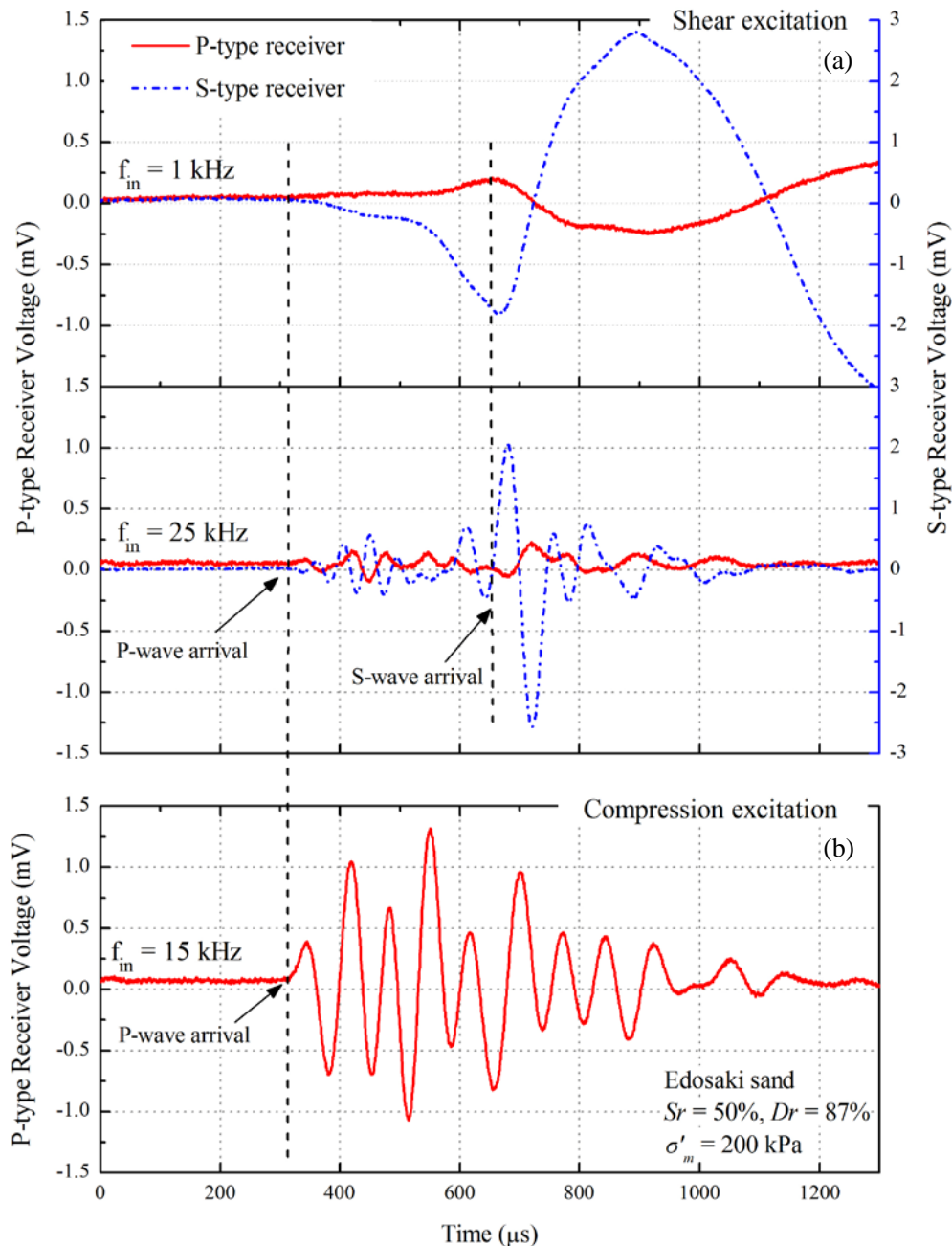


Figure 5.48: Observing near-field effects through simultaneous records of P -type and S -type receivers; (a) Response on shear-type excitation; (b) Response on compression-type excitation.

For the identification of near-field component, shear type exciter of transmitter disk transducer was excited, and the corresponding response was recorded by both *P*-type and *S*-type piezo-elements of receiver disk transducer, as shown in Figure 5.48(a). The response recorded by *P*-type receiver is predominantly due to the compression wave propagation in soil. It is interesting to note that the compression wave response recorded by *P*-type receiver was generated due to the excitation of *S*-type exciter. This provides practical evidence of phenomenon postulated by J. Lee and Santamarina (2005), as shown in Figure 5.25. A comparison with received signals from compression excitation (*P*-type exciter) confirms that the initial deflection of *S*-wave signal represents the arrival of *P*-wave instead (Figure 5.48(b)). Also the *P*-wave velocity obtained through shear excitation and compression excitation is found to exhibit no significant difference in Edosaki sand specimen subjected to varying isotropic confining pressure as shown in Figure 5.49.

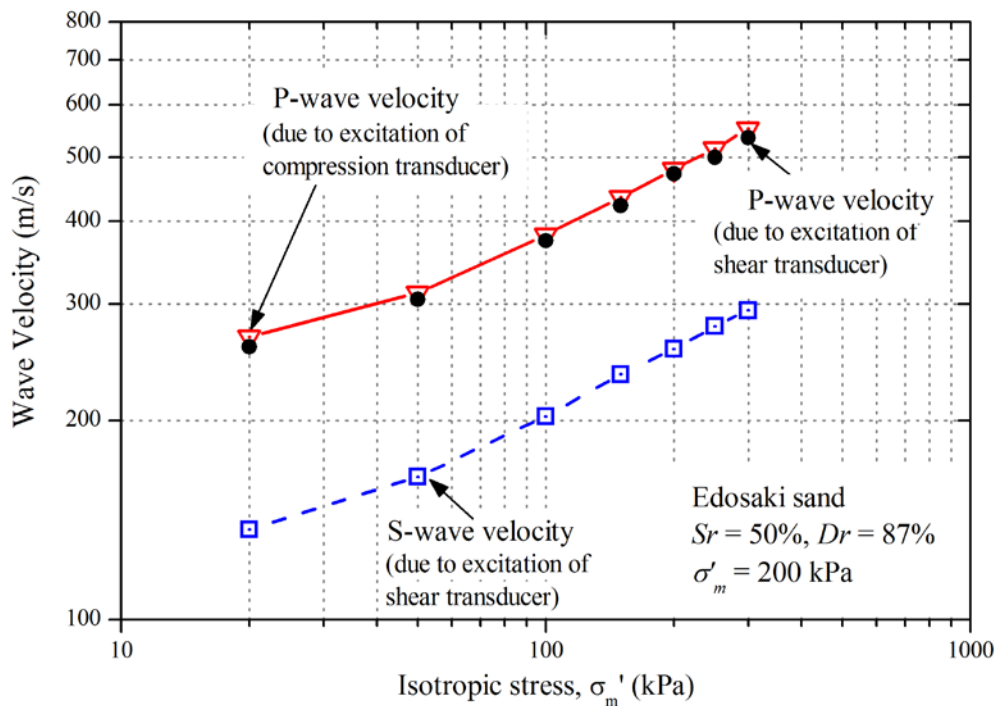


Figure 5.49: Compression and shear wave velocities measured in 50% saturated Edosaki sand specimen.

5.8. CONCLUDING REMARKS

The foundation of this chapter has been laid through a comprehensive overview of existing literature related to piezoelectric ceramic elements, and their use for geotechnical engineering purposes. Disk type piezoelectric transducer is the core component of the elastic wave measurement system used in this study. This chapter discusses in detail its manufacturing, use, and applications. Detailed procedure for the calibration of elastic wave measurement system is presented.

Performance evaluation of wave measurement system was conducted by studying the effects of crosstalk, quality of transmission cables and features of recording unit. The evaluation showed that crosstalk deterioration can successfully be eliminated through proper grounding, and the use of low-noise coaxial cables can significantly enhance signal to noise ratio of received signals. Use of wave recorder with low inherent noise, and high analogue to digital (*A/D*) conversion resolution, sampling rate, and voltage sensitivity can considerably improve the overall performance and signal interpretation of received signals. A thorough investigation was conducted to examine the effects of shape of input waveform, excitation frequency, soil moisture, and isotropic confining pressure on disk transducer received signals. The evaluation showed that the use of sinusoidal input waveform and increasing the number of wavelengths between source and transmitter can diminish near field effects and improve the reliability of shear wave travel time determination. Compression wave travel time on the other hand was not found to be affected by frequency of excitation. However in fully saturated soil specimen, compression wave travel time was observed to reflect travel time in pore fluid instead of soil skeleton. Therefore, determination of compression wave velocity for saturated specimens is not meaningful. Disk transducer also enables combined monitoring of shear and compression wave signals produced by a single excitation. Combined monitoring of shear and compression waves by using disk transducer was found to assist identification of near-field effects in shear wave receiver signals. Disk type piezoelectric transducers show significant future potential for laboratory determination of shear modulus (based on V_s) and constrained compression modulus (based on V_p) of soil because of their robustness and noninvasive nature.

5.9. REFERENCES

- Arroyo, M. (2001). *Pulse Tests in Soil Samples*. PhD Thesis, University of Bristol.
- Arulnathan, R., Boulanger, R. W., & Riemer, M. F. (1998). Analysis of Bender Element Tests. *Geotechnical Testing Journal, GTJODJ*, 21(2), 120-131. doi: 10.1520/GTJ10750J
- ASTM. (2007). Standard Test Methods for Modulus and Damping of Soils by Resonant-Column Method, *ASTM Standard D4015-07*. West Conshohocken, PA.
- ASTM. (2008). Standard Test Method for Laboratory Determination of Pulse Velocities and Ultrasonic Elastic Constants of Rock *ASTM Standard D2845-08*. West Conshohocken, PA.
- ASTM. (2011). Standard Test Method for Consolidated Undrained Triaxial Compression Test for Cohesive Soils *ASTM Standard D4767-11*. West Conshohocken, PA.
- Bates, C. (1989). Dynamic Soil Property Measurements During Triaxial Testing. *Geotechnique*, 39(4), 721-726.
- Blewett, J., Blewett, I. J., & Woodward, P. K. (2000). Phase and Amplitude Responses Associated with the Measurement of Shear-Wave Velocity in Sand by Bender Elements. *Canadian Geotechnical Journal*, 37(6), 1348-1357. doi: 10.1139/t00-047
- Brignoli, E. G. M., Gotti, M., & Stokoe, K. H. (1996). Measurement of Shear Waves in Laboratory Specimens by Means of Piezoelectric Transducers. *Geotechnical Testing Journal, GTJODJ*, 19(4), 384-397. doi: 10.1520/GTJ10716J
- Brocanelli, D., & Rinaldi, V. (1998). Measurement of Low-Strain Material Damping and Wave Velocity with Bender Elements in the Frequency Domain. *Canadian Geotechnical Journal*, 35(6), 1032-1040.

- Carlson, A. B. (1986). *Communication Systems: An Introduction to Signals and Noise in Electrical Communication*. New York: Mc-Graw-Hill.
- Chan, C.-M. (2010). Bender Element Test in Soil Specimens: Identifying the Shear Wave Arrival Time. *Electronic Journal of Geotechnical Engineering*, 15, 1263-1275.
- Clayton, C., Theron, M., & Best, A. (2004). The Measurement of Vertical Shear-Wave Velocity Using Side-Mounted Bender Elements in the Triaxial Apparatus. *Geotechnique*, 54(7), 495-498.
- Curie, J., & Curie, P. (1880). Développement, Par Pression, De L'électricité Polaire Dans Les Cristaux Hémihèdres À Faces Inclinaées. *Comptes rendus de l'Académie des Sciences*, 91, 294-295.
- de Alba, P., & Baldwin, K. C. (1991). Use of Bender Elements in Soil Dynamics Experiments. *Recent Advances In Instrumentation, Data Acquisition And Testing In Soil Dynamics*. Edited by S.K. Bhatia and G.W. Blaney, ASCE Geotechnical Special Publication No. 29. American Society Of Civil Engineers (ASCE), Reston, Va. 86-101.
- de Alba, P., Baldwin, K. C., Janoo, V., Roe, G., & Celikkol, B. (1984). Elastic-Wave Velocities and Liquefaction Potential. *Geotechnical Testing Journal, ASTM*, 7(2), 77-87.
- Dyvik, R., & Madshus, C. (1985). *Lab Measurements of Gmax Using Bender Elements*. Proceedings: Advances in the art of testing soils under cyclic conditions (pp. 186-196).
- Fioravante, V. (2000). Anisotropy of Small Strain Stiffness of Ticino and Kenya Sands from Seismic Wave Propagation Measured in Triaxial Testing. *Soils and foundations*, 40(4), 129-142.
- Fioravante, V., & Capoferri, R. (2001). On the Use of Multi-Directional Piezoelectric Transducers in Triaxial Testing. *ASTM geotechnical testing journal*, 24(3), 243-255.

- Greening, P. D., & Nash, D. F. (2004). Frequency Domain Determination of G₀ Using Bender Elements. *ASTM geotechnical testing journal*, 27(3), 288-294.
- Greening, P. D., Nash, D. F. T., Benahmed, N., Ferriera, C., & da Fonseca, V. (2003). *Comparison of Shear Wave Velocity Measurements in Different Materials Using Time and Frequency Domain Techniques*. Proceedings: International Symposium on Deformation Characteristics of materials (pp. 381-386), Lyon.
- Jovicic, V., Coop, M., & Simic, M. (1996). Objective Criteria for Determining G_{max} from Bender Element Tests. *Geotechnique*, 46(2), 357-362.
- Kawaguchi, T., Mitachi, T., & Shibuya, S. (2001). *Evaluation of Shear Wave Travel Time in Laboratory Bender Element Test*. Paper presented at the 15th International Conference on Soil Mechanics and Geotechnical Engineering (ICSMGE).
- Lawrence, F. V. (1963). Propagation of Ultrasonic Waves through Sand. *Massachusetts Institute of Technology, Boston, Report R63-08*.
- Lawrence, F. V. (1965). Ultrasonic Shear Wave Velocities in Sand and Clay. *Massachusetts Institute of Technology, Boston, Research Report R65-05*.
- Lee, C. J., & Huang, H. Y. (2007). Wave Velocities and Their Relation to Fabric Evolution During the Shearing of Sands. *Soil Dynamics and Earthquake Engineering*, 27(1), 1-13. doi: 10.1016/j.soildyn.2006.05.006
- Lee, J., & Santamarina, J. (2005). Bender Elements: Performance and Signal Interpretation. *Journal of Geotechnical and Geoenvironmental Engineering*, 131(9), 1063-1070. doi: doi:10.1061/(ASCE)1090-0241(2005)131:9(1063)
- Leong, E. C., Cahyadi, J., & Rahardjo, H. (2009). Measuring Shear and Compression Wave Velocities of Soil Using Bender-Extender Elements. *Canadian Geotechnical Journal*, 46(7), 792-812. doi: 10.1139/t09-026
- Leong, E. C., Yeo, S. H., & Rahardjo, H. (2005). Measuring Shear Wave Velocity Using Bender Elements. *ASTM geotechnical testing journal*, 28(5), 488-498. doi: 10.1520/GTJ12196

- Lings, M., & Greening, P. (2001). A Novel Bender/Extender Element for Soil Testing. *Geotechnique*, 51(8), 713-717.
- Lohani, T., Imai, G., & Shibuya, S. (1999). Determination of Shear Wave Velocity in Bender Element Test. *Earthquake Geotechnical Engineering*, 101-106.
- Mancuso, C., & Vinale, F. (1988). Propagazione Delle Onde Sismiche: Teoria E Misure in Sito. *Atti del Convegno Nazionale del Coordinamento per gli Studi di Ingegneria Geotecnica*, 115-138 [In Italian].
- Mohsin, A., & Airey, D. (2003). *Automating Gmax Measurement in Triaxial Tests*. Proceedings: The Prefailure Deformation Characteristics of Geomaterials (pp. 73-80), Lyon.
- Montoya, B. M., Gerhard, R., DeJong, J. T., Wilson, D. W., Weil, M. H., Martinez, B. C., & Pederson, L. (2012). Fabrication, Operation, and Health Monitoring of Bender Elements for Aggressive Environments. *Geotechnical Testing Journal*, 35(5), 728-742.
- Nakagawa, Soga, K., & Mitchell. (1996). Pulse Transmission System for Measuring Wave Propagation in Soils. *Journal of Geotechnical Engineering*, 122(4), 302-308. doi: 10.1061/(ASCE)0733-9410(1996)122:4(302)
- Pantazopoulos, I., & Atmatzidis, D. (2012). Dynamic Properties of Microfine Cement Grouted Sands. *Soil Dynamics and Earthquake Engineering*, 42, 17-31.
- Pennington, D. S., Nash, D. F. T., & Lings, M. L. (2001). Horizontally Mounted Bender Elements for Measuring Anisotropic Shear Moduli in Triaxial Clay Specimens. *ASTM geotechnical testing journal*, 24(2), 133-144. doi: 10.1520/GTJ11333J
- Prakash, S. (1981). *Soil Dynamics*: McGraw-Hill New York.
- Rees, S., Le Compte, A., & Snelling, K. (2013). *A New Tool for the Automated Travel Time Analyses of Bender Element Tests*. Proceedings: 18th International Conference on Soil Mechanics and Geotechnical Engineering (pp. 2843-2846), Paris, France.

- Richart, F. E., Hall, J. R., & Woods, R. D. (1970). *Vibrations of Soils and Foundations*.
- Rodríguez, J. A. D., & Moreno-Carrizales, P. (2001). A Study of Soil Microstructure Using Bender Element Tests. *Proceeding, IVth International Conference on Recent Advances in Geotechnical Earthquake Engineering and Soil Dynamics*, Paper No. 1.39.
- Sanchez-Salineró, I., Roesset, J. M., Stokoe, I., & Kenneth, H. (1986). *Analytical Studies of Body Wave Propagation and Attenuation*. DTIC Document.
- Schultheiss, P. J. (1981). Simultaneous Measurement of P & S Wave Velocities During Conventional Laboratory Soil Testing Procedures. *Marine Geotechnology*, 4(4), 343-367. doi: 10.1080/10641198109379831
- Shirley, D. J. (1978). An Improved Shear Wave Transducer. *The Journal of the Acoustical Society of America*, 63, 1643.
- Shirley, D. J., & Hampton, L. D. (1978). Shear - Wave Measurements in Laboratory Sediments. *The Journal of the Acoustical Society of America*, 63, 607.
- Stokoe II, K., Isenhower, W., & Hsu, J. (1980). *Dynamic Properties of Offshore Silty Samples*. Proceedings: Offshore Technology Conference.
- Strassburger, E. (1982). *Use of Piezoelectric Transducers for Stiffness and Density Measurement of Soil*. M.S. Thesis, University of Texas at Austin, USA.
- Styler, M., & Howie, J. (2012). *Comparing Frequency and Time Domain Interpretations of Bender Element Shear Wave Velocities*. Proceedings: GeoCongress 2012@ sState of the Art and Practice in Geotechnical Engineering (pp. 2207-2216).
- Styler, M. A., & Howie, J. A. (2013). Combined Time and Frequency Domain Approach to the Interpretation of Bender-Element Tests on Sand. *ASTM geotechnical testing journal*, 36(5), 649-659.

- Suwal, L. P., & Kuwano, R. (2009). *Development of Disk Shaped Piezo-Ceramic Plate Transducer for Elastic Wave Measurements in Laboratory Specimens*. Paper presented at the The 3rd NEA-JC Annual Workshop on Current and Future Technologies, The University of Tokyo, Tokyo, Japan.
- Suwal, L. P., & Kuwano, R. (2010a). Development of Disc Shaped Piezo-Ceramic Plate Transducer for Elastic Wave Measurement in Laboratory Sepcimens. *Seisan-Kenkyu, Bimonthly Journal of Institute of Industrial Sciences, The University of Tokyo*, 61(6), 123-128.
- Suwal, L. P., & Kuwano, R. (2010b). Performance of Plate Transducer Having Different Surface Conditions on Elastic Wave Measurement. *Bulletin of Earthquake Resistant Structure Research Center, Institute of Industrial Science*, 43, 1-13.
- Thomann, T., & Hryciw, R. (1990). Laboratory Measurement of Small Strain Shear Modulus under Ko Conditions. *Geotechnical Testing Journal*, 13(2), 97-105.
- Uchimura, T. (2011). *Wave Velocity in Unsaturated Slopes in Relation to Moisture and Stability*. Paper presented at the The 14th Asian Regional Conference on Soil Mechanics and Geotechnical Engineering, Hong Kong.
- Viggiani, G., & Atkinson, J. (1995). Stiffness of Fine-Grained Soil at Very Small Strains. *Geotechnique*, 45(2), 249-265.
- Wang, Y., Lo, K., Yan, W., & Dong, X. (2007). Measurement Biases in the Bender Element Test. *Journal of Geotechnical and Geoenvironmental Engineering*, 133(5), 564-574. doi: doi:10.1061/(ASCE)1090-0241(2007)133:5(564)

INVESTIGATION OF SOIL MOISTURE EFFECTS ON ELASTIC WAVE PROPAGATION

Chapter 6

CHAPTER 6

INVESTIGATION OF SOIL MOISTURE EFFECTS ON ELASTIC WAVE PROPAGATION

6.1. GENERAL REMARKS

Active monitoring of soil moisture content is necessary for effective prediction of landslides (Uchimura et al., 2010). Typical instrumentation to indicate soil moisture in unsaturated soils includes ceramic cups or tensiometers for determining soil matric suction, and dielectric moisture sensors for measurement of volumetric water content of soil (Fredlund & Xing, 1994; Uchimura et al., 2010; Ramesh & Vasudevan, 2012). All such sensors are however, point sensors and hence, sensitive only to local moisture content changes in the vicinity of sensor. To cover a wide potential landslide area, a large number of such sensors would therefore be required. A novel idea of predicting soil moisture changes by monitoring elastic wave velocities is presented in this chapter. This idea mainly comprises of installing a pair of elastic wave exciter and receiver assembly on the slope surface, and monitoring the variation of elastic wave velocities with changing soil moisture. In this way, a single pair of exciter/receiver system can cover a considerably large area.

6.2. TEST CONDITIONS

This chapter covers laboratory element studies exploring the behavior of wave velocities with soil moisture. Two series of triaxial tests were conducted to explore the effects of soil moisture on wave velocities. In the first series of tests, a number of triaxial specimens with different initial saturation ratio were prepared and wave velocities were determined at various isotropic confining pressures. For the sake of

simplicity, this type of test series is defined as *Isotropic Compression Constant Water content Tests (ICCW)*, and the corresponding tests are designated by letters “IC” representing “*Isotropic Compression*”. Although this type of test series explained the behavior of wave velocities with moisture content, but this is not the natural way of soil wetting during rainfall. Hence, to explore the behavior of wave velocities during soil wetting by rainfall, another series of triaxial test was conducted. In this series of tests, the specimens were kept at constant isotropic total stress throughout the test and water was injected from a saturated ceramic disk at specimen’s base to wet the specimen. This test series is designated as *Isotropic Compression Water Injection tests (ICWI)*, and each test is designated by letters “IWI”, i.e. “*Isotropic compression Water Injection*”. The following sections explain the test results and corresponding discussions of these tests. Initial test conditions and other important parameters of each test series are summarized in the following tables;

Table 6.1: Initial test conditions in ICCW tests

<i>Test Designation</i>	<i>S_r</i> (%)	<i>e</i>	<i>R_c</i> (%)	<i>γ_b</i> (g/cm ³)	<i>S_u</i> (kPa)	<i>Remarks</i>
<i>IC-2</i>	0	0.671	89.7	1.581	--	Dry
<i>IC-3</i>	20	0.713	87.5	1.625	69.3	Unsaturated
<i>IC-4</i>	45	0.791	83.6	1.672	5.63	Unsaturated
<i>IC-6</i>	9	0.733	86.4	1.560	--	Unsaturated
<i>IC-7</i>	99	0.733	86.4	1.945	--	Saturated (<i>B = 0.80</i>)
<i>IC-8</i>	74	0.740	86.1	1.832	1.3	Unsaturated
<i>IC-10</i>	99.9	0.722	87.0	1.952	--	Saturated (<i>B = 0.968</i>)

Table 6.2: Initial test conditions in ICWI tests.

<i>Test Designation</i>	<i>Sr</i> (%)	$\sigma_1 = \sigma_3$ (kPa)	<i>e</i>	<i>Rc</i> (%)	<i>Infiltration pressure</i> (kPa)	<i>WI</i> (ml/hr)	<i>Use of helical filter paper</i>
<i>IWI-1</i>	18	100	0.706	87.8	25	16.05	Yes
<i>IWI-3</i>	0	100	0.791	83.6	31	31.84	Yes
<i>IWI-4</i>	0	50	0.813	82.6	27	24.15	Yes
<i>IWI-5</i>	0	200	0.786	83.8	29	26.77	Yes
<i>IWI-6</i>	0	150	0.789	83.7	30	28.03	Yes
<i>IWI-8</i>	0	25	0.800	83.2	30	27.37	Yes
<i>IWI-9</i>	19	200	0.712	87.5	25	18.72	Yes
<i>IWI-10</i>	18	50	0.720	87.1	25	15.97	Yes

6.3. ISOTROPIC COMPRESSION CONSTANT WATER CONTENT (ICCW) TESTS

The primary goal of this test series was to study the effect of soil moisture on elastic wave velocities (V_p and V_s) in soil. Several specimens with different initial moisture content were thus prepared and subjected isotropic confinements. Across all the tests conducted in this series, an attempt was made to keep all factors influencing wave velocities other than soil moisture as constant. Initial test conditions of test specimens used in this test series are presented in Table 6.1.

6.3.1 Methodology

Moist tamping technique of specimen preparation, as outlined in Section 4.3.1.3 of Chapter 4, was used to prepare cylindrical triaxial specimens (75 mm in diameter and 153 mm in height) from Edosaki sand. Placement moisture content was controlled to prepare specimens with initial saturation ratio (S_r) of 0% (dry), 9%, 20%, 45% and 74%. Besides, two saturated specimens having Skempton's B -value (Bishop, 1954; Skempton, 1954) of 0.80 and 0.97 were also tested. Saturation ratio of these saturated specimens can be approximated as 99% and 99.9% respectively (Towhata, 2008; Gu et al., 2013). Each specimen was subjected to isotropic confining stress of 20 kPa, 30 kPa, 50 kPa, 100 kPa, 150 kPa, 200 kPa, 250 kPa and 300 kPa, with P -wave and S -wave velocities measured at each stress level, as shown in Figure 6.1. At each confining pressure elastic wave velocities were recorded for several input frequencies and waveforms (details discussed in Chapter 5). However for this test series, P -wave and S -wave velocities from single cycle of 10 kHz or 15 kHz sinusoidal wave excitation were used respectively.

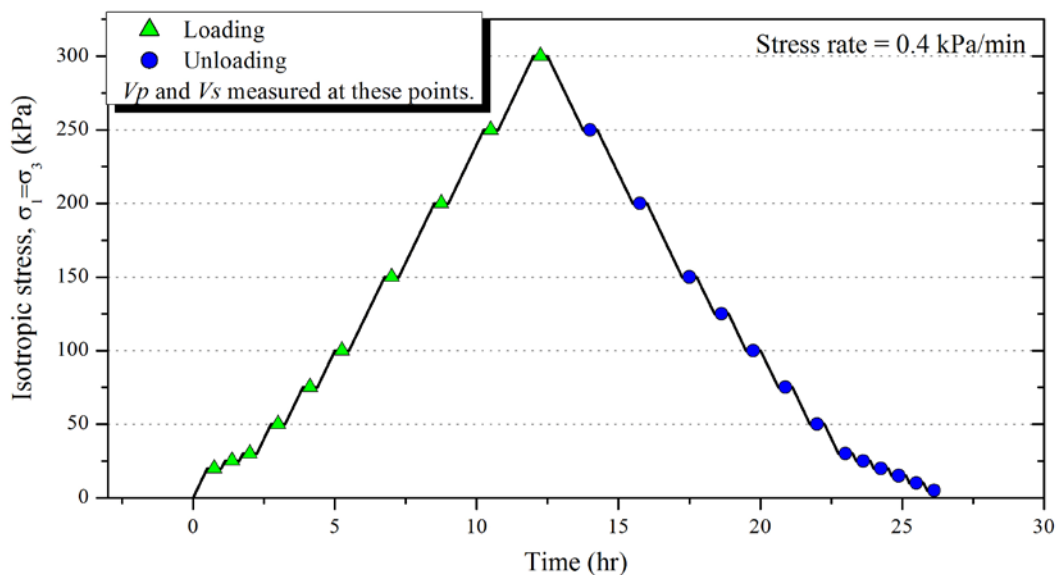


Figure 6.1: Stress path in *ICCW* tests.

Wave velocities are function of mean effective stress, void ratio and bulk density of soil (B. O. Hardin & Richart, 1963; B. O. Hardin & Drnevich, 1972). At each stress level, specimens were required to possess the same void ratio. Otherwise the difference in void ratio could affect wave velocities, and test results from different test

specimens could not be compared. However, it is extremely difficult to predict, with certainty, the volumetric compression of various unsaturated specimens. Therefore, the specimens were prepared at high initial relative density ($Dr = 85\%$ to 90%), so that the overall volumetric compression under isotropic confinement could be reduced. Despite very high initial relative density, each specimen underwent considerable volumetric compression on increasing isotropic confining stress from 20 kPa to 300 kPa. A typical variation of void ratio during isotropic confinement is shown in Figure 6.2. Wave velocity readings were therefore recorded not only during loading the specimen from 20 kPa to 300 kPa but also during unloading from 300 kPa, as shown in Figure 6.1. During unloading wave velocities were recorded at 300 kPa, 250 kPa, 200 kPa, 150 kPa, 100 kPa, 50 kPa, 30 kPa, 20 kPa, 15 kPa, 10 kPa, and 5 kPa. The corresponding variation of void ratio during unloading path was observed to be very small, i.e. of the order of 0.01 (Figure 6.2). For this reason, wave velocities obtained during unloading path were considered more reliable for this study; and thus most of the discussions are derived from the results of wave velocities during unloading path. A more detailed comparison of wave velocities during loading and unloading paths is presented in following sections.

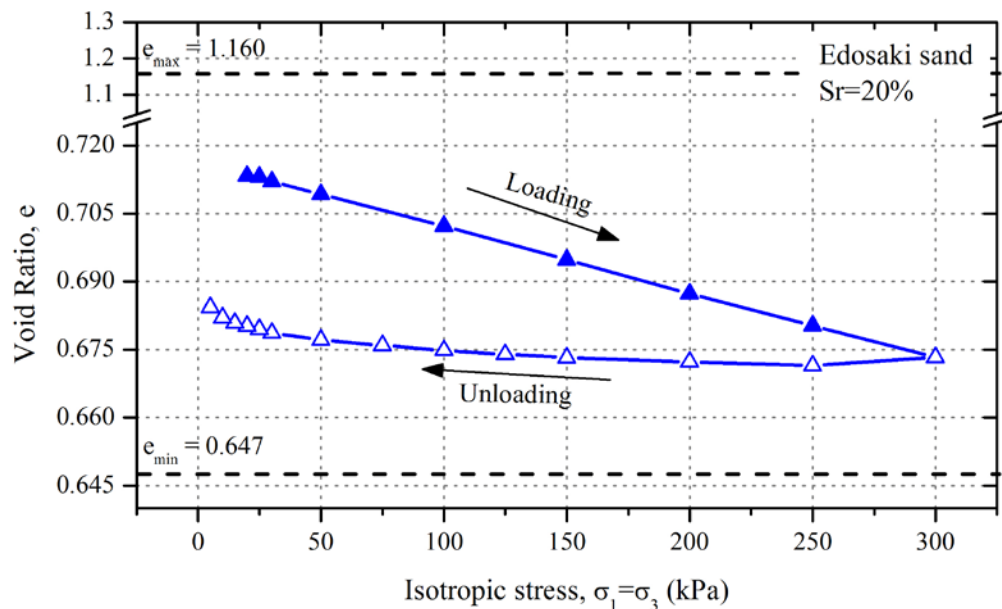


Figure 6.2: Typical variation of void ratio during ICCW tests.

6.3.2 Normalization of Void Ratio and Density

As explained in the previous section, it was extremely difficult to control and/or predict the final void ratio of specimens under isotropic compression. Consequently, the volumetric compression of specimens with different saturation ratio, under the final isotropic stress of 300 kPa, was different, as depicted by Figure 6.3. Initial density of each specimen was therefore controlled to achieve a nearly uniform void ratio during unloading from 300 kPa. However, as evident from Figure 6.3, very small discrepancy in void ratios of various specimens was inevitable. Additionally, even if the void ratios of various specimens are assumed equal, difference in water content would result in different bulk density of each specimen. Wave velocities were therefore normalized corresponding to a reference void ratio, $e_o = 0.673$ ($Dr = 95\%$), and density, $(\gamma_d)_o = 1.578 \text{ g/cm}^3$ ($(\gamma_d)_o = 89.5\%$ of $(\gamma_d)_{max}$). The reference values were selected in such a way that most of the specimens had void ratios and densities close to the reference values during unloading phase. Normalization of wave velocities was done by considering the following relationships.

From elastic continuum mechanics, shear modulus, G , and the constrained compression modulus, M , can be expressed as;

$$G = Vs^2 \times \rho \quad (6.1)$$

$$M = Vp^2 \times \rho \quad (6.2)$$

Rearranging Eq. 6.1 and 6.2, we get shear wave, Vs , and compression wave velocities, Vp , as;

$$Vs = \sqrt{G/\rho} \quad (6.3)$$

$$Vp = \sqrt{M/\rho} \quad (6.4)$$

where, ρ represents the bulk density (total density) of soil.

Elastic wave propagation in soils is a function of void ratio and mean effective stress. A functional relationship representing the dependency of wave velocity on void ratio was proposed by B. O. Hardin and Richart (1963) and is given as;

$$G = A \cdot F(e) \cdot (\sigma'_m)^n \quad (6.5)$$

where G is in MPa and mean effective stress, $\sigma'_m (= (\sigma_1 + 2\sigma_3)/3)$, is in kPa; and void ratio function $F(e)$ is given as,

$$F(e) = \frac{(a - e)^2}{1 + e} \quad (6.6)$$

where, parameter a is equal to 2.17 or 2.97 for round grained or angular sand respectively, A is a fitting parameter reflecting soil fabric formed through various stress-strain histories, n is a dimensionless parameter, and σ'_m is mean effective stress acting on soil. For Edosaki sand used in this study, parameter a equal to 2.17 was found to be suitable. Hence $a = 2.17$ is used in this study.

Substituting Eq. 6.5 in Eq. 6.3, we get;

$$V_s = \sqrt{\frac{G}{\rho}} = \sqrt{\frac{1000 \times A \times F(e)}{\rho}} \times (\sigma'_m)^{\frac{n}{2}} \quad (6.7)$$

$$V_s = \sqrt{1000 \times A} \times \sqrt{\frac{1}{\rho}} \times \sqrt{F(e)} \times (\sigma'_m)^{\frac{n}{2}}$$

where, shear wave velocity, V_s , is in 'm/s'. Normalized shear wave velocity, V_s' , corresponding to designated void ratio, e_o , is given as;

$$V_s' = V_s \times \sqrt{\frac{F(e_o)}{F(e)}} \quad (6.8)$$

where, $F(e_o)$ is the void ratio function corresponding to designated void ratio of 0.673, and is obtained by using Eq. 6.6.

In a similar way, normalized compression wave velocity, V_p' , corresponding to designated void ratio, e_o , can be derived as;

$$V_p' = V_p \times \sqrt{\frac{F(e_o)}{F(e)}} \quad (6.9)$$

Eq. 6.8 can further be modified to accommodate density normalization as;

$$V_s'' = V_s' \times \sqrt{\frac{\gamma_d}{(\gamma_d)_o}} = V_s \times \sqrt{\frac{F(e_o)}{F(e)}} \times \sqrt{\frac{\gamma_d}{(\gamma_d)_o}} \quad (6.10)$$

Similarly, V_p' from Eq. 6.9 when normalized for density appears as;

$$V_p'' = V_p' \times \sqrt{\frac{\gamma_d}{(\gamma_d)_o}} = V_p \times \sqrt{\frac{F(e_o)}{F(e)}} \times \sqrt{\frac{\gamma_d}{(\gamma_d)_o}} \quad (6.11)$$

where, V_s'' and V_p'' are the shear and compression wave velocities respectively normalized for designated void ratio and density, while $(\gamma_d)_o$ represents the reference dry density.

Hence, all the shear wave, V_s , and compression wave velocities, V_p , were normalized corresponding to designated void ratio, $e_o=0.673$, and designated dry density, $(\gamma_d)_o=1.578 \text{ g/cm}^3$, by using Eq. 6.8 – Eq. 6.11. This simplified the comparison of wave velocities among specimens with different water contents.

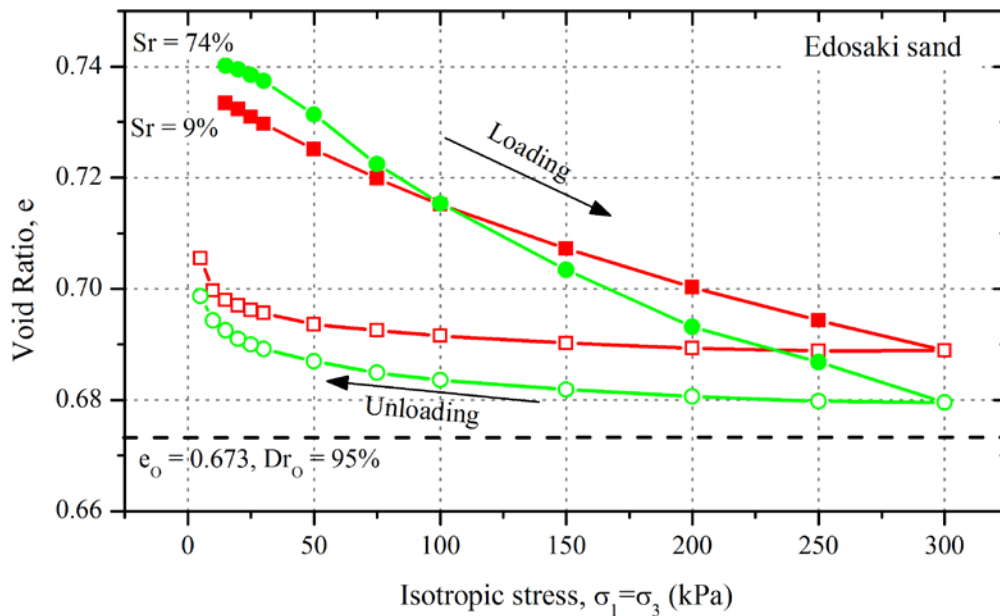


Figure 6.3: Effect of saturation ratio on volume change during ICCW tests.

6.3.3 Effects of Isotropic Stress on Wave Velocities

The dependency of wave velocities on effective stress is well established (B. Hardin & Black, 1968; Iwasaki et al., 1978; Chien et al., 2002; Lee et al., 2012). For all the specimens tested in this study, both the compression (V_p), and shear wave velocities (V_s) increased steadily during the isotropic loading from 20 kPa to 300 kPa. Similarly, V_p and V_s decreased during the unloading path, as the isotropic stress was decreased from 300 kPa to 5 kPa. Figure 6.4 to Figure 6.10 shows the variation of shear wave velocity, V_s , during loading and unloading path for specimens with different saturation ratios. Shear wave velocities normalized with respect to designated void ratio, e_o ($=0.673$), and designated density, $(\gamma_d)_o$ ($=1.578 \text{ g/cm}^3$), V_s'' , are shown as Figure (b) in each of respective figures.

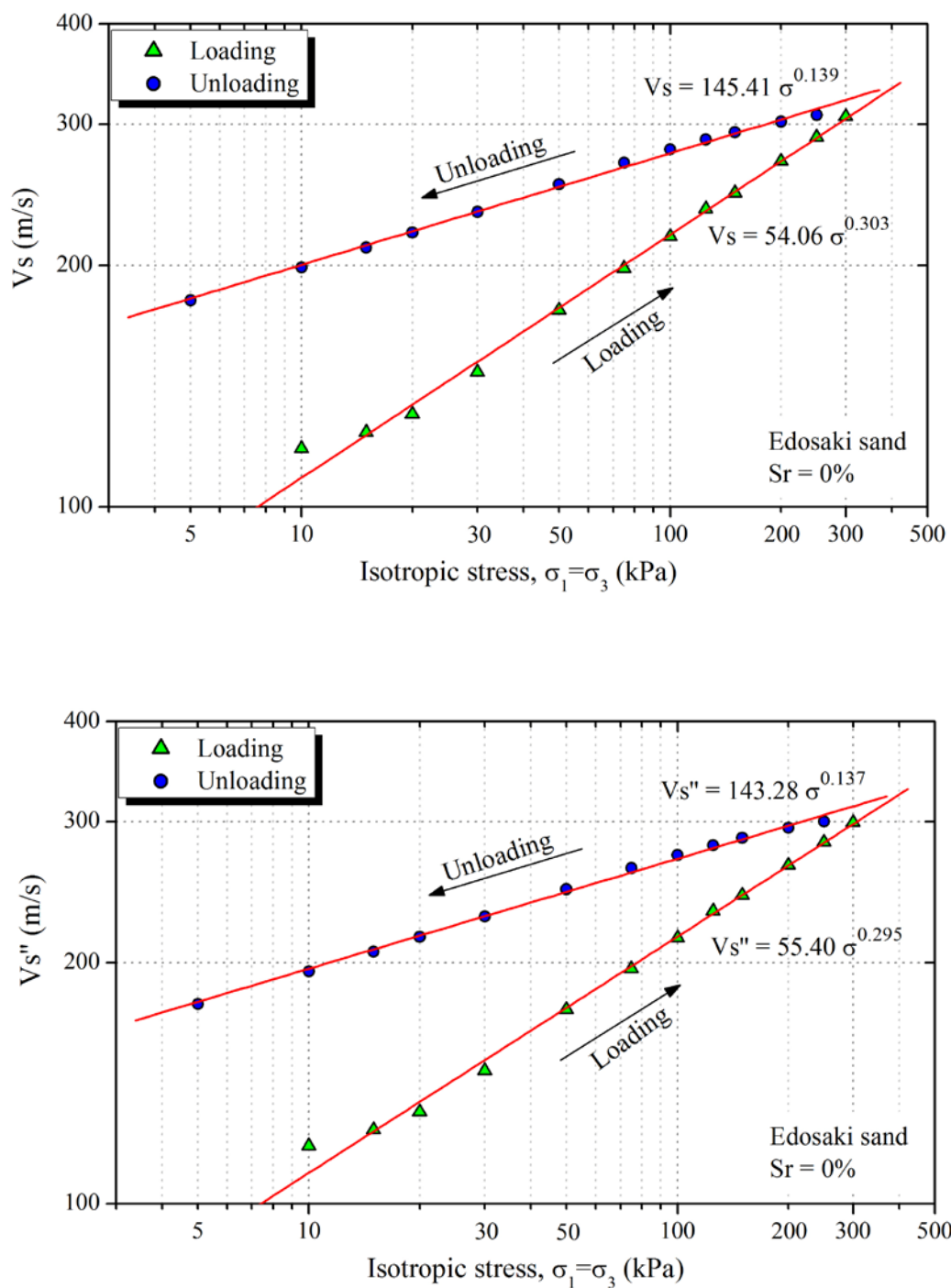


Figure 6.4: Response of shear wave velocity to isotropic loading, $S_r=0\%$; (a) observed shear wave velocity, V_s ; (b) shear wave velocity corrected for void ratio and density, V_s'' .

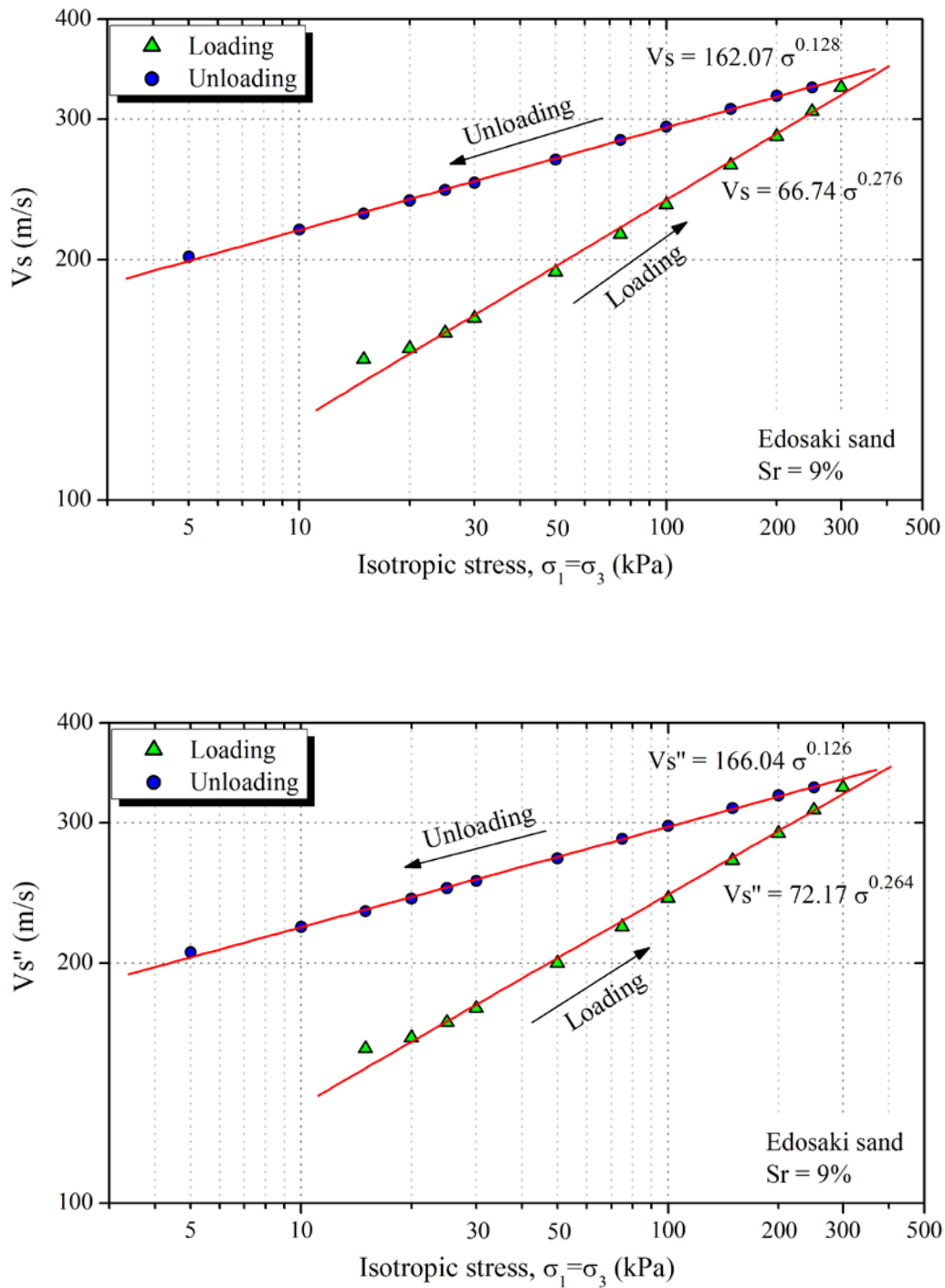


Figure 6.5: Response of shear wave velocity to isotropic loading, $S_r=9\%$; (a) observed shear wave velocity, V_s ; (b) shear wave velocity corrected for void ratio and density, V_s'' .

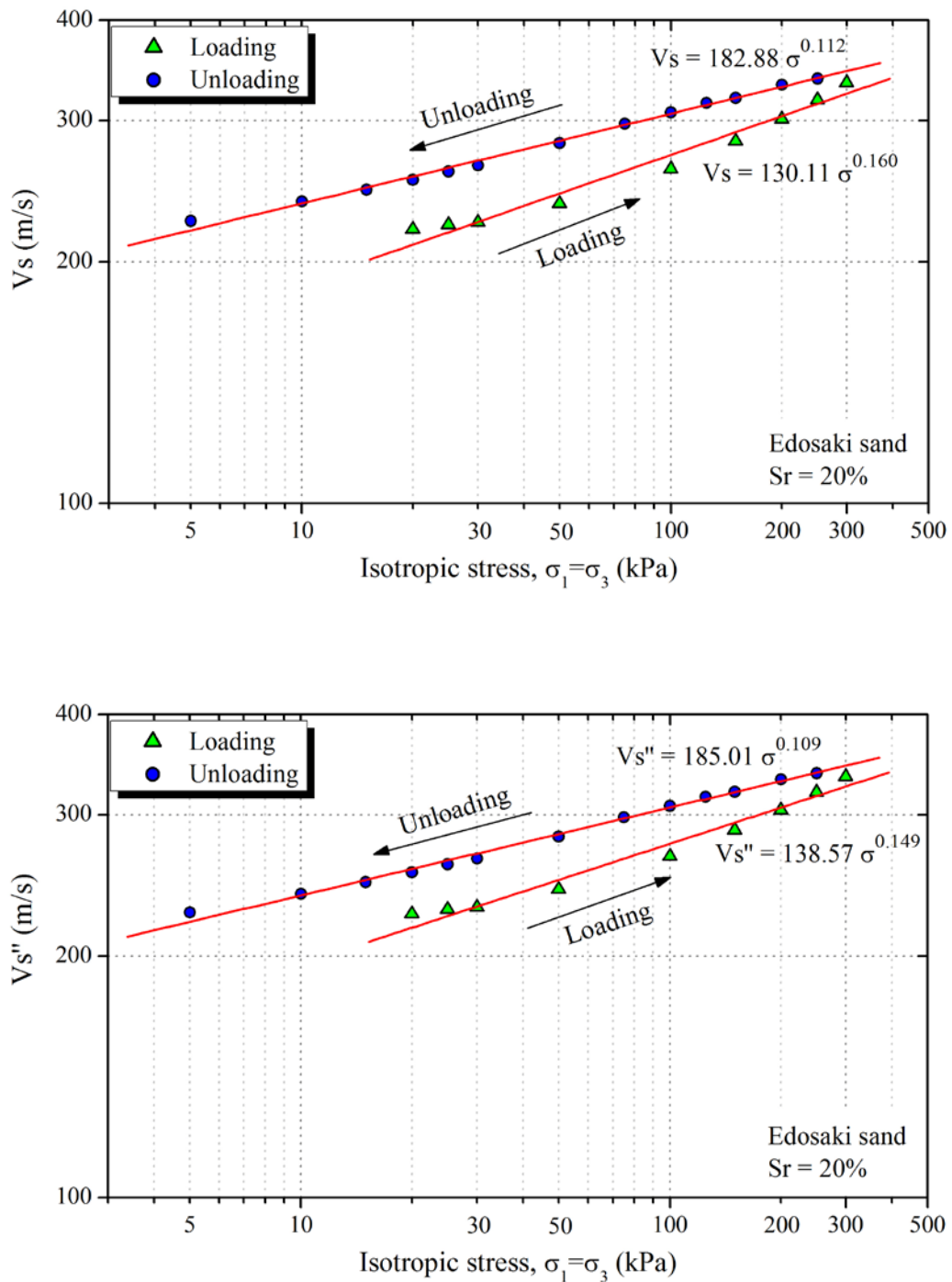


Figure 6.6: Response of shear wave velocity to isotropic loading, $S_r=20\%$; (a) observed shear wave velocity, V_s ; (b) shear wave velocity corrected for void ratio and density, V_s'' .

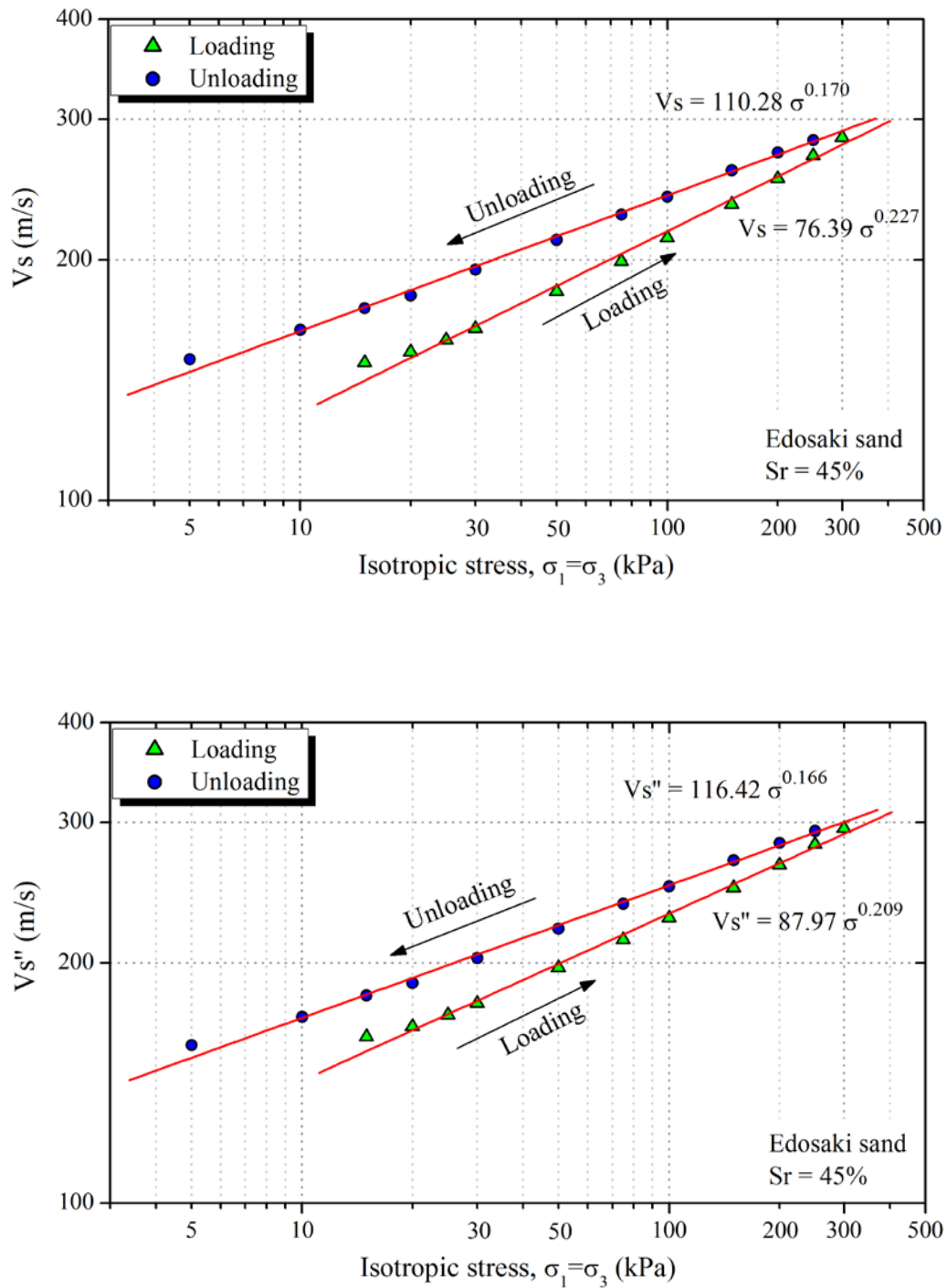


Figure 6.7: Response of shear wave velocity to isotropic loading, $S_r=45\%$; (a) observed shear wave velocity, V_s ; (b) shear wave velocity corrected for void ratio and density, V_s'' .

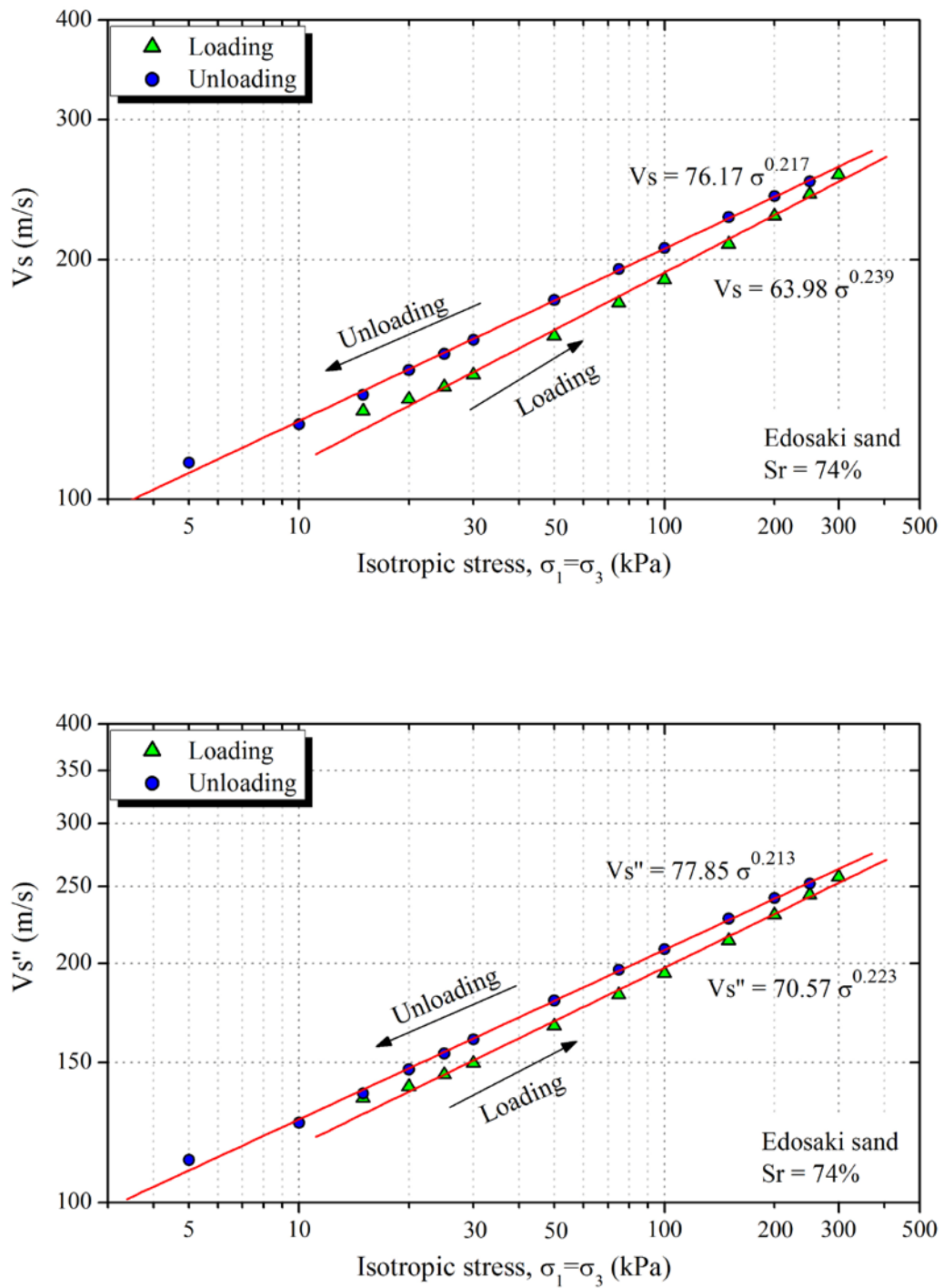


Figure 6.8: Response of shear wave velocity to isotropic loading, $S_r=74\%$; (a) observed shear wave velocity, V_s ; (b) shear wave velocity corrected for void ratio and density, V_s'' .

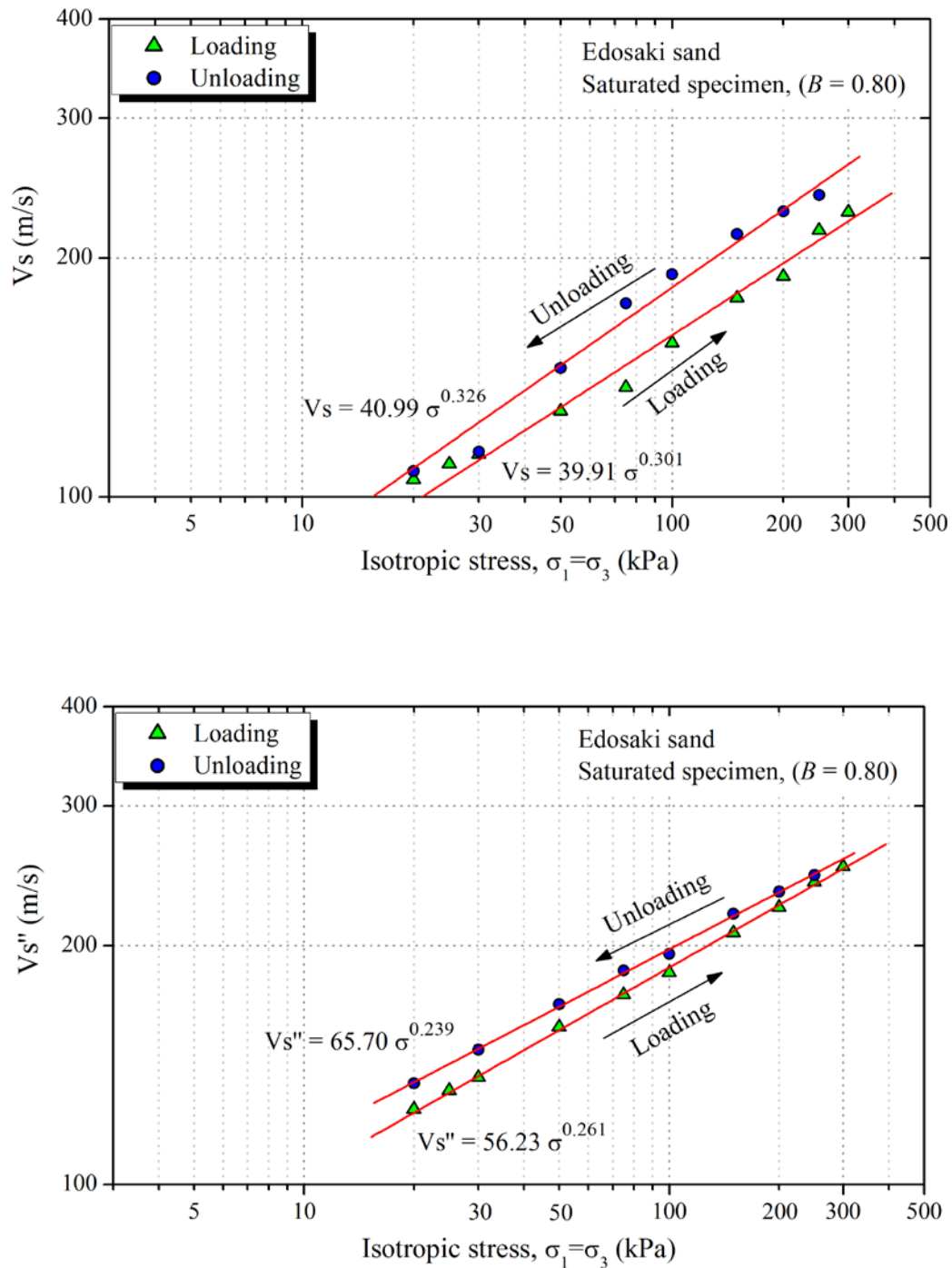


Figure 6.9: Response of shear wave velocity to isotropic loading: Saturated specimen ($B = 0.80$); (a) observed shear wave velocity, V_s ; (b) shear wave velocity corrected for void ratio and density, V_s'' .

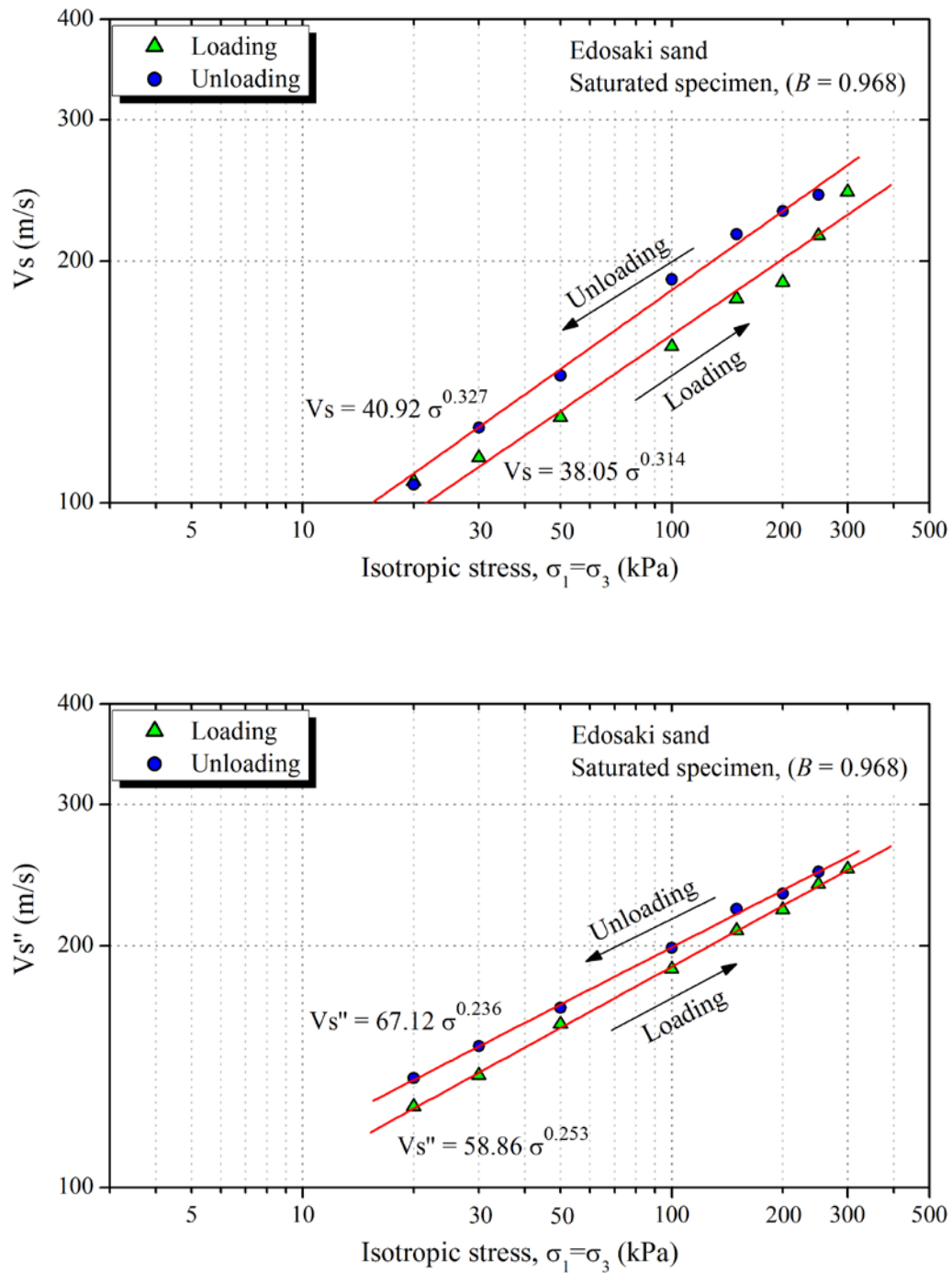


Figure 6.10: Response of shear wave velocity to isotropic loading: Saturated specimen ($B = 0.968$); (a) observed shear wave velocity, V_s ; (b) shear wave velocity corrected for void ratio and density, V_s'' .

From Eq. 6.7, wave velocities, V , can be represented as power function of mean effective stress, σ_m' ;

$$V = C \times (\sigma_m')^n \tag{6.12}$$

where, the variable n is known as the ‘power’ and it governs the shape of the function, i.e. the rate of increase/decrease of V with σ_m' ; and coefficient C is known as the scaling factor (or multiplier), and it moves the value of $(\sigma_m')^n$ up or down the plot (larger C , higher will be the plot and vice versa). From Eq. 6.7 and Eq. 6.12, C is a function of void ratio (e), soil bulk density (ρ), and soil fabric.

The power function presented in Eq. 6.12 appears as a straight line when plotted on a log-log scale as shown in Figure 6.4 to Figure 6.10. Thus, the parameters C and n can be computed by curve fitting. Parameters C and n , derived from shear wave velocities in Figure 6.4 to Figure 6.10, are summarized in Table 6.3 and Table 6.4 respectively.

Table 6.3: Summary of fitting parameter, C , from shear wave velocity plots.

S_r (%)	V_s		V_s''		$A=[(C_2-C_1)/C_2]$ $\times 100$	$B=[(C_2'-C_1)/C_2']$ $\times 100$	$A-B$ (%)
	(loading) C_1	(unloading) C_2	(loading) C_1'	(unloading) C_2'			
0	54.06	145.41	55.4	143.28	62.8	61.3	1.5
9	66.74	162.07	72.17	166.04	58.8	56.5	2.3
20	130.11	182.88	138.57	185.01	28.9	25.1	3.8
45	76.39	110.28	87.97	116.42	30.7	24.4	6.3
74	63.98	76.17	70.57	77.85	16.0	9.4	6.7
99	39.91	40.99	56.23	65.7	2.6	14.4	-11.8
($B=0.80$)							

99.9 ($B=0.968$)	38.05	40.92	58.86	67.12	7.0	12.3	-5.3
-----------------------	-------	-------	-------	-------	-----	------	------

Table 6.4: Summary of fitting parameter, n , from shear wave velocity plots.

Sr (%)	V_s		$V_{s''}$		$A = [(n_2 - n_1)/n_2] \times 100$	$B = [(n'_2 - n'_1)/n'_2] \times 100$	$A - B$
	(loading) n_1	(unloading) n_2	(loading) n_1'	(unloading) n_2'			
0	0.303	0.139	0.295	0.137	54.1	53.6	0.6
9	0.276	0.128	0.264	0.126	53.6	52.3	1.4
20	0.16	0.112	0.149	0.109	30.0	26.8	3.2
45	0.227	0.17	0.209	0.166	25.1	20.6	4.5
74	0.239	0.217	0.223	0.213	9.2	4.5	4.7
99 ($B=0.80$)	0.301	0.326	0.261	0.239	-8.3	8.4	-16.7
99.9 ($B=0.968$)	0.314	0.327	0.253	0.236	-4.1	6.7	-10.9

As depicted from Figure 6.4 to Figure 6.10, shear wave velocity varies linearly with isotropic stress, σ'_m . However, it is noticeable that the rate of increase in V_s (represented by parameter n), during loading is greater as compared to unloading stage. This may be because of the increasing void ratio during the loading path. Thus, V_s during loading is increased not only due to the increase in σ'_m , but also due to the

volumetric compression of specimen. During the unloading path however, change in void ratio is negligible (Figure 6.2), and thus, V_s is only affected by σ'_m . Parameter C , on the other hand, is observed to be greater during unloading path as compared to the loading path. This is because, during unloading, the specimens were in more compacted state.

The use of void ratio function for normalization of V_s (Eq. 6.10) was also found to reduce the discrepancy of V_s during loading and unloading stages. This means that the values of C and n during loading and unloading are better comparable after applying void ratio correction. This can be seen from last column of Table 6.3 and Table 6.4 which shows that the values of C and n during loading and unloading stages are improved up to a maximum of 6.7%.

Similarly Figure 6.11 to Figure 6.17 show the variation of actual compression wave velocities, V_p , and the normalized compression wave velocities, V_p'' , during loading and unloading of isotropic stress at various saturation ratios.

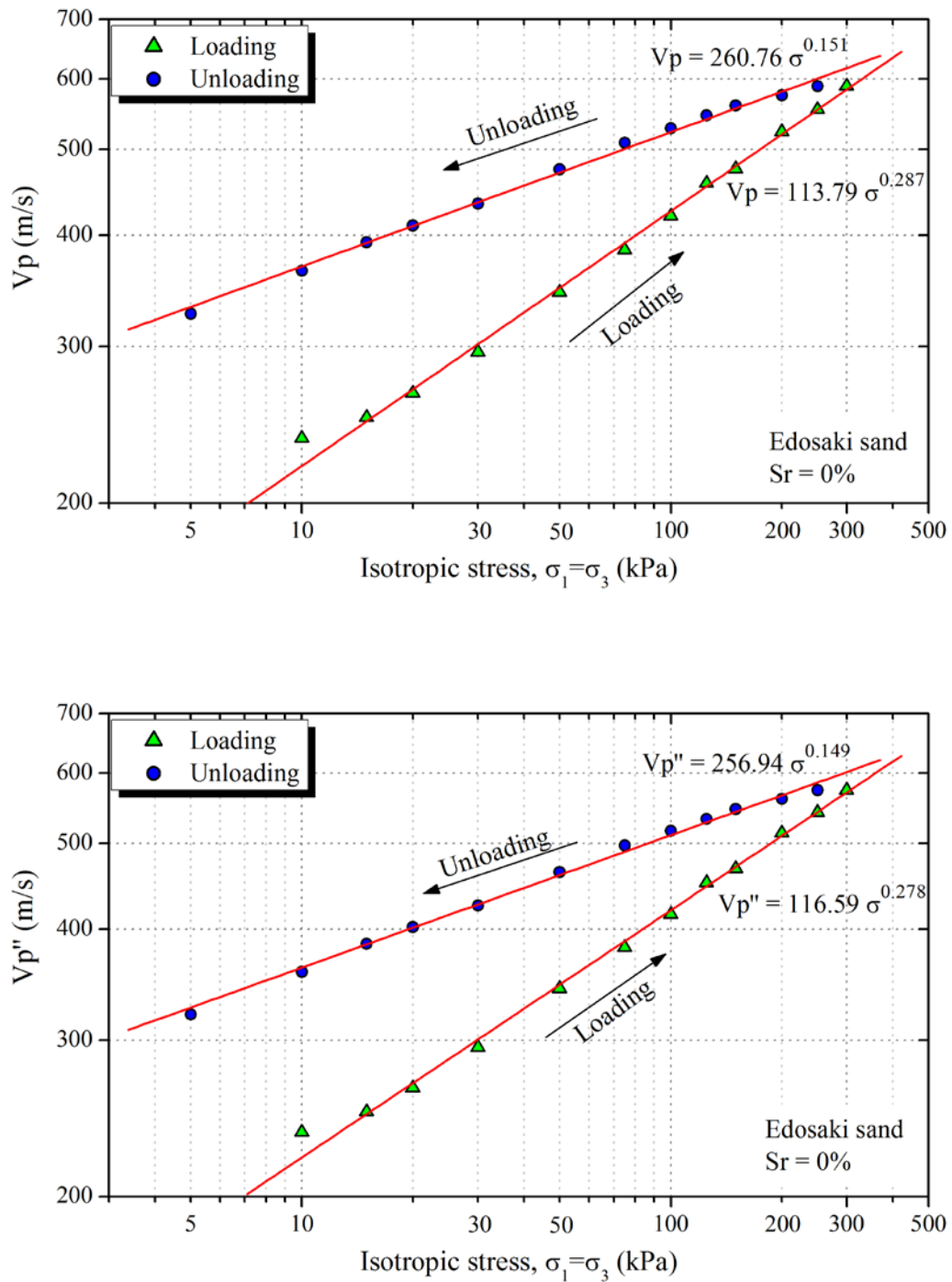


Figure 6.11: Response of compression wave velocity to isotropic loading, $S_r=0\%$; (a) observed shear wave velocity, V_p ; (b) shear wave velocity corrected for void ratio and density, V_p'' .

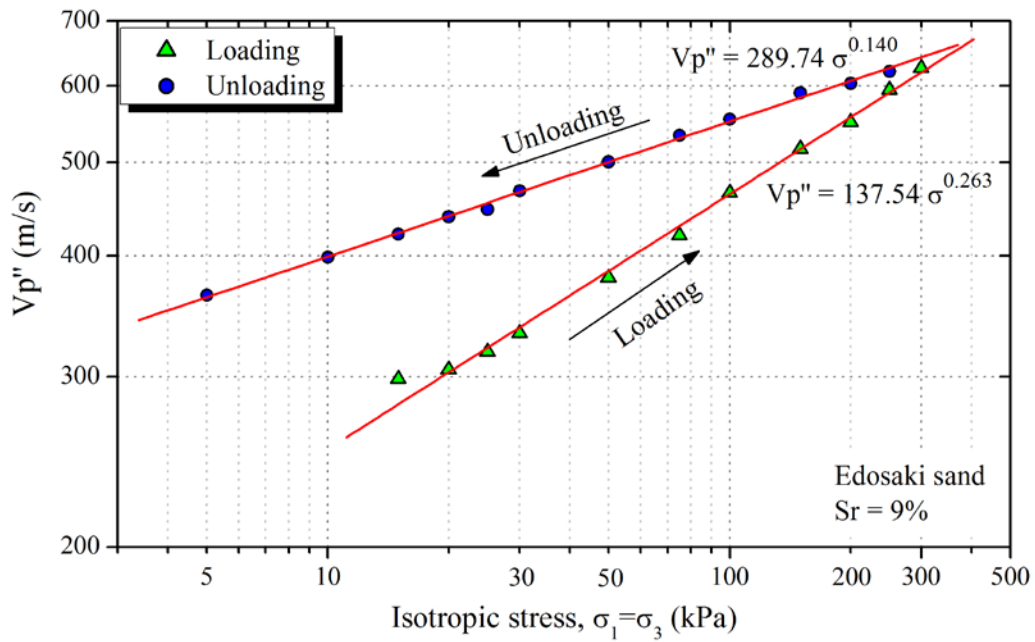
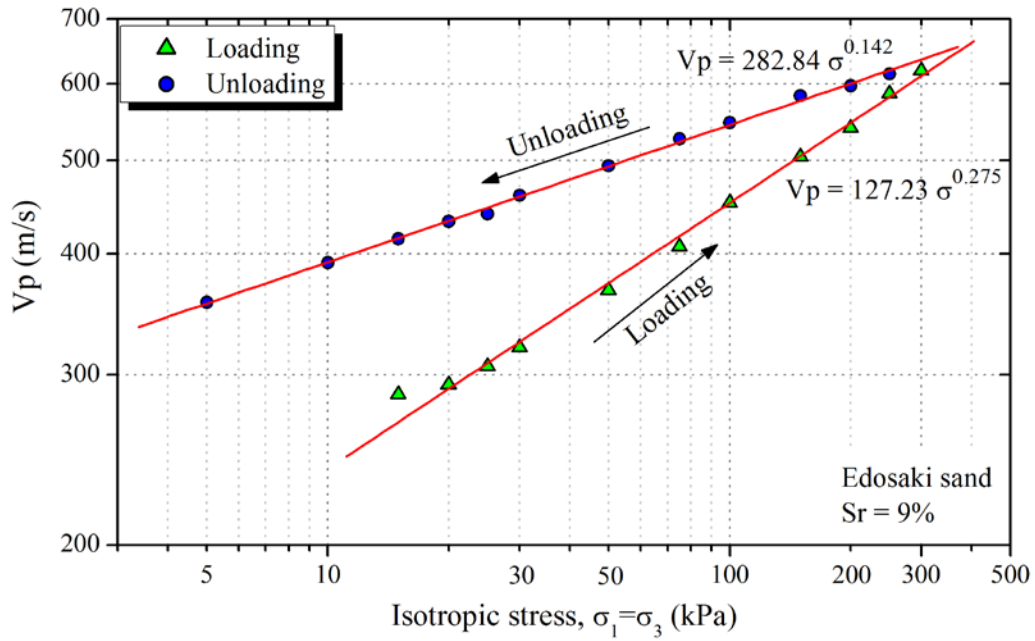


Figure 6.12: Response of compression wave velocity to isotropic loading, $S_r=9\%$; (a) observed shear wave velocity, V_p ; (b) shear wave velocity corrected for void ratio and density, V_p'' .

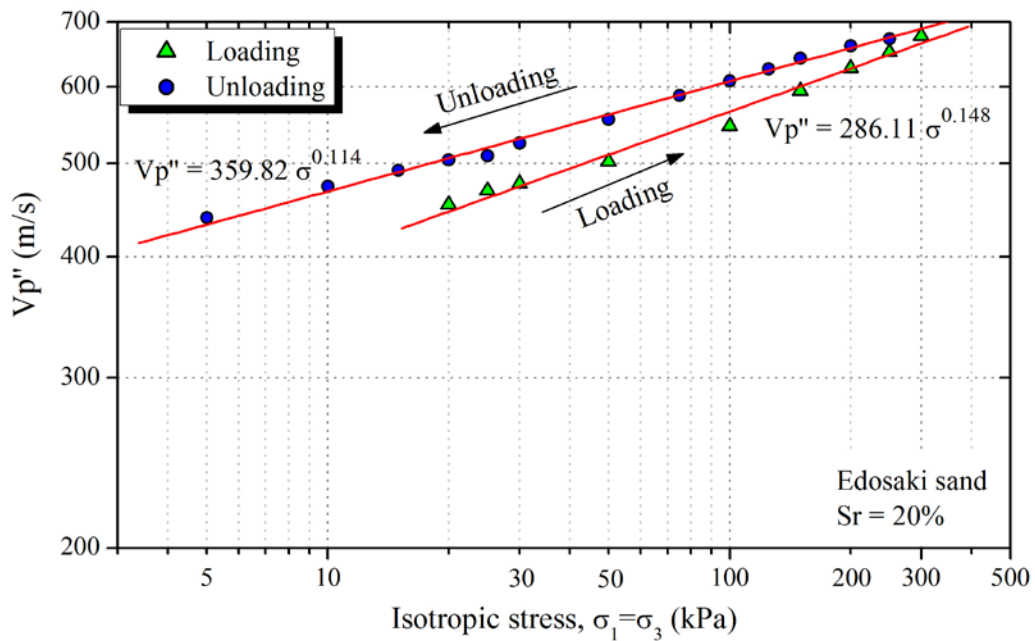
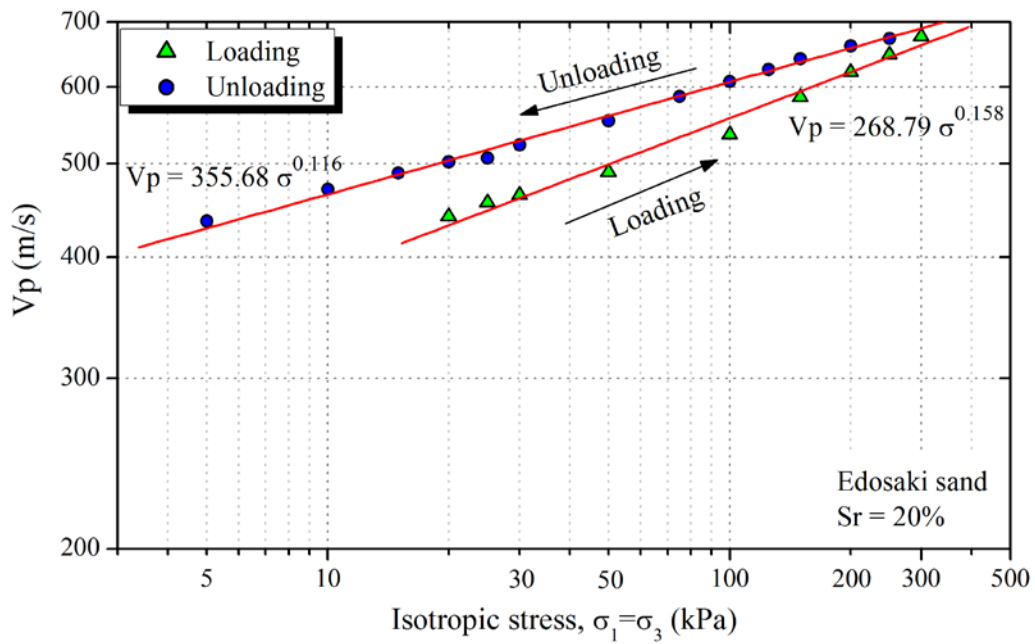


Figure 6.13: Response of compression wave velocity to isotropic loading, $S_r=20\%$; (a) observed shear wave velocity, V_p ; (b) shear wave velocity corrected for void ratio and density, V_p'' .

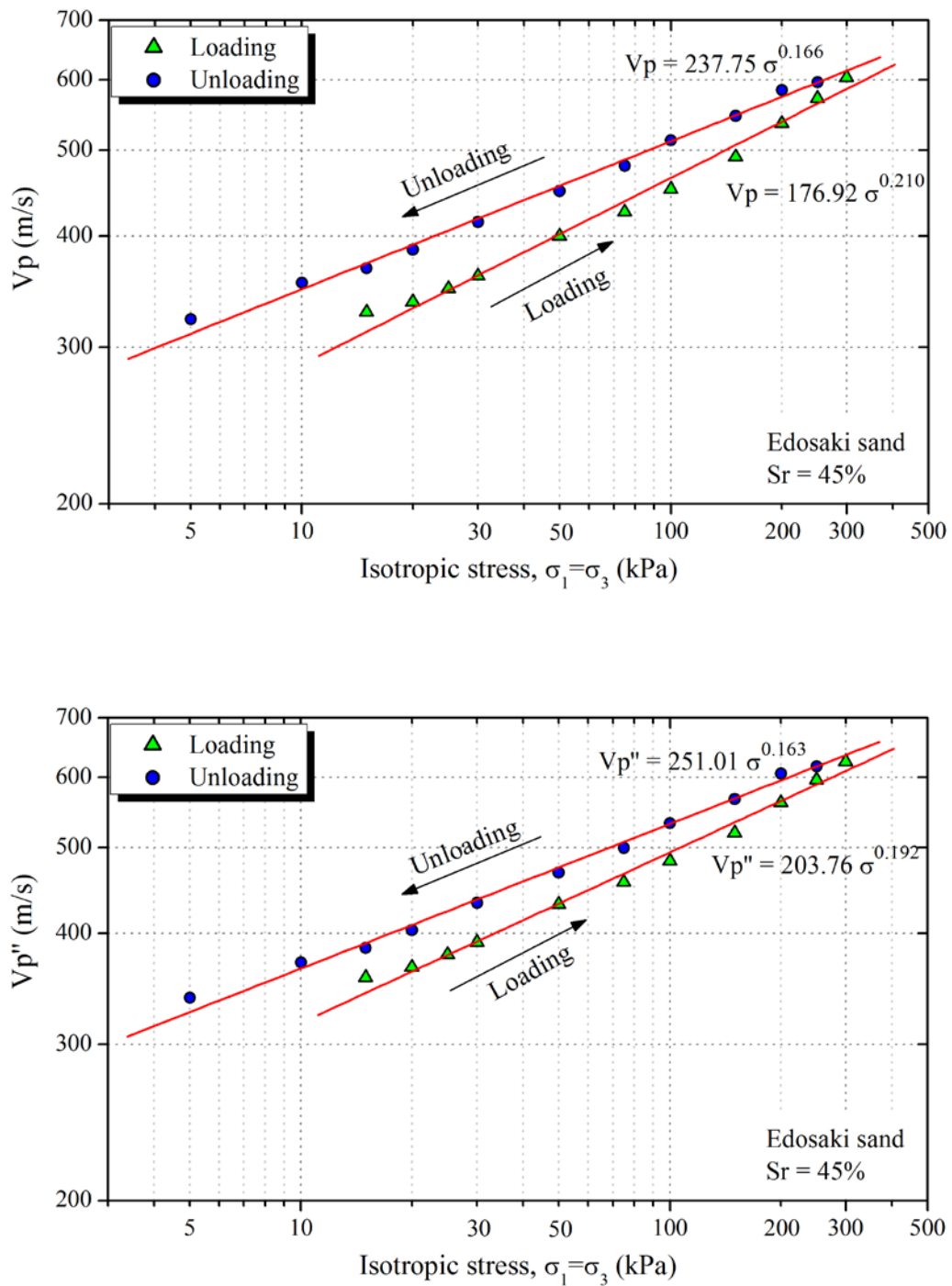


Figure 6.14: Response of compression wave velocity to isotropic loading, $S_r=45\%$; (a) observed shear wave velocity, V_p ; (b) shear wave velocity corrected for void ratio and density, V_p'' .

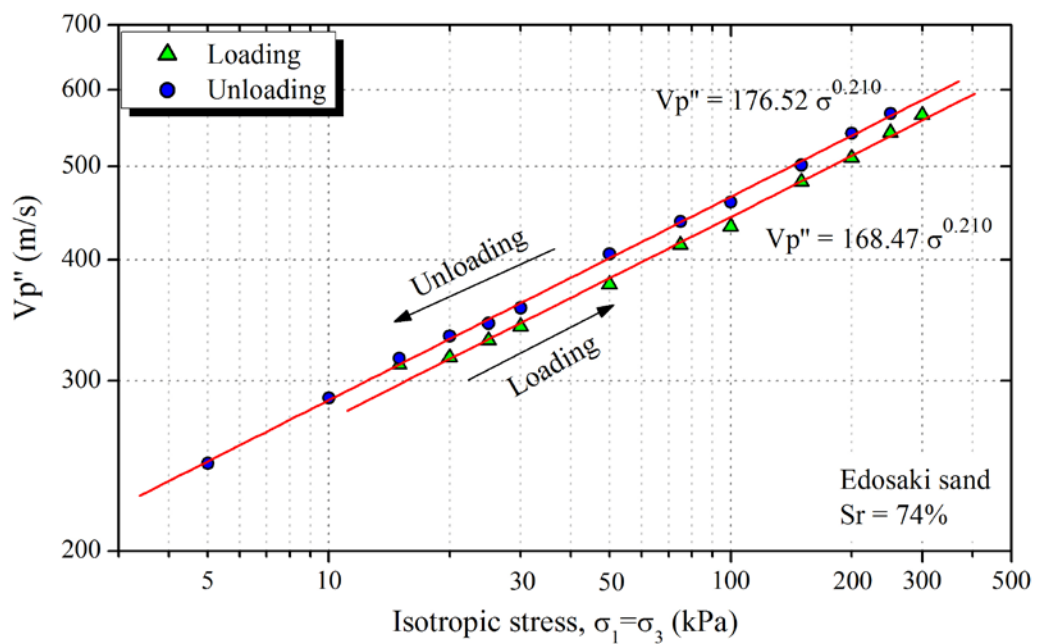
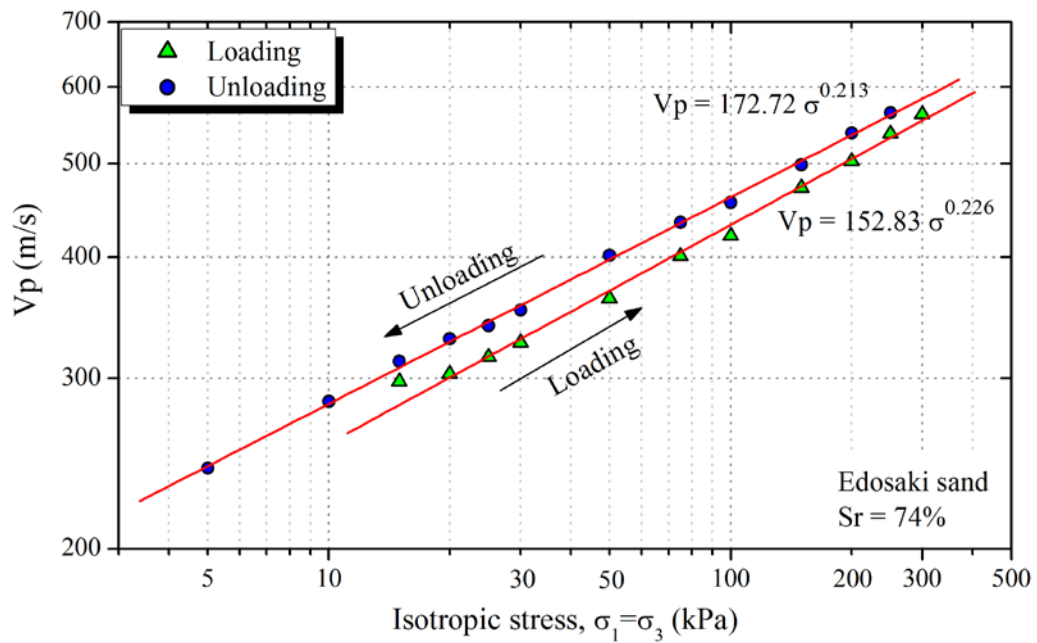


Figure 6.15: Response of compression wave velocity to isotropic loading, $S_r=74\%$; (a) observed shear wave velocity, V_p ; (b) shear wave velocity corrected for void ratio and density, V_p'' .

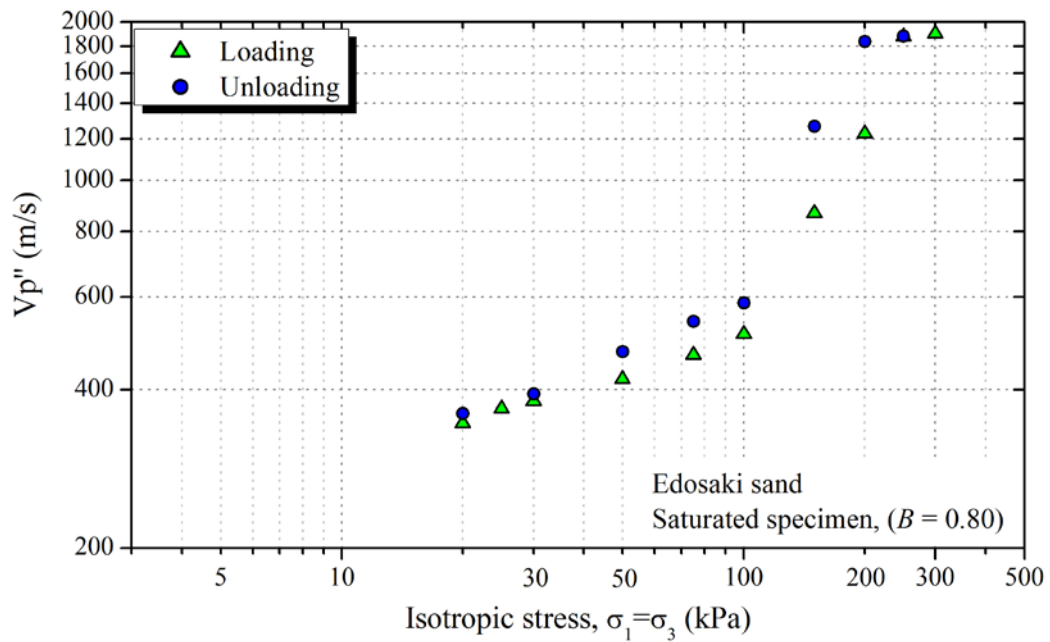
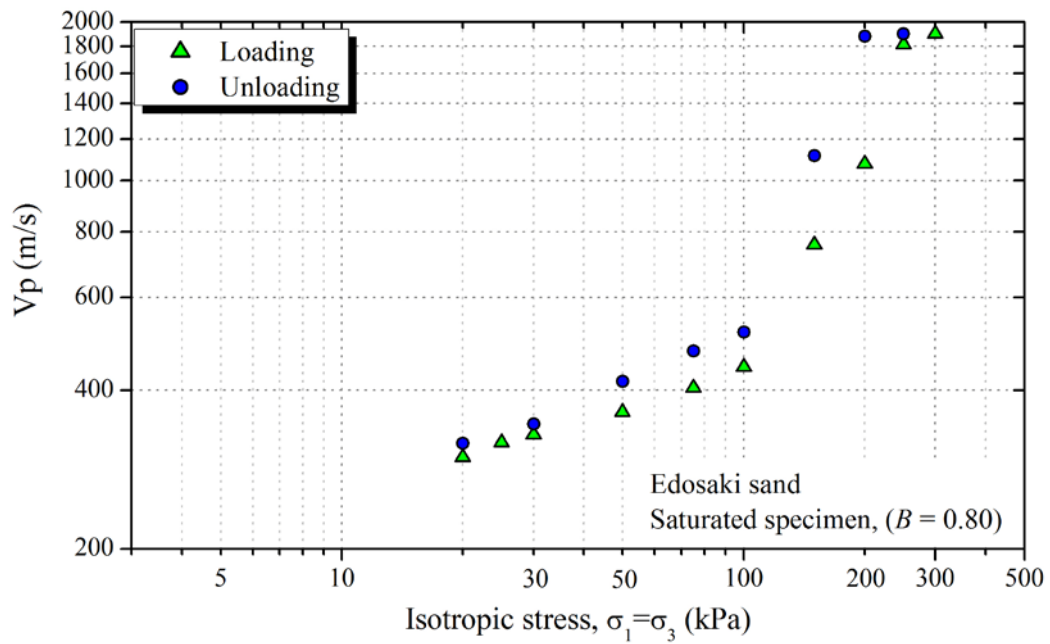


Figure 6.16: Response of compression wave velocity to isotropic loading: Saturated specimen ($B = 0.80$); (a) observed shear wave velocity, V_p ; (b) shear wave velocity corrected for void ratio and density, V_p'' .

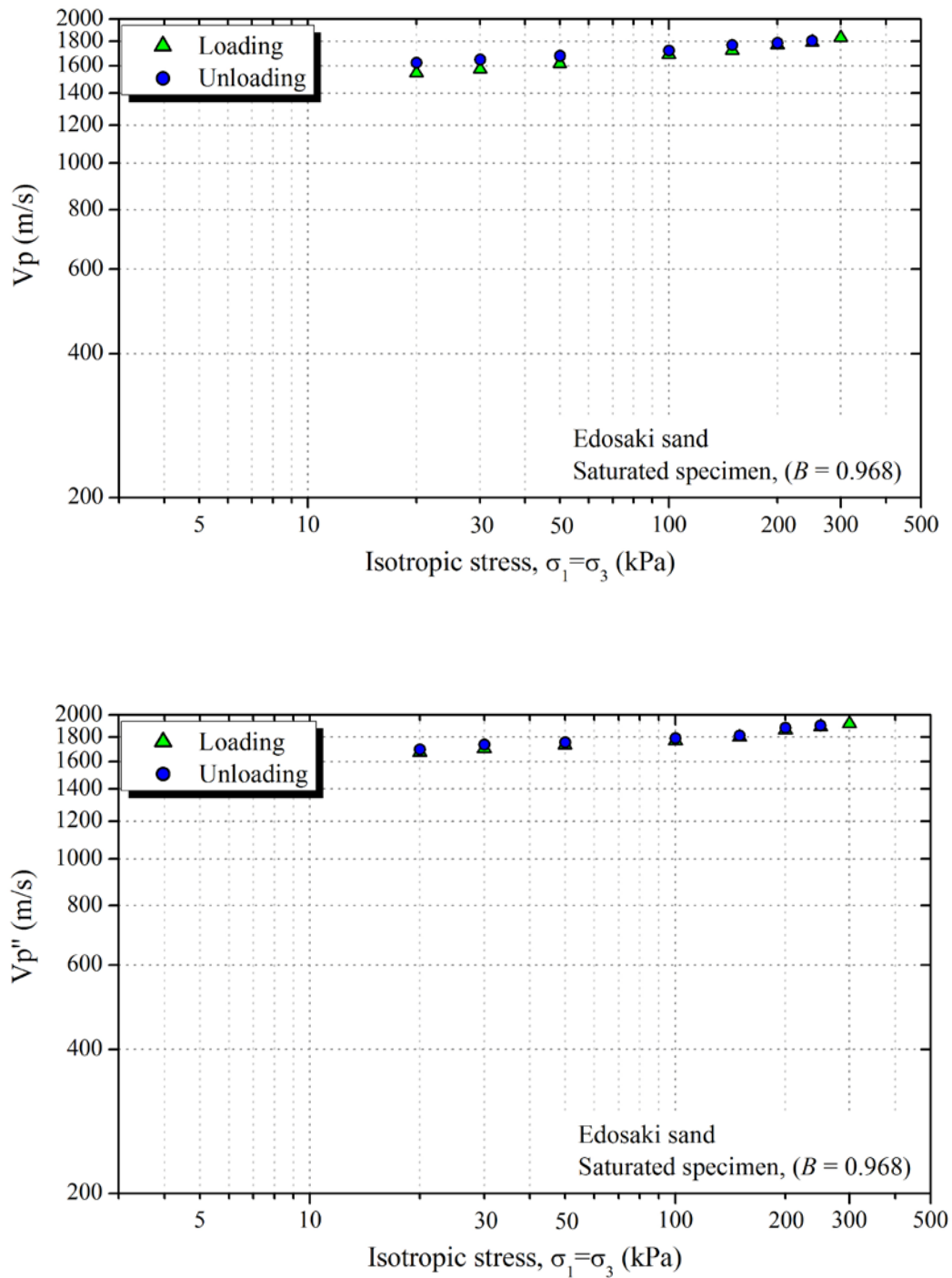


Figure 6.17: Response of compression wave velocity to isotropic loading: Saturated specimen ($B = 0.80$); (a) observed shear wave velocity, V_p ; (b) shear wave velocity corrected for void ratio and density, V_p'' .

The behavior of compression wave velocities in unsaturated specimens was observed to be similar to that of shear wave velocities, with almost twice the magnitude. However, for saturated specimens, the behavior of compression wave velocities was not comparable with shear wave velocities. Under saturated conditions, the compression wave can travel through the continuous water phase instead of the soil skeleton. Thus, the compression wave velocity in saturated conditions appears to approach sonic wave velocity in water. This phenomenon can be observed in Figure 6.16 and Figure 6.17.

For saturated specimens, compression wave velocity is dependent on Skempton's pore pressure parameter ' B ' (Kokusho, 2000; Tsukamoto et al., 2002). In Figure 6.16, for saturated specimen with B -value of 0.80, no considerable anomaly in V_p is observed for σ'_m less than 100 kPa. However, when isotropic stress is increased further, the air inside the soil pores gets compressed, reducing its volume; and thus, V_p starts to increase considerably. Conversely, when isotropic stress is reduced from 300 kPa, air inside soil pores starts expanding thus breaking the continuity of water phase. Therefore, V_p decreased sharply from around 1800 m/s at 300 kPa, to around 500 m/s at 100 kPa. If B -value is high enough, then V_p reaches sonic wave velocity in water even at low confining pressures, as shown in Figure 6.17. No considerable increase in V_p is observed with isotropic stress, when $B=0.968$.

Compression wave velocity, V_p , can also be expressed by the same expression defined in Eq. 6.12. Coefficients C and n , derived from compression wave velocities in Figure 6.11 to Figure 6.17 are summarized in Table 6.5 and Table 6.6 respectively.

Table 6.5: Summary of fitting parameter, C , from compression wave velocity plots.

Sr (%)	Vp		Vp''		$A = [(C_2 - C_1)/C_2]$ $\times 100$	$B = [(C'_2 - C'_1)/C'_2]$ $\times 100$	$A-B$ (%)
	(loading) C_1	(unloading) C_2	(loading) C_1'	(unloading) C_2'			
0	113.79	260.76	116.59	256.94	56.4	54.6	1.7
9	127.23	282.84	137.54	289.74	55.0	52.5	2.5
20	268.79	355.68	286.11	359.82	24.4	20.5	3.9
45	176.92	237.75	203.76	251.01	25.6	18.8	6.8
74	152.83	172.72	168.47	176.52	11.5	4.6	7.0

Table 6.6: Summary of fitting parameter, n , from compression wave velocity plots.

Sr (%)	Vp		Vp''		$A = [(n_2 - n_1)/n_2]$ $\times 100$	$B = [(n'_2 - n'_1)/n'_2]$ $\times 100$	$A-B$
	(loading) n_1	(unloading) n_2	(loading) n_1'	(unloading) n_2'			
0	0.303	0.139	0.278	0.149	47.4	46.4	1.0
9	0.276	0.128	0.263	0.14	48.4	46.8	1.6
20	0.16	0.112	0.148	0.114	26.6	23.0	3.6
45	0.21	0.166	0.192	0.163	21.0	15.1	5.8
74	0.239	0.217	0.21	0.21	5.8	0.0	5.8

Similar to shear wave velocity, a higher value of parameter n is observed during loading as compared to unloading path (Table 6.6). It shows a higher rate of increase of V_p per unit σ'_m during loading as compared to unloading stage. Coefficient C , which is largely dependent on packing of soil particles (i.e. density), is observed to be greater during the unloading path, owing to higher density of soil specimen during unloading. As was the case in shear wave velocities, void ratio function (Eq. 6.9) was found to decrease the difference in V_p during loading and unloading stages. Last columns of Table 6.5 and Table 6.6 show that, the comparison between values of C and n during loading and unloading stages is improved up to a maximum of 7.0%.

It is pertinent to note the presence of small hysteresis in wave velocities during loading and unloading even after normalizing for void ratio and density. As per Eq. 6.7 once void ratio and density are fixed after normalization, wave velocities for same isotropic stress during loading and unloading should be equal. But this is not the case. Although, void ratio and density were normalized but the difference in soil fabric, i.e. spatial arrangement of soil particles and soil voids, during loading and unloading caused a difference in wave velocity. The influence of soil fabric is governed by parameters A and n in Eq. 6.7. In order to confirm this phenomenon, two specimens, $S_r=20\%$ and $S_r=45\%$, were reloaded back to 300 kPa after the initial unloading. Since this reloading occurred when the specimen was in over-consolidated state, thus the variation in void ratio was expected to be very small. Figure 6.18 shows the typical variation of void ratio during such a test. Due to this extremely small variation in volumetric strain during reloading, soil fabric was not expected to change much, and the wave velocities were only expected to be affected by mean stress.

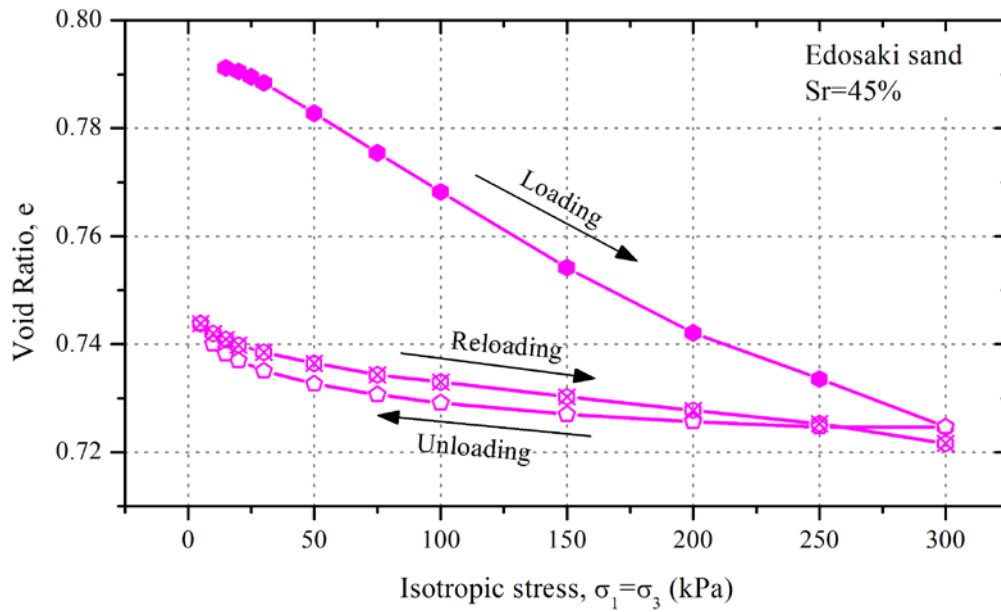


Figure 6.18: Typical variation of void ratio during reloading of isotropic stress.

Figure 6.19 and Figure 6.20 show the variation of V_s and V_p in two unsaturated specimens during loading, unloading, and reloading paths respectively. Owing to similar void ratio and soil fabric, wave velocities in unloading and reloading paths are observed to be quite similar. This highlights the significance of soil particle arrangement and distribution of voids in soil matrix, on elastic wave propagation.

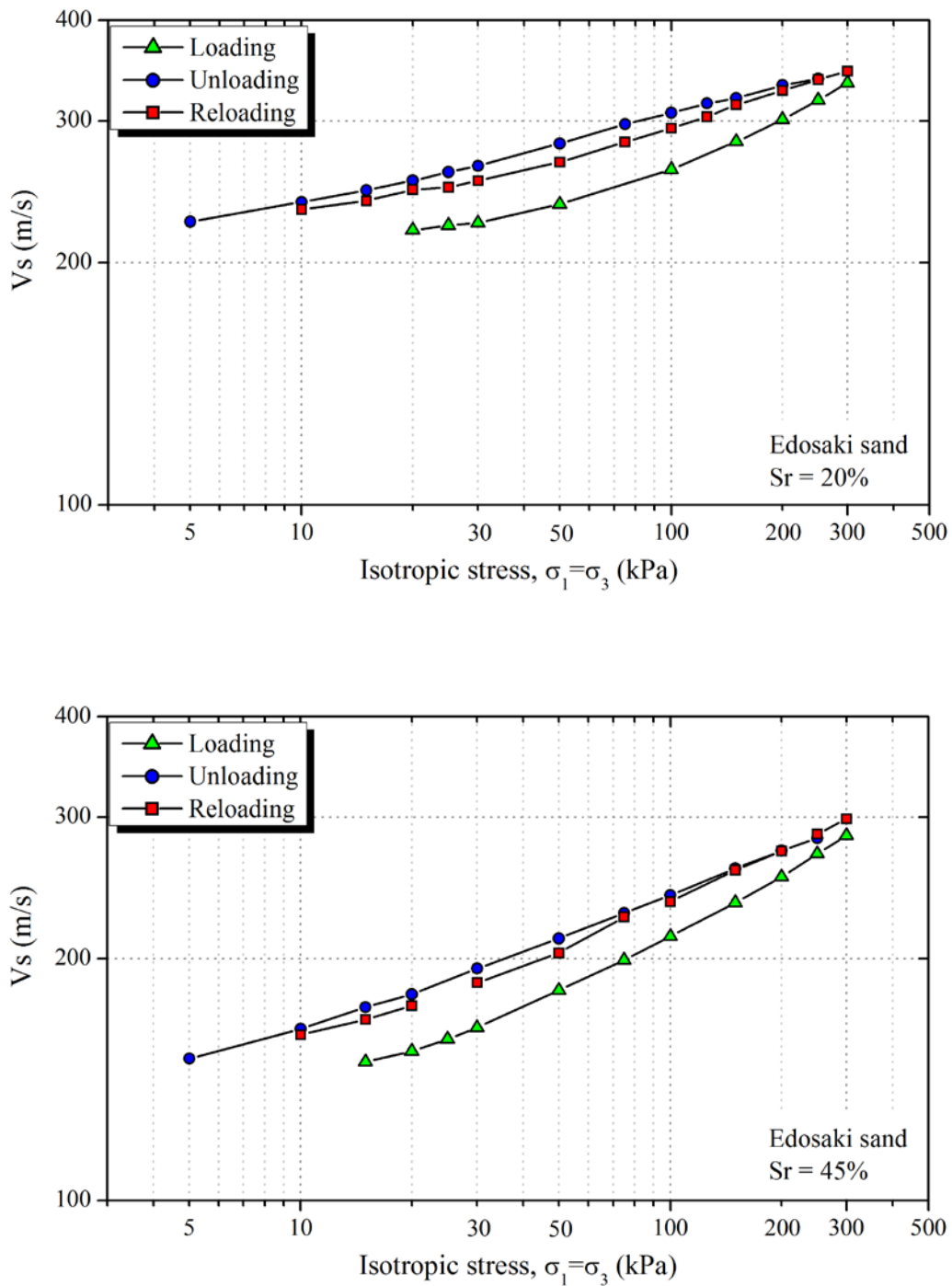


Figure 6.19: Typical variation of shear wave velocity during reloading of isotropic stress; (a) $Sr=20\%$; (b) $Sr=45\%$.

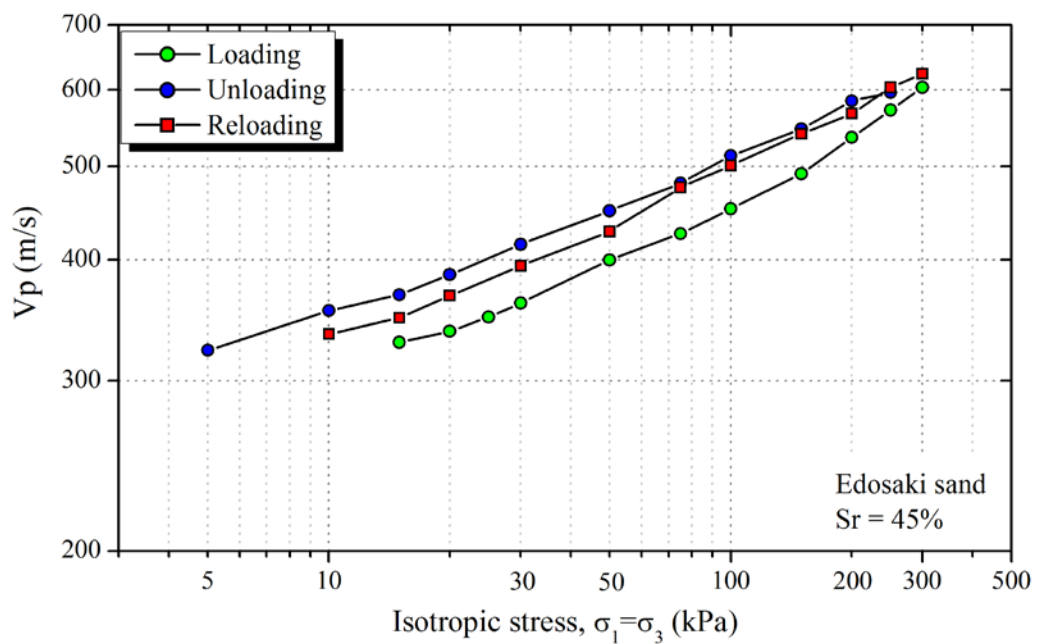
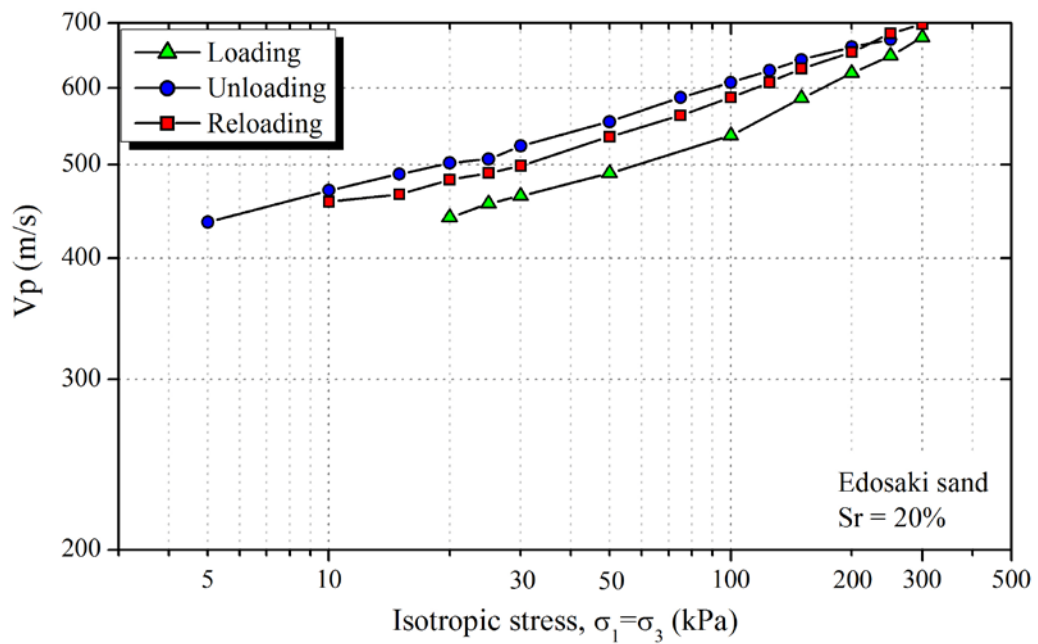


Figure 6.20: Typical variation of compression wave velocity during reloading of isotropic stress; (a) $S_r=20\%$; (b) $S_r=45\%$

6.3.4 Deformation Characteristics of Specimens

All the specimens underwent volumetric compression with the increase in isotropic stress. Volume change behavior of various specimens is shown in Figure 6.2, Figure 6.3, and Figure 6.18. With the increase in isotropic stress, axial compressive strains started developing in the specimens, as shown in Figure 6.21(b), and Figure 6.22(b). Similarly, during the unloading path, axial strains were observed to retreat. Axial strains recorded by externally mounted *LVDT* were slightly larger than those recorded by *LDTs*. It may be because *LDTs* used in this study were 112 mm in length. When fixed in between the pseudo-hinges, they covered about 75% length of specimen. The deformations occurring in the remaining 25% length of specimen, close to its ends, may not have been recorded by *LDTs*. Otherwise the trend of axial deformations obtained from *LVDT* and *LDTs* are quite similar.

Three clip gauges attached at different levels along the specimen height recorded radial deformations during the experiments. Figure 6.21(c) and Figure 6.22(c) show the response of these clip gauges. Nearly uniform radial strains were observed throughout specimen height. Similar to axial deformations, radial deformations increased (compression) during the loading path. Whereas, the specimens started to expand radially when isotropic stress was decreased from 300 kPa during the unloading path.

Close observation of the plots also reveals that, axial and radial deformations stopped soon after stopping the stress increment/decrement. Since the rate of isotropic stress was kept very low (~ 0.4 kPa/min), soil particles had enough time to rearrange during stress increase/decrease. In a trial test, stress rate of 5 kPa/min was used, and it was observed that axial and radial deformations stabilized 30min~60min after stopping the stress increment/decrement.

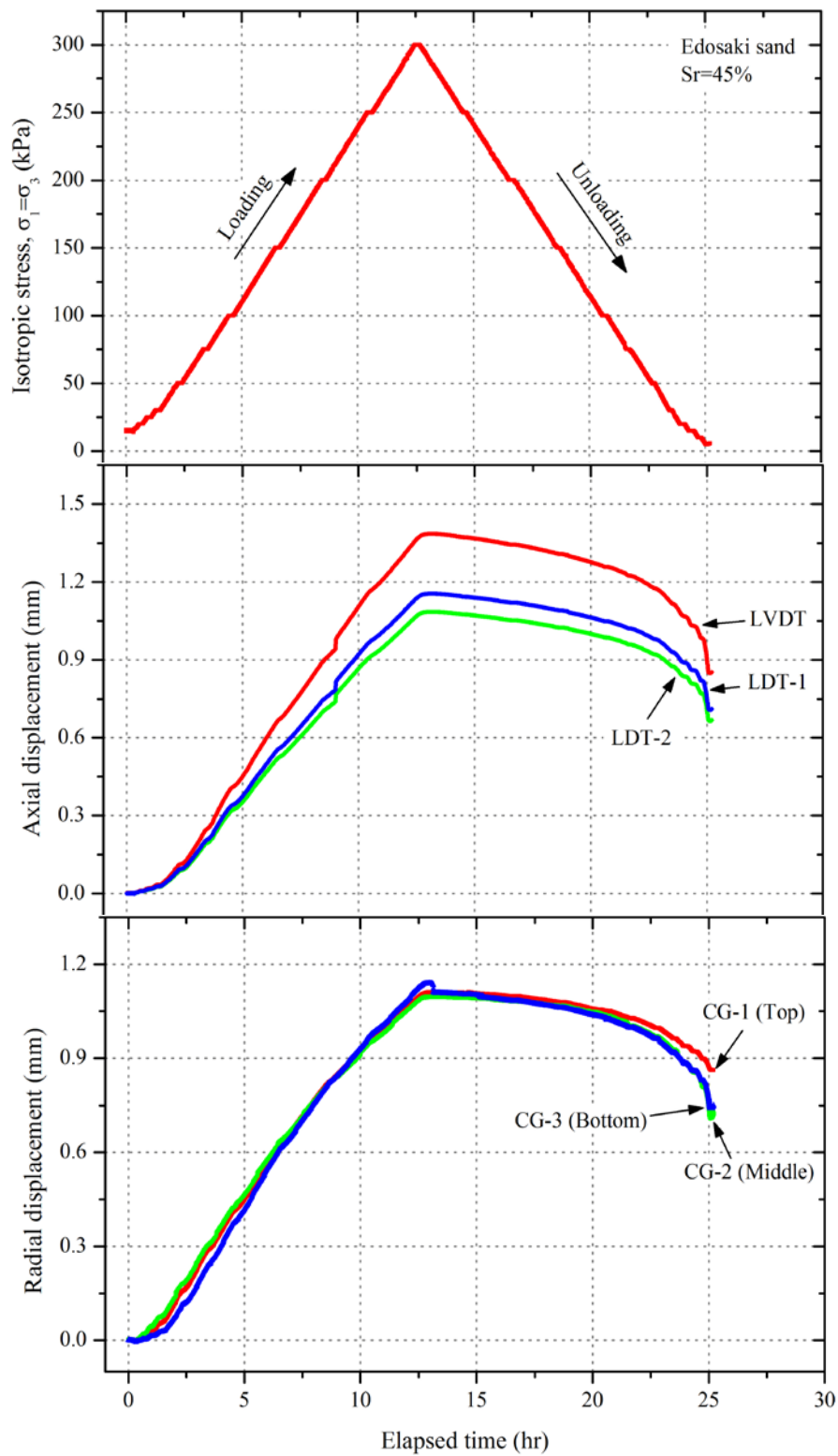


Figure 6.21: Deformation characteristics of unsaturated specimen, $S_r=45\%$; (a) Variation of isotropic stress; (b) Comparison of axial displacement transducers; (c) Radial deformation characteristics.

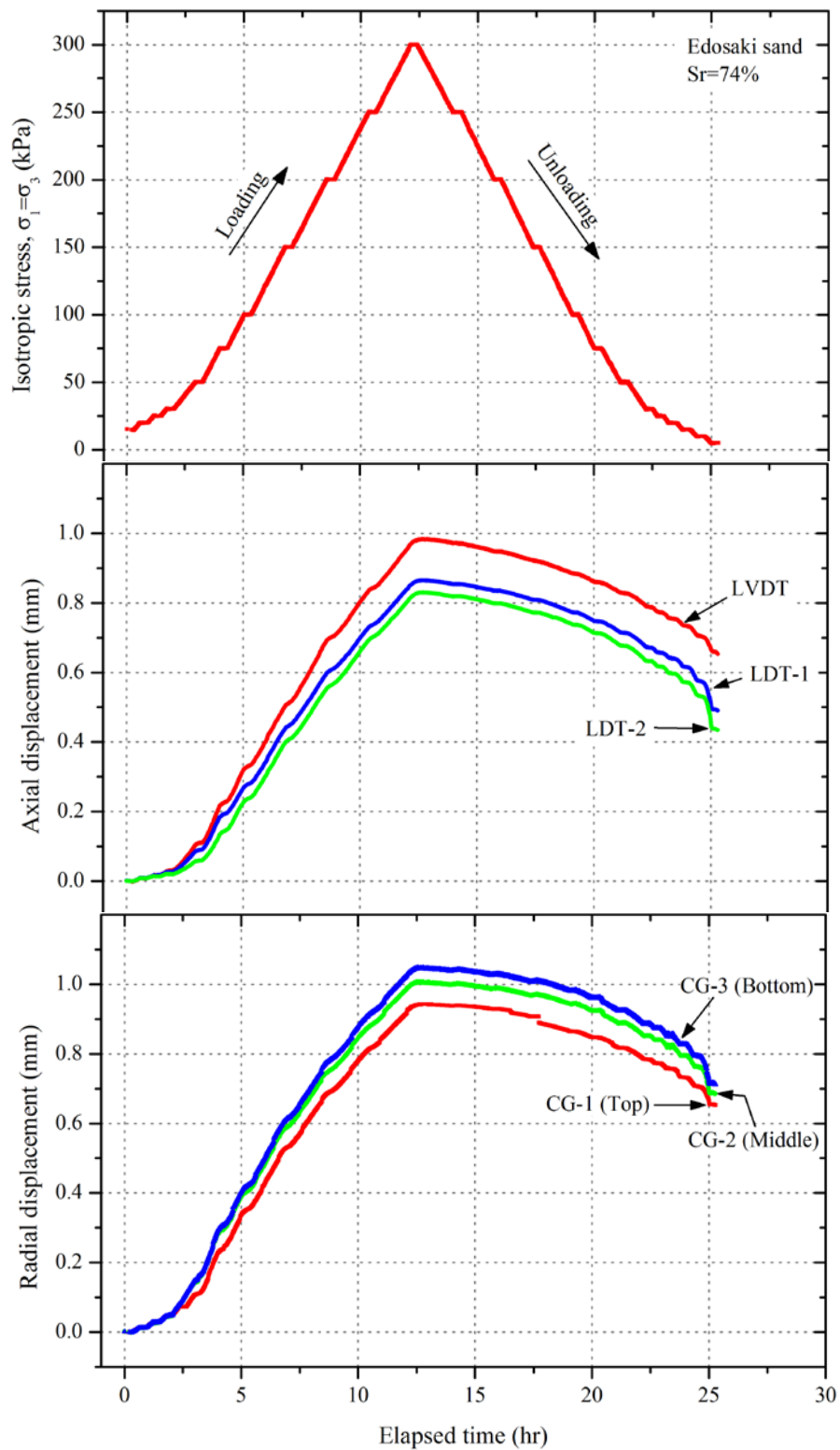


Figure 6.22: Deformation characteristics of unsaturated specimen, $S_r=74\%$; (a) Variation of isotropic stress; (b) Comparison of axial displacement transducers; (c) Radial deformation characteristics.

6.3.5 Effects of Soil Moisture on Wave Velocities

Figure 6.23 summarizes the effects of saturation ratio on corrected shear wave velocity, V_s'' , at various confining pressures during unloading of isotropic stress, whereas the corresponding response during isotropic stress increment (loading path) is shown in Figure 6.24. As explained in previous section, results have been normalized to $e = 0.673$, and $\gamma_d = 1.578 \text{ g/cm}^3$ in order to simplify the comparison. Clear relationship between saturation ratio and shear wave velocities can be observed. It is notable that S -wave velocity for dry soil was low and it increased to a peak value at around 20% saturation ratio. Increasing saturation ratio beyond the peak value of 20% caused a decrease in S -wave velocity. However, the rate of decrease in V_s diminished as the soil approached saturation state. Although no significant difference in V_s'' was observed during loading and unloading stages, but still the curves during unloading stage were more smooth due to small variation of void ratio.

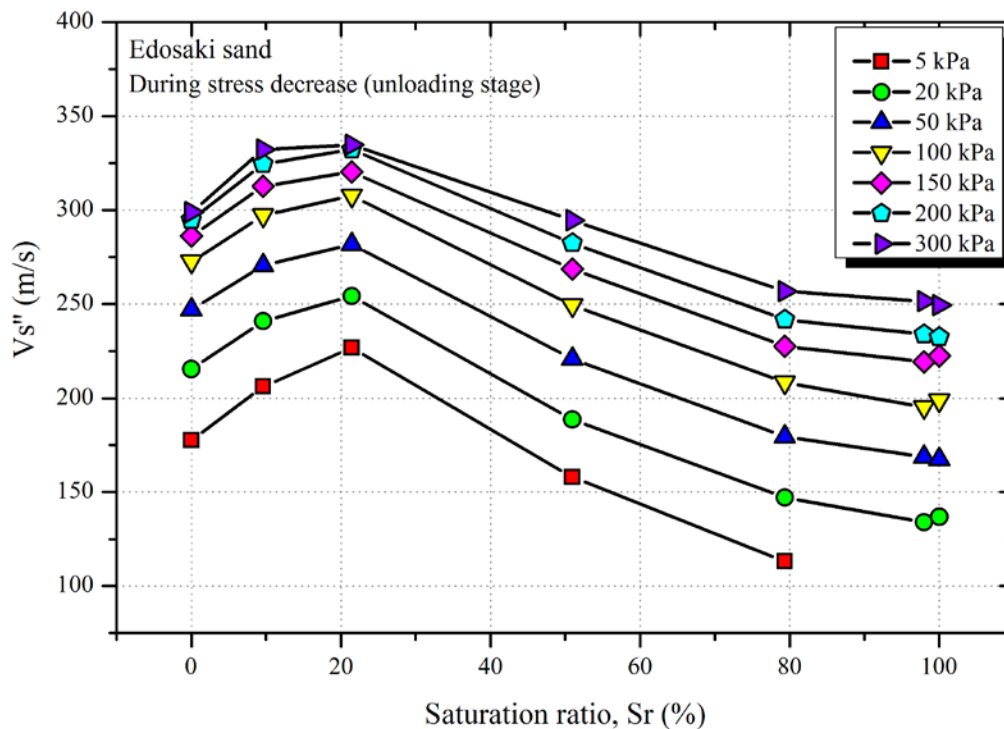


Figure 6.23: Behavior of V_s'' with soil saturation during unloading of isotropic stress in *ICCW* tests.

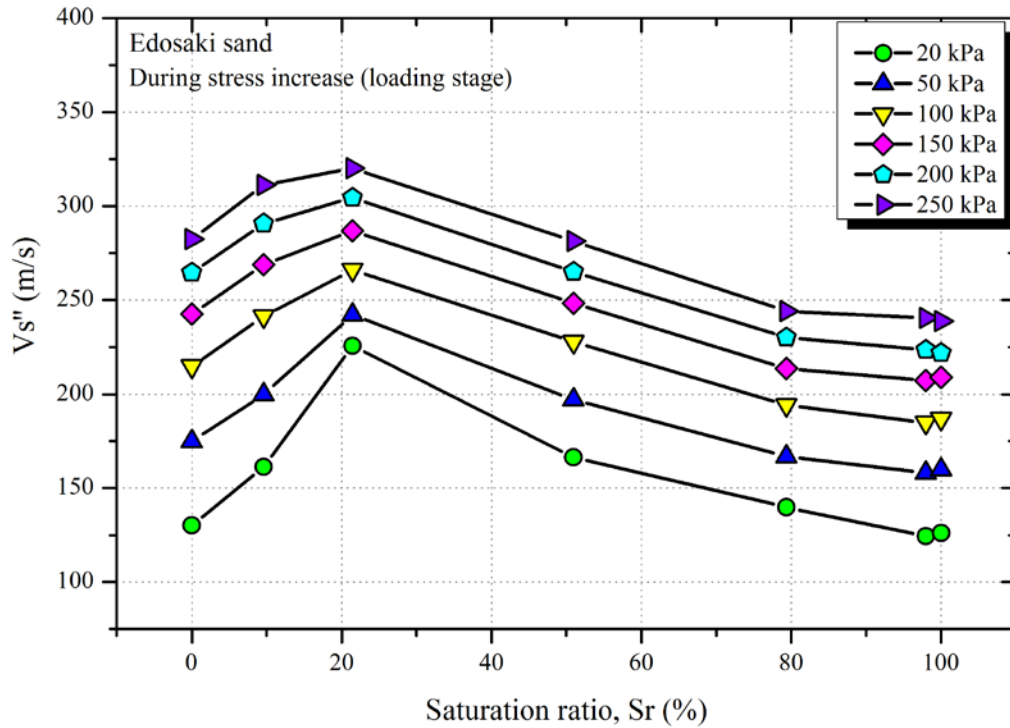


Figure 6.24: Behavior of V_s'' with soil saturation during loading of isotropic stress in *ICCW* tests.

Figure 6.25 and Figure 6.26 show the behavior of compression wave velocities corrected for void ratio and density, V_p'' , during unloading and loading of isotropic stress respectively. For saturated conditions, compression wave velocities are observed to approach the speed of sound in water (~ 1500 m/s – 2000 m/s); as under saturated conditions the compression wave propagates through the water phase instead of soil skeleton (Kokusho, 2000; Tsukamoto et al., 2002). This behavior is quite different to the one observed for shear wave velocities. Ignoring saturated conditions, the trend of *P*-waves is identical to *S*-wave velocities (Figure 6.25(b), and Figure 6.26(b)). Since the variation of void ratio during unloading phase was very small, hence the behavior of V_p'' during unloading (Figure 6.25) was observed to be more consistent/smooth compared to the loading path (Figure 6.26).

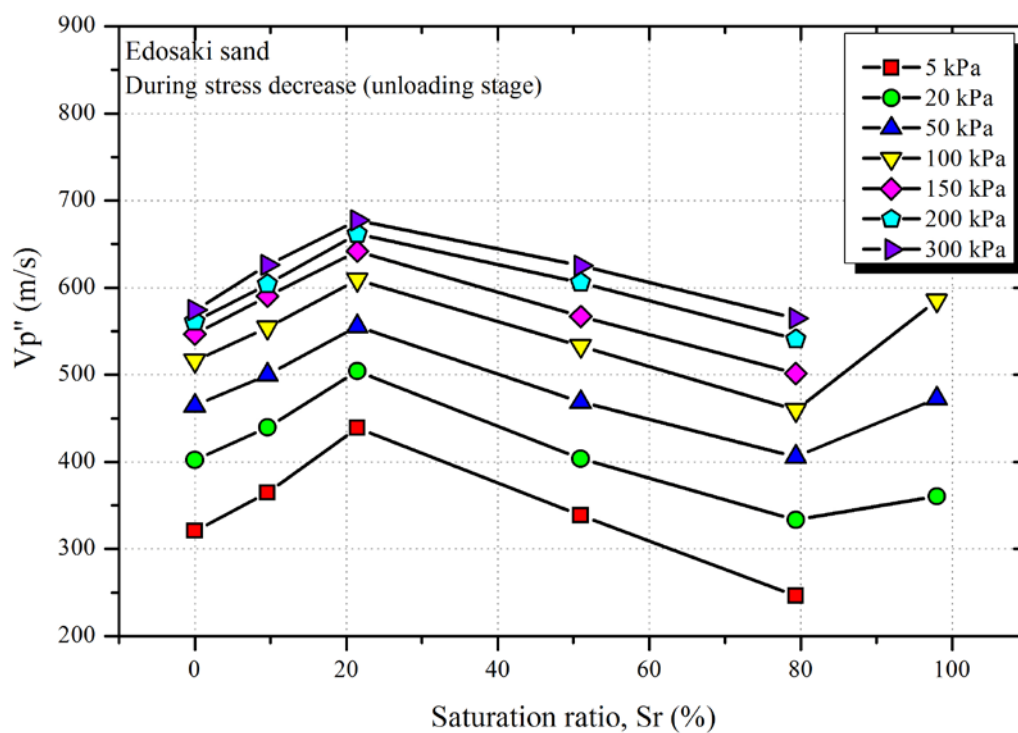
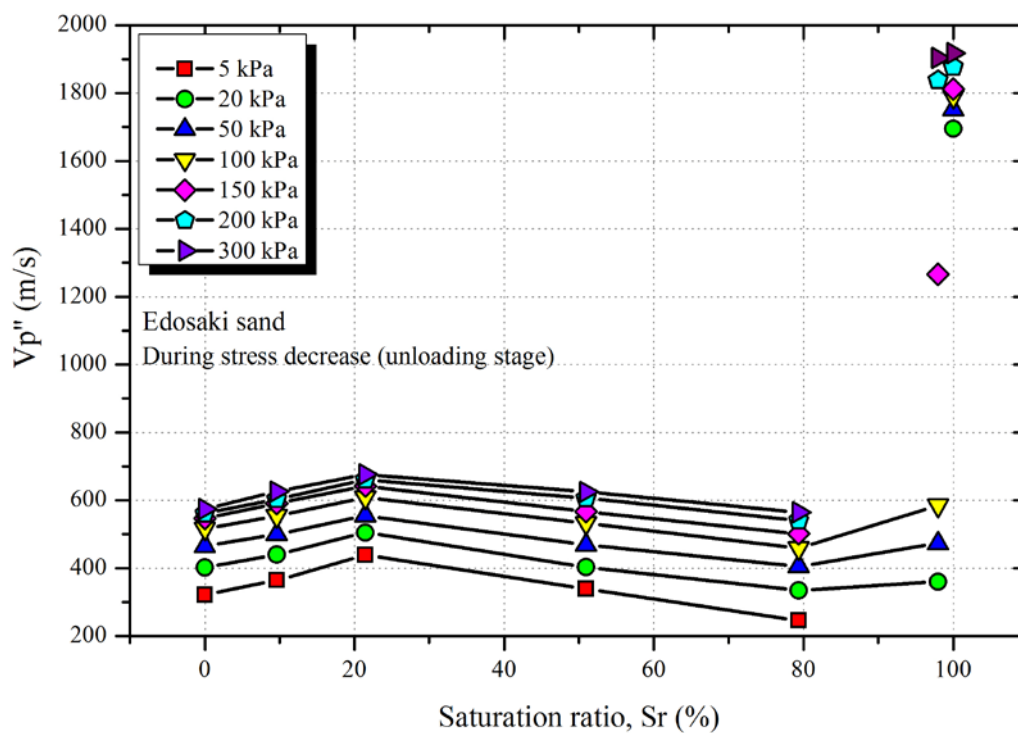


Figure 6.25: Behavior of V_p'' with soil saturation during unloading of isotropic stress in ICCW tests; (a) V_p'' ; (b) V_p'' (Zoomed-in).

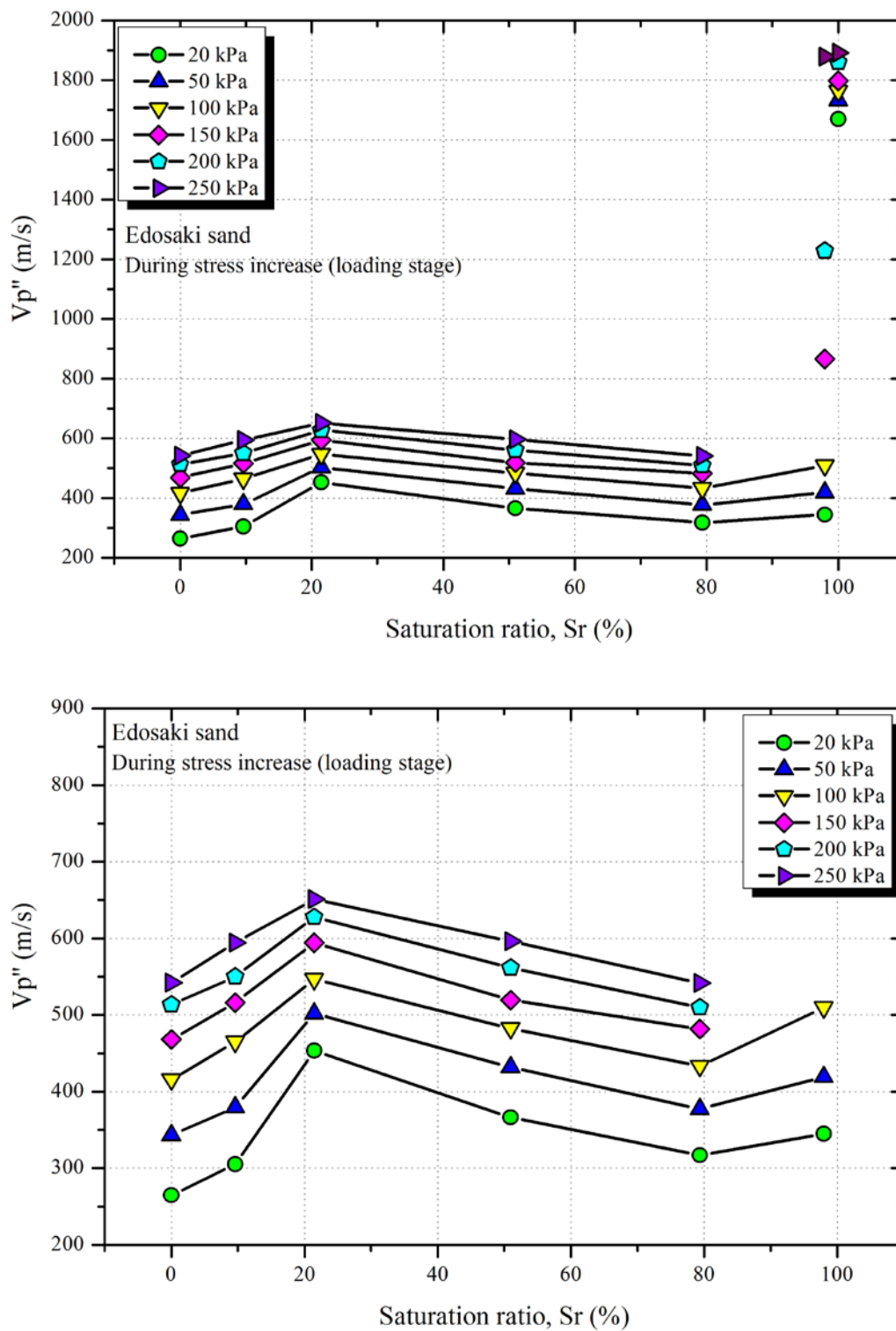


Figure 6.26: Behavior of $V_{p''}$ with soil saturation during loading of isotropic stress in ICCW tests; (a) $V_{p''}$; (b) $V_{p''}$ (Zoomed-in).

The effects of void ratio and density normalization can be observed by comparing Figure 6.23–Figure 6.26 with Figure 6.27 and Figure 6.28. Since the specimens were prepared at a very high initial density, the overall change in void ratio while undergoing loading and unloading of stress was not very large. Therefore, the possible variation in wave velocity due to changing void ratio was already limited. This is why, the general trends of wave velocities without normalization are not much different to those after normalization.

Considering the application of these results for predicting landslides, the initial saturation ratio on slope surface may be around 30% which increases to 80%-90% during heavy rainfall. From Figure 6.23–Figure 6.28 it can be deduced that, the corresponding reduction in *P*-wave and *S*-wave velocities would be around 30%-40%. This reduction in wave velocities is prominent enough to be used for landslide prediction. Further details of field application of elastic wave velocities for landslide prediction are presented in Chapter 9.

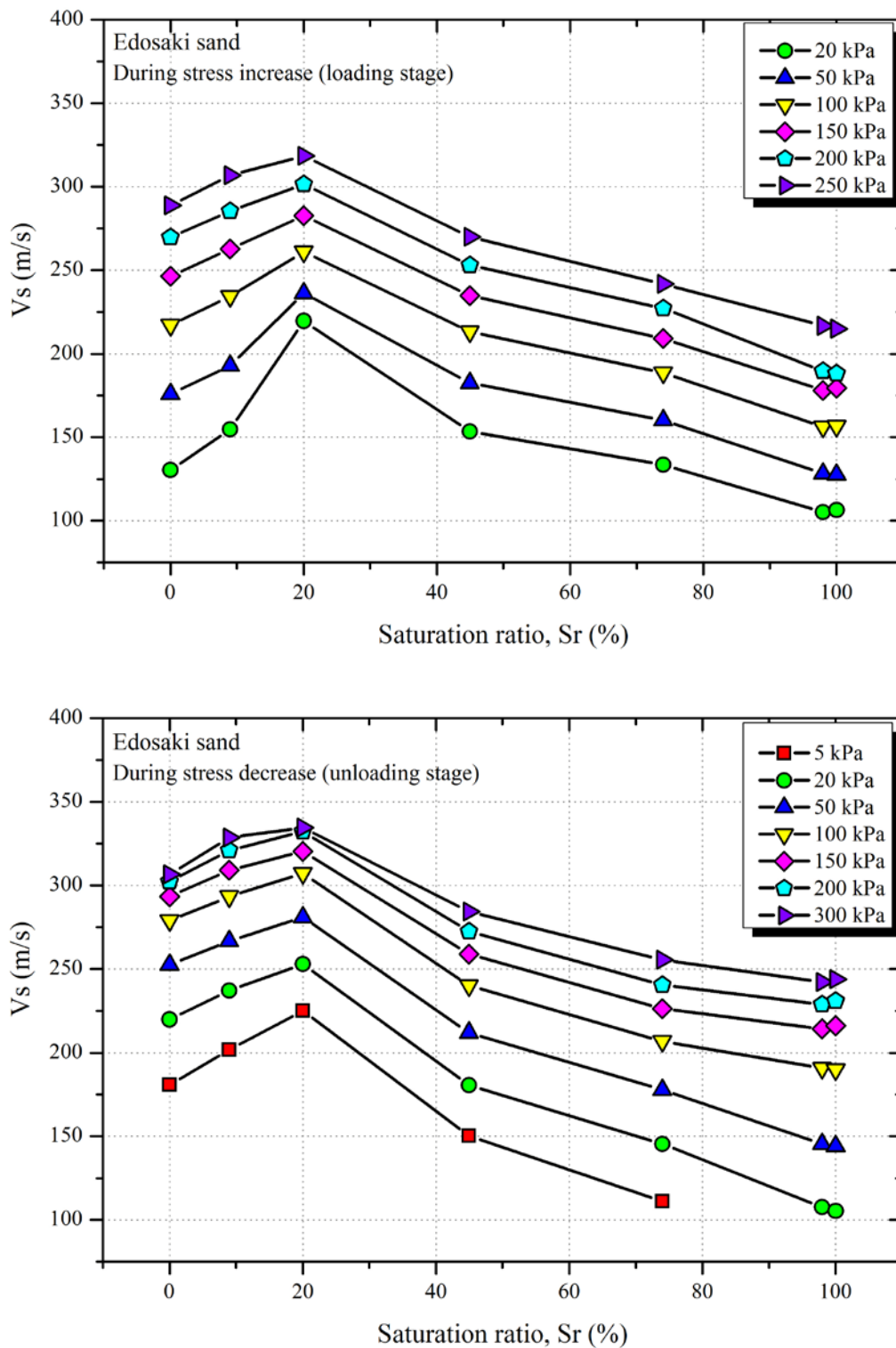


Figure 6.27: Behavior of shear wave velocity, V_s , with soil saturation in ICCW tests; (a) During loading phase; (b) During unloading phase.

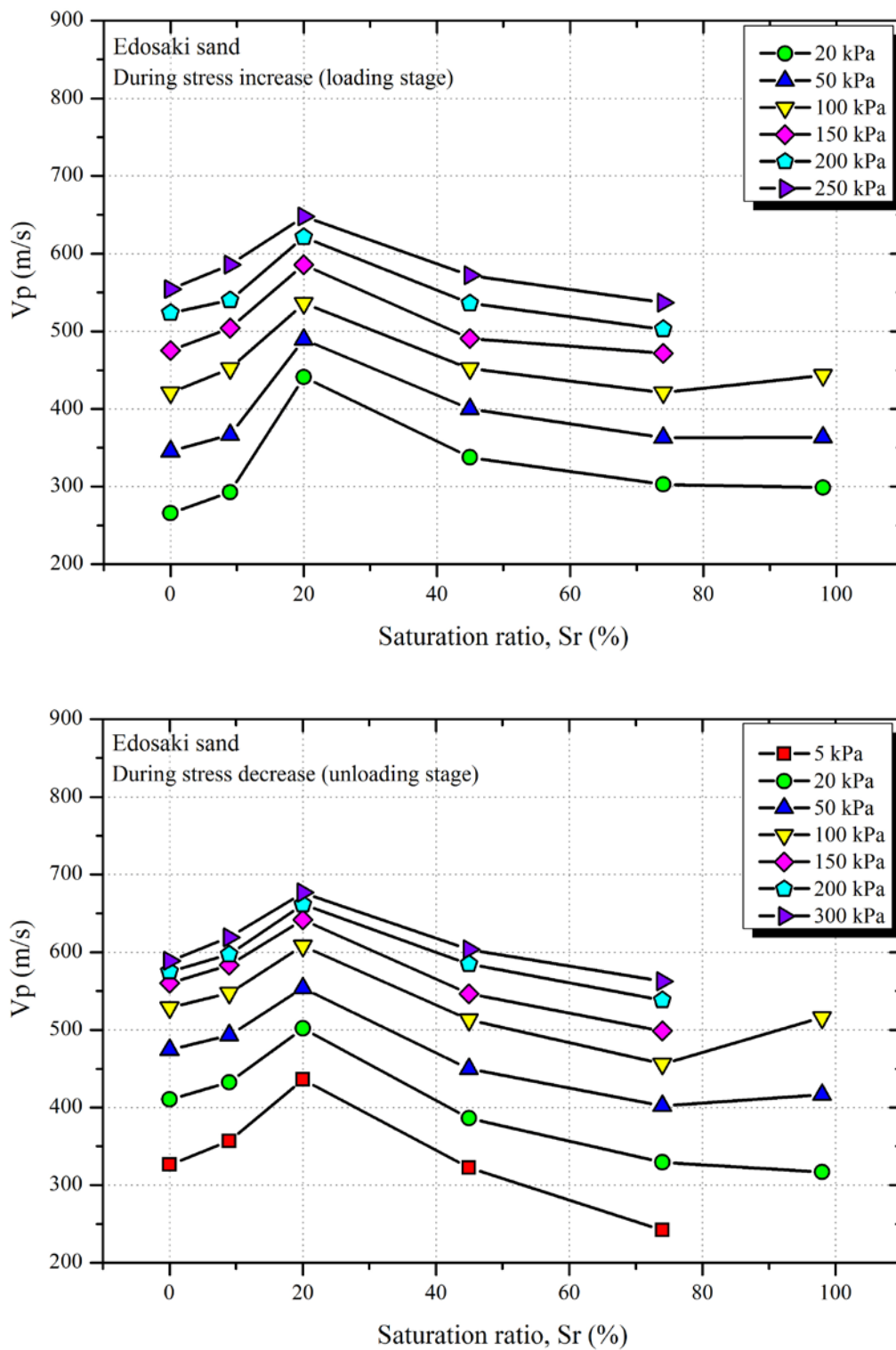


Figure 6.28: Behavior of compression wave velocity, V_p , with soil saturation in ICCW tests; (a) During loading phase; (b) During unloading phase.

6.4. ISOTROPIC COMPRESSION WATER INJECTION (ICWI) TESTS

The general behavior of V_s and V_p with changing soil moisture was explained by *ICCW* tests. However, the results of *ICCW* tests presented in Figure 6.23 to Figure 6.28 does not replicate the actual wetting of soil during rainfall; in which rain water gradually percolates into soil thereby changing its moisture content. The primary goal of this test series (*ICWI* tests) was to confirm the behavior of V_s and V_p during water injection; and to ascertain its dependence on wetting method.

6.4.1 Methodology

The specimens were prepared by tamping Edosaki sand to the desired density directly over the ceramic disk (sealed to the base pedestal). Each specimen was set to the desired isotropic confining pressure and then water was injected by applying constant infiltration pressure on top of the burette connected with ceramic disk. As the water percolated into the specimen through the ceramic disk, saturation ratio of specimen changed. The amount of water entering the specimen was determined by recording water level in the burette by means of differential pressure transducer (*DPT*). Wave velocity readings were taken at regular intervals during the water injection process. Table 6.2 summarizes the initial test conditions of various test specimens used in this set of experiments.

Since water was injected essentially through the base of specimen, thus naturally it was expected to wet the bottom of specimen first. To ensure a more uniform distribution of injected water, a helical shaped filter paper was placed inside the latex membrane in such a way that it wrapped around the specimen. The use of helical filter paper ensured more uniform water distribution upon water injection through the base. A detailed analysis of filter paper use for uniform moisture distribution is presented in Section 7.5 of Chapter 7.

For the experiments performed on initially dry specimens, the ceramic disk was not initially saturated (specimens were prepared over dry ceramic disk) since very high matric suction of dry specimens would quickly suck all the water from ceramic disk. Water line connecting the burette with ceramic disk was closed during sample

preparation so as to avoid water flowing into the specimen before the test. At the start of water injection some amount of water was consumed in saturating the initially dry ceramic disk, chamber underneath it, and the associated piping. The amount of water required to saturate the ceramic disk, its chamber, and piping was determined by comparing the weight of the saturated assembly with that of dry assembly, i.e.

$$\begin{array}{l} \text{weight of water} \\ \text{for saturating} \\ \text{ceramic disk} \end{array} = \begin{array}{l} \text{weight of saturated} \\ \text{ceramic disk assembly} \end{array} - \begin{array}{l} \text{weight of dry} \\ \text{ceramic disk assembly} \end{array} \quad (6.13)$$

The amount of water required for saturating the system was thus computed immediately at the start of water injection. This was then deducted from the total amount of water draining out from the burette to calculate the corrected saturation ratio of specimens at any time during water injection. An initially saturated ceramic disk was however used in case of moist specimens. Since the ceramic disk at the base pedestal was used for water injection, thus the measurement of matric suction was not possible in these tests.

Majority of the specimens used in *ICWI* tests were initially dry and thus had very high initial matric suction (possibly of the orders of 10^6 kPa). Thus the miniature pore water pressure sensor could not be used as it de-saturated soon after it was brought in contact with dry soil. Therefore, the use of miniature pore pressure sensors was limited to *CSWI* tests.

P-wave and S-wave velocities were determined at regular intervals during the course of experiments. Excitation frequency of 10 kHz was found suitable for the determination of V_p and V_s in this series of experiments. Single cycle of sinusoidal wave was used as input waveform. Additionally for each reading, twenty measurements of each type of wave were stacked in order to remove any anomalies and to enhance the signal to noise ratio of the signals.

6.4.2 Initially Dry Specimens

A constant infiltration pressure was applied at the top of burette which was connected with ceramic disk. This ensured a nearly uniform water injection through the base of specimen. The variation of saturation state of soil with water injection is shown in

Figure 6.29. Since the rate of water injection was constant, so saturation ratio (S_r) increased linearly with time. However, the rate of S_r was decreased once water started draining out from the specimen.

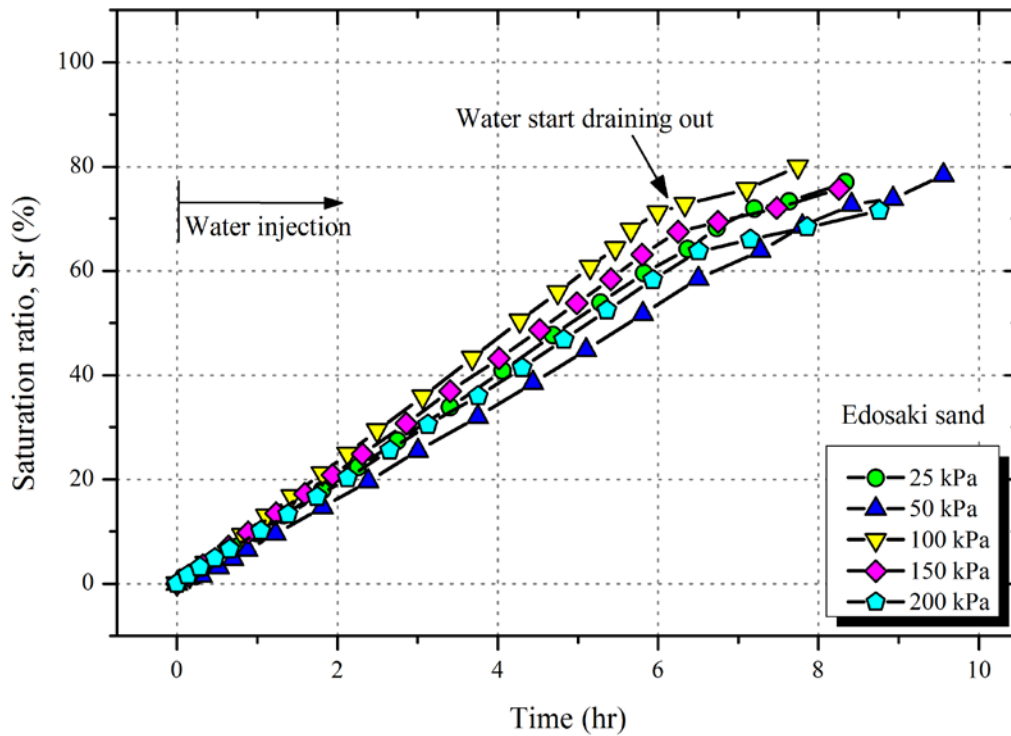


Figure 6.29: Variation in saturation ratio, S_r , of ICWI specimens upon water injection.

All the specimens exhibited compressive behavior upon water injection, as shown in Figure 6.30. The magnitude of volumetric compression however, increased with isotropic stress level which is consistent with fundamental principles of soil mechanics.

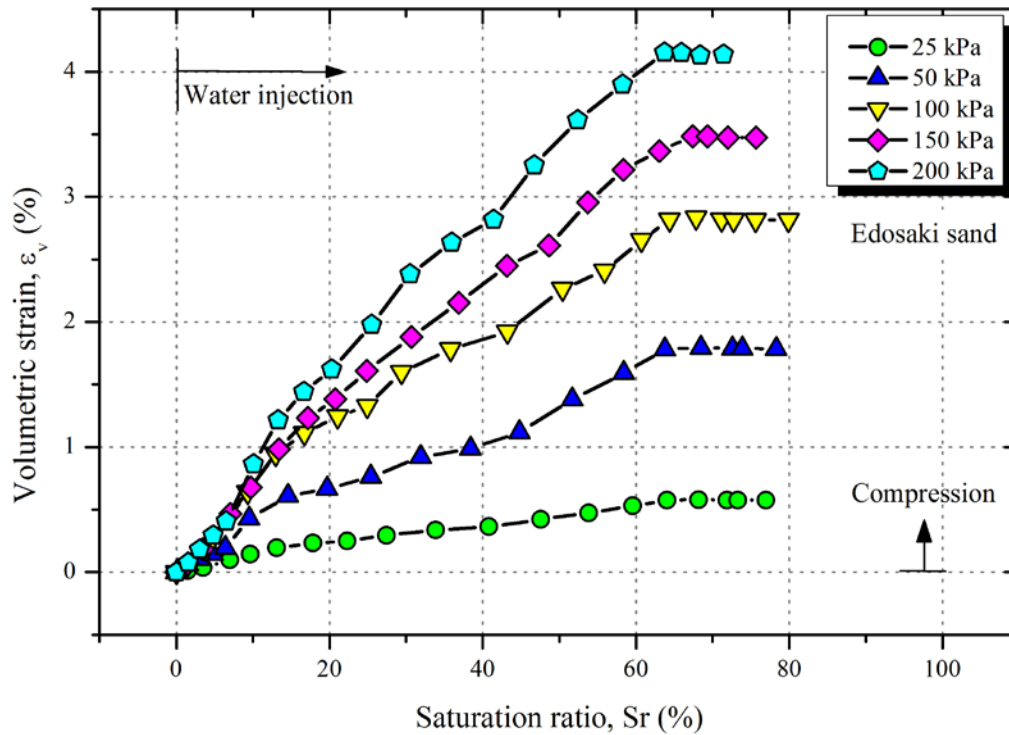


Figure 6.30: Volume response of *ICWI* specimens upon water infiltration.

Figure 6.31 shows the behavior of shear wave (V_s), and compressive wave velocities (V_p) on increasing soil moisture by injecting water from an initially dry state. Both V_s and V_p increase slightly, before start decreasing with S_r . The initial increase in wave velocities may be attributed to the increased particle to particle contact area due to adsorbed water film around soil particles. Similar phenomenon has previously been reported by Cho and Santamarina (2001) and also by Alramahi et al. (2009).

Although, the overall trend is somehow consistent with the results obtained from *ICCW* tests but the magnitude of V_s and V_p differ from those presented in Figure 6.23 & Figure 6.25. This difference is mainly due to the difference in void ratio. To draw a better comparison, wave velocities were normalized to void ratio, $e = 0.673$, and dry density, $\gamma_d = 1.578 \text{ g/cm}^3$ by using Eq. 6.8 and Eq. 6.11. The normalized shear wave (V_s'') and compression wave velocities (V_p'') presented in Figure 6.32 show reasonable consistency, in trend as well as magnitude, with *ICCW* tests.

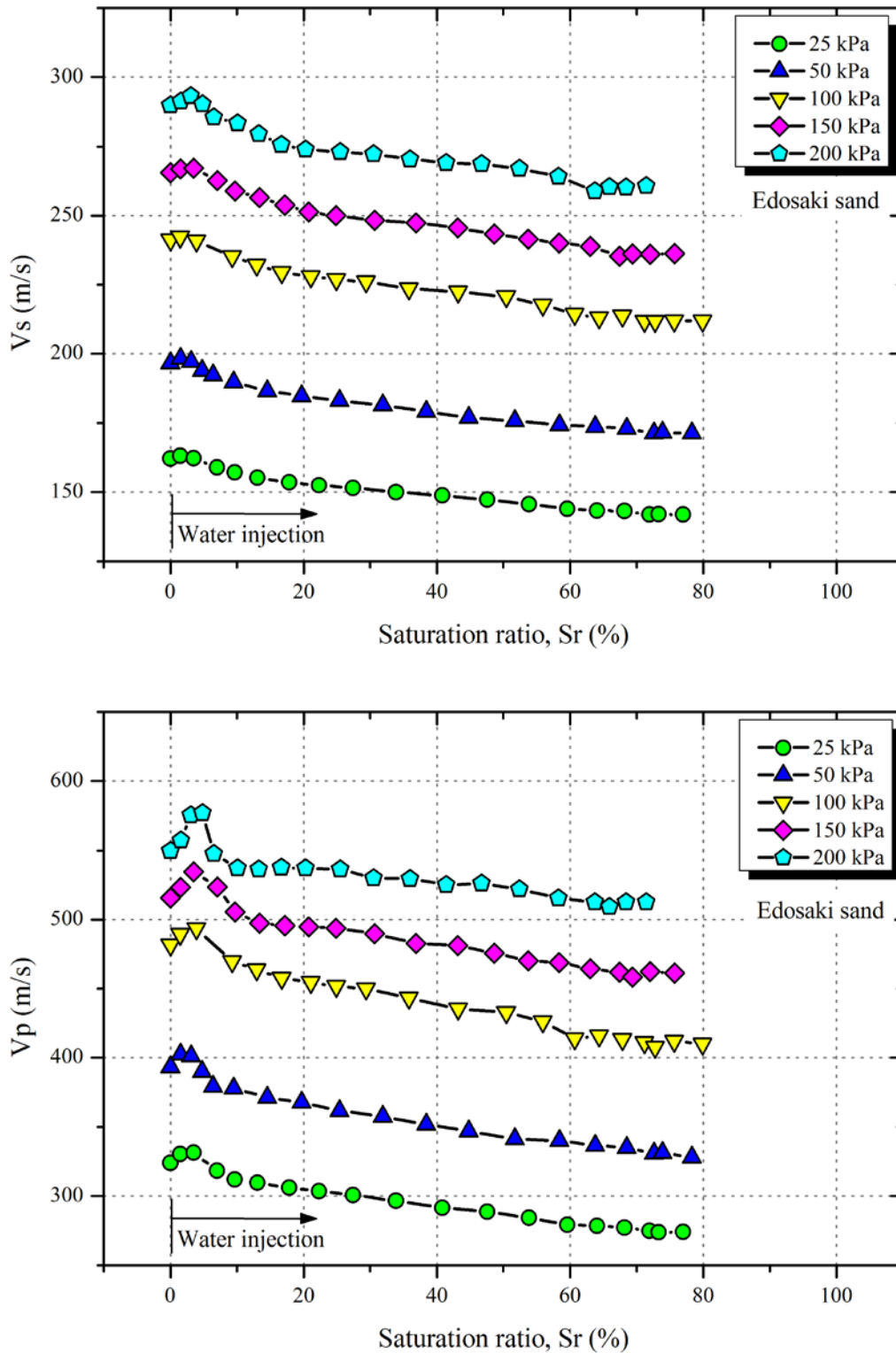


Figure 6.31: Variation of elastic wave velocities upon water injection in *ICWI* tests; (a) Shear wave velocity, V_s ; (b) Compression wave velocity, V_p .

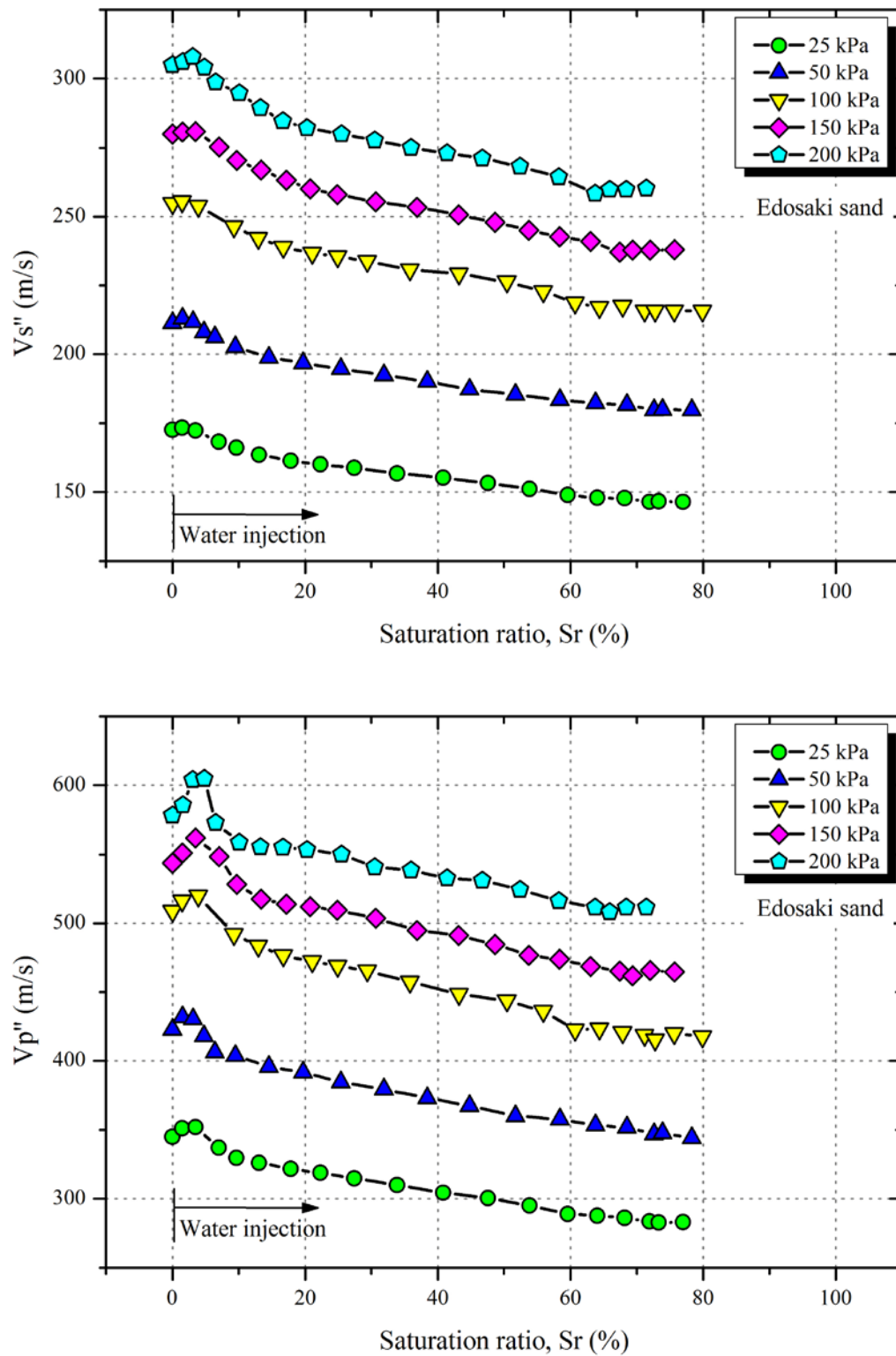


Figure 6.32: Variation of normalized elastic wave velocities upon water injection in ICWI tests; (a) Normalized shear wave velocity, V_s'' ; (b) Normalized compression wave velocity, V_p'' .

6.4.3 Initially Moist Specimens

Some *ICWI* tests were performed on partially saturated specimens ($S_r = 20\%$). Three identical specimens were subjected to different isotropic confining pressures. Water was then injected through the bottom ceramic disk by applying constant infiltration pressure on top of the burette connected with the ceramic disk. The variation of saturation ratio upon water injection is shown in Figure 6.33.

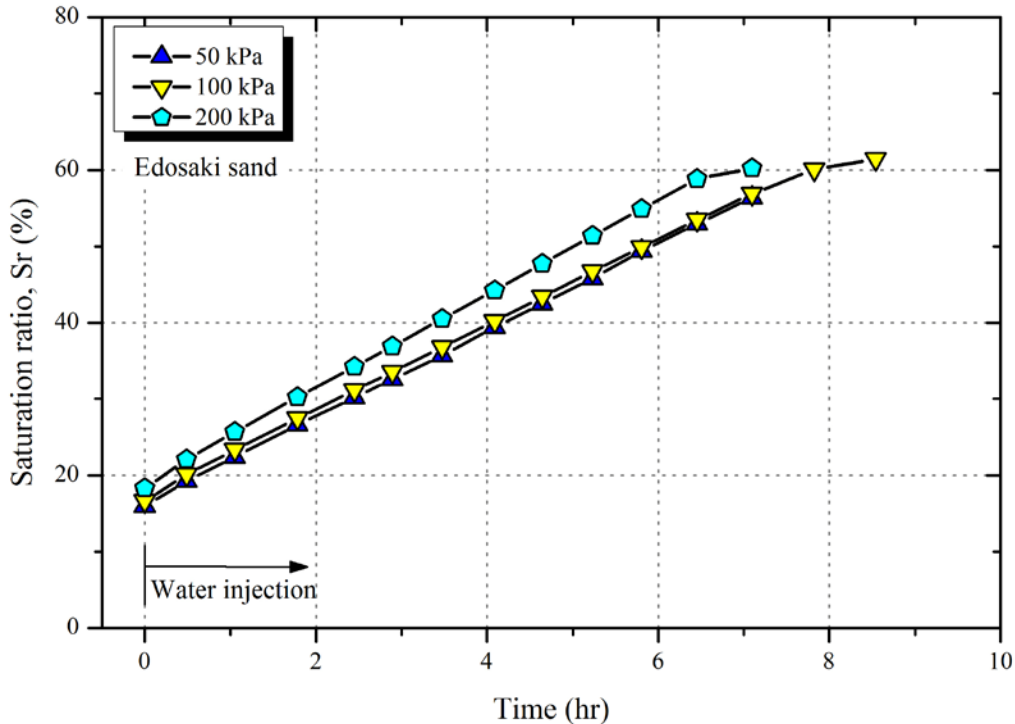


Figure 6.33: Variation in saturation ratio, S_r , of initially moist *ICWI* specimens upon water injection

Figure 6.34 shows the volume change behavior of specimens. Extremely small strain was observed initially upon water injection. This extremely small strain may be attributed to the very high initial relative density of specimens ($D_r \approx 90\%$). After considerable water was injected, the specimens started to shrink in volume (compressive strains). This compression continued, until water started draining out from specimen causing it to dilate by small amount. The initial compression upon water injection may be because of the collapse of soil fabric due to loss of matric suction. Pore water pressure gradually develops upon water injection, and once pore

pressure exceeds the effective stress, the specimen dilates allowing the pore water to drain out.

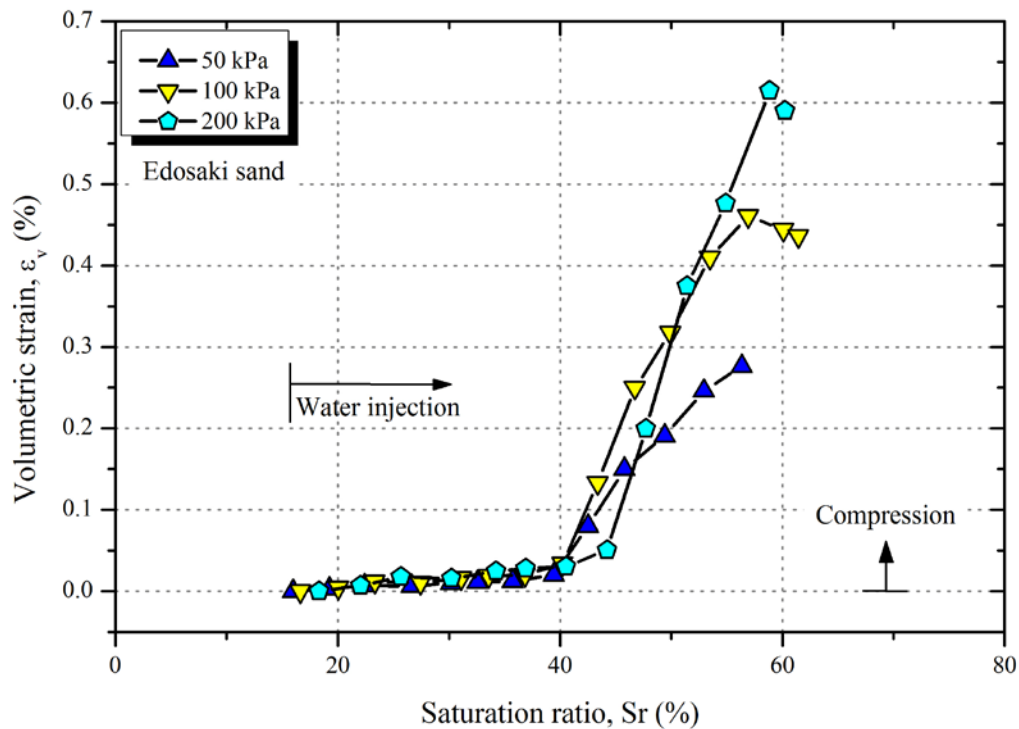


Figure 6.34: Volume response of initially moist *ICWI* specimens upon water infiltration.

Figure 6.35 shows normalized shear wave (V_s''), and compression wave velocities (V_p'') plotted against saturation state of soil. Wave velocities were normalized corresponding to a designated void ratio, $e = 0.673$, and dry density, $\gamma_d = 1.578 \text{ g/cm}^3$ by using Eq. 6.8 and Eq. 6.11. Both V_s'' and V_p'' show a distinct decreasing trend with saturation ratio, and decreased by about 20% to 25% when saturation ratio of soil was increased from 20% to about 60%. This confirms the sensitivity of wave velocities to soil saturation state; and thus can be utilized on actual slope surfaces to estimate the saturation state of soil. Wave velocities before normalization, also show similar trends, as can be noticed from Figure 6.36.

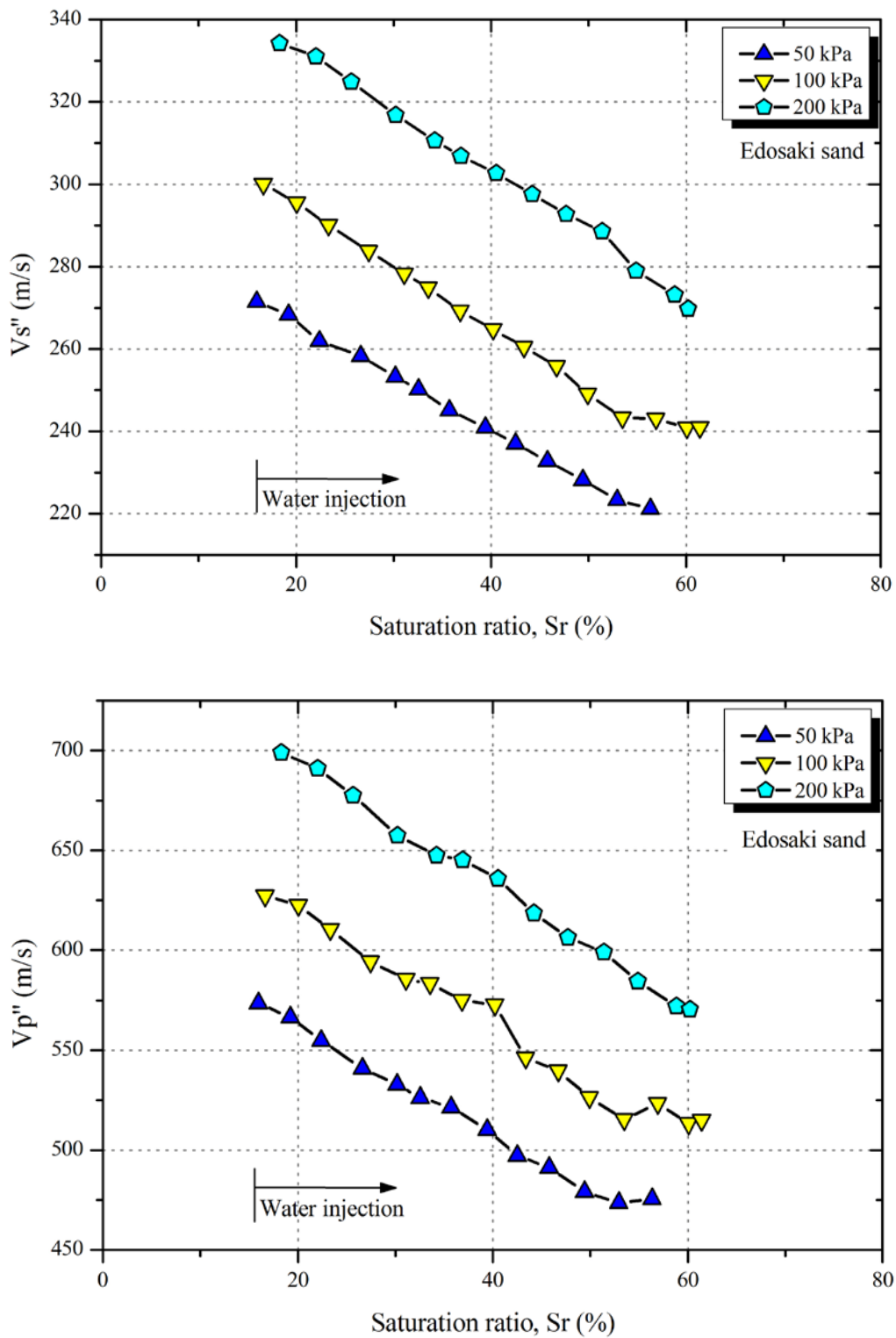


Figure 6.35: Variation of normalized elastic wave velocities upon water injection in initially moist *ICWI* tests; (a) Normalized shear wave velocity, V_s'' ; (b) Normalized compression wave velocity, V_p'' .

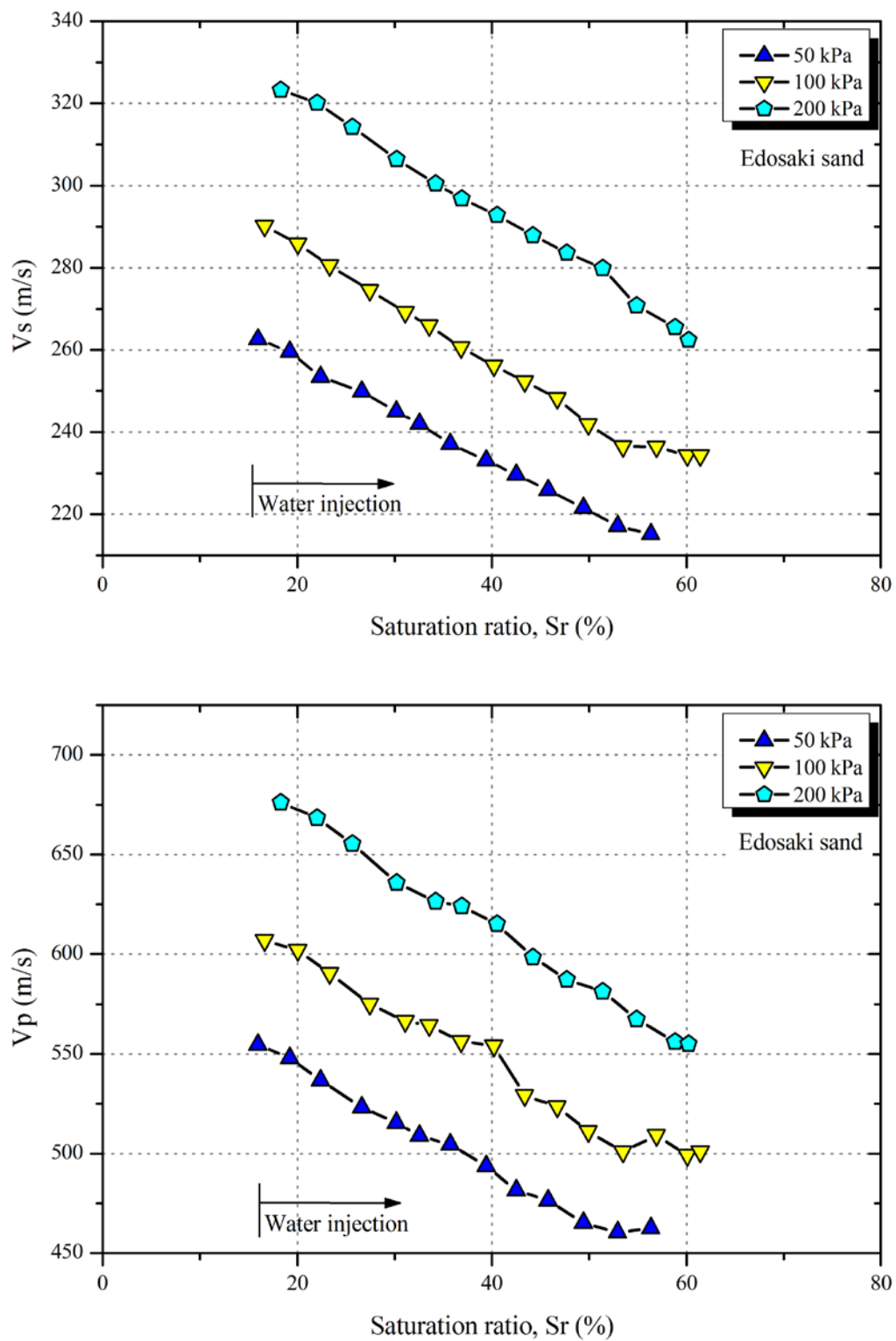


Figure 6.36: Variation of elastic wave velocities upon water injection in initially moist ICWI tests; (a) Shear wave velocity, V_s ; (b) Compression wave velocity, V_p .

As discussed previously with reference to Figure 6.34, extremely small strains were observed during the initial phase of water injection. This phenomenon is very interesting with reference to wave velocities, since the behavior of wave velocities only due to changing soil moisture (no volume change) can be observed. Figure 6.37 plots the behavior of V_s and V_p with volumetric strain. In the initial phase of plot, wave velocities decrease without any appreciable change volumetric strain. This shows that the decrease in wave velocities is solely due to moisture change and volumetric strains had negligible effect on wave velocities.

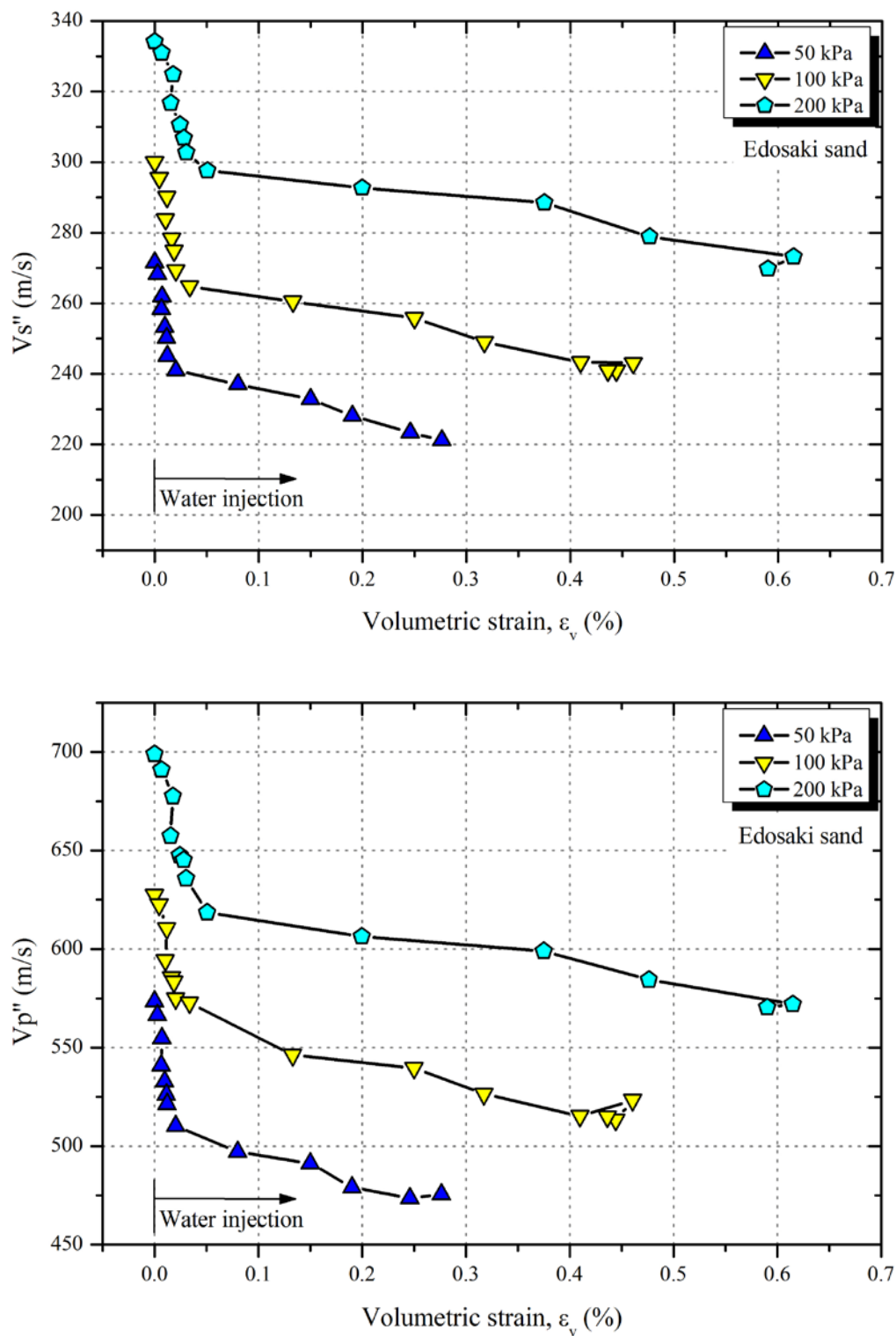


Figure 6.37: Wave velocities plotted against volume response of specimens during ICWI tests on initially moist specimens; (a) Normalized shear wave velocity, V_s'' ; (b) Normalized compression wave velocity, V_p'' .

6.5. WAVE VELOCITIES AS A FUNCTION OF MATRIC SUCTION

The soil water characteristic curve (*SWCC*) of soil is generally obtained by a pressure plate or a tempe pressure cell apparatus (Fredlund et al., 2012). Such a test was not part of this study. However, initial matric suction at different saturation ratios was determined during setting up specimens for *ICCW* tests. After preparing the specimen and setting up the triaxial cell, a small isotropic confining pressure (about 10 kPa) was applied to support the specimens in standing. This isotropic stress was maintained for a long duration so as to allow matric suction to stabilize. A constant value of matric suction was generally obtained in 24~48 hours, as shown in Figure 4.10 (Chapter 4). Once matric suction was equalized, it was recorded as initial matric suction of soil specimen at a particular saturation ratio. Further discussion on the determination of initial matric suction is presented in Section 4.3.1.5 of Chapter 4. Initial matric suction from various specimens was recorded and plotted against saturation ratio, as shown in Figure 6.38.

However, it is to be noted that the air entry value (*AEV*) of ceramic disk governs the maximum magnitude of matric suction that can be measured with the assembly. Since the *AEV* of ceramic disk was limited to 100 kPa, hence the ceramic disk/pressure sensor assembly was not able to measure suction greater than 100 kPa. In such cases when matric suction of specimen exceeded *AEV* of ceramic disk, air from the specimen broke the capillary barrier at the soil-ceramic disk interface and diffused through the ceramic disk. This diffused air entered the pipes connecting the ceramic disk with external pore pressure transducer, thus disturbing the readings of matric suction, as shown in Figure 6.38.

Moreover, *SWCC* data of Edosaki sand from Gallage and Uchimura (2010) was back-calculated to present *SWCC* in terms of saturation ratio. Considering the effects of density on *SWCC* (Yang et al., 2004; Gallage & Uchimura, 2010; Zhou et al., 2012), the *SWCC* was selected in such a way to possess similar density as *ICCW* tests. Similarly, the experimental data was fitted by using Eq. 6.14 proposed by Fredlund and Xing (1994).

$$\theta_v = \left[\frac{\theta_s}{\{\ln [e + (\psi / a)^n]\}^m} \right] \left[1 - \frac{\ln (1 + \psi / \psi_r)}{\ln (1 + 10^6 / \psi_r)} \right] \quad (6.14)$$

where,

θ_v = volumetric water content

θ_s = saturated volumetric water content

a = soil parameter related to *AEV* of soil (kPa)

n = soil parameter related to slope between *AEV* and residual suction on *SWCC*

m = parameter related to residual water content portion of *SWCC*

e = natural number = 2.71828...

ψ = soil matric suction (kPa)

ψ_r = residual soil suction (kPa) corresponding to residual water content, θ_r

Eq. 6.14 is commonly used for fitting *SWCC* data and provides a good fit for sand, silt, and silty sand over a wide range of matric suction. The fitting parameters in Eq. 6.14 (a , m , n) describe the shape of the *SWCC*. To best-fit the experimental data, these parameters can be obtained by least squares optimization method using experimental data and nonlinear curve-fitting algorithms as explained by (Fredlund & Xing, 1994). The air-entry value, residual suction, and fitting parameters (a , m , n) of *SWCC* were obtained using *SoilVision* computer software (*SoilVision systems Ltd. Ver. 4.14*). The fitting parameters used for *SWCC* shown in Figure 6.38 are $\psi_r=10.13$ kPa, $a=3.320$ kPa, $m=0.403$, and $n=5.453$.

Figure 6.38 shows that the data of initial matric suction from *ICCW* tests, which is although limited but agrees well with the *SWCC* obtained from Gallage and Uchimura (2010) as well as Fredlund and Xing (1994). Therefore, it was assumed reasonable to consider this *SWCC* as the representative of specimens used in *ICCW* tests.

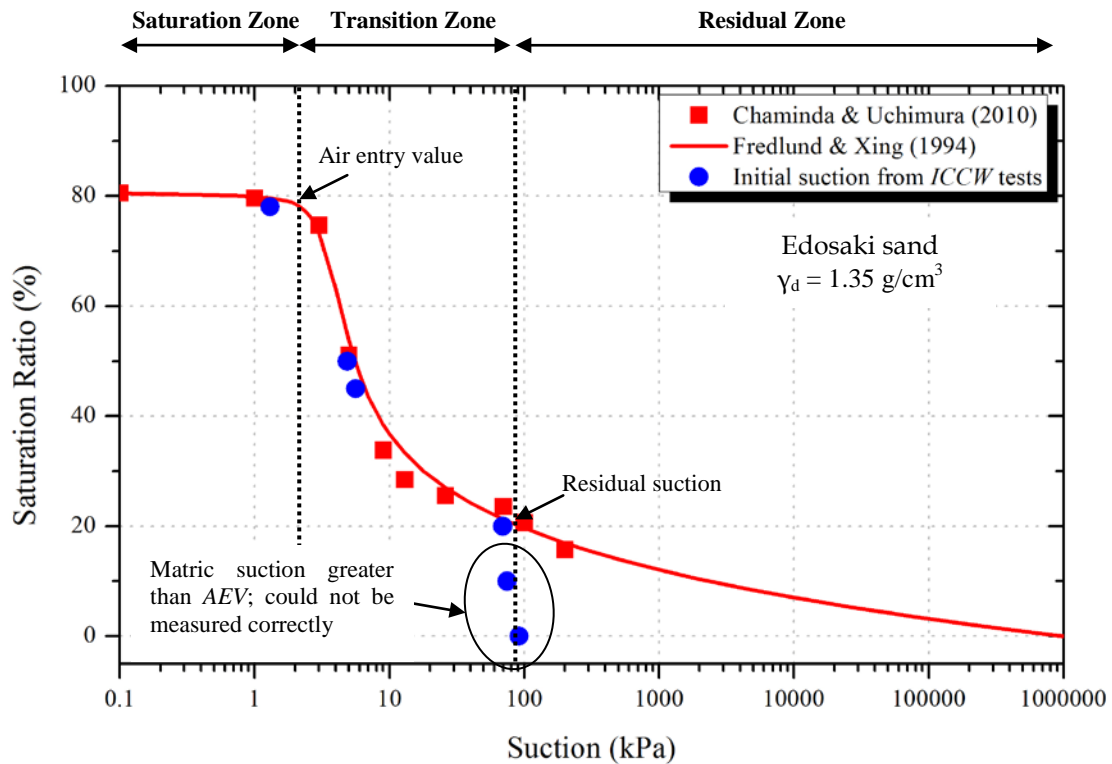


Figure 6.38: Soil water characteristic curve (SWCC) of Edosaki sand based on initial suction of *ICCW* tests, test data from Gallage and Uchimura (2010), and Fredlund and Xing (1994) curve fitting.

SWCC is typically divided into three zones; (i) saturation zone, (ii) transition zone, and (iii) residual zone. In the saturation zone, all the voids are completely filled with water, thus the matric suction is extremely low. In the transition zone, inter-particle voids are filled partially with water and partially with air, and changes in soil moisture are sharply reflected by variation of matric suction. In the residual zone, most of the voids are filled with air; water is only coating soil particles in the form of adsorbed water film. This behavior is schematically shown in Figure 6.39.

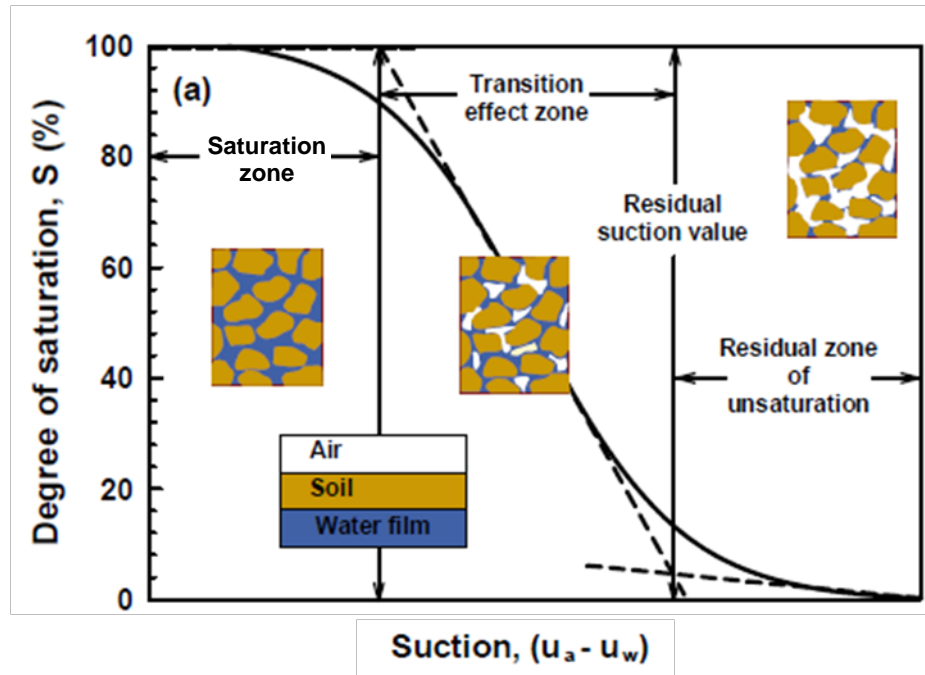


Figure 6.39: Zones of a typical SWCC (after Oh and Vanapalli (2011)).

The behavior of wave velocities, as observed in Figure 6.23 to Figure 6.26 can be explained qualitatively on the basis of soil particle contact points and matric suction, using the SWCC (Oh and Vinapalli, 2011). Figure 6.40 overlays normalized shear wave velocities, V_s'' , (from Figure 6.23) obtained through ICCW tests on SWCC of Edosaki sand. For comparison purposes, the axes of SWCC are exchanged.

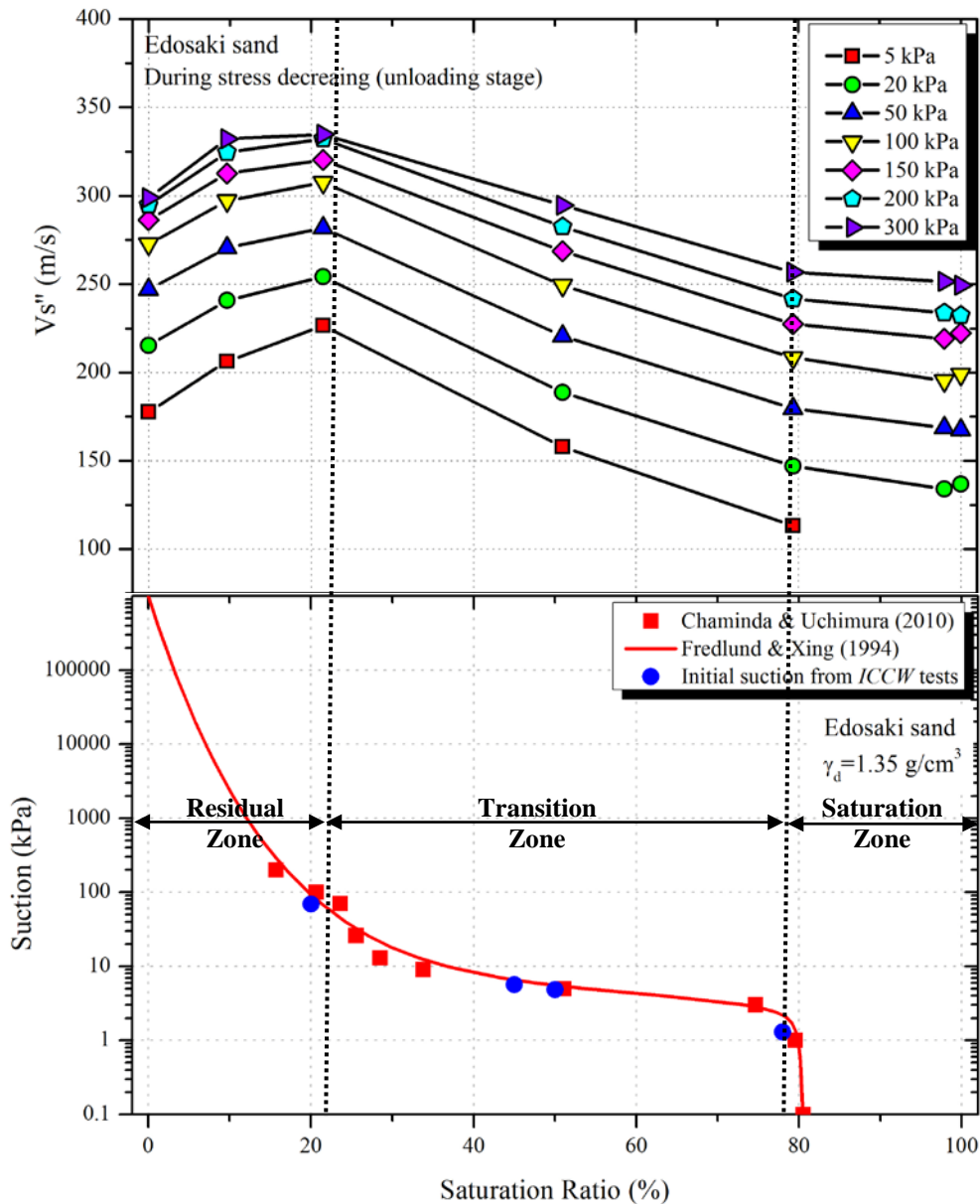


Figure 6.40: Dependence of elastic wave velocities on zones of *SWCC*.

S-wave velocity for dry soil specimen is low since no capillary forces exist and wave is transmitted only through inter-particle contact points (Figure 6.41(a)). However, on increasing saturation ratio, a thin layer of adsorbed water surrounds soil particles; schematically shown in Figure 6.41(b) & Figure 6.41(c). In this condition wave propagates through inter-particle contact points plus the soil-water meniscus points, hence increasing wave velocity. Additionally, the presence of meniscus water also increase the meniscus stresses which in turn increase effective stress and the wave

velocity. This trend continues unless soil reaches optimum saturation (corresponding to maximum wave velocity) beyond which soil matric suction and the corresponding stresses govern wave velocity. Increase in saturation ratio beyond optimum saturation results in loss of matric suction. The corresponding decrease in effective stresses causes reduction in wave velocity. In the saturation zone however, there is negligible change in matric suction, and thus the effective stress, with changing soil moisture. Therefore, the rate of wave velocity decrease becomes lower.

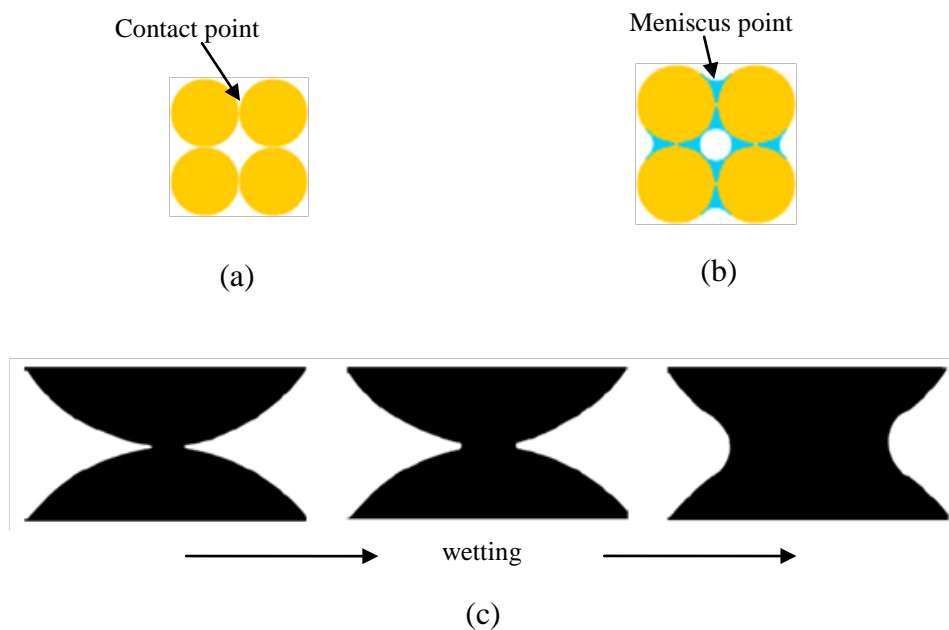


Figure 6.41: Change in the particle contact area with saturation of soil; (a) Dry soil, wave travel possible only through inter-particle ‘*contact points*’; (b) Partially saturated soil, wave travels through inter-particle contacts plus ‘*meniscus points*’; (c) Evolution of inter-particle contact area with soil wetting (after Santamarina (2003)).

A similar explanation is also valid for compression wave velocities. However in the saturation zone, the voids are completely (or nearly) filled with water, and a continuous water phase exists in the specimen. In such a condition, the compression wave propagates through water instead of soil skeleton, and thus very high wave velocities are observed. This phenomenon is not observed in case of shear waves, since the shear strength of water is zero and thus shear waves can not travel through water.

6.6. SUMMARY

This chapter summarizes test results and discussions related to the effects of soil moisture on elastic wave propagation. Level of applied stress, void ratio, and specimen density were found to affect wave velocities, and wave velocities increased with an increase in any of these parameters. The effects of soil saturation on wave velocities were envisaged by means of two distinct triaxial test series. Wave velocities were found to decrease with soil saturation. This behavior was found to be consistent irrespective of the mode of wetting. Also the decrease in wave velocities with increasing saturation was found to be significant enough to be used as an indicator of soil saturation state during rainfall. For saturated soil however, compression wave velocity approached sonic wave velocity in water. Since most of the rain-induced landslides initiate in nearly saturated conditions therefore this phenomenon could serve as a useful indicator to predict the time when soil attains full saturation in the field. Lastly, the behavior of wave velocities with soil saturation was explained on the basis of soil matric suction. It was showed that the behavior of wave velocities with soil saturation state during *ICCW* tests could be divided into two distinct sections. An initial drier section, in which wave velocities increased with saturation because of the increased inter-particle contact area produced by adsorbed water film. And a relatively wet second zone in which wave velocities were mainly governed by matric suction; and wave velocities decreased rapidly with the decrease in soil matric suction.

6.7. REFERENCES

- Alramahi, B., Alshibli, K. A., & Fratta, D. (2009). Effect of Fine Particle Migration on the Small-Strain Stiffness of Unsaturated Soils. *Journal of Geotechnical and Geoenvironmental Engineering*, 136(4), 620-628.
- Bishop, A. W. (1954). The Use of Pore-Pressure Coefficients in Practice. *Geotechnique*, 4(4), 148-152.
- Chien, L.-K., Oh, Y.-N., & Chang, C.-H. (2002). Effects of Fines Content on Liquefaction Strength and Dynamic Settlement of Reclaimed Soil. *Canadian Geotechnical Journal*, 39(1), 254-265.
- Cho, G. C., & Santamarina, J. C. (2001). Unsaturated Particulate Materials-Particle-Level Studies. *Journal of Geotechnical and Geoenvironmental Engineering*, 127(1), 84-96.
- Fredlund, D. G., Rahardjo, H., & Fredlund, M. D. (2012). *Unsaturated Soil Mechanics in Engineering Practice*: John Wiley & Sons.
- Fredlund, D. G., & Xing, A. (1994). Equations for the Soil-Water Characteristic Curve. *Canadian Geotechnical Journal*, 31(4), 521-532.
- Gallage, C., & Uchimura, T. (2010). Effects of Dry Density and Grain Size Distribution on Soil-Water Characteristic Curves of Sandy Soils. *Soils and foundations*, 50(1), 161-172.
- Gu, X.-q., Yang, J., & Huang, M.-s. (2013). Laboratory Investigation on Relationship between Degree of Saturation, B-Value and P-Wave Velocity. *Journal of Central South University*, 20(7), 2001-2007. doi: 10.1007/s11771-013-1701-x
- Hardin, B., & Black, W. (1968). Vibration Modulus of Normally Consolidated Clay. *J. Soil Mech. and Found. Div., ASCE*, 94, 353-369.
- Hardin, B. O., & Drnevich, V. P. (1972). Shear Modulus and Damping in Soils: Design Equation and Curves. *J. Soil Mech. Found. Engng. Div., ASCE* 98(7), 667-691.

- Hardin, B. O., & Richart, F. E. (1963). Elastic Wave Velocities in Granular Soils. *J. Soil Mech. and Found. Div., ASCE*, 89(1), 33-65.
- Iwasaki, T., Tatsuoka, F., & Takagi, Y. (1978). Shear Moduli of Sands under Cyclic Torsional Shear Loading. *Soils and Foundations*, 18(1), 39-56.
- Kokusho, T. (2000). Correlation of Pore-Pressure B-Value with P-Wave Velocity and Poisson's Ratio for Imperfectly Saturated Sand or Gravel. *Soils and foundations*, 40(4), 95-102.
- Lee, C.-J., Wang, C.-R., Wei, Y.-C., & Hung, W.-Y. (2012). Evolution of the Shear Wave Velocity During Shaking Modeled in Centrifuge Shaking Table Tests. *Bulletin of Earthquake Engineering*, 10(2), 401-420.
- Oh, W., & Vanapalli, S. (2011). *Relationship between Poisson's Ratio and Soil Suction for Unsaturated Soils*. Paper presented at the 5th Asia-Pacific Conference on Unsaturated Soils, Pattaya, Thailand.
- Ramesh, M., & Vasudevan, N. (2012). The Deployment of Deep-Earth Sensor Probes for Landslide Detection. *Landslides*, 9(4), 457-474. doi: 10.1007/s10346-011-0300-x
- Santamarina, J. C. (2003). Soil Behavior at the Microscale: Particle Forces. *Geotechnical Special Publication, ASCE*, 119, 25-56.
- Skempton, A. (1954). The Pore-Pressure Coefficients a and B. *Geotechnique*, 4(4), 143-147.
- Towhata, I. (2008). *Geotechnical Earthquake Engineering*: Springer.
- Tsukamoto, Y., Ishihara, K., Nakazawa, H., Kamada, K., & Huang, Y. (2002). Resistance of Partly Saturated Sand to Liquefaction with Reference to Longitudinal and Shear Wave Velocities. *Soils and foundations*, 42(6), 93-104.
- Uchimura, T., Towhata, I., Lan Anh, T., Fukuda, J., Bautista, C. B., Wang, L., . . . Sakai, N. (2010). Simple Monitoring Method for Precaution of Landslides

Watching Tilting and Water Contents on Slopes Surface. *Landslides*, 7(3), 351-357. doi: 10.1007/s10346-009-0178-z

Yang, H., Rahardjo, H., Leong, E.-C., & Fredlund, D. G. (2004). Factors Affecting Drying and Wetting Soil-Water Characteristic Curves of Sandy Soils. *Canadian Geotechnical Journal*, 41(5), 908-920.

Zhou, A.-N., Sheng, D., & Carter, J. (2012). Modelling the Effect of Initial Density on Soil-Water Characteristic Curves. *Geotechnique*, 62(8), 669-680.

BEHAVIOR OF ELASTIC WAVE VELOCITIES DURING RAIN- INDUCED LANDSLIDES

Chapter 7

BEHAVIOR OF ELASTIC WAVE VELOCITIES DURING RAIN-INDUCED LANDSLIDES

7.1. GENERAL

For the development of a rainfall-induced landslide early warning system based on elastic wave velocities, it was first necessary to envisage the response of elastic wave velocities during actual landslide conditions. For this purpose, the available options included full scale field experiments (e.g. artificial rainfall on a natural slope and studying the wave velocity response before and during failure initiation), scaled down model experiments, or element tests. Among these, element tests provided the best possibility to explore the said phenomenon under controlled conditions, without the influence of several external factors which may be encountered during field, or model experiments. Element tests were therefore conducted to explore the behavior of elastic wave velocities during controlled conditions replicating rainfall-induced landslide initiation. The said experiments, and the related discussions are presented in this chapter.

7.2. TEST CONDITIONS

The stress path followed by a soil element during rain-induced landslides is a special one. As discussed in Chapter 2, such a stress path can be reproduced in laboratory element tests by the following test approaches (Brand, 1981);

1. Decreasing the radial stress (σ_3) while maintaining the axial stress (σ_1) constant.
2. Application of constant total stress (σ_1, σ_3 : constant) and increasing pore water pressure from initial negative value until the failure occurs.

In this research, soil specimens were subjected to each of the above mentioned stress paths, and the corresponding response of elastic wave velocities during the prevailing landslide conditions was studied. For simplicity's sake, the former test series was labeled as *Constant Water Radial Stress Reduction tests (CWRSR)*, and the corresponding tests were designated by letters “RSR” representing “*Radial Stress Reduction*”. Similarly, the second set of experiments was labeled as *Constant Shear stress Water Injection tests (CSWI)*, and each test was designated as “CSI” i.e. “*Constant Shear water Injection*”. Initial test conditions of specimens used in both test series are summarized in Table 7.1 and Table 7.2.

Table 7.1: Initial test conditions in CWRSR tests.

<i>Test Designation</i>	<i>Sr</i> (%)	<i>e</i>	<i>γ_b</i> (g/cm ³)	<i>Remarks</i>
<i>RSR-3</i>	21	0.670	1.667	Unsaturated
<i>RSR -4</i>	47	0.730	1.724	Unsaturated
<i>RSR -6</i>	10	0.719	1.573	Unsaturated
<i>RSR -8</i>	79	0.681	1.887	Unsaturated
<i>RSR -9</i>	97	0.691	1.959	Saturated (<i>B=0.08</i>)

Table 7.2: Initial test conditions in CSWI tests.

<i>Test Designation</i>	σ_3 (kPa)	K (σ_1/σ_3)	Dr (%)	Sr (%)	Su (kPa)	<i>Infiltration pressure (kPa)</i>	WI (ml/hr)	<i>Use of helical filter paper</i>
<i>CSI-2</i>	25	3.0	56	29.4	--	30	19.08	No
<i>CSI-4</i>	25	3.0	30	32.0	11.71	50	32.4	No
<i>CSI-5</i>	25	3.0	56	32.6	--	25	17.28	Yes
<i>CSI-6</i>	25	3.7	56	28.2	28.52	25	16.92	No
<i>CSI-7</i>	25	3.7	56	28.5	30.13	27.5	16.92	Yes
<i>CSI-8</i>	25	3.7	56	28.5	27.83	28	14.76	No
<i>CSI-9</i>	25	2.5	56	28.0	32.28	25	19.08	Yes
<i>CSI-10</i>	25	3.4	56	28.1	28.19	25	16.92	Yes
<i>CSI-11</i>	25	3.0	56	28.1	31.15	28.5	16.92	Yes
<i>CSI-12</i>	25	3.0	56	27.7	36.86	31	18.72	No
<i>CSI-13</i>	25	3.4	30	29.3	15.36	31	18.00	No
<i>CSI-14</i>	25	3.4	75	33.5	--	28	16.56	Yes
<i>CSI-15</i>	25	3.4	65	27.9	42.27	28	15.84	Yes
<i>CSI-16</i>	25	3.4	30	29.7	16.95	25	13.32	Yes
<i>CSI-18</i>	25	2.0	56	29.8	29.18	25	16.92	Yes

7.3. CONSTANT WATER RADIAL STRESS REDUCTION (CWRSR) TESTS

The chief goal of this test series was to examine the effects of soil yielding (during landslides) on elastic wave velocities. Typical element tests involving reproduction of rainfall-induced landslides include injecting water into soil specimens (Brand, 1981; Brenner et al., 1985; Anderson & Sitar, 1995; K. Farooq et al., 2004). However, as discussed in Chapter 6, wave velocities are sensitive to soil moisture. Thus the effects of soil yielding alone, on wave velocities, can not be studied during water injection tests. Brand (1981), however, postulated that the stress path followed by a soil element during landslides can also be reproduced in triaxial tests by reducing radial stress while keeping the axial stress constant. Brand's idea of radial stress reduction was thus adopted in this set of experiments to study the effect of soil yielding on elastic wave velocities during landslides, without changing moisture state of soil.

7.3.1 Methodology

One of the main advantages of elastic wave measurement by piezoelectric transducers is the non-destructive nature of tests. This advantage was brought to use by reusing the specimens which were initially used for *ICCW* tests. During *ICCW* tests, the specimens were only subjected to increase and then decrease of isotropic stress. At the end of each test, the specimens were still intact without any appreciable change in gravimetric moisture content. Same specimens were thus used for *CWRSR* tests.

Having undergone isotropic compression during *ICCW* test, the void ratio of these specimens was different from the initial void ratio of *ICCW* specimens. This resulted in a small change in initial saturation ratio as well. Besides unsaturated specimens, a saturated specimen with Skempton's *B*-value (Skempton, 1954) of 0.08 was also tested. This corresponded to a saturation ratio of about 97%, as shown in Figure 7.1 (Towhata, 2008; Gu et al., 2013). Initial test conditions of various specimens tested as part of this series are summarized in Table 7.1.

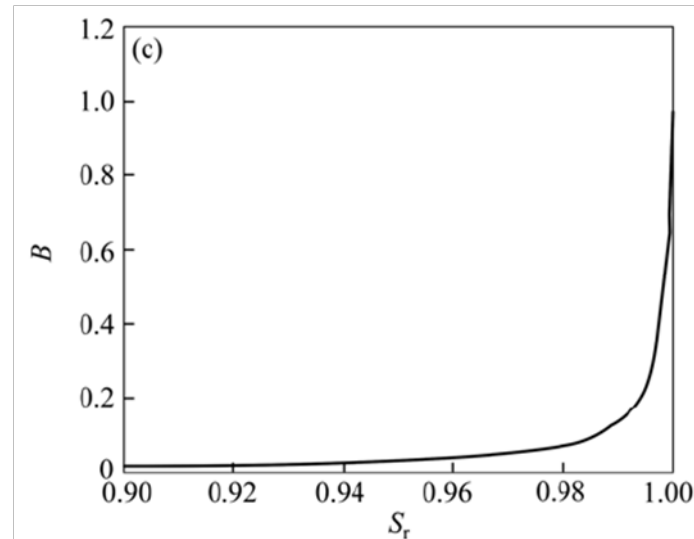


Figure 7.1: Relationship between saturation ratio and Skempton's B -value (after Gu et al. (2013)).

Each specimen, at the end of *ICCW* test, was at isotropic stress of 5~10 kPa. Isotropic confining pressure was increased to 150 kPa (stress increment = 1 kPa/min). For the equalization of stress in the specimen, this stress level was maintained for about 1 hour. From 150 kPa initial isotropic confining pressure, radial stress (σ_3) was gradually decreased at a rate of 0.016 kPa/s so that the specimen reached failure. The magnitude of axial load was adjusted accordingly to maintain a constant axial stress (σ_1) throughout the test. Elastic wave velocities were recorded at various points along this stress path. A single pulse of sinusoidal wave of 10 kHz or 15 kHz was used for the determination of P -wave and S -wave velocities respectively. Stress path employed in these tests is schematically shown in Figure 7.2. Moreover, drainage valve was kept open throughout the test, so as to keep pore air pressure at atmospheric level which is true for most shallow rainfall-induced landslides.

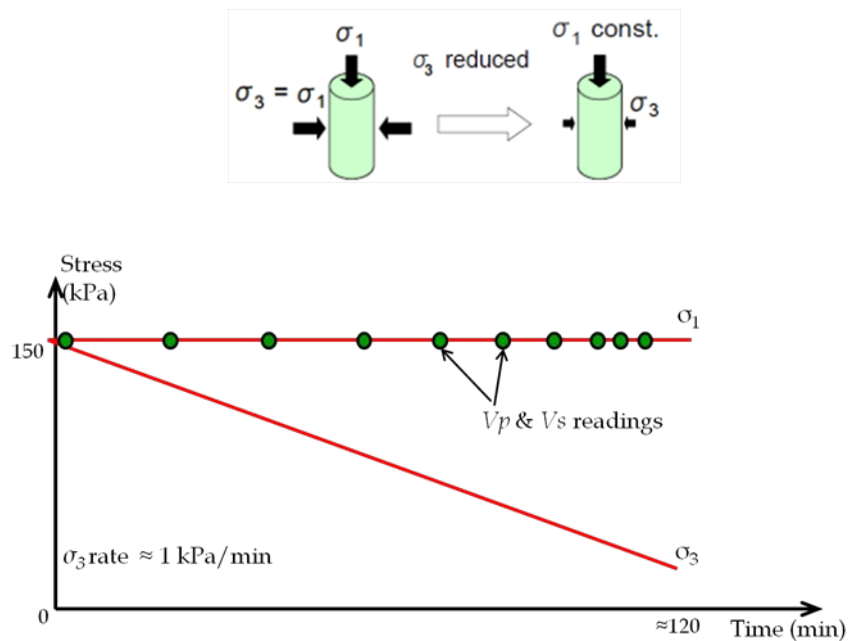


Figure 7.2: Stress path adopted for *CWRSR* tests.

Rain-induced landslides typically occur at shallow depths of less than 3 meters (Anderson & Sitar, 1995; Ng & Pang, 2000; K. Farooq et al., 2004). Element tests reproducing in-situ landslide conditions are therefore required to be conducted at low stress levels (<50 kPa). However, the specimens subjected to stress path shown in Figure 7.2, could not initiate failure when axial stress was kept low. Due to this limitation, a high axial stress of 150 kPa was adopted for this test series.

7.3.2 Effects of Initial Saturation on Failure Initiation

Field stress path tests were carried out on specimens with different initial saturation ratio, by maintaining the axial stress constant and gradually reducing the radial stress to the point of failure. Figure 7.3 shows the response of various specimens when subjected to field stress path. On reducing radial stress (σ_3) from an initial isotropic stress of 150 kPa, extremely small strain was observed during the early phase of tests. However, after sufficient reduction in radial confinement, axial strain started to increase first slowly and then at a rapid rate. Such transition in strain rate can be defined as *yield point* of specimen. Once the yield point is reached, there is continuous straining of the specimen without any appreciable change in stress. Moreover, the strains beyond yield point are irrecoverable. Hence, the yield point can

be said to represent failure initiation of the specimen as indicated by “ Δ ” in Figure 7.3.

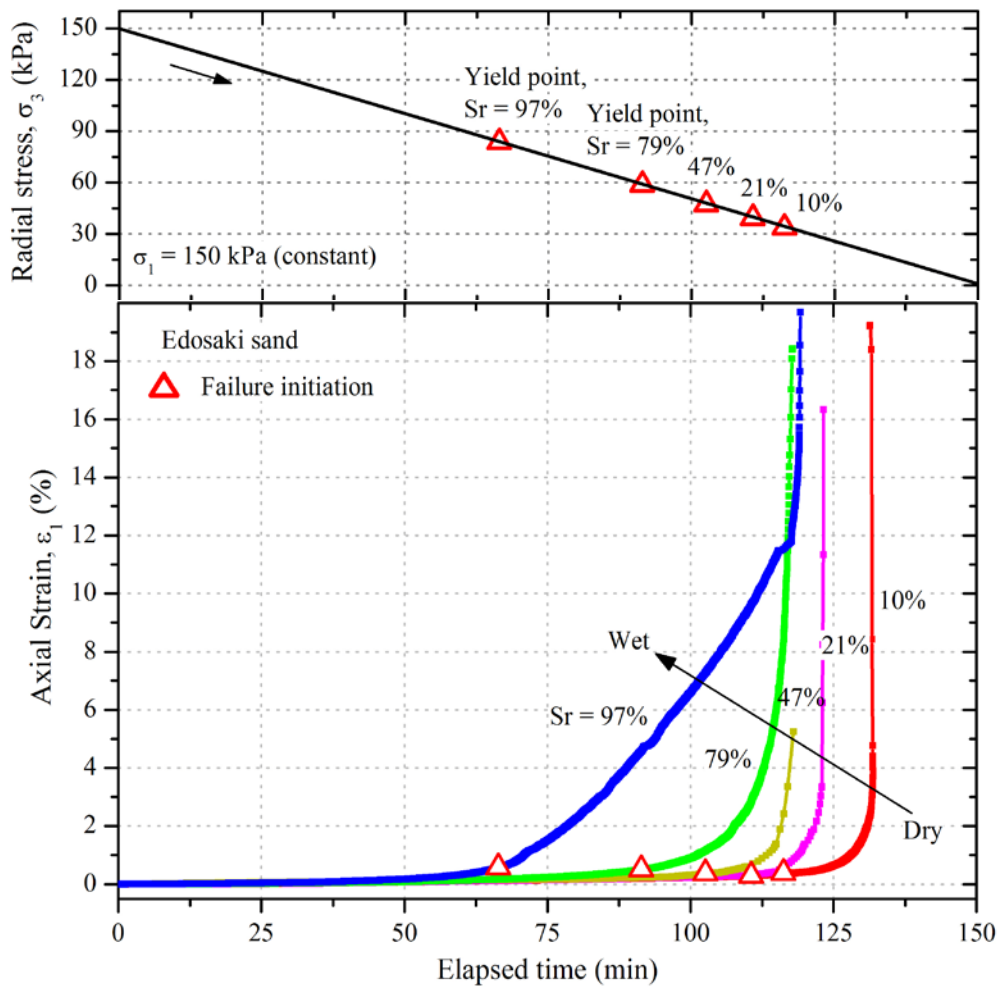


Figure 7.3: Response of *CWRSR* specimens to radial stress reduction.

A systematic approach adopted for the definition of Δ is explained in Figure 7.4. Using the radial stress (σ_3) ~ axial strain (ϵ_1) plot, a tangent corresponding to 0.2% axial strain (point A) was drawn. Another line, tangent to the final part of the curve, was extended backwards to intersect the first tangent. The intersection point of these two tangents (point B) represented the yield point of soil specimen and the corresponding magnitude of radial stress indicated the yield strength. Thus, the failure was initiated when the specimen reached its yield strength, and yield point of each specimen is indicated by Δ in Figure 7.3.

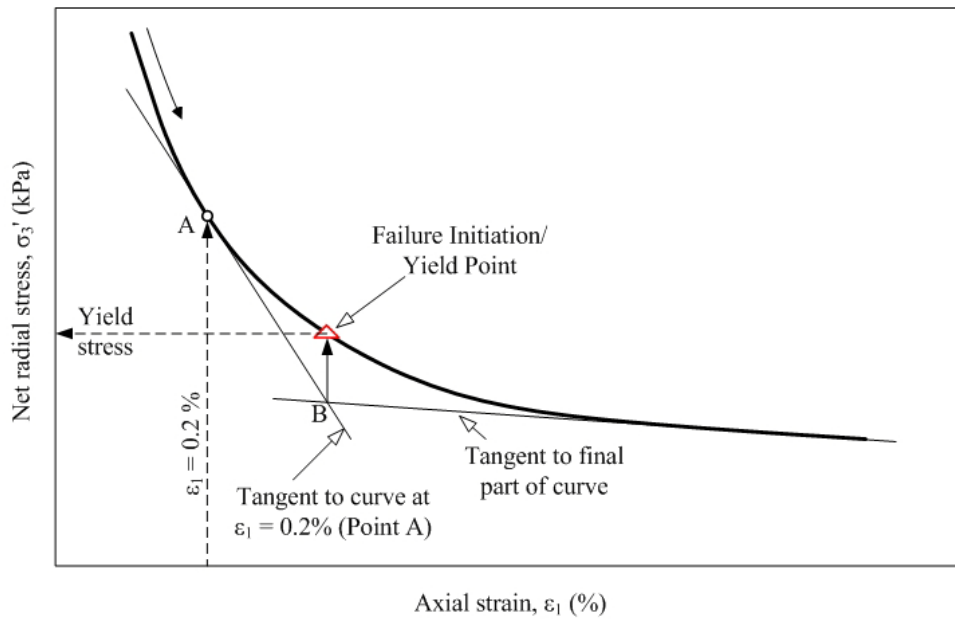


Figure 7.4: Definition of yield point in *CWRSR* tests.

From Figure 7.3, yielding of soil specimen subjected to field stress path is a function of initial saturation state. Although the rate of radial stress decrement was same for all test cases, yet specimens with higher saturation initiated failure much earlier than relatively drier specimens. Therefore, it can be surmised that wetter slopes are closer to failure stage than relatively drier slope surfaces.

Test results presented in Figure 7.3 also help understand the post failure behavior of unsaturated slopes. Post-yielding strain rate decreases with increasing saturation. For instance, 20% saturated specimen developed very large strains in a very short time after yielding. However, it took a very long time after yielding for 90% saturated specimen to reach the failure strain. Dry slopes undergoing failure process are therefore expected to fail at a rapid pace (brittle in nature) as compared to wet slopes which are rather expected to fail in a more ductile manner. Large post-yielding strain in wet slopes can hence be used as a warning before complete failure.

7.3.3 Effects of Soil Yielding on Wave Velocities

As the specimens were subjected to field stress path, elastic wave velocities (V_s : shear wave velocity, and V_p : compression wave velocity) were determined at various intervals. Figure 7.5 summarizes the effects of soil yielding on shear and compression wave velocities. With the decreasing radial stress (σ_3), there is a very small (or in some cases no) decrease in wave velocities. However, as soon as the failure is initiated, as indicated by Δ , wave velocities decrease at a rapid pace. It is also noticeable that, except specimen having $S_r=21\%$, wave velocities decrease with increasing saturation ratio. This observation is consistent with conclusions derived from Chapter 6. For $S_r=21\%$, wave velocities are higher because of the increased inter-particle contact due to adsorbed water film around soil particles, as previously discussed in Section 6.5 of Chapter 6.

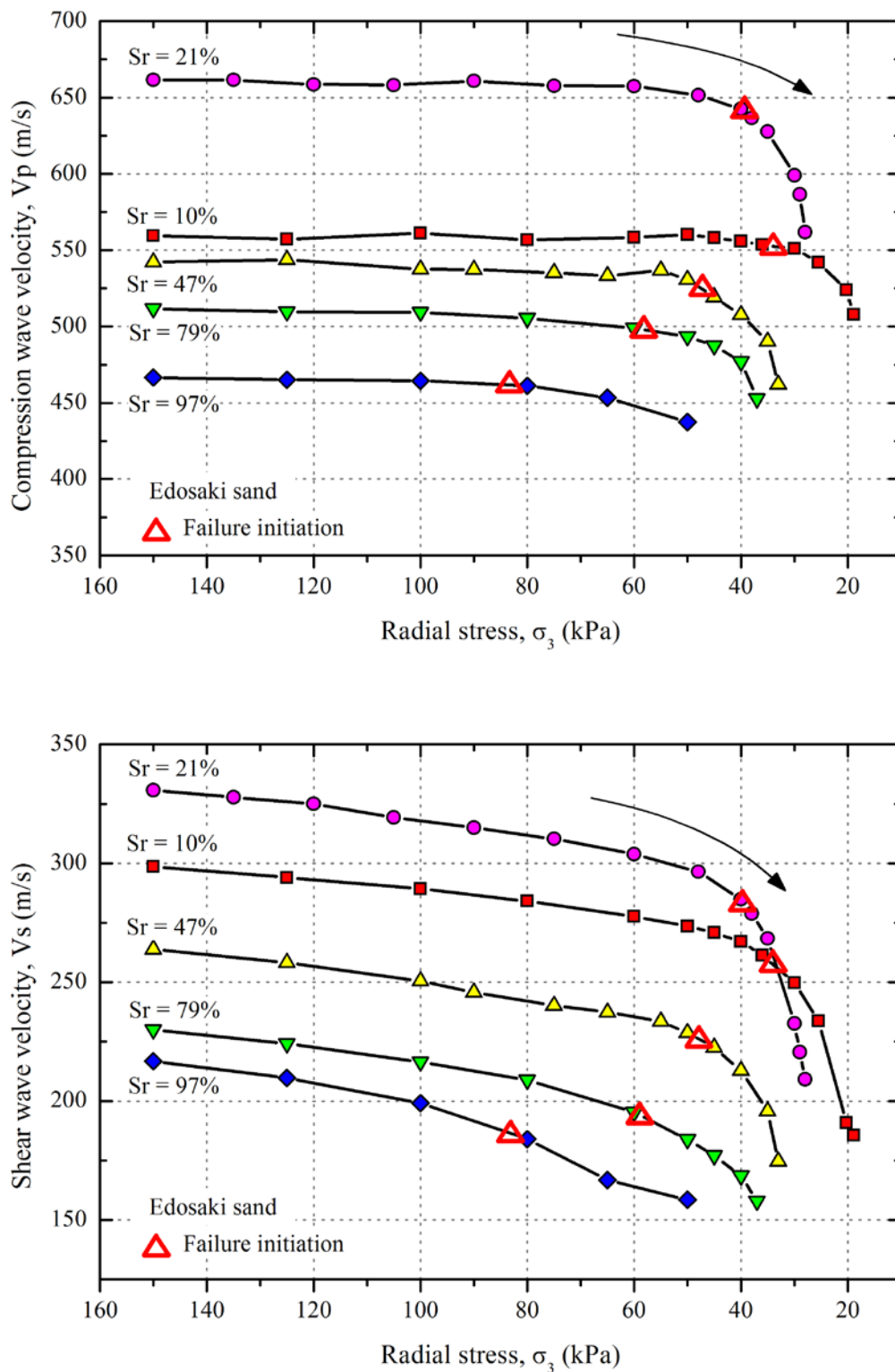


Figure 7.5: Effects of soil yielding on elastic wave velocities; (a) Compression wave velocities, V_p ; (b) Shear wave velocities, V_s

There was a small difference in the initial density of all the specimens, as shown in Figure 7.6. This could affect wave propagation as discussed previously in Section 6.3.2 (Chapter 6). Thus to draw a better comparison among specimens with different initial density and saturation ratio, wave velocities were normalized corresponding to void ratio $e_o = 0.673$, and dry density, $(\gamma_d)_o = 1.578 \text{ g/cm}^3$, by using Eq. 6.10 and Eq. 6.11. Compression, and shear wave velocities corrected for void ratio and density were represented by V_p'' and V_s'' respectively and are shown in Figure 7.7.

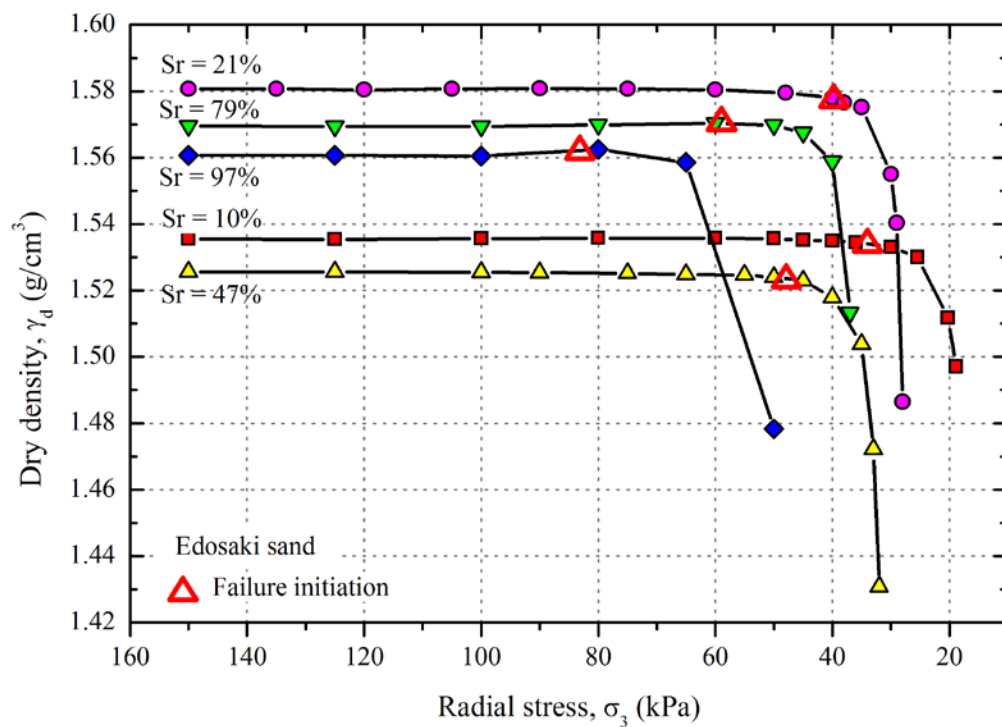


Figure 7.6: Variation of dry density during the course of CWRSSR tests.

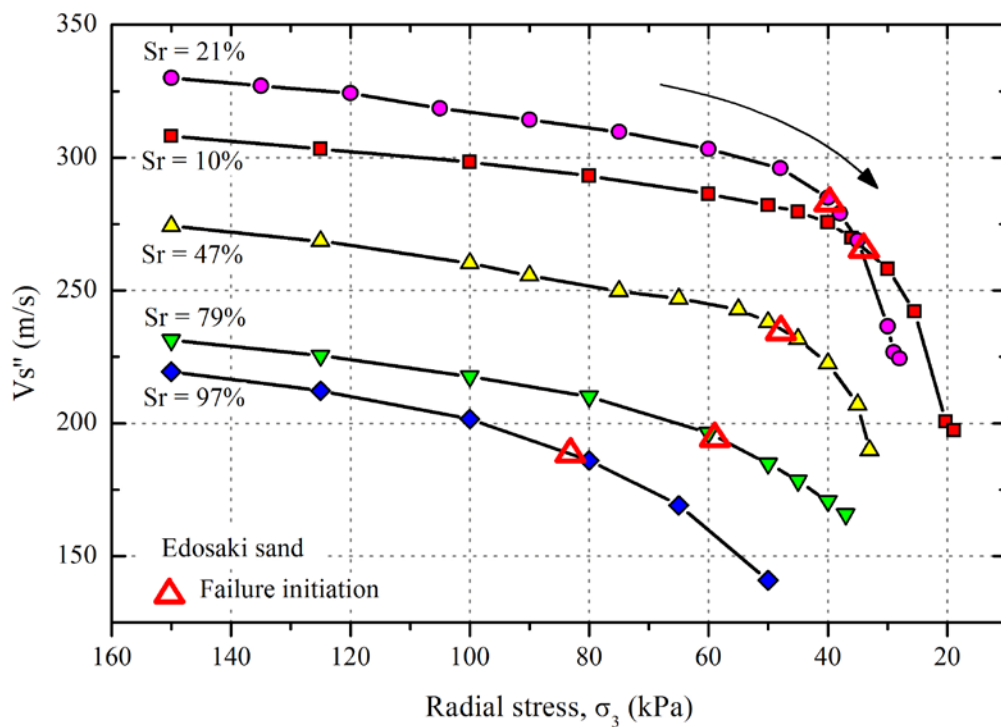
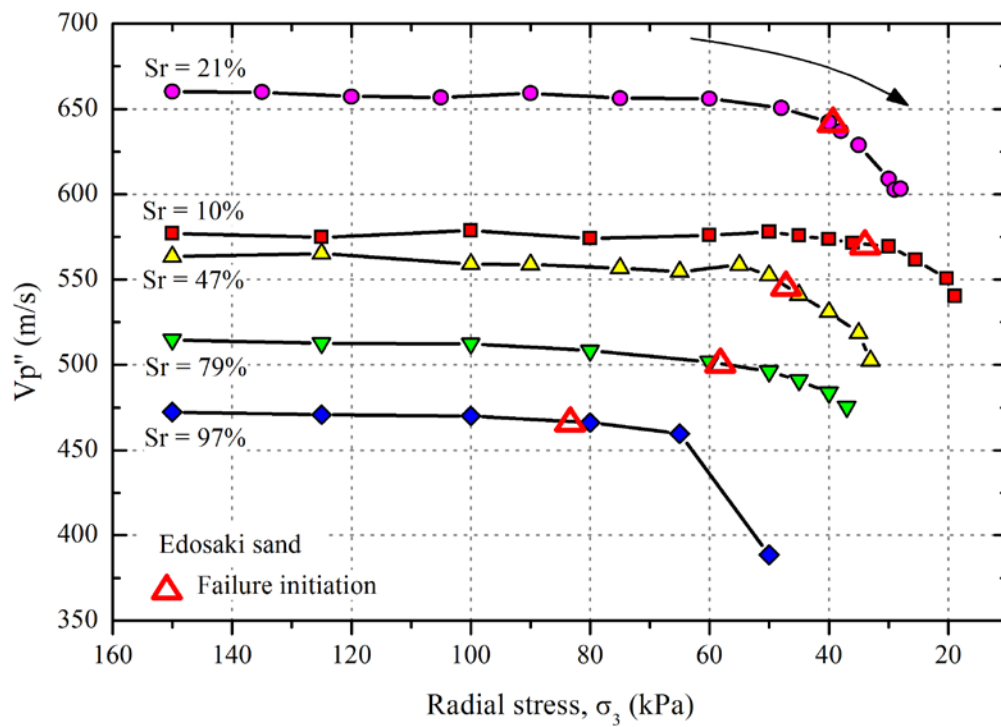


Figure 7.7: Effects of soil yielding on elastic wave velocities normalized for void ratio ($e_o = 0.673$) and density ($(\gamma_d)_o = 1.578 \text{ g/cm}^3$); (a) Normalized compression wave velocity, V_p'' ; (b) Normalized shear wave velocity, V_s'' .

With the reduction of radial stress (σ_3), V_s started decreasing slowly (Figure 7.7(a)). This decrease in V_s can be attributed to the gradual loss of inter-particle contact force due to decreasing radial stress. As the radial stress approached yield strength of specimen (represented by Δ), a sharp decrease in V_s was observed. Normalized compression wave velocity (V_p) however, nearly remained constant before failure initiation, but dropped at an accelerated speed once the failure was initiated (Figure 7.7(b)).

Shear strength of unsaturated specimens subjected to field stress path is function radial stress (σ_3) and soil matric suction (negative pore water pressure). Higher the saturation ratio, lower would be matric suction, and shear strength would be more sensitive to radial stress (σ_3) only. This phenomenon can be observed from Figure 7.8, a plot of radial stress versus wave velocities normalized with respect to the respective initial wave velocity. The rate of pre-yielding V_s decrement was higher for 90% saturated specimen as compared to the relatively drier specimens. Moreover, while undergoing the field stress path shear and compression wave velocities were observed to decrease by about 40% and 15% respectively. This decrease in wave velocities due to soil yielding can be used as an indicator of landslide initiation in actual field conditions.

Elastic waves travel through soil skeleton via inter-particle contacts. Larger the number of inter-particle contacts, greater will be the wave velocity and vice versa. Specimen dilatation would loosen the soil skeleton and reduce the number of particle contact points, thus wave velocity would decrease with dilatation. This observation is depicted in Figure 7.9 in which wave velocities are plotted against volumetric strains. Both compression and shear wave velocities were observed to decrease rapidly with specimen dilatation. With reference to rain-induced landslides, the increase in ground water table, and the corresponding pore water pressure during rainfall, generally makes the soil structure loose, causing it to dilate. This would cause the wave velocities to decrease, hence enabling the prediction of slope movements.

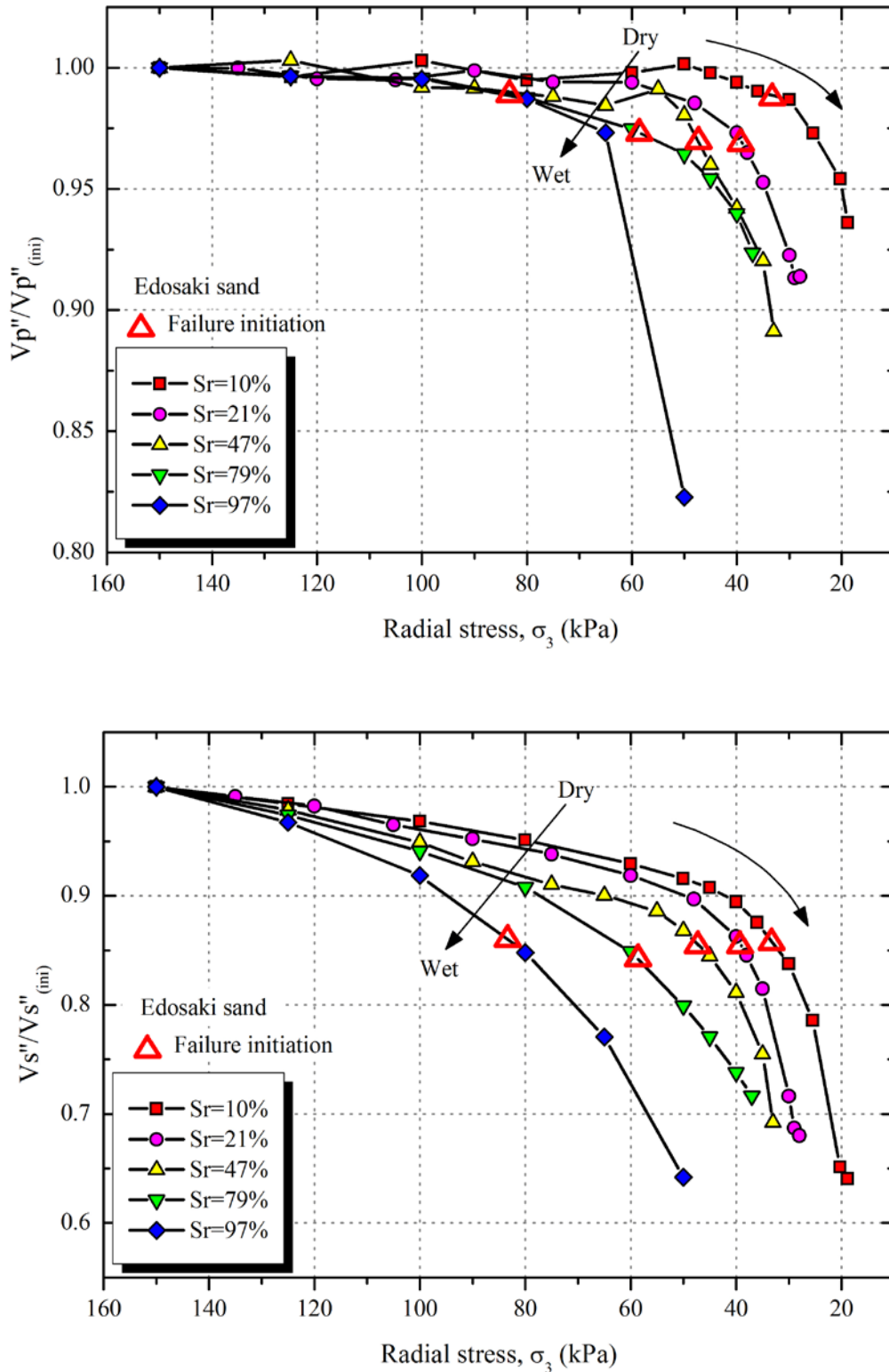


Figure 7.8: Variation of corrected elastic wave velocities ($e_o = 0.673$; $(\gamma_d)_o = 1.578$ g/cm³), normalized with respective initial values; (a) Compression wave velocities, $V_p''/V_{p''(ini)}$; (b) Shear wave velocities, $V_s''/V_{s''(ini)}$.

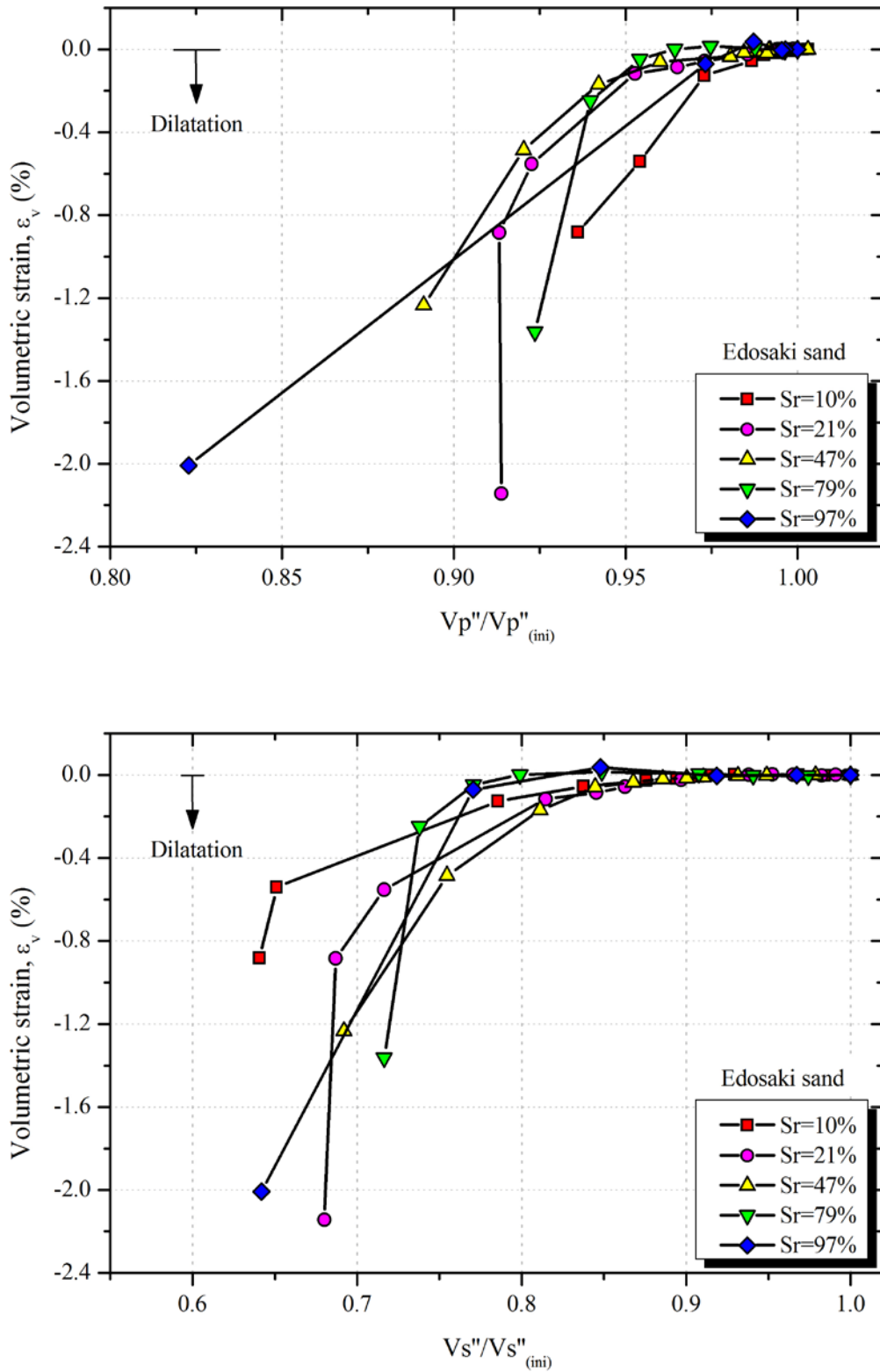


Figure 7.9: Dependence of elastic wave velocities on specimen dilatation; (a) Compression wave velocities, $V_p''/V_p''(ini)$; (b) Shear wave velocities, $V_s''/V_s''(ini)$.

7.3.4 Dependency of V_s and V_p on Principle Stress Direction

A close observation of Figure 7.8 reveal that the pre-yielding behavior of V_s and V_p is different; i.e. V_s start decreasing immediately with the decrease in radial stress, whereas V_p remains nearly constant in the initial phase of radial stress reduction, and decrease only once the specimen has yielded. This is because of the difference in stress dependency of two waves i.e. shear wave is a function of both axial (σ_1) and lateral stress (σ_3), whereas compression wave is solely dependent on axial stress (σ_1) (Hardin & Richart, 1963; Stokoe II et al., 1995). Therefore, decrease of radial stress (σ_3) in the pre-yielding phase only causes reduction in V_s , while V_p remains unaffected. However, once failure is initiated, the specimen starts to dilate at an accelerated pace and the structural rearrangement of particles causes rapid reduction of both V_p and V_s . This phenomenon is further highlighted in Figure 7.10, in which the responses of volumetric strain, compression wave velocity, and shear wave velocity with axial strain of the specimen are plotted. Wave velocities in this figure are normalized with the corresponding initial values. Initially, with radial stress reduction, axial strain decreased without any dilation. After considerable axial strain, specimen started to dilate until it reached failure. Since axial stress (σ_1) was constant (at 150 kPa), compression wave velocity remained nearly constant as long as there was no volumetric strain in the specimen. Shear wave velocity, on the other hand, kept on decreasing right from the beginning, because of the decrease in radial stress (σ_3). This provides an experimental confirmation of postulate made by Hardin and Richart (1963).

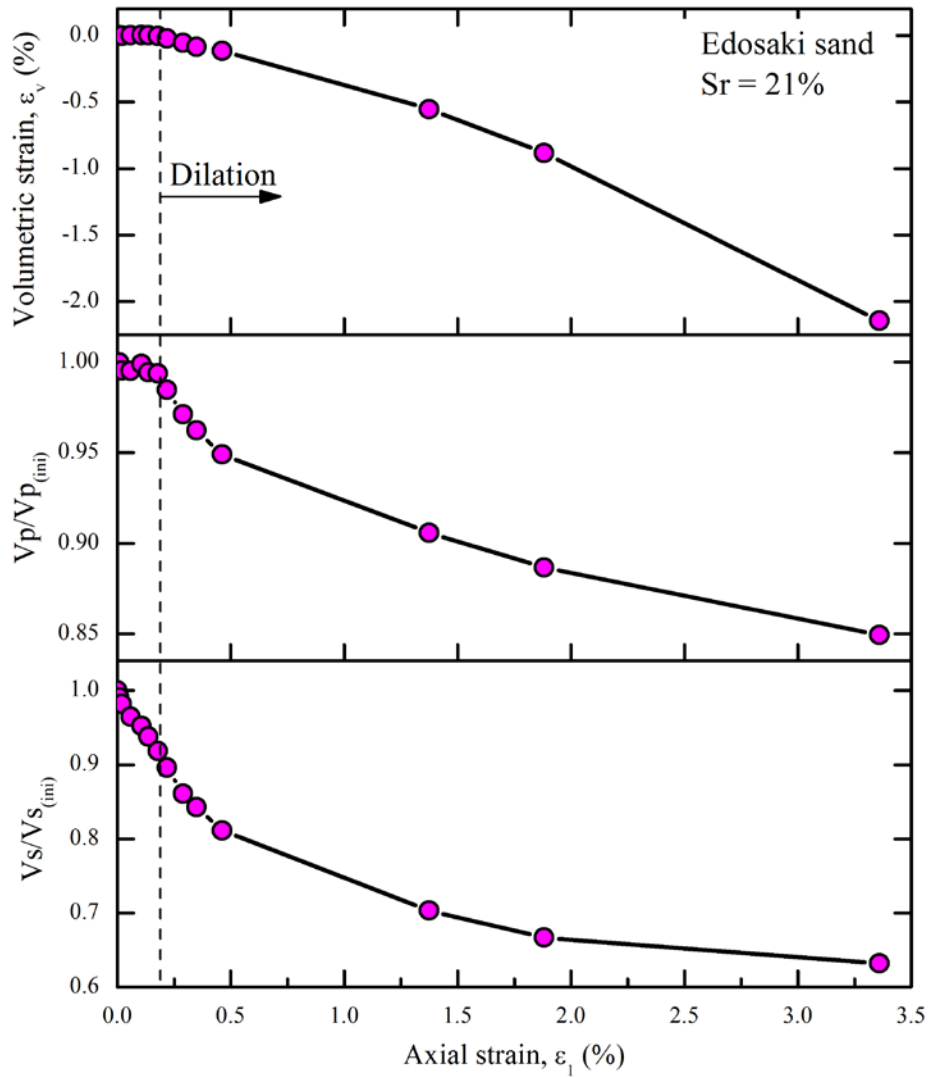


Figure 7.10: Dependence of shear and compression wave velocities on principle stress direction.

A closer observation of Figure 7.9 confirms that this explanation is valid for all the specimens of this test series. At zero (or nearly zero) volumetric strains, shear wave velocities of all the specimens decrease considerably because of the decreasing radial stress (σ_3). On the contrary, compression wave velocities remained nearly constant at zero (or nearly zero) volumetric strains, since axial stress was not changed ($\sigma_1=150$ kPa: constant).

7.3.5 Application for Landslide Monitoring

Soil on a slope surface may initially be in unsaturated state with soil matric suction contributing significantly towards its shear strength. Percolation of rainwater in the soil reduces soil matric suction, thereby causing a stress relief. Moreover, near the failure stage, pore water pressure may start to develop, which would effectively push the particles away from each other, causing it to dilate. From the discussions in previous sections, it can be surmised that stress relief, and soil dilation cause wave velocities to decrease. Thus a continuous record of wave velocities on the slope surface can provide indication of dilation and stress relief in soil during rainfall, helping in the prediction of landslides.

Wave velocities can also be helpful in predicting the rate of slope movement during landslides. Before yielding, shear wave velocities were found to decrease almost linearly with axial strain, as shown in Figure 7.11. However, the rate of decrease of wave velocity reduced after yielding of specimen. This can be useful for the prediction of soil yielding in actual field conditions.

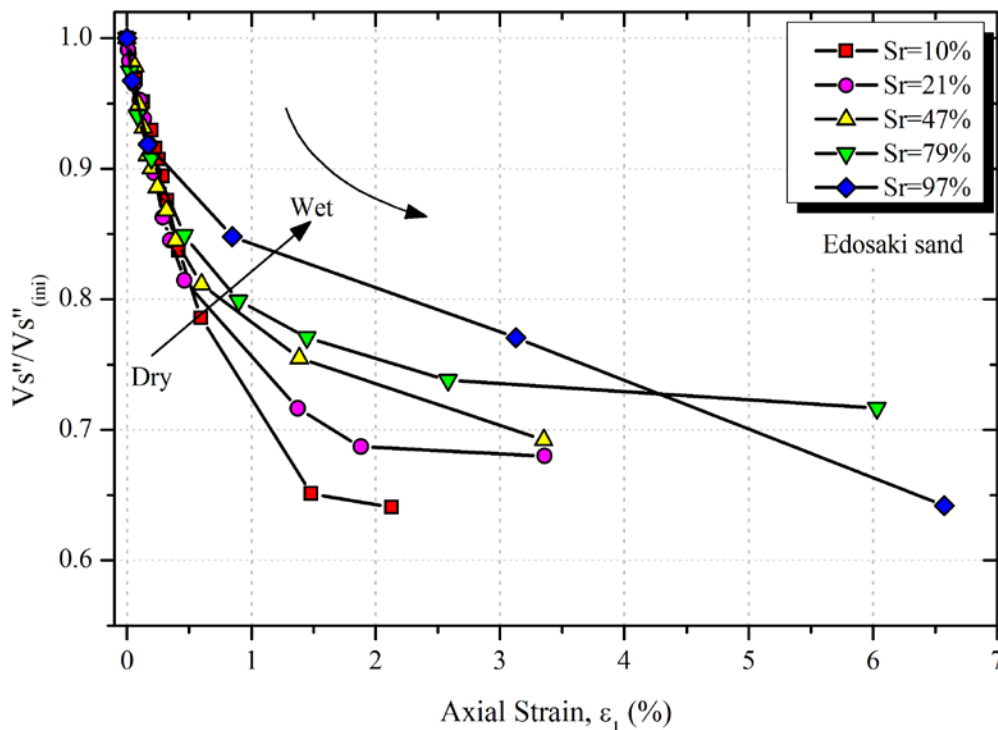


Figure 7.11: Variation of normalized shear wave velocities with axial strain in specimens.

7.4. CONSTANT SHEAR STRESS WATER INJECTION (CSWI) TESTS

Test series presented in previous section (*CWRSR* tests) could simulate the field stress path followed by a soil element during landslides. However, the actual mechanism of rain-induced landslides could not be reproduced in *CWRSR* tests. The actual mechanism of rain-induced landslides includes permeation of water into initially unsaturated soil; under constant total stress, soil loses its strength initially due to the loss of matric suction, and then due to the development of pore water pressure. This series of experiments was thus designed to reproduce not only the field stress path, but also to mimic the actual mechanism of rain-induced landslides. During the experiments elastic wave velocities were determined at regular intervals, to study the behavior of wave velocities during rainfall-induced slope failures.

7.4.1 Methodology

Cylindrical triaxial specimens (75 mm in diameter and 150 mm in height) were prepared by wet tamping Edosaki sand to a specified density in ten equal layers, as described in Section 4.3.1.3 (Chapter 4). All the specimens were prepared at an initial saturation ratio of 30%. Initial isotropic confining pressure was maintained at 25 kPa for 12~24 hours in order to allow equalization of matric suction, which was then taken as initial matric suction of soil specimen, as discussed in Section 4.3.1.5 (Chapter 4). Axial stress was then increased gradually at a rate of 1 kPa/min to the specified level of principle stress ratio ($K = \sigma_1/\sigma_3$) which represented the field consolidation state of soil element along the potential failure plane. After one hour of consolidation, for equalization of stress, water was infiltrated through the bottom ceramic disk by applying a constant infiltration pressure on a burette connected to the ceramic disk (Figure 3.2). The amount of water entering the specimen was determined by recording water level in the burette by means of differential pressure transducer (*DPT*). Infiltration pressure at the ceramic disk was recorded through a pressure transducer connected to the line connecting the burette and ceramic disk (Figure 3.2; Chapter 3). As the water level in burette decreased, infiltration pressure acting on ceramic disk also decreased (due to decreasing pressure head). Air pressure acting on top of burette was therefore adjusted to keep the infiltration pressure constant. The

burette used in this study was of 100 ml capacity. Once the burette got empty, injection of water into specimen was stopped momentarily, and burette was refilled by connecting it to a de-aired water tank and applying negative pressure on its top. The whole process of refilling the burette was completed in about 5 minutes, and was not observed to disturb the trend of strain development. K Farooq (2002) also reported that development of strain in unsaturated specimens is a function of water infiltration, and strain development stopped once water injection was stopped.

Water was continuously injected into the specimen until its failure, which was indicated by a sharp increase in axial strain. The amount of water entering and leaving the specimen was continuously recorded, based on which overall saturation ratio of specimen was computed. Elastic wave velocities were recorded at regular intervals during water injection process. Excitation frequencies of 7 kHz and 5 kHz were used for the determination of P -wave and S -wave velocities respectively. In order to reduce random signal noise, transmitter was triggered several times for each measurement and the corresponding received signals were stacked. Typically each recorded signal was obtained by stacking twenty wave signals. However after failure initiation, specimens started deforming rapidly and a number of readings were required to be taken in a very short time. Thus, the number of stacks for each measurement was reduced to 5 stacks/reading. Stress path adopted in $CSWI$ tests is schematically shown in Figure 7.12.

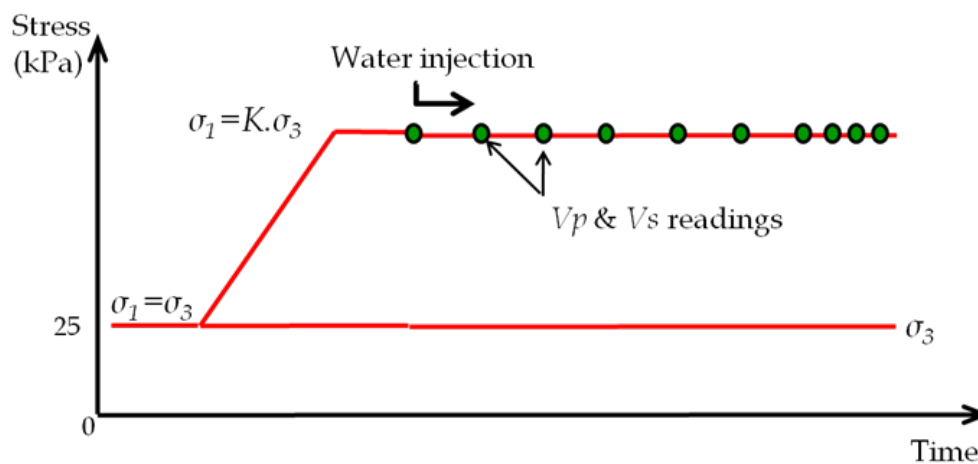


Figure 7.12: Schematic representation of stress path adopted for $CSWI$ tests.

It is worth noting that wave velocities measured during water injection experiments (e.g. *ICWI* tests, and *CSWI* tests) represent the average wave velocity through the specimen. Moisture content along the height of specimen may not be constant during water infiltration. Thus, the recorded wave velocity may be slightly different from the localized wave velocity at specimen's base, at its center or near the top, etc.

Rain-induced slope failures typically occur at shallow depths, generally less than 3 m (Anderson & Sitar, 1995; Ng & Pang, 2000; K. Farooq et al., 2004). Such failures are characterized by low confining pressures acting on soil elements along failure plane, and a conjuncture of pore air pressure equivalent to atmospheric pressure can reasonably be assumed. Hence all the tests were conducted at a low confining pressure (σ_3) of 25 kPa, and pore air pressure in the specimens, was vented to atmosphere through top cap throughout the course of experiments. Soil matric suction could therefore be measured by simply monitoring pore water pressure in the specimens. A miniature pore water pressure, fitted with a saturated ceramic disk at its front, was placed mid-height inside the specimen to continuously record variation of pore water pressure during the course of water injection. Schematic description of the specimens used in this study is shown in Figure 7.13.

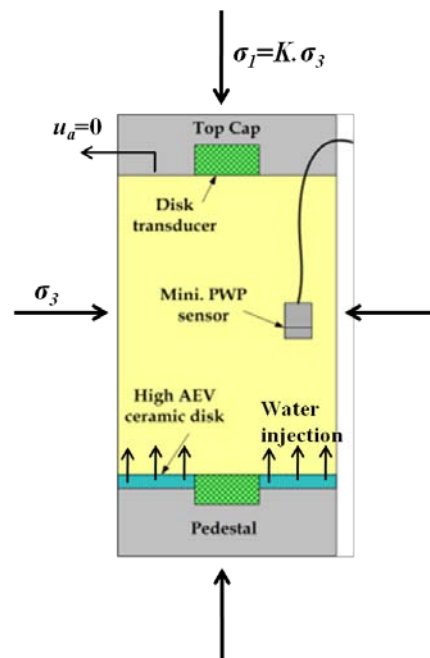


Figure 7.13: Schematic description of triaxial specimens used in this study.

Since water was being injected into the specimens through the high *AEV* ceramic disk at the base pedestal, it was thus natural for the specimen's bottom to be wetted first. At any time during the water injection process, there was non-uniform distribution of water along specimen's height. A sheet of ordinary filter paper was cut in such a way so that it could be rolled to form a helix. This helix shaped filter paper was placed inside the latex membrane such that it covered the periphery of soil specimens. To explore the effects of helical filter paper, specimens in identical conditions, were tested with and without helical filter paper. The use of helical filter paper and the corresponding initial conditions of various specimens used in this study are summarized in Table 7.2. The use of helical filter paper ensured a more uniform water distribution in the soil specimen. More detailed discussion on the use of helical filter paper is presented in Section 7.5.

For time saving, ceramic disk was sometimes reused for various experiments without undergoing the complete process of re-saturation which generally takes 1~2 days. Prior to reuse, saturation condition of ceramic disk was ensured by using a process described by Huang (1994). In this process, saturated ceramic disk was connected to pressure transducer and its surface was wiped with a tissue paper. Saturation was assumed to be correct if the ceramic disk could develop a negative pressure of 60~70 kPa. Details of this process are outlined in Section 4.3.1.1 (Chapter 4). During the course of experiments, air diffused through the ceramic disk may get entrapped underneath it (Muraleetharan & Granger, 1999; Nishiumura et al., 2012). Therefore at the same infiltration pressure, rate of water injection kept on decreasing upon reuse of saturated ceramic disk. This explains the difference in water injection rates in Table 7.2, even when the infiltration pressure was constant.

7.4.2 Effects of Initial Relative Density

In order to investigate the effect of initial relative density on landslide initiation and the corresponding response of elastic wave velocities, water injection tests were performed on specimens with relative densities ranging from 30% to 75%. Figure 7.14 shows the response of Edosaki sand on water injection for various relative densities. The confining pressure (σ_3), principle stress ratio (K), and initial saturation ratio (S_r) were kept constant at 25 kPa, 3.4, and 30% respectively. With the start of

water injection, all the specimens started deforming at a nearly constant rate. However, once the failure was initiated (represented by Δ) strain rate (represented by ϵ_{II}) increased rapidly. Relative density affected the failure pattern in two ways. Firstly, loose specimens initiated failure much earlier as compared to dense specimens. This can be explained on the bases of initial matric suction of each specimen, as shown in Figure 7.14(c). Matric suction is a function of inter-particle pore size and can be illustrated by using Kelvin's equation as (Aitchison, 1960; Fredlund & Rahardjo, 1993; Fredlund et al., 2012);

$$u_a - u_w = \frac{2T_s}{R_s} \quad (7.1)$$

where, u_a and u_w are pore air and pore water pressures respectively. T_s represents surface tension of air-water interface (e.g., $T_s = 72.75$ mN/m at 20 °C), and R_s is the radius of maximum pore size in soil. Thus from Eq. 7.1, small pore size of dense soil specimens would result in high matric suction and vice versa is true for loose specimens. Variation of soil matric suction with its density has been studied in detail by Gallage and Uchimura (2010) and Zhou et al. (2012). Low initial matric suction of loose specimens can dissipate very quickly on water injection. Hence, loose specimens tend to lose their strength much rapidly and initiate failure earlier than dense specimens. On a second front, variation in relative density affected the rate of strain after the initiation of failure (ϵ_{II}). Post failure strain rate (ϵ_{II}) was observed to decrease with increasing relative density. This implies that once the failure is initiated, a slope surface composed of loose deposits would undergo more rapid movement compared to dense soil deposits.

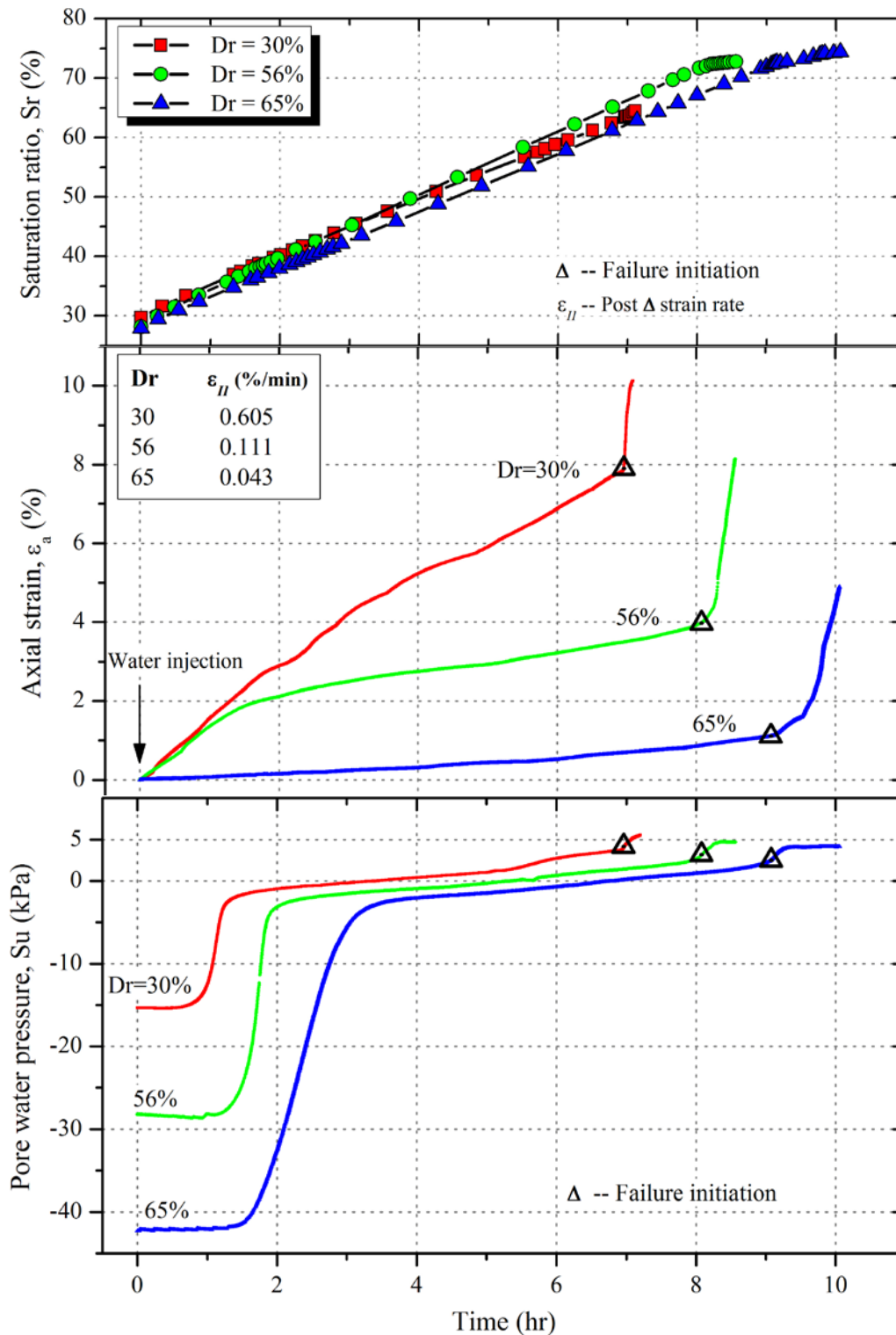


Figure 7.14: Effect of relative density of soil on failure initiation during rain-induced landslides; (a) Variation of saturation ratio (S_r) with time; (b) Axial strain (ϵ_a) response upon water infiltration; (c) Variation of pore water pressure/matric suction (S_u).

The corresponding response of compression wave (V_p) and shear wave (V_s) velocities to water injection is shown in Figure 7.15. Elastic waves travel faster in dense mediums; thus, V_p and V_s for dense specimens were observed to be higher. Consistent with the observations made in Chapter 6, V_p and V_s decrease gradually upon water injection. Gradual softening of soil specimen upon water injection may be responsible for decreasing wave velocities. This decrease continues until the specimens reach failure stage (indicated by Δ), after which V_p and V_s start decreasing rapidly. Rapid decrease in wave velocities upon failure initiation may be attributed to specimen dilation. As shown in Figure 7.16, all the specimens showed compressive behavior upon water injection; where volumetric strain, ε_v , and shear strain, γ , were calculated by using the following expressions;

$$\varepsilon_v = \varepsilon_a + 2 \varepsilon_r \quad (7.2)$$

$$\gamma = \varepsilon_a - \varepsilon_r \quad (7.3)$$

where, ε_a is the axial strain, and ε_r represents average radial strain of the specimens. Moreover, according to the typical sign convention employed in soil mechanics, compressive strains were assumed positive while tensile strains were considered as negative. Once the failure was initiated, the specimens which were initially being compressed upon water injection, started to expand. This gradual expansion of specimens, combined with the increase in specimen saturation ratio, and reorientation of particles upon failure initiation contributed towards rapid decrease in wave velocities.

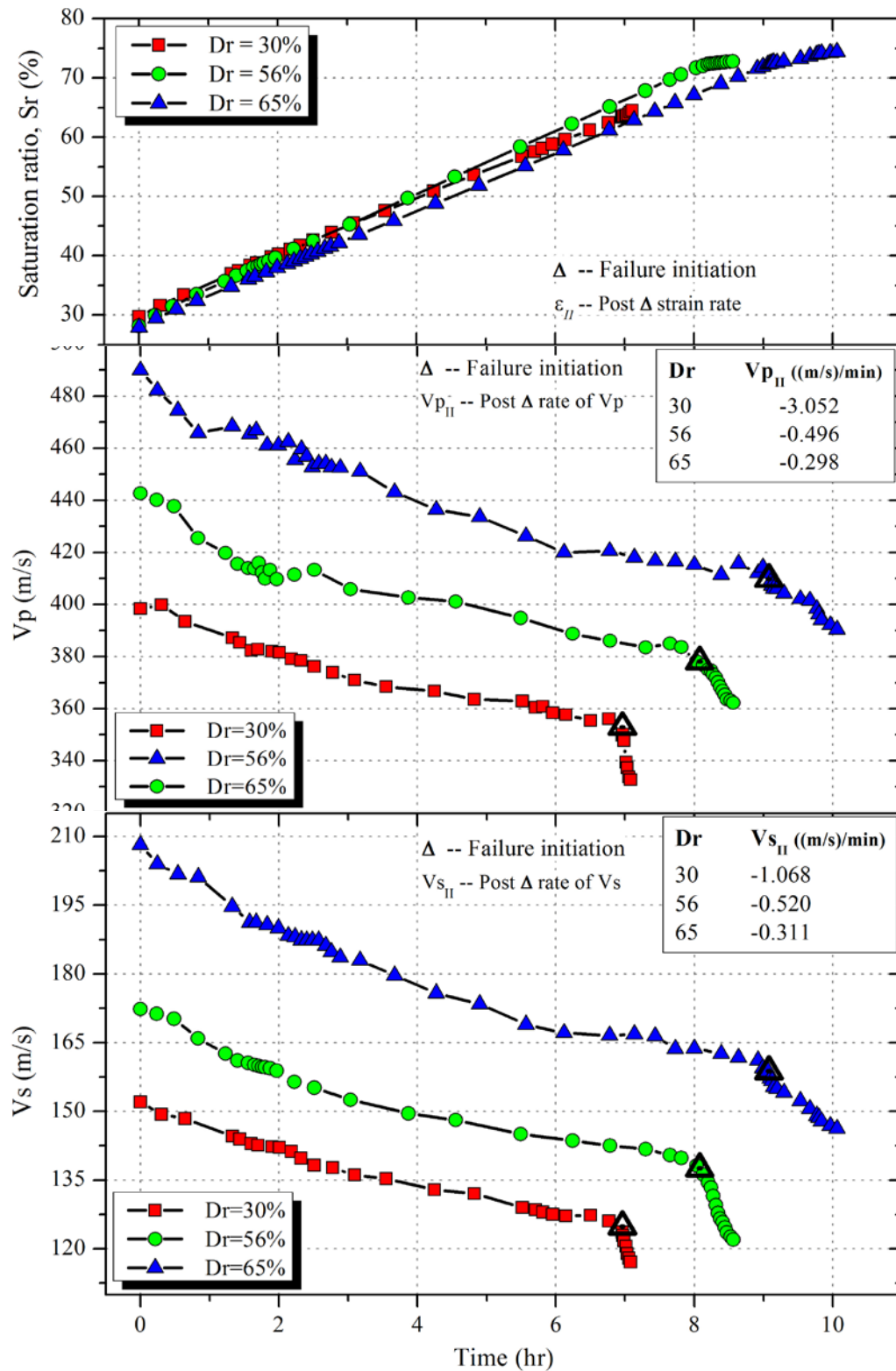


Figure 7.15: Response of elastic wave velocities at different specimen densities during shearing infiltration tests; (a) Variation of saturation ratio (S_r) with time; (b) Compression wave velocity (V_p) response; (c) Shear wave velocity (V_s) response.

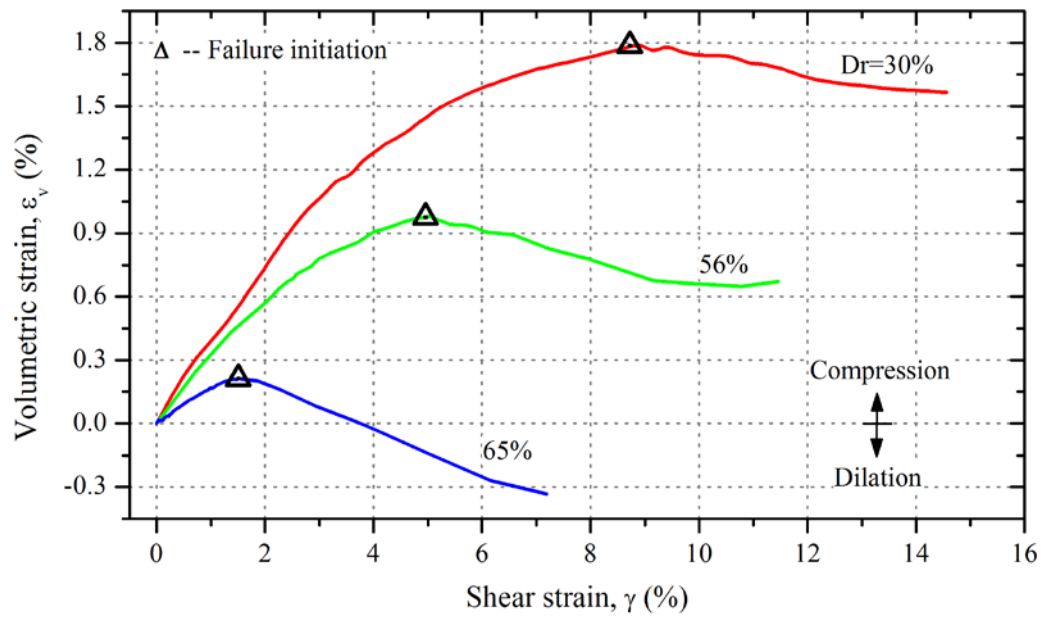


Figure 7.16: Effect of relative density on strain path during shearing infiltration tests.

In order to draw a better comparison among different specimens, wave velocities were corrected for changes in void ratio and density, as discussed in Section 6.3.2 (Chapter 6). Wave velocities were corrected corresponding to $e_o=0.673$, and $\gamma_b=1.578 \text{ g/cm}^3$ by using Eq. 6.10 and Eq. 6.11. Moreover, the corrected wave velocities were normalized corresponding to the respective initial values and are shown in Figure 7.17. Decrease in wave velocities before failure initiation was mainly due to water infiltration. Irrespective of specimen density, this decrease was observed to be nearly constant for both V_p and V_s . It means that irrespective of nature of slope surface (loose, dense, etc.), the state of saturation of soil can be predicted simply by monitoring the drop in wave velocities. It is pertinent to consider that the rate of decrease of normalized V_p and V_s after failure initiation (represented by $V_{pII(Norm)}$, and $V_{sII(Norm)}$), is consistent with the post failure strain rate (ϵ_{II}); i.e. $V_{pII(Norm)}$, and $V_{sII(Norm)}$ decrease with relative density, as does axial strain rate (ϵ_{II}). Also clear from Figure 7.17 is that, the time of failure initiation can easily be identified by monitoring the wave velocity record. This observation can be of practical importance for wave velocity based landslide early warning systems.

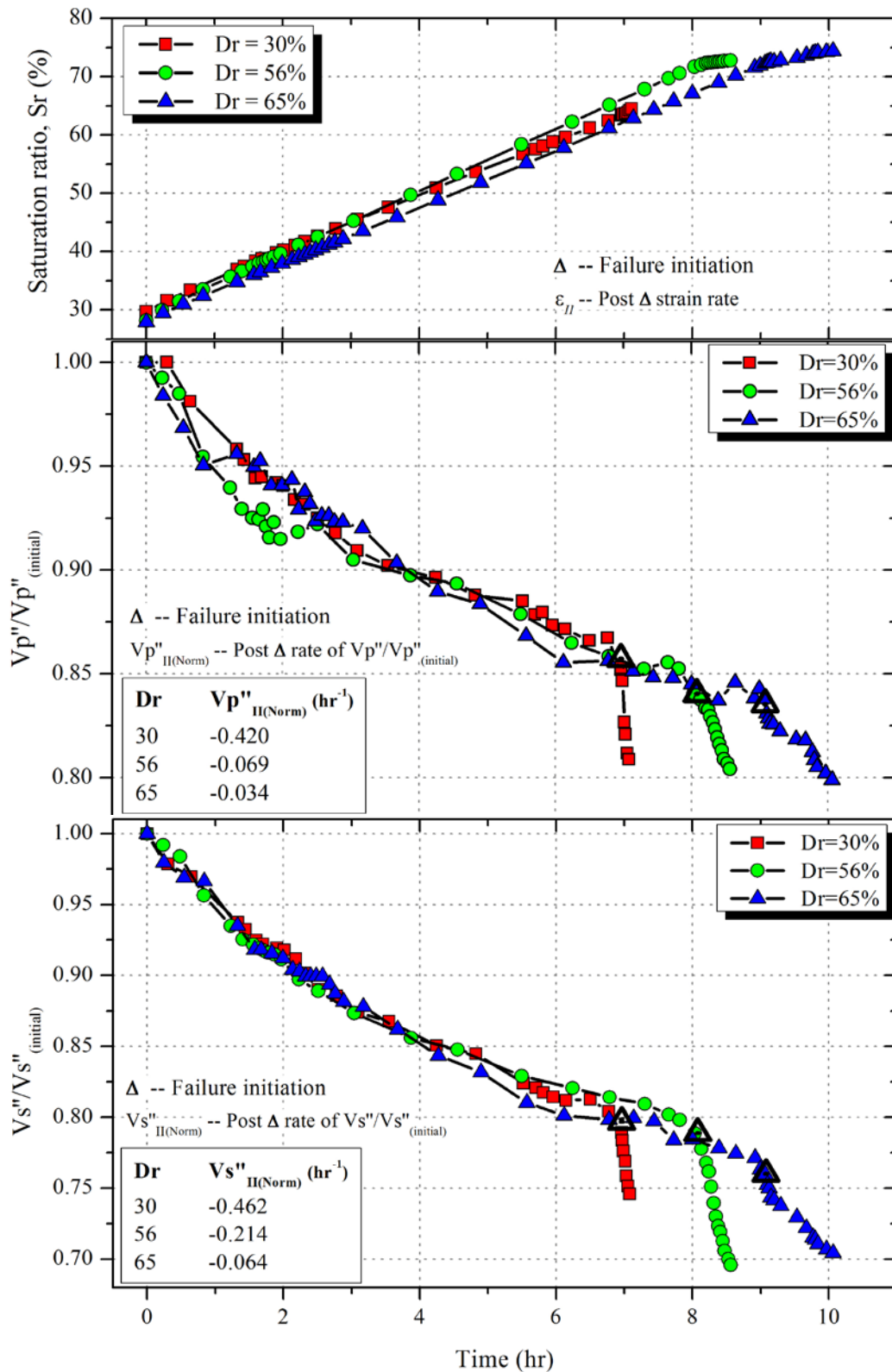


Figure 7.17: Response of elastic wave velocities (normalized corresponding to $e_o = 0.673$, and $\gamma_d = 1.578 \text{ g/cm}^3$) at different specimen densities during shearing infiltration tests; (a) Saturation ratio (Sr) versus time; (b) Normalized compression wave velocities ($Vp''/Vp''_{(initial)}$); (c) Normalized shear wave velocities ($Vs/Vs_{(initial)}$).

7.4.3 Effects of Principle Stress Ratio

The initial principle stress ratio ($K=\sigma_1/\sigma_3$) represents the field stress state of soil element along the potential failure plane, and K is mainly a function of angle of slope surface (Anderson & Sitar, 1995; Zhu & Anderson, 1998). Considering an infinite slope with failure plane parallel to the ground surface, K is principally a function of slope inclination, as explained by Das (2001);

$$\sigma_1 = \gamma H \cdot (1 + \sin \alpha) \quad (7.4)$$

$$\sigma_3 = \gamma H \cdot (1 - \sin \alpha) \quad (7.5)$$

Principle stress ratio can be obtained as a ratio of major to minor principle stress, given as;

$$K = \frac{\sigma_1}{\sigma_3} = \frac{\gamma H \cdot (1 + \sin \alpha)}{\gamma H \cdot (1 - \sin \alpha)} \quad (7.6)$$

Additionally, the applicability of Eq. 7.6 for steep slopes was also showed by Tsukamoto et al. (1998). The relationship between principle stress ratio, K , and slope inclination, α , is shown in Figure 7.18 (after K Farooq (2002)). A vast majority of natural slopes made up of soft deposits possess slope inclinations ranging from $\alpha = 0^\circ$ to $\alpha = 45^\circ$ (Ishihara et al., 1999). Thus for laboratory element tests, the principle stress ratio, K , can safely be assumed to be lying between 1 and 5.8 (K Farooq, 2002).

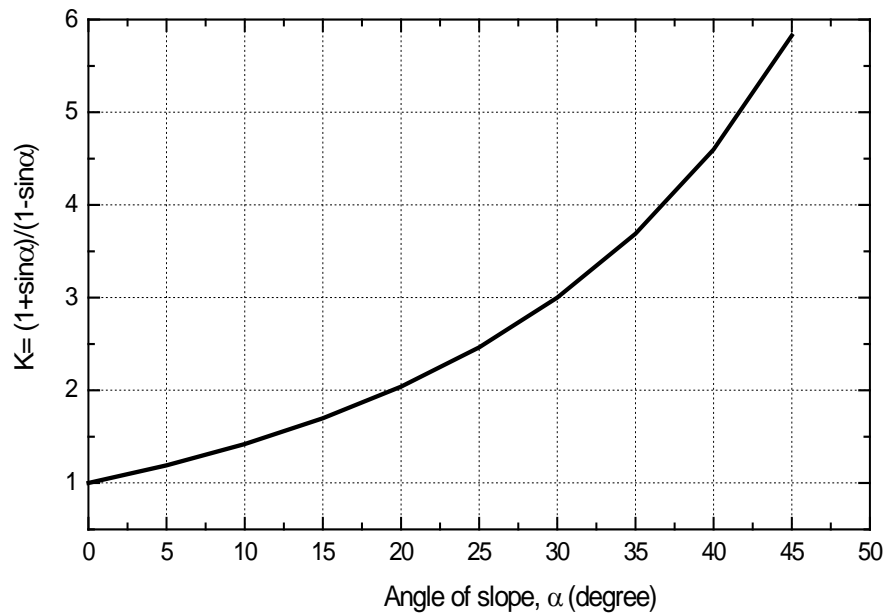


Figure 7.18: Relationship between principle stress ratio (K) and slope inclination (after K Farooq (2002)).

To investigate the effect of slope inclination on landslide patterns and the corresponding response of elastic wave velocities, water injection tests were conducted on Edosaki sand specimens with initial principle stress ratio between 2.0 and 3.7. Relative density, D_r , initial saturation ratio, S_r , and confining pressure, σ_3 , were maintained constant at 56% 30% and 25 kPa respectively for all the tests. Results of these experiments are summarized in Figure 7.19. Axial strains started to develop gradually with water injection, but the strains increased rapidly once the failure was initiated and the specimens were observed to deform by a large magnitude in a short span of time.

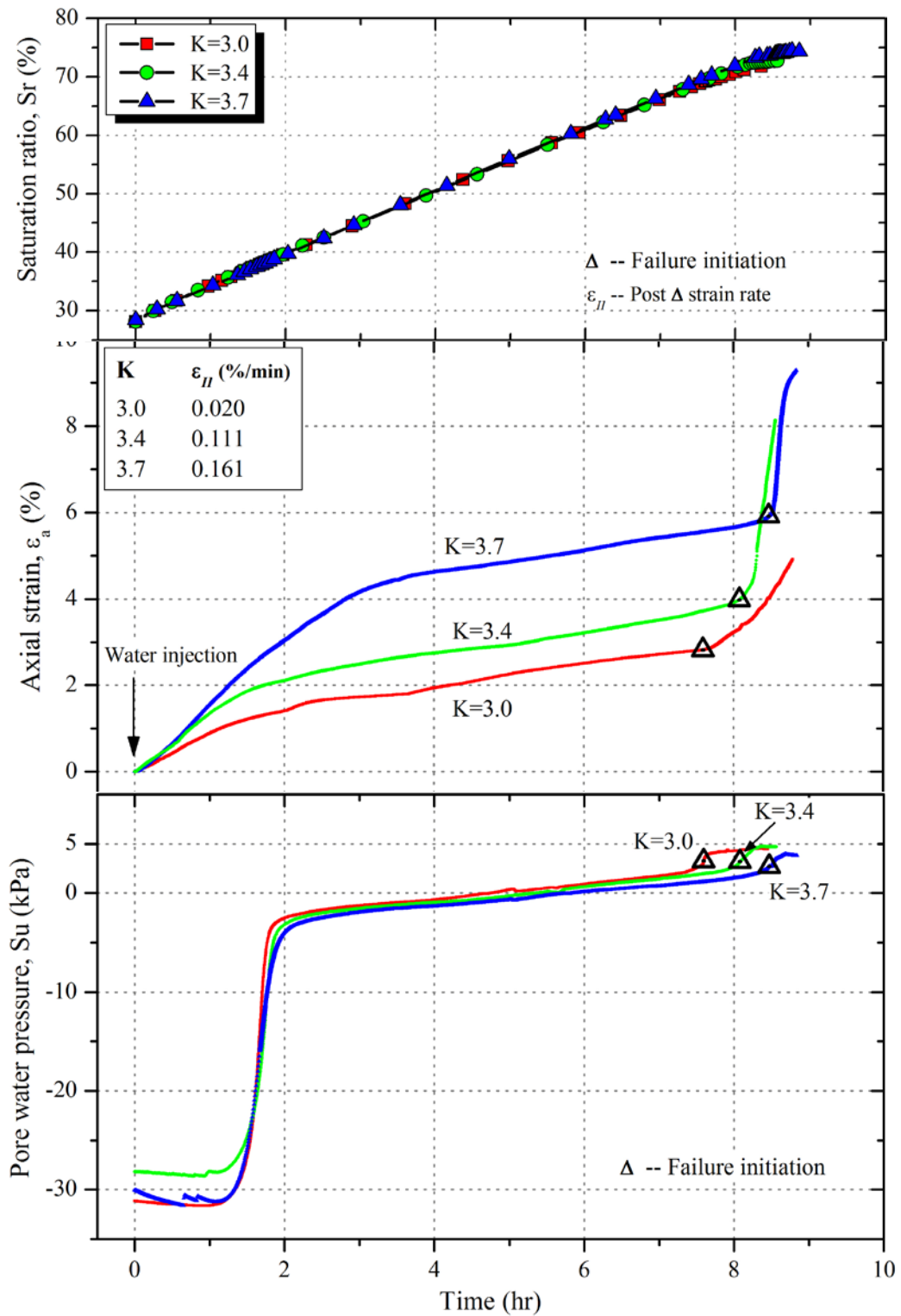


Figure 7.19: Effect of principle stress ratio (K) on failure initiation during rain-induced landslides; (a) Variation of saturation ratio (S_r) with time; (b) Axial strain (ϵ_a) response upon water infiltration; (c) Variation of pore water pressure/matric suction (S_u).

Since initial density of all the specimens was same ($Dr=56\%$), each specimen exhibited nearly equal initial matric suction, as highlighted from Figure 7.19(c), yet the failure time of each specimen was slightly different. This difference in failure initiation may be explained on the basis of specimen density at the time of failure. Specimens subjected to large K values underwent large volumetric compression, as indicated in Figure 7.20. This large volumetric compression can also be apprehended from large axial strain prior to failure initiation (Figure 7.19(a)). Due to large volumetric compression, specimens with high K value were denser at the time of failure initiation and hence failed at a later time (dense specimens initiate failure later – section 7.4.2). Specimens with large K exhibited a much larger post-failure strain rate (ε_{II}). This shows that once the failure is initiated, steep slopes are expected to fail at a very rapid pace.

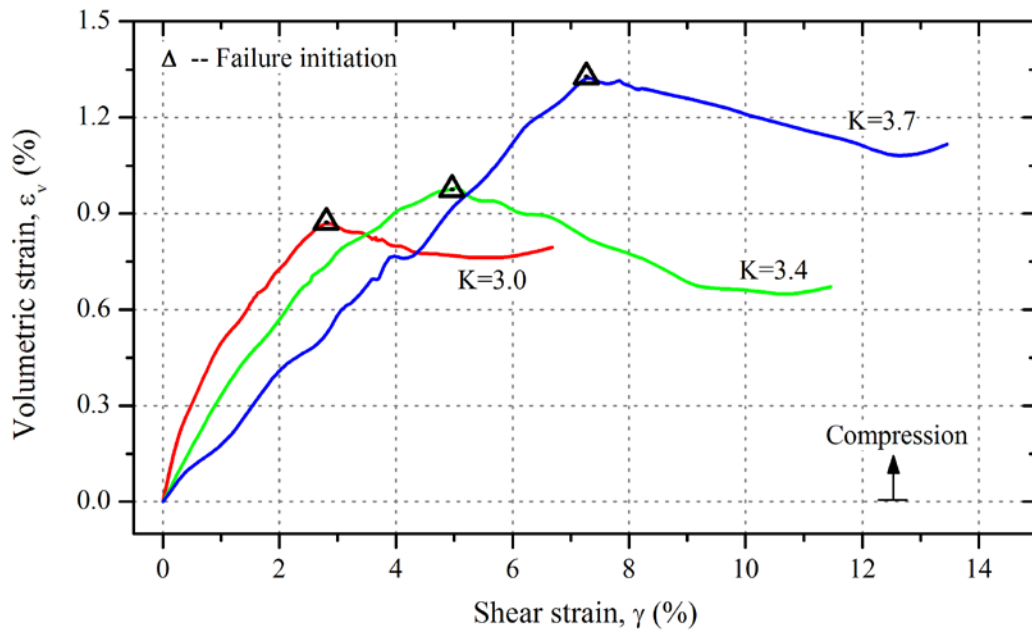


Figure 7.20: Effect of principle stress ratio (K) on strain path during shearing infiltration tests.

The response of V_p and V_s to water infiltration is shown in Figure 7.21. Since initial density and saturation ratio of all the specimens were similar, magnitude of initial wave velocities for all the specimens were therefore comparable. Wave velocities of all the specimens first decreased slowly upon water injection, and then after failure initiation dropped rapidly. Strain path of specimens, shown in Figure 7.20, reveals that the specimens which were initially being compressed upon water infiltration started to expand after failure initiation. This slight expansion of specimens contributed to the drop in wave velocities.

It is interesting to note that the response of shear wave velocities is quite smooth as compared to compression wave velocities. Magnitude of compression wave signals is very weak as compared to shear waves. Thus the determination of arrival time of compression waves is often obscured by noise in received signals, and its determination often involves some educated guesswork. On the contrary, signal to noise ratio of shear wave signals is generally very high, ensuring the determination of shear wave arrival time with relative confidence; detailed discussion on this phenomenon is presented in Chapter 5.

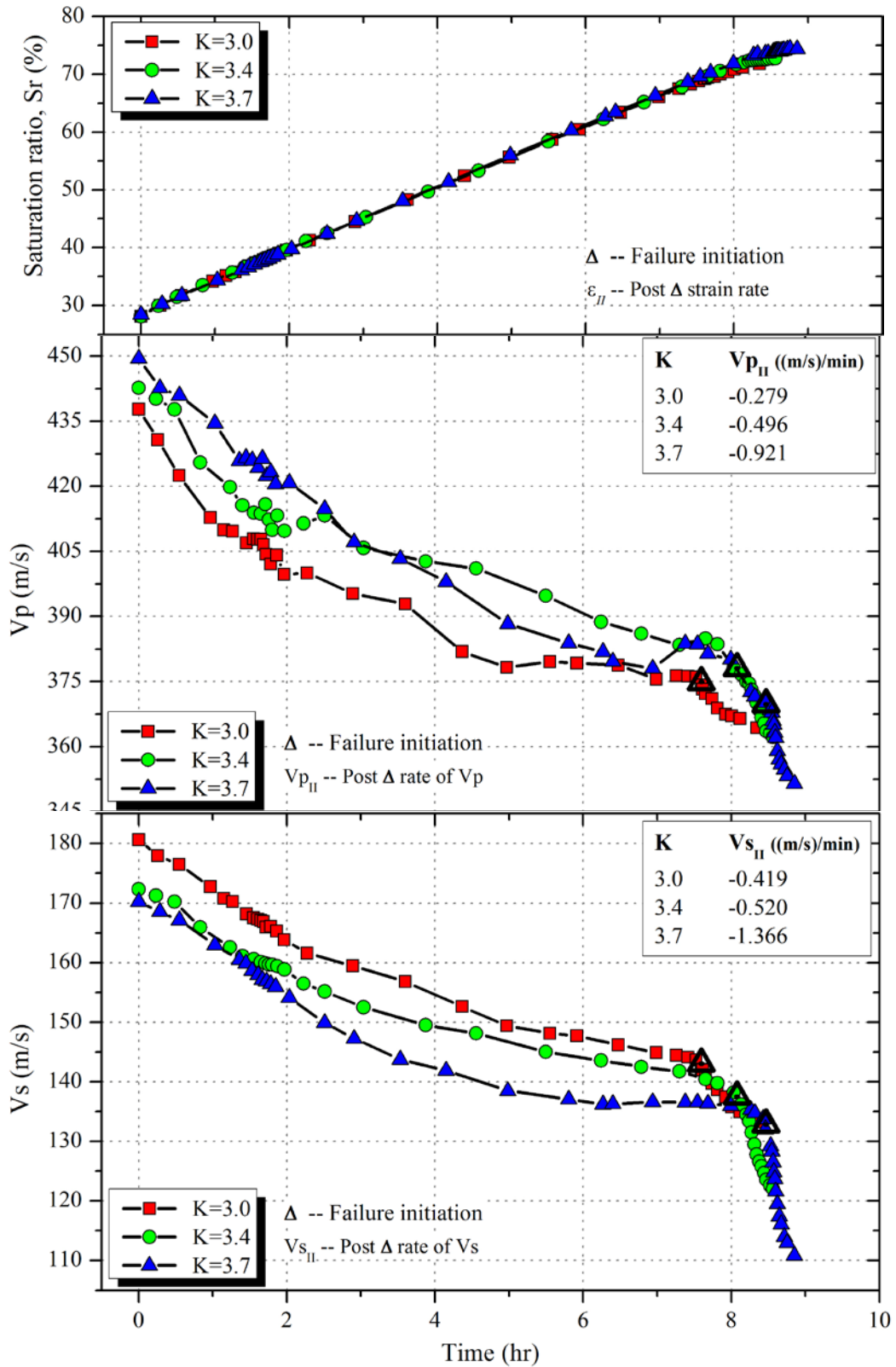


Figure 7.21: Response of elastic wave velocities at different principle stress ratios (K) during shearing infiltration tests; (a) Variation of saturation ratio (S_r) with time; (b) Compression wave velocity (V_p) response; (c) Shear wave velocity (V_s) response.

In order to draw a better comparison of wave velocities, V_p and V_s were corrected for changes in void ratio. Eq. 6.10 and Eq. 11, described in Section 6.3.2 were used to normalize wave velocities corresponding to $e_o = 0.673$, and $(\gamma_d)_o = 1.578 \text{ g/cm}^3$, and the normalized wave velocities were represented as V_p'' and V_s'' for compression wave and shear wave velocities respectively. Wave velocities were further normalized with respect to the corresponding initial values and are shown in Figure 7.22. Wave velocities which were first normalized with respect to designated void ratio and density, and then by their respective initial values were designated as $V_p''_{(Norm)}$ and $V_s''_{(Norm)}$ for compression wave and shear wave velocities respectively. Upon water infiltration but before failure initiation, $V_p''_{(Norm)}$ and $V_s''_{(Norm)}$ were observed to decrease by about 16% and 20% respectively. This decrease corresponded to an increase in saturation ratio from about 30% to 70%.

After failure initiation, both $V_p''_{(Norm)}$ and $V_s''_{(Norm)}$ decreased rapidly. Rate of wave velocities decrease after failure initiation is indicated as $V_p''_{II(Norm)}$ and $V_s''_{II(Norm)}$ for compression wave and shear wave velocities respectively. An important observation with respect to landslide monitoring is that, the rate of decrease of $V_p''_{(Norm)}$, and $V_s''_{(Norm)}$ are consistent with the corresponding post-failure axial strain rates (ϵ_{II}). For example, post-failure axial strain rate, ϵ_{II} , is largest for $K=3.7$, this is indicated by largest values of $V_p''_{II(Norm)}$ and $V_s''_{II(Norm)}$ as well. Thus, it can be surmised that elastic wave velocities are function of axial strain. This phenomenon is of significant importance with reference to landslide monitoring, and highlights the applicability of elastic wave velocities for actual landslide prediction.

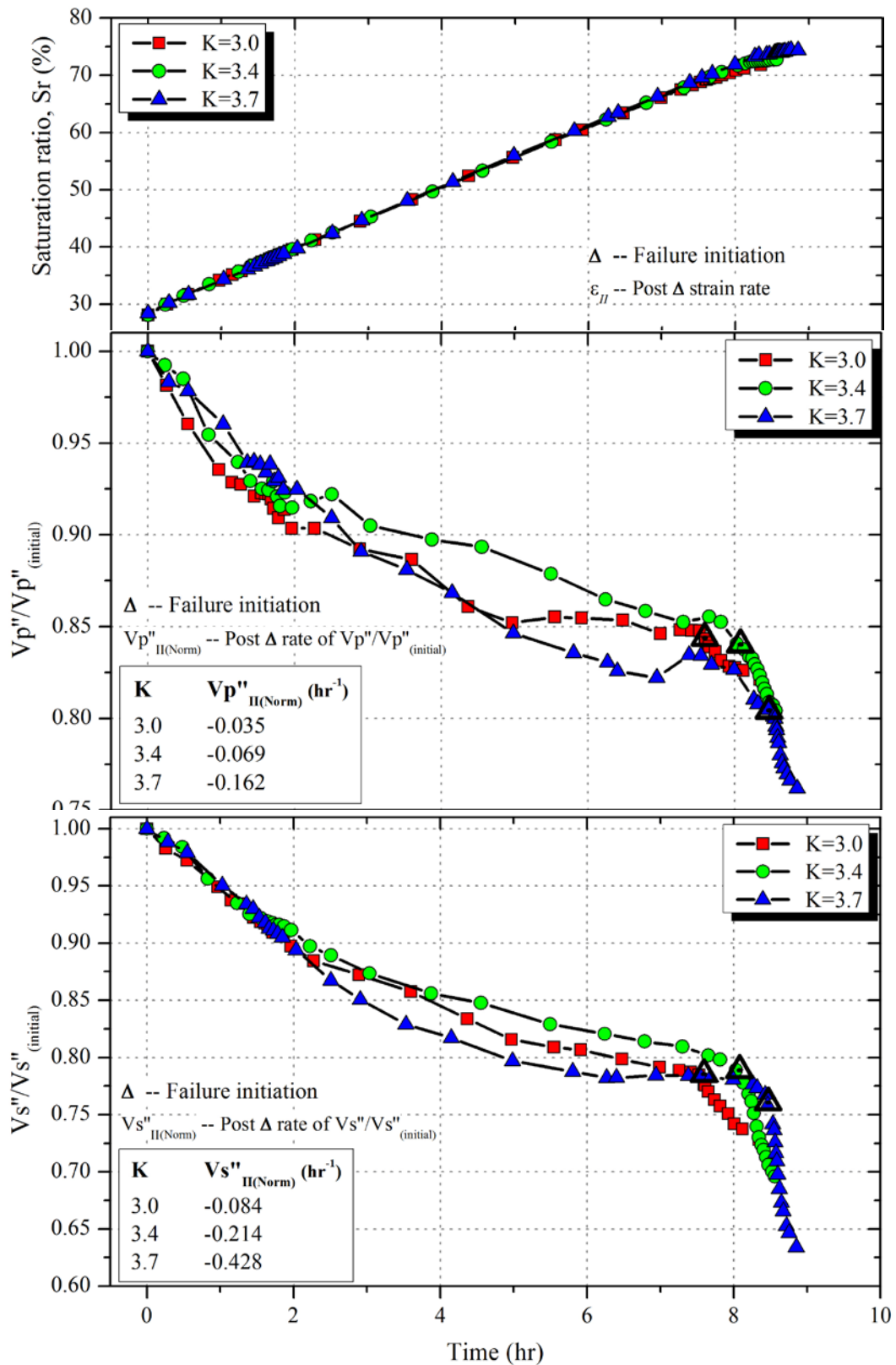


Figure 7.22: Response of elastic wave velocities (normalized corresponding to $e_o = 0.673$, and $\gamma_d = 1.578 \text{ g/cm}^3$) at different principle stress ratios (K) during shearing infiltration tests; (a) Saturation ratio (S_r) versus time; (b) Normalized compression wave velocities ($V_p''/V_p''_{(initial)}$); (c) Normalized shear wave velocities ($V_s''/V_s''_{(initial)}$).

7.5. MOISTURE DISTRIBUTION THROUGH HELICAL FILTER PAPER

Realistic reproduction of rain-induced landslides mechanism in laboratory element tests requires water injection into unsaturated soil specimen (Brand, 1981). Han (1997) and Melinda et al. (2004) attempted to reproduce such conditions by injecting water into a direct shear specimen whereas Getie (2012) injected water into a soil specimen in a simple shear apparatus. In all such cases water was injected into the soil specimen through a high air entry value ceramic disk fitted at the base of shear box. Water injected during simple shear/direct shear tests can be distributed evenly in soil specimens due to their small height to diameter ratio. However, similar attempts to inject water through ceramic disk fitted in pedestal of triaxial apparatus have been less fruitful. Water injected in a triaxial specimen through pedestal essentially wets the bottom of specimen first, before rising to the top of specimen through capillary suction. At any given time there is unequal distribution of water along the longitudinal axis of specimen. This makes the sample non-uniform, leading to progressive failure. For more uniform distribution of water in a triaxial specimen, a technique using a ceramic disk and a helical shaped filter paper wrapped around the specimen has been suggested in this section.

7.5.1 Ceramic Disk/Filter Paper Technique

Water can be injected uniformly in a triaxial specimen by using a ceramic disk fitted in pedestal (Figure 7.23(a)). Constant infiltration pressure applied on a burette, containing de-aired water and connected to the saturated ceramic disk, ensured more or less uniform water injection in triaxial specimen, as shown in Figure 7.14(a) and Figure 7.19(a), etc. The rate of water injection depended on magnitude of infiltration pressure applied on the burette. Rate of injection higher than soil permeability could cause accumulation of water at base of specimen, thereby, causing non-uniformity in specimen. This non-uniformity of moisture can be avoided if water is not allowed to accumulate at the base by providing additional drainage path around the periphery of specimen. Any material having permeability higher than soil, and soft enough not to disturb the stress ~ strain characteristics of the specimen can be made to cover the sides of specimen. This would allow water to flow towards the top of specimen

without being accumulated at the bottom. A filter paper (which has high permeability as compared to soil) cut specifically to form a helix around the specimen was utilized for this purpose (Figure 7.23(b), (c) and (d)). The helix shaped filter paper covered about 50% surface area of specimen. Helical shape of filter paper was adopted so that natural expansion/contraction of specimen during shearing is not disturbed. Pedestal having ceramic disk sealed to it was fitted in the triaxial cell (Figure 7.23(a)). Filter paper, forming a helix was assembled inside latex membrane (Figure 7.23(b)). Soil was poured-in very carefully by using a card-board funnel. Wet tamping technique of sample preparation was utilized for specimen preparation (Figure 7.23(c)). Figure 7.23(d) shows finalized shape of a completed specimen.

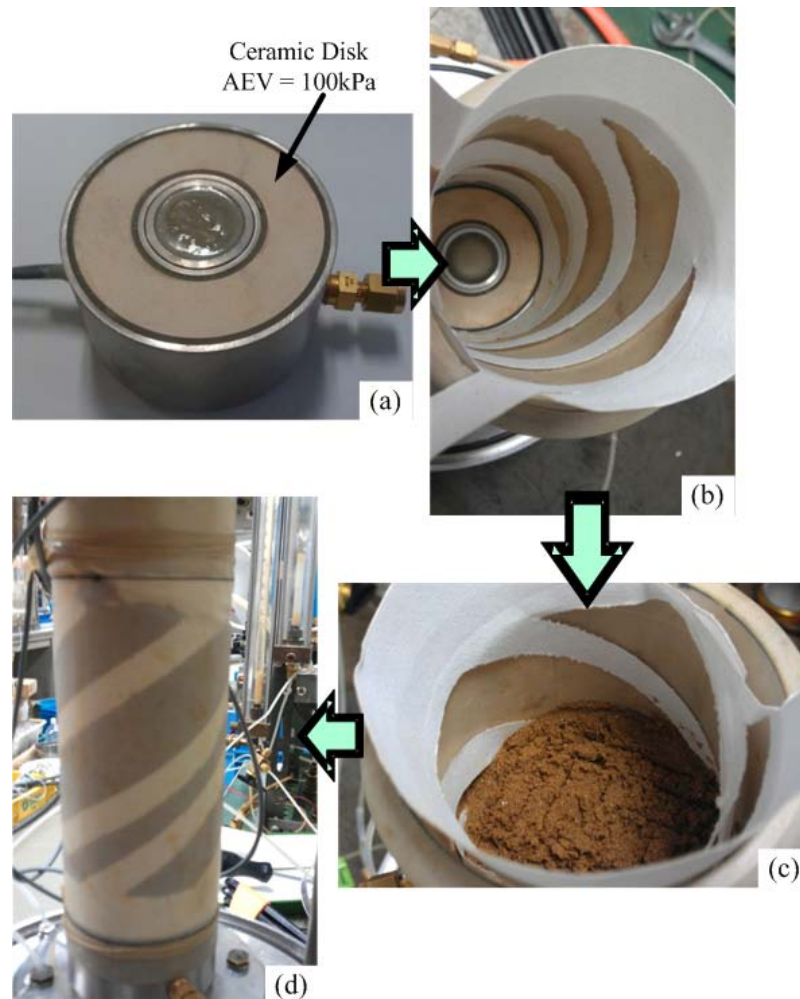


Figure 7.23: Water injection in a triaxial specimen using a ceramic disk and filter paper; (a) High AEV ceramic disk embedded in pedestal; water injected through application of back pressure; (b) Helical filter paper assembled inside latex membrane; (c) Specimen preparation by wet tamping; (d) Completed soil specimen.

To verify the effectiveness of filter paper technique, moisture content distribution in various sections of specimen was determined at the end of water injection tests. For this purpose specimens were carefully removed from triaxial cell Figure 7.24(a); pedestal was carefully taken out and membrane was cut open (Figure 7.24(b)). The specimens were divided into fifteen equal parts (Figure 7.24(c) and (d)) and gravimetric water content of each part was determined by placing them in oven for 24 hours (105 ± 5 °C). Care was practiced to procure samples from the center of each part, so that it truly represented the moisture content of each of fifteen parts. By knowing the end of test void ratio (e) and specific gravity (G_s) of Edosaki sand, gravimetric water content (w) was then used to calculate the actual saturation ratio (S_r) of each part by using the following expression;

$$S_r = \frac{w \cdot G_s}{e} \quad (7.7)$$

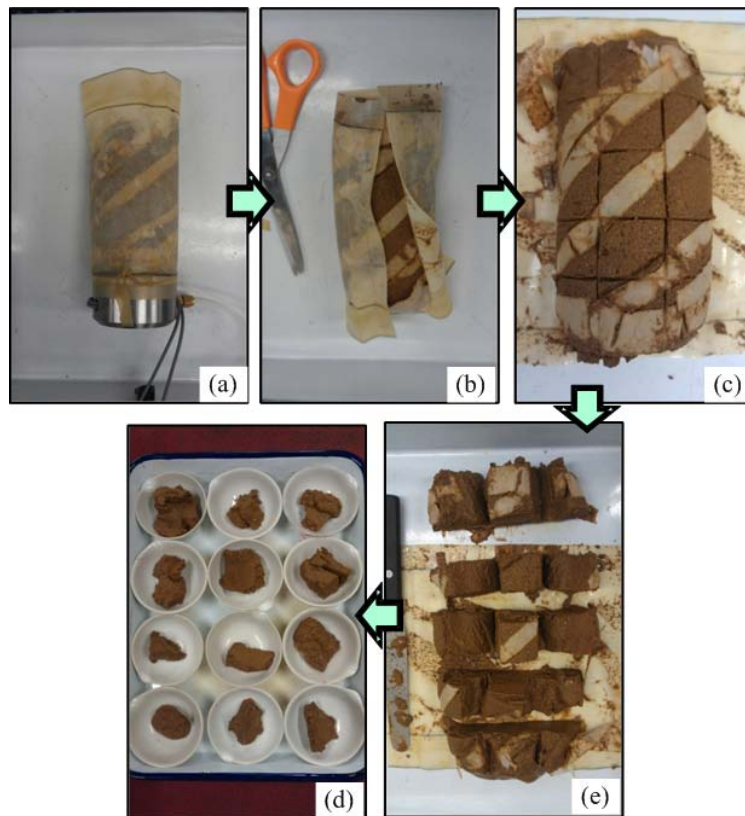


Figure 7.24: End of test moisture distribution in triaxial specimen; (a) Specimen removed from triaxial cell; (b) Pedestal is detached carefully and membrane is cut open; (c)(d) Fifteen equal sections are marked and specimen is divided into 15 equal parts; (e) Sample collected for moisture content from center of each part.

For the sake of simplicity, specimens were divided into three vertical section viz., *V1*, *V2*, and *V3* and five horizontal sections viz., *H1*, *H2*, *H3*, *H4*, and *H5*, as shown in Figure 7.25(a) and (b) respectively. Similar nomenclature is used in various figures to represent the moisture distribution in various specimens in the following sections.

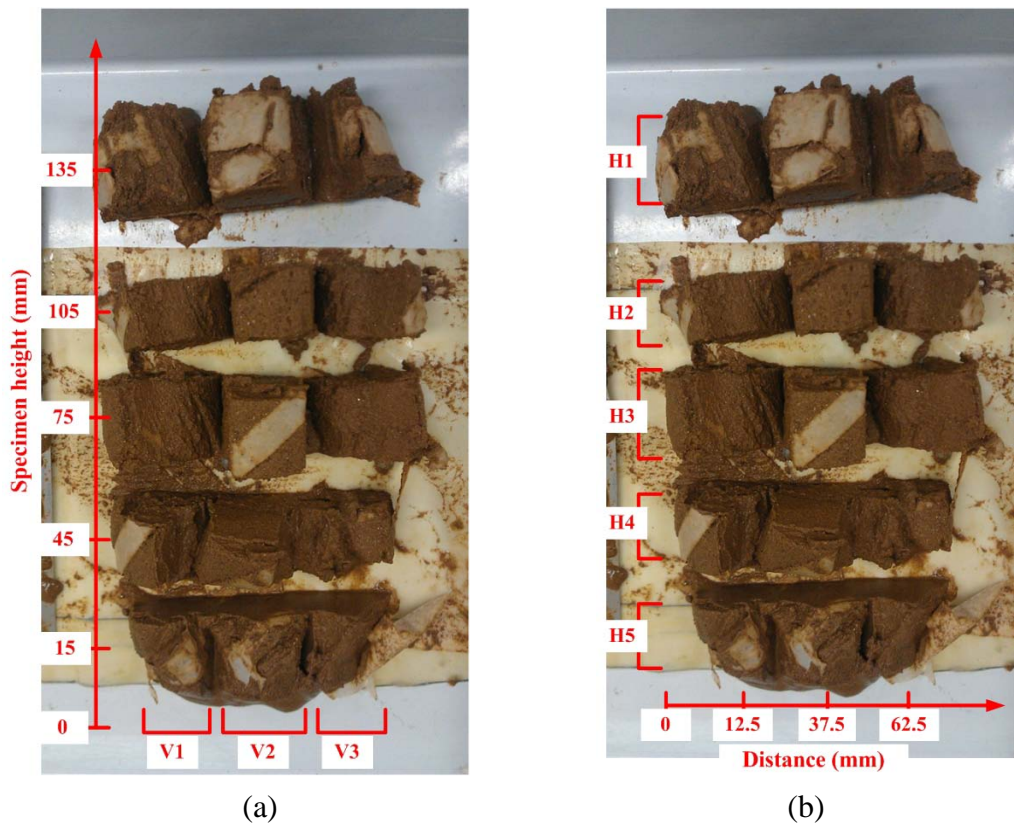


Figure 7.25: Nomenclature for labeling end of test moisture distribution; (a) Longitudinal sections; (b) Transverse sections.

7.5.2 Moisture Distribution in Specimens

Efficiency of helical filter paper system is based on the assumption that it will facilitate moisture distribution in the specimen because of having high permeability as compared to compacted soil. To test the validity of this hypothesis, end of test moisture content at various sections of specimens were determined. Behavior of specimens upon water injection was compared with the corresponding moisture distribution in order to find out the relationship between mode of failure and moisture distribution.

Figure 7.26 summarizes the response of water injection experiments, on 56% dense Edosaki sand specimens subjected to principle stress ratio (K) of 3.0, with and without using the filter paper. Various specimens are designated by their code names listed in Table 7.2. Nearly uniform water injection rate was achieved by controlling the infiltration pressure applied on top of burette. Specimens *CSI-11* (with filter paper), and *CSI-12* (without filter paper) started straining identically with water infiltration. However, a momentary increase in strain rate was observed at about 50% saturation ratio for specimen without helical filter paper. This increased strain rate depicts a localized failure in the specimen which may have occurred due to the localized accumulation of water in the specimen. Similarly, specimen *CSI-2*, which was also without helical filter paper, exhibited multiple failures, i.e., progressive failure, before the final failure at about 90% saturation ratio. However, such intermediate failures were not observed when helical filter paper was used around the specimen, as observed for specimen *CSI-11*. Such specimen is marked with only a single failure at around 70% saturation ratio. This final failure was identified by dissipation of pore water pressure in the specimen i.e., water started to come out of the drainage valve as indicated by the decrease in rate of saturation ratio (Figure 7.26(a)). For intermediate failures however, no water came out of the specimens. This is probably because pore water pressure first developed near the base of specimen, once failure occurred (indicated by increased strain rate) in the bottom zone, pore water started accumulating in other zones of specimen. With further water injection pore water pressure increased in the rest of the specimen. This net increase in pore water pressure finally led to failure initiation in the specimen, as indicated by a rapid increase in strain rate. At this point water started coming out of the drainage valve, indicating the

presence of a continuous drainage path inside the specimen. Thus the tests were stopped at this point.

It is also noticeable that specimens undergoing progressive failure failed at later time (and consequently higher saturation ratio), compared to specimen without progressive failure. It may be explained on the basis of specimen density at the time of failure initiation. As discussed in Section 7.4.2, time of failure initiation is a function of specimen density; greater the density, the specimen would require more time (and higher saturation ratio) to fail. Each progressive failure increased specimen density as indicated by larger magnitude of corresponding axial strains. Thus the specimens being denser, required more time for failure to initiate.

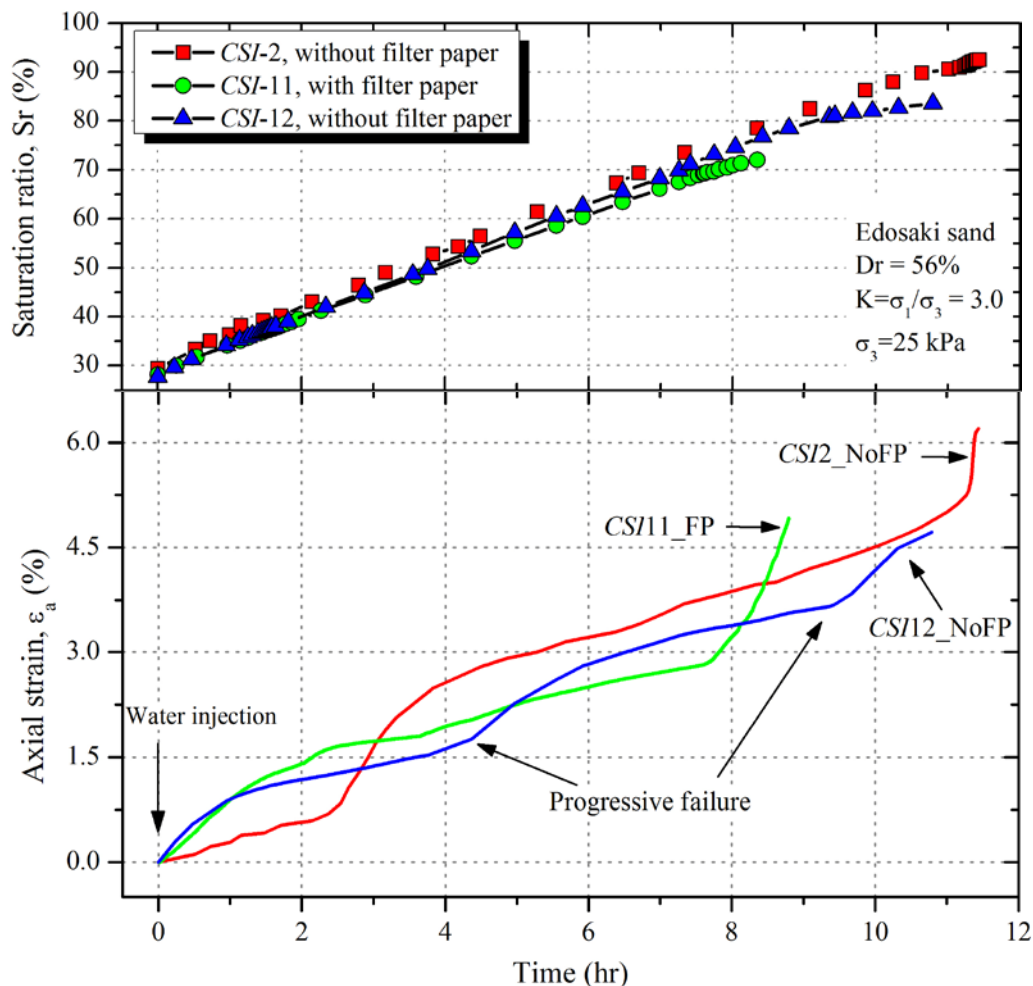


Figure 7.26: Effect of helical filter paper on strain response of Edosaki sand specimens ($Dr = 56\%$, $K = 3.0$, $\sigma_3 = 25$ kPa).

As explained in the previous section specimens were divided into fifteen parts, i.e., three vertical sections *V1*, *V2*, and *V3*; and five horizontal sections namely, *H1*, *H2*, *H3*, *H4*, and *H5*. Figure 7.27 represents the end of test moisture distribution in specimen *CSI-12* in which helical filter paper was not used and which underwent progressive failure upon water injection. An analysis of three vertical sections (Figure 7.27(a)), show variation of end of test saturation ratio along the height of specimen. Saturation ratio near the base of specimen was observed to be much higher than the top. This large difference in saturation ratio along specimen height causes non-uniformity in the specimen and is responsible for progressive failure as shown in Figure 7.26. Moisture distribution along specimen diameter was not observed to fluctuate much (Figure 7.27(b)). This may be because of the uniform water injection across the specimen diameter. However, for section *H5*, representing the bottom most section, saturation ratio was higher in the center of specimen than its sides. Since the water was not injected through the central part of base pedestal (since it was occupied by piezoelectric disk transducer), center of the specimen was expected to have lower saturation but this was not the case. A possible explanation of this anomaly may be that water in vertical sections *V1*, and *V3* (at the sides of specimen) was pushed upwards by a continuous stream of water percolating through the ceramic disk. Thus, water on the sides of specimen continued to move upwards. Whereas in the central section, *V2*, water kept accumulating in the lower most part because of the absence of any upward push, hence is the reason for its high saturation. A vertical dashed line at about 83% represents the overall saturation ratio of specimen at the time of failure initiation.

A comparison of end of test saturation ratio of test specimen *CSI-11*, shown in Figure 7.28, represents a much uniform moisture distribution throughout the specimen. For simplicity of comparison, axes scales are kept similar for Figure 7.27 and Figure 7.28. Even after using the helical filter paper, the bottom of specimen was wetter compared to the top but the maximum difference in saturation ratio between specimen bottom and top was reduced from about 30% to around 10%. This shows the effectiveness of helical filter paper in uniform distribution of injected water. Similar to the without filter paper case, central part of specimen exhibited slightly higher moisture compared to the sides, as shown in Figure 7.28(b). Owing to a

relatively uniform moisture distribution, the specimen did not show progressive failure as was observed without filter paper (Figure 7.26).

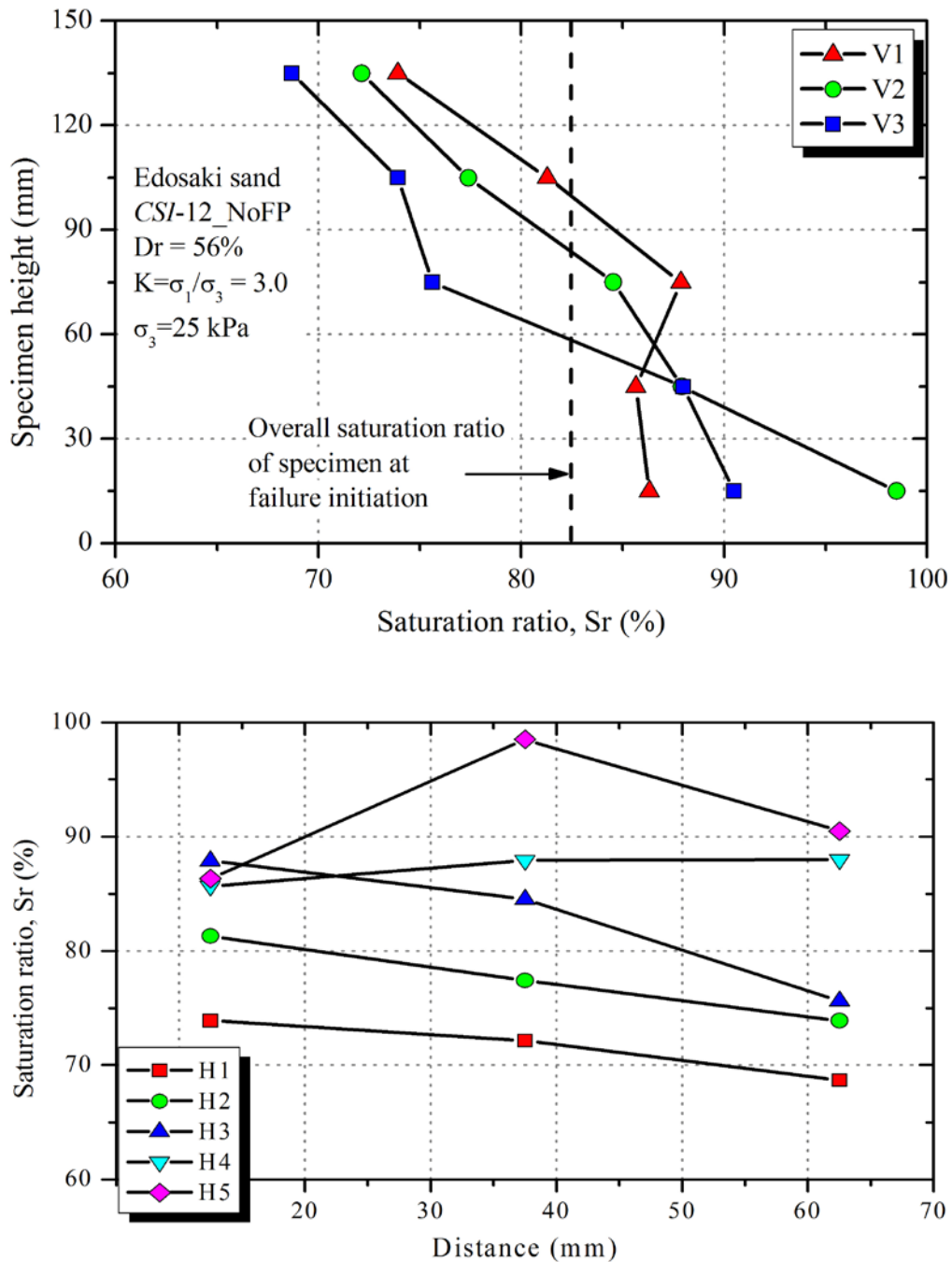


Figure 7.27: End of test moisture distribution when helical filter paper was not used ($Dr = 56\%$, $K = 3.0$, $\sigma_3 = 25$ kPa); (a) Moisture variation along specimen height; (b) Moisture variation along specimen diameter.

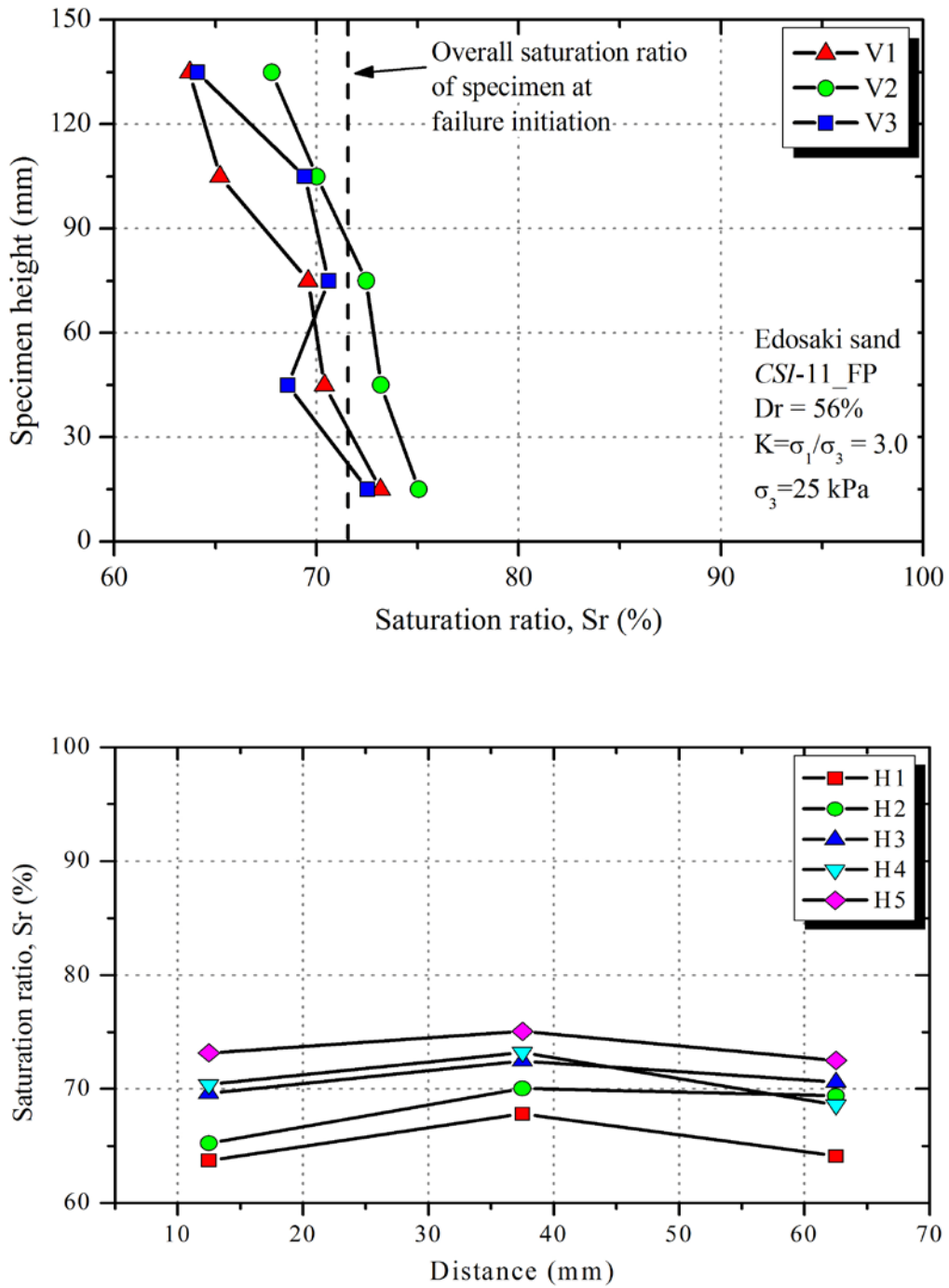


Figure 7.28: End of test moisture distribution when helical filter paper was used ($D_r = 56\%$, $K = 3.0$, $\sigma_3 = 25 \text{ kPa}$); (a) Moisture variation along specimen height; (b) Moisture variation along specimen diameter.

Figure 7.29 shows end of test moisture distribution of specimens, with and without helical filter paper when water was injected into Edosaki sand specimens with initial relative density (Dr) 30% and principle stress ratio (K) of 3.4; whereas a similar plot for initial test conditions $Dr = 56\%$ and $K = 3.7$ is shown in Figure 7.30. Moisture contents shown in these figures are calculated by averaging the moisture contents of three vertical sections $V1$, $V2$, and $V3$ at each level of specimen height. The use of helical filter paper around the specimen provided additional drainage paths to injected water without letting it to accumulate at the base of specimen. Thus, moisture distribution of specimens with filter paper were observed to be much uniform compared to the specimens without filter paper. On average non-uniformity of moisture between specimen top and bottom decreased by about 50% with the use of helical filter paper. Owing to the uniform distribution of water, specimens with helical filter paper did not show tendency of progressive failure, as shown in Figure 7.31 and Figure 7.32.

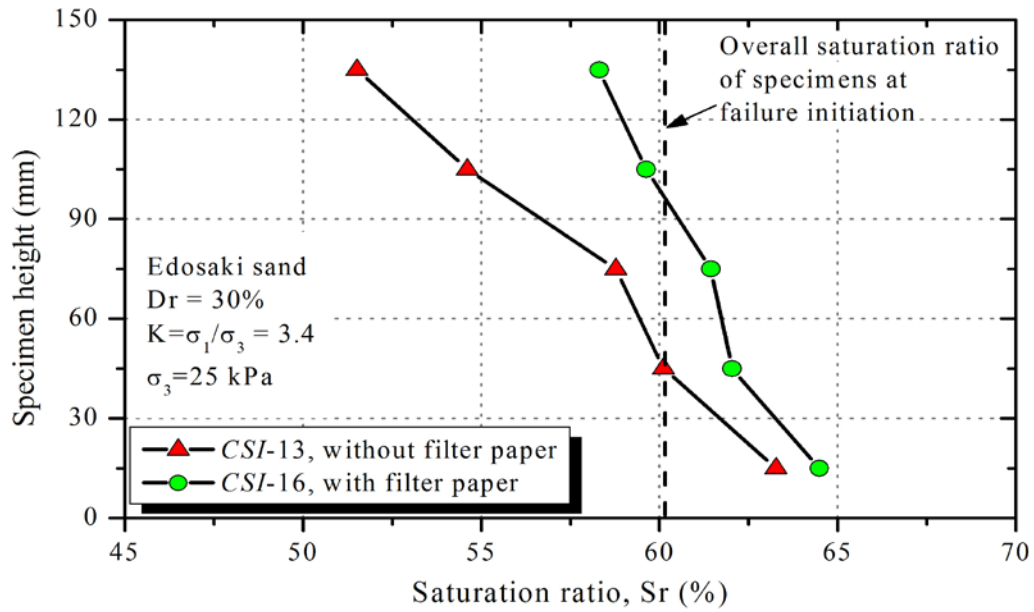


Figure 7.29: Comparison of end of test moisture distribution in the specimens with, and without using helical filter paper ($D_r = 30\%$, $K = 3.4$, $\sigma_3 = 25$ kPa).

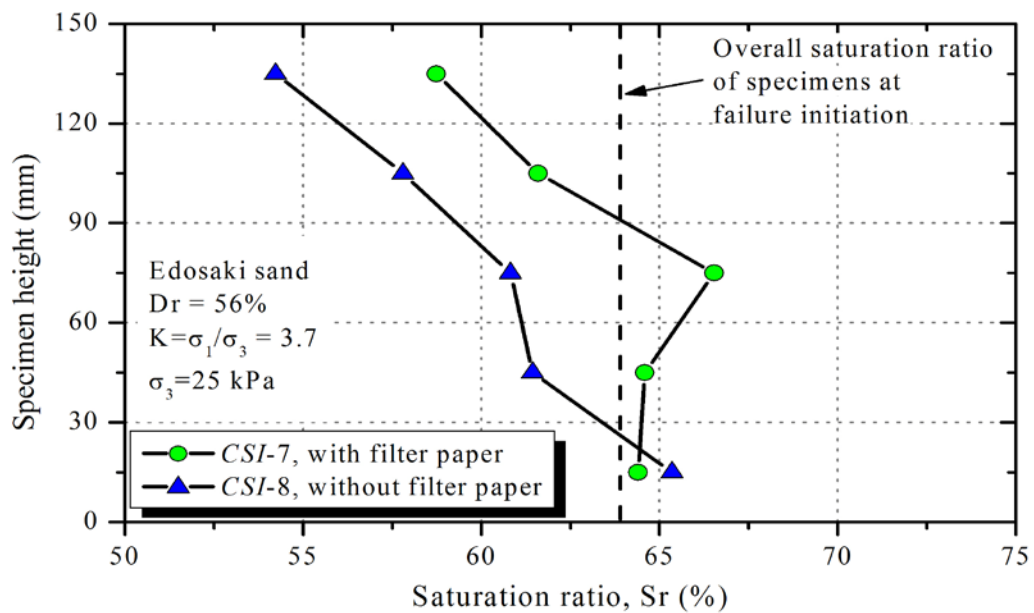


Figure 7.30: Comparison of end of test moisture distribution in the specimens with, and without using helical filter paper ($D_r = 56\%$, $K = 3.7$, $\sigma_3 = 25$ kPa).

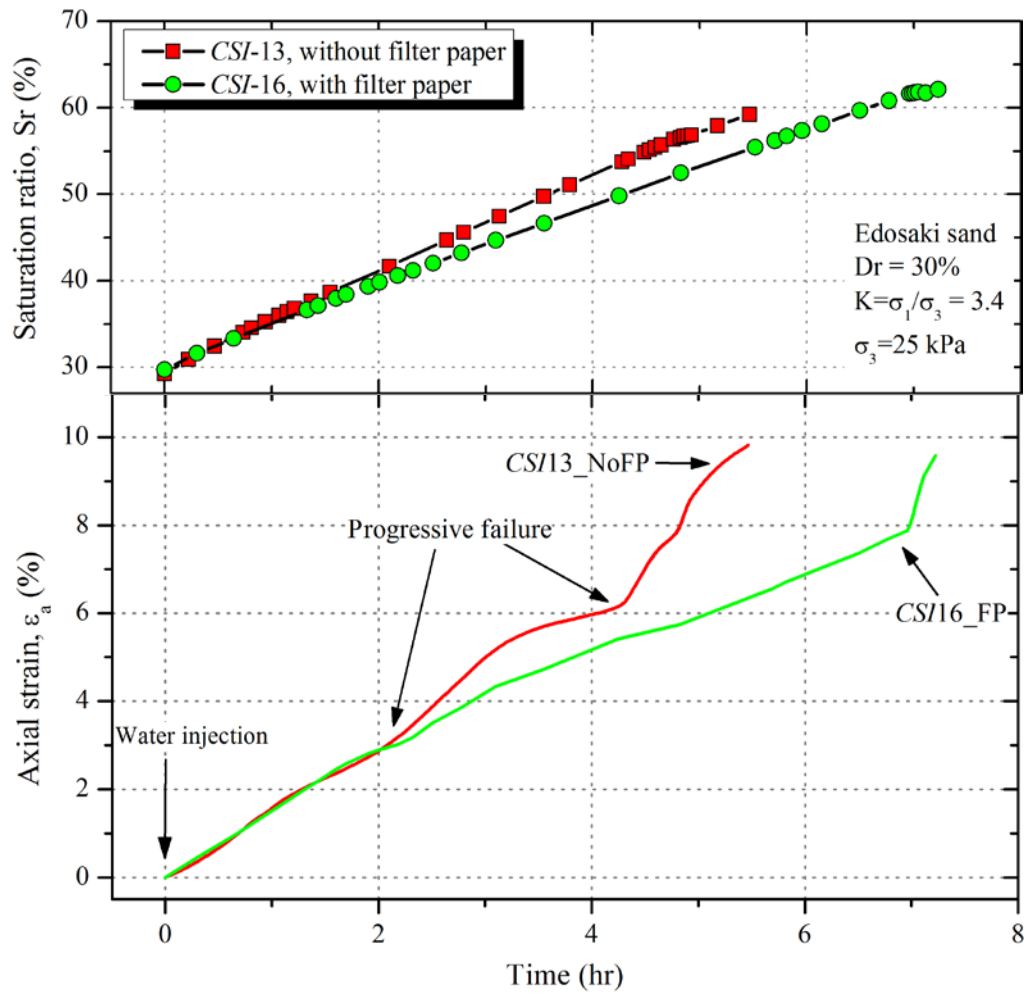


Figure 7.31: Comparison of strain response of specimens with, and without using helical filter paper ($D_r = 30\%$, $K = 3.4$, $\sigma_3 = 25$ kPa).

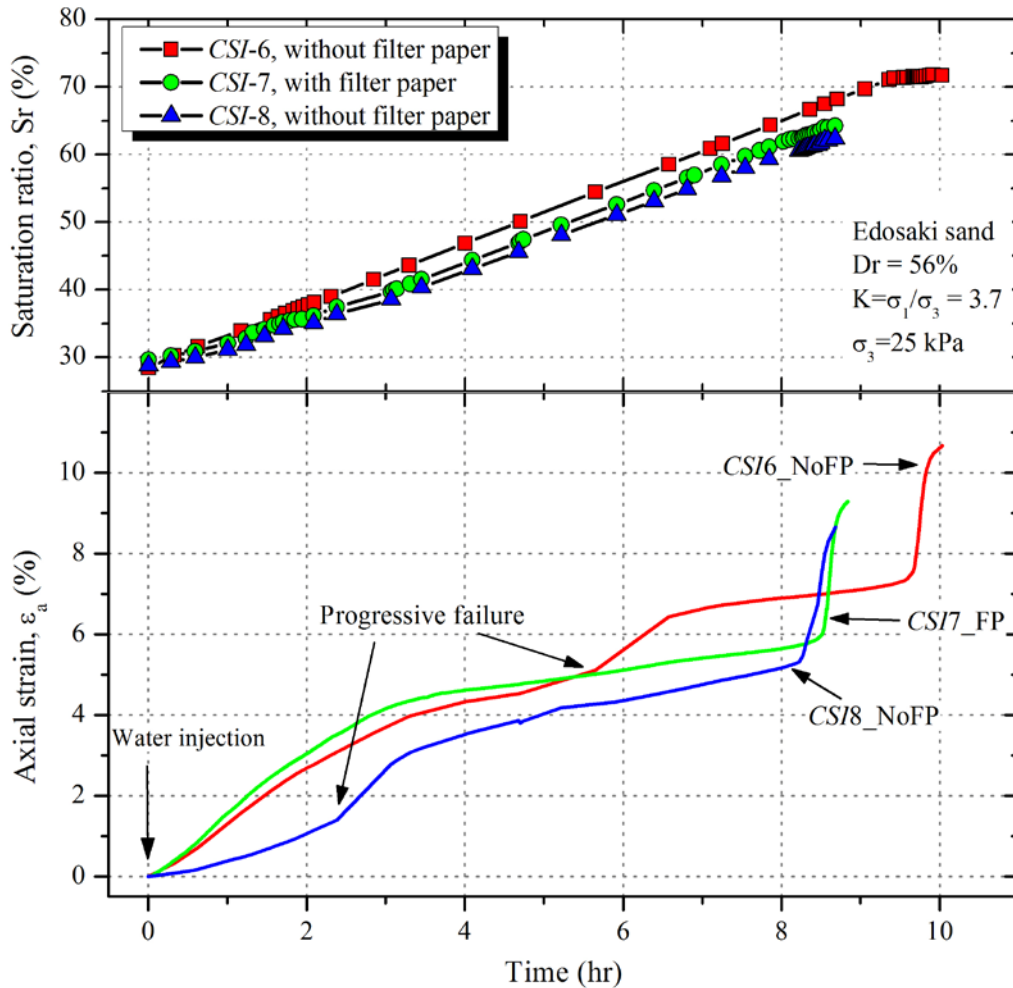


Figure 7.32: Comparison of strain response of specimens with, and without using helical filter paper ($Dr = 56\%$, $K = 3.7$, $\sigma_3 = 25$ kPa).

It is surmised that, the helical filter paper wrapped around the specimen provides additional drainage paths along the periphery of specimen; and prevents water from accumulating at the base of specimen. Injected water rises along the periphery of soil specimen through the filter paper and simultaneously makes its way radially inwards towards the center of specimen; thereby considerably reducing the wetting time. This improves the uniformity of moisture inside the specimen at any given time during water injection process. This also helps avoiding localized water accumulation inside the specimens, thereby reducing the possibility of progressive failure.

7.5.3 Deformation Characteristics

Figure 7.33 and Figure 7.34 show the response of specimen *CSI-10* ($Dr = 56\%$, $K = 3.4$), and *CSI-5* ($Dr = 56\%$, $K = 3.0$) respectively, plotted against saturation ratio. In both of these specimens helical filter paper was used for moisture distribution and thus progressive failure was not observed. Figure 7.33(a), and Figure 7.34(a) compare the response of axial strain obtained by means of *LVDT* with that recorded with *LDTs*. *LDTs* could only measure strain up to 3%~4%, and thus were removed as soon as they reached their maximum capacity, as indicated in each figure. Axial strain measured by *LDTs* was observed to be slightly less compared to *LVDT*. This may be because *LDTs*, 11cm in length, were used in this study. These were fixed in the center of specimens and thus were not able to determine strains that could develop close to end platens (i.e., near specimen's longitudinal edges). A close observation of initial part of Figure 7.33(a) reveals that, *LVDT* started recording axial strain immediately upon water infiltration. However, *LDTs* did not show any axial strain initially, since initially the strains were localized only in the bottom most part of the specimen close to end platen, which was outside the range of *LDT*. As soon as the water front reached the limit of *LDTs*, they started recording axial strains with nearly the same magnitude as *LVDT*; this can be confirmed by near parallel trend between *LVDT* and *LDT* response beyond this point.

Since water was being injected through the ceramic disk, it was thus natural for the bottom of specimen to get wet first. This can be observed from the response of radial deformation clip gauges, as shown in Figure 7.33(b) and Figure 7.34(b). In both cases, *CG-3*, located near the bottom of the specimen, started developing strains first. As the water permeated towards the top, *CG-2* (located at the center of specimens), and then *CG-1* (located near the top of specimens) started deforming radially. Negative magnitudes of radial deformations indicate radial expansion of specimens (increase in diameter). Although the center of specimen initiated deforming at a later time majority of post-failure strains appear to be accumulated in the central part of the specimen, as indicated by very large radial strain of *CG-2* after failure initiation (Figure 7.33(b), and Figure 7.34(b)).

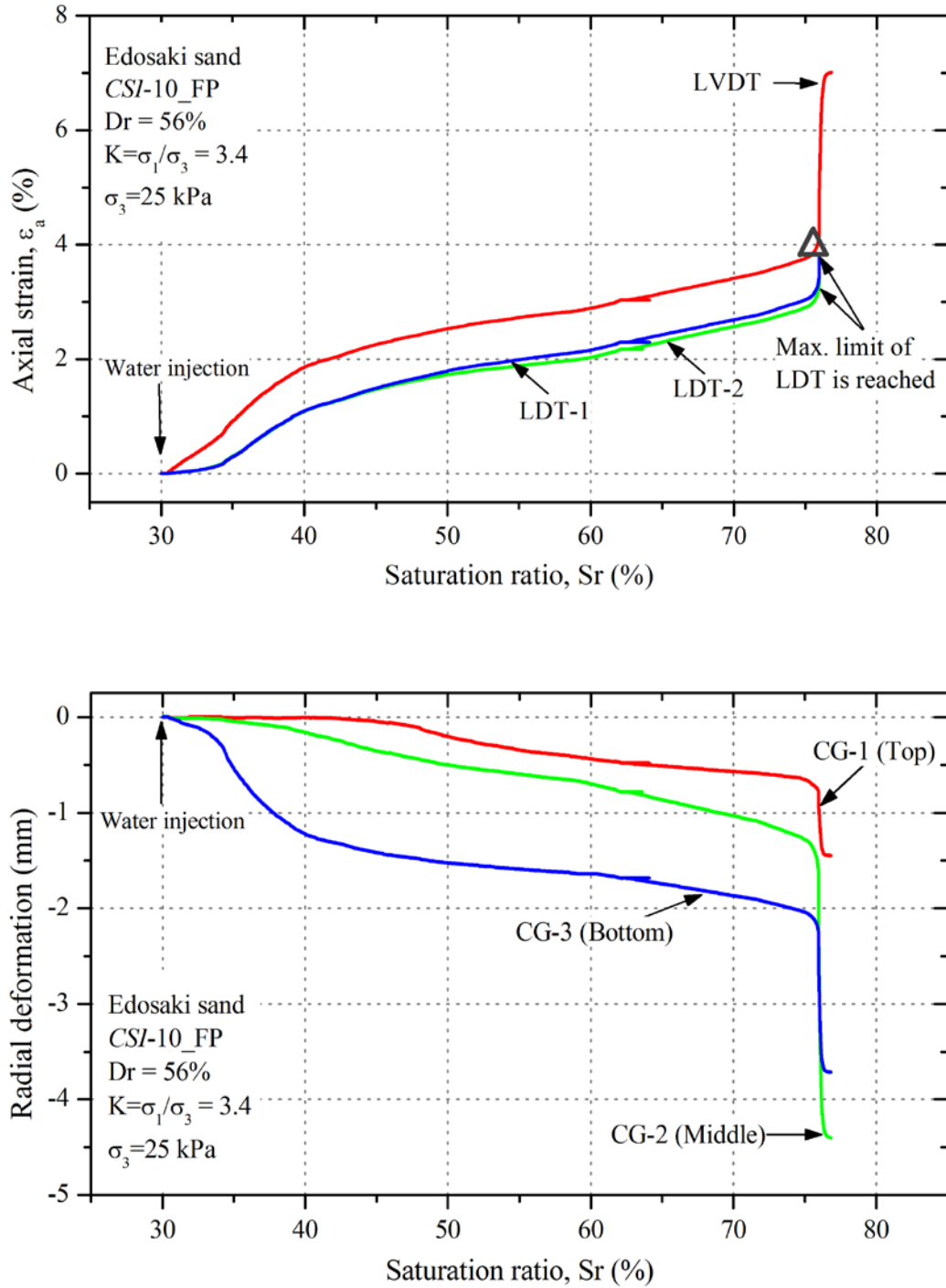


Figure 7.33: Deformation characteristic during shearing infiltration test when helical filter paper was used ($D_r = 56\%$, $K = 3.4$, $\sigma_3 = 25$ kPa); (a) Axial strain response; (b) Radial strain response.

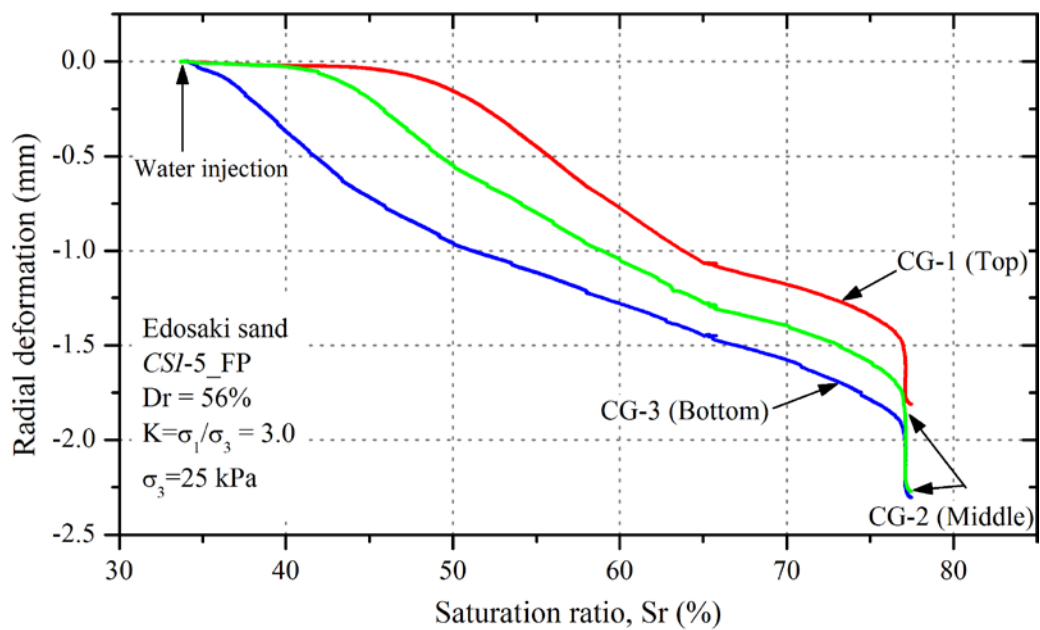
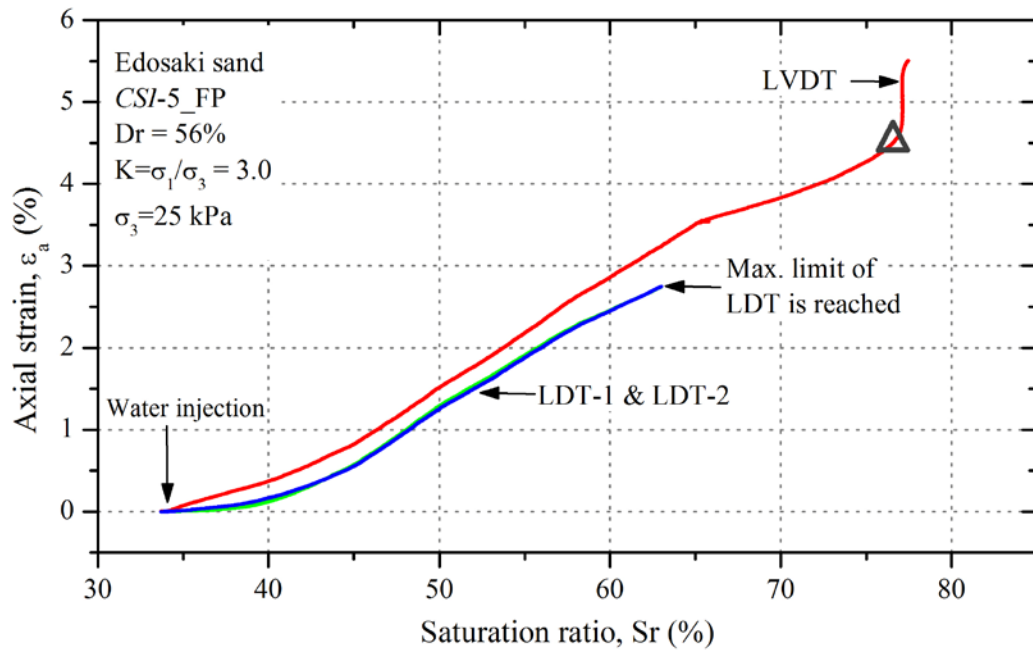


Figure 7.34: Deformation characteristic during shearing infiltration test when helical filter paper was used ($Dr = 56\%$, $K = 3.0$, $\sigma_3 = 25 \text{ kPa}$); (a) Axial strain response; (b) Radial strain response.

Figure 7.35 and Figure 7.36 show the response of specimens *CSI-6*, and *CSI-8* respectively. Both the specimens had an initial relative density (D_r) of 56% and a principle stress ratio (K) of 3.7. Helical filter paper was not used in these specimens. Both the specimens failed progressively before final failure (indicated by Δ). Unlike the specimens with filter paper, radial strains were more or less accumulated near specimen's base. This was primarily because of the non-uniform distribution of water along specimen's height. Since water kept accumulating in the lower part of specimens, radial strains observed by middle and bottom clip gauges (*CG-2* and *CG-3*) kept on increasing without any appreciable increase in radial strain near the top of specimen (*CG-1*). Radial strains thereby kept on decreasing along the height of specimens.

Monitoring radial strains along different levels of the specimen also gives an indication of location of initiation of any intermediate failure, as can be seen in Figure 7.36(b). The first failure of specimen *CSI-8* was mainly concentrated near the base of specimen, as indicated by the increased strain of *CG-3*; whereas no significant variation was observed for *CG-1*. Similarly, increased strain rate of *CG-1* around second failure indicates that the failure was mainly concentrated in the top part of specimen.

From the discussions presented in hereinbefore it can be surmised that water injection through a ceramic disk in unsaturated triaxial specimen causes accumulation of water at the base of specimen; leading to progressive failures. Such localized water accumulation, and the resulting progressive failures can be avoided by using a helix shaped filter paper around the periphery of the specimens. This ensures a more uniform water distribution along the height of specimens, resulting in radial deformations which are concentrated near the center of the specimens. This assists in reproducing the natural mechanism of rain-induced landslides in laboratory element tests.

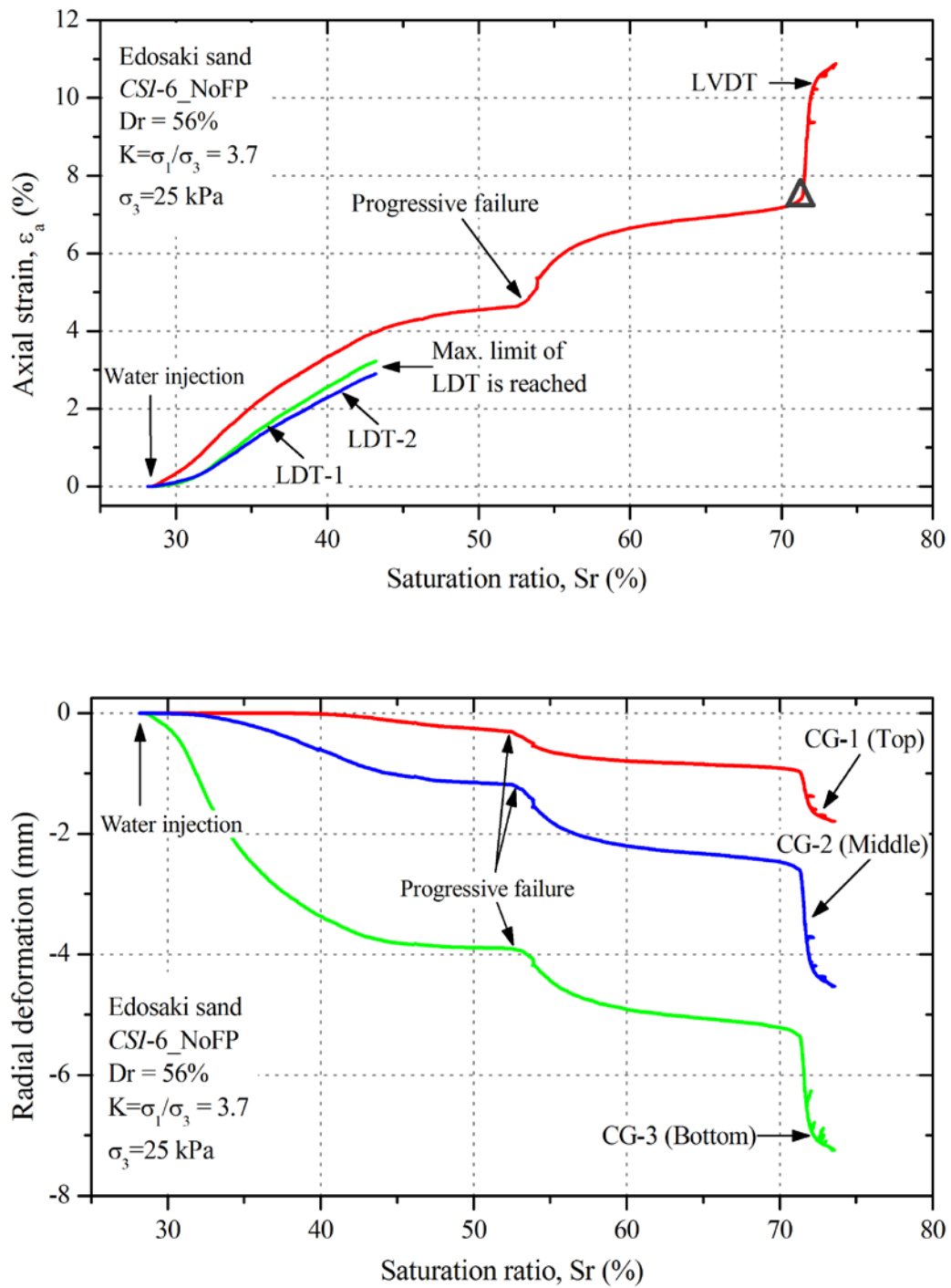


Figure 7.35: Deformation characteristic during shearing infiltration test when helical filter paper was not used ($D_r = 56\%$, $K = 3.7$, $\sigma_3 = 25$ kPa); (a) Axial strain response; (b) Radial strain response.

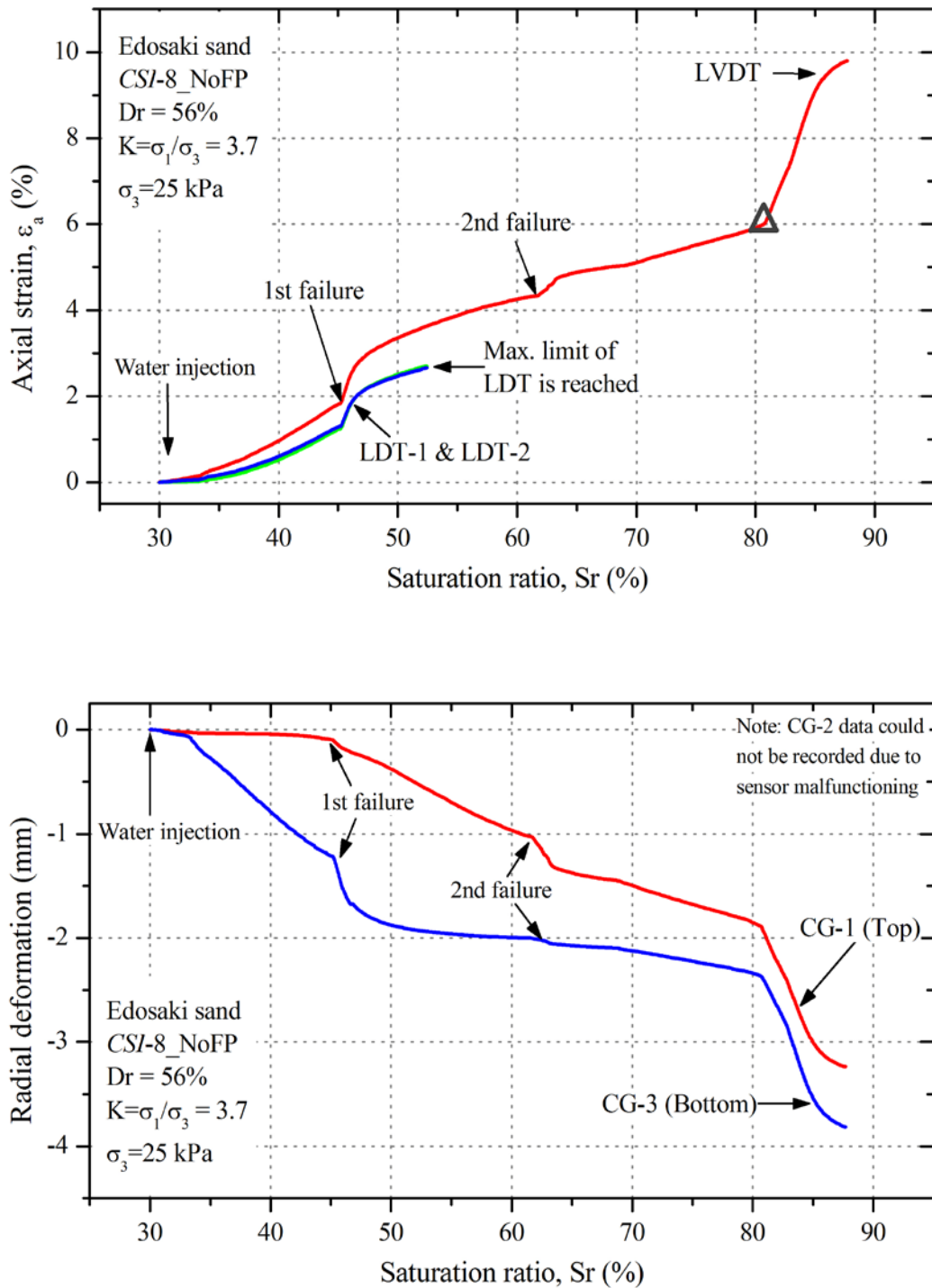


Figure 7.36: Deformation characteristic during shearing infiltration test when helical filter paper was not used ($D_r = 56\%$, $K = 3.7$, $\sigma_3 = 25$ kPa); (a) Axial strain response; (b) Radial strain response.

7.6. SUMMARY

This chapter summarizes experimental studies exploring the mechanism of rainfall-induced landslides, and the corresponding behavior of elastic wave velocities during landslide initiation. Wet slopes were found to initiate failure earlier and hence were surmised to be in a relatively unstable condition as compared to dry slopes. The mode of failure also changed from brittle (immediate/sudden) to ductile for relatively moist slopes. Experimental evidence exploring the effects of initial relative density on failure initiation revealed that, under identical rainfall, loose slopes initiate failure earlier than dense slopes. Also after failure initiation, loose slopes tend to deform very quickly compared to dense slopes. The effects of slope inclination on landslide initiation were also studied by modeling slope inclination in terms of principle stress ratio. Steep slopes were found to exhibit very rapid movement after failure initiation.

Behavior of elastic wave velocities was found to be sensitive to soil wetting as well soil deformations. With changes in soil moisture due to water injection, elastic wave velocities gradually kept on decreasing. As soon as soil initiated failure, wave velocities decreased at an accelerated rate. Such sharp decrease in wave velocities can be useful for predicting failure initiation in actual landslide conditions. Moreover in post-failure stage, rate of wave velocities followed the rate of axial strain. This observation can be useful for predicting the rate of slope movement in the field.

Water infiltration in an unsaturated triaxial specimen generally results in non-uniform distribution of water in the specimen. A new technique for distributing the injected water in triaxial specimen by using a helical filter paper has been proposed in this chapter. Comparison of end of test moisture distribution from various experiments confirms a more uniform water distribution in the specimen with helical filter paper. Strain responses of various experiments also show the presence of helical filter paper reducing the possibilities of progressive failure upon water infiltration.

7.7. REFERENCES

- Aitchison, G. D. (1960). *Relationships of Moisture Stress and Effective Stress Functions in Unsaturated Soils*. Proceedings: Conference on pore pressure and suction in soils (pp. 47-52), London, UK.
- Anderson, S. A., & Sitar, N. (1995). Analysis of Rainfall-Induced Debris Flows. *Journal of Geotechnical Engineering*, 121(7), 544-552.
- Brand, E. W. (1981). Some Thoughts on Rain-Induced Slope Failures. *Proc. of 10th International Conference on Soil Mechanics and Foundation Engineering*, 3, 373-376.
- Brenner, R. P., Tam, H. K., & Brand, E. W. (1985). Field Stress Path Simulation of Rain-Induced Slope Failure. *Proc. of 11th International Conference on Soil Mechanics and Foundation Engineering*, 2, 991-996.
- Das, B. M. (2001). *Principles of Geotechnical Engineering* (5th ed.). United States: Thomson-Engineering.
- Farooq, K. (2002). Experimental Study on Failure Initiation in Sandy Slopes Due to Rainfall Infiltration (Phd Thesis). *Tokyo, The University of Tokyo*.
- Farooq, K., Orense, R., & Towhata, I. (2004). Response of Unsaturated Sandy Soils under Constant Shear Stress Drained Condition. *Soils and foundations*, 44(2), 1-13.
- Fredlund, D. G., & Rahardjo, H. (1993). *Soil Mechanics for Unsaturated Soils*: Wiley-Interscience Publication, John Wiley & Sons, New York.
- Fredlund, D. G., Rahardjo, H., & Fredlund, M. D. (2012). *Unsaturated Soil Mechanics in Engineering Practice*: John Wiley & Sons.
- Gallage, C., & Uchimura, T. (2010). Effects of Dry Density and Grain Size Distribution on Soil-Water Characteristic Curves of Sandy Soils. *Soils and foundations*, 50(1), 161-172.

- Getie, G. (2012). *Shear Deformation and Failure of Unsaturated Soil Due to Injection of Water under Constant Stress*. MSc, University of Tokyo, Tokyo, Japan.
- Gu, X.-q., Yang, J., & Huang, M.-s. (2013). Laboratory Investigation on Relationship between Degree of Saturation, B-Value and P-Wave Velocity. *Journal of Central South University*, 20(7), 2001-2007. doi: 10.1007/s11771-013-1701-x
- Han, K. K. (1997). *Effect of Hysteresis, Infiltration and Tensile Stress on the Strength of an Unsaturated Soil*. MSc Thesis, Nanyang Technological University, School of Civil and Structural Engineering.
- Hardin, B. O., & Richart, F. E. (1963). Elastic Wave Velocities in Granular Soils. *J. Soil Mech. and Found. Div., ASCE*, 89(1), 33-65.
- Huang, Y. (1994). *Effect of Suction on Strength and Deformation Behavior of Unsaturated Collapsible Soils*. PhD Thesis, University of Tokyo, Japan.
- Ishihara, K., Tsukamoto, Y., & Nakayama, S. (1999). *Flow-Type Failure of Slopes Based on Behavior of Anisotropically Consolidated Sand*. Proceedings: IS-SHIKOKU'99, Proceedings of the International Symposium on Slope Stability Engineering (pp. 3-12).
- Melinda, F., Rahardjo, H., Han, K., & Leong, E. (2004). Shear Strength of Compacted Soil under Infiltration Condition. *Journal of Geotechnical and Geoenvironmental Engineering*, 130(8), 807-817. doi: doi:10.1061/(ASCE)1090-0241(2004)130:8(807)
- Muraleetharan, K. K., & Granger, K. K. (1999). The Use of Miniature Pore Pressure Transducers in Measuring Matric Suction in Unsaturated Soils. *ASTM geotechnical testing journal*, 22(3), 226-234.
- Ng, C. W., & Pang, Y. (2000). Influence of Stress State on Soil-Water Characteristics and Slope Stability. *Journal of Geotechnical and Geoenvironmental Engineering*, 126(2), 157-166.

- Nishiumura, T., Koseki, J., Fredlund, D. G., & Rahardjo, H. (2012). Microporous Membrane Technology for Measurement of Soil-Water Characteristic Curve. *ASTM geotechnical testing journal*, 35(1), 201-208.
- Skempton, A. (1954). The Pore-Pressure Coefficients a and B . *Geotechnique*, 4(4), 143-147.
- Stokoe II, K., Hwang, S., Lee, J.-K., & Andrus, R. D. (1995). *Effects of Various Parameters on the Stiffness and Damping of Soils at Small to Medium Strains*. Proceedings: Pre-Failure Deformation of Geomaterials (pp. 785-816), Sapporo, Japan.
- Towhata, I. (2008). *Geotechnical Earthquake Engineering*: Springer.
- Tsukamoto, Y., Ishihara, K., & Nosaka, Y. (1998). On the Initiation of Rainfall Induced Soil Failure. *Geotechnical Hazards*, 883-890.
- Zhou, A.-N., Sheng, D., & Carter, J. (2012). Modelling the Effect of Initial Density on Soil-Water Characteristic Curves. *Geotechnique*, 62(8), 669-680.
- Zhu, J.-H., & Anderson, S. (1998). Determination of Shear Strength of Hawaiian Residual Soil Subjected to Rainfall-Induced Landslides. *Geotechnique*, 48(1), 73-82.

FIELD APPLICATION OF ELASTIC WAVE VELOCITIES FOR LANDSLIDE PREDICTION

Chapter 8

FIELD APPLICATION OF ELASTIC WAVE VELOCITIES FOR LANDSLIDE PREDICTION

8.1. GENERAL

The challenge envisaged in this study is to predict the behavior of soil during landslides by using elastic wave velocities. Rain-induced landslides typically occur at shallow depths (Anderson & Sitar, 1995; Ng & Pang, 2000; Farooq et al., 2004). Slope surfaces, at shallow depths, are generally in unsaturated state with soil matric suction (negative pore water pressure) playing an important role in their stability. During rainfall events, as water percolates the slope surface, matric suction is gradually lost resulting in reduction of shear strength. With the loss of available shear strength slope surface starts to become more and more unstable and this destabilization continues to a point at which equilibrium can no longer be sustained and the slope ultimately fails. The following sections outline the approaches which may be adopted for the prediction of such rain-induced landslides using elastic wave velocities.

8.2. CONCEPTUAL FRAMEWORK

Experimental results and discussions presented in Chapter 6, and Chapter 7, explain the fundamental mechanism of elastic wave velocity variation in unsaturated soils. This information can be used to lay down the basic framework and fundamental guidelines for the use of elastic wave velocities for landslide prediction. Principle outcomes of from discussions which are directly related landslide monitoring can be outlined as follow;

- Elastic wave velocities decrease with increasing soil moisture content. Thus, wave velocities are expected to decrease as soil gets wet during rainfall.
- Wave velocities increase with confining pressure, i.e., elastic wave velocities measured at deeper depths would be larger compared to shallow depths. This behavior is the same irrespective of saturation state. The only exception to this rule is compression wave velocity in fully saturated conditions, which reaches sonic wave velocity in water when the soil is fully saturated.
- Yielding of soil during landslides causes wave velocities to decrease at an accelerating rate. This phenomenon is observed to be the same irrespective of soil saturation state, confining pressure, field consolidation state, or density of soil deposit, etc.
- Post failure decrease in wave velocities is consistent with the strain rate. Thus, simply by monitoring the rate of wave velocities, an indication of rate of slope movement can be obtained.

These points provide the basic guidelines for the use of wave velocities for slope monitoring. Using these points, a conceptual idea of landslide prediction is presented in Figure 8.1. A pair of exciter/receiver assembly placed on the slope surface can be used to obtain wave velocities in slope at regular intervals. Start of a rainfall event would increase soil saturation hence reducing wave velocity. Simply by monitoring the decrease in wave velocities, average saturation state of the soil can be estimated. Meanwhile, slope failures may occur when the slope ground is already nearly saturated and water contents are constant at a high level. Some failures happen even after the rainfall has stopped. Wave velocities are expected to decrease sharply once failure is initiated and soil has started to yield. Change in rate of decrease in wave velocities can provide an indication of failure initiation. Additionally, since the rate of wave velocity decrease is proportional to strain rate in soil, it can provide an estimate of speed of movement of failing slope as well.

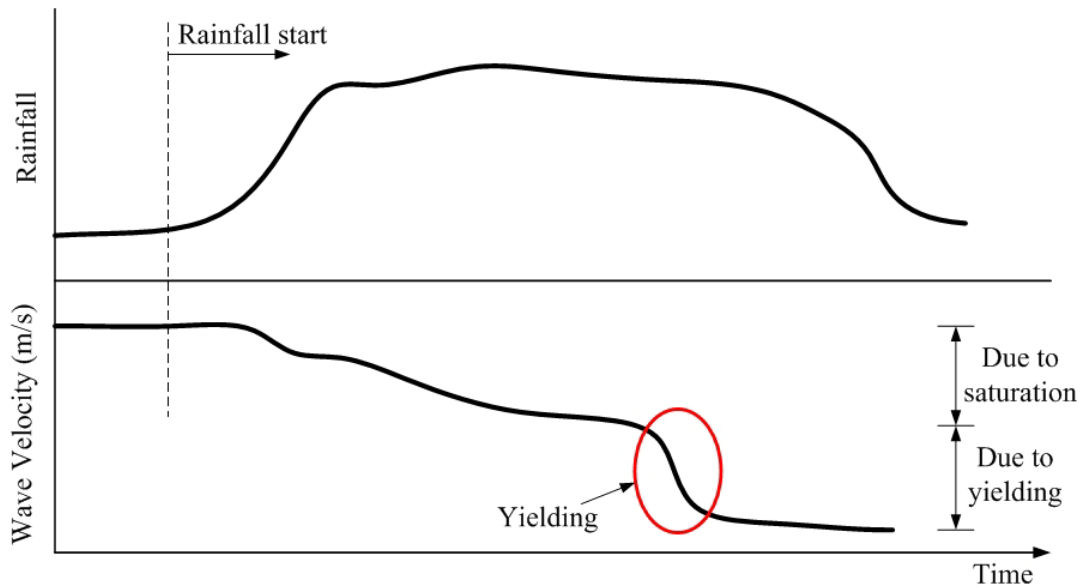
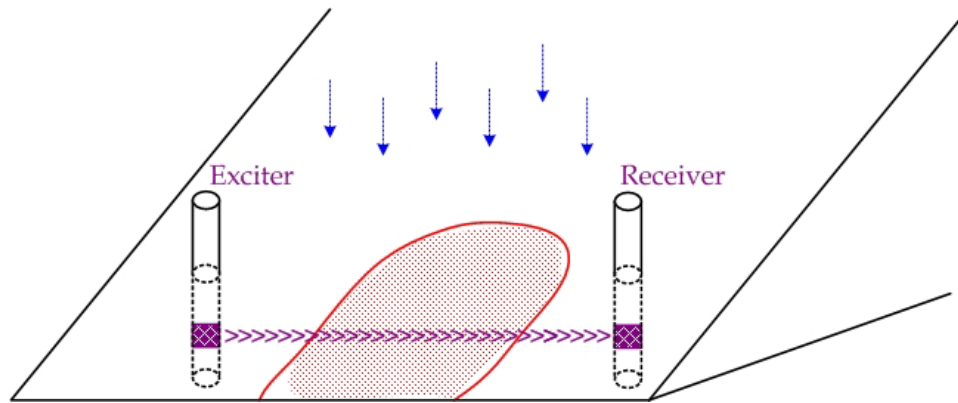


Figure 8.1: Expected response of elastic wave velocities during rainfall-induced landslides.

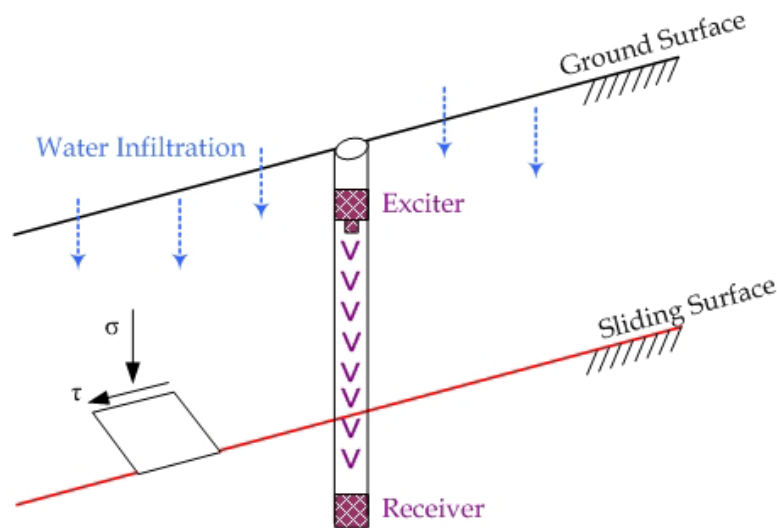
8.3. KEY CONCERNS FOR PRACTICAL APPLICATION

This study has established the mechanism of elastic wave velocities in unsaturated soils and during landslide conditions using laboratory element tests. However, the applicability of these concepts, in a cost beneficial way, to actual landslide problems is still unexplored. The key questions which need to be answered to make this technology a success may be summarized into following points;

1. The best suited orientation of elastic wave transmitter/receiver devices in the field, for the time being is not known. A possible orientation may include placing transmitter/receiver assembly in cross-hole type assembly, as shown in Figure 8.2(a). Another possibility is the down-hole type orientation as shown in Figure 8.2(b). Both types of orientations have their own advantages and disadvantages; some of them have been discussed in the following section related to the possible approaches of landslide monitoring by using elastic wave velocities.



(a) Cross-hole



(b) Down-hole

Figure 8.2: Possible orientations of exciter and receiver in field conditions; (a) Cross-hole type; (b) Down-hole type.

2. Optimal location of exciter/receiver assembly on the slope surface is still unexplored. It is not known whether to place the exciter/receiver assembly near the toe, close to the top, at the center, or any other location is best suited for landslide monitoring. Farooq et al. (2004), Orense et al. (2004), and Gallage and Uchimura (2010) indicated that slope failures generally initiate in high saturation zones near the toe of slope. Although this gives us an idea

about the possible ideal location of wave measurement devices but this idea is yet to be tested in actual landslide conditions.

3. A continuous source of excitation is required for generating waves on the slope surface. Selection of an optimal exciting device is quite a challenging task. The exciter device is required to generate wave impulses strong enough to reach the receiving devices with sufficiently high signal to noise ratio. On the other hand, the excitations should not be so strong so as to mechanically destabilize the slope. Piezoelectric or electromagnet type exciters may be used, however, they may require sufficiently high power source for continuously developing excitations over long periods of time. This may become quite challenging particularly when installed in remote locations.
4. To receive the pulses of waves generated by excitation devices, receivers are required. These receivers are required to be of high quality so that they can discern between the actual received signal and surrounding noise. They are required to be energy efficient so that the installed batteries are not required to be replaced every now and again. Most importantly, the receiving devices are required to be cost efficient. This is because a number of receiving devices may be required to be placed on the slope surface to receive excitations from a single transmitter, thus cost of receiving devices can considerably affect the overall economics of the project. Some possible options which can be used as receivers include piezoelectric sensors, contact microphones, geophones, accelerometers, etc.

With the rapid technological advancements, the problems related to efficient transmitting and receiving devices are relatively easy to overcome. However, the real task lying ahead for geotechnical engineers is the development of efficient criteria for issuing such warnings. Questions such as, “*by observing the decreasing wave velocities in actual slopes, when to issue a preliminary warning, and when does the risk level become so high to issue a final emergency warning?*” are very difficult to answer solely based on laboratory experiments. Answers to these questions are extremely important and can only be obtained through rigorous field experience gained by monitoring wave velocities during actual landslide conditions.

8.4. FIELD APPLICATION – IDEAS

8.4.1 Single Exciter, Multiple Receivers Approach

One of the biggest concerns of any rational idea is its economic feasibility. In order to convince the masses of the effectiveness of the product, and make them bring it into their use, demands the product to be cost beneficent. Two key components controlling the cost of wave velocity based landslide monitoring system are the ‘wave exciter/transmitter’ and ‘receiver’ devices.

A variety of receiving devices like electromagnets, piezoelectric ceramics, accelerometers, microphones, geophones, etc. are already available commercially. Many of these receiving devices are available literally at throw away prices e.g., contact microphones can be purchased as low as \$1. Compensating for overhead expenditures including modification and upgrading of these sensors, and water proofing, etc, a good quality receiving unit may be prepared for about \$10 cost. Development of a cost-efficient wave exciter/transmitter is however going to be a challenging task. In general context, transmitters can be divided into two broad categories; (i) without any mechanical moving parts, e.g., piezoelectric or electromagnetic type transmitters, etc, and (ii) excitation by means of mechanical movements, e.g., drop hammer, etc. Transmitters of the former category may require less driving voltage but are generally capable of generating excitations which are low in amplitude. These low amplitude excitations may not be able to be transmitted to receivers, a few meters from the exciter. On the other hand, transmitters of the latter category can generate high amplitude excitations which may be received several meters away. However, a continuous source of large driving voltage may be required for them; which may be a concern for landslide monitoring in remote areas.

In any case, a more cost-efficient approach for landslide monitoring based on elastic waves may be to install several receiving units on the slope surface which are made to receive excitations from a single excitation device. This concept is schematically shown in Figure 8.3. General procedure for landslide monitoring using this approach is outlined in the following points;

- A single exciter is strategically located on the slope surface to transmit waves to several receiving units.
- The exciter is triggered at regular intervals and wave velocity record of each receiver is monitored regularly.
- Each receiver represents a specific section of slope geometry. Variation of wave velocity recorded by each receiver can give an indication of saturation state across the slope surface.
- As per Figure 8.1, sharp decrease in wave velocity recorded by any receiver can not only provide an idea about possible failure initiation but can also indicate its location on the slope surface.

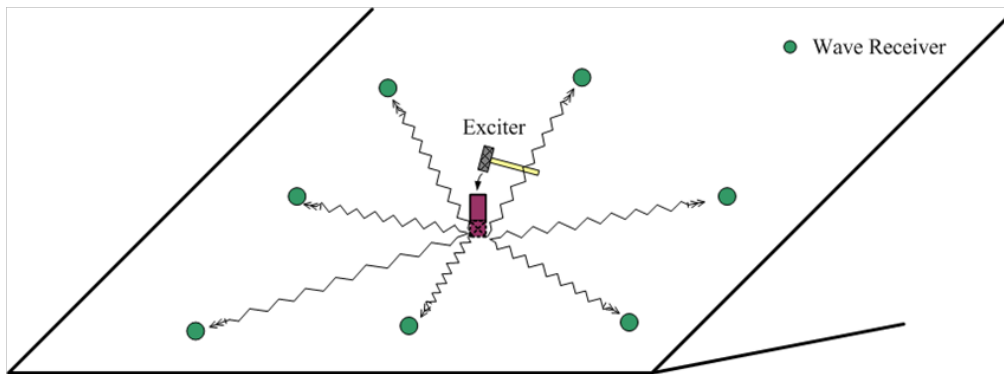


Figure 8.3: Schematic showing single exciter, multiple receiver assembly.

In such an assembly it may still be very difficult to determine the location of potential failure plane. This can be improved by placing the excitation source at a certain depth inside the soil. Excitation source in the form of a hollow cylindrical rod can be pushed into the slope surface by ramming. Ramming is continued until it reaches hard strata, which is indicated by rebounding. A drop hammer, as shown in Figure 8.4, can then be used to generate excitations deep into the slope surface. Waves from the point of excitation would travel towards the receivers which can be interpreted to monitor any variations in the travel time. Development of yielding in the failure plane could thus be identified and the location of development of failure plane could better be realized. This concept is schematically shown in Figure 8.4. One possible limitation in this approach may be that, the thickness of failure plane may be too small to cause any

variation in wave velocities. However, this phenomenon is yet unexplored and requires further research to confirm the affect of failure plane thickness on wave velocities.

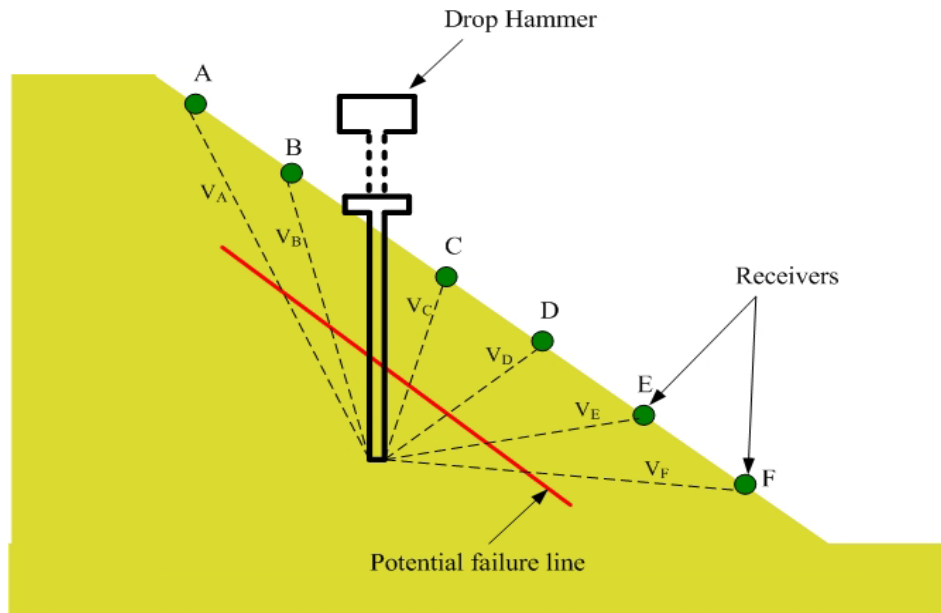


Figure 8.4: Schematic representation of wave excitation deep into soil surface.

8.4.2 Monitoring Based on Seismic Refraction

Movement of slope surface and location of potential failure plane can be identified by using seismic refraction method. The basic assumption of this approach is that the potential failure plane lies on the interface of two layers; the unstable surficial deposit and the underlying stable deposit.

8.4.2.1 Principle of Seismic Refraction

Seismic refraction method is based on the refraction of seismic waves at the interface of geological layers. Seismic waves travel at different velocities in different subsurface layers. Wave velocity generally increases with the depth of soil deposits since deeper deposits are expected to be having higher densities.

Upon exciting the seismic source (shot), a part of wave propagates along the surface in the form of *direct waves* whereas the other part travels into the soil stratum. The

behavior of wavefront propagating through soil stratum is governed by Snell's law. When this wave comes across an interface between two geological layers, a part of it is reflected back into the same layer while the remaining is refracted into the deeper deposit. However, for *critical angle* of incidence, the wave is *critically refracted* and continues to propagate parallel to the interface at the speed of underlying layer, as shown in Figure 8.5. According to Huygen's principle every point on the interface excited by seismic waves acts as a secondary source of waves. Thus, energy travelling through this interface is continually refracted back to the upper medium at an angle equivalent to critical angle (i_c), and is known as *head wave* (Figure 8.5 and Figure 8.6).

Receivers which are *critical distance* (x_c) apart from the source receive these critically refracted waves in the form of *head waves*, which arrive at the receivers before direct waves. This concept is schematically shown in Figure 8.6.

Travel time recorded by each receiver is plotted against their respective distances from the source, as shown in Figure 8.7. Because of the difference in propagation speed of direct waves and refracted waves, a bi-linear plot is achieved. Depth of the underlying layer can then be computed by comparing the slopes of these two lines

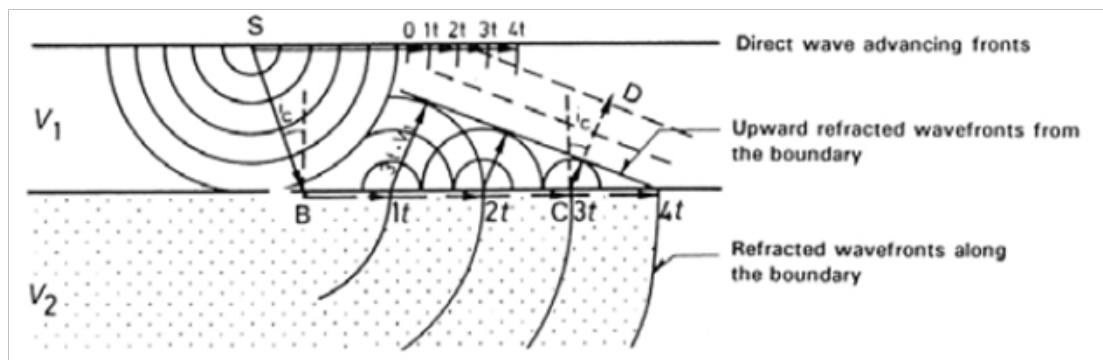


Figure 8.5: Schematic illustration showing the ray paths of the incident wave (SB) striking the boundary at critical angle (i_c), and the refracted wave (BC) traveling along the boundary with velocity $V_2 (>V_1)$. The latter is refracted back to the first medium (V_1) at the same angle (i_c) and re-emerges with a ray path such as CD. Advancement of the wavefronts is shown from the instant ($t = 0$) when the incident ray strikes the boundary B. (after Palmer (1986))

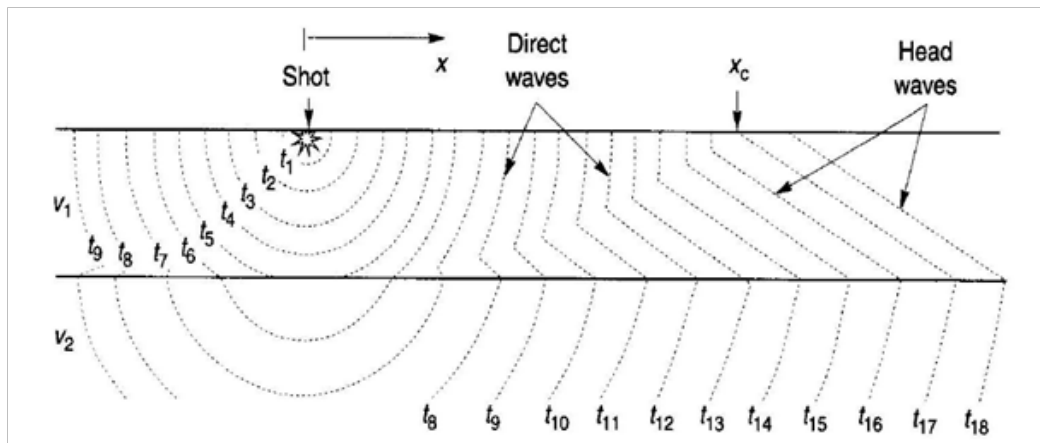


Figure 8.6: Wavefronts for the first-arriving waves in a seismic refraction survey. Note that first arrivals near the source are from direct waves but, at the distance greater than the critical distance, x_c , the first arrivals are from the head waves. (after U.S. Corps of Engineers (1979)).

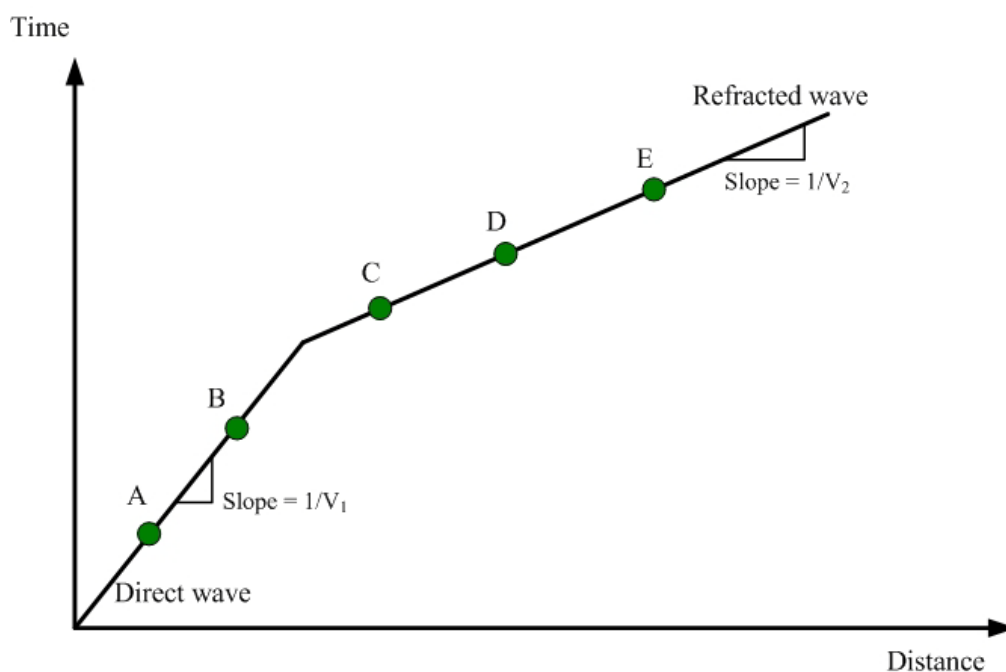


Figure 8.7: Typical plot of seismic refraction test.

8.4.2.2 Use of Seismic Refraction for Landslide Monitoring

The fundamental assumption of this method is that the potential failure plane lies at the interface of two layers. Thus, by monitoring the change in wave velocity of *critically refracted wave*, criteria can be developed for landslide early warning. An exciter and a series of receivers can be aligned on the slope surface. Any wave generated by the exciter would travel in the form of direct wave on slope surface, and as critically refracted wave at the potential failure plane, as shown in Figure 8.8.

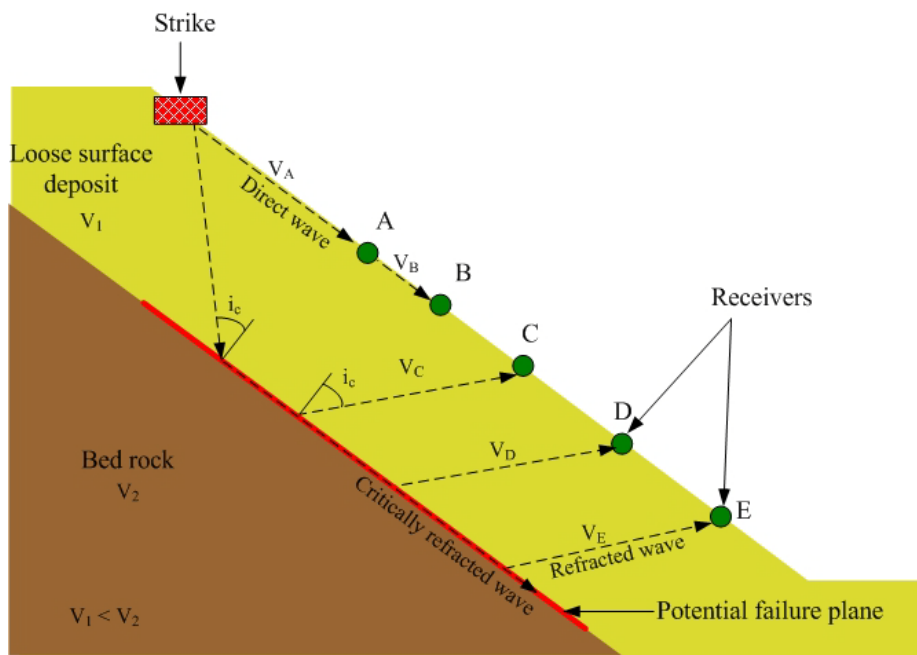


Figure 8.8: Schematic illustration describing the layout of sensors and wave propagation paths of seismic waves when used for landslide monitoring.

Figure 8.9 shows response of direct wave and refracted wave at various stages of landslide. V_A represents velocity of direct waves (i.e. travelling on the slope surface), whereas V_{FP} represents the velocity of critically refracted waves which travel along the failure plane. Path 'A' in the plot, represents the initial conditions before the start of rainfall. During rainfall, soil surface starts getting wet and therefore wave velocity decreases, as indicated by the trend of V_A in path 'B' (Figure 8.9). However, wave velocity along the potential failure plane, which is a function of wave velocity in the underlying stable layer is not expected to drop. This is indicated by a near-parallel response of V_{FP} during path 'A' and path 'B'. However, once the failure is initiated

along the failure plane, no change in V_A is expected, however, V_{FP} is expected to decrease due to soil yielding along the slip surface. By following this approach, wave propagation in soil can be utilized to predict the initiation of landslides.

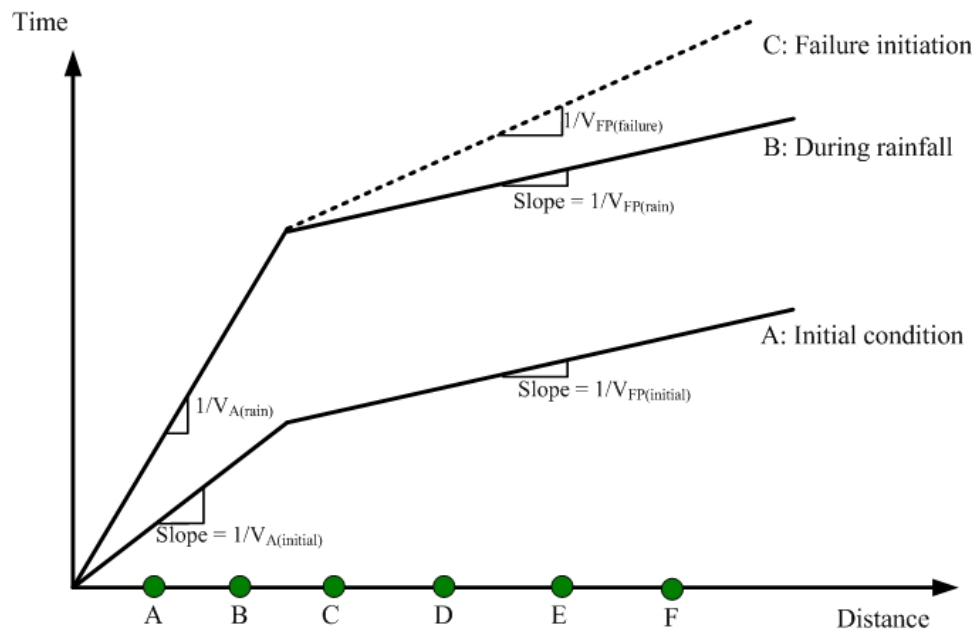


Figure 8.9: Schematic illustration of variation of wave velocities in a seismic refraction test during rainfall-induced landslides.

8.5. CONCLUDING REMARKS

This chapter is a step forward towards the practical application of elastic wave propagation for landslide early warning. Besides summarizing the most important findings of previous chapters related to wave propagation during landslides, this chapter presents future avenues for its practical use in the field. Several ideas related to the type of transmitting devices, type of receiving devices, location and orientation of these devices on the slope surface, etc were discussed. In addition, two possible approaches for landslide early warning using elastic waves were discussed in detail.

8.6. REFERENCES

- Anderson, S. A., & Sitar, N. (1995). Analysis of Rainfall-Induced Debris Flows. *Journal of Geotechnical Engineering*, 121(7), 544-552.
- Farooq, K., Orense, R., & Towhata, I. (2004). Response of Unsaturated Sandy Soils under Constant Shear Stress Drained Condition. *Soils and foundations*, 44(2), 1-13.
- Gallage, C., & Uchimura, T. (2010). *Investigation on Parameters Used in Warning Systems for Rain-Induced Embankment Instability*. Proceedings: Proceedings from the 63rd Canadian Geotechnical Conference (GEO2010) (pp. 1025-1031).
- Ng, C. W., & Pang, Y. (2000). Influence of Stress State on Soil-Water Characteristics and Slope Stability. *Journal of Geotechnical and Geoenvironmental Engineering*, 126(2), 157-166.
- Orense, R. P., Shimoma, S., Maeda, K., & Towhata, I. (2004). Instrumented Model Slope Failure Due to Water Seepage. *Journal of Natural Disaster Science*, 26(1), 15-26.
- Palmer, D. (1986). *Refraction Seismics: The Lateral Resolution of Structure and Seismic Velocity*: Geophysical Press London.
- U.S. Corps of Engineers (1979). *Geophysical Exploration Engineering Manual EM 1110-1-1802*. U.S. Government Printing Office, Washington, D.C.

CONCLUSIONS & RECOMMENDATIONS

Chapter 9

CONCLUSIONS & RECOMMENDATIONS

9.1. GENERAL

Human beings are pushing the limits of ‘possible’ through research and innovation. What was unthinkable a few decades back is pretty much in the realm of possibility in present days. An equally innovative idea is the ability to predict a rainfall-induced landslide. The underlying concept is to watch the variation of different slope parameters during rainfall, and issue a landslide warning when these parameters approach their respective critical values. One of the key questions in doing so is “*Which parameters to watch?*”. So far real-time early warning of landslides has been attempted by watching actual slope movements (through tilt sensors, inclinometers, extensometers, etc), and monitoring soil moisture variation (through dielectric moisture sensors, tensiometers, etc). However, there are several shortcomings associated with these measurements. A new idea to predict slope movements by using elastic wave propagation in soil has been presented in this study. A thorough laboratory investigation was conducted to explore the validity of this idea.

Laboratory investigations conducted as part of this study started with the development of an appropriate triaxial system which could not only test unsaturated specimens but could also measure elastic wave velocities (compression wave velocity and shear wave velocity). A novel disk type piezoelectric transducer which was capable of measuring both compression and shear wave velocities was fabricated for this purpose. Detailed performance evaluation of elastic wave measurement system in terms of quality of transmission cables, electromagnetic coupling (crosstalk), signal recorder, shape of input waveform, excitation frequency, etc. was conducted.

Rainfall-induced landslides are primarily associated with a continuous change in soil moisture. Two separate series of triaxial experiments were conducted to explore the

behavior of elastic wave velocities with changing soil moisture. An attempt was made to explain elastic wave variation in terms of soil matric suction. Response of elastic waves during rainfall-induced landslides was investigated by two additional series of triaxial experiments. Field stress conditions were reproduced by injecting water in soil specimens through a saturated ceramic disk at its base. Effects of initial relative density, and principle stress ratio were examined. A novel technique of distributing the injected water in unsaturated triaxial specimen through a helical filter paper was also proposed in this study. Major conclusions derived from these studies are summarized in the following section.

9.2. CONCLUSIONS

9.2.1 Disk Transducer – Performance Analysis

A new disk shaped piezoelectric transducer that enables both shear and compression wave velocities to be determined by using a single pair of transducers mounted across a soil specimen was described. The proposed disk transducer is advantageous over conventional bender elements due to its non-invasive nature. Performance of disk transducer with respect to resolution of A/D recorder, quality of transmission cables, grounding conditions, shape of input waveform, and excitation frequency was analyzed and the following conclusions were drawn;

- A time lag between initial excitation of transmitter and first deflection of receiver exist in disk transducer measurements. For accurate evaluation of elastic wave velocities, time lag corrections are required to be made to disk transducer readings.
- Use of low noise coaxial cables reduces self-induced cables noise and improves signal to noise ratio of received signals by 2.5 times compared to ordinary coaxial cables.
- For disk type piezoelectric transducers, the use of recording unit with low inherent noise is essential. Signal recording unit with high A/D conversion resolution, sampling rate and voltage sensitivity was found to facilitate signal interpretation.

- Electromagnetic coupling between source and receiver piezo-transducer, commonly known as crosstalk, was found to distort receiver signals. First arrival of received signals is masked by crosstalk particularly when testing with low input frequencies. Crosstalk was found to be removed by grounding both transmitter and receiver piezoelectric transducers.
- Large number of frequency components contained within square excitation leads to exceedingly distorted receiver signals. Interpretation of first arrival and determination of shear wave travel time is considerably easy when sinusoidal excitation waveform is used.
- The *S*-wave signals are affected by near-field effects. Near-field effect diminishes with an increase in L/λ ratio, i.e. increasing excitation frequency. For minimizing shear wave distortions, an empirical lower bound of $L/\lambda = 0.33$ has been suggested in literature. The validity of this relationship for different soil saturation states was tested, and it was observed to serve well irrespective of soil moisture condition.
- Amplitude of received signals is affected by magnitude of input frequency. The strongest response of received signals indicates the resonance frequency of soil – disk transducer system. Increasing/decreasing input frequency away from resonance frequency weakens the received signals.
- Amplitude of received signals is also weakened by decrease in soil stress state, or increase in soil moisture.

9.2.2 Soil Moisture Effects on Wave Velocities

Two sets of triaxial test series were conducted to explore the effects of soil moisture on the propagation of elastic wave velocities. In *ICCW* tests, specimens with controlled initial moisture were subjected to various levels of isotropic confining pressures. Whereas in *ICWI* tests, isotropic confining pressure was maintained constant and saturation state of specimens was varied by injecting water through a saturated ceramic disk at the base of specimens. Conclusions drawn from these experiments are summarized in the following points;

- Elastic wave velocities decrease with soil saturation. Shear and compression wave velocities decrease by about 30%~40% when soil saturation is increased

from 20% to about 90%. This decrease in elastic wave velocities with soil saturation is significant enough to be used as an indicator of soil saturation state for actual landslide monitoring.

- Decrease in elastic wave velocities with soil saturation is independent of mode of wetting. This was confirmed by an identical behavior observed during *ICCW*, and *ICWI* experiments.
- Elastic wave velocities increase with isotropic stress increase. This behavior is independent of soil saturation state. Thus for in-situ monitoring, elastic wave velocities are expected to be influenced by soil overburden pressure. This observation could be of significant importance when measuring wave velocities at various depths through cross-hole techniques.
- In fully saturated conditions, compression wave velocities approach sonic wave velocities in water (1500 m/s ~ 2000 m/s). However, this phenomenon is significantly affected by *B*-value of tested specimen. In any case, such behavior of compression waves can be utilized in the field to determine full saturation of soil.
- Elastic wave propagation in soil depends not only on void ratio, stress state, moisture state, etc., but is also governed by soil fabric and arrangement of particles in the soil matrix. This was confirmed by subjecting a few specimens to cycles of loading, unloading, and then reloading of isotropic stress. After primary consolidation during initial loading, negligible change in void ratio as well as soil fabric was expected, hence during unloading and reloading paths wave velocities remained largely comparable.
- The behavior of elastic wave velocities with soil saturation state can be expressed as a function of soil water characteristic curve. This can be explained as an initial *residual zone*, in which wave velocities increase with saturation. This is due to increase in thickness of contractile skin/meniscus water and the corresponding increase in inter-particle contact area available for wave propagation. In the *transition zone*, inter-particle stress is governed largely by soil matric suction. Rapid decrease in soil matric suction cause reduction of effective stress, which in turn reduces elastic wave velocities. In the *saturation zone* of *SWCC*, there is negligible decrease in matric suction, and hence, the rate of wave velocity decrease reduces.

9.2.3 Wave Velocities during Landslides

The behavior of elastic wave velocities during landslides was investigated through two distinct series of triaxial experiments. Both sets of experiments produced an identical stress path which was representative of field stress path during rainfall-induced slope failures. *CWRSR* specimens were prepared by adding predefined amount of moisture. From an initial isotropic stress state, radial stress was reduced gradually until the failure of specimens. In *CSWI* tests, axial and radial stress were set initially according to field consolidation state. Without changing the externally applied axial or radial stress, the specimens were brought to failure by injecting water into the specimens through a saturated ceramic disk at the base of specimen. Main findings of these studies are summarized below;

- Failure initiation (yielding) due to reduction of radial stress was found to be a function of initial saturation ratio. Wet specimens were found to yield earlier than dry specimens reflecting the wet slopes to be much closer to failure stage.
- Post-yielding behavior is dependent on saturation state. Time lapse between failure initiation and complete failure can be considerably large in nearly saturated slopes. However, dry slopes may tend to fail in a brittle manner i.e. very small time between failure initiation and complete failure. This observation could indicate the available response time for disaster managers e.g., if an early warning system indicates failure initiation in a relatively wet slope, sufficient time may be available for evacuation and vice versa.
- In *CWRSR* experiments, both shear and compression wave velocities were found to decrease rapidly on failure initiation. A decrease of about 40% was observed in shear wave velocity whereas the corresponding decrease in compression wave velocity was about 15%. Such a sharp decrease in wave velocities can be useful in predicting failure initiation of landslides.
- During *CSWI* tests, looser specimens were found to initiate failure earlier as compared to dense specimens. This was because loose specimens exhibited low initial matric suction which dissipated very quickly upon water infiltration. This implies, real slopes surfaces comprising of loose deposits would fail earlier than a dense slopes subjected to identical rainfall.

- Strain rate after failure initiation of dense soils is lower compared to loose deposits. This indicates that once the failure is initiated, loose deposits would undergo faster deformations than dense slopes.
- Post-failure strain rate also increases with principle stress ratio. Thus, steep slopes would undergo more rapid movements compared to mild/gentle slopes.
- Both compression wave (V_p) and shear wave (V_s) velocities decrease gradually with water saturation. But once failure is initiated, both start decreasing rapidly. This phenomenon can be utilized in actual slopes for identification of failure initiation.
- Rate of decrease in wave velocities after failure initiation is consistent with post-failure strain rates. This observation can be useful in predicting the rate of slope movement after failure initiation. It also finds practical significance with respect to site-specific early warning.
- A new method of distributing the injected water in an unsaturated specimen by using a helical filter paper is proposed. End of experiment water distribution determined in various specimens confirmed a more uniform moisture distribution with the use of helical filter paper. Uniform water distribution along specimen height was also found to decrease chances of progressive failure.

9.3. RECOMMENDATIONS FOR FUTURE RESEARCH

Several avenues of future research were discovered during the course of this study. Based on the experiences, results and discussions of this research presented hereinbefore, some recommendations for future researches are summarized below;

- The scope of present study was limited to Edosaki sand only. Validity of these findings on other soil types is required to be confirmed. This observation is of real significance with respect to clayey soils. A definite influence of soil matric suction was observed on elastic wave propagation. Therefore, it would be very interesting to explore this effect in clays because of the major role matric suction plays in unsaturated clay behavior.

- In present study, the sensitivity of elastic wave velocities to soil saturation as well as soil deformations was well explored by means of element tests in controlled laboratory environment. However, practical application of these concepts for actual landslide early warning requires similar confirmations in actual field conditions where several unforeseen parameters may also play their part. Scaled model experiments or artificial rainfall experiments on actual landslide sites may help in establishing a more realistic and practical approach for landslide early warning.
- Measurement of elastic wave velocities in the field would require sophisticated transmitter and receiver devices. Cross-disciplinary research, bringing together the knowledge of electrical engineering and geotechnical engineering, is therefore required to develop efficient, low energy, low noise transmitter and receiver devices for landslide early warning systems.
- During *ICCW* test on dry Edosaki sand, a hysteresis was observed in loading and unloading paths of wave velocities plotted against confining pressure. The hysteresis was found to diminish with increasing soil saturation. However, previous research conducted on pure sand (dry and saturated conditions only) does not indicate the presence of any such hysteresis. Exploring the effects of fines content and soil saturation on loading/unloading hysteresis in wave velocity ~ confining pressure/effective stress plot would make an interesting study from soil mechanics view point.
- Matric suction changes rapidly during water injection tests. Miniature pore water pressure sensor used in *CSWI* experiments used a ceramic disk in its front part for suction determination. Although this sensor performed well in the negative pore water pressure zone, but it failed to detect rapid changes in the positive pore water pressure zone near the failure of specimen. As a result, all the specimens appeared to have failed at nearly the same positive pore water pressure. The ceramic disk in the front cap of miniature sensor can be replaced with a micro-porous membrane (Nishiumura et al., 2012) which, owing to its very small thickness, is expected to give more realistic response of pore pressure variation inside the specimen.
- *CSWI* experiments exploring the effects of water infiltration rate on elastic wave velocities would form a very interesting study. Such experiments are of

significant importance to observe the behavior of slopes (and corresponding elastic wave velocities) subjected to rainfalls of different intensities. For high intensity rainstorms (typhoons, etc), elastic wave velocities may decrease rapidly right from the beginning of the storm. In such cases, failure initiation may not be detectable by monitoring elastic wave velocities alone.

9.4. REFERENCES

Nishiumura, T., Koseki, J., Fredlund, D. G., & Rahardjo, H. (2012). Microporous Membrane Technology for Measurement of Soil-Water Characteristic Curve. *ASTM geotechnical testing journal*, 35(1), 201-208.

TRIAXIAL APPARATUS EQUIPMENTS

Appendix A

APPENDIX A

TRIAXIAL APPARATUS EQUIPMENTS

A.1. GUIDE TO MAKE LOCAL DEFORMATION TRANSDUCER (LDT)

July 22, 1993

SATO, Takeshi

Translated into English by YOSHIDA, Teru

Tatsuoka Laboratory, 5th Division, Institute of Industrial Science, University of Tokyo

1. Materials and tools

(a) Phosphor bronze sheet (strip)

Example of size:

Soil specimen size	Width×Length×Thickness
φ 50 × 100mm	3.5 × 70 × 0.2mm
φ 75 × 150mm	3.5 × 120 × 0.3mm 4.0 × 120 × 0.3mm
φ 100 × 200mm	⊙ 4.0 × 170 (160) × 0.3mm 4.5 × 170 × 0.3mm
φ 300 × 600mm	5.0 × 540 × 1.0mm 6.0 × 540 × 1.0mm

(b) Strain gauges

KFG-2N-120-C1-16 (for φ300mm soil specimen)

KFG-1N-120-C1-16 (for others)

Kyowa Electronic Instruments Co., Ltd.

(c) Adhesive agent

CC-35A

Kyowa Electronic Instruments Co., Ltd.

(d) Gauge terminals

T-F7

Kyowa Electronic Instruments Co., Ltd.

(e) Coating agent

1 component RTV (Silicone): KE-47T, KE-45T

Surface treatment agent: Primer FA, FB

Shin-Etsu Chemical Co., Ltd.

(f) Leadwire

4-wire shield or PTFE wire

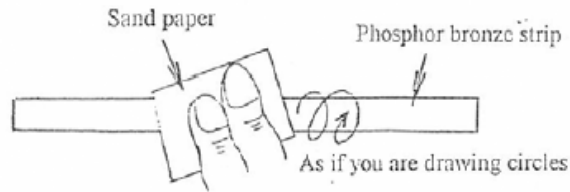
Tokyo Sokki Kenkyujo Co., Ltd.

(g) Others

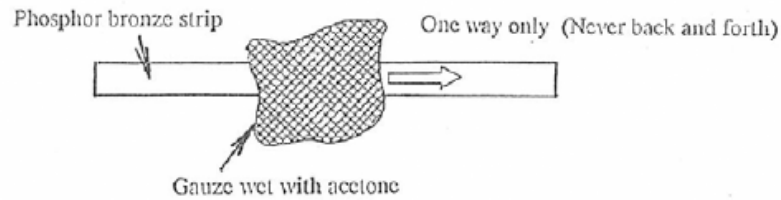
Scotch mending tape, tweezers, nipper, blade (cutter), sand paper (#320, #800, #1000), silicone rubber, gauze, 1mm section paper, tooth pick (2 or 3 pieces), swab, solvent (acetone), soldering iron, solder string ($\phi 0.8$ to 1.0mm)

2. Method to fix gauges on the phosphor bronze strip

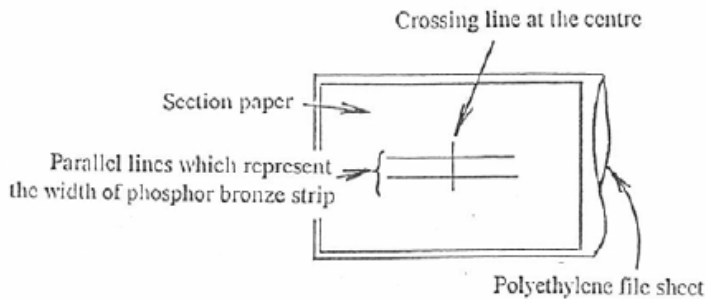
(1) Smooth the cut edges of the strip with a fine file. Cut the phosphor bronze strip into desirable length (can be cut with cutting pliers). File the both ends so that it would become rectangular to the two edges. File the central part (larger than the area of gauges and terminals) with sand paper (firstly, #320, then #800, and finally #1000) as if you are drawing circles.



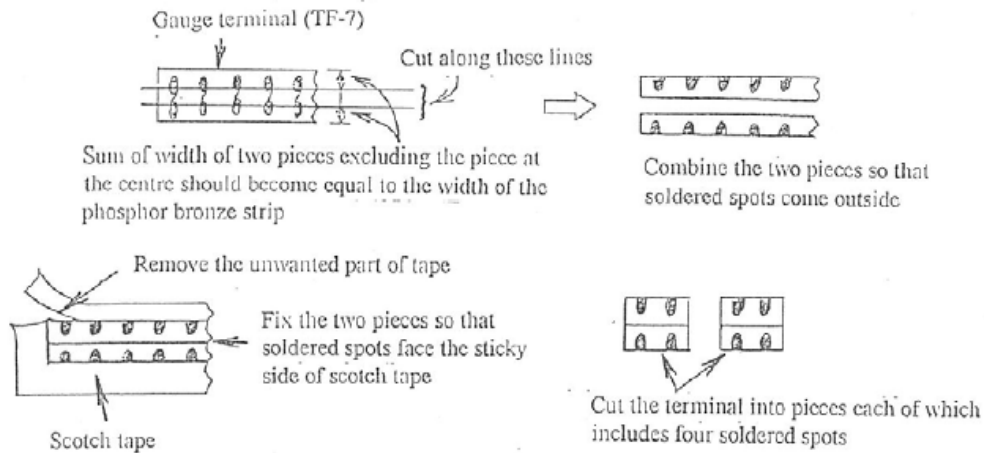
(2) Remove fats and dirt from phosphor bronze strip. With gauze having absorbed acetone (i.e. volatile solvent which dissolves oils and fats (Solvent which contains water, such as alcohol, cannot be used)), wipe firmly in one direction (never back and forth).



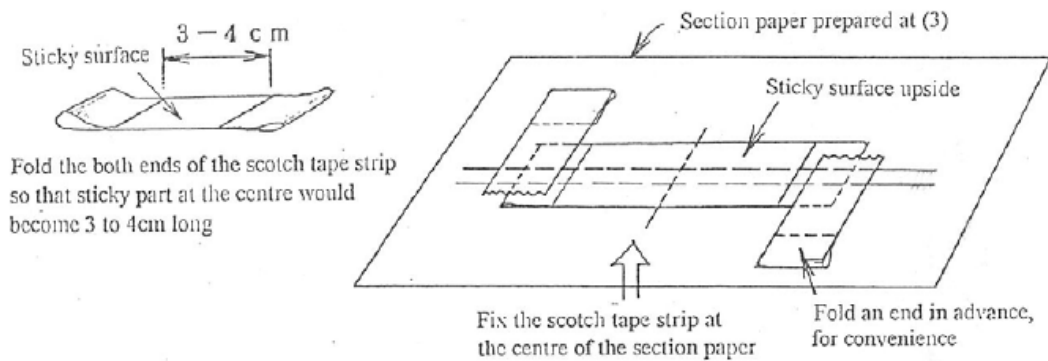
(3) Draw parallel lines on the section paper with an interval equal to the width of phosphor bronze strip, and also draw a crossing line at the centre. Put the section paper into a polyethylene file sheet (the thicker, the better).



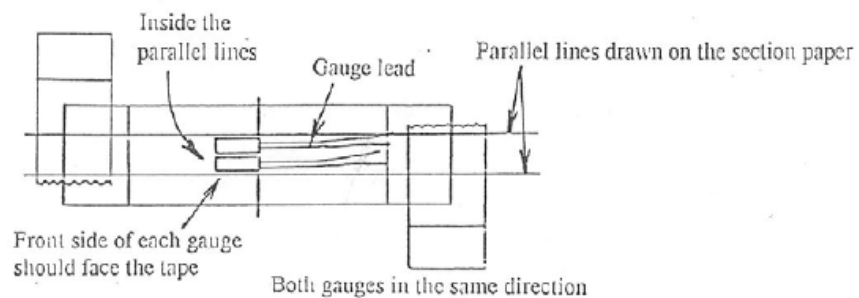
(4) Reconstruct the gauge terminal. Cut the terminal into three pieces so that the sum of the width of two pieces excluding the piece at the centre equals to the width of the phosphor bronze strip. Combine the two pieces using scotch tape, so that soldered spots come outside and that soldered spots face the sticky side of scotch tape. Remove the unwanted part of scotch tape. Cut the terminal into pieces each of which includes four soldered spots (Two pieces are needed for every L.D.T.).



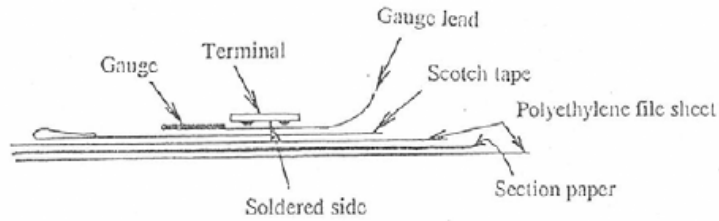
(5) Preparation for the following stages. Prepare a strip of scotch tape about 10cm long. Fold both ends of the scotch tape strip so that the sticky part at the centre would become 3 to 4cm long. Fix the scotch tape strip on the section paper (prepared at (3)) with tape, so that the strip comes just on the lines and sticky side comes upside. Take care not to touch with finger, and keep away from dust.



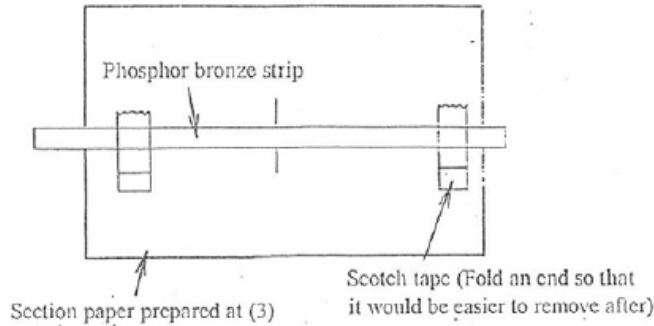
(6) Fix two strain gauges on the scotch tape strip, inside the parallel lines, and in the same direction, front side (Make sure carefully) of each gauge facing the tape.



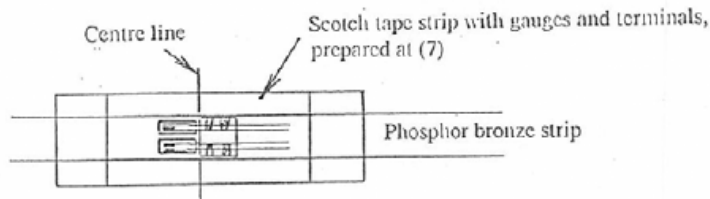
(7) Fix a gauge terminal, which has been prepared at (4), just on the gauge leads, and next to the strain gauges, with soldered spots on it looking downward. If finished, remove the scotch tape strip from the section paper. Take care not to touch the strain gauges, terminal and sticky surface by hand, and to keep them away from dust.



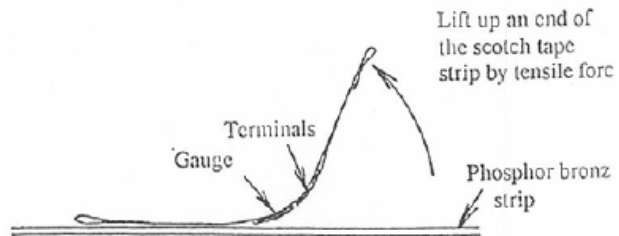
(8) Fix the phosphor bronze strip on the section paper, symmetrically against the line at the centre, with tape.

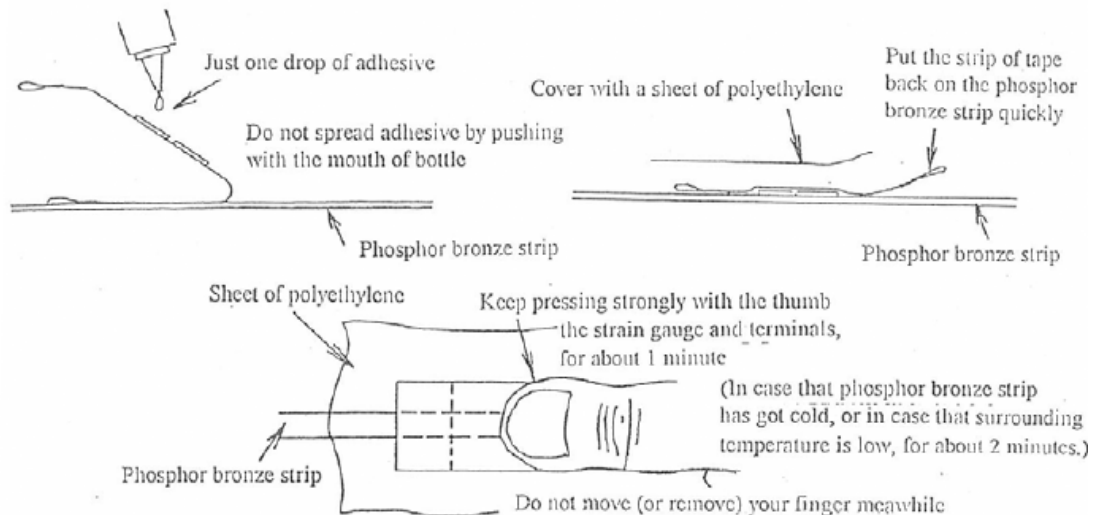


(9) Fix the strip of scotch tape prepared at (7), with the border between strain gauges and terminals being just upon the centre line. Strain gauges and terminals must not come out of the phosphor bronze strip.



(10) Stick the gauges and terminals on the phosphor bronze strip. Lift up an end of the scotch tape strip prepared at (9) (terminal's side) off the phosphor bronze strip (This time you should not bend the strain gauges extremely. Best raise the tape end by tensile force.) Drop adhesive, one drop on the gauge and another on the terminals. Do not spread adhesive by pushing with the mouth of bottle or other tool or finger (Otherwise adhesive will harden too fast and also adhesive does not show enough strength.) Put the strip of tape on the phosphor bronze strip quickly. Put a sheet of polyethylene on it and keep pressing strongly the strain gauge and terminals with the thumb, for about 1 minute at 20°C. Do not move (or remove) your finger meanwhile. (In case that phosphor bronze strip has got cold, or in case that surrounding temperature is low, for about 2 minutes.)





(11) Leave the device alone for at least 4 hours at room temperature. It is possible to continue your work on the reverse side, but do not apply strong compressive or bending force.

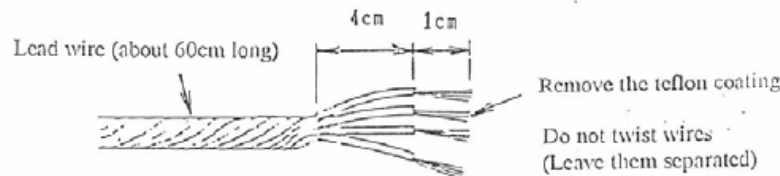
(12) After one day of curing, remove the scotch tape strip. Take care not to hurt gauges and gauge leads, and do little by little, because the tape is also hardened by adhesive. (You may wipe off the sticky substance with alcohol, but acetone cannot be used because it dissolves or could be harmful for adhesive.)

3. Wiring

(1) Preparation for wiring the lead wire (1. (f))

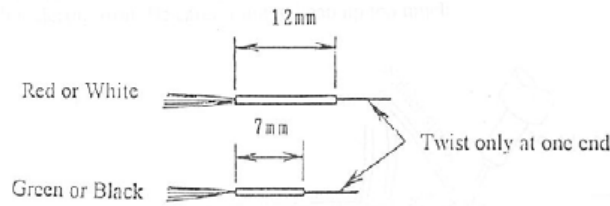
(a) Cut the lead wire into desirable length (about 60cm for small specimen). Remove the outer coating (black chloroprene coating). Remove also shield wires and thin transparent film sheet so that only four teflon leads (red, white, black and green) remain.

(b) Cut the leads into two pieces at the point about 4cm away from one end. Untie (loosen) an end of the longer one for about 4cm, and remove the teflon coating for about 1cm from each end (Do not twist wires. Leave them separated).

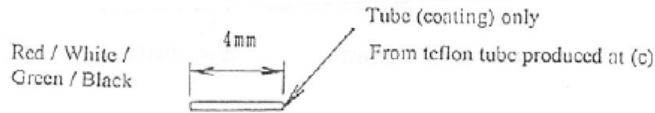


(c) Take into 4 pieces (4 colors) the shorter piece of lead (about 4cm long). For red and white leads, remove the coating at both ends, leaving the coating at the centre for 12mm. Twist wires at only one side, for both pieces. Similarly, for black and green pieces, remove the coating at both ends, leaving the coating at the centre for 7mm long, and twist wires at only one end. This time, do not throw the

teflon tubes into dust box. Keep them to utilize at following stages.

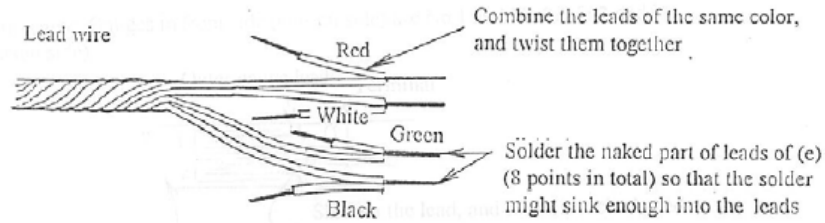


(d) Prepare a 4 mm long teflon tube for each color (red, white, black and green) from the tubes produced at (c).



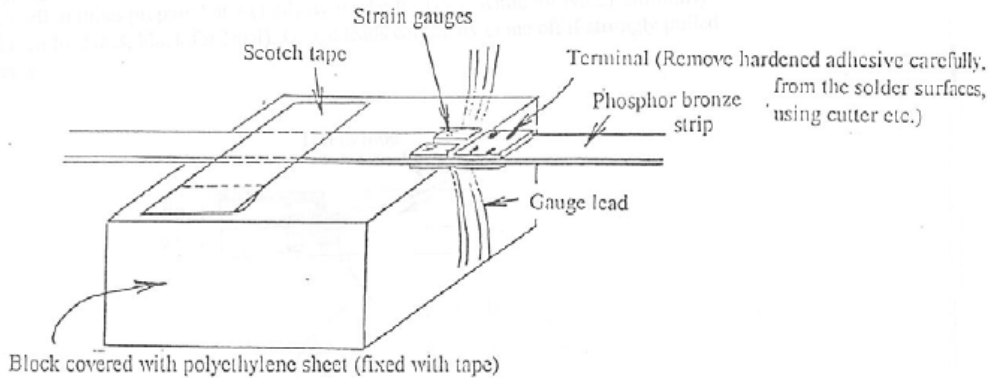
(e) Twist the lead wires of (b) together with the non-twisted end of the lead of (c) (Put same color's together).

(f) Solder the naked part of leads of (e) (8 points in total) so that the solder might sink enough into the leads.



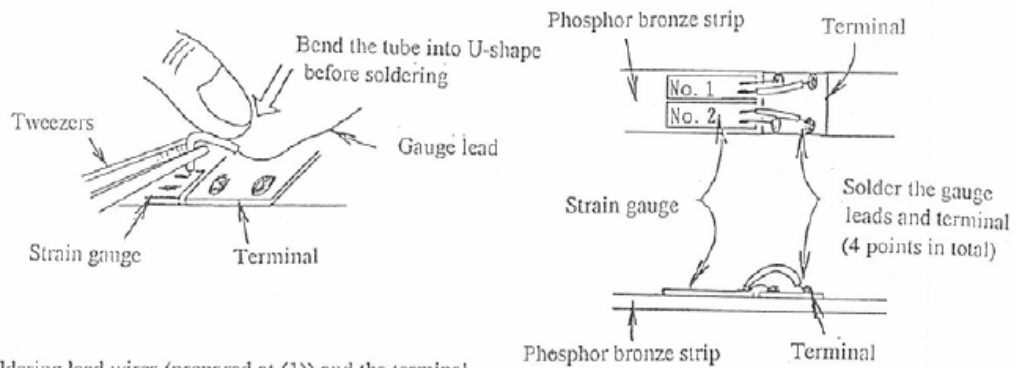
(2) Soldering terminals and strain gauges

(a) At the following stages, it is very convenient to use a block (about 5cm×3cm×3cm), covered with polyethylene sheet (fixed with tape) as a working table. Fix the phosphor bronze strip on the table with tape, so that the gauge leads might come slightly out of the table. Remove hardened adhesive agent (and also particles of tape) carefully, from the solder surfaces (8 in total) on the terminals, using cutter etc.



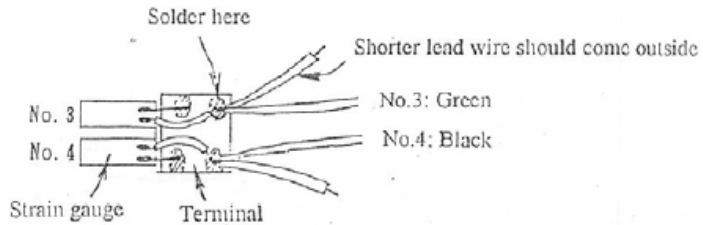
Fix the phosphor bronze strip on the table with tape, so that the gauge leads come slightly out of the table.

-Bend each tube covering the lead into U-shaped, with tweezers and a finger tip in advance, and solder the lead and the terminal (4 points in total).

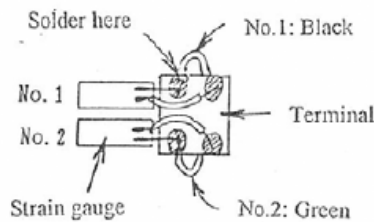


(3) Soldering lead wires (prepared at (1)) and the terminal

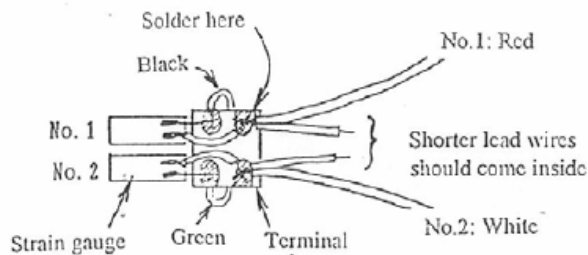
-Lay the phosphor bronze strip so that strain gauges No.3 and No.4 come upside. Solder the gauge No.3 and green lead wires so that the shorter lead wire comes outside. Similarly, solder the gauge No.4 and black lead wire.



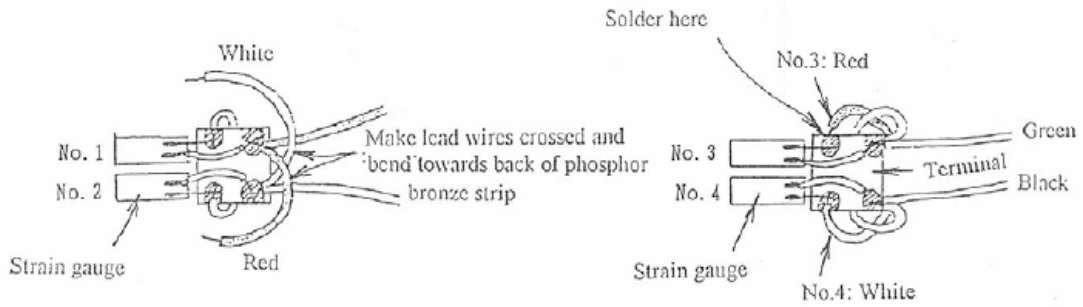
-Bend the shorter lead wires towards backside. Reverse the phosphor bronze strip so that gauges No.1 and No.2 come upside. Solder black lead wire and gauge No.1, and also green lead wire and gauge No.2, as illustrated.



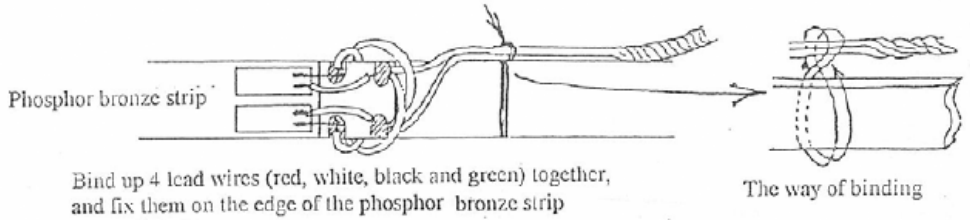
-Lay the phosphor bronze strip with surface of gauge No.1 and No.2 upside. Solder the gauge No.1 and red lead wire so that the shorter lead wire turns inside. Similarly, solder the gauge No.2 and white lead wire.



-Make the shorter lead wires (red and white) crossed, and bend them towards the back side. Reverse the phosphor bronze strip so that gauges No.3 and No.4 come upside. Solder the gauge No.3 and red lead wire, and also gauge No.4 and white lead wire (See the illustration).



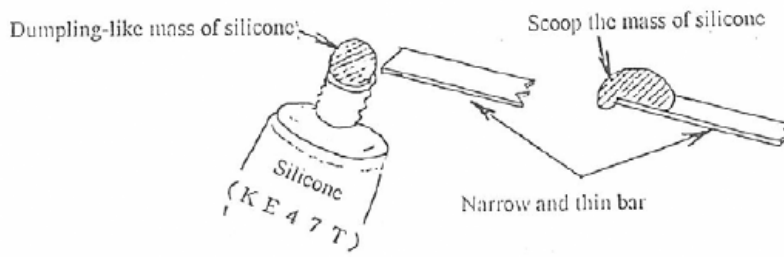
-Put the 4 lead wires (red, white, black and green) together, and fix them on the edge of the phosphor bronze strip by binding them up.



4. Coating

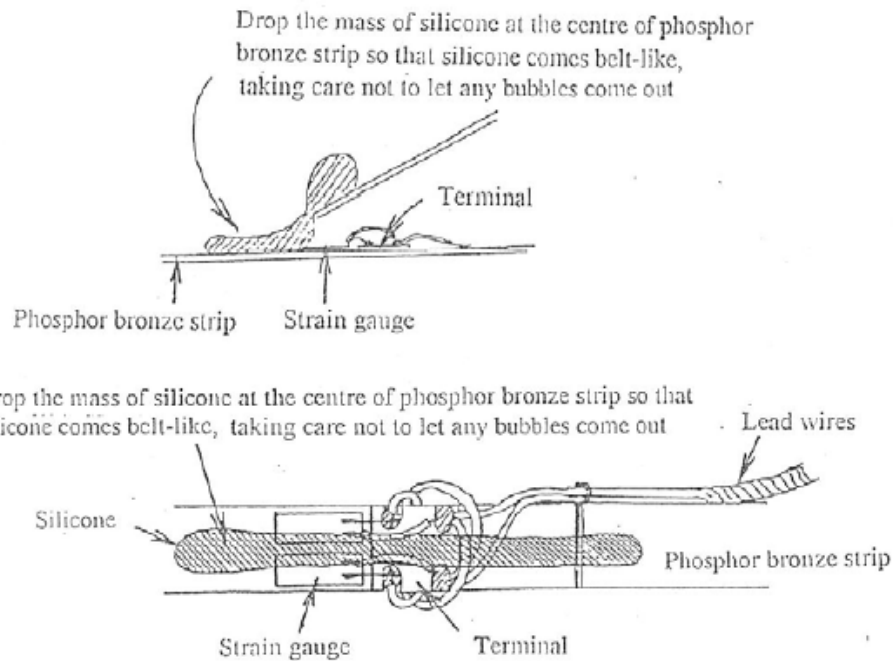
(1) Stir Primer FA and FB well, mixed at the ratio of 4 to 1 respectively, within a container such as evaporating dish. After cleaning the surface for application, spread the agent on the area including strain gauges, terminal and the tie of lead wires (both sides of phosphor bronze strip). Leave it alone until it gets dry. Be careful not to touch the Primer processed surface.

(2) Push the silicone KE47T out of the tube so that a mass of silicone gets dumpling-like. Take care not to let any bubbles come out. Scoop the mass of silicone with a thin, narrow plate (A piece of phosphor bronze that has come out as odds and ends when preparing the phosphor bronze strip is suitable for this).



(3) Drop the mass of silicone at the centre of phosphor bronze strip so that silicone comes belt-like. Take care not to let any bubbles come out. Leave it alone for a full day without touching silicone, and silicone will spread by itself to the edge of the phosphor bronze strip and no bubble will come out.

(4) Coat another side similarly.



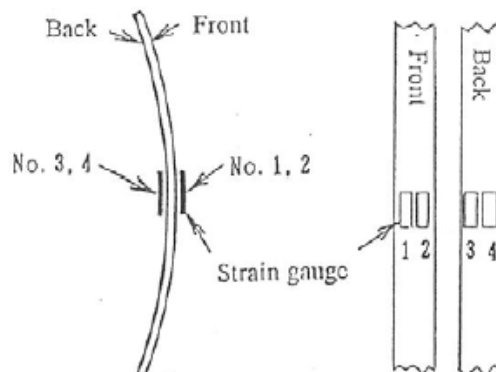
5. Composition of the bridge and connection with amplifier

-The illustration shows the arrangement of strain gauges; No.1 and No.2 are on tension side, while No.3 and No.4 are on compression side.

-The circuit is Wheatstone bridge; gauge A and C are for input of voltage, while B and D are for output. Both tensile and compressive strain are not out-put; only bending strain can be measured. The output is stable against temperature fluctuation and is amplified to 4 times.

-Relationships between each strain gauge and color of the lead wire are as below;

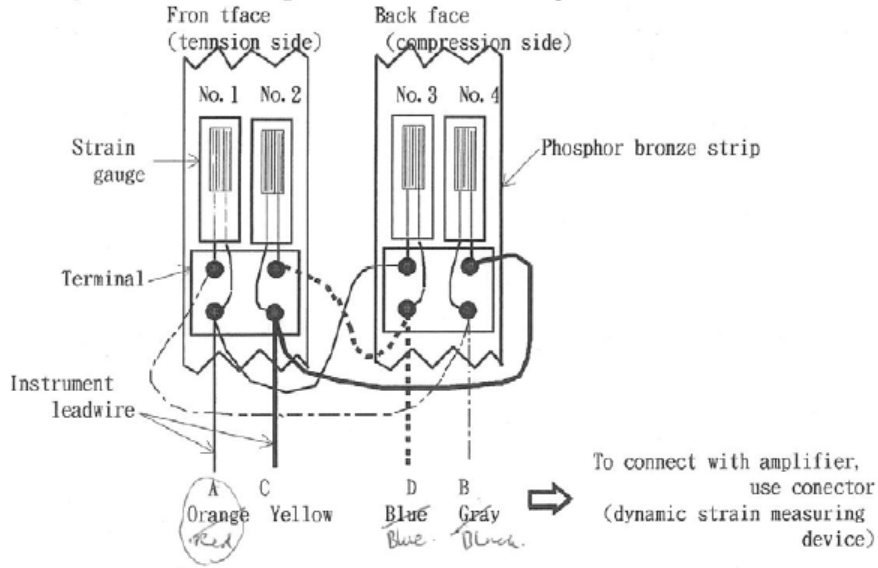
- Gauge A: Red (+)
- Gauge B: Black (-)
- Gauge C: White (-)
- Gauge D: Green (+)



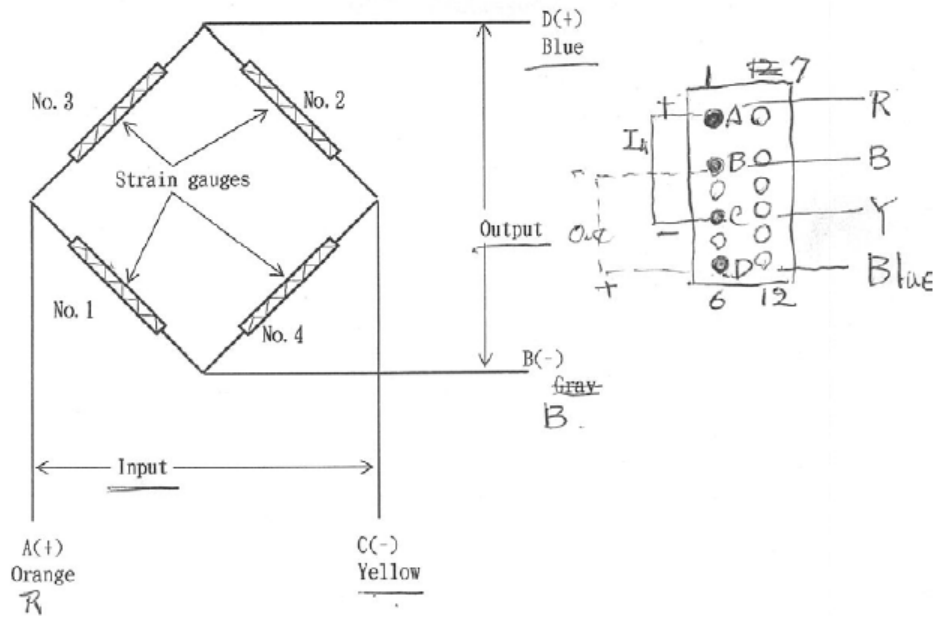
-To connect with the amplifier (dynamic strain measuring device), use 7-pin connector (a plug, PRC03-12A-10-7M-10, Tajimi Musen Co., Ltd. (See the illustration)).

L. D. T.

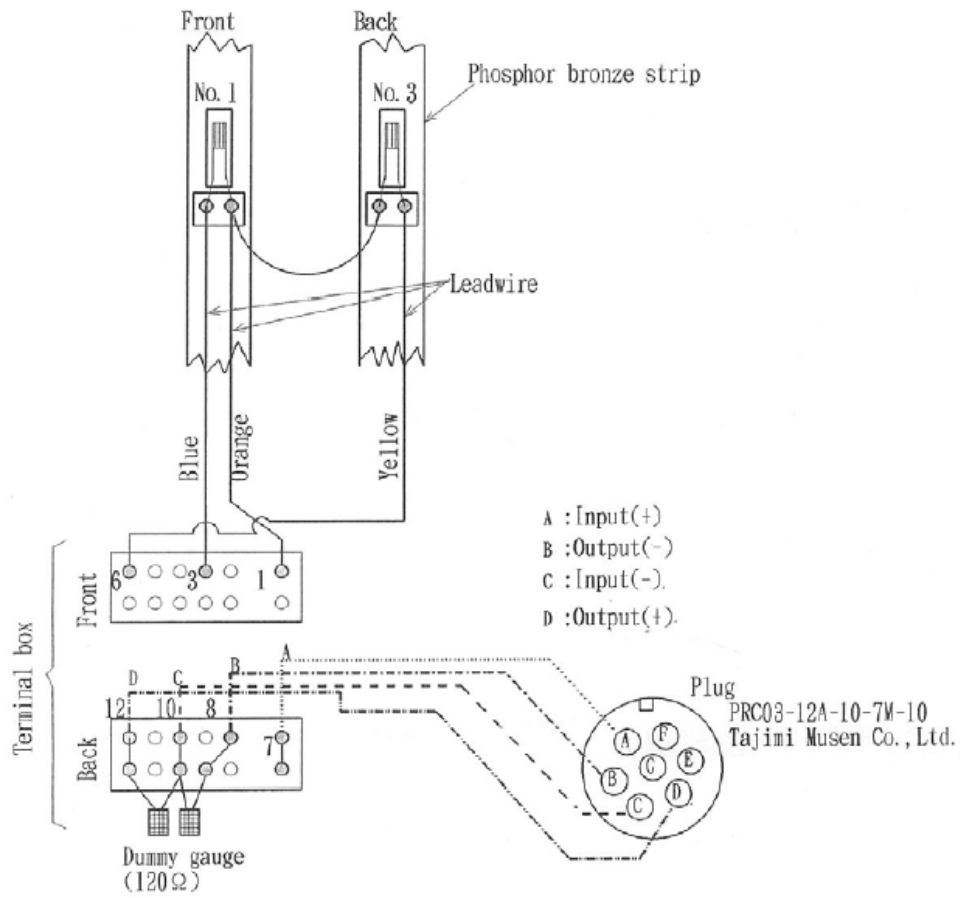
Composition of bridge connection with amplifier



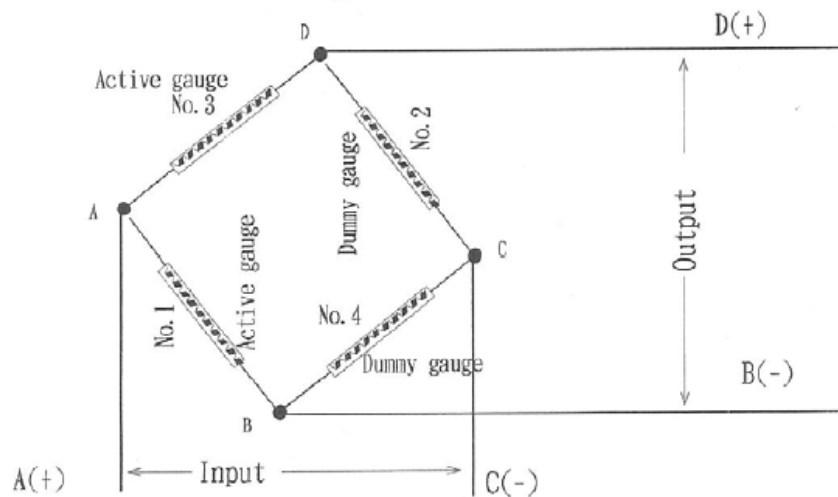
Composition of the bridge by strain gauges (Wheatstone bridge)



L. D. T.



Composition of the bridge by strain gauges
Wheatstone bridge



A.2. DETERMINATION OF LOAD CELL CAPACITY

The load cell used in this study is an electronic-resistant strain gauge type transducer shown in Figure A.1. Its main body is made from a block of phosphore-bronze. Following the basic design by Tani et al. (1983), four suitably placed electronic-resistant strain gauges (two on compression zone and two on extension zone), forming a Wheatstone bridge, are the essential elements of this type of load cell. The maximum capacity of the load cell was determined by using the following expression;

$$W = \frac{e_{po} * E * B * t * t * 2}{6L} \quad (A.1)$$

where,

W = capacity of load cell (kg_f)

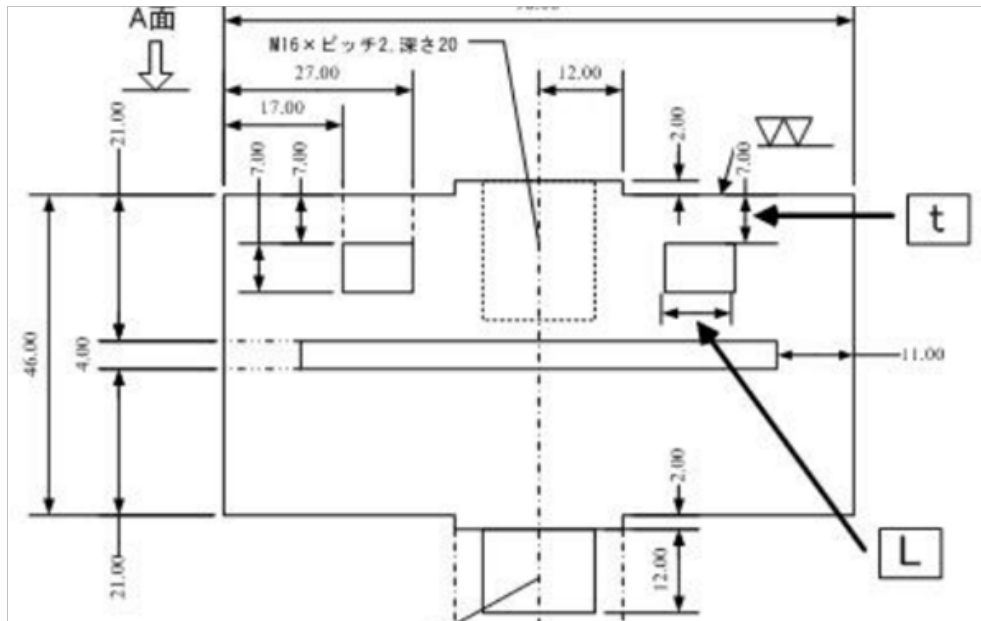
E = Young's Modulus of material (phosphor bronze = 1,220,000 (kg_f/cm²))

B = width (cm)

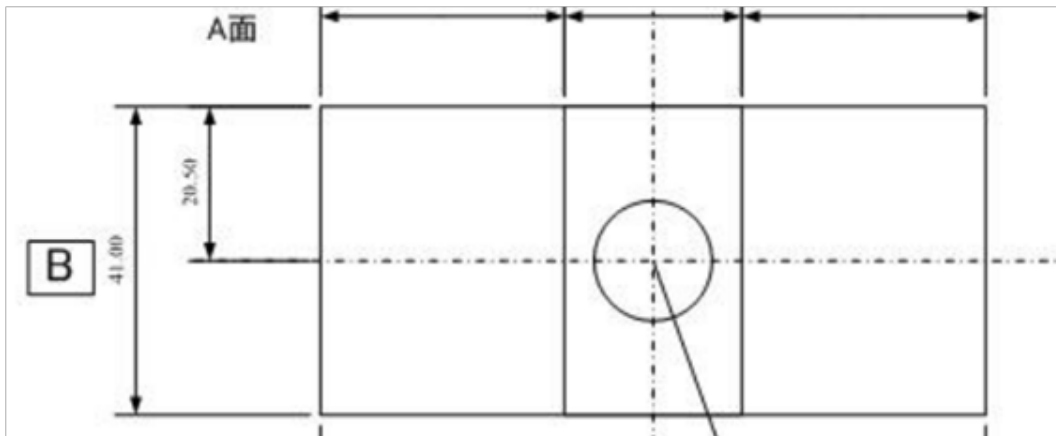
L = width of rectangular space hole (cm)

t = thickness of load cell (cm)

$e_{po} = 0.008$: acceptable strain in elastic range



(a) Side view



(a) Top view

Figure A.1: Schematic views of load cell used in this study.

Table A.1: Capacity of load cell, as determined from Eq. A.1.

E	B	L	T	e_{p0}	W
(kg/cm^2)	(cm)	(cm)	(cm)	$(strain)$	(Ton_f)
1220000	4	0.8	0.23	0.008	0.860507

A.3. REFERENCES

Tani, Y., Hatamura, Y., & Nagao, T. (1983). Development of Small Three Component Dynamometer for Cutting Force Measurement. *Bulletin of the Japanese Society of Mechanical Engineering*, 26(214), 650-658.

TRIGGER AND RECEIVER DEVICES FOR ELASTIC WAVE MEASUREMENT IN LAB

Appendix B

APPENDIX B

TRIGGER AND RECEIVER DEVICES FOR ELASTIC WAVE MEASUREMENT IN LAB

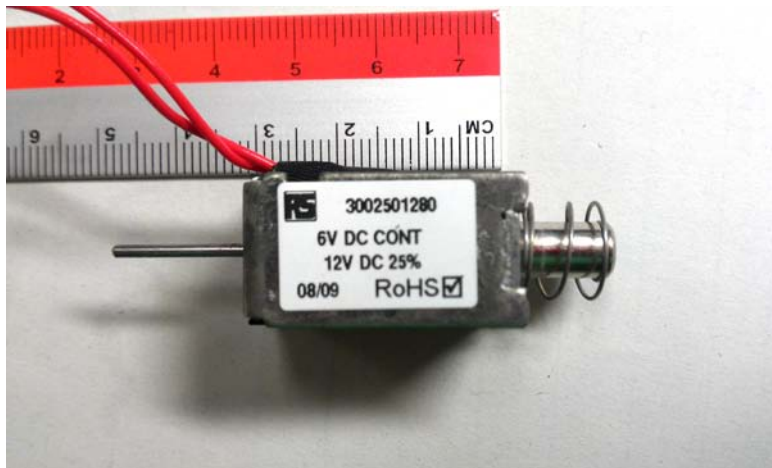
Before ultimately deciding disk transducers (presented in Chapter 5) as the best suited elastic wave measurement devices for this study, several ideas were attempted for the simultaneous measurement of *P*-wave and *S*-wave velocities in triaxial experiments. Although these ideas may not have been good enough for the purpose of this study yet they may be useful in other scenarios. A brief summary of attempted trials along with their benefits and shortcomings is summarized in the following sections.

B.1. TRIGGER DEVICES

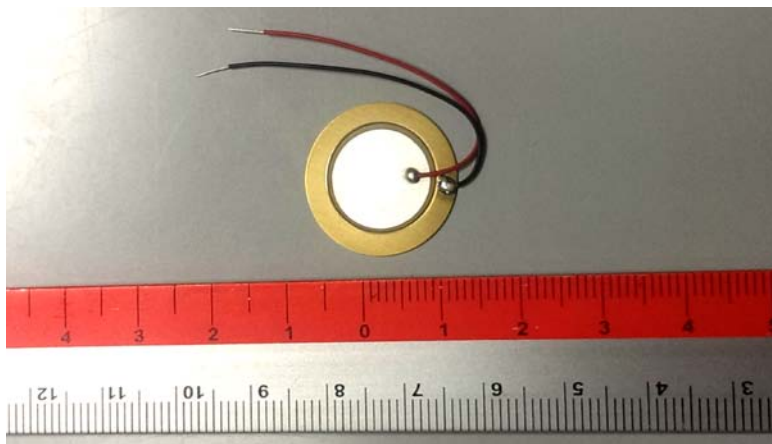
Two types of trigger devices were used for the generation of elastic wave velocities in this study.

- i. Electromagnet type trigger device
- ii. Piezoelectric Speaker type trigger device

Photographs of these trigger devices are shown in Figure B.1.



(a) Electromagnet type trigger device



(b) Piezoelectric speaker type trigger device

Figure B.1: Different excitation devices used for generating elastic waves in triaxial specimen.

B.1.1 Electromagnetic Type Trigger Device

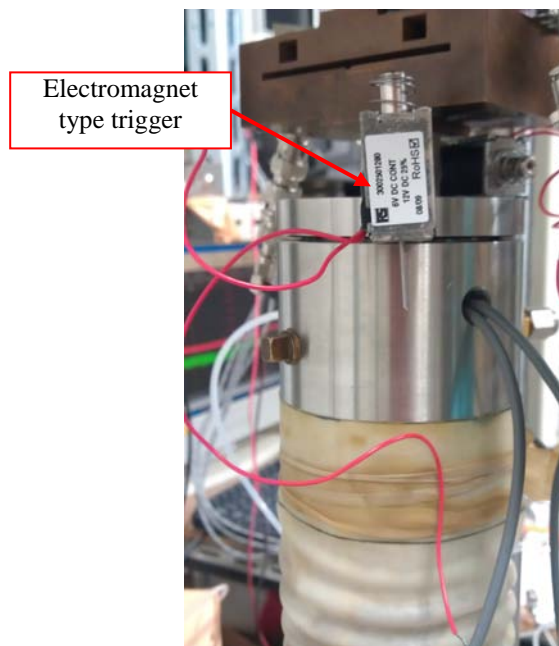
It comprised of a cylindrical rod placed inside a solenoid. On the application of current, magnetic field generated in the solenoid pushed the rod forward to generate a trigger. The rod was pushed back to its initial position by a spring coil.

Type of wave generated by the trigger was governed by the installation orientation on the specimen. Movement of the trigger rod was aligned parallel to the specimen's longitudinal axis for the generation of *P*-waves, and it was oriented transverse to the

longitudinal axis of specimen for generation of *S*-waves. Figure B.2 describes the orientation of sensors for the generation of *P*-waves and *S*-waves. The triggers were glued to the top cap, and the wave velocity was determined by knowing the time difference of wave travel from receiver in the top cap to the receiver in base pedestal.



(a) *S*-type trigger



(b) *P*-type trigger

Figure B.2: Orientation of electromagnetic type trigger for generating *P*-waves and *S*-waves in triaxial specimen.

Typical results obtained due to excitation of electromagnet type trigger device are shown in Figure B.3.

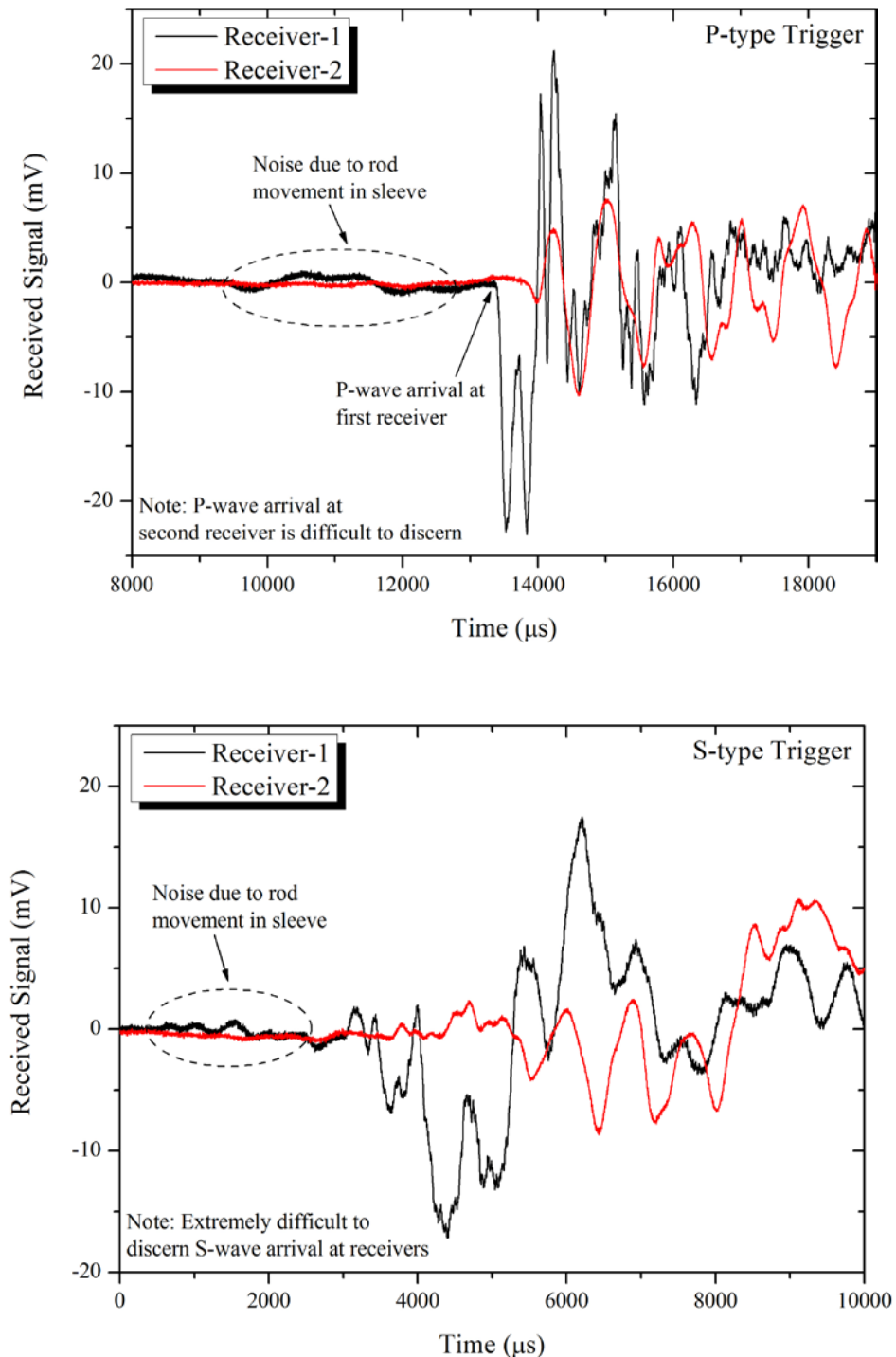


Figure B.3: Typical test results obtained by electromagnet type exciter. Receiver-1 is the piezoelectric wave receiver located in top cap whereas receiver-2 is a similar receiver located in base pedestal.

Main problems experienced in using such trigger devices are summarized as below;

1. Since the triggers were installed on the top cap, the generated wave travelled through the metal frame of triaxial apparatus instead of the soil specimen. This was confirmed by triggering the sensor without any soil specimen installed i.e., top cap suspended in air away from the base pedestal.
2. Sliding of the trigger rod inside the sleeve generated friction which appeared as distortion on the recorded signals thus making it difficult to identify the first deflection (Figure B.3).
3. Rebound of the trigger rod as it was pulled back by spring coil generated additional noise.
4. Elimination of random noise by stacking was impossible because repeated triggering under identical conditions yielded very different received signal.
5. Impossible to control the excitation frequency, as in case typical bender element testing.

B.1.2 Piezoelectric Speaker Type Trigger Device

The main problem with the electromagnet type trigger device was the additional noise generated due to sleeve friction as the trigger rod slid inside the solenoid. To overcome this problem a trigger device without any mechanical movement was required. Speaker type trigger device which mainly comprised of a very small piezoelectric element, helped eliminating this problem. Piezoelectric speaker of 20 mm diameter was glued to the top cap as shown in Figure B.4. On the application of an electric pulse, it generated very small vibrations which could be used for elastic wave velocity determination.

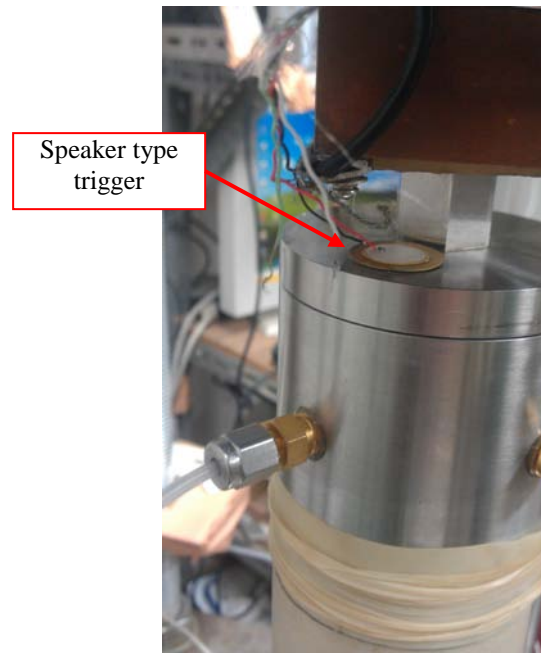


Figure B.4: Piezoelectric speaker type trigger device glued to triaxial top cap.

Typical problems experienced with piezoelectric speaker type trigger devices are as follows;

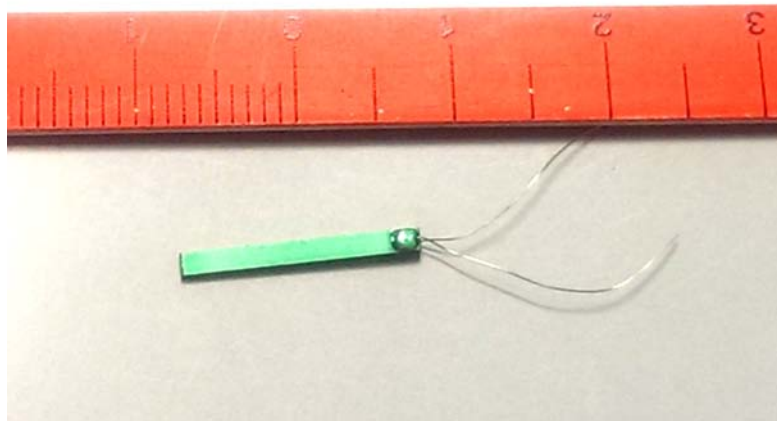
1. Amplitude of excitation is lower than electromagnetic type triggers. Due to low amplitude of excitation, signal to noise ratio (*SNR*) may not be sufficient to efficiently determine wave velocity (especially for aggressive environments like high saturation ratio, or very low confining pressure, etc).
2. Generated wave travelled through triaxial apparatus instead of soil specimen.

B.2. RECEIVING DEVICES

Since both the trigger devices described in the previous section were mounted on the top cap, waves generated by them travelled through the metal frame of triaxial apparatus instead of soil skeleton. Receiving sensors were therefore required to be installed directly on the surface of the specimen so as to avoid external noise distortions.

Beam type piezoelectric receivers were formed by using 15 mm long piezoelectric bender elements (Figure B.5(a)). Bender elements were glued to a tiny wooden piece (Figure B.5(b)). This wooden piece when glued to the specimen surface could receive any vibrations travelling through the specimen. Typical orientation of *P*-type and *S*-type piezo-beams is shown in Figure B.6. Actual photographs of piezo-beams installed on the specimen surface are shown in Figure B.7.

In order to reduce the effects of any external vibrations, extremely thin cables were used for connections. Connections between piezo-beam and extending cables were glued on the same wooden piece so as to make it sturdy (Figure B.5(b)).

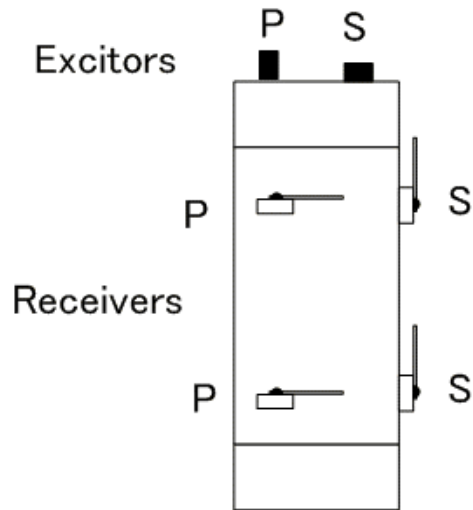


(a) Bender elements used to form piezo-beam receiver

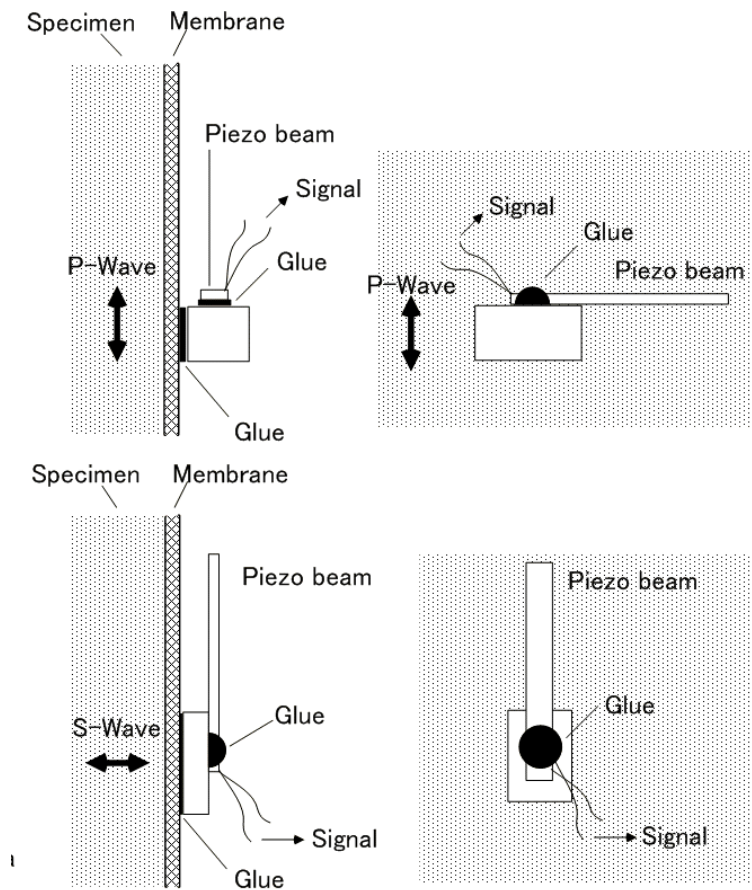


(b) Completed piezo-beam receiver assembly

Figure B.5: Development of piezo-beam receivers.



(a) Orientation of *P*-type and *S*-type piezo-beam receivers on triaxial



(b) Cross-sectional view

(c) Front view

Figure B.6: Schematic illustration explaining installation of piezo-beam receivers.

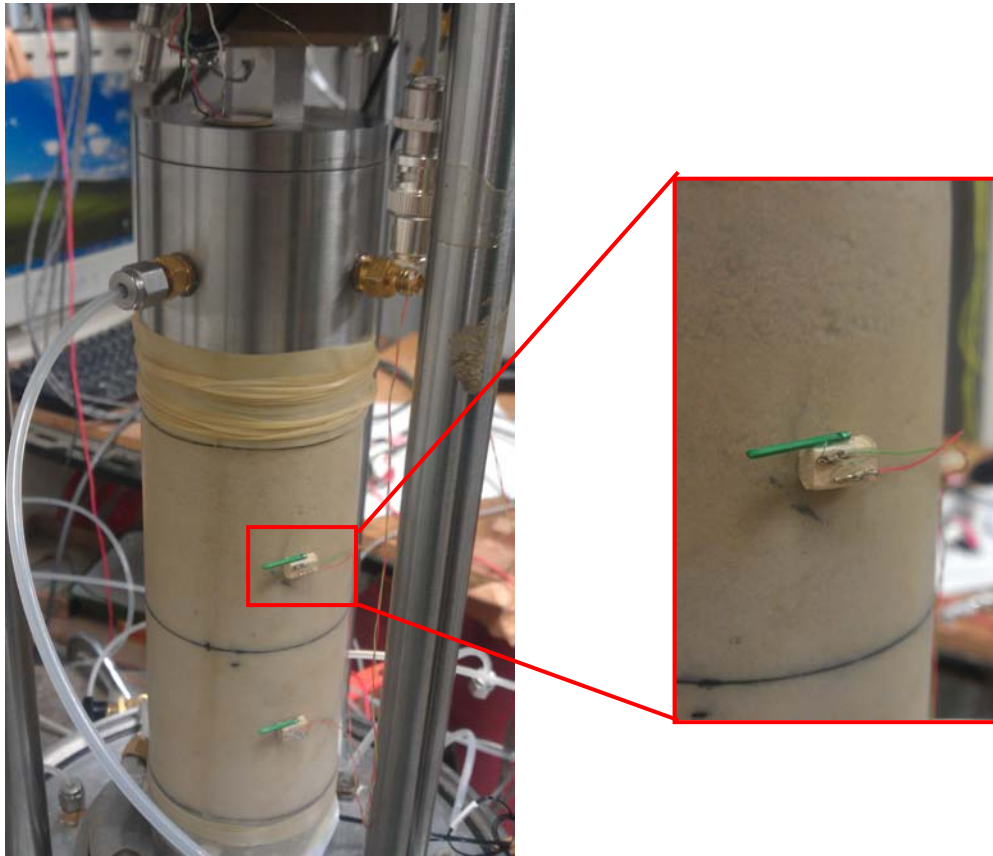


Figure B.7: Piezo-beam receivers installed on triaxial specimen.